

Studies in Surface Science and Catalysis

Advisory Editors: B. Delmon and J.T. Yates

Vol. 79

CATALYSIS

An Integrated Approach to Homogeneous, Heterogeneous and Industrial Catalysis

Editors

J.A. Moulijn

*Department of Chemical Engineering, Delft University of Technology,
Delft, The Netherlands*

P.W.N.M. van Leeuwen

*Department of Chemical Engineering, University of Amsterdam,
Amsterdam, The Netherlands*

R.A. van Santen

*Schuit Institute of Catalysis, Eindhoven University of Technology,
Eindhoven, The Netherlands*



ELSEVIER

Amsterdam — London — New York — Tokyo 1993

ELSEVIER SCIENCE PUBLISHERS B.V.
Sara Burgerhartstraat 25
P.O. Box 211, 1000 AE Amsterdam, The Netherlands

ISBN 0-444-89229-X

© 1993 Elsevier Science Publishers B.V. All rights reserved.

No part of this publication may be reproduced, stored in a retrieval system or transmitted in any form or by any means, electronic, mechanical, photocopying, recording or otherwise, without the prior written permission of the publisher, Elsevier Science Publishers B.V., Copyright & Permissions Department, P.O. Box 521, 1000 AM Amsterdam, The Netherlands.

Special regulations for readers in the U.S.A. – This publication has been registered with the Copyright Clearance Center Inc. (CCC), Salem, Massachusetts. Information can be obtained from the CCC about conditions under which photocopies of parts of this publication may be made in the U.S.A. All other copyright questions, including photocopying outside of the U.S.A., should be referred to the copyright owner, Elsevier Science Publishers B.V.

No responsibility is assumed by the publisher for any injury and/or damage to persons or property as a matter of products liability, negligence or otherwise, or from any use or operation of any methods, products, instructions or ideas contained in the material herein.

This book is printed on acid-free paper.

Printed in the Netherlands

Preface

Catalysis is a fascinating science for those who are actively involved in it, but perhaps even more so for those who know only a little about it. Chemical reactions, for which one would expect half-life times as long as centuries, can be accomplished in minutes to hours with the magic power of a mysterious black box containing a catalyst. Most of our liquid fuels and some 80% of our chemical products are manufactured with the aid of catalytic conversions. In the near future most of our automotive exhaust gases will be cleaned by a catalyst. The ever-increasing yield of fuel from a barrel of crude oil, the continuing increase of the quality of our polymeric materials, the steadily decreasing production cost of bulk and fine chemicals, etc., can be ascribed, to a great extent, to improvements in catalytic systems. Nevertheless, to the layman catalysis does not play a glamorous role, or at least it didn't until the catalytic converter in automobiles entered his life. Even to the modern chemist who is not familiar with it, catalysis has the aura of an empirical discipline, containing some of the ingredients of a black art. Indeed, entirely new catalysts and processes have been discovered mostly by accident, but the majority of the enormous improvements in catalyst performance which we have seen have been brought about by progress in the underlying sciences.

To a large extent catalysis is concerned with the transformations of organic molecules. Nevertheless, the subject is not the realm of organic chemists but rather that of catalysis specialists who are interested in the (often simple) conversions of basic organic molecules while using highly complex catalyst systems. Apart from a large body of acid-base catalysis and catalysis by 'organic' catalysts, heterogeneous and homogeneous (metal) catalysts have been developed in isolation from organic chemistry. There are several factors which have a bearing on this: (i) the synthesis of a catalytic material requires a knowledge of inorganic and organometallic chemistry, surface science, and spectroscopic techniques; (ii) the industrial importance of catalysis ensured that a great deal of the empirical development of the catalysts was not readily available to the scientific community, which concentrated its efforts on more fundamental aspects of the catalyst; (iii) industrial catalysis deals with simple organic molecules, the synthesis of which, quite justifiably, did not attract the interest of modern organic chemists; and (iv) the differing requirements imposed by the industrial manufacture and small-scale laboratory synthesis of chemicals made the gap even larger.

In this book we will concentrate on industrially relevant reactions which are catalyzed by heterogeneous and homogeneous catalysts. This is a somewhat arbitrary choice, but some choice is necessary. Unfortunately, this leaves large areas of industrial biocatalysis and catalysis science uncovered. In keeping with this industrial focus, the topic of catalytic reaction engineering has been included. In industrial applications reaction engineering forms an integral part of catalysis; the constraints of the catalyst material are determined by chemical and reactor engineering aspects, and the related problems have to be solved in close harmony.

Clearly, catalysis is a multidisciplinary activity and this is reflected in the present book. We have chosen a novel combination of basic disciplines which we hope will be of value to our readers. Homogeneous catalysis by metal complexes is treated jointly with heterogeneous catalysis using metallic and non-metallic solids. In both areas the high degree of sophistication of spectroscopic techniques and theoretical modelling has led to an enormous increase in our understanding at the molecular level. This holds for the kinetics of the reactions and the reactivities of the catalysts, as well as for the syntheses of the catalytic materials. In homogeneous catalysis, the time span between the discovery of a new catalytic process and the delineation of the reaction mechanism on a molecular level has usually been relatively short. Hence, while homogeneous catalysis with organometallics is a young branch of catalysis science, its rapid development can be ascribed to a successful molecular approach in the early stages of its development. Heterogeneous catalysis has to a great extent been developed within the context of catalytic reaction engineering. The more recent advances in surface science have contributed to an understanding of the catalytic materials and processes on a molecular level. It therefore seems timely to deal with the organometallic chemistry of heterogeneous and homogeneous catalysis in a concerted manner. The analogies between the bonding of discrete complexes on surfaces and in solution has been noted many times. Many studies have been published on the analogies and differences between bonding in cluster compounds and metal surfaces. There are, however, also fundamental differences between elementary events on metal surfaces and elementary steps on isolated metal complexes. The study of the basic principles is refreshing and inspiring to both worlds.

Outline

The *introductory section* (Chapter 1) presents a brief survey of the history of industrial heterogeneous and homogeneous catalysis. The survey shows that the availability of the feedstocks has had a decisive influence on the catalysts that have been developed. In some instances the chemical ‘leads’ for new catalysts have lain dormant in the literature for a number years before they were developed into industrial processes. Subsequently (Chapter 2) a very limited selection of current industrial catalytic processes is described. These include the

industrial context of the features to be discussed later in the sections on fundamental and applied catalysis. A broad spectrum of important catalytic applications is presented. Each summary contains the basic chemistry, some engineering aspects, feedstock sources and product utilisation. In Chapter 3 the kinetic principles are treated, since in a way they form the basis for catalysis.

The section on *fundamental catalysis* starts off (Chapter 4) with a description of the bonding in complexes and to surfaces. The elementary steps on complexes and surfaces are described as they are relevant to catalysis. The chapter on heterogeneous catalysis (Chapter 5) deals with the mechanistic aspects of three groups of important reactions: syn-gas conversions, hydrogenation, and oxidation. These three reactions give us an opportunity to present the main principles of metal and metal oxide catalysis. Likewise, in the chapter on homogeneous catalysis (Chapter 6) we concentrate on only three reactions, representing examples from three areas: carbonylation, polymerization, and asymmetric catalysis. Identification by *in-situ* techniques has been included, since it was felt to be more appropriate to outline this here than to devote separate chapters to the preparation and characterization of organometallic catalysts (*vide infra* for heterogeneous catalysts).

Many constraints on the industrial use of a catalyst have a macroscopic origin. In *applied catalysis* (Chapter 7) we show how catalytic reaction engineering deals with such macroscopic considerations. The transport and kinetic phenomena in both model reactors and industrial reactors are outlined.

The section on *catalyst preparation* (Chapters 8 and 9) is concerned with the preparation of catalyst supports, zeolites, and supported catalysts, with an emphasis on general principles and mechanistic aspects. For the supported catalysts the relation between the preparative method and the surface chemistry of the support is highlighted. The molecular approach is maintained throughout.

The first chapter (Chapter 10) in the section on *catalyst characterization* summarizes the most common spectroscopic techniques used for the characterization of heterogeneous catalysts, such as XPS, Auger, EXAFS, etc. Temperature programmed techniques, which have found widespread application in heterogeneous catalysis both in catalyst characterization and the simulation of pretreatment procedures, are discussed in Chapter 11. A discussion of texture measurements, theory and application, concludes the section on the characterization of solid catalysts (Chapter 12).

The final chapter (Chapter 13) gives an outline of *current trends* in catalysis. Two points of view are adopted: the first one focuses on developments in process engineering. Most often these have their origin in demands by society for better processes. The second point of view draws attention to the autonomous developments in catalysis, which is becoming one of the frontier sciences of physics and chemistry.

Final remarks

The main theme of the book is the molecular approach to industrial catalysis. The integrated way in which the subject matter has been treated involves many disciplines; as a consequence, the writing of the book has been entrusted to a number of authors. The editors envisaged a careful planning and harmonization of the contents of the chapters. The latter is important, because a rigorous selection of subject matter is necessary in order to keep the size of the book within the limits of a practicable textbook.

The editors have enjoyed working together on this project. We have learned a great deal about our mutual fields while discussing which essential elements should be included and what reactions should serve as instructive examples. The order of the editors' names is alphabetical and does not in any way reflect the outcome of these discussions, nor the magnitude of our efforts! We are very grateful to our authors, who have contributed a number of very good chapters. Some of them were well in time with their responses, while others enjoyed the privilege of having written the most up to date contributions!

When we started putting together the national course on catalysis, on which this book is based, we were a loosely organised foundation for the promotion of catalysis. In the meantime we have organised ourselves into the Netherlands Institute for Catalysis Research, NIOK. We express our wish that this book may contribute in shaping the new Dutch School of Catalysis by providing a broad, general training for our Ph.D. students in the essential elements of catalysis.

*Jacob A. Moulijn
Piet W.N.M. van Leeuwen
Rutger A. van Santen*

List of contributors

E.B.M. Doesburg

Netherlands Energy Research Foundation ECN, Westerduinweg 3,
Petten, The Netherlands

J.W. Geus

Center for Heterogeneous Catalysis, Utrecht University, Transitorium 4,
3508 TB Utrecht, The Netherlands

F. Kapteijn

Department of Chemical Engineering, Delft University of Technology,
Julianalaan 136, 2600 GA Delft, The Netherlands

G.B. Marin

Schuit Institute of Catalysis, Eindhoven University of Technology,
5600 MB Eindhoven

J.A. Moulijn

Department of Chemical Engineering, Delft University of Technology,
Julianalaan 136, 2600 GA Delft, The Netherlands

J.W. Niemantsverdriet

Schuit Institute of Catalysis, Eindhoven University of Technology,
5600 MB Eindhoven

B.E. Nieuwenhuys

Gorlaeus Laboratories, Leiden University, 2300 RA Leiden,
The Netherlands

V. Ponec

Gorlaeus Laboratories, Leiden University, 2300 RA Leiden,
The Netherlands

J.J.F. Scholten

Department of Chemical Engineering, Delft University of Technology,
Julianalaan 136, 2600 GA Delft, The Netherlands

R.A. Sheldon

Laboratory of Organic Chemistry, Applied Chemistry Department,
Delft University of Technology, Julianalaan 136, 2628 BL Delft,
The Netherlands

A. Tarfaoui

Department of Chemical Engineering, Delft University of Technology,
Julianalaan 136, 2600 GA Delft, The Netherlands

H. van Bekkum

Laboratory of Organic Chemistry, Applied Chemistry Department,
Delft University of Technology, Julianalaan 136, 2628 BL Delft,
The Netherlands

J.H.C. van Hooff

Schuit Institute of Catalysis, Eindhoven University of Technology,
5600 MB Eindhoven

G. van Koten

Department of Metal-Mediated Synthesis, Faculty of Chemistry,
Utrecht University, Padualaan 8, 3584 CH Utrecht, The Netherlands

P.W.N.M. van Leeuwen

Department of Chemical Engineering, University of Amsterdam,
Nieuwe Achtergracht 166, 1018 WV Amsterdam, The Netherlands

R.A. van Santen

Schuit Institute of Catalysis, Eindhoven University of Technology,
5600 MB Eindhoven

J.A.R. van Veen

Shell Research B.V., Badhuisweg 3, 1031 CM Amsterdam

Chapter 1

History of catalysis

1.1 INTRODUCTION

The name 'catalysis' was coined by Berzelius in 1836. He concluded that besides 'Affinity' a new force is operative, the 'Catalytic Force'. Reaction occurred by catalytic contact. The word 'catalysis' stems from the Greek: it has the sense of 'down' and 'loosen'. At that time affinity was known as a chemically driving force, but no understanding existed, on a molecular level, of reaction rates. Catalysis — as a tool for carrying out reactions — had already been exploited much earlier. It has been applied for thousands of years in processes such as fermentation. An interesting example is the production of sulphuric acid. In the Middle Ages this was synthesized in small quantities in glass equipment by burning sulphur with nitric acid in humid air. In 1746 lead was used as a construction material for the reaction chambers and larger production volumes became possible. In 1793 Clement and Desormes showed that the quantity of nitre could be much reduced by admitting additional air to the reactor. They were aware of the fact that the nitrous vapours are only intermediates and that the oxidising agent is air. Their conclusion was correct, and nitre is what we would nowadays call a catalyst.

At the end of the eighteenth and the beginning of the nineteenth century the influence of metals and oxides on the decomposition of several substances was studied by many scientists. It was noticed that contact with different substances gives very different products. An example is the decomposition of alcohol: in the presence of copper or iron, carbon and an inflammable gas is produced. In the presence of pumice stone decomposition into ethene and water was observed. In other words, selectivity was demonstrated. Many other important milestones can be mentioned: we limit ourselves to a few. Thenard investigated the dissociation of ammonia in contact with metals. In 1813 he found that the dissociation occurs over various metals, provided they are hot. Later he systematically studied the dissociation of hydrogen peroxide. He concluded that some of the solids studied

changed and others did not. Humphry Davy performed systematic investigations with the objective of developing a miner's safety lamp. He discovered that the oxidation of coal gas is catalyzed by platinum. He found that palladium was also active whereas copper, silver and gold did not show any catalytic activity. Davy found that the platinum wires he used had to be hot and, as a consequence, he concluded that the action of platinum was to heat the reacting mixture. The fact that only platinum and palladium were active was explained on the basis of their low heat capacity and low thermal conductivity. Later it was found that finely dispersed platinum is active even at room temperature and Davy's explanation was thus not correct. Platinum catalyzes the combustion of the components of coal gas, in particular CO and CH₄, which in the absence of a catalyst can lead to an explosion. Copper and silver are also active in the oxidation of CO, but they are not sufficiently active in CH₄ oxidation. Of course, depending on the construction, a wire can function as a flame arrester in which radical terminations take place and, as a consequence, explosions are avoided.

In 1834 Faraday proposed that the reactants have to adsorb simultaneously at the surface, but he did not really explain the catalytic action. Of course, neither did Berzelius give an explanation, but he nicely generalized many results in a simple description. Later, Ostwald gave the definition that a catalyst does not influence the thermodynamic equilibrium of reactants and products but affects the rates of the chemical reactions. The conclusions of Berzelius and Faraday proved to be correct.

1.2 INDUSTRIAL CATALYSIS

Industrial catalysis is an old practice. Catalysts have always been used in the production of wine and beer. Among the first industrial catalytic processes are a few inorganic oxidation processes, viz. the Deacon process (oxidation of HCl into Cl₂) and the production of sulphuric acid. These processes were developed before a scientific basis of chemical reactivity was established. Only after the formulation of the theory of chemical equilibria by van 't Hoff did a framework for catalyst development become available. This had a major impact on the development of a process for the synthesis of ammonia at the beginning of the twentieth century, allowing a systematic, scientifically based search for a good catalyst to be performed. It also initiated the development of chemical process engineering as we know it today.

1.2.1 Sulphuric Acid

The production of sulphuric acid was commercialized in the mid-18th century. In the so-called lead chamber process the oxidation of SO₂ into SO₃ was catalyzed by NO. The acid produced is not very concentrated. The raw material used was elemental sulphur from Sicily. Later pyrite was used because of its lower price.

One of the consequences was a much higher impurity level in the feed to the reactor. As early as 1831 a process was patented in which SO_2 was oxidized in the presence of finely divided platinum. The commercial application, however, was strongly delayed due to technical difficulties, the major one being catalyst poisoning.

In the First World War the explosives industry demanded highly concentrated sulphuric acid, which required a different technology. A logical way to go was to use the heterogeneous metal catalysts which had just been developed at that time. Initially, platinum supported on silica or asbestos was used as a catalyst. Subsequently, platinum was substituted by V_2O_5 -based catalysts because of the high price of the metal and the fact that it is easily poisoned by the pollutants present in the raw material, such as arsenic. The raw material has also changed. Nowadays it is once again mainly elemental sulphur, which, to a considerable degree, is a product from the hydrotreatment of oil.

1.2.2 Ammonia Synthesis

Initially, the source of ammonia was coke oven gas and Chile saltpetre. In Germany, in particular, it was recognized as early as the turn of the 20th century that insufficient ammonia was available for agricultural needs. Moreover, the use of ammonia for the manufacture of explosives increased dramatically due to the beginning of the First World War. Extensive efforts were made by teams in many countries, but particularly in Germany, to synthesise NH_3 directly from N_2 . Non-catalyzed routes were discovered and were commercialised; but they were very inefficient. The breakthrough was the development of a catalytic process.

In 1905 Haber reported a successful experiment in which he succeeded in producing NH_3 catalytically. However, under the conditions he used (1293 K) he only found minor amounts of NH_3 . He extrapolated his value to lower temperatures (at 1 bar) and concluded that a temperature of 520 K was the maximum temperature for a commercial process. This was the first application of chemical thermodynamics to catalysis, and precise thermodynamic data were not then known. At that time Haber regarded the development of a commercial process for ammonia synthesis as hopeless and he stopped his work. Meanwhile, Nernst had also investigated the ammonia synthesis reaction and concluded that the thermodynamic data Haber used were not correct. He arrived at different values and this led Haber to continue his work at higher pressures. Haber tried many catalysts and found that a particular sample of osmium was the most active one. This osmium was a very fine amorphous powder. He approached BASF and they decided to start a large program in which Bosch also became involved.

The process development studies were carried out in a systematic way. A good catalyst had to be formulated; the reactor was to be scaled up; and an integrated process had to be designed, including the production of sufficiently pure synthesis gas. Haber envisaged the process scheme given in Fig. 1.1.

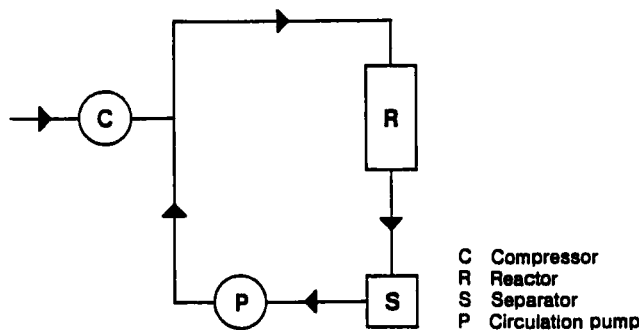


Fig. 1.1. Process scheme for the production of ammonia according to Haber.

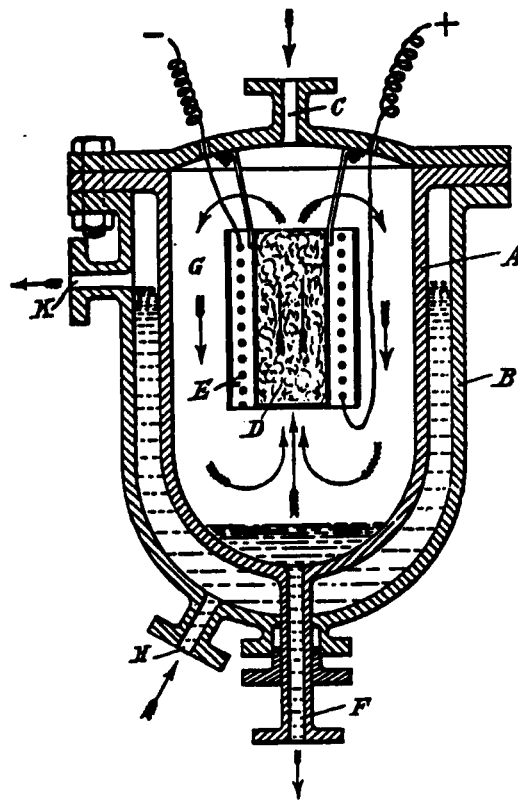


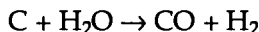
Fig. 1.2. Reactor for the synthesis of ammonia (BASF 1910).

Systematic studies were carried out in order to discover a suitable catalyst. Iron catalysts were especially tried, because it was known that iron catalyzes the decomposition of ammonia, which is the reverse of the reaction being studied. It

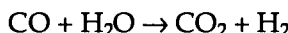
was discovered that iron alone was only slightly active but its activity could be improved (promoted) or worsened (poisoned) by additives. In their studies over 10 000 catalysts were prepared and over 4000 were tested.

When the laboratory studies gave promising results, scale-up studies commenced. The major problem was the construction of a reactor which was able to withstand the reaction conditions. Due to the high pressure, high-strength carbon steel was used; however, this steel is corroded by H₂ under the severe reaction conditions used, and consequently loses its strength. Bosch designed a reactor which contained an outer wall of high carbon steel, lined internally with soft, low carbon steel (Fig. 1.2). The catalyst was also heated internally, so that the external wall was continuously kept at a low temperature.

Very pure, electrically generated H₂ was available for the pilot studies, but for a commercial plant, this was of course not practical. The solution was found in coal gasification:



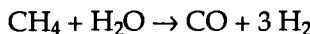
followed by the water–gas shift reaction:



Haber received the Nobel prize in 1919 for his work on ammonia synthesis. Bosch was awarded the 1931 Nobel prize for his achievements in high-pressure technology.

Up to the 1950s the technology for ammonia synthesis did not change very much. Fundamental changes became possible in the '60s. These changes are of both a chemical and a technological nature.

Technically, the most attractive hydrocarbons for the production of H₂ are methane and, to a lesser extent, oil ('CH₂):



These reactions are carried out catalytically using nickel catalysts. However, a side reaction is carbon deposition. Since the rate of this side reaction increases with pressure, the production of synthesis gas at high pressure was not feasible. The addition of promoters, which catalyze the carbon steam reaction, suppresses carbon deposition, thus allowing higher pressures. This made a revolution possible in the ammonia synthesis industry. At the same time progress in the development of centrifugal compressors enabled large, single-train plants to be constructed. These developments have led to much more efficient ammonia plants. Figure 1.3 illustrates the process development since the beginning of commercial ammonia production by nitrogen fixation.

Still further process improvements may be possible, but potential improvements should be analyzed by considering the whole process integrally.

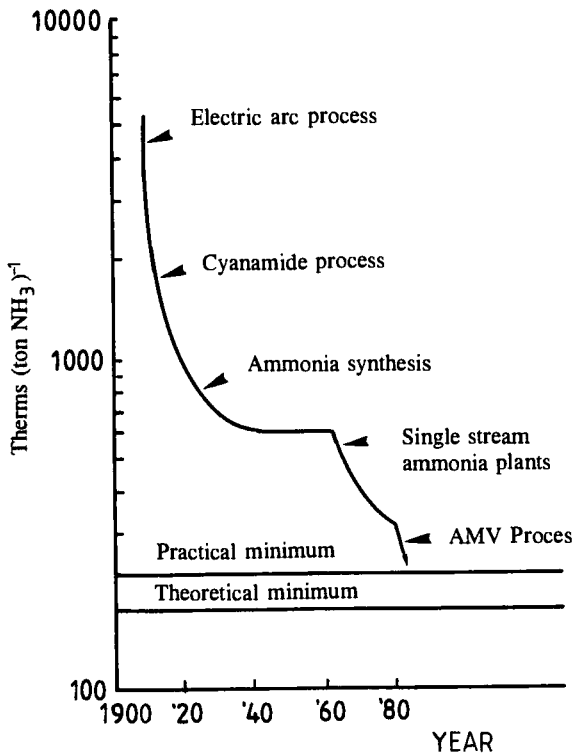


Fig. 1.3. Efficiency of nitrogen fixation.

1.2.3 Coal, Oil, Natural Gas

Industrial catalysis has always been closely connected with changes in society. If we confine ourselves to the last 100 years, it is appropriate to highlight the fuel market. In this period a transition is observed from coal to oil and, more recently, to natural gas.

1.2.3.1 Coal

Essentially, in all coal utilization processes the first step is a heating step and a variety of pyrolysis products are formed, depending on the technology. This is illustrated in Fig. 1.4 [7].

A major application of coal was the production of coke. This process is a mild pyrolysis process and, besides coke, large quantities of coke oven gas are also produced containing many of the base materials for the chemical industry, e.g., ammonia, acetylenes and aromatics.

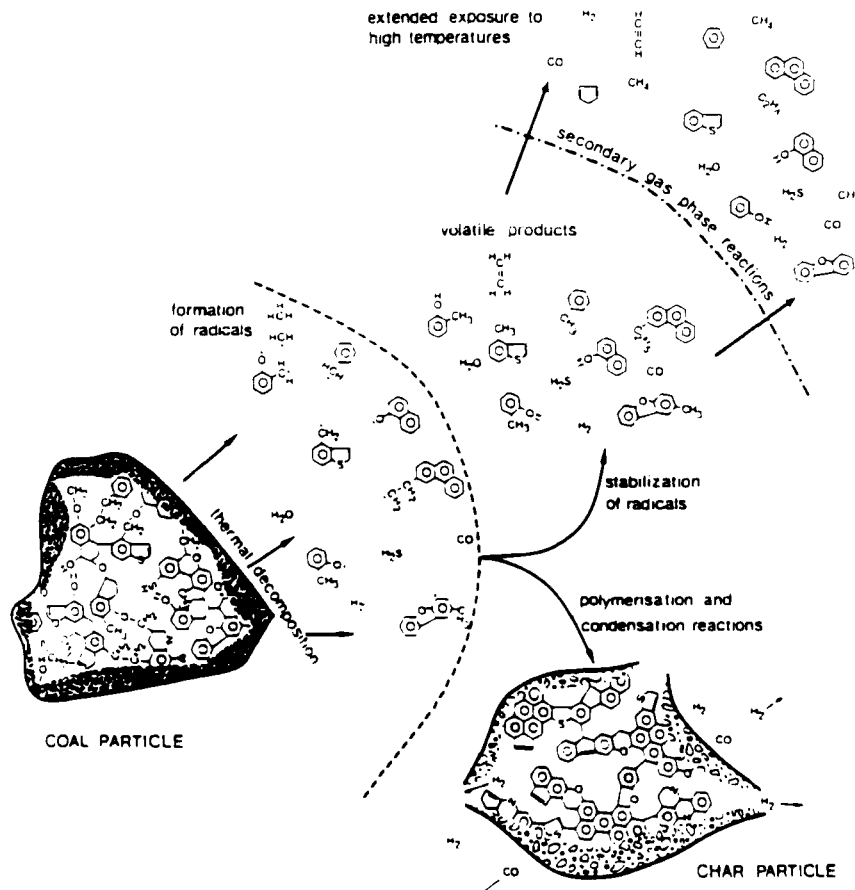


Fig. 1.4. Reactions occurring during the pyrolysis of coal.

In Germany, before and during the Second World War, a large amount of ethylene was produced from acetylene derived from coke oven gas. Coke ovens also provided essentially all the aromatics in Germany. Coal was also gasified, giving synthesis gas, a mixture of CO and H₂. Products such as ammonia and methanol were catalytically produced from this synthesis gas. Fischer-Tropsch technology was also developed to convert synthesis gas to motor fuels.

Coal was also directly hydrogenated into liquids which could be used as feedstocks in the chemical industry. The first catalytic hydrogenation of coal was reported by Berthelot in 1869, using HI as a catalyst. The success in developing catalytic high pressure processes for ammonia and methanol also stimulated process development in catalytic coal hydrogenation. Catalyst deactivation appeared to be a major problem. The solution was found in carrying out the process in two steps: first a liquid phase hydrogenation was carried out in a slurry of coal particles, oil produced from coal and highly dispersed catalyst. Many catalysts

were tried, e.g. iron oxide and sulphide. In the second stage the oils from the first stage were hydrogenated in a fixed bed reactor. As early as 1924 it was known that sulphides of Mo, W, Co and Fe were suitable hydrogenation catalysts which were not poisoned by the heteroatoms (S, N, O) in the feedstock. Later, in the development of hydrotreating processes for the oil refinery industry, the same catalysts were applied, but now in the treatment of oils.

The extensive activity in Germany in the '40s is well illustrated by Table 1.1.

TABLE 1.1
German hydrogenation plants 1943/44

Start-up date	Location	Raw material	Pressure bar		Product capacity 1943/44 (t per year)
			Liquid phase	Vapour phase	
1927	Leuna	Brown coal	200	200	650 000
		Brown coal tar			
1936	Boehlen	Brown coal tar	300	300	250 000
1936	Magdeburg	Brown coal tar	300	300	220 000
1936	Scholven	Bituminous coal	300	300	230 000
1937	Welheim	Coal tar pitch	700	700	130 000
1939	Gelsenberg	Bituminous coal	700	300	400 000
1939	Zeitz	Brown coal tar	300	300	280 000
1940	Luetzkendorf	Tar oils	500	500	50 000
1940	Poelitz	Bituminous coal oils	700	300	700 000
1941	Wesseling	Brown coal	700	300	250,000
1942	Bruex	Brown coal tar	300	300	600 000
1943	Blechhammer	Bituminous coal and tar	700	300	420 000
<hr/>			<hr/>		
12 Plants			<hr/>		
			<hr/>		
			about 4 million		

1.2.3.2 Oil and Natural Gas

In the U.S. oil and natural gas were playing a significant role, together with coal, as early as the 1920s. It was obvious that, compared with coal, oil was a superior chemical feedstock since the hydrocarbons are present in a gaseous or liquid form. The problem was that crude oil is very unreactive; this applies particularly to the paraffins which are main constituents of crude oil. The situation changed when thermal and, later, catalytic cracking processes were developed.

Distillation of crude oil does not result in large amounts of gasoline of a satisfactory octane number. Cracking of larger molecules, isomerization and

aromatization have to be carried out in order to produce sufficient amounts of high quality gasoline.

As early as 1915 AlCl_3 was used in a batch process. It is not surprising that there was a severe problem in the disposal of the sludges consisting of spent catalyst dissolved in hydrocarbons. At the same time activated clays were found to exhibit catalytic activity. A major breakthrough was the work of Houdry — a mechanical engineer and an automobile racing driver. He concluded that the limitations on the engine performance were not of a mechanical nature; the constraints were due to the performance of the gasoline. He developed a fixed bed process in which activated clay was the catalyst. Activated clays had been used before to produce kerosene for lamp oil. The cracking unit consisted of parallel reactors which were operated cyclically. A scheme of an early design is given in Fig. 1.5.

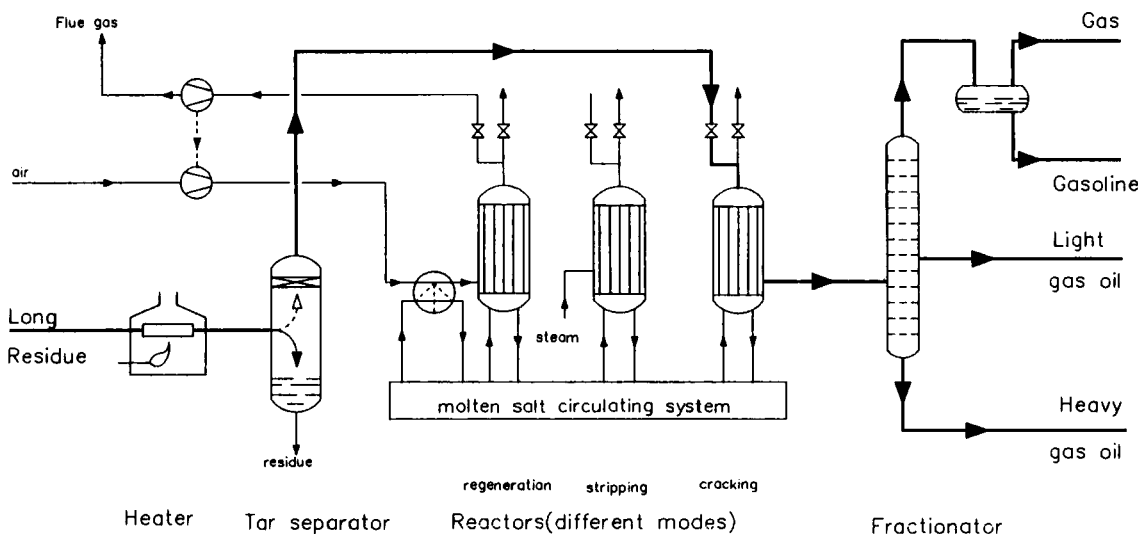


Fig. 1.5. Houdry catalytic cracking process.

Three catalytic converters are present in order to enable the process to operate continuously. Under typical conditions a reactor was on stream for 10 min. Subsequently, it was purged for 10 min and regenerated for 10 min. In regeneration the coke deposited on the catalyst was removed by burning, so continuous operation was possible. Heat was supplied by a molten salt system. In a next generation an adiabatic process was implemented, thus eliminating the molten salt heat transfer system. The heat produced during the regeneration was stored in the bed and provided the heat needed for heating the feedstock to the reaction temperature and providing the heat of reaction. Most of the aviation gasoline used in the Battle of Britain was produced in Houdry units. The next generation

of catalytic crackers was developed immediately after the commercialization of the Houdry units. These were based on the principle that the catalyst particles move between a cracking zone and a regeneration zone. Conveyor type reactors have been used and commercialized. A particularly successful approach, developed mainly by the Standard Oil Company of New Jersey, has been the Fluid Catalytic Cracking (FCC) technology. This technology was introduced at the beginning of the '40s. The reactor and the regenerator were fluidized beds and silica-alumina catalysts were used. The FCC process has been continuously improved both with respect to the catalyst and to the design of the reactor and the process. The acid treated clays were gradually replaced by synthetic silica-alumina catalysts. In the early '60s these were replaced by zeolite-based catalysts. The fluid cracking reactor was replaced by a riser reactor after the mechanical strength and the activity of the catalyst particles had been sufficiently improved.

Catalytic cracking was not the only technology being developed for gasoline needs. iso-Octane was produced as early as 1930 by oligomerization of lower olefins followed by hydrogenation. Ipatieff discovered paraffin alkylation in 1935, in which isobutane was alkylated with butenes or propene, the catalysts being sulphuric acid and hydrofluoric acid. This is an example of homogeneous catalysis. Alkylation was the basis of large volumes of aviation gasoline in World War II. While sufficient amounts of alkenes were available, there was a shortage of isobutane. Isomerization processes were commercially applied to convert n-butane into isobutane with a catalyst consisting of a mixture of AlCl_3 and HCl .

1.2.4 Catalytic Reforming

During the Second World War methylcyclohexane was transformed into toluene over molybdena/alumina catalysts. An attempt was made to use the same process for the 'catalytic reforming' of naphtha in order to increase the octane number by carrying out isomerization, cyclization and dehydrogenation of paraffins into aromatics. The stability of the catalyst was unsatisfactory because a large amount of coke was deposited. The breakthrough came with a catalyst developed at Universal Oil Products (about 1950). This catalyst was Pt supported on an acidic support. The process was called 'Platforming'. This catalyst could be used over a period of 6–12 months and could be regenerated by careful oxidation. It was observed that small amounts of sulphur did not poison the catalyst but even enhanced the reaction rate. Although a scientific success, further catalyst development was needed because the catalyst contained 3% Pt and this was considered far too expensive. Catalysts with satisfactory activity were developed with Pt concentrations between 0.2 and 0.7%. A major improvement was the application of bimetallic catalysts. The first commercially successful one, developed by Chevron, contained Re besides Pt, and was much more stable. The process based on this catalyst is called 'Rheniforming'. Catalytic reforming has

had a great impact: in 1950 about 2% of the U.S. gasoline pool was from catalytic reforming; by the late '50s this figure had risen to 30%.

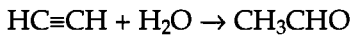
1.2.5 Hydrorefining

Hydrorefining is directly related to the technology developed in coal liquefaction. In this process heteroatoms, in particular S and N, are removed by catalytic hydrogenation. This is done in order to abate pollution and to prevent extensive catalyst deactivation in further catalytic processing. The most common catalysts are $\text{CoS}-\text{MoS}_2/\text{Al}_2\text{O}_3$ and $\text{NiS}-\text{MoS}_2/\text{Al}_2\text{O}_3$. This technology has seen widespread application only since the late '50s. A recent development is the processing of residual oils. Catalyst poisoning is more severe, here, in particular because these feedstocks contain large amounts of metals which deposit on the catalysts. The most abundantly occurring metals are Ni and V. A typical feature of these feedstocks is the presence of large hydrocarbon molecules. The answer has been found in the production of catalysts supported on wide-pore carriers.

It was not only gasoline production that was fundamental in the late '30s; synthetic rubber was just as important. In 1934 BASF and Bayer had developed Buna-S rubber, which was a copolymer containing styrene. Processes were also developed in the U.S. to produce styrene.

1.2.6 Acetaldehyde

Acetaldehyde is an intermediate in acetic acid and vinyl acetate production. Since 1916 it has been produced from the addition of water to acetylene, a reaction catalyzed by divalent mercury in sulphuric acid (20%)/water. Acetylene was made from coal. In Germany in particular, a lot of research was carried out on the use of acetylene as a chemical feedstock.

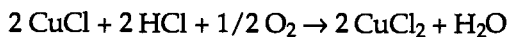
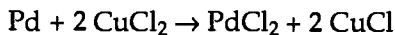


Coal was also the feedstock for synthesis gas (*vide infra*). Many contributions to acetylene chemistry are due to Reppe. His work on new homogeneous metal (mainly nickel) catalysts for acetylene conversion, carried out in the period from 1928 to 1945, was not published until 1948. Under the influence of nickel iodide catalysts, acetylene, water and CO were found to give acrylic acid. A process based on this chemistry was commercialized in 1955.

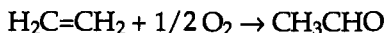
When the oil era started ethene became a much cheaper C_2 feedstock than acetylene and a search was started for new catalytic conversion routes for ethene. In their attempts to epoxidize ethene over a palladium catalyst Smidt and co-workers at Wacker-chemie discovered that ethene and water produced acetaldehyde. They rediscovered a stoichiometric reaction that had been known since 1894 (Phillips):



Smidt combined this reaction with a redox system, which led to a catalytic process ('Wacker process'):



The overall reaction reads:



1.2.7 Butanol

Since the twenties and thirties butanol together with acetone was produced by fermentation of carbohydrates (corn). In the sixties the process was replaced by the hydroformylation of propene. In the OXO process alkenes react with synthesis gas in the presence of a homogeneous catalyst to give a mixture of branched and linear aldehydes:



In formal terms, the addition of formaldehyde across the double bond has taken place. The reaction was discovered by Roelen while working on the conversion of synthesis gas to hydrocarbons. The process was first patented in 1938 and a commercial plant was briefly operated at the end of the war after which it was dismantled. In 1948 a commercial plant was put on stream by Exxon in the U.S.

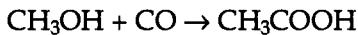
The primary aldehyde product is reduced to the desired butanol, or it is subjected to a base-catalyzed aldol condensation and then hydrogenated to give 2-ethylhexanol. The phthalic ester of the latter is used as a plasticiser in PVC. The first process was based on a $\text{Co}_2(\text{CO})_8$ catalyst, a precursor of $\text{HCo}(\text{CO})_4$. The pressure is high, ca. 200–300 bar, in order to maintain the catalyst's stability. In the '60s Shell developed a process using phosphine ligands which allowed the use of lower pressures. The catalyst is less active but it directly produces alcohols with a somewhat higher linearity.

A breakthrough occurred in the mid-seventies when Union Carbide and Celanese introduced Rh/phosphine catalysts in commercial processes. This catalyst is based on the work by Wilkinson's group; he received the Nobel prize for his work in 1973. Rhodium-based catalysts are much more active than cobalt catalysts and, under certain conditions, at least for 1-alkenes, they are also more selective. The processes for the hydroformylation of higher alkenes (detergent alcohols) still rely on cobalt catalysis. A new development is the use of water-soluble complexes obtained through sulphonation of the ligands (Ruhrchemie).

The new hydroformylation plants for the production of butylaldehyde from propene are all based on rhodium catalysts.

1.2.8 Acetic Acid

Originally, acetic acid was produced by fermentation; this is still the major process for the production of vinegar. Modern production is by acetaldehyde oxidation, liquid phase hydrocarbon oxidation and preferentially by methanol carbonylation. The latter process is to be preferred because of the low raw material and energy costs. As early as 1913 BASF described the carbonylation of methanol at high temperature and pressure:



Due to the extreme conditions commercialization was not successful. Corrosion was very important; only gold and graphite appeared to be resistant enough. Even gold-lined autoclaves were used. In the early '30s the process was abandoned for economic reasons.

Carbonylation with homogeneous nickel catalysts was very extensively studied by Reppe in the thirties and forties. This work was not published until 1953. This process was commercialized in 1955.

In 1941 Reppe demonstrated the potential of many metal carbonyls in several reactions including hydroformylation. This work resulted in 1960 in a process based on CoI_2 operating at 700 bar and 250°C. Corrosion problems were overcome by applying Hastelloy C.

In 1968 Monsanto reported a chemically related process based on rhodium iodide complexes. Due to its high reaction rates, high selectivity and different kinetics, the process differs substantially from the cobalt process. Commercialization was achieved in 1970. Operating conditions are remarkably mild: 30 bar, 180°C.

1.2.9 Polymerization

The first polymerizations were free radical reactions. In 1933 researchers at ICI discovered that ethene polymerizes into a branched structure that is now known as low density polyethene (LDPE). In the mid-'50s a series of patents were issued for new processes in which solid catalysts were used to produce polyethene at relatively low pressures. The first was granted to scientists at Standard Oil (Indiana) who applied nickel oxide on activated carbon and molybdenum oxide on alumina. Their research did not lead to commercial processes. In the late '40s Hogan and Banks of Phillips were assigned to study the di- and trimerization of lower olefins. The objective was to produce high octane motor fuels. When they tried a chromium salt as promoter of a certain catalyst (Cr was a known reforming

catalyst) they found solid white material which appeared to be polyethene. It is worth mentioning that the same scientists discovered the metathesis of alkenes! The Phillips catalyst has been improved and is used in many commercial plants. About a year later Ziegler's group patented a catalyst based on $TiCl_4$ and aluminium alkyls.

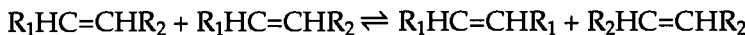
Initially, the activity of these catalysts was poor and, as a result, a high concentration of catalytic material was present in the product. An expensive catalyst removal step was necessary. Catalysts were later improved and a process became feasible in which the polymer formed precipitates and catalyst removal is no longer needed.

In 1956 Natta discovered that propene can be polymerized with a titanium catalyst and that a highly regular polymer is formed.

Ziegler and Natta shared the Nobel prize in 1963.

1.2.10 Metathesis

A novel catalytic reaction was discovered independently by scientists of Phillips Petroleum Company, du Pont and Standard Oil in Indiana. They found that alkenes can react according to the following stoichiometry:



The mechanism has been subject to much debate. The research in this field has had a large impact on transition metal catalysis. It is also interesting that in this field the usually large gap between heterogeneous and homogeneous catalysis does not exist. There was never much doubt that the reaction mechanisms were not the same in both cases.

The first large-scale application was the Phillips Triolefin Process (1966) in which propene was converted into ethene and 2-butene. Due to market changes the reverse process, in which propene is produced, became more attractive later. This process has been in operation since 1985. Another process is the Shell Higher Olefin Process (SHOP) in which ethene is oligomerized and the products are metathesized into detergent range olefins. The same company developed a process in speciality chemicals in which alpha-, omega-dienes are formed from cyclic alkenes.

Metathesis is not limited to acyclic alkenes. Cyclic alkenes also undergo metathesis with the formation of polymers. Homogeneous catalysts are used in most cases. New polymers are produced in this way by Huls, CdF Chimie and Hercules.

1.2.11 Motor Vehicle Emission Control

The development of catalytic reactors for cleaning the exhaust gases of motor vehicles has been stimulated enormously by Californian legislation. In 1959 and

1960 laws on motor vehicle emission standards were enacted which would become operative when at least two different devices were developed which could measure these standards. This gave a large impetus for the research. However, in the mid-'60s, the car industry announced that engine modifications were successful and that the standards could be met without catalytic converters. This delayed further research in the development of catalytic converters. In the late '60s a further tightening of the standards was announced and catalytic research increased considerably. The Clean Air Act of 1970 set standards that went well beyond existing technology and it was clear that catalytic mufflers would be essential.

The initial objective was to reduce the emission of CO and hydrocarbons. The mixture in the engine was fuel-rich and under those conditions the concentrations of CO and hydrocarbons are relatively high, whereas the NO_x concentration is low. The exhaust gases were oxidized in a converter to which air was supplied. Somewhat later the NO_x standards tightened and also the amount of NO had to be reduced. So both oxidation and reduction reactions were required. In the beginning, a so-called dual bed system with separate reduction and oxidation catalysts was envisaged. The engine would be operated under fuel-rich conditions in the first bed; reduction would take place. After air injection into the second bed, CO and the hydrocarbons would be oxidized. The next generation of catalysts could catalyze all reactions simultaneously, provided the fuel-air ratio in the gas mixture was stoichiometric. A typical example of the influence of the fuel-air ratio (lambda) is given in Fig. 1.6.

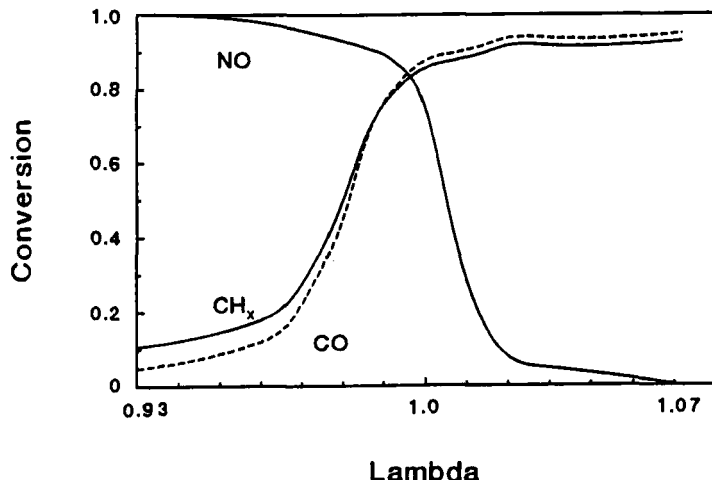


Fig. 1.6. The concentration of CO, NO, CH_x , and O_2 emitted by a gasoline engine as a function of λ , the fuel-air ratio.

At $\lambda < 1$ the activity for NO reduction is high, but not for the oxidation of CO and hydrocarbons. At $\lambda > 1$ the reverse is the case. A special control system had to be developed to guarantee the desired exhaust gas composition. The control system appears to be more critical than the catalyst itself.

The catalysts in use contain Pt and Rh as major constituents. A converter typically contains 1–2 g Pt and 0.2–0.3 g Rh. The design of the reactor has received a lot of attention. Beads were also applied initially, but nowadays monolithic honeycombs are used almost exclusively.

The introduction of catalytic converters has had a tremendous impact on the composition of gasoline. The catalysts used became poisoned by small amounts of impurities; in particular the lead compounds present in high octane gasoline were detrimental. Processes which produce high octane number compounds were therefore stimulated. First, cracking and reforming increased in importance. More recently, the aromatics content is also expected to have to decrease and alternative processes are in use or under way, e.g. the production of MTBE (methyl tertiary-butyl ether).

1.3 SUMMARY

The discussion of the history of catalysis in this chapter has been limited to the major events, so many interesting developments could not be mentioned. Moreover, the selection of topics has been subject to a personal bias. A more comprehensive overview is given in Table 1.2 of the development of industrial catalytic processes. The list is impressive and it is also clear that catalysis remains a very fascinating area.

Many reasons underlie the development of the science and technology of catalysis. One of the driving forces that should not be overlooked is the availability of the raw materials. Originally, biomass was predominant. Later coal became the most important industrial feedstock. Coke oven gas components played the role of base chemicals. Subsequently, oil took over the place of coal and the technological scene changed profoundly. More recently, natural gas resources appear to have become much more important than had been expected. Therefore it is not surprising that a lot of research in catalysis is aimed at processes based on natural gas. It is also clear that biomass is experiencing a revival. Figure 1.7 illustrates this point: it shows that for a number of important chemicals, the development of processes is linked to the availability of different raw materials. In recent years environmental considerations have been the major driving force for novel processes, often catalytic processes.

TABLE 1.2
Historical summary of the development of industrial processes

Year	Process	Catalyst
1750	H ₂ SO ₄ lead chamber process*	NO/NO ₂
1870	SO ₂ oxidation	Pt
1880	Deacon process (Cl ₂ from HCl)	ZnCl ₂ /CuCl ₂
1885	Claus process (H ₂ S and SO ₂ to S)	Bauxite
1900	Fat hydrogenation	Ni
	Methane from syngas	Ni
1910	Coal liquefaction	Fe
	Upgrading coal liquids	WS ₂
	Ammonia synthesis (Haber–Bosch)	Fe/K
	NH ₃ oxidation to nitric acid	Pt
1920	Methanol synthesis (high pressure process)	Zn, Cr oxide
	Fischer–Tropsch synthesis	Promoted Fe, Co
	SO ₂ oxidation	V ₂ O ₅
	Acetaldehyde from acetylene*	Hg ²⁺ /H ₂ SO ₄
1930	Catalytic cracking (fixed bed, Houdry)	Clays
	Ethene epoxidation	Ag
	Polyvinyl chloride*	Peroxide
	Polyethylene (low density, ICI)*	Peroxide
	Oxidation of benzene to maleic anhydride	V
	Alkylation*	HF/H ₂ SO ₄
1940	Hydroformylation, alkene to aldehyde*	Co
	Catalytic reforming (gasoline)	Pt
	Cyclohexane oxidation (nylon 66 production)*	Co
	Benzene hydrogenation to cyclohexane	Ni, Pt
	Synthetic rubber, SBR*	Li, peroxide
	BNR*	Peroxide
	Butylrubber*	Al
1950	Polyethylene (high density), Ziegler–Natta	Ti
	Phillips	Cr
	Polypropene, Ziegler–Natta	Ti
	Polybutadiene, Ziegler–Natta	Ti
	Hydrodesulphiding (HDS)	Co, Mo sulphides
	Naphthalene oxidation to phthalic anhydride	V, Mo oxides
	Ethylene oxidation to acetaldehyde*	Pd, Cu
	p-Xylene oxidation to terephthalic acid*	Co, Mn
	Ethylene oligomerization*	Co
	Hydrotreating of naphtha	Co–Mo/Al ₂ O ₃
1960	Butene oxidation to maleic anhydride	V, P oxides

Continued

TABLE 1.2 (*Continuation*)

Year	Process	Catalyst
1970	Acrylonitrile via ammoxidation of propene (Sohio)	Bi, Mo oxides
	Propene oxidation to acrolein/acrylic acid	Bi, Mo oxides
	Xylene hydroisomerization	Pt
	Propene metathesis	W, Mo, Re
	Adiponitrile via butadiene hydrocyanation*	Ni
	Improved reforming catalysts	Pt, Re/Al ₂ O ₃
	Improved cracking catalysts	Zeolites
	Acetic acid from MeOH (carbonylation)*	Co
	Vinyl chloride via ethene oxychlorination	Cu chloride
	Ethene oxidation to vinyl acetate	Pd/Cu
	o-Xylene oxidation to phthalic anhydride	V, Ti oxides
	Propene oxidation to propene oxide*	Mo
	Hydrocracking	Ni-W/Al ₂ O ₃
	HT water-gas shift process	Fe ₂ O ₃ /Cr ₂ O ₃ /MgO
	LT water-gas shift process	CuO/ZnO/Al ₂ O ₃
	Methanol synthesis (low pressure, ICI)	Cu-Zn-Al oxide
	Acetic acid from MeOH (carbonylation, low pressure process, Monsanto)*	Rh
	Improved process for xylene isomerization	Zeolite
	α-Alkenes via ethene oligomerization*/isomerization/metathesis (SHOP)	Ni, Mo
	Improved hydroformylation*	Rh
	Auto exhaust gas catalysts	Pt/Rh
	L-DOPA (Monsanto)*	Rh
	Cyclooctenamer (metathesis)*	W
	Hydroisomerization	Pt/zeolite
	Selective reduction of NO (with NH ₃)	V ₂ O ₅ /TiO ₂
1980	Gasoline from methanol process (Mobil)	Zeolite
	Vinyl acetate from ethene and acetic acid	Pd
	Methylacetate (carbonylation)*	Rh
	Methylacrylate via t-butanol oxidation	Mo oxides
	Improved coal liquefaction	Co, Mo sulphides
	Diesel fuel from syngas	Co
1990	Polyketone (from CO and ethene)*	Pd

The data refer to activities of a pilot plant scale at least.

*Homogeneous catalyst system.

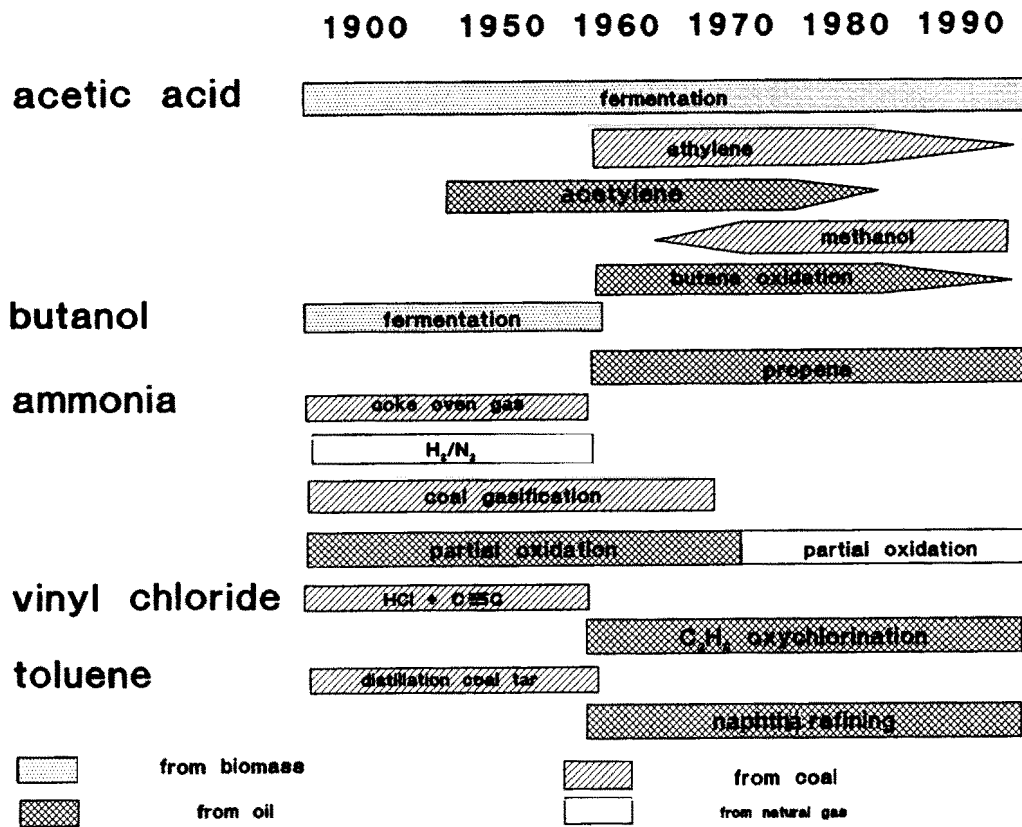


Fig. 1.7. Raw materials for some important chemicals.

REFERENCES

- 1 H.S. Bell, *American Petroleum Refining*, 3rd edition, Constable and Company Ltd., Lancaster, PA, USA, 1945.
- 2 E.E. Donath, History of Catalysis in Coal Liquefaction, in J.R. Anderson and M. Boudart (Editors), *Catalysis, Science and Technology*, Springer Verlag, Berlin, 1982, Vol. 3, pp. 1–38.
- 3 H. Heinemann, A Brief History of Industrial Catalysis, in J.R. Anderson and M. Boudart (Editors), *Catalysis, Science and Technology*, Springer Verlag, Berlin, 1981, Vol. 1, pp. 1–42.
- 4 A.J.B. Robertson, The Early History of Catalysis, *Platinum Metals Review*, 19(2) (1975) 64–69.
- 5 S.A. Topham, The History of the Catalytic Synthesis of Ammonia, in J.R. Anderson and M. Boudart (Editors), *Catalysis, Science and Technology*, Springer Verlag, Berlin, 1985, Vol. 7, pp. 1–50.
- 6 J. Trofast, J.J. Berzelius and the Concept of Catalysis, in *Perspectives in Catalysis: In commemoration of Jöns Jacob Berzelius*, CWK Gleerup, pp. 9–17.
- 7 P.J.J. Tromp and J.A. Moulijn, Slow and Rapid Pyrolysis of Coal, in Y. Jürüm (Editor), *New Trends in Coal Sciences*, Kluwer Acad. Publ., Dordrecht, 1988, pp. 305–309.

Chapter 2

Catalytic processes in industry

2.1 INTRODUCTION

In this chapter a dozen industrial catalytic processes will be described with the aim of giving the reader an impression of the use of catalysis. We have chosen to do this before going into the scientific aspects of catalysis, catalyst preparation and characterization, and catalytic reaction engineering. In this way we set the scene with the industrial applications, so that the reader may keep it in mind when studying the various aspects of catalysis. The choice of the processes is arbitrary, of course. We have tried to represent as many elements as possible within this limited number of processes. From the viewpoint of applications we have looked for catalytic processes from the oil industry, petrochemical industry, exhaust gas technology, fine chemical industry, polymer preparation, etc. A broad variation in chemical reactions has also been pursued, ranging from cracking to denoxing and asymmetric catalysis. Within this limited number of examples we have tried to introduce as many reactor types as possible. Separation of catalyst and product is often a point of interest. The descriptions include a brief survey of the chemistry, the catalyst, the process and the reactor. Occasional reference is made to alternative processes, and the use of the product is briefly indicated.

2.2 CATALYTIC PROCESSES IN THE OIL REFINERY

Oil refineries are complex plants. Besides physical processes such as distillation and extraction, a large number of different chemical conversion processes are applied. Catalysis plays a crucial role in these processes. The most important ones are:

- catalytic reforming;
- hydrotreatment;
- fluid catalytic cracking;
- alkylation.

The place of these processes can best be understood from a simplified scheme of a typical oil refinery (Fig. 2.1). The crude oil is first separated by distillation into a number of fractions. The naphtha fraction has the right boiling point for gasoline, but does not have an acceptable performance. The 'octane number' is too low and has to be increased. This is achieved by 'catalytic reforming'. The catalysts for this process contain acid sites and noble metals, which are poisoned by nitrogen-containing bases and sulphur-containing compounds. That is why a hydrotreatment step precedes the reforming reactors. A catalytic hydrogenation is carried out in this hydrotreatment step, removing nitrogen and sulphur as NH₃ and H₂S. These gaseous compounds can easily be recovered by absorption in a special liquid.

Cracking reactions are carried out in order to reduce the molecular size and to produce more valuable transport fuel fractions (gasoline and diesel). Fluid catalytic cracking is acid catalyzed (zeolites) and a complex network of carbeneum ion reactions occur leading to size reduction and isomerization (see Chapter 4, Section 4.4). Hydrogenation also takes place in hydrocracking, as well as cracking.

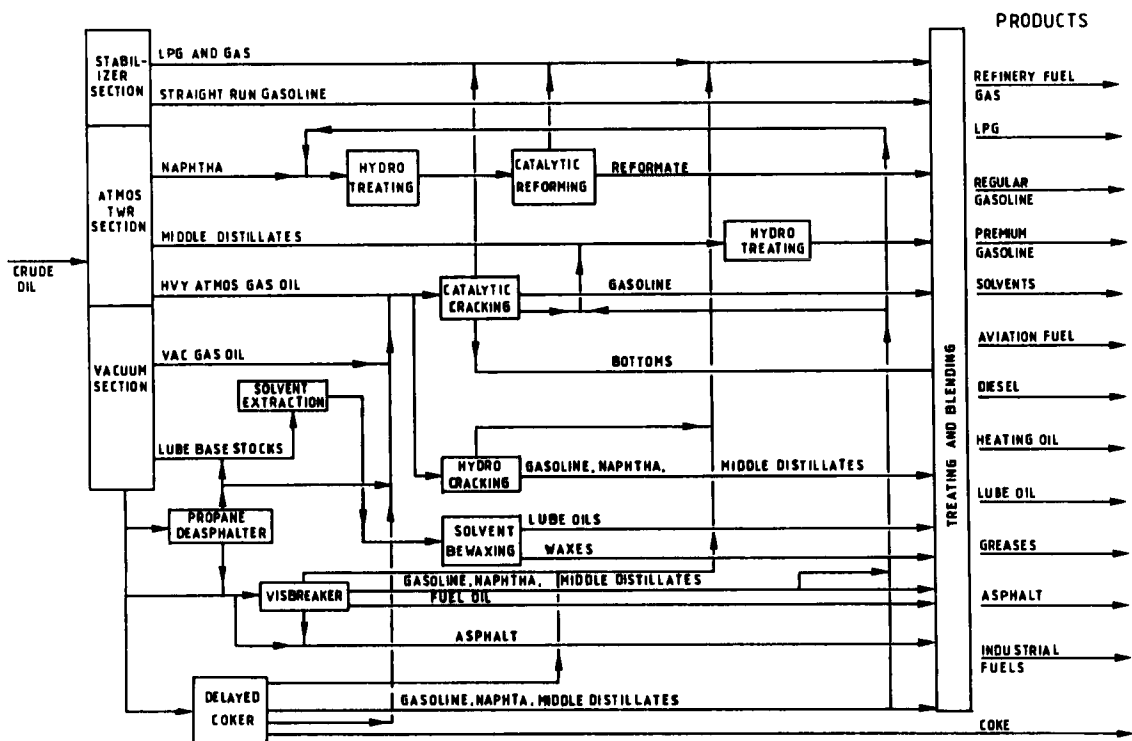


Fig. 2.1. Advanced refinery.

2.2.1 Catalytic Reforming

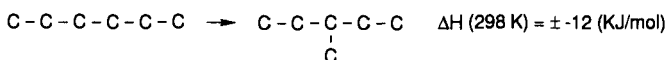
The purpose of catalytic reforming is to boost the octane number by converting molecules with a low octane number into molecules with a high octane number (see Table 2.1).

TABLE 2.1
Overview of octane number of different hydrocarbons

Hydrocarbon	Octane number	Boiling point (K)
<i>n</i> -pentane	62	309
2-methyl butane	90	301
cyclopentane	85	322
<i>n</i> -hexane	26	342
2-methyl pentane	73	333
2,2-dimethylbutane	93	323
1-hexene	63	337
2-hexene	81	341
benzene	>100	353
cyclohexane	77	354
<i>n</i> -octane	0	399
2-methylheptane	13	391
2,2,4-trimethylpentane	100	372
1-octene	35	395
2-octene	56	398
3-octene	68	396
xlenes	>100	—
ethylbenzene	98	410
1,2-dimethylcyclohexane	79	403
ethylcyclohexane	41	403
methyl tert.-butyl-ether (MTBE)	118	328
ethyl tert.-butyl-ether (ETBE)	118	345
tert.-amyl methyl-ether (TAME)	115	359

The capacity of catalytic reforming is very large. In the western world alone it amounts to over 1 million t/d. The major reactions occurring are:

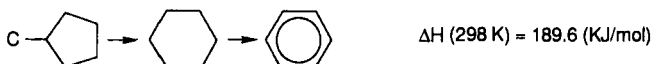
Isomerization



Aromatization



Isomerization and aromatization



Clearly, favourable reaction conditions are a high temperature and a low pressure. However, a low pressure is not possible because large carbon deposits are formed. Carbon deposition is lowered by increasing the hydrogen partial pressure. Typical practical conditions are 800 K and 30 bar. Under these conditions, catalyst activity is typically retained over a period of 3 to 6 months. Regeneration is performed by removing the carbon deposits by careful burning in diluted air.

In practice catalytic reforming is usually carried out in fixed bed reactors (see Fig. 2.2). Because the reactions are endothermic, heat has to be introduced. A conventional scheme is based upon a series of three or four adiabatic fixed bed reactors with interstage heating. Part of the hydrogen produced is recycled to maintain high hydrogen partial pressures. The product mixture from the last reactor is cooled and separated into a gas phase and a liquid phase. The latter is purified by distillation.

The catalyst is called 'bifunctional'; both the carrier and the metallic particles dispersed over the carrier exhibit different catalytic functions. The carrier contains chlorine ions and, as a consequence, it has acid properties and exhibits isomerization and cyclization activities. The metal particles consist of alloys of, for example, Pt/Re which exhibit hydrogenation/dehydrogenation activity.

2.2.2 Catalytic Cracking

The purpose of catalytic cracking is to increase the fraction of gasoline. Originally cracking was performed thermally, but cracking in the presence of a catalyst predominates nowadays. Catalytic cracking is one of the largest applications of catalysis: worldwide 500 million ton/y. Catalytic cracking was the first large-scale application of fluid beds. This explains the name 'fluid catalytic cracking' (FCC) which is still used, although the modern catalytic cracking reactor is an entrained flow reactor.

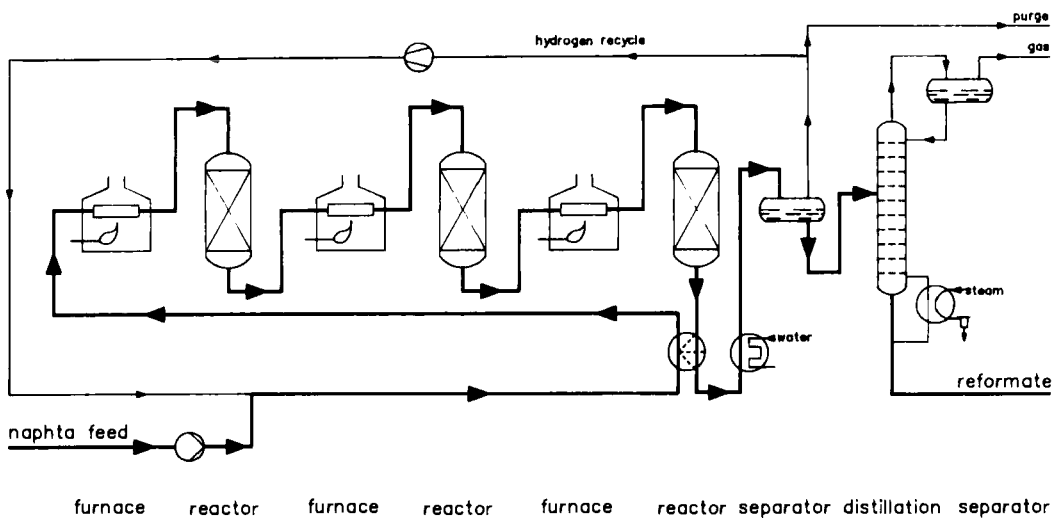
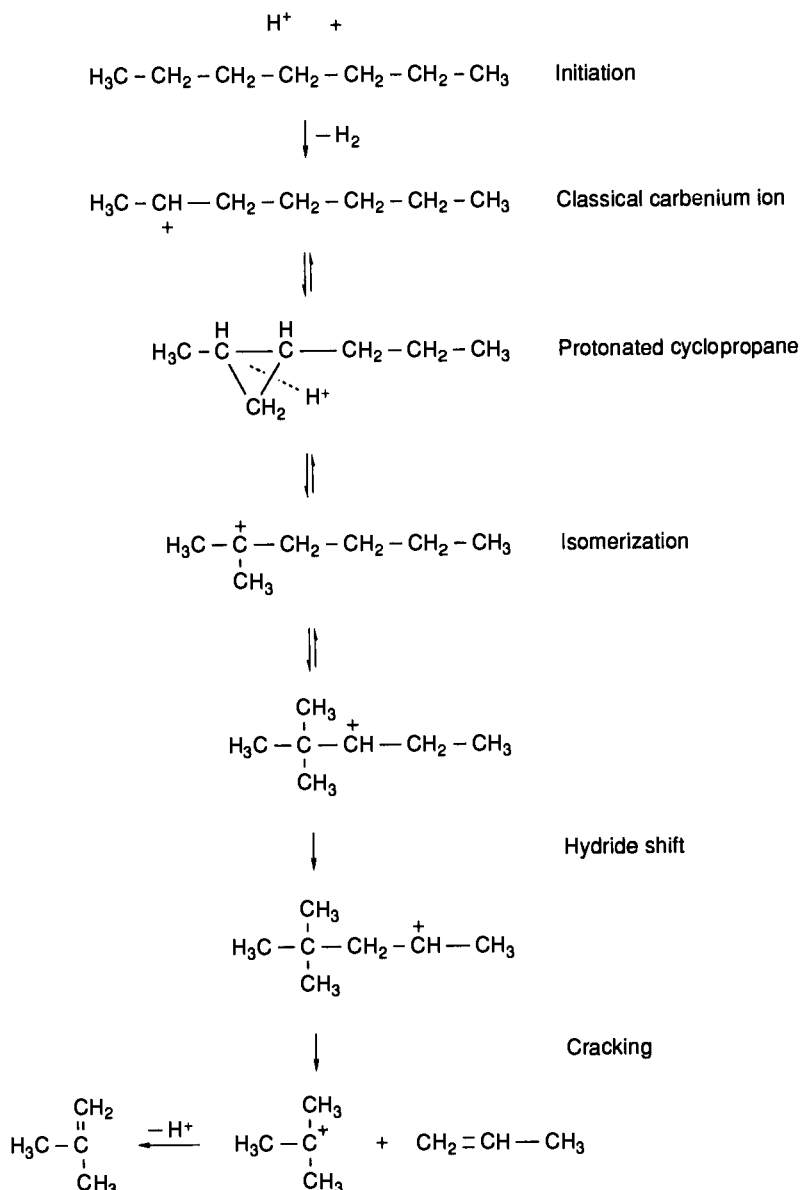


Fig. 2.2. Catalytic reforming.

The mechanism

In catalytic cracking many reactions take place simultaneously. Cracking occurs by C–C bond cleavage of paraffins, dealkylation etc. Isomerization and even condensation reactions also take place. These reactions occur via positively charged hydrocarbon ions (carbocations). The nature of the carbocations is the subject of debate. For the cracking of paraffinic hydrocarbons it is usually assumed that carbenium ions are the crucial intermediates, which decompose via beta fission into olefins and (smaller) carbenium ions (see Chapter 4, Section 4.4). A typical reaction mechanism for catalytic cracking (and hydrocracking) under the relatively mild conditions used in FCC is shown on page 28.

The catalyst causes a ‘classical’ carbenium ion to be formed by acid catalyzed activation reactions. The classical carbenium ion is transformed into the key intermediate which can be described as a protonated cyclopropane structure. After some rearrangements cracking occurs. The formation of branched paraffins is very fortunate since branched paraffins have high octane numbers and the isobutane produced can be used in alkylation. The preferred products are those of which the formation proceeds via tertiary carbenium ions. Carbenium ions can also be generated by intermolecular hydride transfer reactions between alkane and carbenium ions that are not able to form tertiary carbenium ions (see Chapter 4, Section 4.4). Under more severe conditions lower paraffins can also be cracked.



Process description

Extensive coke deposition takes place during catalytic cracking, resulting in loss of activity. Typically, the catalyst loses 90% of its activity within one second. An elegant solution has been found for this problem. The clue to this solution is a combination of a reactor in which cracking takes place with a reactor used for regeneration of the catalyst by burning the deposited coke. In this set-up coke is

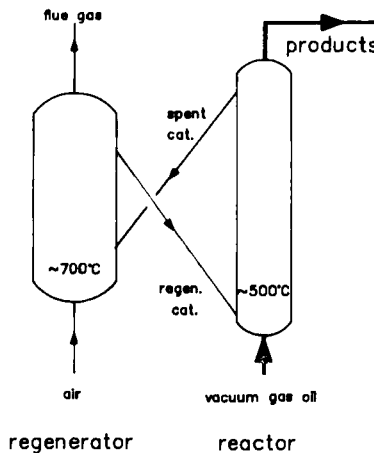


Fig. 2.3. The principle of catalytic cracking.

often referred to as a 'mixed blessing' because, although it poisons the catalyst, it also enables the production of the heat required for the endothermic cracking reactions.

The principle is as follows (see Fig. 2.3). The feed is vaporized and entrains the catalyst particles (size ca. $70\text{ }\mu\text{m}$). The residence time in the riser is about one second. Such risers are very high: typically 30 m (reactor diameter 1 m). The catalyst particles are separated by a cyclone and transferred to the regenerator, in which the coke is burned. After regeneration the catalyst particles are returned to the riser. So a catalyst particle is actually a batch reactor. It enters the riser at a high activity and temperature. While it is travelling through the riser, it acts as a catalyst, its temperature drops due to the endothermic nature of the cracking reactions, coke is deposited and its activity decreases strongly. Subsequently, it is transferred to the regenerator and coke burning starts. It recovers its activity and the temperature is increased by the exothermic combustion.

A diagram of a cracking unit is shown in Fig. 2.4.

Catalyst

The catalyst particles consist of a silica-alumina matrix containing zeolite crystals. Zeolites contain pores of molecular dimensions, and as a consequence they have to be very small to give the reactant molecules the opportunity to reach the active sites. Typically, they have a diameter of $1\text{--}5\text{ }\mu\text{m}$. Such a fine powder cannot be handled in the reactors used and the particles used are therefore composed of a matrix containing the zeolite particles. The matrix itself has large pores and also exhibits activity. Special additives are added, among other things to catalyze the CO oxidation reaction since when large amounts of CO are present, a separate burner is needed to recover the energy present in the gas.

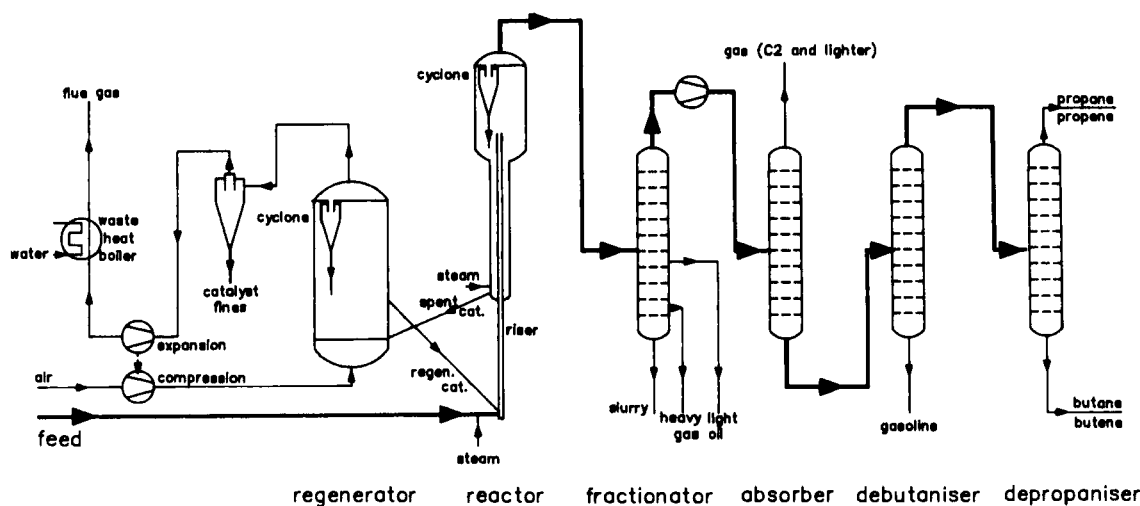


Fig. 2.4. Scheme of a catalytic cracking unit.

Environmental aspects

A catalytic cracking plant emits dust, nitrogen oxides and sulphur oxides. The first stream is derived from attrition of the catalyst particles in the regenerator, which is a fluidized bed. Nitrogen oxides are formed in the regeneration and the sulphur oxides arise from the sulphur compounds present in the feed. Part of the sulphur is released in the riser, and part in the regenerator. From an environmental point of view these two modes have quite different impacts. In the riser S is released in the form of H_2S and is recovered downstream in the gas cleaning sections. In the regenerator the gas phase is oxidized and S is released as sulphur oxide in a highly diluted gas stream containing as major component the large amount of N_2 from the air used for burning the coke. In contrast to H_2S from the regenerator gas effluent, the recovery of the sulphur oxides from the diluted regenerator gas is difficult. Recently attention has been given to the question of what to do with the spent catalyst.

2.2.3 Hydrotreatment

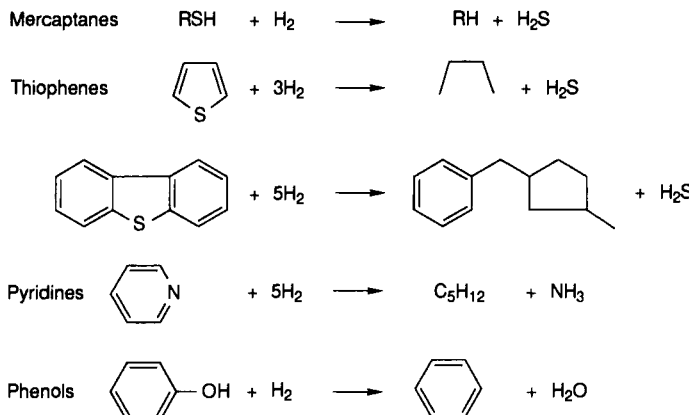
Hydrotreatment belongs to the class of conversions involving reaction with hydrogen. In this section 'hydrotreatment' is limited to hydrogenation and hydrogenolysis reactions in which removal of heteroatoms (in particular S,N,O) and some hydrogenation of double bonds and aromatic rings take place. In these reactions — in contrast to hydrocracking, in which size reduction is the objective — the

molecular size is not drastically altered. Hydrotreatment as defined here is sometimes called hydropurification.

The major objectives are:

- protection of downstream catalysts;
- improvement of gasoline (odour, colour, stability, corrosion);
- protection of the environment.

Typical reactions that occur are:



In naphtha reforming, hydrotreatment is always applied to protect the platinum-containing catalyst against sulphur poisoning. The specification of sulphur content for the feed for the reforming unit is less than 1 ppm.

The hydrogen used in naphtha hydrotreatment is a by-product of the catalytic reforming. When hydrotreatment of heavy residue is performed, separate H₂ production units are often required.

Unstable byproducts are formed in naphtha cracking, and these are hydrotreated in order to increase their stability. One of the important reactions occurring is the saturation of diolefins.

Process description

In simple naphtha hydrotreatment the feed is vaporized and led through a fixed bed reactor. When heavier feed stocks are treated, vaporization is not possible and trickle phase operation will be more suitable. In this mode the liquid and gas flow concurrently downwards. Most of the hydrotreatment of heavy residues is performed in trickle bed reactors. The major concern is to guarantee a complete wetting of the catalyst particles, because dry regions will cause extensive coking. When more extensive hydrogenation occurs (often from the hydrogenation of aromatic rings) interstage cooling is often applied.

Typical process conditions are:

Temperature: 350–420°C

Pressure: 40–100 bar

LHSV: 1–6 h⁻¹

The severity of the processing conditions depends on the feed; for light petroleum fractions it will be milder than for heavy residues. Moreover, it is common practice to compensate for deactivation of the catalyst by increasing the temperature of the reactor. A simplified flow scheme involving a trickle flow reactor is shown in Fig. 2.5.

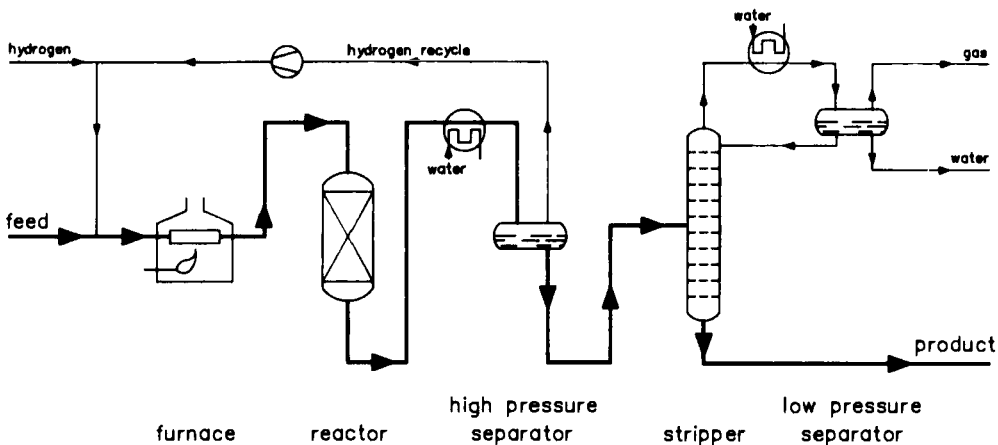


Fig. 2.5. Simplified scheme of hydrotreatment involving a trickle flow reactor.

Catalysts

Catalysts are mixed metal sulphides on a carrier. The major examples are supported mixed phases of CoS and MoS₂, of NiS and MoS₂ and NiS and WS₂. There is as yet no full agreement on the structure. For the first catalyst the best description is small MoS₂ clusters with CoS units at the edges. Typical dimensions of these clusters are 1 nm and a stacking between 1 and 3.

Environment

From the point of view of clean technology hydrotreatment is gaining increasing interest. A recent example is diesel fuel. Sulphur-containing compounds in diesel fuel cause serious difficulties in catalytic cleaning of the exhaust gases. Undoubtedly, in the near future, novel processes will be needed for the deep desulphurization of diesel.

2.3 TOTAL ISOMERIZATION PROCESS OF PARAFFINS

Overall Reaction

Hydroisomerization of C₅ and C₆ paraffins (250°C, Pt–H–mordenite as the catalyst) combined with separation of normal and branched paraffins (over zeolite CaA).

Feedstock

Straight run C₅–C₆ paraffins ('light ends') from refinery distillation.

Product Use

As gasoline component with improved octane number, cf. Table 2.1.

Scale

Over 25 plants are operating the total isomerization process (TIP) and this number is growing continuously. Many millions of tons of isomerized paraffins are produced annually by this process.

Process Description

The TIP process is a combination of Shell's Hysomer process and Union Carbide's ISOSIV process. Both processes are zeolite based.

In the Hysomer process the catalyst is a Pt(O)-loaded zeolite of the H-mordenite type. The temperature applied has a strong bearing on the composition of the equilibrium mixture obtained, see Fig. 2.6 for the hexane isomers: the lower the temperature applicable, the more dimethylbutanes are present. The temperature dependence is not easily explained, but it will be clear that a low temperature is favourable for the purpose of the process.

Hydroisomerization is thought to start with dehydrogenation of paraffins, giving carbenium ions and alkenes. Secondary carbenium ions can rearrange to tertiary cations, probably via protonated cyclopropane derivatives. Transfer of hydride towards the tertiary carbenium ions provides the isomerized branched paraffins (see Chapter 4, Section 4.4). A side reaction is C–C scission of carbenium ions leading to cracked products. Hydrogenolysis on the metal function can also contribute to this undesired reaction. The larger the alkane, the more hydrocracking takes place, which may be the reason that the TIP process so far has focused on the C₅ and C₆ fractions.

It should be noted that H-mordenite itself is also able to isomerize alkanes such

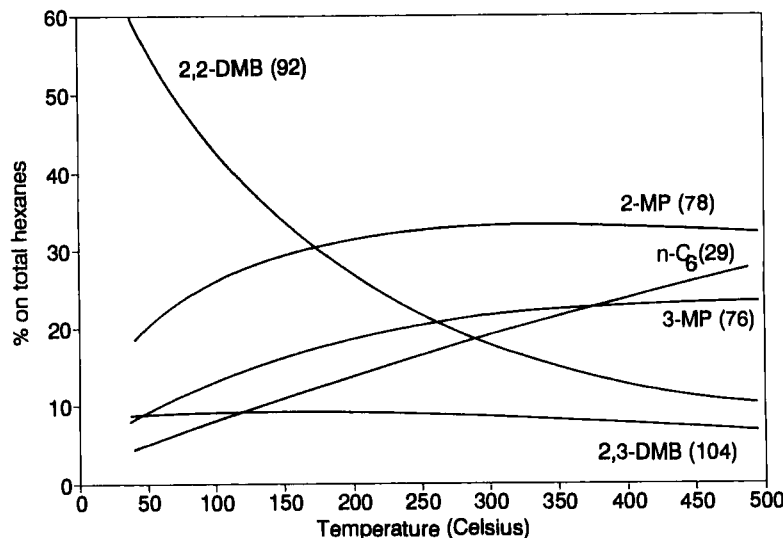


Fig. 2.6. Thermodynamic equilibria for hexane hydroisomerization (RON).

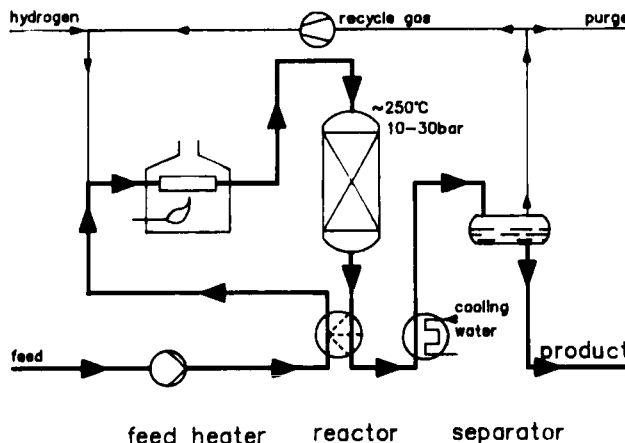


Fig. 2.7. Diagram of Shell Hysomer process.

as pentane. However, the presence of platinum greatly improves its selectivity and stability, as shown in Fig. 2.8. Apparently the hydrogenation function prevents oligomerization etc. leading to coke formation.

In the TIP process the Hysomer process is combined with the ISOSIV process which separates normal paraffins from branched ones by selectively adsorbing the normal fraction into zeolite CaA (pressure swing adsorption). After desorption (by applying vacuum) the normal paraffins are recycled. A schematic view

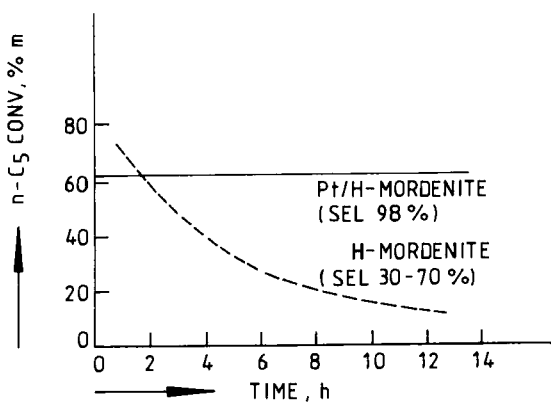


Fig. 2.8. Influence of metal function in pentane hydroisomerization.

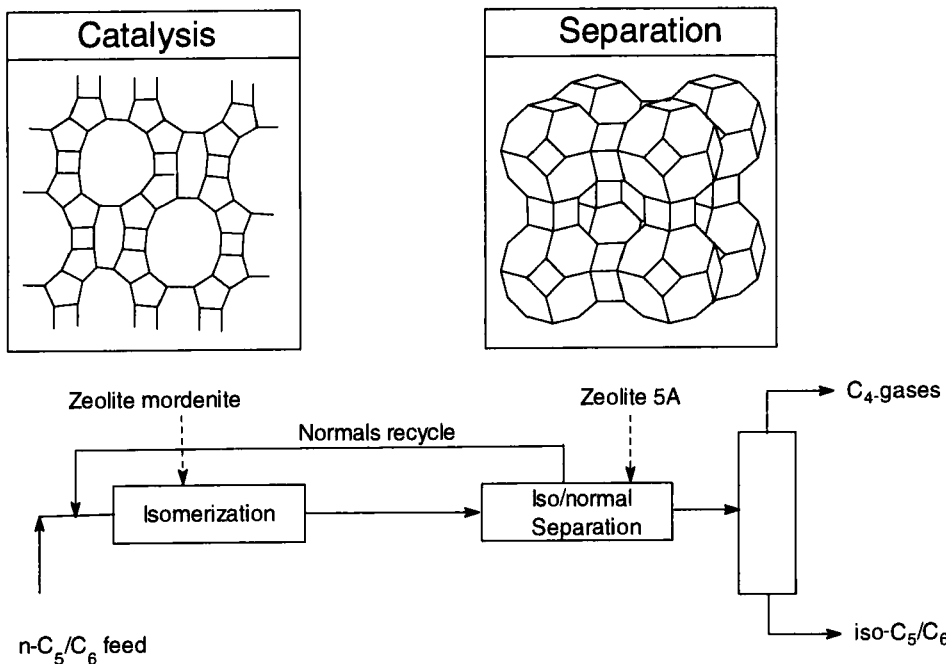


Fig. 2.9. Paraffin total isomerization process (TIP).

of the TIP process, including a structural picture of the two zeolites involved, is given in the Fig. 2.9.

The pore openings of zeolite A just allow normal alkanes to enter the pore system of the crystal. It might be of interest to have a zeolite available which adsorbs the normals and the mono methyl-branched paraffins and leaves the high octane dimethyl branched compounds unadsorbed.

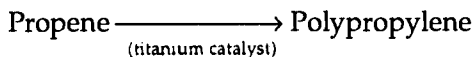
Catalysts

Mordenite is a strong zeolite the Si/Al ratio of which can easily be changed from 5 to higher values. Its parallel channels having a somewhat elliptical cross section (0.65×0.7 nm) allow all C_5 and C_6 isomers to enter and to leave. Platinum is introduced by ion exchange with $Pt(NH_3)_4^{2+}$. Competitive exchange with NH_4^+ (excess) is recommended in order to obtain a high Pt dispersion. A careful calcination follows in which local high temperatures in the zeolite crystal have to be prevented. Finally the Pt catalyst is reduced with hydrogen.

The selective adsorbent CaA is prepared in the sodium form (the detergent zeolite NaA) and subsequently partially exchanged with Ca(II).

2.4 ISOTACTIC POLYPROPYLENE

Overall Reaction



Isotactic polypropylene is a stereoregular polymer with all methyl groups pointing in the same direction when the backbone is stretched. In syndiotactic polypropylene the methyl groups alternate along the chain. The atactic polymer lacks regularity. All three forms retain a perfect head-to-tail structure.

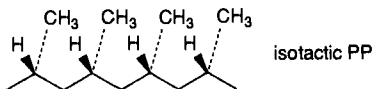


Fig. 2.10. Isotactic PP.

Feedstock

Propene from oil refinery crackers.

Product Use

Polypropylene is a plastic which finds many end uses with a variety of product property requirements. In general, isotactic polypropylene has a high tensile strength, a low density, a good heat and abrasion resistance, and it has a nice looking optical gloss. The melting point (by dsc) is 162°C , the density is 0.9 g/cm^3 . The chemical properties, determined in the manufacture, include stereoregularity, molecular weight and molecular weight distribution. The process gives a powder that is first extruded into pellets (nibs). During the processing many organic and inorganic chemicals may be added, such as antioxidants, UV stabi-

lizers, fillers, reinforcing fibres, dyes, etc. Processing may involve injection moulding, film extrusion, and pipe extrusion. The processing parameters in the second transformation — temperature, cooling rate, etc. — determine the mechanical properties of the consumer product. The product has a crystallinity of 60%. The crystalline spherulites may have different morphological forms which strongly depend on the processing conditions.

Scale

Nine million tons (1990) of polypropylene are produced annually. In 1973 this was only 3 million tons.

Process Description

The performance of the catalyst is of crucial importance to the design of the plant. Figure 2.11 shows the scheme of a high-yield liquid process for which the catalyst was pioneered by Montedison and Mitsui. The catalyst is a titanium tetrachloride supported on magnesium dichloride which, in the presence of various modifying donor compounds, is reduced by triethylaluminium. This leads to a highly active catalyst, a product with a high stereoregularity, and a high bulk density. The propene feed has to be thoroughly purified. Traces of contaminants such as water, oxygen, carbon monoxide and sulphur compounds would destroy the catalyst. The components are fed to the reactor ($60\text{--}70^\circ\text{C}$, 10 bar), a CSTR. The reaction is highly exothermic (2500 kJ/kg, from gaseous C_3H_6). Cooling coils are used in slurry processes and the feed may be additionally cooled. In the second step the unreacted propene is removed by flashing and recycled. The solid isotactic product is separated by centrifugation. Depending on the catalyst,

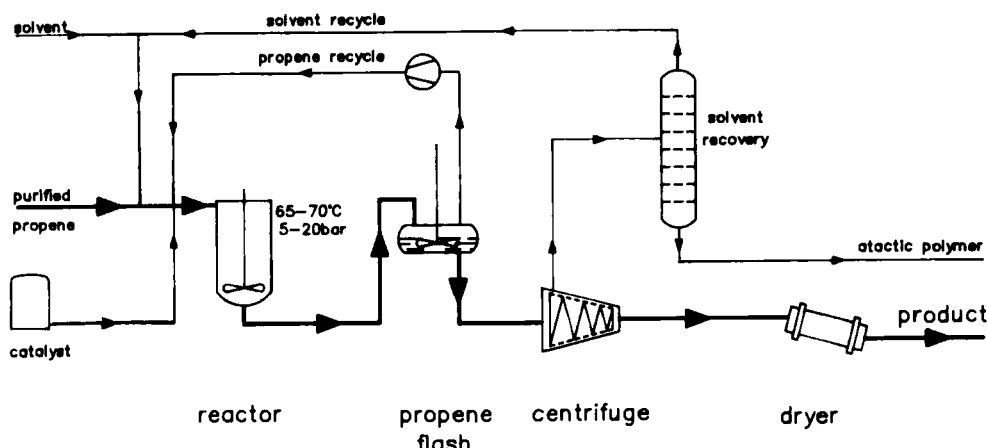


Fig. 2.11. Slurry process for polypropylene with high activity catalyst.

the liquid from the centrifugation stage may contain dissolved atactic polypropylene which is collected by removal of the solvent with steam. The isotactic product from the centrifugation is dried and the solvent is recycled after thorough drying. In this process the catalyst concentrations are low and no catalyst removal ('de-ashing') is needed. The fluffy powder is very sensitive to oxidation and a stabilization package is added to the product before it is exposed to air. The dried powder is pelletized in an extruder.

Alternatives

The similar, older slurry process uses a less active catalyst. The monomer is dissolved in isoctane, the titanium catalyst and aluminium cocatalyst are added and this mixture is fed to the reactor which is maintained at 70°C. The inorganic corrosive (Cl) residues are removed in a washing step with alcohols. The atactic material is removed by extraction. A third process employs propene as the liquid in combination with a high activity catalyst. The Himont 'Spheripol' process, which uses spherical catalyst particles, gives spherical polymer beads of millimetre size that need no extrusion for certain purposes. A more recent development is the gas-phase polymerization using an agitated bed. All processes are continuous processes, where the product is continuously removed from the reactor. Over the years we have seen a reduction of the number of process steps. The process costs are very low nowadays, propene feed costs amounting to more than 60% of the total cost.

The Catalyst

The catalyst was discovered by Ziegler who mixed $TiCl_4$ and aluminium alkyls and thus polymerized ethene. Natta recognized the peculiar structural properties that a substituted alkene might confer in the polymer. Commercial production of both polymers with the new catalysts started very soon after its discovery in 1954. Titanium is reduced to the trivalent state and it is generally accepted that propene insertion into the titanium alkyl bond leads to the polymer. The stereoregularity is determined by the geometry of the site of the catalytic centre. This is known as the Cossee-Arlman mechanism. The solid $TiCl_3$ catalysts contain different sites, some of which give atactic and some of which give isotactic polymer. The major improvement in the second generation catalysts was in the preparation of a high surface area $TiCl_3$, free of cocrystallized $AlCl_3$. The modern high-yield catalysts consist of very small crystallites of $MgCl_2$ with supported $TiCl_4$ and a Lewis base, e.g. dimethyl phthalate. They are reduced by $AlEt_3$.

The productivity of the catalyst has been the topic of continuous research. Table 2.2 gives a review of development of the catalyst in the last three decades.

In addition to the molecular properties, the macroscopic growth of the polymer particles is important; they should be sufficiently large and dense,

TABLE 2.2
Development of PP catalyst activity

PP catalysts	Year	Yield (kg/g)	Isotacticity (%)
TiCl ₃ , 1st generation	1954	4	92
TiCl ₃ , 2nd	1971	16	96
MgCl ₂ , TiCl ₄ , 3rd	1975	325	92
MgCl ₂ , TiCl ₄ , 3rd	1981	1300	96

otherwise there is no means of collecting and processing the product. What is more, the capacity of the plant also increases with the bulk density of the product. The theoretical bulk density for ideal uniform spheres is 540 kg/m³. Values obtained in modern plants are of the order of 500 kg/m³. The morphology is also determined by the solid catalyst preparation. The morphology of the macroscopic catalyst particles is 'reproduced' by the growing polymer particles.

2.5 CATALYSTS FOR AUTOMOTIVE POLLUTION CONTROL

Automobiles contribute significantly to air pollution, especially in urban areas. Typical concentrations in the exhaust gases of a gasoline engine are given in Fig. 2.12.

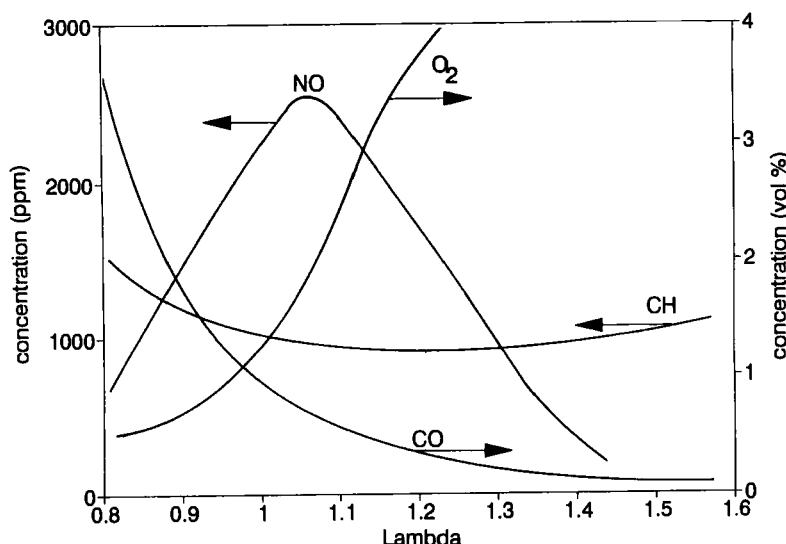


Fig. 2.12. The concentration of CO, NO, CH_x, and O₂ emitted by a gasoline engine as a function of λ (the dimensionless air-fuel ratio).

Here lambda (λ) is the dimensionless air to fuel ratio ($\lambda = 1$ corresponds to stoichiometric combustion). For low values, the amount of air is substoichiometric and a lot of CO and hydrocarbons are produced. At higher values of λ ($\lambda > 1$), combustion is more complete and much less unburned hydrocarbons and CO are emitted. However, the temperature in the cylinder increases and, as a consequence, more NO_x is emitted. At still higher values of λ , because of the large excess of air, the temperature drops and less NO_x is formed. Operation under a large excess of air is referred to as 'lean' burning. With respect to the amounts of CO and NO formed, lean burning is very attractive. However, it also has disadvantages: emission of unburned hydrocarbons increases and ignition gives problems. The latter problem can be solved by applying a higher compression ratio. Recently, an attempt has been made to develop and manufacture engines working at high λ values. If lean-burning engines can be used, only oxidation of hydrocarbons would be needed in the catalytic converter.

Catalysis has been remarkably successful in reducing emissions. Table 2.3 shows typical emissions for Otto (gasoline) engines with and without a 'three-way catalyst' are shown. Data for diesel engines are also included.

Clearly, catalysis essentially solves the problem of the air pollution. The data illustrate the good performance of diesel engines as far as the emission of NO_x and CO are concerned. Until recently, the NO_x emission was below the legislation limits in the developed countries. More recent limits are stricter, however. Also, it is clear that for diesel engines the emission of particulates (mainly soot) is very large compared to that of Otto engines. As diesel engines are considerably more efficient than Otto engines, intensive research is being carried out in order to eliminate the environmental problems of diesel engines. Both primary measures (engine modifications) and secondary measures (catalyzed NO_x reduction and soot combustion) are adopted. Diesel emissions are also specifically associated with the presence of SO₂. SO₂ emissions are low in gasoline engines because gasoline is thoroughly desulphurized. For diesel fuel this is not yet the case, but it is expected that this will change in the near future.

TABLE 2.3

Emission of particulates, hydrocarbons, NO_x, and CO for gasoline engines, gasoline engines with a catalyst and diesel engines

Engine	Particulates (mg/mi)	Hydrocarbons (g/mi)	NO _x (g/mi)	CO (g/mi)
Otto engines without catalyst	15–30	2.2–3.8	2.6–8.0	13–33
Otto engines with three-way catalyst	5–10	0.1–0.3	0.2–0.6	1–4
Diesel engines	200–650	0.1–0.8	1.0–2.0	1–3

mi = mile, measured for 18 engines in a standard driving cycle (FTP); data from Volkswagen, 1988.

Catalysts

For three-way catalysts in converters for Otto engines Pt/Rh supported on La-stabilized alumina are used. Promoters are present, e.g., CeO₂. The alumina is usually situated as a ‘washcoat’ layer in a monolith (typically with a cell density of 400 cells/in²) consisting of cordierite. In practice, the catalysts appear to be very stable. In fact, the durability of the electronic control system (for the regulation of the λ value in the converter) is more critical than the catalyst itself.

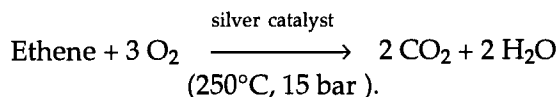
Recently, in academic circles and in industry, a renewed interest can be observed in the development of non-noble metal catalysts, e.g., Cu-based catalysts. If lean-burning systems were to become available, oxidation would be the only reaction to be catalyzed and catalyst composition will certainly be changed accordingly. Catalytic converters are still in the development stage for diesel engines.

2.6 ETHENE OXIDE

Overall Reaction



Side reaction:



Feedstock

Ethene from oil refinery crackers.

Product Use

The main use of ethene oxide is as ethylene glycol, half of which is used in as anti-freeze and the other half is used in the production of polyesters. Other products are glycol ethers, polyurethanes and poly(ethylene glycols). We find these in many consumer products such as fibres, foils, bottles, solvents, plasticizers, adhesives, detergents, brake fluids, etc.

Scale

Nine million tons of ethene oxide are produced annually.

Process Description

Here we will describe the process using pure oxygen. The catalyst used is a silver catalyst supported ($\pm 10\%$) on a highly pure porous alumina with a low

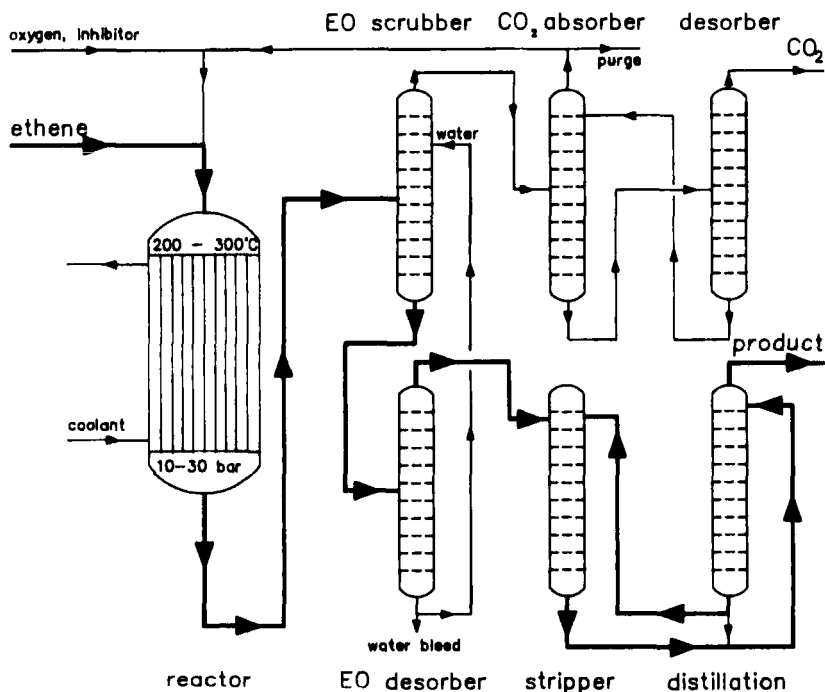


Fig. 2.13. Oxidation of ethene with oxygen (heat exchangers omitted).

surface area ($\sim 1 \text{ m}^2$). The side reaction is highly exothermic (1300 kJ/mol of ethene under the conditions given, and with a selectivity of 80% most of the heat is produced by the side reaction) and the reactor therefore consists of a huge bundle of pipes of a few centimetres in diameter and several meters long to obtain good heat transfer. The tubes are cooled by water or a high-boiling hydrocarbon. The heat of the heat transfer liquid is used to heat the reactants and for steam generation. The mass conversion of ethene is of the order of 10%. The concentration of ethene oxide in the gas that leaves the reactor is only 1 or 2% which is necessary for suppression of complete combustion. The inlet gas is made up from the recycle gas and, in addition to ethene ($\pm 25\%$) and oxygen ($\pm 8\%$), contains carbon dioxide, argon and methane. After the gas is cooled it is sent to a scrubber where ethene oxide is removed with water. It is then led through a basic solution to remove the carbon dioxide. The ethene oxide (b.p. 10.8°C at 100 kPa) is removed from the water. Likewise the carbon dioxide is removed in a desorber.

Alternatives

The alternative process uses air instead of oxygen. The operation of this system is totally different since now large amount of inert nitrogen would end up in the

recycle. Therefore a large amount of the gas is vented, which simultaneously circumvents the removal of carbon dioxide. The conversion per pass, however, must be much higher, and the amount of ethene in the off-gas is still too high for direct venting into the atmosphere and hence a secondary reactor is needed.

Another process, the chlorohydrin process, is now obsolete. On a weight basis this process produced more calcium chloride than ethene oxide!

The Catalyst

The silver catalyst was discovered by Lefort in 1931. Today's catalyst is much more active and selective. It contains silver particles with a diameter of 0.1–1 µm. Alkali metal salts, cesium for instance, may be added as promoters. The feed also contains organic chlorides such as vinyl chloride, which suppress the side reaction. The selectivity in commercial plants has never exceeded 86%, according to published records. This has long been regarded as a magic number, since it was argued that only half of the dioxygen molecule could be utilized for epoxidation, and that the other oxygen atom should be removed from the catalyst by 'burning' ethene. Laboratory experiments have now proved that this is not necessarily the case and that, in principle, higher selectivities may be expected (see Section 5.4.2).

Propene oxide cannot be made directly from propene and oxygen with this catalyst since the total combustion predominates. Instead, it is produced using hydroperoxides as the oxidant, see the next section (Section 2.7).

2.7 STYRENE AND PROPYLENE OXIDE (SMPO PROCESS)

Feedstock

Ethylbenzene and propene. The former is produced from benzene and ethene.

Product Use

Styrene is the monomer for polystyrene and styrene–butadiene rubber. Propylene oxide is mainly used for the manufacture of propylene glycol and polyurethanes.

Scale

About 10 million tons of styrene and 3.5 million tons of propylene oxide are produced annually, worldwide. Most of the styrene is still produced by dehydrogenation of ethylbenzene and it is estimated that ca. 800,000 tons of styrene and 400,000 tons of propylene oxide are produced by the SMPO process.

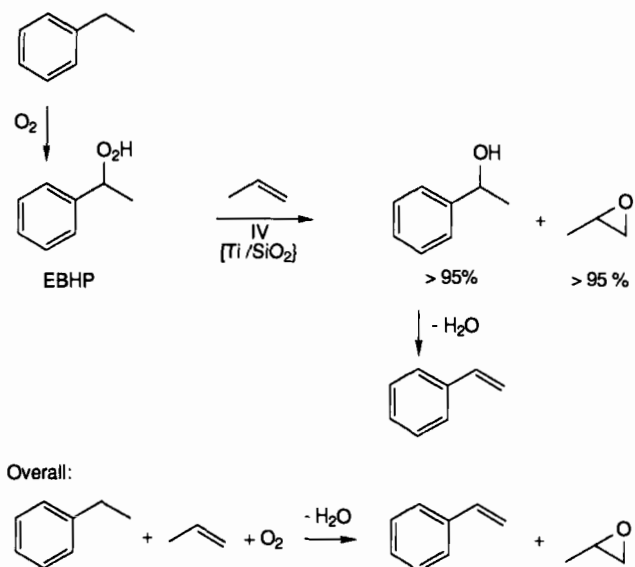


Fig. 2.14. The SMPO process.

Process Description

The process involves three steps (see Fig. 2.14):

- autoxidation of ethylbenzene to the corresponding hydroperoxide (EBHP);
- liquid phase catalytic epoxidation of propylene with EBHP, affording propylene oxide and α -methylbenzyl alcohol;
- Dehydration of α -methylbenzyl alcohol over a titania catalyst at 180–280°C to give styrene.

Two variations of the process are used, the only essential difference being the catalyst employed in the epoxidation step. In the Arco (Atlantic Richfield) process a homogeneous molybdenum catalyst is used. The Shell process employs a heterogeneous titanium/silica catalyst.

The stoichiometry of the reaction is such that ca. 2 tons of styrene are produced per ton of propene oxide. The SMPO route to styrene is 'cleaner' and much less energy intensive than the conventional dehydrogenation route. The amount of styrene that can be produced is limited by the amount of propylene oxide that can be sold. The flow diagram for the process is shown in Fig. 2.15.

Alternatives

An alternative to the use of the ethylbenzene hydroperoxide is tertiary-butyl hydroperoxide obtained from isobutane and dioxygen. The product alcohol is converted with methanol to MTBE (methyl tertiary butylether).

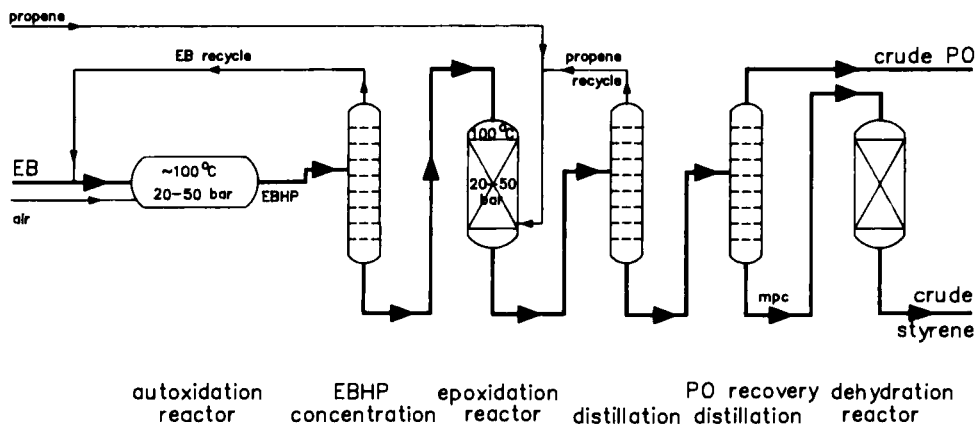
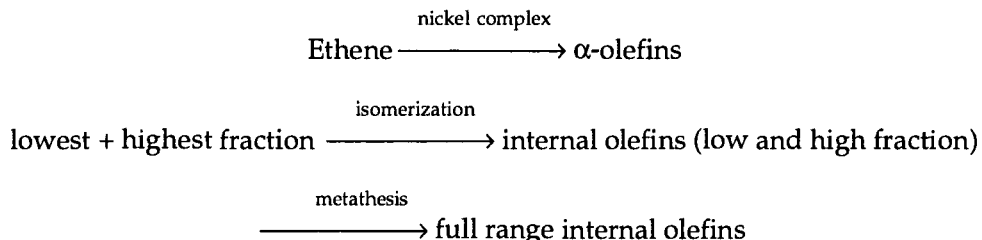


Fig. 2.15. Simplified flow diagram of the SMPO process.

2.8 HIGHER OLEFINS

Overall Reaction



Feedstock

Ethene from oil refinery crackers.

Product Use

The desired α -alkenes in the C_{10} – C_{20} range are used as feedstock in the production of detergent alcohols and in the synthesis of lubricants, the C_6 – C_{10} alkenes are used as plasticizer alcohols in phthalates for PVC, and as comonomers in low-density polyethylene, and a variety of other products. The internal by-products are mainly used for the production of alcohols via a cobalt-catalyzed hydroformylation.

Scale

The typical size of the Shell process plant described here is 250,000 tons per year. The total production of higher olefins includes several alternative routes

and is estimated to be 2 million tons annually. A large part of the alkenes is produced for captive use.

Process Description

Many transition metal hydrides will polymerize ethene to polymeric material or, alternatively, dimerize it to butene. Fine-tuning of these catalysts to one that will give a mixture of, say, predominantly C₁₀–C₂₀ oligomers is not at all trivial. Nickel complexes have been extensively studied by Wilke and his coworkers for their activity as alkene oligomerization catalysts. In the late sixties Keim and coworkers at Shell discovered a homogeneous nickel catalyst which selectively oligomerizes ethene to higher homologues. A simplified flow diagram is shown in Fig. 2.16. The catalyst is prepared in a prereactor from nickel salts with boron hydrides as the reducing agent under a pressure of ethene, and a ligand is added. Polar solvents, such as alcohols (1,4-butanediol), are used for the dissolution of

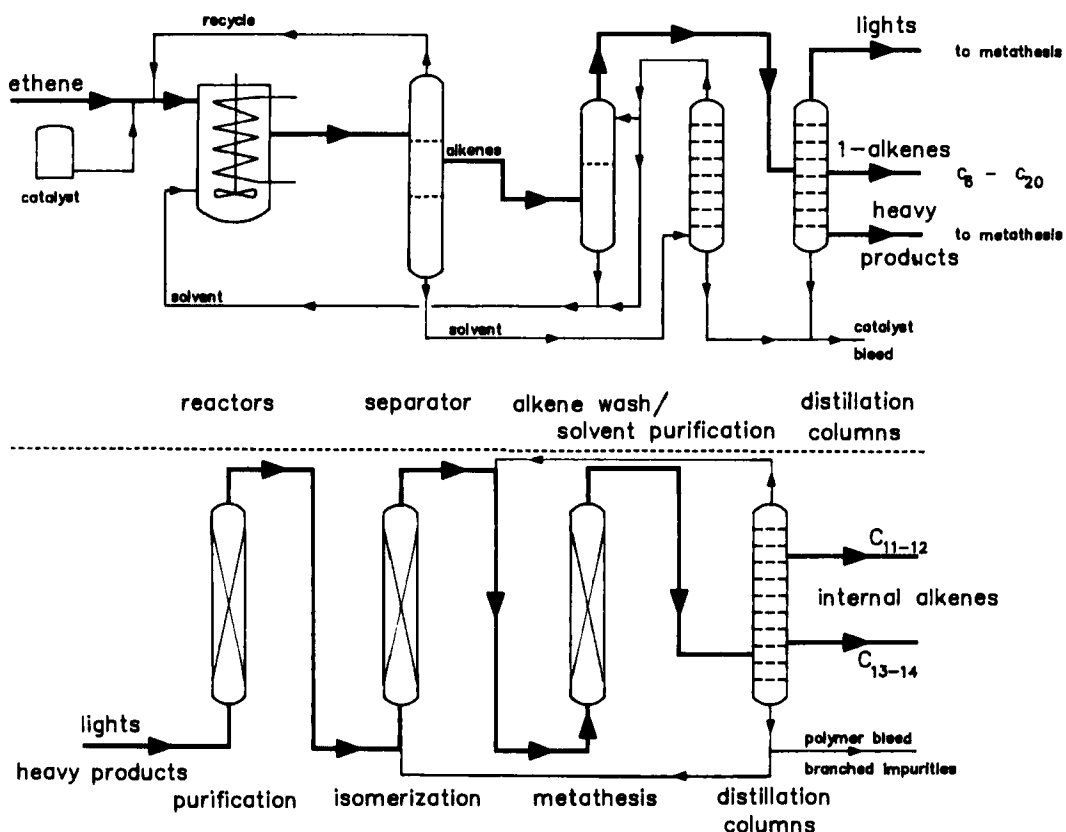


Fig. 2.16. Shell higher olefins process.

the catalyst. The catalyst solution and ethene are led to the reactor, a stirred autoclave, which is maintained at 80–120°C and 100 bar of ethene. The product alkenes are insoluble in the alcohol and phase separation takes place. After settling, the alcohol layer goes to a regeneration unit. The alkene layer is washed and ethene is recycled to the reactor. The products are distilled and the desired fractions are collected. The lower alkenes, the composition of which depends on the demand, and the heavy alkenes must be 'disproportionated' to give the full range of alkenes. Direct metathesis of the higher and lower 1-alkenes is not the way to go, since metathesis of e.g. C₂₂ and C₄ 1-alkenes would give ethene and an internal C₂₄, which is no improvement. The light and heavy alkenes are sent to an isomerization reactor after having passed a purification bed, a simple absorbent to remove alcohol and ligand impurities. The isomerized mixture is then passed over a commercial molybdenum metathesis catalyst (CoMo), also in a fixed bed reactor, to give a broad mixture of internal alkenes. After distillation the C_{11–13} fraction ($\pm 15\%$) is used as a feedstock for alcohol production via cobalt catalysts (hydroformylation and reduction). The product is now a mixture of internal, linear alkenes. The bottom and the top ends of this mixture are again recycled, and eventually all material leaves the isomerization/metathesis plant as internal C_{11–13} alkenes. This 'by-product' constitutes a large part of the production, and only half of the production or less amounts to the more valuable 1-alkenes. In spite of the high selectivity of the oligomerization reaction, there is a build-up of the branched alkenes in the isomerization–metathesis recycle, which may be as high as 50%. A bleed stream of the heavies controls the amount of branched material and the amount of (continuously growing) polymers.

Alternatives

Two aluminium-based processes are in use. The one-step process is operated at high temperature and with aluminium alkyls as the catalyst. This process resembles the nickel process discussed above; as a matter of fact Ziegler's group was working with this aluminium catalyst when they accidentally discovered the influence of nickel which, under these drastic conditions, gave the unwanted butenes! The second aluminium-based process is a two-step process that employs aluminium stoichiometrically in each pass; the alkyls are grown at a lower temperature, decomposed in the next reactor at higher temperature, and the aluminium complexes are recycled. This procedure leads to 'peaking' in the C_{10–C₁₆} range.

Higher alkenes can be obtained from thermal cracking of wax, and although a thermodynamic mixture of internal alkenes might have been expected, the wax-cracker product contains a high proportion of 1-alkenes, the kinetically controlled product. For the cobalt-catalyzed hydroformylation the nature of the alkene mixture is not relevant, but for other derivatizations the isomer composition is

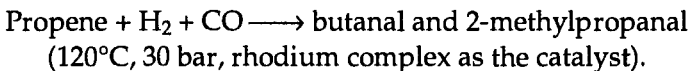
pivotal to the quality of the product. Another process involves the catalytic dehydrogenation of alkanes over a platinum catalyst.

Catalyst

The oligomerization catalyst is a homogeneous nickel complex of a phosphino-carboxylic acid. The other catalysts are fixed bed catalysts: a Co/Mo oxide for the metathesis reaction and a solid catalyst for the isomerization.

2.9 RHODIUM CATALYZED HYDROFORMYLATION OF PROPENE

Overall Reaction



Feedstock

Propene from oil refinery crackers, and syngas from coal or natural gas.

Product Use

Butanal is reduced to 1-butanol, which is used as a solvent. Butanal is dimerized with base to give 2-ethylhexan-1-ol which is used as the phthalate ester in PVC as a plasticizer.

Scale

The estimate is that 3 million tons of butanal are produced annually via the process described here.

Process Description

The low pressure oxo process was jointly developed by Union Carbide, Davy Powergas (Davy McKee), and Johnson Matthey. The latter two companies possess the rights of the Wilkinson patents. The catalyst is a rhodium complex, with a large excess of triphenylphosphine. Temperature and pressure have to be controlled very carefully because the linearity strongly depends on these parameters. Ligand and rhodium (300 ppm) are very sensitive to impurities and the feed must be very thoroughly purified. The rhodium stays in the reactor, apart from a small purification cycle, employed for the reactivation of inactive rhodium

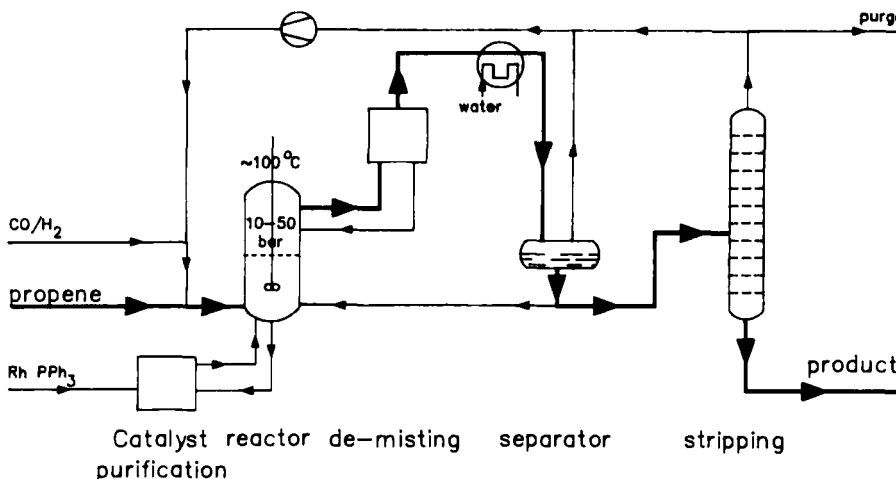


Fig. 2.17. Low pressure rhodium hydroformylation.

complexes, the removal of heavy ends and ligand decomposition products that slowly build up. The gases are led into the reactor at the bottom via a sprinkler (see Fig. 2.17). The alkene conversion per pass is estimated to be 30%, and the propene is recycled. Only propene is hydroformylated with the use of this process; high-boiling alkanals cannot be removed with the gases in this manner. The demister is a crucial part of the system; the fine droplets which might be present in the gas will, of course, contain rhodium. In view of the high costs this should be transferred back into the reactor very rigorously. After the product has condensed and separated from the gaseous feedstock in the separator the butanal, containing a few percent 2-methylpropanal, is led to the distillation column. The flow to the reactor from the separator must maintain the minimum liquid level in the reactor. The small catalyst recycle is necessary because slow decomposition of the ligand occurs. Triphenyl-phosphine decomposes in the rhodium catalyzed process to a phenyl fragment and a diphenylphosphido fragment. Diphenylphosphide forms very stable, though inactive rhodium complexes. Impurities in the feed may also cause the formation of inert rhodium complexes. A variety of reagents can be applied for the regeneration of the inactive complexes to the active $\text{HRh}(\text{CO})(\text{PPh}_3)_3$ precursor.

Alternatives

The alternative processes include cobalt-catalyzed hydroformylation and similar rhodium-based processes. Hydroformylation with cobalt requires much higher temperatures ($140\text{--}170^\circ\text{C}$) and pressures (70–200 bar). The activity ratio of rhodium and cobalt may be of the order of 1000 but the costs of the metals

counterbalance this effect. The selectivity of the rhodium catalyst is of the order of 99% or higher, whereas certain cobalt catalysts may show a selectivity as low as 90%. The by-products are alkanes, through hydrogenation of the feedstock, and heavy ends through condensation of the aldehyde products. Cobalt still is the preferred catalyst for the hydroformylation of internal higher alkenes to detergent aldehydes (alcohols). In the eighties a new process has come on stream employing a two-phase system with rhodium in a water phase and the substrate and the product in an organic phase. The catalyst used is a rhodium complex with a sulphonated triarylphosphine, which is highly water soluble. The process has been commercialized by Ruhrchemie for the production of butanal from propene, after the initial work had been done by workers at Rhone-Poulenc.

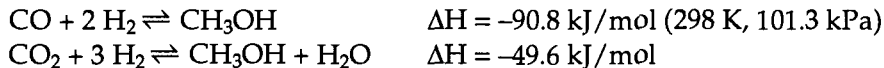
Recently, Union Carbide has announced the replacement of the triphenylphosphine ligand by bulky phosphites. The new catalysts lead to higher reaction rates, selectivity and catalyst stability and may also be of interest for the hydroformylation of 2-butenes.

The Catalyst

With all the characteristics of the cobalt process in mind, it can be seen that there was a sizable incentive to improve on this performance. Fundamental work by Wilkinson demonstrated that rhodium triphenylphosphine catalysts allowed the operation of the hydroformylation reaction at much lower pressure (1 bar was reported by Wilkinson) which consequently lead to the hope of much lower capital and operating costs. The selectivity was also reported to be considerably higher; virtually no hydrogenation was observed and the linearity was in some cases as high as 90%. A convenient catalyst precursor is $\text{RhH}(\text{CO})(\text{PPh}_3)_3$. Under ambient conditions this will slowly convert 1-alkenes into the expected aldehydes. Internal alkenes undergo hardly any reaction and, in contrast to the cobalt catalyst, it has little isomerization activity. At higher temperatures pressures of 10 bar or more are required. Unless a large excess of ligand is present the catalyst will also have some isomerization activity, but the internal alkenes thus formed will not be hydroformylated. This makes the rhodium catalyst less suitable for the conversion of alkenes other than propene. Propene hydroformylation can be performed with a linearity ranging from 60 to 95%, depending on the phosphine concentration. At very high phosphine concentration the rate is low, but the linearity attains its maximum value. The commercial process presumably operates around 30 bar, at 120°C, at high phosphine concentrations, and linearities around 92%. The estimated turnover frequency of mols of product per mol of rhodium complex per hour is of the order of 300. Low ligand concentrations, with concomitant low linearities (70%), will give turnover frequencies of the order of 10,000 at 10 bar and 90°C.

2.10 METHANOL SYNTHESIS

Overall Reaction



Feedstock

Synthesis gas (CO/H₂) manufactured by reforming of a hydrocarbon, usually natural gas.

Product Use

Methanol is one of the most important chemicals. The major application is in the chemical industry, where it is used as a solvent or as an intermediate. It is increasingly used in the energy sector. A survey of the most important reactions is given in Fig. 2.18.

Scale

Methanol is a major bulk chemical. In 1989 the production capacity exceeded 21×10^6 ton/y.

Process Description

The thermodynamic equilibrium is most favourable at high pressure and low temperature. The methanol synthesis process was developed at the same time as NH₃ synthesis. In the development of a commercial process for NH₃ synthesis it was observed that, depending on the catalyst and reaction conditions, oxygenated products were formed as well. Compared with ammonia synthesis, catalyst development for methanol synthesis was more difficult because selectivity is crucial besides activity. In the CO hydrogenation other products can be formed, such as higher alcohols and hydrocarbons that are thermodynamically favoured. Figure 2.19 illustrates this.

It is clear that methanol is less stable than many possible by-products, such as methane. The catalyst has to be selective. The selectivity of modern catalysts is above 99%. The original catalysts were active only at high temperature (300–400°C). The pressure applied was 25–35 MPa. Until the end of the 1960s basically the original catalyst was used. More active catalysts were known, but they were not resistant to impurities such as sulphur. In modern plants the synthesis gas is very pure and very active catalysts can be used. This has led to 'low pressure plants' (260°C, 50–100 bar). The temperature is critical. A low temperature is favourable from a thermodynamic point of view.

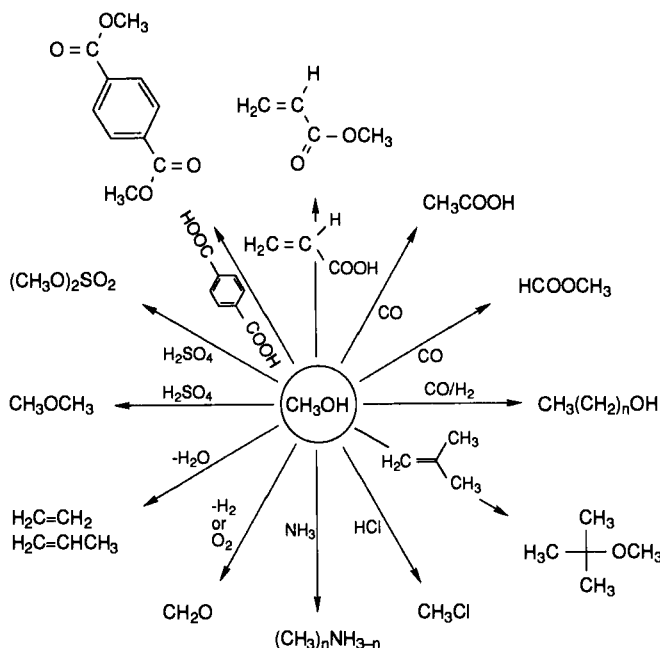


Fig. 2.18. Reactions of methanol.

Methanol production plants consist of three parts:

- production of synthesis gas;
- synthesis of methanol;
- processing of the crude methanol produced.

The composition of synthesis gas depends on the feedstock used. When naphtha is the raw material, the stoichiometry is about right. However, when CH_4 is used, H_2 is in excess. In practice the excess of H_2 is burnt as fuel or CO_2 is added to the process in order to convert all H_2 into methanol. In general the last approach is the preferred one.

Most modern processes are low pressure processes. Plant capacities range from 150–3000 tons/day. The plants differ mainly in reactor design and, interrelated with this, in the way the heat produced by the reaction is removed. In the ICI process an adiabatic reactor is used with a single catalyst bed. The reaction is quenched by adding cold reactant gas at different heights in the catalyst bed. The temperature profile in the bed has a sawtooth profile. A flow scheme of the ICI process is given in Fig. 2.20.

The product mixture leaving the reactor flows through heat exchangers in order to heat the reactant mixture to the desired temperature. Subsequently, the mixture is further cooled and raw methanol condenses while the unconverted synthesis gas is recycled to the reactor. The raw methanol is purified by distillation.

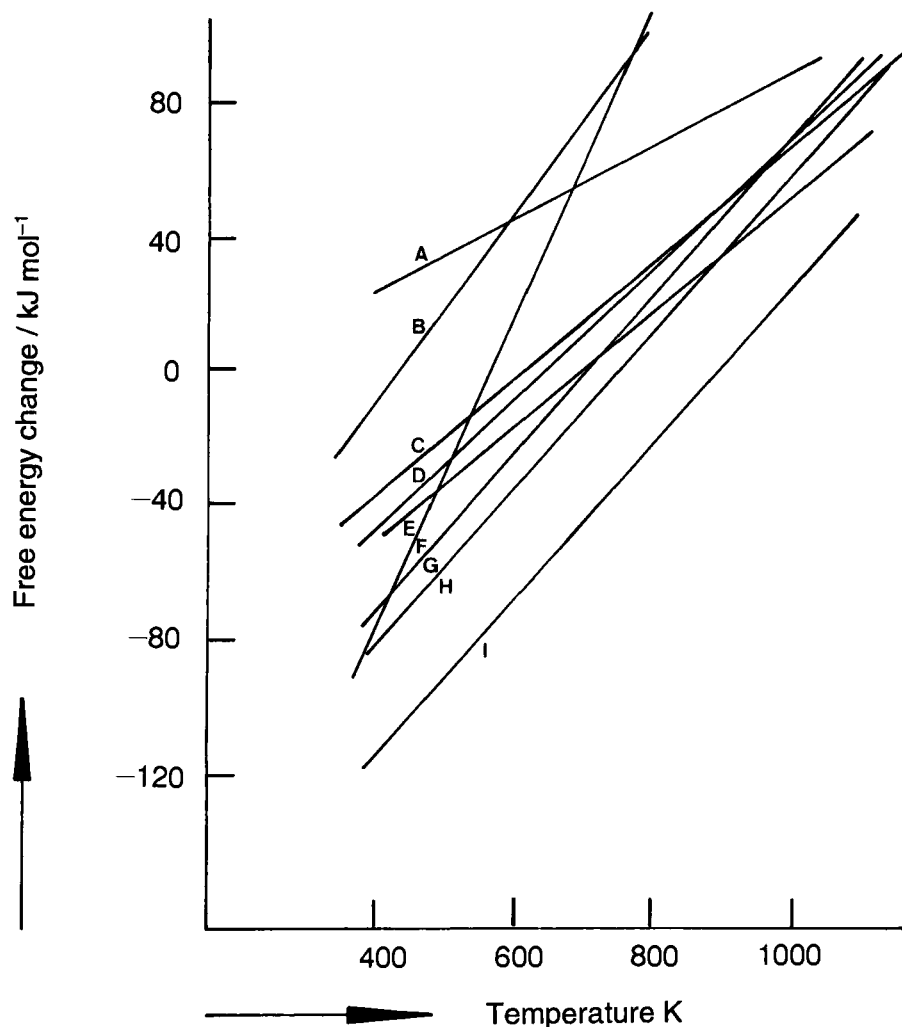


Fig. 2.19. Standard free energies of formation of hydrocarbons and alcohols from carbon monoxide and hydrogen with water as by-product. A, ethanol; B, methanol; C, acetylene; D, benzene; E, propylene; F, ethylene; G, propane; H, ethane; I, methane [7].

In the Lurgi process a cooled tube reactor is applied. The catalyst particles are located in the tubes and cooling takes place by boiling water. The most important difference between the two reactor types is the temperature profile. In the Lurgi reactor it is much flatter than in a quench reactor.

In the Haldor Topsoe process several reactors are used, arranged in series. The heat of reaction is removed by intermediate coolers. The synthesis gas flows radially through the catalyst beds.

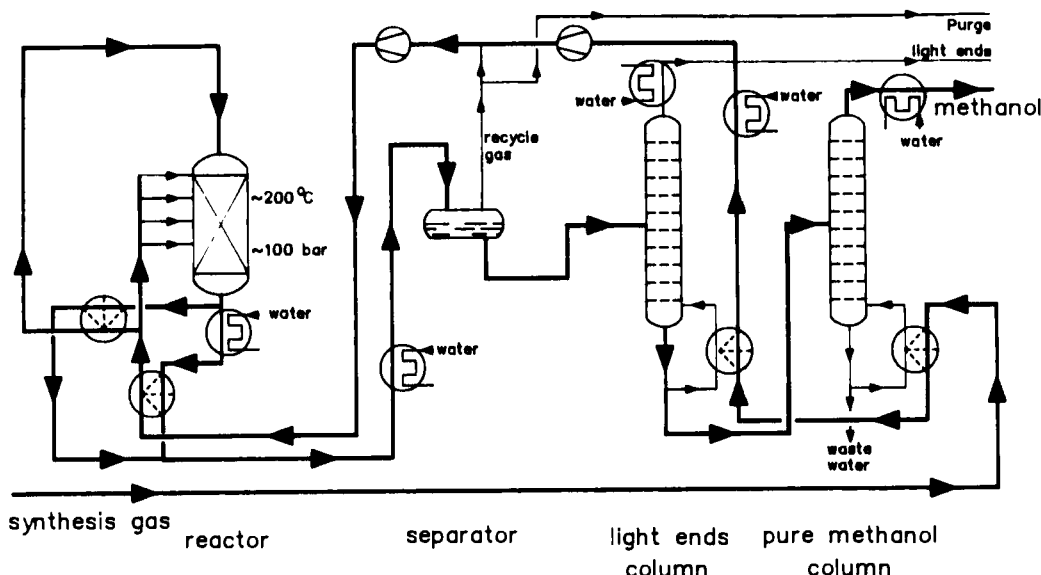


Fig. 2.20. The ICI low-pressure methanol process.

Deactivation will always occur. The usual practice (increasing temperature) is not recommended because of the sensitivity of the catalyst to sintering. Hence, the pressure is increased to compensate for the decline in activity.

Alternatives

Although a classical process, research and development are still being carried out, aiming at the realization of novel processes. These are based either upon shifting the equilibrium by removing the product or by developing a dramatically improved catalyst, permitting operating at much lower temperature.

Catalysts

Originally, a catalyst based on chromia and zinc oxide was developed. In fact, during the first 40 years this catalyst was applied without fundamental changes. In 1966 ICI introduced a Cu/ZnO/Al₂O₃ catalyst with much higher activity. This catalyst allowed reaction temperatures lower than 300°C, affording a commercial process at much lower pressure: 50–100 bar instead of the 250–350 bar used in the older process.

2.11 MALEIC ANHYDRIDE

Overall Reaction



Feedstock

Butane and butenes from refinery crackers and natural gas. Since 1985 butane was introduced to replace benzene as the feedstock. The first commercial production, based on benzene, started in 1930.

Product Use

Maleic anhydride is an important intermediate in the chemical industry [8–9]. It is used in polycondensation and addition reactions. The end products of these reactions are polyesters, alkyd resins, lacquers, plasticizers, copolymers and lubricants. For example, the copolymer of styrene and maleic anhydride is an engineering plastic.

Scale

The typical size of the plant of the process described here is 20,000–30,000 tons per year. World production is 0.5 million tons per year.

Process Description

The commercial processes are based on fixed-bed technology. Tubular reactors are used in order to obtain good heat transfer. A fixed-bed reactor, however, is not optimal. The thermal characteristics of the reaction network are highly unfavourable; the reactions are exothermic, and intermediate products are much more reactive than butane while hot spots lead to total combustion. Low feed concentrations and an extensive heat transfer surface area are required. The butane concentration in the feed is only 1.8%, which is below the explosion limit. The butane process produces more water than the benzene process and only 35% of the maleic anhydride yield can be recovered directly from the product stream. The remainder is condensed together with water leading to maleic acid. This is then dehydrated at >130°C. The product is purified by fractional distillation. Alternatively, maleic anhydride is condensed from the product stream in a high boiling organic solvent such as phthalic acid or tetra- or hexahydrophthalic acid. The waste gases are sent to an incineration unit.

Catalysts

The basis of the commercial success was the development of highly selective catalysts [10-12], i.e. the vanadium phosphorus oxide (VPO) catalyst which is prepared from V_2O_5 digested in a refluxing acidic solution (aqueous HCl or butanol or benzyl alcohol) and orthophosphoric acid. The precipitate is filtered off and dried below 200°C. The solid is calcined in air at 400°C. A high mechanical strength is required for VPO used in a fluid-bed operation and therefore silica is also incorporated. After calcination a thin layer of silica is located at the periphery of the particles which are now very durable while the silica layer is porous to reactants and products. There are many promoters for the VPO catalysts, the most important being Zn, U, Ti, Co, Mo, Mg and Zr. There seems to be a general consensus that there is an optimum averaged valence state of vanadium, which is slightly higher than 4 (the alcohols may act as reductors during the preparation). Figure 2.21 gives a schematic view of a spray-dried particle prepared from colloidal silica and polysilicic acid.

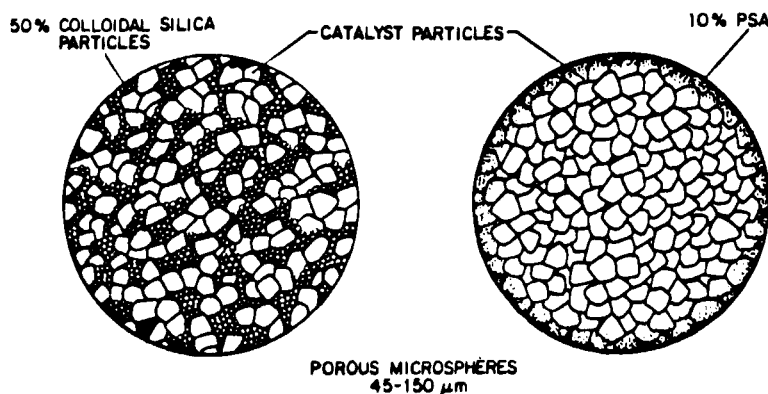
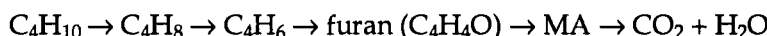


Fig. 2.21. Spray dried particles prepared from 50% colloidal silica (~20 nm diameter) and 10% silica derived from polysilicic acid [13].

The elucidation of the kinetic network has received a lot of attention. The following simplified scheme has been proposed:



From the extensive literature it can be concluded that a Mars-van Krevelen mechanism applies; the oxidation of the hydrocarbons is achieved using the surface oxygens and the reoxidation of the catalysts is accomplished by reduction of oxygen at separate sites.

Alternatives

In the past the most important process was based on the partial oxidation of benzene. Typical production units are 10,000–20,000 tons/y, which is smaller than those using butane. Benzene gives rise to smaller amounts of water and more maleic anhydride can be produced in the first condensation step.

Fluidized-bed reactors have proposed as alternatives to circumvent the problems mentioned above (ALMA process, Alusuisse, Lummus). These allow better control of the temperature and higher feed concentrations. In addition the reactor system is less prone to explosions. A major problem in this reactor is attrition of the catalyst. In recent literature this problem has received a great deal of attention. A second drawback of the fluidized-bed reactor is the intrinsic mixing behaviour, which lowers the conversion.

An interesting option (Monsanto, Du Pont) involves the use of a riser reaction as shown in Fig. 2.22. The configuration is analogous to a modern FCC unit (see Fig. 2.3). In the riser reactor the (oxidized) catalyst transfers oxygen to the butane substrate giving maleic anhydride. The catalyst is separated from the product in

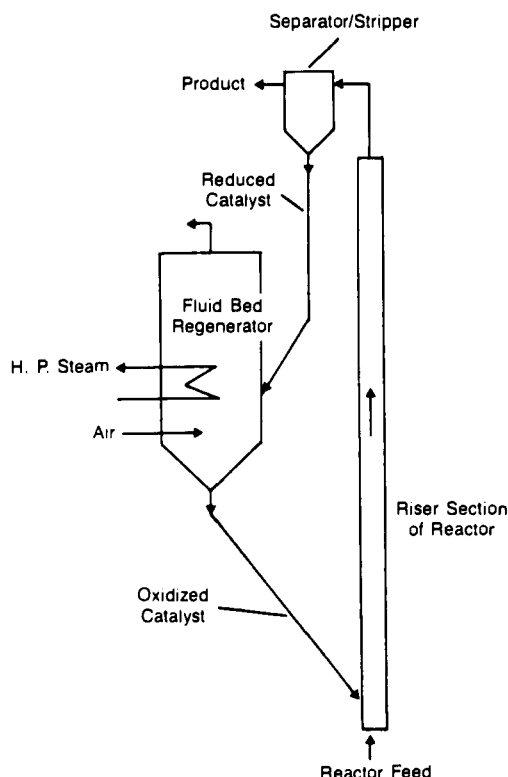


Fig. 2.22. Riser reactor for selective oxidation [10].

a stripping zone. Subsequently the catalyst is reoxidized in the fluid-bed reactor. Data from pilot studies indicate that the catalyst is able to transfer an amount of oxygen to the substrate equivalent to a monolayer capacity, thus confirming the Mars–van Krevelen mechanism for this reaction. Separation of the two steps enables a fine tuning of the reaction conditions:

- the oxidation is performed in the absence of molecular oxygen which improves the selectivity (75% has been reported [4]). Moreover the reaction mixture is always out of the explosion zone.
- residence times in the reactor and the regenerator can be chosen independently and, as a consequence, optimal conditions for selectivity can be obtained.

2.12 METHYL *t*-BUTYL ETHER (MTBE)

Overall Reaction

Addition of methanol to isobutene to yield MTBE (80–110°C, 7–20 bar, ion exchange resin in the H⁺ form as the catalyst).

Feedstock

Isobutene is present in refinery streams. Especially C₄ fractions from catalytic cracking are used. Such streams consist mainly of *n*-butenes, isobutene and butadiene, and generally the butadiene is first removed by extraction. For the purpose of MTBE manufacture the amount of C₄ (and C₃) olefins in catalytic cracking can be enhanced by adding a few percent of the shape-selective, medium-pore zeolite ZSM-5 to the FCC catalyst (see Fig. 2.23), which is based on zeolite Y (large pore). Two routes lead from *n*-butane to isobutene (see Fig. 2.24); the isomerization/dehydrogenation pathway (upper route) is industrially practised. Finally, isobutene is also industrially obtained by dehydration of *t*-butyl alcohol, formed in the Halcon process (isobutane/propene to *t*-butyl alcohol/propene oxide). The latter process has been mentioned as an alternative for the SMPO process (see Section 2.7).

Product Use

The main use of MTBE is as an octane booster in gasoline formulations. Table 2.1 (above) compares octane number and boiling points of some tertiary ethers and hydrocarbons. The volatility is another important property of gasoline components. In fact, the lower volatility of ETBE is an advantage with respect to MTBE. Another (smaller scale) application of MTBE is the synthesis of high purity isobutene by cracking MTBE over amorphous silica–alumina. This isobutene serves as a monomer for polyisobutene.

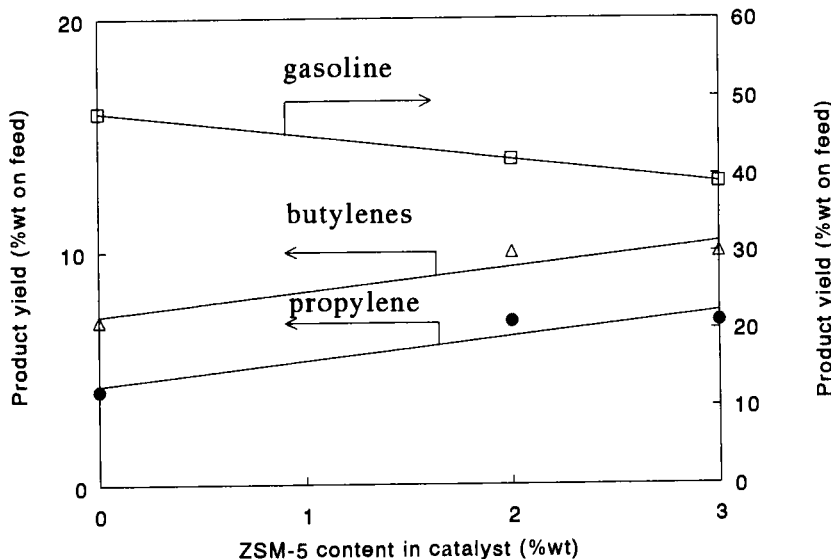


Fig. 2.23. Product yields in catalytic cracking vs. ZSM content in FCC catalyst.

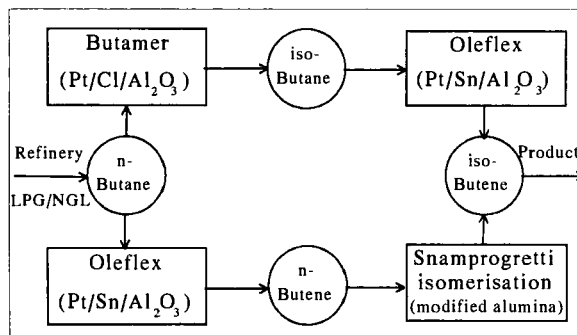


Fig. 2.24. Two routes for isobutene from butane.

Scale

MTBE is the fastest growing chemical of the last decade. Presently, over 11 million t/y capacity has been installed. Further growth is foreseen. Essentially the success of MTBE is founded (i) on its outstanding antiknock properties as a gasoline component, and (ii) its function as a key product in the C₄ hydrocarbon processing within a refinery.

Process Description

The synthesis of MTBE is carried out in the liquid phase over a fixed bed of ion

exchange resin in the H⁺ form. The rate of reaction of isobutene with methanol is much higher than that of the *n*-butenes (isobutene forms a relatively stable tertiary carbenium ion in the first step), which enables the selective conversion of isobutene in the presence of the *n*-butenes. In fact, streams with an isobutene content as low as 5% can be converted.

A C₄ fraction and methyl alcohol (molar ratio methyl alcohol:*i*-C₄ = 1:1) is preheated to about 70°C before being sent to the reactor containing a fixed bed of sulphonated polystyrene resin. The reaction is exothermic ($\Delta H_{298} = -37.7 \text{ kJ/mol}$) and the heat produced is removed by means of cooling jackets so as to keep the temperature below 120°C. The reaction mixture from the top of the reactor is distilled and any unreacted butene is collected overhead with the azeotropic amount of methyl alcohol. The bottom contains pure MTBE. The distillate, together with additional methyl alcohol, is passed to a second reactor. The products from the second stage are extracted with water to remove residual methyl alcohol. The water-methyl alcohol solution is distilled to recover methyl alcohol, which is recycled.

The second stage in the process is required because the MTBE formation is an equilibrium reaction. The temperature needed (~100°C) to achieve a sufficiently high *rate* of conversion means a decrease in isobutene equilibrium conversion ($X_{iB} = 0.9$ at 65°C, $X_{iB} = \sim 0.75$ at 100°C). The main side reaction in the MTBE process is the dimerization of isobutene towards di-isobutene (two isomers). Side reactions with essentially no significance are the formation of *t*-butyl alcohol (due to the presence of water as feed impurity), the formation of dimethyl ether from methyl alcohol, and the oligomerization of isobutene towards tri- and tetramers. A (three stage) process is also in operation which tolerates butadiene. The butadiene/methyl alcohol reaction is faster than that of the *n*-butenes but considerably slower than that of isobutene, so high isobutene selectivity can still be obtained. Similar liquid phase processes, as described above for MTBE, are recommended for the reaction of isopentenes and methanol to yield TAME and for the conversion of isobutene and ethanol to give ETBE. The use of higher iso-olefins — as for TAME — leads to somewhat lower yields of methyl *t*-alkyl ethers than are obtained for MTBE. As an alternative to fixed bed catalytic conversion the formation of MTBE by 'reactive distillation' is applied. Here *in situ* separation of feed and product components is aimed at, leading to a higher isobutene conversion. A flow scheme is given in Fig. 2.25.

The Catalyst

The catalysts used industrially in the MTBE process are sulphonated polystyrene resins of the macroreticular type. These strongly acidic materials are prepared by copolymerizing styrene and *p*-divinylbenzene in the presence of an organic compound that is a good solvent for the monomers but a poor swelling

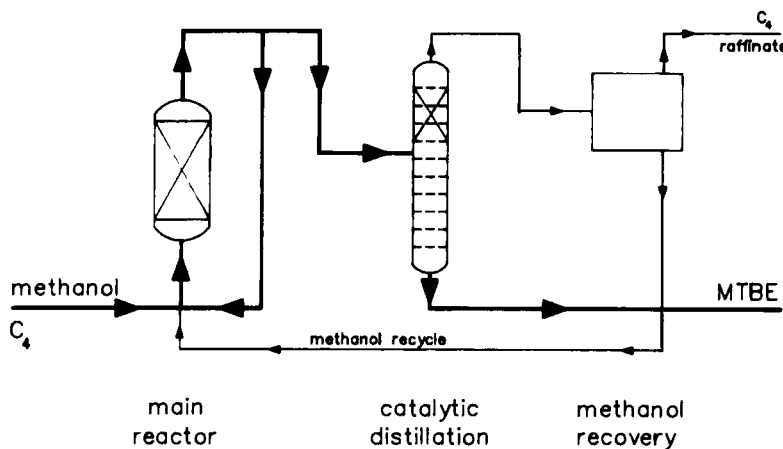


Fig. 2.25. Flow scheme of the MTBE process with catalytic distillation.

agent for the polymer. Opaque round particles are obtained, which are subjected to sulphonation.

Amberlyst 15 (A15) is often used, and is prepared by using some 20% (wt.) of divinylbenzene in the formulation. The highly crosslinked product has a surface area of ~50 m²/g and an exchange capacity of 4–5 meq/g resin.

In the preparation of MTBE it is accepted that methyl alcohol adsorbs more strongly but diffuses more slowly in the domain of the resin than the less polar isobutene. In order to keep the side reaction (isobutene to di-isobutene) at a low level, relatively small resin particles should be used.

Other catalysts for the isobutene/methyl alcohol reaction include: sulphuric acid (homogeneous), heteropolyacids (homogeneous or heterogeneous) and zeolites (heterogeneous).

2.13 CAPROLACTAM

Feedstock

Benzene or toluene via cyclohexanone (see Fig. 2.27).

Product Use

Caprolactam is the raw material for Nylon-6 (see Fig. 2.26).

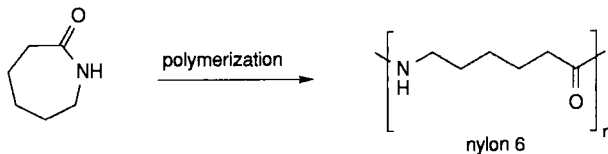


Fig. 2.26. Conversion of caprolactam into Nylon-6.

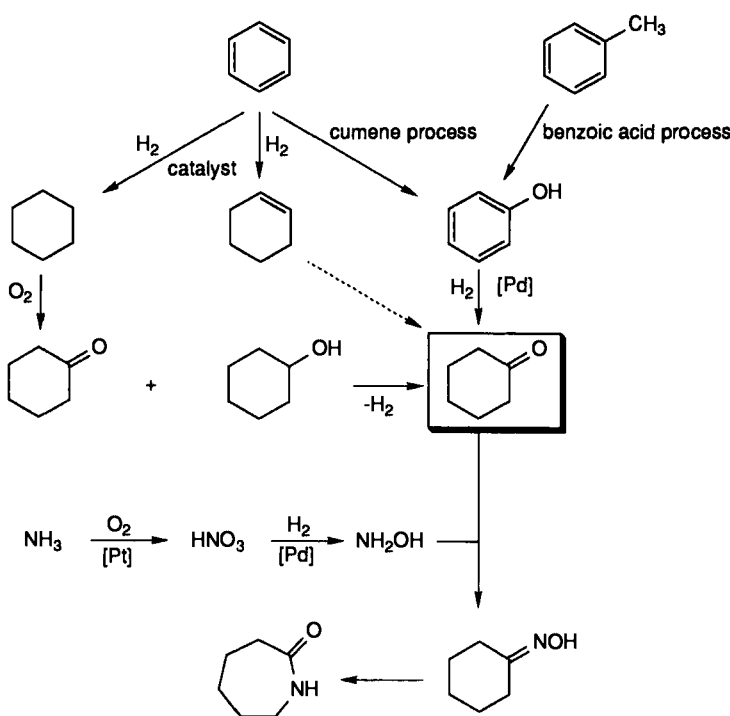


Fig. 2.27. Caprolactam manufacture.

Scale

Worldwide annual production is ca. 2 million tons.

Process Description

Several processes are used for the industrial production of caprolactam. Generally cyclohexanone is the key intermediate and it is produced by catalytic hydrogenation of phenol (ex benzene or toluene) or the catalytic autoxidation of cyclohexane (from benzene hydrogenation) as shown in Fig. 2.27.

In the phenol hydrogenation process phenol is fed in the gas phase with hydrogen at 140–170°C through a catalyst bed at atmospheric pressure. The catalyst generally consists of 0.2–0.5 wt.% palladium on a zeolite carrier. The yield exceeds 95% at quantitative conversion. Figure 2.28 shows the flow diagram for the process.

In the cyclohexane oxidation route cyclohexane is oxidized with air at 125–126°C and 8–15 bar in the liquid phase using Co or Mn naphthanates as the catalyst. This affords a mixture of cyclohexanol and cyclohexanone via a classical free radical autoxidation mechanism. Cyclohexane conversion is limited to 10–12% in order to minimize by-product formation via further oxidation. The selectivity to cyclohexanol/cyclohexanone is 80–85%.

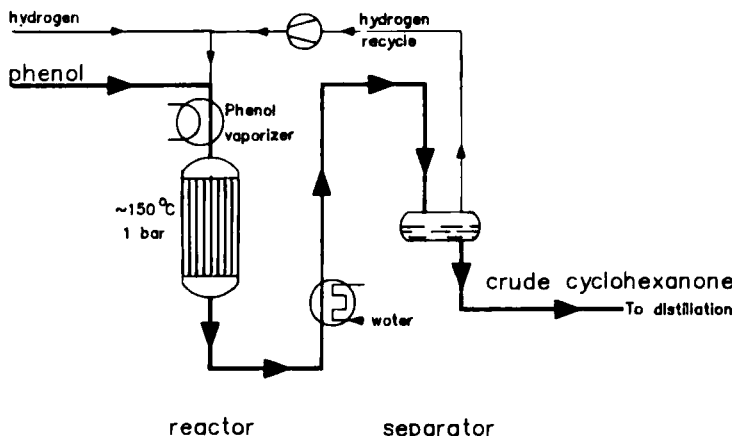


Fig. 2.28. Flow diagram for cyclohexanone production from phenol.

The unreacted cyclohexane is distilled off and recycled. The ca. 1:1 mixture of cyclohexanol and cyclohexanone is then subjected to dehydrogenation over a palladium catalyst (the same catalyst as is used in phenol hydrogenation) to give pure cyclohexanone.

In classical processes cyclohexanone is converted to the corresponding oxime by reaction with hydroxylamine (see Fig. 2.27). The oxime subsequently affords caprolactam via the Beckmann rearrangement with sulphuric or phosphoric acid. Alternatively, in a more recent development, not yet commercialized, a mixture of cyclohexanone, ammonia and hydrogen peroxide is directly converted to cyclohexanone oxime over a titanium(IV)-silicalite (TS-1) catalyst. This route is more direct than the classical route and reduces the amount of salt formation but it involves the use of a more expensive oxidant (H_2O_2 rather than O_2).

2.14 VITAMIN A INTERMEDIATES

Feedstock

The major feedstocks in the modern routes to key vitamin A intermediates are butadiene, isobutene and formaldehyde.

Product Use

Vitamin A is widely used as a pharmaceutical and a food and feed additive.

Scale

Worldwide production of vitamin A is ca. 3000 tons.

Process Description

Two key intermediates in the production of vitamin A are citral and the so-called C₅ aldehyde. In the modern routes to these intermediates, developed by BASF and Hoffmann-La Roche, catalytic technologies are used (see Fig. 2.29 and 2.30). Thus, in the synthesis of citral, the key intermediate is 2-methyl-1-butene-4-ol, formed by acid-catalyzed condensation of isobutene with formaldehyde. Air oxidation of this alcohol over a silver catalyst at 500°C (the same catalyst as is used for the oxidation of methanol to formaldehyde) affords the corresponding aldehyde. Isomerization of 2-methyl-1-butene-4-ol over a palladium-on-charcoal catalyst affords 2-methyl-2-butene-4-ol. The latter is then reacted with the aldehyde from the oxidation step to form an enol ether. Thermal Claisen rearrangement of the enol ether gives citral (see Fig. 2.29).

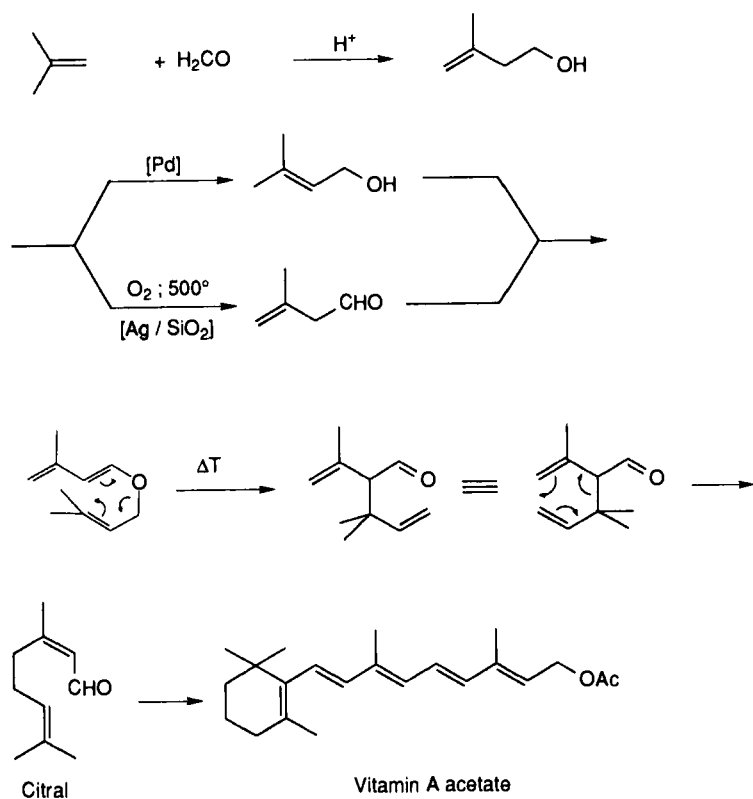


Fig. 2.29. BASF route to citral.

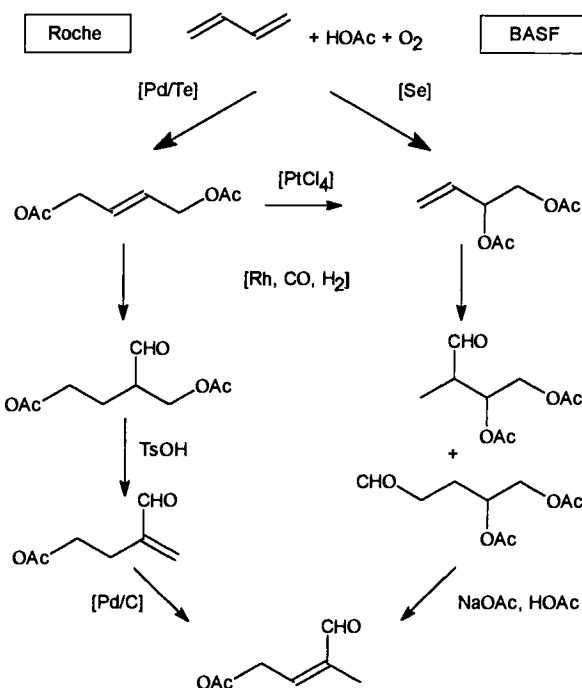


Fig. 3.30. Synthesis of vitamin A intermediate.

The C₅ aldehyde intermediate is produced from butadiene via catalytic oxidative acetoxylation followed by rhodium-catalyzed hydroformylation (see Fig. 2.30). Two variations on this theme have been described. In the Hoffmann-La-Roche process a mixture of butadiene, acetic acid and air is passed over a palladium/tellurium catalyst. The product is a mixture of *cis*- and *trans*-1,4-diacetoxy-2-butene. The latter is then subjected to hydroformylation with a conventional catalyst, RhH(CO)(Ph₃P)₃, that has been pretreated with sodium borohydride. When the aldehyde product is heated with a catalytic amount of *p*-toluenesulphonic acid, acetic acid is eliminated to form an unsaturated aldehyde. Treatment with a palladium-on-charcoal catalyst causes the double bond to isomerize, forming the desired C₅-aldehyde intermediate.

In the BASF process the 1,2-diacetate is the substrate for the hydroformylation step. It can be prepared either directly via oxidative acetoxylation of butadiene using a selenium catalyst or via PtCl₄-catalyzed isomerization of the 1,4-diacetate (see above). The latter reaction affords the 1,2-diacetate in 95% yield. The hydroformylation step is carried out with a rhodium catalyst without phosphine ligands since the branched aldehyde is the desired product (phosphine ligands promote the formation of linear aldehydes). Relatively high pressures and temperatures are used and the desired branched aldehyde predominates. The product mixture is then treated with sodium acetate in acetic acid to effect selective elimination of acetic acid from the branched aldehyde, giving the desired C₅ aldehyde.

2.15 IBUPROFEN

Feedstock

p-Isobutylbenzene (see Fig. 2.31).

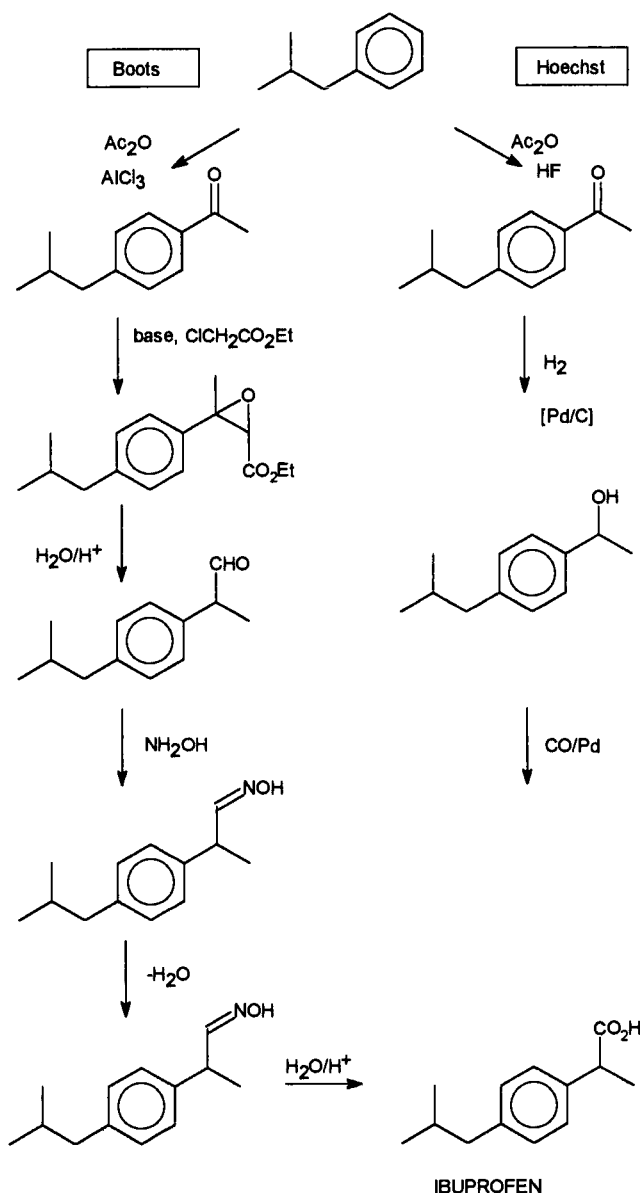


Fig. 2.31. Two routes for the production of ibuprofen.

Product Use

Ibuprofen is an over-the-counter drug that is widely used as an antiinflammatory and a general analgesic, where it competes with aspirin.

Scale

Worldwide annual production is of the order of 7000–8000 tons which is very large for a pharmaceutical.

Process Description

There are basically two processes for the production of ibuprofen (see Fig. 2.31). Both involve a Friedel–Crafts acylation as the first step. In the classical route, developed by Boots, the *p*-isobutylacetophenone is subsequently converted to ibuprofen in five steps involving conventional organic chemistry. In the catalytic route, more recently developed by Hoechst, the *p*-isobutylacetophenone is converted in two steps.

The first step is catalytic hydrogenation to the corresponding alcohol over a 5% palladium-on-charcoal catalyst in methanol solvent at 30°C and 7 bar. The selectivity is 97% at >99% conversion. In the second step the alcohol is carbonylated at 35 bar CO and 125–130°C in the presence of a PdCl₂(Ph₃P)₂ and HCl as catalyst. Selectivities to ibuprofen are ca. 70% at 99% conversion.

The catalytic route has the advantages of being shorter and producing considerably lower amounts of inorganic salts than the classical route.

REFERENCES

- 1 I. Maxwell, C. Williams, F. Muller and B. Krutzen, *Zeolite catalysis for high quality fuels*, Shell brochure, 1992.
- 2 G.A. Mills and E.E. Ecklund, 'Alternative Fuels', Parts 1 and 2, *ChemTech* (1989) pp. 549 and 626.
- 3 G.M. Wells, *Handbook of Petrochemicals and Processes*, 1991, p. 270.
- 4 M. Iborra, J.F. Izquierdo, J. Tejero and F. Curill, 'Getting the lead out with ethyl *t*-butyl ether', *ChemTech* (1988) 120.
- 5 I.E. Maxwell and W.H.J. Stork, *Stud. Surf. Sci. Catal.*, 58 (1991) 571.
- 6 D.M. Ruthven, *Chem. Eng. Progress*, Feb. (1988) 42.
- 7 T. Sie, *Ind. Eng. Chem. Res.* 31 (1992) 1881.
- 8 G.J. Hutchings, *Appl. Catal.*, 72 (1990) 1–32.
- 9 V.A. Zazhigalov, *Katal.* 27 (1990) 1–20 (in Russian).
- 10 R.M. Contractor and A.W. Slight, *Catal. Today*, 3 (1988) 175–184.
- 11 B.K. Hodnett, *Catal. Rev.-Sci. Eng.*, 27 (1985) 373–424.
- 12 US Patent 3,931,046 (1976).
- 13 R.M. Contractor, H.E. Bergna, H.S. Horowitz, C.M. Blackstone, B. Malone, C.L. Torardi, B. Griffiths, U. Chowdhry and A.W. Sleight, *Catal. Today*, 1 (1987) 54.
- 14 *Eur. Chem. News*, 50 (Dec. 1988) 12, 36.

Chapter 3

Chemical kinetics of catalysed reactions

3.1 INTRODUCTION

Rate expressions are indispensable in the application of catalysed reactions, in the design of chemical reactors, and their process control. Insight into the dependence of the reaction rate on catalyst variables, the temperature and concentrations of reactants, products and other relevant species are needed to predict the sizes of catalytic reactors and the optimum operating conditions.

$$r = f(\text{catalyst}, T, p_i \dots, k_i \dots, K_i \dots, K_{\text{eq}}) \quad (3.1)$$

Catalytic reactions consist of a reaction cycle formed by a series of elementary reaction steps. Hence the rate expression is in general a function of many parameters. In heterogeneously catalysed reactions reactant molecules are adsorbed on the catalyst surface (characterized by equilibrium constants K_i), undergo chemical modifications on the surface to give adsorbed products with rate constants k_i and these products finally desorb. The overall catalyst activity and selectivity is determined by the composition and structure of its surface. Hence it is important to relate constants, such as k_i and K_i with the chemical reactivity of the catalyst surface.

Since many different modes of adsorption and rearrangement of molecule fragments are possible on catalyst surfaces, many reactions can occur in parallel. Therefore these catalysts often have a low selectivity. Selectivity is increased by the use of promoters or catalyst modifiers that create particular surface sites and increase selectivity by suppressing undesired reaction paths.

In homogeneous catalysis ligands play a related role with respect to selectivity. Many different complexes may be formed in a solution; the desired reaction occurs only on a particular one. Ligand choice determines the particular complex formed that results in the desired product.

Complex formation in homogeneous catalysis and adsorption on a catalyst surface share the same principle: the total number of sites is constant. The rate expressions for homogeneous and heterogeneous catalysts therefore have a similar form. Usually, for gas phase reactions, partial pressures are used, whereas concentrations are employed for liquid phase reactions. This only has consequences for the dimensions of the constants in the rate expressions. The following approach to the derivation of these rate expressions can be applied to homogeneous as well as to heterogeneous catalyst systems.

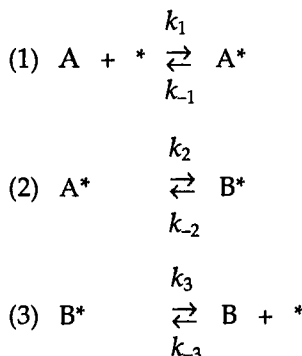
Two principles are important:

- (i) catalysts do not affect the overall equilibrium of a reaction, but only the reaction rate of the reacting molecules;
- (ii) the total number of catalytically active sites is a constant. In heterogeneous catalysis this site density is expressed as the number of sites per kg catalyst or per unit of surface area; in homogeneous catalysis it is expressed as the concentration of catalytically active complex molecules.

The rate expressions should be compatible with these boundary conditions.

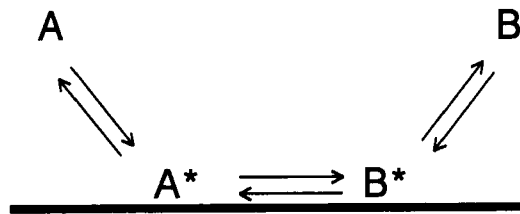
3.2 RATE EXPRESSION (SINGLE SITE MODEL)

Consider the reversible (e.g. isomerization) reaction $A \rightleftharpoons B$ proceeding according to the following three elementary steps (see Fig. 3.1):



This kinetic model can be interpreted as follows:

- a molecule A is adsorbed at an active site * at the catalyst with formation of an adsorbed complex A^* ;
- this adsorbed complex reacts at the active site by rearrangement to an adsorbed complex B^* .
- finally, product B desorbs from the active site, liberating the site for a new catalytic cycle.

Fig. 3.1. Schematic representation of the reaction $A \rightleftharpoons B$.

Since these steps are considered to be elementary processes their rates can be derived directly from their reaction equations.

$$r_1 = k_1 N_T p_A \theta_* - k_{-1} N_T \theta_A \quad (3.2)$$

$$r_2 = k_2 N_T \theta_A - k_{-2} N_T \theta_B \quad (3.3)$$

$$r_3 = k_3 N_T \theta_B - k_{-3} N_T p_B \theta_* \quad (3.4)$$

Here θ_* , θ_A and θ_B represent the fractions of the total number of sites that are vacant, or occupied by A and B, respectively. N_T is the total concentration of active sites present. For this gas phase reaction the partial pressures of A and B are preferred, but in the liquid phase molar concentrations should be used.

Conservation of the number of active sites leads to the site balance expression:

$$1 = \theta_* + \theta_A + \theta_B \quad (3.5)$$

Under steady state conditions the time derivatives are zero. These conditions are often satisfied when flow conditions are used. Therefore:

$$\frac{d\theta_A}{dt} = 0 = k_1 p_A \theta_* - k_{-1} \theta_A - k_2 \theta_A + k_{-2} \theta_B \quad (3.6)$$

$$\frac{d\theta_B}{dt} = 0 = k_{-3} p_B \theta_* - k_{-2} \theta_B - k_2 \theta_B + k_2 \theta_A \quad (3.7)$$

Since all steps are in series the overall rate equals the difference between the forward and the reverse rate of each step.

$$r = r_1 - r_{-1} = r_2 - r_{-2} = r_3 - r_{-3} \quad (3.8)$$

The unknowns θ_* , θ_A and θ_B can be eliminated from Eqns. (3.5–3.7) followed by substitution in Eqn. (3.8). Finally Eqn. (3.9) follows for the reaction rate expression.

$$r = \frac{N_T k_1 k_2 k_3 [p_A - p_B / K_{eq}]}{(k_1 k_3 + k_1 k_{-2} + k_3 k_{-3})p_A + (k_{-1} k_{-3} + k_2 k_{-3})p_B + (k_{-1} k_{-2} + k_{-1} k_3 + k_2 k_3)} \quad (3.9)$$

with $K_{\text{eq}} = K_1 K_2 K_3$ being the overall equilibrium constant for the reaction. N_T represents the total concentration of active sites with possible dimension mol (kg cat) $^{-1}$.

Rate expression (3.9) has been derived for a relatively simple kinetic model by application of the site balance and the steady state hypothesis. More complex models will result in more complex expressions, which are hard to handle. Fortunately, some simplifications can be applied.

3.3 RATE DETERMINING STEP — QUASI-EQUILIBRIUM

The reaction $A \rightleftharpoons B$ proceeds according to three elementary processes in series. Consequently, the net rates of the individual steps are equal to the overall rate. It can be imagined that the forward and reverse rates of two of these steps are relatively large compared with that of the third one. They are so large that, relatively speaking, the forward and the reverse rates are nearly equal. These steps are said to be in *quasi-equilibrium*. The other step is then called the *rate determining step* (rds). Figure 3.2 depicts the case where the surface reaction is rate determining, whereas the adsorption and desorption steps are in *quasi-equilibrium*.

The rate expression is now obtained as follows. Starting with the rate determining step:

$$r = r_2 - r_{-2} = k_2 N_T \theta_A - k_{-2} N_T \theta_B \quad (3.10)$$

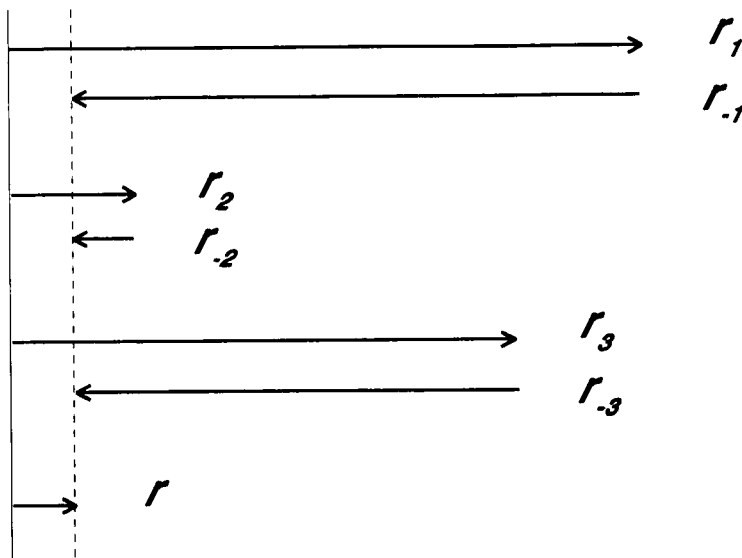


Fig. 3.2. Visualisation of the *quasi-equilibrium* and rate determining steps. The lengths of the arrows are proportional to the rates of the relevant steps.

and using the *quasi*-equilibrium condition:

$$K_1 = \frac{k_1}{k_{-1}} = \frac{\theta_A}{\theta_* p_A} \rightarrow \theta_A = K_1 p_A \theta_* \quad (3.11)$$

$$K_3 = \frac{k_3}{k_{-3}} = \frac{\theta_* p_B}{\theta_B} \rightarrow \theta_B = \frac{p_B \theta_*}{K_3} \quad (3.12)$$

This enables the elimination of the unknown quantities θ_A and θ_B from (3.10). The remaining θ_* can be eliminated by use of the site balance (3.5).

$$\theta_* = \frac{1}{1 + K_1 p_A + p_B / K_3} \quad (3.13)$$

Finally the resulting rate expression for the surface reaction rate determining is given by (3.14).

$$r = \frac{N_T k_2 K_1 [p_A - p_B / K_{eq}]}{1 + K_1 p_A + p_B / K_3} \quad (3.14)$$

In a similar way, if adsorption is rate determining, one can derive:

$$r = \frac{N_T k_1 [p_A - p_B / K_{eq}]}{1 + (1 + 1 / K_2) p_B / K_3} \quad (3.15)$$

and, if desorption is rate determining:

$$r = \frac{N_T k_3 K_1 K_2 [p_A - p_B / K_{eq}]}{1 + (1 + K_2) K_1 p_A} \quad (3.16)$$

If other species also adsorb on the active sites they occupy these catalytic centres and hence lower the reaction rate. The effect of these inhibitors should be included in the rate expression and can be summarised in Eqn. (3.17) for the reaction under consideration:

$$r = \frac{k' [p_A - p_B / K_{eq}]}{1 + K_A p_A + K_B p_B + \sum K_I p_I} \quad (3.17)$$

Here K_A , K_B and K_I represent the adsorption equilibrium constants of the components A, B and I, respectively, if the surface reaction is rate determining; k' represents here the apparent (observed) overall reaction rate constant

3.3 ADSORPTION ISOTHERMS

Reaction step (3.1) represents an adsorption step. Under equilibrium conditions the forward and reverse rates are equal and the equilibrium is described by Eqn. (3.11). This does not mean *per se* that K_1 is constant. It may vary as a function

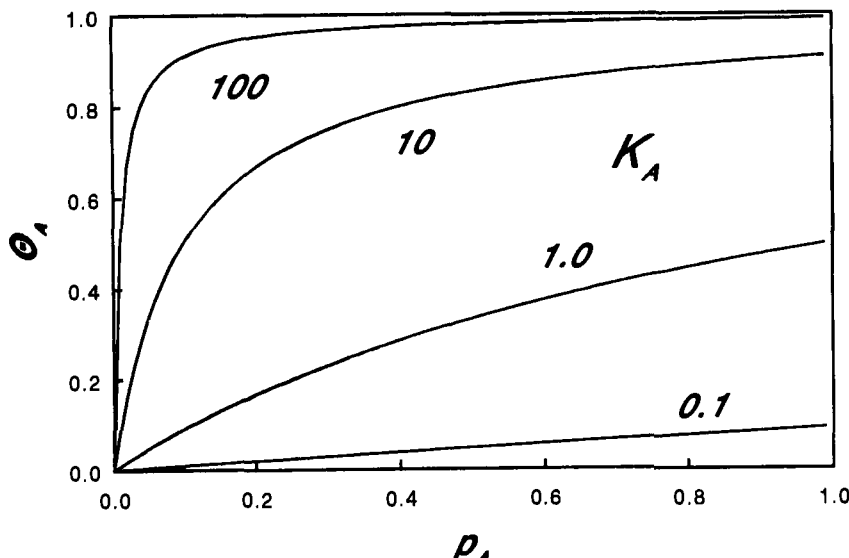


Fig. 3.3. Surface coverage with A as a function of p_A for various values of K_A .

of the surface occupancy for a non-uniform surface, due to the interaction of adsorbed species. In the derivation of rate expressions it is generally assumed that one is dealing with a homogeneous surface.

Under the assumptions that:

- the surface contains a constant number of identical adsorption sites
- a site can contain only one molecule; and
- no interaction takes place between adsorbed molecules; then so-called Langmuir adsorption is operative.

From the foregoing one can easily derive that for the fractional coverage of A in case of a one-component adsorption, Eqn. (3.18) is valid. Figure 3.3 gives a graphical representation for several values of K_A ($= K_1$), the adsorption equilibrium constant of A.

$$\theta_A = \frac{K_A p_A}{1 + K_A p_A} \quad (3.18)$$

In the case of a gas-solid system the partial pressure of a component is usually used.

Three regions can be distinguished for the Langmuir isotherm:

- (i) At low values for $K_A p_A$ a linear relation exists between θ_A and p_A , with slope K_A . This is equivalent to Henry's law.
- (ii) At high values of $K_A p_A$ the relation can be represented by

$$(1 - \theta_A) = \frac{1}{K_A p_A} \quad (3.19)$$

and approaches 1 asymptotically, i.e. nearly all sites are occupied.

(iii) For values of $K_A p_A$ around 1, θ_A can be represented by

$$K_A p_A^{1/n} \quad (n > 1) \quad (3.20)$$

With increasing temperatures K_A decreases and a transition from (ii) to (i) can be expected. The dimension of K_A has units of (pressure) $^{-1}$. If atm $^{-1}$ (the standard thermodynamic reference state for gases) is used, K_A can be expressed as

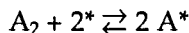
$$K_A = \exp\left(\frac{-\Delta G_A^\circ}{RT}\right) = \exp\left(\frac{\Delta S_A^\circ}{R} - \frac{\Delta H_A^\circ}{RT}\right) \quad (3.21)$$

where ΔH° and ΔS° represent the enthalpy and entropy of adsorption, respectively. Both quantities are generally negative since adsorption is an exothermic process and the molecule loses at least its translational degrees of freedom.

The assumptions for the Langmuir isotherm imply an ideal surface, and few real systems will follow this ideal. Experimental determinations of the heat of adsorption ($-\Delta H_{ads}^\circ$) as a function of θ show that it decreases with increasing coverage. This indicates that catalyst surfaces are non-uniform and/or the adsorbed molecules exhibit a mutual interaction. Other adsorption isotherms that take this coverage dependency into account are, among others, the Freundlich and the Temkin isotherms. In the practice of kinetic modelling, however, these are hardly ever used since the derivation of rate expressions becomes a difficult job (see e.g. Ref. [1]) and multicomponent adsorption can nearly always only be described by the Langmuir model, although this situation might rapidly change with the increasing use of high capacity computers. Within the Langmuir approach the general expression for the fractional coverage by component j in the case of multicomponent adsorption is given by (3.22).

$$\theta_j = \frac{K_j p_j}{1 + K_j p_j + \sum_i K_i p_i} \quad (3.22)$$

Only molecular adsorption has been considered above. Upon adsorption some molecules dissociate (e.g. H₂, CO) and two sites are needed. Consider the following dissociative adsorption equilibrium

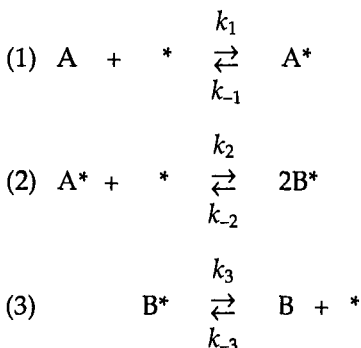


In an analogous way as in the preceding section for the adsorption isotherm, one can derive that the coverage with A follows Eqn. (3.23). The pressure dependency now follows the square root of the partial pressure of A₂ at low coverages.

$$\theta_A = \frac{(K_A p_A)^{1/2}}{1 + (K_A p_A)^{1/2}} \quad (3.23)$$

3.4 RATE EXPRESSION (OTHER MODELS)

In many reactions it has been demonstrated that more than one site is involved in the catalytic process. This is particularly often the case for dissociation reactions. The same procedure as depicted above for a single site model can be used for the derivation of the rate expression for a dual site model, but the result is somewhat different. This is exemplified for the following dissociation reaction $A \rightleftharpoons 2B$, which is thought to proceed according to the three step sequence:



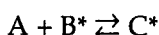
in which the last step must proceed twice in order to complete the overall reaction. Its stoichiometric number equals two, that of the other steps is one.

By application of the steady-state hypothesis, a site balance and the assumption that the surface dissociation is rate determining while the other steps are in quasi-equilibrium, the following rate expression is derived:

$$r = \frac{s N_T k_2 K_A K_B^2 [p_A - p_B^2 / K_{eq}]}{(1 + K_A p_A + K_B p_B)^2} \quad (3.24)$$

here the numerator includes a parameter, s , which represents the number of nearest neighbours of an active site. K_A and K_B are the adsorption equilibrium constants for A and B and are equal to K_1 and $1/K_3$. The denominator is now squared compared with a single site model. This indicates that two active sites are involved in the rate determining step. These types of models are called Langmuir–Hinshelwood models.

Reactions of a molecule directly from the gas phase with a surface complex, as:



are called Eley–Rideal models.

Other variants of kinetic models can be derived, of course. Froment and Bischoff [2] presented an extended treatment of this approach and it follows that rate expressions based on sequences of elementary steps, one of which is rate determining, can be represented by the following expression

$$\text{rate} = \frac{(\text{kinetic factor}) (\text{driving force})}{(\text{adsorption group})^n} \quad (3.25)$$

The kinetic factor always contains the rate constant of the rate determining step, together with the concentration of active sites and adsorption equilibrium constants.

The driving force represents the chemical affinity of the overall reaction in reaching thermodynamic equilibrium. It is proportional to the concentration difference of the reactants with respect to their equilibrium concentrations. It does not contain any parameter associated with the catalyst, consistent with the fact that the catalyst does not affect chemical equilibrium.

The adsorption group represents the reduction of the number of active sites due to adsorption. The individual terms represent the distribution of the active sites over the different intermediate surface species and vacancies. It may contain square roots of partial pressures, indicating dissociative adsorption. The power n in the rate expression indicates the number of sites involved in the rate determining process, usually 0, 1 or 2.

In heterogeneous catalysis these models are generally referred to as the Langmuir–Hinshelwood–Hougen–Watson (LHHW) models. The term Michaelis–Menten kinetics is often used in homogeneous catalysis, enzyme reactions and reactions of microbial systems.

3.5 INITIAL RATE EXPRESSIONS

A further simplification of the rate expressions is obtained if the product concentrations or partial pressures are negligibly small. For the single site model this results in the following expressions:

Adsorption rate determining:

$$r = N_T k_1 p_A \quad (3.26)$$

Surface reaction rate determining:

$$r_0 = \frac{N_T k_2 K_1 p_A}{1 + K_1 p_A} \quad (3.27)$$

Desorption rate determining:

$$r_0 = \frac{N_T k_2 K_1 K_2 p_A}{1 + (1 + K_2) K_1 p_A} \quad (3.28)$$

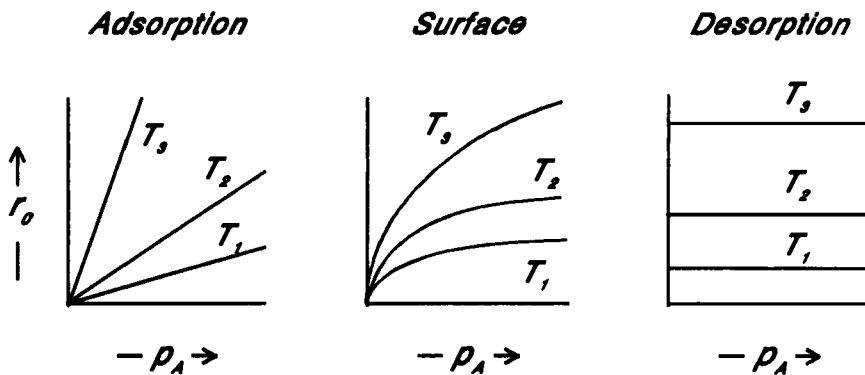


Fig. 3.4. Pressure dependency of the initial reaction rate of r_0 for three different rate determining steps, and at increasing temperatures.

In the latter case the surface is nearly fully occupied and the last expression reduces to:

$$r_0 = N_T k_3 \quad (3.29)$$

Figure 3.4 represents the pressure dependencies of r_0 for these three cases. It is evident that this initial dependency of rate on pressure gives a quick insight into which kinetic model best describes the experimental results of the reaction under consideration. It is ideal for model discrimination purposes where one tries to select the best kinetic description for a process. In applying this, two important aspects must be realised:

- (i) The product partial pressure may be low, but not all the terms in the denominator can be cancelled by a strong adsorption. Only the numerator can be simplified.
- (ii) Other components may compete for adsorption sites and occupy part of the active sites. Hence, a variation of the pressure will have less effect than might be expected.

In the case of the dual site model the initial rate even passes through a maximum if the surface reaction step is rate determining (cf. Eqn. (3.24)).

3.6 TEMPERATURE DEPENDENCY — LIMITING CASES

In this section we consider the temperature dependency of the rates of catalysed reactions, since a typical behaviour can be expected for catalysed reactions, due to the effect of (competitive) adsorption. This will be demonstrated with some simplified cases, starting with a consideration of the rate determining step.

According to the transition state theory, the reaction rate of the rate determining step can be computed from expression (3.30).

$$k_T = k_{\text{barrier}} K_T^{\#} = k_{\text{barrier}} \left(\frac{k_{T+}^{\#}}{k_{T-}^{\#}} \right) \quad (3.30)$$

It is assumed that the reacting complex is in equilibrium with the transition state complex (T.S.) and that the number of molecules in the transition state that react to give the product per unit of time is given by the frequency k_{barrier} . The rate of this step is assumed to be rate limiting. It implies that energy exchange is fast compared to the overall reaction rate. This is depicted in Fig. 3.5. Because $K_T^{\#}$ is an equilibrium constant it can be written as in Eqn. (3.31), where $\Delta G^{\#}$, $\Delta H^{\#}$ and $\Delta S^{\#}$ are the free enthalpy, the enthalpy and the entropy differences between the transition state and the ground state, respectively.

$$K_T^{\#} = \exp\left(\frac{-\Delta G^{\#}}{RT}\right) = \exp\left(\frac{\Delta S^{\#}}{R} - \frac{\Delta H^{\#}}{RT}\right) \quad (3.31)$$

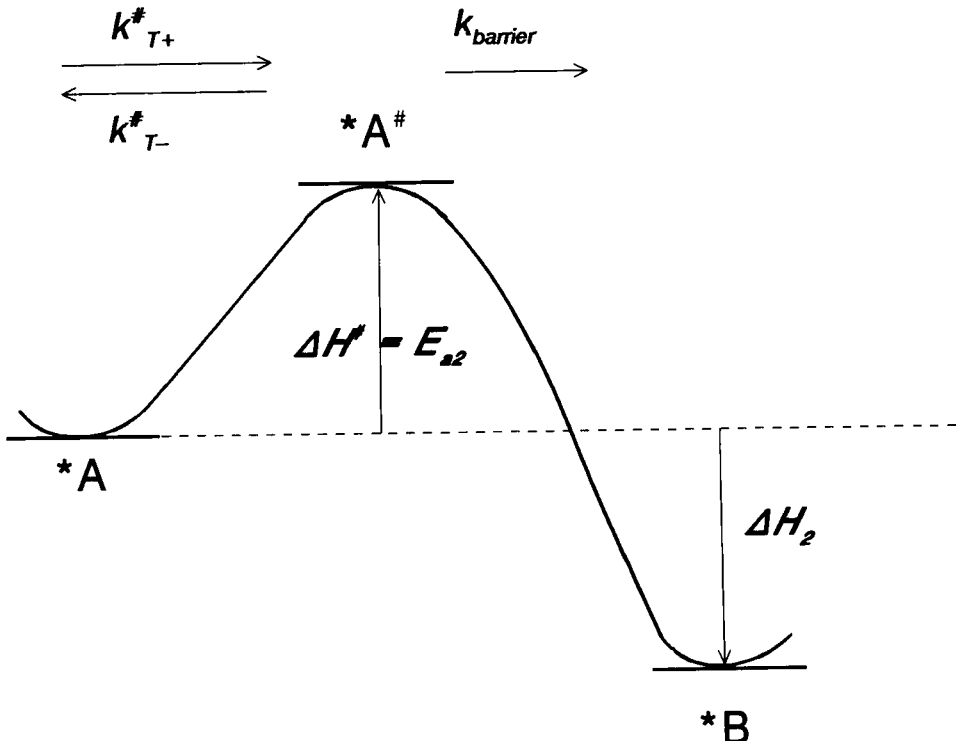


Fig. 3.5. Energy diagram for the rate determining surface reaction.

As long as quantum-mechanical corrections can be ignored:

$$k_{\text{barrier}} = \frac{kT}{h} \quad (3.32)$$

For the rate constant of the rate determining step this results in:

$$k = \frac{kT}{h} \exp (\Delta S^\# /R - \Delta H^\# /RT) = k_0 \exp (-E_a /RT) \quad (3.33)$$

$\Delta H^\#$ can be identified approximately with the activation energy E_a (neglecting the degree of freedom along the reaction coordinate, resulting in a contribution of RT) of the reaction step, and $\Delta S^\#$ with the entropy of activation. This relation will be used together with the derived rate expressions to illustrate that the overall activation energy is a complex function of the reaction enthalpies and activation energies of the individual elementary reaction steps. More detailed treatments are presented in Refs. [3] and [4]. This approach can lead to selection of the best kinetic model on the basis of thermodynamic considerations.

Starting with Eqn. (3.14) and assuming that the reverse reaction can be neglected, the rate expression for this single site reaction, with the surface reaction being rate determining, can be written as

$$r = \frac{N_T k_2 K_A p_A}{1 + K_A p_A + K_B p_B} \quad (3.34)$$

The following special cases can be distinguished:

- (i) A strong adsorption of A results in $K_A p_A \gg 1$ and $K_B p_B$, and Eqn. (3.34) reduces to:

$$r = N_T k_2 \quad (3.35)$$

Physically this means that the whole surface is occupied by A. Varying the pressure of A has no effect on the rate. The reaction is said to be zero order in A (and B) and the overall activation energy $E_a^{(\text{obs})} = E_{a2}$ provided the number of active sites N_T is temperature independent. This situation is depicted in Fig. 3.5.

- (ii) A and B are only weakly adsorbed and $K_A p_A$ and $K_B p_B \ll 1$, so the rate expression becomes:

$$r = N_T k_2 K_A p_A \quad (3.36)$$

the reaction is now first order in A and zero order in B, while the observed overall activation energy will be lower than in the previous case, since:

$$E_2^{(\text{obs})} = E_{a2} + \Delta H_A \quad (3.37)$$

and ΔH_A represents the adsorption enthalpy of A, which is negative since adsorption is an exothermal process. The energy diagram is represented by Fig. 3.6.

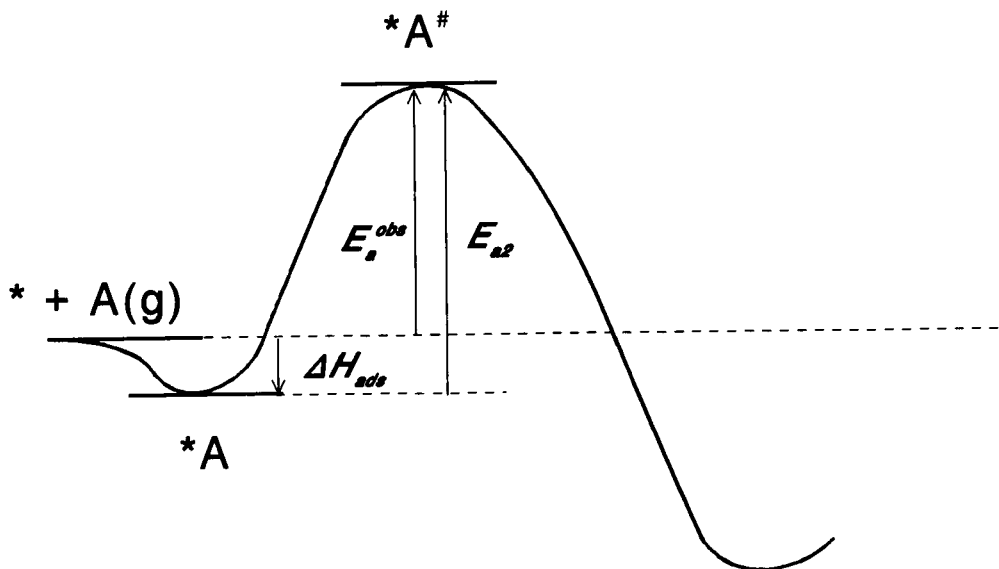


Fig. 3.6. Energy diagram for the case (ii), $K_A p_A$ and $K_B p_B \ll 1$.

- (iii) The adsorption of B is very strong, so that $K_B p_B \gg 1$, $K_A p_A$, and the rate expression becomes:

$$r = \frac{N_T k_2 K_A p_A}{K_B p_B} \quad (3.38)$$

The reaction is now first order in A and -1 in B (B inhibits the reaction strongly). The surface is nearly completely covered with B and the observed activation energy is now higher than in the previous cases:

$$E_a^{(\text{obs})} = E_{a2} + \Delta H_A - \Delta H_B \quad (3.39)$$

since $-\Delta H_B > -\Delta H_A$ as a consequence of the stronger adsorption of B.

This overall activation energy can be interpreted as follows from the energy diagram in Fig. 3.7. Since B is strongly adsorbed it mainly covers the available active sites, so the initial state for the reaction is in fact gaseous A and adsorbed B. For A to be able to react firstly a molecule of B has to be desorbed and the desorption enthalpy has to be overcome. Subsequently, A adsorbs, gaining adsorption enthalpy, and reacts further in the rate determining step where the activation energy barrier E_{a2} has to be taken.

- (iv) For intermediate values of $K_A p_A$ and $K_B p_B$ the reaction order for A will between 0 and 1, and for B between -1 and 0. The observed overall activation energy will have intermediate values between the two extremes of (ii) and (iii).

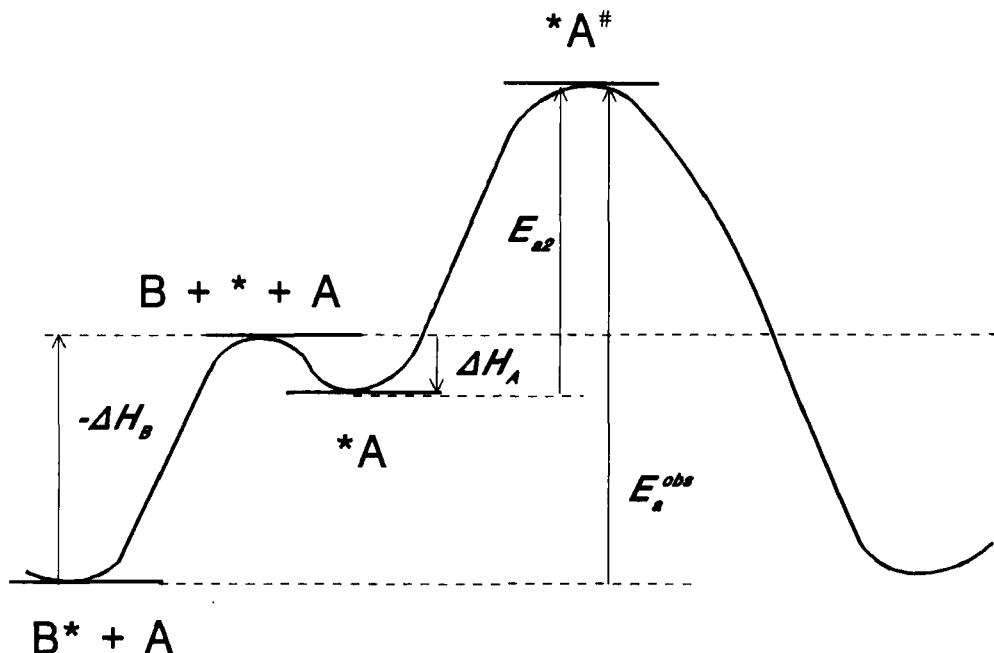


Fig. 3.7. Energy diagram for case (iii), $K_B p_B > 1$, $K_A p_A$.

$$E_{a2} + \Delta H_A < E_a^{obs} < E_{a2} + \Delta H_A - \Delta H_B \quad (3.40)$$

Transitions between these different situations will occur as a function of the temperature, since the rate and equilibrium constants vary exponentially with the reciprocal temperature. With increasing temperature the adsorption equilibrium constants decrease, so a gradual transition can be envisaged from (iii) via (iv) to (ii), during which:

- the order of A remains nearly 1
- the order of B changes from -1 to 0
- the observed overall activation energy will change from (3.39) via (3.40) to (3.37).

Large changes in partial pressure can also result in changes in the apparent reaction order of a component. At low p_A the reaction is first order in A, while at high p_A the rate approaches a limit as can be expected for Langmuir adsorption, and the reaction becomes zero order in A. Generally, this means that the overall activation energy and the apparent reaction order of components is dependent of the coverage of the active sites.

In an analogous way limiting cases can be distinguished for the dual site model, where even the order in A can become negative (cf. Eqn. (24)).

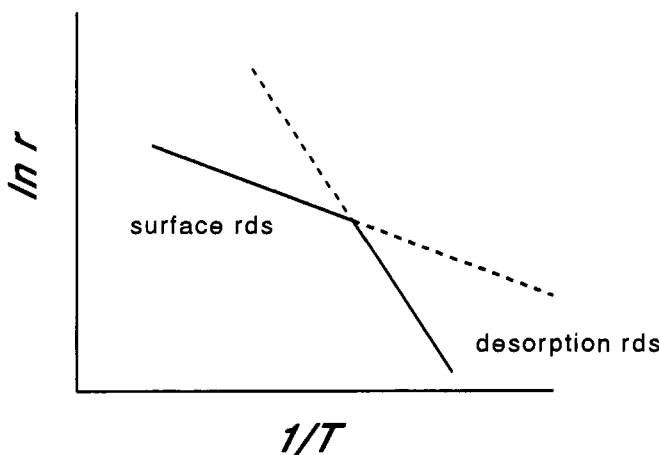


Fig. 3.8. Change of observed activation energy due to a changing rate determining step as a function of temperature.

Until now it has been assumed that the rate determining step remained the same, but it can change, especially under the influence of temperature [2], but also pressure changes can induce this [4]. Suppose that the rate determining step is the desorption at low temperature. Generally this implies that the activation energy barrier for desorption is the highest. A temperature increase will enhance this step most, compared to the other steps with lower activation energies, until the rate of another step becomes the lowest, as depicted in Fig. 3.8. This implies that the observed overall activation energy decreases with increasing temperature upon a change in the rate determining step.

In these cases one cannot comply with only one rate determining step. To obtain an adequate rate expression, valid over the whole temperature range under consideration, two or even more steps should be assumed not to be in *quasi-equilibrium*, and are, hence, rate determining.

3.7 SABATIER PRINCIPLE — VOLCANO PLOT

According to Eqns. (3.36) and (3.37) it is apparent that the larger the heat of reactant adsorption, the larger the overall rate of the reaction. The increase in the heat of adsorption enhances the surface coverage (and changes the reaction order) and consequently the reaction rate. A relation between the overall rate of reaction and the heat of adsorption is often found. Generally, however, the rate passes through a maximum as a function of the heat of adsorption. This trend is given in Fig. 3.9. Volcano plots, as in this figure, have been measured for very different reactions, varying from formic acid decomposition [5], the ammonia synthesis reaction, to hydrodesulphurization or hydrogenation reactions.

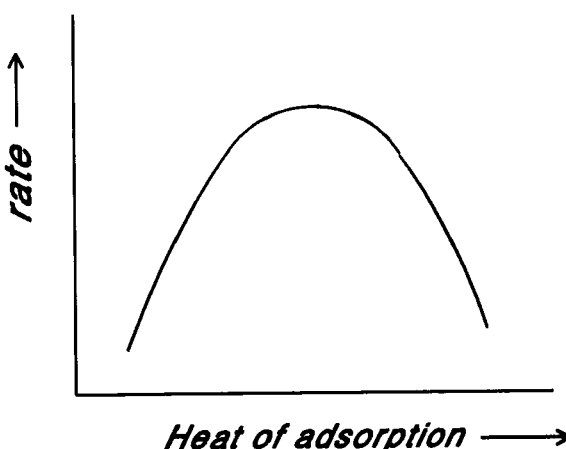


Fig. 3.9. Volcano curve for the rate as a function of the heat of adsorption.

As explained above the increase of the rate is due to the increased site coverage with the reactant (case (ii) above). A limit of the increase is reached once the optimum surface coverage is reached. The rate is then controlled by the rate of product formation (case (i)). The reason for the decrease in reaction rate with a further increase in heat of adsorption is the resulting increase in the overall activation energy. Not only will the reactants be adsorbed more strongly, but the products will also be held more strongly (case (iii) above). Other effects may be that the surface interacts too strongly with the reactants or molecule fragments, that they follow other reaction paths and the reaction becomes non-selective, or that they cannot leave the catalyst, the catalyst deactivates (e.g. carbon deposition).

Clearly, an optimum for the interaction of the catalytically active surface and the adsorbates exists, resulting in a maximum for the reaction rate (the Sabatier principle). To the left of the maximum the reaction has a positive order in the reactants, whereas to the right the order has become negative.

For practical heterogeneous catalyst kinetics this principle has the following consequence. Usually, the assumption of a homogeneous surface is not valid. It would be more realistic to assume the existence of a certain distribution in the activity of the sites. From the above, certain sites will, however, contribute most to the reaction, since these sites activate the reactants most optimally. This might result in an apparently uniform reaction behaviour, and can explain why Langmuir adsorption often provides a good basis for the reaction rate description. This also implies that adsorption equilibrium constants determined from adsorption experiments can only be used in kinetic expressions when coverage dependence is explicitly included; otherwise they have to be extracted from the rate data.

In this respect it can be mentioned that several authors have derived rate expressions for non-uniform surfaces. In Ref. [4], Boudart and Djégà-Mariadassou

(1984) show that relations are obtained that have a mathematical similarity with those obtained for a uniform surface.

3.8 CONCLUDING REMARKS

In the preceding paragraphs we have indicated how a useful approximate reaction rate expression can be derived for catalysed reactions, starting from an assumed kinetic model of elementary reaction steps.

The derivation is based on the following assumptions:

- the reaction system is in a steady state
- a uniform surface for adsorption and reaction
- a constant number of active sites, independent of the reaction conditions
- adsorbed species do not interact, apart from their reaction paths

The form of the resulting expression differs from the gas phase reaction rate expressions due to the presence of a denominator which represents the reduction in rate due to adsorption phenomena and of which the individual terms represent the distribution of the active sites among the possible surface complexes and vacancies. These expressions are termed the Langmuir–Hinshelwood–Hougen–Watson (LHHW) rate expressions.

The steady-state approach generally yields complex rate expressions. A simplification is obtained by the introduction of the rate determining step and *quasi-equilibrium* steps, and by the initial reaction rate approach.

In practice useful relations result even for the non-ideal heterogeneous surfaces of solid catalysts. Some reasons can be:

- similar mathematical relations for uniform and non-uniform adsorption models
- Sabatier's principle of the optimum site activity. Only optimum sites contribute to the reaction, resulting in an apparently uniform behaviour

In this chapter the aspects of model selection/discrimination and parameter estimation and the experimental acquisition of kinetic data are not dealt with, since they fall outside its scope. Moreover, in interpreting the observed temperature dependency of the rate coefficients in this chapter it was assumed that we are dealing with intrinsic kinetic data. As will be shown in a Chapter 7, other, parasitic, phenomena of mass and heat transfer may interfere, disguising the intrinsic kinetics. Criteria will be presented there, however, to avoid this experimental problem.

REFERENCES

- 1 M.I. Temkin, 'The Kinetics of Some Industrial Heterogeneous Catalytic Reactions' in *Advances in Catalysis*, Vol. 28, Academic Press, New York, 1979, p. 173.
- 2 G.F. Froment and K.B. Bischoff, *Chemical Reactor Analysis and Design* 2nd ed., Wiley, New York, 1991.

- 3 R.W. Maatman, '*Site Density and Entropy Criteria in Identifying Rate-Determining Steps in Solid-Catalyzed Reactions*' in *Advances in Catalysis*, Vol. 29, Academic Press, New York, 1980, p. 97.
- 4 M. Boudart and G. Djégà-Mariadassou, *Kinetics of Heterogeneous Catalytic Reactions*, Princeton University Press, Princeton, NY, 1984.
- 5 W.J.M. Rootsmaert and W.M.H. Sachtler, *Z. Physik. Chem.* 25 (1960) 16.
- 6 J.J. Carberry, '*Physico-Chemical Aspects of Mass and Heat Transfer in Heterogeneous Catalysis*' in *Catalysis, Science and Technology*, Vol. 8, Springer, Berlin, 1987, p. 131.
- 7 O.A. Hougen and K.M. Watson, *Chemical Process Principles*, Vol. III, Wiley, New York, 1947.
- 8 J.M. Thomas and W.J. Thomas, *Introduction to the Principles of Heterogeneous Catalysis*, Academic Press, London, 1967.

Chapter 4

Bonding and elementary steps in catalysis

4.1 INTRODUCTION

In this chapter we discuss the bonding to transition metal elements and the elementary reactions that can occur in transition metal complexes and on surfaces of solids. The bonding will be discussed in Section 4.2 in terms that are applicable to both homogeneous and heterogeneous catalysts, the emphasis being on what they have in common and what distinguishes the bonding in the two instances. Section 4.3 gives a summary of the organometallic reactions that are important as elementary steps in homogeneous catalysts; working with this 'basis set' it is in many cases possible for the reader to write down a likely mechanism for a reaction for which only the overall formula is known. In part these reactions are also relevant to heterogeneous catalysis and this section forms a good introduction to the next, Section 4.4, which deals with reactions on metal surfaces and solid acids. It will be very instructive to compare the steps of the organometallic complexes with the new possibilities created by the metal and oxide surfaces. In passing, we have also tried to point out the differences existing in the vocabulary between the homogeneous schools and the heterogeneous schools in catalysis. We do not propose that unique meanings can be attached to the words used, but it is necessary, and hopefully sufficient, that the reader is made aware of these minor obstacles.

4.2 BONDING

4.2.1 *Bonding to Transition Metal Surfaces*

The valence electron distribution of a transition metal surface is sketched in Fig. 4.1. A narrow d valence electron band is overlapped by a broad $s-p$ valence

electron band. Per atom, the number of electrons in the s,p valence electron band can be considered to be constant and equal to 1. The s character of the atomic orbitals dominates in this valence band. The d valence electron content varies. For the metals Cu, Ag and Au the d valence electron band is completely occupied. When one moves from right to left in a row of the periodic system, the d valence electron occupation of the metal decreases. In Ni, Pd and Pt the d valence electron occupation is 9, etc. The width of the d valence electron band increases when moving down in a column of the periodic system or to the left, moving along a row. For a metal (i.e. the solid) the ionization potential is less than for an atom (the resulting positive charge is screened better in the metal) and is called the work function. The work function decreases when moving from right to left along a row, and increases when moving downward along a column in the periodic system. The d atomic orbitals have a smaller spatial expansion than the s atomic orbitals, which explains the smaller width of the d valence atomic orbitals.

The bond strength to transition metal surfaces decreases with increasing d valence electron occupation. It tends to decrease when moving downward along a column of the periodic system. The metal–metal bond strength becomes larger because the metal electrons become more delocalized due to the larger orbital overlap. Upon chemisorption electrons have to localize on the surface involved in the chemisorptive bond. The larger the delocalization of the metal electrons, the higher is the cost involved in localization of the electrons and the smaller the chemisorptive bond energy. In addition the work function tends to increase, resulting in a decrease of polarity of the adatom surface chemical bond. For instance carbon, oxygen and hydrogen atoms are bonded more strongly to Ni

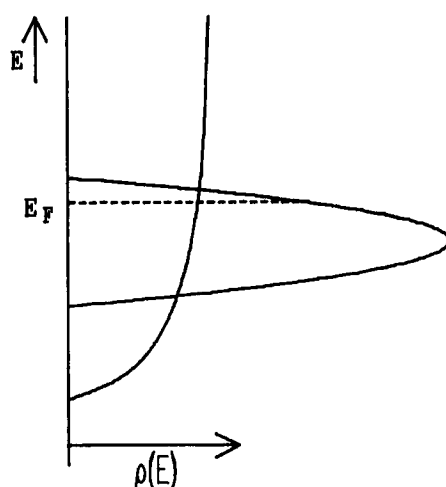


Fig. 4.1. The valence electron distribution at a transition metal surface (schematic).

than to Pt. Exceptions to this rule exist, however. For example CO binds more strongly to Pt than to Ni, but O₂ and N₂ show the expected, reverse behaviour. The angular dependence of *d* atomic orbitals is of relevance when orbital symmetry arguments are important. This will become especially apparent in Section 4.4 where association and dissociation reactions will be discussed [1,2].

Generally, the bonding of adatoms other than hydrogen to a metal surface is highly coordination-dependent, whereas molecular adsorption tends to be much less discriminative. For the different metals the bond strength of an adatom also tends to vary much more than the chemisorption energy of a molecule. Atoms bind more strongly to surfaces than molecules do. Here we will discuss the quantum chemical basis of chemisorption to the transition metal surfaces. We will illustrate molecular chemisorption by an analysis of the chemisorption bond of CO [3] in comparison with the atomic chemisorption of a C atom.

The valence electron orbitals and energies of CO and C are sketched in Fig. 4.2. In a molecule, atomic orbitals form bonding and antibonding orbitals, separated by an energy gap. In CO the highest occupied molecular orbital, the 5σ orbital is σ symmetric with respect to the molecule's axis. It is separated by approximately 7 eV from the lowest two unoccupied degenerate 2π* orbitals, of π symmetry with respect to the molecule's axis. The unoccupied 2π* orbitals are antibonding and result from the interaction between the C_{p_x} and O_{p_x} and C_{p_y} and O_{p_y} orbitals. In the atom, atomic *p* orbitals are partially occupied, separated by approximately 20 eV from the doubly occupied 2s atomic orbital. CO adsorbs perpendicular to the transition metal surface, attached via its carbon atom. When adsorbed atop the surface valence s-electrons will interact with the 5σ orbital, but their interaction is symmetry forbidden with the *p*-symmetric 2π* orbitals.

Interaction of π-type CO orbitals with the *s* valence atomic orbitals is only possible in high coordination sites (in the organometallic nomenclature these are called bridging sites, denoted μ, μ₃, and μ₄ for sites involving 2, 3 and 4 metal atoms, respectively). As illustrated in Fig. 4.3 they can then interact with asymmetric group orbitals that are linear combinations of atomic *s* orbitals of the surface atoms.

When CO is adsorbed atop (monometallic, end-on), the π-type CO 2π* orbitals will interact with the symmetric metal *d* atomic orbitals as well as *p_x* or *p_y* orbitals. The 5σ orbital will interact with *d_{z²}* as well as *s* and *p_z* metal atomic orbitals. To illustrate the formation of the surface chemical bond, the interaction scheme of bond formation between the CO valence orbitals (5σ and 2π*) and metal *d* valence electrons is sketched in Fig. 4.4. Both bonding and antibonding orbital fragments are formed. Bonding π-type fragment orbitals are occupied. They are mainly located on the metal atom. Bonding as well as antibonding σ-type surface fragment orbitals become occupied. The σ-type bonding (σ_{*b*}) orbital fragments are mainly located on CO, the σ-type antibonding (σ_{*a*}) orbital fragments are mainly located on the metal atom.

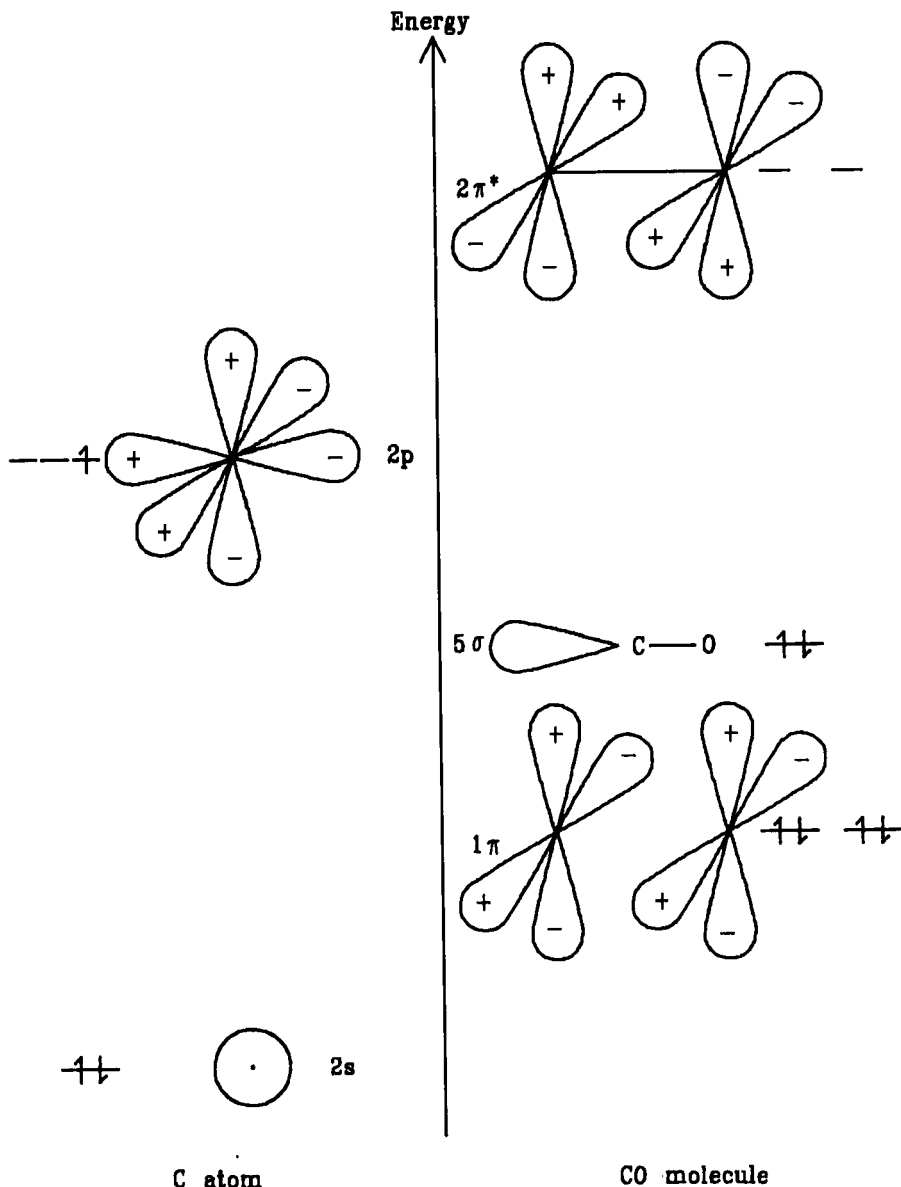


Fig. 4.2. Atomic and molecular valence electron levels.

When the d valence electron band is nearly completely filled, interaction with the doubly occupied CO 5σ orbital, leading to a significant fraction of occupied antibonding orbital fragments σ_a between adsorbate and surface atoms, will be repulsive. This Pauli repulsion is proportional to the number of surface atom neighbours and hence is a minimum in atop coordination. This counteracts the

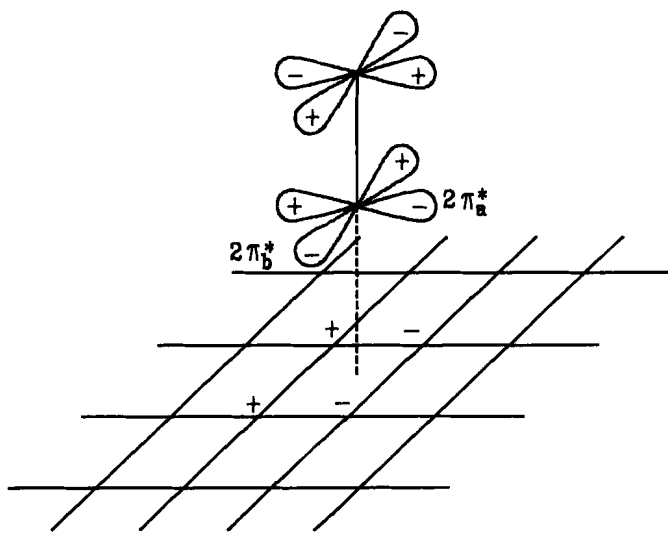


Fig. 4.3. Interaction of CO with a (100) surface in fourfold coordination. The $2\pi_a^*$ orbital interacts with the asymmetric surface group orbital $\psi_g^S = \frac{1}{2}(\varphi_a + \varphi_c - \varphi_c - \varphi_d)$.

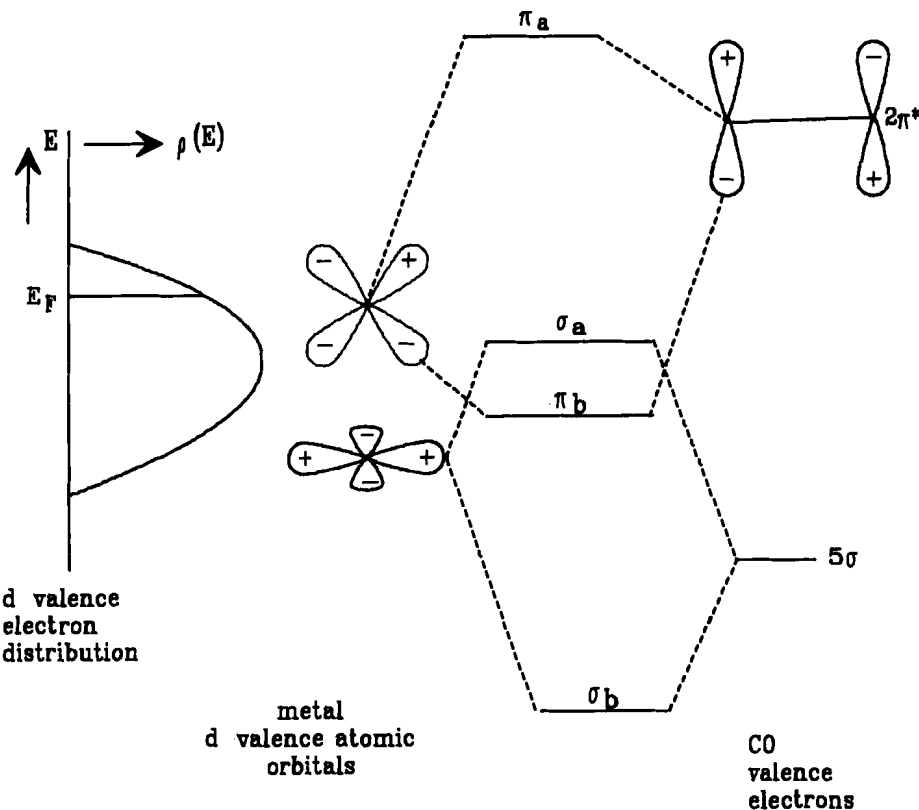


Fig. 4.4. Quantum chemistry of the CO d valence electron interaction (schematic). On the left the d valence electron distribution is sketched, which is typical of a transition metal.

interaction with the $2\pi^*$ -CO molecular orbitals, which favours high coordination sites. Different from the CO 5σ orbital, the energy of the unoccupied $2\pi^*$ orbitals is higher than the metal surface Fermi energy. The occupied orbital fragments resulting from the interaction with the metal surface are mainly of bonding nature and are located on the metal surface atoms. Occupied bonding orbital fragments favour adsorption in high coordination sites.

A decrease in the d valence electron occupation decreases the occupation of the bonding π -type orbitals. This decreases the interaction energy. For the σ -type symmetric orbital fragments a decrease in electron occupation depletes antibonding orbital fragments, which results in an increase of the interaction energy. Changes in the interaction of π - and σ -type orbitals give a counteracting contribution to the overall bond strength.

Bonding between occupied adsorbate orbitals and the surface (the σ -type interaction in the case of CO chemisorption) is also referred to as electron donation. The electron occupation of the CO 5σ orbital is depleted in comparison with its occupation in the free CO molecule. Similarly, the interaction with adsorbate orbitals, which are unoccupied before adsorption (for instance the CO $2\pi^*$ orbitals of CO), is called back donation because of the increase in electron density in the CO $2\pi^*$ orbital upon bond formation. The increase is proportional to the $2\pi^*$ orbital participation in the occupied surface fragment orbitals. The $2\pi^*$ electron occupation increases with coordination. Because of the antibonding nature of the $2\pi^*$ orbital with respect to the CO bond energy, electron population of the $2\pi^*$ orbital weakens the CO bond strength. This is observed in IR spectroscopy by a decreasing frequency of the CO stretching mode. The description of surface chemical bonding in terms of electron donation and back donation is called the Blyholder model. As we will discuss in the next section it is very similar to the Chatt–Dewar–Duncanson chemical bonding model in transition metal complexes.

Bonding of the C atom to the transition metal surface is dominated by interaction with the three low-lying $2p$ C atomic orbitals. The p atomic orbitals parallel to the metal surface can only interact with the s valence orbitals in high-coordination sites. This interaction is much stronger than the corresponding CO interaction (the $2\pi^*$ orbitals should be compared), because of the lower energy of the atomic orbitals. Also these C p atomic orbitals are not part of a molecular orbital as in CO, which increases orbital overlap significantly. The overlap of the $2\pi^*$ orbital with a surface group orbital ψ_g is given by:

$$S_{2\pi^*, \psi_g} = \int (c_1 \psi_{p_x}^C - c_2 \psi_{p_x}^O) \cdot \psi_g \, d\tau \quad (4.1a)$$

$$= c_1 \int \psi_{p_x}^C \cdot \psi_g \, d\tau \quad (4.1b)$$

$$= c_1 S_{p_x, \psi_g} \quad (4.1c)$$

Equation (4.1c) relates the carbon p_x overlap to the overlap with a CO $2\pi^*$ orbital. The value of $|c_1|^2$ is significantly less than 1. Whereas the interaction with a molecular $2\pi^*$ orbital results only in occupied bonding orbital fragments, interaction with the atomic p_x , p_y or p_z orbitals results in a bonding orbital fragment as well as antibonding ones. This is due to the lower energy of the atomic $2p$ orbitals, as compared with molecular $2\pi^*$ orbitals.

In the atom three $2p$ orbitals are involved in the surface chemical bond. The interaction with the p_z orbital has σ symmetry with respect to the surface. Apart from an interaction with different surface symmetry orbitals and a larger overlap energy with the surface orbitals, its dependence on electron occupation is qualitatively similar to that of the p_x and p_y orbitals. Because the p_x and p_y orbitals can only interact with the surface s atomic orbitals in high coordination sites, and this bonding interaction contributes significantly to the total surface bond energy, bonding to high coordination sites is favoured.

The covalent interaction with the adatom $2p$ orbitals increases with decreasing surface d valence electron occupation, because fewer antibonding orbital fragments then become occupied. The adsorption energy of atoms varies much more strongly with d valence electron occupation than that of molecules because compensating effects occur in the surface chemical bond of molecules. As we discussed above for CO, variation in the interaction with the 5σ orbital is partially compensated for by changes in the interaction with the $2\pi^*$ orbital.

In general, therefore, high coordination sites are favoured when adsorbates interact that have partially occupied p or π type orbitals [4]. This is typically the case for most adatoms. The interaction of s or σ type orbitals with partially filled metal valence orbitals usually also shows a preference for high coordination sites. When the interaction with d valence orbitals dominates atop adsorption is favoured in group 8–11 metals. Hydrogen atoms will adsorb in high coordination sites as long as their interaction with the d valence electrons is small. This generally appears to be the case. Methyl fragments adsorbed to the Ni surface tend to favour high coordination sites. The CH_3 fragment mainly interacts via its σ -symmetric lone-pair orbital. For a transition metal like Pt, with spatially more extended d atomic orbitals, one expects the methyl radical to show less preference for high coordination sites and to adsorb strongly atop. Chemisorption of ammonia to a metal surface also occurs mainly by way of its σ type lone-pair orbital. Calculations show that on Cu, with a completely filled d valence electron band, NH_3 adsorbs preferentially atop. Bonding with the CH_3 radical or ammonia occurs mainly by the electron donating interaction with their highest occupied molecular orbital (HOMO), the σ orbital, because of the weak interaction with their lowest unoccupied molecular orbital (LUMO), which has an unfavourably high energy.

Often, as we saw for CO, interaction with HOMO as well as LUMO type adsorbate orbitals is important. This is also the case for a molecule like ethylene.

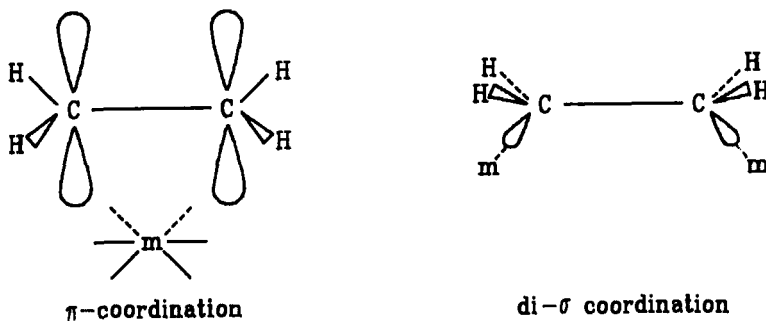


Fig. 4.5. Coordination of ethylene.

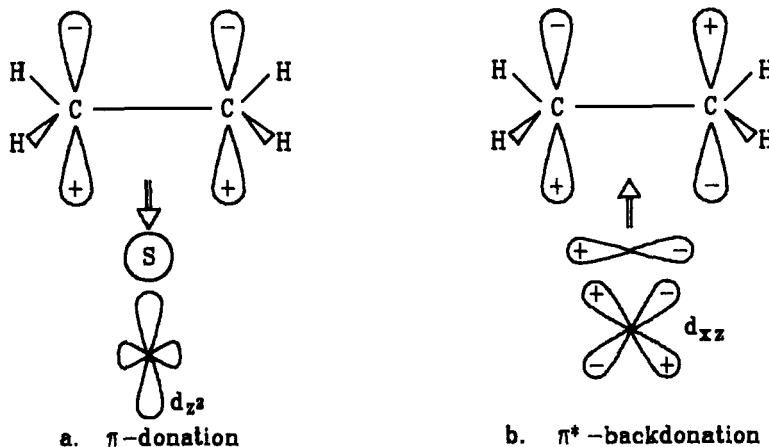


Fig. 4.6. Chatt-Dewar-Duncanson chemical bonding scheme of chemisorbed ethylene.

This can coordinate in two ways to the transition metal surface, namely in π coordination or di- σ coordination (Fig. 4.5) (η^2 and $\mu\text{-}\eta^1\text{:}\eta^1$, respectively).

The chemical bonding of π coordinated ethylene is very similar to the Chatt-Dewar-Duncanson picture of CO coordination (Fig. 4.6). The donating orbital is the doubly occupied π orbital that is σ -symmetric with respect to the normal to the surface. When adsorbed atop it interacts with the highly occupied d_{z^2} surface atomic orbital and the partially filled s and p_z orbitals. The ethylene LUMO is the empty asymmetric π^* orbital, which interacts with the surface d_{xz} and p_x orbitals. The corresponding overall interaction is relatively weak and no hybridization on ethylene is assumed to occur. The orbital interaction diagram of the occupied ethylene π orbital with surface atom d_{z^2} orbital is analogous to that sketched for the CO 5σ orbital in Fig. 4.4. When this d_{z^2} becomes nearly completely occupied, as occurs, for instance, for Pd or Pt, the ethylene- π surface atom d_{z^2} interaction

becomes repulsive. Because the spatial extension of Pt d atomic orbitals is larger than those of Pd or Ni, the repulsive interaction is largest for Pt. In order to overcome this repulsive interaction ethylene rehybridizes on Pt and adsorbs in di- σ coordination, as sketched in Fig. 4.5b ($\mu-\eta^1:\eta^1$). The orbitals on the C atom of ethylene rehybridize from sp_2 to sp_3 hybridization, as in ethane. The CH bonds bend away from the surface and two lone pair orbitals, one in each carbon atom, develop along the missing CH bonds. They are directed towards the surface metal atoms. Ethylene now prefers coordination to two surface metal atoms [8]. Chemisorption controlled by ad-molecule hybridization generally appears to be important when the interaction with highly occupied surface d valence atomic orbitals dominates. On Pt CH_3 adsorbs atop but CH_2 adsorbs in twofold position (μ , without the subscript 2) and CH in threefold position (μ_3). On Ni, with a relatively unimportant d valence orbital interaction, all three molecule fragments prefer high coordination [9].

When surface atoms participate in more open surfaces, their average coordination number decreases, resulting in an increase of coordinative unsaturation. The width of the valence band electron density is related to the coordination number of the metal atoms. The larger the coordination number, the larger is the number of metal–metal bonds per atom, and the electrons have to be shared over more bonds. This increases the degree of delocalization of the surface electrons, which is reflected in an increased valence electron bandwidth. Because the total electron density per atom remains constant, an increased bandwidth implies a decreased average electron energy density. As is illustrated in Fig. 4.7, the electron density decreases with decreasing coordinative unsaturation in the centre of the valence electron band. This is because the integrated density is constant.

As a result, the interaction of adsorbate orbital and surface orbitals is largest for surface atoms that have the lowest surface metal atom coordination number. The bonding orbital surface fragment has a larger downward shift and the antibonding orbital fragments shift more upward. For the situation sketched in Fig. 4.7, fewer antibonding orbital fragments become occupied for the coordinatively most unsaturated atoms. This, in combination with the larger downward shift of the bonding orbital fragments, results in a stronger interaction with the coordinatively most unsaturated surface atoms. A similar overall result can be derived when empty adsorbate orbitals interact, forming only occupied bonding surface orbital fragments.

Changes in bond strength with variation of coordinative unsaturation of surface atoms are very similar to the effects of coadsorption [11]. When two adsorbate atoms share a bond with the same surface atoms, the surface atom effectively has an increased coordination number. Therefore the adatom bond strength is weaker than when there is no sharing between metal surface atoms. The heat of adsorption generally decreases at high adsorbate surface coverage as a result of this effect.

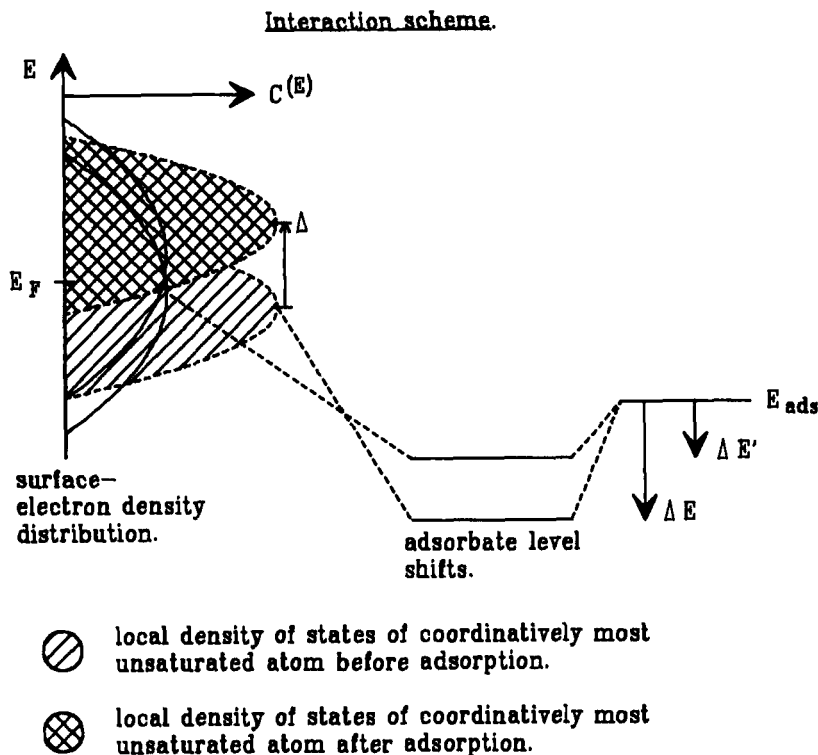


Fig. 4.7. Interaction of adsorbate orbital with surface atoms of different coordination number.

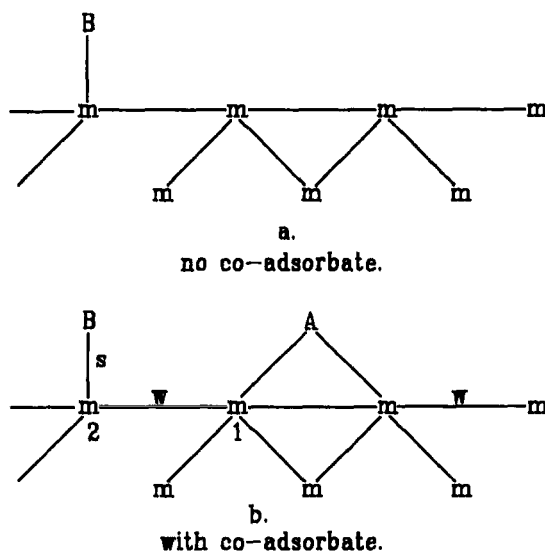


Fig. 4.8. Change in bond strength with a surface atom by a coadsorbate in the second coordination shell with respect to adsorbate (schematic). w = bond weakening, s = bond lengthening.

On the adsorption of strongly interacting surface atoms, in particular, the neighbouring metal–metal bonds between surface metal atoms weaken strongly. The surface–adatom interaction enhances the total number of surface atom neighbour atoms. The delocalization of the surface electrons increases, which results in a decrease of bond strength between the other atoms. This also holds for the interaction between the surface metal atoms. An alternative way of viewing this is the concept of conservation of bond order [10]. The bond order of a chemical bond is a measure of its bond strength. To a very good approximation the sum of the bond orders of the chemical bonds with a single atom is a constant. Because the total bond order per metal surface atom is conserved, an increase in coordination number decreases the bond order per bond, and hence the bond strength of the atom bonds.

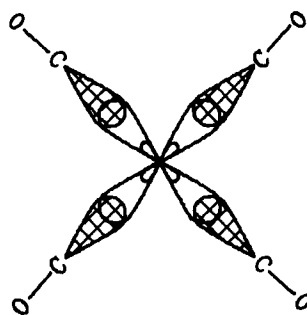
The effect on the bond strength of a coadsorbate adatom B, adsorbed in the second coordination shell with respect to adatom A, is an increase of the bond energy (see Fig. 4.8). The weakened interaction between metal atoms 1 and 2, results in an increase of the M–B bond strength.

4.2.2 Chemical Bonding in Organometallic Coordination Complexes and on Surfaces of Transition Metal Compounds

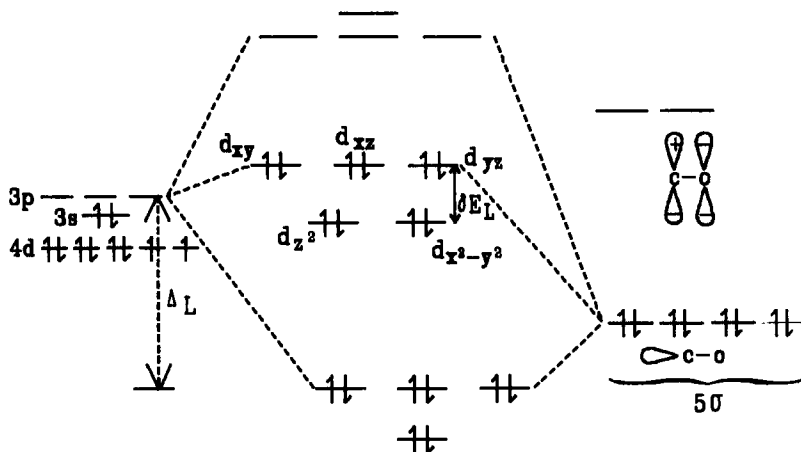
Ligands and molecules bind to organometallic and coordination complexes with energies comparable to the adsorption energies found for surfaces. As on surfaces, the chemical bond formed in such complexes also contains significant s or p character. A major difference with metal surfaces is the importance of discrete valence electron occupation numbers on complex stability. A prototype coordination compound is $\text{Ni}(\text{CO})_4$.

Figure 4.9 shows a schematic illustration of the chemical bonds of tetrahedral $\text{Ni}(\text{CO})_4$. Bonding can be best understood by initially ignoring the (weak) interaction between Ni and CO $2\pi^*$ electrons. The interaction is dominated by the CO 5σ and Ni 4s and $4p$ electrons. Four approximate sp^3 hybridized orbitals are formed, directed to the four CO 5σ orbitals. Eight new orbitals, four bonding and four antibonding, are formed separated by an energy gap 2Δ .

The d atomic orbitals interact only weakly with the CO molecular orbitals. The d atomic orbitals that have orbital lobes directed to the CO ligand positions acquire an antibonding character. A small splitting of the d orbitals results. Electron counting shows that 18 electrons give a stable complex. In that case the five d orbitals and four bonding sp^3 orbitals are occupied. The next electron has to be placed in the highly antibonding s,p -type orbitals. This is a very general principle in the bonding of transition metal complexes. Compounds are stable as long as no antibonding orbitals become occupied. For Co, one finds that since it has one electron fewer than Ni, $\text{Co}(\text{CO})_4$ can accept one additional electron. This



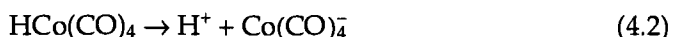
a. Hybridization orbital interaction scheme



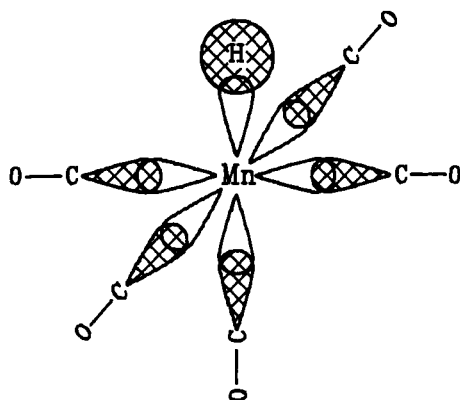
b. molecular orbital scheme.

Fig. 4.9. Chemical bonding in $\text{Ni}(\text{CO})_4$.

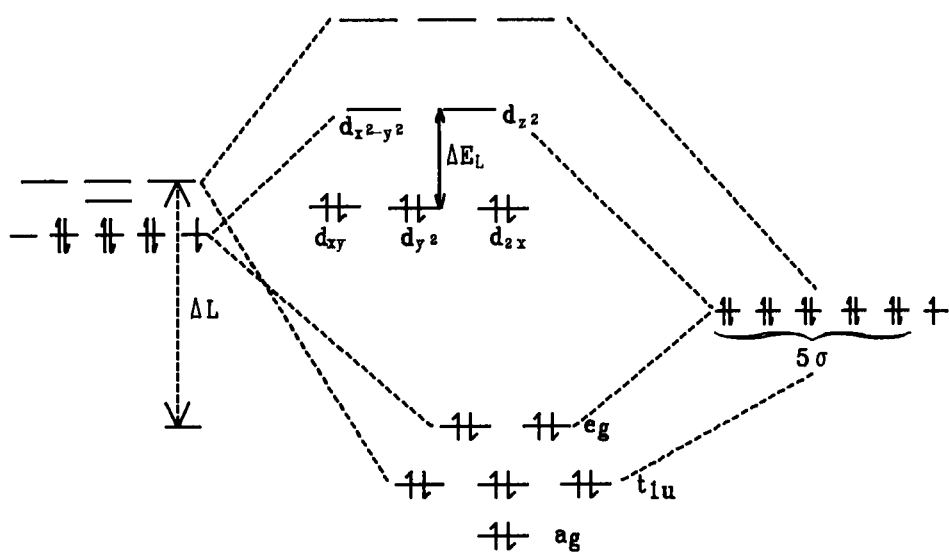
is the reason why dimerization occurs giving $[\text{Co}(\text{CO})_4]_2$, but bonding with hydrogen can also occur. Because of the stability of the $\text{Co}(\text{CO})_4$ anion, the hydrogen atom in the hydrogen cobalt carbonyl complex has an acidic character.



A covalent metal hydride bond is formed in $\text{HMn}(\text{CO})_5$: its bonding scheme is shown in Fig. 4.10. Manganese has seven valence electrons: the H atom donates one electron. Again, bonding with CO is considered to occur mainly with the CO



a.. Hybridized orbital scheme



b. molecular orbital scheme

Fig. 4.10. Chemical bonding in HMn(CO)₅.

5σ orbitals. Because the 5σ CO orbitals participate in bonding occupied complex orbitals and antibonding unoccupied orbitals, the electron occupation of the CO 5σ orbitals is found to decrease. Electron back donation occurs between the doubly occupied d_{xy} , d_{yz} and d_{zx} atomic orbitals and empty CO $2\pi^*$ orbitals. The d orbitals shift slightly downwards and the CO $2\pi^*$ orbitals shift slightly upwards

due to this interaction. This is the Chatt–Dewar–Duncanson picture of chemical bonding, which we discussed earlier in the context of the surface chemical bond [12]. In addition to Mn *s* and *p* electrons, the atomic $d_{x^2-y^2}$ and d_{z^2} also become involved in the bonding and antibonding orbitals formed with the CO 5σ orbitals.

A large splitting occurs between the *d* atomic orbitals on Mn. The d_{z^2} and $d_{x^2-y^2}$ orbitals are part of the six antibonding orbitals combinations with the CO 5σ orbitals. A stable complex is formed once again with an electron count of 18. More electrons would occupy the antibonding $d_{x^2-y^2}$ and d_{z^2} orbitals, weakening the complex. The hybridized bond orbitals formed here can be considered as d^2sp^3 hybrids. A strong MnH orbital is formed. When the molecule dissociates one bonding–antibonding orbital pair is removed from the orbital scheme, Fig. 4.11. The ligand field splitting changes, too. The degeneracy of the $d_{x^2-y^2}$ and d_{z^2} orbitals disappears and the $d_{z^2} - p_z$ hybridized orbital becomes the lowest unoccupied molecular orbital, directed towards the empty ligand position of hydrogen. It contains one electron.

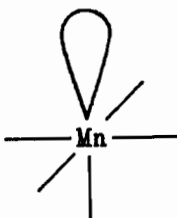


Fig. 4.11. Dangling bond orbital of Mn(CO₅).

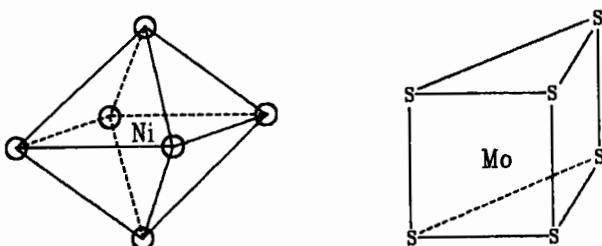


Fig. 4.12. Local cation coordination in NiO and MoS₂.

The distribution of electrons over *d* orbitals in complexes of different geometry controls the most stable geometric configuration. This principle can also be used to understand the chemical bonding of transition metal compounds and their surfaces. We will illustrate this first by analyzing the relative stability of octahedral NiO versus trigonal prismatic MoS₂.

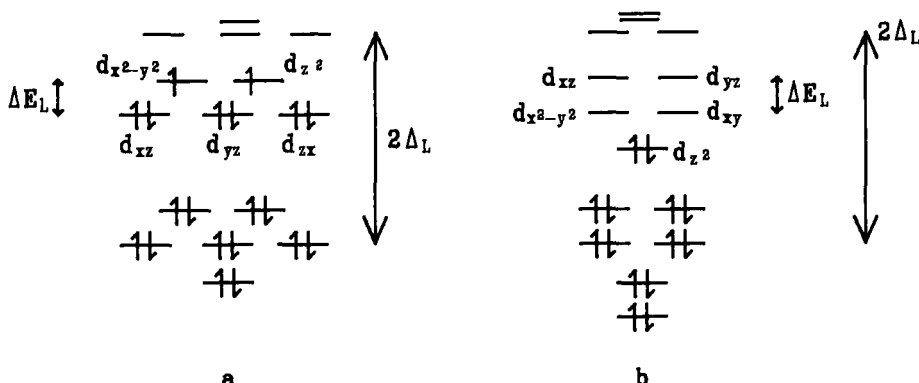


Fig. 4.13. Orbital schemes.

Bonding in transition metal compounds can be analyzed analogously to that in transition metal complexes, by considering each oxygen or sulphur atom to contribute two electrons to the complex and an *s*-type orbital. The resulting orbital schemes are given in Fig. 4.13.

In NiO, the Ni²⁺ ion contributes eight electrons. Bonding is dominated by population of the bonding, mainly *s,p*-type, orbitals. The octahedron can be considered a 20 electron complex. Two electrons have to be placed in the bond-weakening antibonding $d_{x^2-y^2}$ and d_{z^2} orbitals. As a result of Hund's rule, this results in a triplet state. Clearly, a more stable situation exists in octahedrally coordinated Co³⁺, forming an 18 electron complex.

When an oxygen anion is removed from a surface, a surface dangling bond appears, as described for Mn(CO)₅, directed towards the vacancy position. In NiO this will contain two electrons. Because it is doubly occupied, in the case of coordination to Ni²⁺ ions, interaction with the dangling bond will be weak. However for Co³⁺, strong coordination of basic molecules containing occupied σ lone pair orbitals becomes possible.

Interestingly sulphidic compounds, having a cation coordination which is similar to that of the oxides, show large differences in their sensitivity with respect to basic molecules like NH₃. Whereas the desulphurization activity of cobalt sulphide catalysts is readily poisoned by ammonia, nickel sulphide maintains its activity to a significant extent. This agrees with the observed weak interaction of the adsorbent with the doubly occupied dangling bond orbital of the Ni²⁺ ion.

In MoS₂, which has trigonal symmetry only the nonbonding d_z^2 orbital becomes occupied. The bond strength of MoS₂ is controlled by the occupation of bonding orbitals of low energy. Whereas, in Ni²⁺ and Co³⁺ complexes, antibonding orbitals are occupied which are also antisymmetric and able to donate electrons into antibonding adsorbate orbitals, such orbitals are not occupied in MoS₂. The

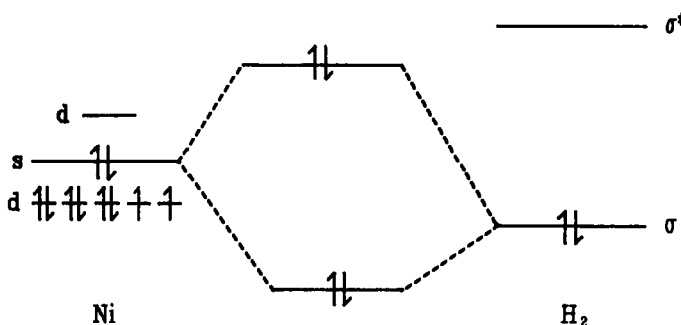


Fig. 4.14. The interaction between a Ni atom and a hydrogen molecule.

corresponding surfaces are expected to behave chemically as Lewis acids.

We have learned that the atomic orbitals on transition metal surfaces or in organometallic complexes are rehybridized to a significant extent. This changes the nature of the chemical bond considerably from that in the free atom. We will illustrate this by comparing dissociation of the H_2 molecule by a Ni atom and the $Ni(PH_3)_2$ complex [15–18].

In the Ni atom, the 4s orbital contains two electrons. This spatially extended, doubly occupied orbital experiences a large repulsive interaction with the doubly occupied $H_2 \sigma$ orbital of the same symmetry. Dissociation of H_2 has a large activation energy because electron promotion has to occur from 4s to 3d atomic orbitals in order for dissociation to occur. Coordination by ligands, as in $Ni(PH_3)_2$, decreases the promotion energy. The $Ni(PH_3)_2$ complex has linear geometry (Fig. 4.15).

Occupied bonding orbitals and non occupied antibonding orbitals between the Ni atom and the two phosphoric ligands are formed when two electrons of the Ni 4s orbitals are promoted into the Ni 3d orbitals. The Ni 4s and 4p atomic

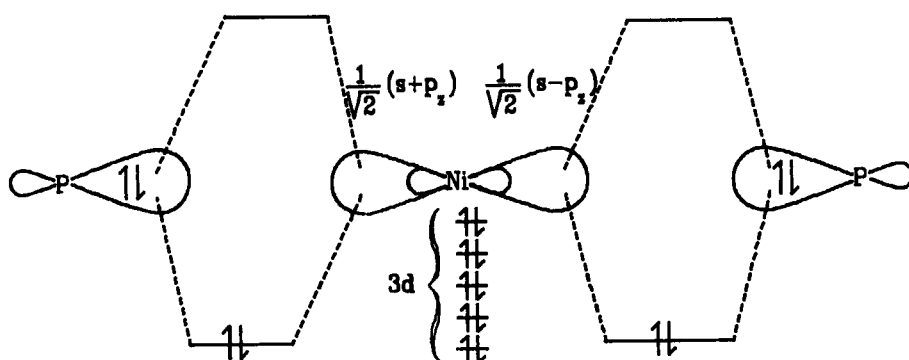


Fig. 4.15. The electronic structure of $H_3P-Ni-PH_3$.

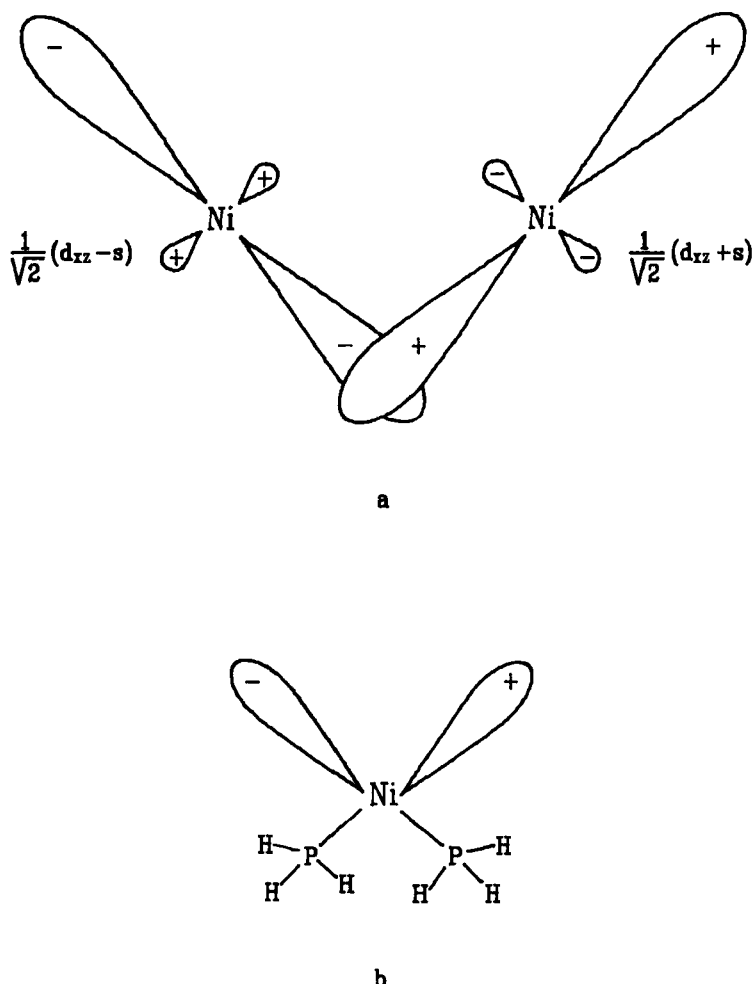


Fig. 4.16. Rehybridization of Ni atomic orbitals in the deformed $\text{Ni}(\text{PH}_3)_2$ complex.

orbitals hybridize into two empty atomic orbitals directed to the occupied lone pair on the phosphorus atom. When the hydrogen molecule approaches this complex, the interaction is again weak. The empty, spatially extended Ni *s*-atomic type orbitals required for bonding have been pushed upwards to a high energy. Dissociation occurs only when the $\text{Ni}(\text{PH}_3)_2$ molecule is deformed in such a way that empty spatially extended orbitals become available.

When the $\text{H}_3\text{P}-\text{Ni}-\text{PH}_3$ angle becomes 90° , hybridization between the d_{xz} and *s* atomic orbitals, rather than *s-p* hybridization, results in directed orbitals suitable for coordination with the PH_3 ligands. In the process, empty antibonding orbitals having an *s* and d_{xz} nature are created, as sketched in Fig. 4.16. Their orientation and symmetry are suitable for interaction with the hydrogen molecule. Now the

antibonding $H_2\sigma$ orbital can be populated and the molecule will dissociate. Note that hybridization on the Ni atom is now d^9s^1 , which is very similar to the hybridization of a Ni atom in the Ni metal surface.

When discussing the chemical bonding in $M(CO)_4$ complexes we observed that complexes become stabilized for particular electron counts. When an increase in electron count results in the population of antibonding orbitals no stable clusters are formed. An analogous rule has been formed for the stability and hence reactivity of metal clusters. It stems from the large overlap of the s and p atomic orbitals and the resulting importance of the s and p valence electrons to the cohesive energy of the metal clusters. Each atom can be considered to contribute one electron per atom to the s,p valence electron bonds of the cluster. In a closed packing geometry the clusters are approximately spherical, and hence, a stable cluster will be one with $n = 2, 8, 18$, etc. Indeed, beam experiments indicate exceptional stability or nonreactivity for such cluster atom numbers for many metals. The shell rule, however, is very approximate and in most cases it is better to consider surface atom coordination numbers when studying cluster reactivity.

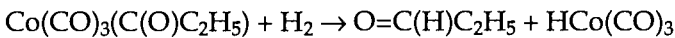
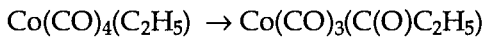
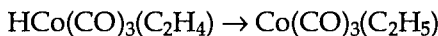
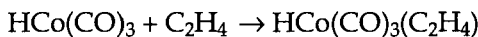
4.3 ELEMENTARY STEPS IN ORGANOMETALLIC COMPLEXES

The following paragraphs deal with the elementary steps that occur at a metal centre in a homogeneous catalytic reaction. Although the greater part of the elementary steps described have been studied in detail in model reactions of homogeneous organometallic complexes [19–23], there is general consensus that many of them can also take place at metal ions on surfaces [24]. At metallic surfaces, however, several additional reactions can take place that, by their nature, do not occur with low molecular weight, soluble organometallic complexes. The latter will be discussed in Section 4.4.

4.3.1 *Creation of a Vacant Site*

The function of a catalytic centre is to bring reactants together and to lower the activation barrier of their reaction. In homogeneous catalysis the catalytic centre comprises a metal centre and surrounding organic molecules. The latter molecules are called ligands and they can be neutral molecules (solvent, phosphines, CO, alkenes) or anions (e.g. halides). The ligands are usually σ donors, bringing the electron count of the complex to 18 or 16 or, especially on the left-hand-side of the periodic table, to 14 electrons, so that no electrons are forced into antibonding orbitals (see Section 4.2.2). To bring the reactants together, the metal centre must have vacant sites, i.e. it must be coordinatively unsaturated. Metal catalysis begins, we could say, with the creation of these vacant sites. In the condensed phase solvent molecules will always interact with the metal ion. The reactant

molecules are present in excess, and so may the ligands be. Therefore, a competition exists in complex formation between the desired substrate and other potential ligands present in the solution. With heterogeneous catalysts the presence of competing molecules in the gas phase controls the state of the surface. A negative order in one of the concentrations of the reactants can often be found in the expression for the rate of product formation (see the chapter on kinetics). In homogeneous catalysis this order can also be negative in ligand concentration. When the substrate coordinates strongly to the metal centre this may give rise to a zeroth order in the concentration of the substrate, i.e. Michaelis–Menten kinetics. Furthermore, coordination of the product formed during the reaction may slow down or inhibit the catalytic process. As an illustration, we may mention the cobalt-catalyzed hydroformylation reaction [25,26]:



The catalyst is $\text{HCo}(\text{CO})_4$, which must lose one molecule of CO in order to make room for an alkene molecule (Fig. 4.17).

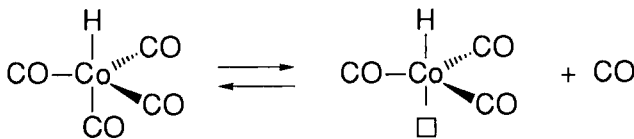


Fig. 4.17. Desorption of carbon monoxide.

A high CO pressure would shift equilibrium (4.3) to the left and the catalytic reaction would become slower. In this complex CO is a far better ligand than an alkene. On the other hand the reaction uses CO as a substrate, so it cannot be omitted. Furthermore, low pressures of CO may lead to decomposition of the cobalt carbonyl complexes to metallic cobalt and CO, which is also undesirable. Finally, the product alcohol may stabilize divalent cobalt species which are not active as a catalyst:



In a nutshell, we see several counteracting factors.

4.3.2 Coordination of the Substrate

The vacant site created in the required initial step of the catalytic process at the metal centre can now be occupied by the incoming substrate. Another way of looking at the question of 'creation of a vacant site' and 'coordination of the substrate' is the classical way of studying substitution reactions [27]. This is particularly useful for homogeneous complexes. Two extreme mechanisms are distinguished: a (complex) associative and a (complex) dissociative one. The discussion above concurs with the dissociative mechanism, that is to say the rate-controlling step is the breaking of the bond between the metal and the leaving ligand. In the associative process the displacement is a bimolecular process with simultaneous bond breaking and bond formation. The bond being broken or formed denotes here the bond between the reactant *molecule* and the *metal*. Note the difference in terminology between heterogeneous catalysis and coordination chemistry, the terminology adopted in homogeneous catalysis:

Homogeneous catalysis:	Meaning:	Heterogeneous catalysis:
dissociation	metal ligand bond breaking	desorption
association	metal ligand bond forming	desorption
oxidative addition	fission of bond in substrate	dissociation
reductive elimination	making of bond giving substrate	association

In square-planar, 16-electron complexes (i.e. coordinatively unsaturated) as found for many group 9 (Co, Rh, Ir) and 10 (Ni, Pd, Pt) metals, the associative process is most common. The *trans* effect and *trans* influence ligand series [19–23] are also useful measures in the study of homogeneous catalysis. Apart from very small ligands, such as CO, H₂ and NO, steric repulsion between ligands, as well as complexes and incoming substrates, plays a dominant role in determining the kind of intermediates and complexes formed and their equilibria in solution.

Carbon monoxide and ethylene are common substrates involved in homogeneous catalysis. The bonding of carbon monoxide to a transition metal has been depicted in Fig. 4.4. The bonding of alkenes to transition metals is described by the Chatt–Dewar–Duncanson scheme involving σ donation by the filled π orbital of the alkene, and π back donation from the metal into the π^* orbital of the alkene (see Fig. 4.6).

4.3.3 Insertions and Migrations

Elementary steps involving insertion or migration reactions are of prime importance for catalysis employing alkenes and carbon monoxide. Two examples taking place on a platinum centre have been depicted in Figs. 4.18 and 4.19. In these reactions an acetyl fragment is formed on the platinum centre from a coordinated CO and a methyl group. The important mechanistic difference

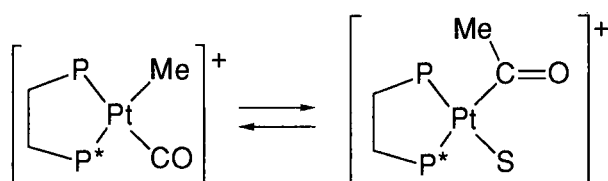


Fig. 4.18. Insertion reaction.

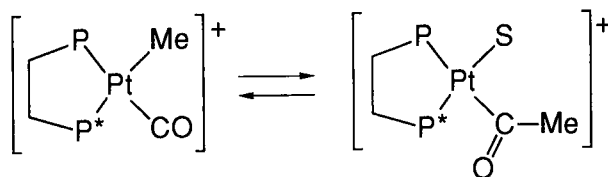


Fig. 4.19. Migratory insertion reaction.

between insertion and migration is that, in the insertion mechanism, CO inserts into the metal methyl bond and consequently the acyl bond formed takes the position of the former methyl group, i.e. the σ bonded fragment retains its position *trans* to P^* (Fig. 4.18). In the migration mechanism the methyl group migrates to the coordinated CO, and now the resulting acetyl group occupies the position *cis* to P^* (Fig. 4.19). There is convincing experimental evidence [28] (see below) in support of the migration mechanism versus the insertion mechanism, though not for the simplest platinum complexes shown in Figs. 4.18 and 4.19. Results of theoretical calculations [30–32] are in better agreement with the migration mechanism, i.e. with the anionic methyl group moving to the positively charged carbon atom of carbon monoxide. Hence the most accurate description for this process is migration. In the literature, however, the reaction is usually referred to as ‘insertion’, perhaps mainly because the reactive unsaturated species (CO or ethene) is chosen as the linguistic subject of our sentences: ‘carbon monoxide inserts giving an acyl complex’. To do justice to the intimate details of this reaction one also writes ‘migratory insertion’.

So far we have automatically presumed that the reacting carbon monoxide is coordinated to the metal. For the platinum example shown that might not be an easy thing to prove, but there is experimental evidence for complexes in which methyl migration to coordinated CO occurs. The classic proof stems from a relatively inert complex in which both the migration and the exchange of coordinated CO with free CO is slow. The reaction of $\text{CH}_3\text{Mn}(\text{CO})_5$ in the presence of ^{13}C labelled free ^{13}CO results in the formation of $\text{CH}_3(\text{CO})\text{Mn}(\text{CO})_4(^{13}\text{CO})$ in which the labelled CO is present as carbon monoxide and not in the acetyl group (Fig. 4.20).

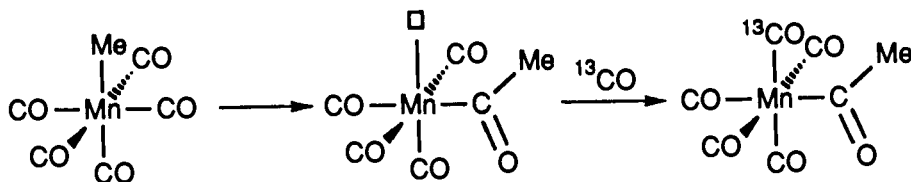


Fig. 4.20. Migratory insertion to pre-coordinated CO.

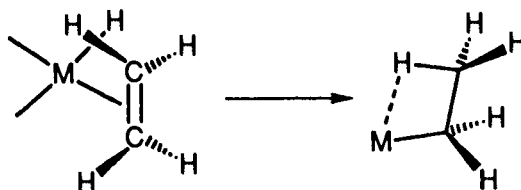


Fig. 4.21. Hydride migration to ethene.

Hence there is no direct reaction between the methyl manganese unit and the newly incoming carbon monoxide. Later, when we discuss the activation of a coordinated substrate molecule toward nucleophilic attack, the latter will turn out to be an alternative for the insertion/migration process. In the reaction involving nucleophilic attack at the coordinated, activated, unsaturated substrate, the anionic fragment is an uncomplexed species. There is, as yet, no proven example of an insertion of an uncomplexed unsaturated substrate into a metal–carbon σ bond.

A second important migration reaction takes place with alkenes, rather than carbon monoxide. Figure 4.21 gives a schematic representation of a hydride that migrates to a coordinated ethene molecule *cis* to the hydride. The figure shows the hydride migration which would leave an empty space in the coordination sphere of the metal. This coordinative unsaturation can be lifted in two ways: firstly, an agostic [33] interaction with the β -hydrogens may occur; secondly, an incoming ligand may occupy the vacant site [34]. How and whether activation of a coordinated alkene takes place prior to migration is not always clear-cut. Coordinated alkenes are subject to σ donation and π back donation, and the overall outcome of the shift of electron density from and to the coordinated alkene cannot be predicted. Molecular orbital calculations [35] show that, to a simple first approximation, the coordinated alkene is not activated towards migration (i.e. nucleophilic attack) and it cannot be predicted *a priori* whether rapid migration of the hydride will occur. However, a strong polarization of the alkene will be achieved when an asymmetric bonding of the alkene is arranged, as shown in Fig. 4.22.

The migration reaction takes place in a *cis* fashion with respect to the alkene; the two atoms M and H add on the same face of the alkene (2+2 *cis*-addition). This

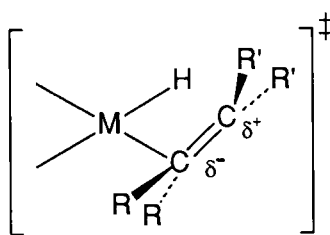


Fig. 4.22. Asymmetric coordination giving activation for nucleophilic attack.

has been unequivocally established by experiments. Later we will see reactions where this is not the case, although the overall stoichiometry is the same for both types.

Thermodynamically the insertion of an alkene into a metal–hydride bond is much more favourable than the insertion of carbon monoxide into a metal–methyl bond. The latter reaction is more or less thermoneutral and the equilibrium constant is near unity under standard conditions. The metal–hydride bond is stronger than a metal–carbon bond and the insertion of carbon monoxide into a metal hydride is thermodynamically most often uphill. Insertion of alkenes is also a reversible process, but slightly more favourable than CO insertion. Formation of new σ bonds at the cost of the loss of the π bond of the alkene during alkene hydrogenation etc., makes the overall processes of alkenes thermodynamically exothermic, especially for early transition metals.

Other insertions may involve isonitriles, alkynes, alkadienes, CO_2 , and SO_2 . They will not be dealt with here.

4.3.4 β -Elimination and Deinsertion

The reverse reaction of the migration of η^1 -bonded anionic groups to coordinated alkenes is named β -elimination. (Compare Figs. 4.23 and 4.24).

The migration reaction diminishes the total electron count of the complex by two, and creates a vacant site at the metal; β -elimination does the opposite. β -Elimination requires a vacant site at the metal centre, and the electron count of the complex increases by two electrons during the process. The reaction resembles the β -elimination reaction occurring in many organic processes, but the difference lies in the intramolecular nature of the present process, as the eliminated alkene may be retained in the complex. In organic chemistry the reaction may well be a two-step process, e.g. proton elimination with a base followed by the leaving of the anion. In transition metal chemistry, however, it is the availability of d orbitals that greatly facilitates a concerted *cis* β -elimination.

Suppression of β -elimination in catalytic processes is often a desirable feature. It can be achieved in several ways, although these recommendations in many

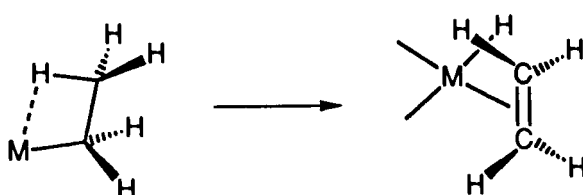
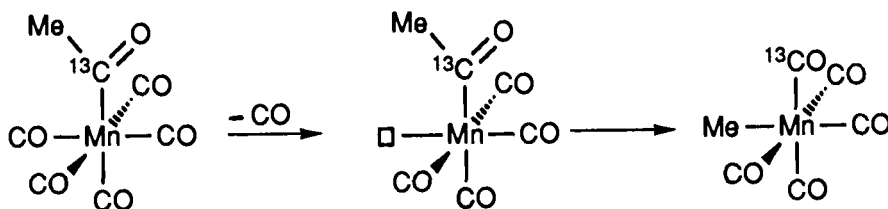
Fig. 4.23. β -Elimination.

Fig. 4.24. Cis-deinsertion.

instances have limited practical value. Rule number one would be to avoid β -hydrogens! When carrying out a polymerization reaction with a specific alkene carrying three hydrogens this will indeed be impractical. Rule number two is to maintain coordinative saturation. Again, in a catalytic cycle this may be a counterproductive suggestion, since the next reaction in the catalytic cycle will also require a vacant site in order to bring the next substrate molecule into the coordination sphere of the metal. Thirdly, steric hindrance may hamper the correct stereochemistry required for β -elimination, and perhaps this can be used to stabilize our metal alkyl complex. The last recommendation is to seek the metals for which the metal alkyl complexes are stable with respect to the corresponding hydride/alkene metal complexes. The relative stability of metal alkyls with respect to hydrides increases for the metals on the left-hand side of the periodic table: the early transition metals and the lanthanides [36–38]. It is not surprising that the best alkene polymerization catalysts are found amongst these metals.

For metal hydride elimination from a metal alkyl (to produce an alkene) one will also find the terms 'deinsertion' and 'extrusion' rather than β -elimination. For alkenes ' β -elimination' is correct, but for CO the deinsertion nomenclature is obligatory. We have seen that insertion takes place between a σ -bonded, anionic fragment and a neutral ligand in mutual *cis* positions, as was described for the manganese complex in Figure 4.20. By the same token, the deinsertion reaction can only proceed if there is a vacant site *cis* to the acyl group. A further modification of the experiment outlined in Fig. 4.20 proves this point. A manganese acetyl complex which is ^{13}C labelled at the acyl carbonyl group was synthesized and

heated to give deinsertion of CO. The result was that the only product formed contained the methyl substituent in a position *cis* to the labelled ^{13}C , see Fig. 4.24.

4.3.5 Oxidative Addition

In an oxidative addition reaction an electrophilic compound XY adds to a metal complex during which the XY bond is broken and two new bonds are formed: MX and MY. X and Y are reduced, and will at least *formally* have a minus one charge and hence the *formal* oxidation state of the metal is raised by two. The coordination number of the metal also increases by two. The electron count of the metal complex increases by two, while the electron count of the metal decreases by two. Figure 4.25 gives a formal representation. Clearly, the oxidative addition will be faster when the starting metal centre is more electron rich and/or more nucleophilic and hence the reaction is promoted by electron-releasing donor atoms at the metal. The simplest form of an oxidative addition has been presented in Section 4.2.2 (Figs. 4.14–16), the reaction of nickel with dihydrogen. It has already been mentioned that both the electron count and the geometry of the coordination complex play an important role in determining the energetics of such an electron. In the following only one popular example will be described.

The oxidative addition has been most extensively studied on iridium complexes, particularly Vaska's complex. The latter is a square planar complex, *trans*-L₂IrCl(CO), with a d⁸ electron count containing iridium(I). After the oxidative addition we formally obtain iridium(III), an octahedral complex, with a d⁶ electron configuration; i.e. the 16-electron square-planar complex is converted into an octahedral 18-electron complex. In Fig. 4.26 we have depicted the oxidative addition of methyl iodide to Vaska's complex (L = phosphine) [39]. A large

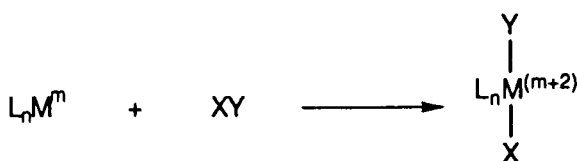


Fig. 4.25. Oxidative addition.

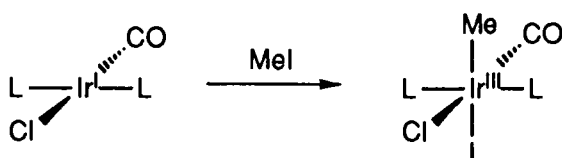
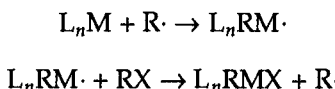


Fig. 4.26. Oxidative addition to Vaska's complex.

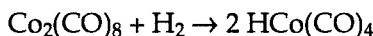
series of organic and inorganic molecules have been added to d^8 -iridium and d^8 -rhodium centred complexes in this manner.

The oxidative addition of alkyl halides can proceed in different ways, although the result is usually a *trans* addition independent of the mechanism [40]. In certain cases the reaction proceeds as an S_N2 reaction, as in organic chemistry. That is to say that nucleophilic attack is carried out by the electron-rich metal at the carbon atom attached to the halide, the halide being the leaving group. This process leads to inversion (Walden inversion) of the stereochemistry of the carbon atom (this can be observed only when the carbon atom is asymmetric). Note that effects of steric hindrance in the electrophile RX on the relative rates of the reaction is the same as in organic chemistry, i.e. $\text{MeI} \gg \text{EtI} \gg \text{PrI} \gg \text{iPrI}$. There are also examples in which racemization occurs. In some cases this has been explained on the basis of a radical chain mechanism. Indeed, radical scavengers have proved the presence of radicals by slowing the reaction down, and radical traps have demonstrated the expected ESR signals. The reaction sequence for the radical chain process reads as follows:



The oxidative addition of dihydrogen to low-valent metal complexes is a common reaction in many catalytic cycles. Common electronic configuration changes involved are $d^2 \rightarrow d^0$, $d^8 \rightarrow d^6$, and $d^{10} \rightarrow d^8$. In spite of the high strength of the dihydrogen bond the reaction proceeds smoothly to afford *cis* dihydrido complexes. The bond energy of a metal–hydrogen bond is in the order of $240 \pm 40 \text{ kJ mol}^{-1}$ which is sufficient to compensate for the loss of the H–H bond (436 kJ mol^{-1}). The hydride anion is formally charged with a minus one charge and this electron count gives dihydrogen the role of an oxidizing agent!

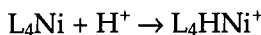
In general, oxidative addition reactions occur at mononuclear complexes as discussed above. Oxidative addition of dihydrogen often occurs at binuclear complexes. The reaction of dicobalt octacarbonyl may illustrate this:



The electronic configuration of the metals change from d^7 to d^6 . This reaction has also been referred to as the homolytic cleavage of dihydrogen, although no hydrogen radicals are involved in the cleavage reaction itself. In subsequent reactions this type of catalysts may indeed give rise to organic radicals. We will call it an ‘oxidative addition’ to a binuclear metal centre. One may have some doubt about the hydridic nature of the hydrides formed, because in the hydrido cobalt carbonyl the hydrogen atom shows an ‘amphoteric’ character: sometimes it reacts as an H^- anion, and in other cases its reactions are best described as an H^+ cation (it is reported to be as acidic as sulphuric acid). Note that in the former

case the Co centre is formally monovalent, whereas in the proton case its valency is minus one. This demonstrates the ability of the metal centre to accommodate changes in effective oxidation states.

The oxidative addition of acids is another instructive example. It resembles the reactions with alkyl halides and may result in another 'amphoteric' hydride:



The starting material is an 18-electron nickel(0) complex which is protonated forming a divalent five-coordinate nickel hydride [41]. This can react further with alkenes to give alkyl groups, but it can also react as an acid with hard bases to regenerate the nickel(0) complex. Similar oxidative addition reactions have been recorded for phenols, water, amines, carboxylic acids, mineral acids (e.g. HCN), etc.

Intermolecular oxidative additions involving C–H bond breaking is a topic which has been extensively studied recently. It is usually referred to as C–H activation; the idea is that the M–H and M–hydrocarbyl bonds formed will be much more prone to functionalization than the unreactive C–H bond [42–44]. Intramolecular oxidative additions of C–H bonds have been known for quite some time [45] (see Fig. 4.27). This process is termed orthometallation. It occurs frequently in metal complexes, and is not restricted to 'ortho' protons. It has considerable importance in metal-mediated synthesis.

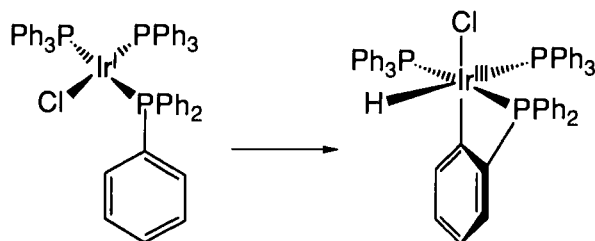


Fig. 4.27. Orthometallation.

4.3.6 Reductive Elimination

Reductive elimination is simply the reverse reaction of oxidative addition: the formal oxidation state of the metal is reduced by two (or one in a bimetallic reaction), and the total electron count of the complex is reduced by two. While oxidative addition can also be observed for main group elements, this reaction is more typical of the transition elements in particular the electronegative, noble metals. In a catalytic cycle the two reactions occur pairwise. At one stage the oxidative addition occurs, followed by, for example, insertion reactions; and then the cycle is completed by a reductive elimination of the product. Reductive

elimination can be enhanced by electron-withdrawing ligands on the metal, i.e. when the state of lower valency (electron-rich metal centre) is stabilized. Chemical oxidation (one or two electron) of a complex may also initiate reductive elimination. Only one example will be discussed here, as most reactions are directly the reverse of the ones discussed above under oxidative additions.

Reductive elimination of molecules with carbon–carbon bonds has no counterpart in oxidative addition reactions because the metal–carbon bond energies ($120\text{--}240\text{ kJ mol}^{-1}$) may not always be large enough to compensate for the energy of the carbon–carbon bond (370 kJ mol^{-1}), and secondly, the carbon–carbon bond is much less reactive than a carbon–hydrogen bond or a dihydrogen bond due to repulsive interactions between the attacking substituted C–C bond and the ligands surrounding the metal centre.

Examples of reductive elimination are present in the literature mostly for group 10 metals, e.g. Fig. 4.28. As outlined above, the reaction can be induced by the addition of electron-withdrawing ligands; in this case electron-poor alkenes are very effective as ligands.

In practice the reactions are less straightforward than is shown in Fig. 4.28, and several other decomposition pathways are available (see α -elimination below).

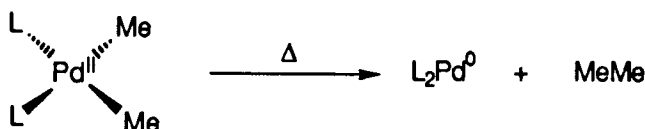


Fig. 4.28. Reductive elimination of a C–C bond.

4.3.7 α -Elimination Reactions

α -Elimination reactions have been the subject of much study since the mid-seventies, mainly due to the pioneering work of Schrock [47,48]. The early transition metals are most prone to α -elimination, but the number of examples of the later elements is growing. A now classic example (1973!) is shown in Fig. 4.29.

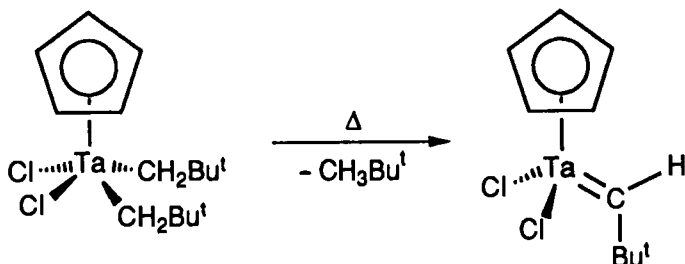


Fig. 4.29. α -Elimination.

The process is called α -elimination because a hydrogen at the alpha carbon at the metal is being eliminated (if we regard the product as a metalla-alkene the process should be called β -elimination, but this only adds to the confusion). The electron-deficient tantalum atom forms 'agostic' bonds with hydrogens in the α -positions. (Agostic interaction implies electron donation by nearby atoms or bonds to highly electrophilic metal centres which is observed spectroscopically or as a distortion in the crystal structure). In the starting material this activates one hydrogen that will then leave with the neopentyl anion as neopentane. In the alkylidene complex formed there is a strong interaction between tantalum and the electrons of the α -hydrogen of the alkylidene. Consequently, in suitable complexes α -elimination can occur twice, yielding alkylidyne complexes. See Fig. 4.30 for a simplified example with tungsten.

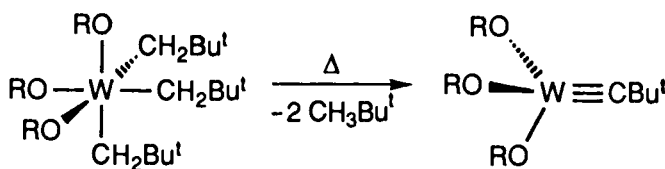


Fig. 4.30. α -Elimination giving alkylidyne complexes.

In decomposition reactions of dimethyl–metal complexes of palladium(II) and nickel(II) one finds the formation of only traces of methane [49] which may also attributed to an α -elimination process. In regard to the valence state, note that, formally, the alkylidene ligand is considered as a neutral ligand and therefore, in the tantalum–alkylidene complex in Fig. 4.29, tantalum is trivalent. The electronic structure of the alkylidene is of course reminiscent of the corresponding oxide $\text{CpTa}(\text{Cl})_2\text{O}$, which we would definitely call pentavalent. All that matters is that there should be a sufficient number of electrons for the multiple bonds which we draw.

4.3.8. Cyclometallation

Cyclometallation refers to a process in which unsaturated moieties form a metallacyclic compound. It is sometimes categorized under oxidative additions, but we prefer this separate listing. Examples of the process are presented in Fig. 4.31. Metal complexes which actually have displayed these reactions are M = L₂Ni for reaction **a**, M = Cp₂Ti for reactions **b** and **c**, M = Ta for **d**, and M = (RO)₃W for **e**. The latter examples involving metal–carbon multiple bonds, have only been observed for early transition metal complexes, the same ones mentioned under the α -elimination heading.

In examples **a** and **b** in Fig. 4.31, the metals increase their valency by two, and this is not just a formalism as the titanium(II) and the nickel(0) are indeed very electron-rich metal centres. During the reaction a flow of electrons takes place from the metal to the organic fragments which end up as anions. In these two reactions the metal provides two electrons for the process, as in oxidative addition reactions. The difference between cyclometallation and oxidative addition is that, during oxidative addition, a bond in the adding molecule is being broken, whereas in cyclometallation, fragments are added together. For reactions **c** and **d** the situation is slightly different. The formal valency of the metal increases in **c** and **d** with two units again when the alkylidene is considered as a two-electron neutral ligand. The two electrons donated by the metal in the 'oxidative addition' process were already involved in the bonding of the alkylidene, and not present at the metal centre as a surplus nonbonding lone pair (cf. square planar d^8 complexes, or the above d^2 Ti and d^{10} Ni cases). The reaction of the alkylidyne **e** is a cyclometallation reaction for which other descriptions make little sense.

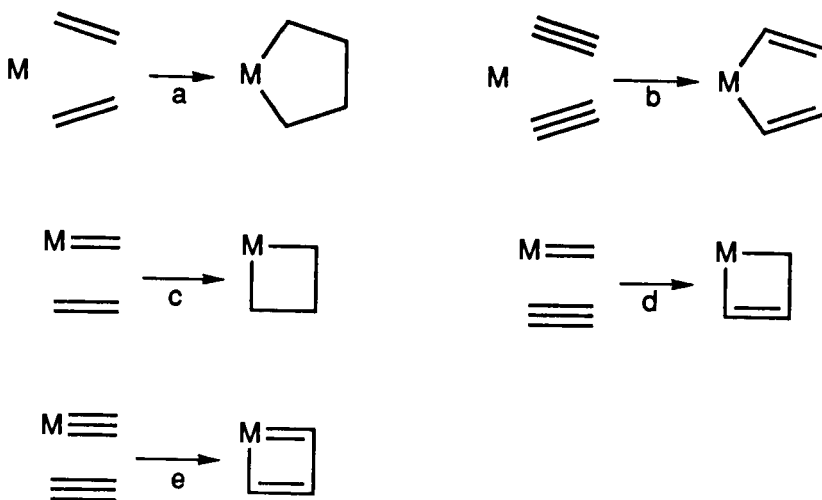


Fig. 4.31. Cyclometallations.

Three mechanisms can be proposed for the intimate reaction mechanism for **c–e**, analogous to the organic 2+2 cycloadditions: a pericyclic (concerted) mechanism, a diradical mechanism, and a diion mechanism. In view of the polarization of the metal(+) carbon(–) bond, an ionic intermediate may be expected. The retention of stereochemistry, if sometimes only temporary, points to a concerted mechanism.

The reverse reaction of a cyclometallation is of importance for the construction of catalytic cycles. The simple retrocyclometallations of **a** and **b** are not produc-

tive, since they would again lead to ethene and ethyne, and additional reactions have to be invoked for a productive catalytic cycle. For **c–e** the following retro reactions can be envisaged, leading to new products: see Fig. 4.32.

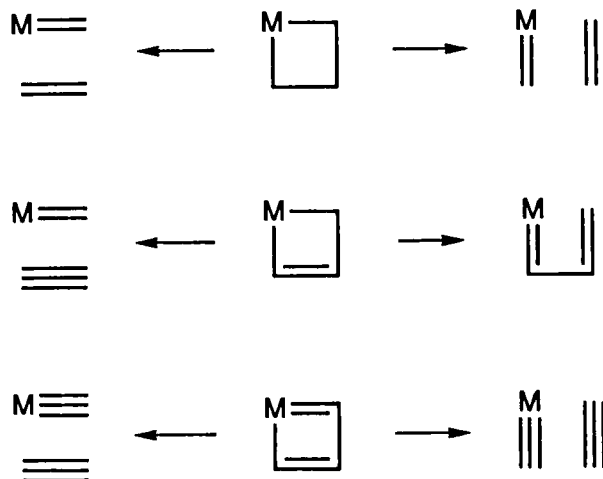


Fig. 4.32. Retro-cyclometallations.

Reaction **a** in Fig. 4.31 may be succeeded by various other reactions such as insertions, β -eliminations or regular reductive eliminations (see Fig. 4.33).

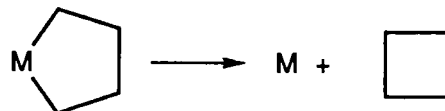


Fig. 4.33. Cyclisation through reductive elimination.

The reductive elimination reaction is governed by the common rules given in Section 4.3.6. Nickel-catalyzed cyclodimerization [50] affords 1,5-cyclooctadiene which is used as such in a variety of chemical applications or is reduced to cyclooctene which is, *inter alia*, used for the production of cyclooctenemers, a ring-opening metathesis product. The first step involves the coordination of a diene molecules to zerovalent nickel (and an additional ligand L). Then a cyclometallation takes place during which the nickel is transferred into divalent nickel. A reductive elimination completes the cycle regenerating nickel(0) and the two carbon–carbon bonds have been formed. Figure 4.34 shows the essential details.

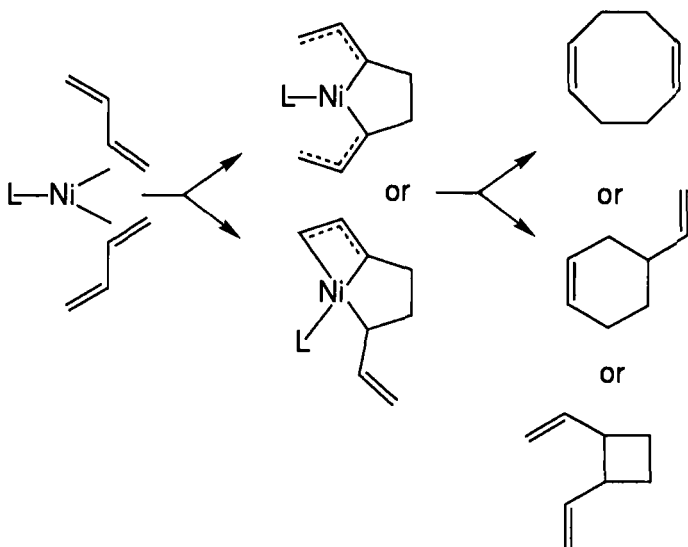


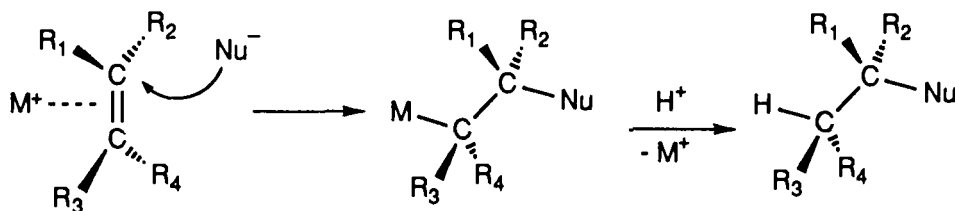
Fig. 4.34. Cyclodimerisation mechanism.

4.3.9 Activation of a Substrate toward Nucleophilic Attack

Alkenes

Coordination of an alkene to a relatively electronegative metal (it may often carry a positive charge) activates the alkene toward attack of nucleophiles. After the nucleophilic attack the alkene complex has been converted into a σ -bonded alkyl complex with the nucleophile at the β position. With respect to the alkene (in the ‘organic’ terminology) the alkene has undergone *trans*-addition of M and the nucleophile Nu, see Fig. 4.35. As indicated in Section 4.35, the overall result is the same as that of an insertion reaction, the difference being that insertion gives rise to a *cis*-addition and formation of a vacant site, and nucleophilic attack to a *trans*-addition. There is ample proof for the *trans* fashion; the organic fragment can be freed from the complex by treatment with protic acids and the organic product can be analyzed. Suitably substituted alkenes will show the *trans* or *cis* fashion of the addition. Hydrides can be added *trans* to an alkene by taking a borohydride anion as the nucleophile and adding that to a coordinated, and thus activated, alkene.

In Fig. 4.35 the nucleophile depicted is anionic, but Nu may also be a neutral nucleophile, such as an amine or H_2O . There are many alkene complexes of middle and late transition elements which undergo this type of reaction, e.g. M = Pd^{2+} , Pt^{2+} , Hg^{2+} , Zn^{2+} , $\text{FeCp}(\text{CO})^{2+}$. The addition reaction of this type is the key step in the Wacker-type processes catalyzed by palladium.

Fig. 4.35. Nucleophilic *trans*-attack on a coordinated alkene.

Alkynes

Alkynes show the same reaction, and again the product obtained is the *trans* isomer. After a suitable elimination from the metal the alkene obtained is the product of the *trans*-addition. Earlier we have seen that insertion into a metal–hydride bond and subsequent hydrogenolysis of the M–C bond will afford the *cis*-alkene product. Thus, with the borohydride methodology and the hydrogenation route, both isomers can be prepared selectively.

Carbon monoxide

Carbon monoxide, when coordinated to a metal centre, is subject to activation toward nucleophilic attack. Through σ donation and π back donation into the antibonding CO π^* orbitals the carbon atom has obtained a positive character. This makes it not only more susceptible to a migrating anion at the metal centre, but also to a nucleophile attacking from outside the coordination sphere. In this instance it is more difficult to differentiate between the two pathways. There are examples showing that the electrophilicity of the carbon atom can be further increased by the action of Lewis acids complexing to the oxygen atom of the coordinated CO. Figure 4.36 shows an alkoxide attack at coordinated CO giving a carboalkoxy complex, and a borohydride attack at coordinated CO in which the boron simultaneously acts as a Lewis acid in the final product [51]. The BH₃ complexation now stabilizes the formyl complex that would otherwise be

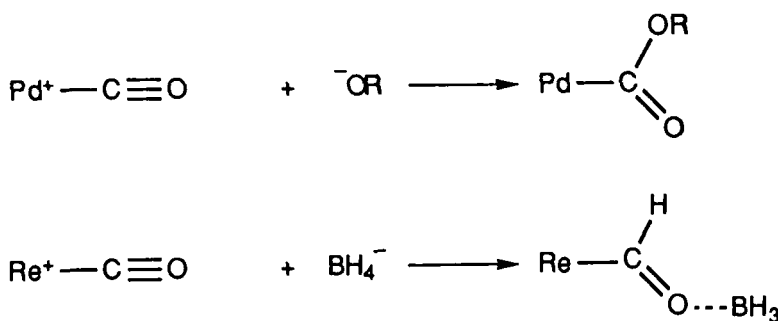
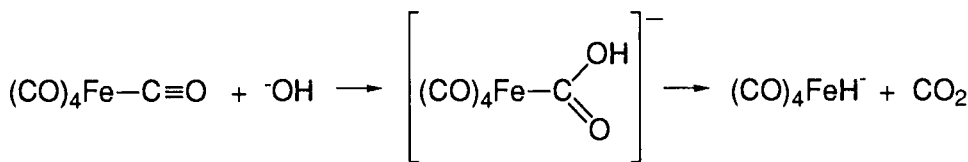


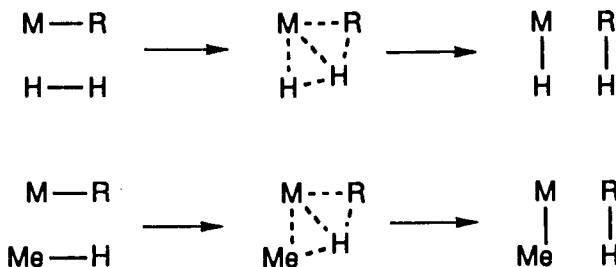
Fig. 4.36. Nucleophilic attack at coordinated CO.

Fig. 4.37. Nucleophilic attack at $Fe(CO)_5$.

thermodynamically inaccessible. The latter reaction has so far only been of academic interest in homogeneous systems (it may be relevant to heterogeneous systems though proof is lacking). The nucleophilic attack by alkoxides, amines, and water is of great interest to homogeneous catalysis. A dominant reaction in syn-gas systems is the conversion of carbonyls with water to metal hydrides and carbon dioxide ('shift reaction'), see Fig. 4.37.

4.3.10 σ -Bond Metathesis

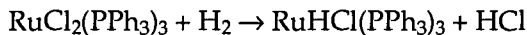
A reaction which is relatively new is the so-called σ -bond metathesis [52]. The word metathesis is used because of the now well-known metathesis of alkenes and alkynes. It is a concerted 2+2 reaction immediately followed by its retrograde reaction giving metathesis. The transition state is strongly polarized, such that in the reaction of $M-R$ with $H-H$ (Fig. 4.38), the transition state contains a $[H\cdots H\cdots R]^-M^+$ unit with large negative charges at the terminal groups. The highly electronegative metal ion affords the appropriate empty orbitals for the stabilization of the complex anion in the transition state. Both late and early transition metal alkyls are prone to this reaction, but its occurrence had to be particularly invoked in the case of the early transition metals. Many similar reactions, such as the reaction of metal alkyls with other $H-X$ compounds, could be described as if they followed this pathway, but the use of the term σ -bond metathesis is restricted to those reactions in which one reacting species is a metal hydrocarbyl or metal hydride and the other reactant is a hydrocarbon or dihydrogen. Two reactions have been depicted in Fig. 4.38. There are, of course, borderline cases; when the reacting hydrocarbon is acidic, as in the case of 1-alkynes, a direct attack of the proton at

Fig. 4.38. σ -Bond metathesis.

the carbanion can be envisaged. It has been proposed that acyl metal complexes of the late transition metals may also react with dihydrogen according to a σ -bond metathesis mechanism. However, an alternative exists for the late elements in the form of an oxidative addition reaction. This alternative does not exist for d^0 complexes such as Sc(III), Ti(IV), Ta(V), W(VI), etc. and in such cases σ -bond metathesis is the most plausible mechanism. σ -Bond metathesis can also be regarded as a special case of heterolytic cleavage (see Section 4.3.11), but the latter reaction has only been observed for dihydrogen, so far, and not for alkanes.

4.3.11 Heterolytic Cleavage of Dihydrogen

Dihydrogen is said to be heterolytically cleaved when it is dissociated into a proton and a metal bonded hydride. It has been the topic of much study and discussion, and the evidence for its occurrence has been growing steadily [54,55]. In the ideal case the heterolytic splitting is catalyzed by the metal ion and a base which assists in the abstraction of the proton. In this reaction there is no formal change in the oxidation state of the metal. The mechanism has been proposed for Ru(II) complexes which can react with dihydrogen according to:



Note, however, that ruthenium has a sufficient number of d electrons to allow for oxidative addition of dihydrogen, which could then be quickly followed by reductive elimination of HCl. It is difficult to distinguish between the two pathways experimentally. Recent observations on dihydrogen complexes of ruthenium have thrown a new light on the heterolytic splitting of dihydrogen. $\text{CpRu(L)(L')(\eta}^2\text{-H}_2\text{)}^+$ reacts rapidly with NEt_3 , as can be deduced from the dynamic ^1H NMR spectra, which indicate a rapid exchange of the dihydrogen complex with its conjugate base, CpRu(L)(L')H . This reaction is much faster than the exchange with the corresponding dihydride complex. The present studies on dihydrogen complexes may lead to a better understanding of the heterolytic splitting of dihydrogen, which is now shown to be activated towards reaction with a base through complexation to a cationic complex.

4.4 ELEMENTARY REACTION STEPS ON SURFACES

It is convenient to subdivide the reactions discussed in this section into three groups:

(a) *Reactions catalysed by metals*

In the substantial majority of cases the reaction takes place between the adsorbed molecule, or their fragments. This is known as the Langmuir–Hinshelwood mechanism. For very few reactions a so-called Eley–Rideal mechanism has been postulated, in which an adsorbed molecule or its fragment reacts with a molecule impinging from the gas(liquid)phase.

(b) Oxidation/reduction reactions catalysed by oxides

In many of these reactions a lattice constituent — oxygen or hydrogen — is brought into reacting molecules and the lattice defect is subsequently removed by a reaction with another reaction component, or by a reaction with another reactive centre of the same molecule. This is the so-called Mars and van Krevelen mechanism. With some oxides peroxide groups are formed on the surface (from adsorbed oxygen molecules). Radicals may form at high temperatures (1000 K).

(c) Acid base reactions catalysed by oxides

Examples are reactions initiated by the protonation, as for example carbenium ion formation from — for example — olefins (Brønsted acidic centres) or deprotonation reactions like base-catalysed aldol condensation.

4.4.1 Metal Catalysed Reactions

General features

Let us start with some features of mechanisms which are typical of metals. First, clean surfaces have a very high reactivity. Therefore, under conditions in which we usually determine the rates (or apply a reaction in practice), the surface is almost completely covered by one or another component of the reaction catalysed. For example, upon a (model) reaction $H_2+D_2 = 2HD$, the surface of active metals is covered by a hydride like layer. Upon reaction of hydrocarbons, carbide-like species or graphitic layers can be formed. Actually, a really 'clean' reaction on metals does not exist under conditions in which one wants to measure the rate. We do not know the extent to which modifying layers retain some activity of their own. But some authors claim that these layers are very active indeed [56–59]. It has also been postulated that the firmly bound species (carbides, sulphides, graphitised carbon islands, etc.) modify the surface structure to such an extent that this change of surfaces cannot be ignored when discussing the mechanism of reactions on metals because new centres are created [60,61]. An artist's view of a working surface of a model metal catalyst (stepped single crystal surface) in contact with gas mixtures containing hydrocarbons is shown in Fig. 4.39.

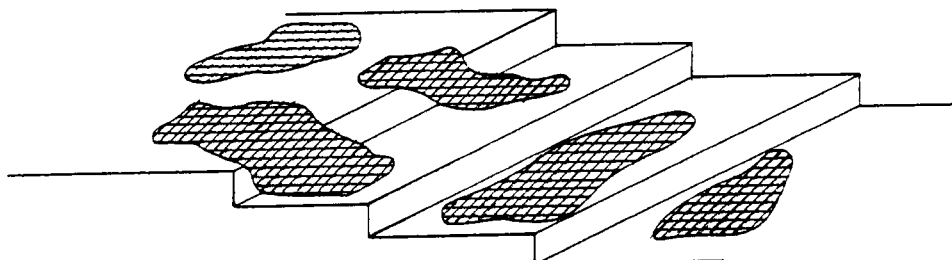


Fig. 4.39. Single crystal metal surface with cut forming steps. After adsorption of a hydrocarbon, islands are formed (preferentially on terraces) of hydrogen-lean–carbon-rich species.

A second important feature of reactions on metals is that a metal surface is a locus of very high density of active atoms. A molecule can thus be very easily bound to several contiguous atoms simultaneously or, as one says, to an ensemble of atoms [62,63]. For example, it is known that CO can be coordinated to 1, 2 or 3 (perhaps also 4) metal atoms, whereby each form shows a different frequency of CO stretching vibration $\nu(\text{C}\equiv\text{O})$.

All reactions on metals can be subdivided into two groups:

- (i) reactions which are not sensitive to the ensemble size variations such as (de)hydrogenations on the C–C, C–O or C–N bonds; and
- (ii) reactions sensitive to the ensemble size, such as hydrogenolysis of hydrocarbons (fission of a C–C bond), Fischer–Tropsch synthesis reactions (fission of the C–O bond), hydrogenolysis of C–O, C–N and most likely N–O bonds.

Also the mode of adsorption (e.g. of CO, hydrocarbons, etc.) can depend on the available ensemble size or given composition of the surface [64–68]. It appears that the heat of adsorption of various modes of CO adsorption is only marginally influenced when the required ensemble (1, 2 or 3 and more) is transferred from a pure metal into a matrix of another metal (for instance alloys with Cu, Au and Ag). When a CO molecule, monitored by IR spectroscopy, is taken as a probe of the local electronic structure of atoms (or ensembles of atoms), no pronounced effects of alloying are found [69–71].

4.4.1.1 Adsorption modes and reactivity of diatomic molecules

The adsorption of diatomic molecules on a metal surface may be considered as a competition between molecular and dissociative adsorption



Dissociative adsorption can occur when the bonds formed between the fragments of the dissociated molecule and the surface are much stronger than the bonds within the molecule and between the molecule and the surface. For example, molecular dihydrogen, dioxygen or dinitrogen are only weakly adsorbed on the transition metals. Oxygen, hydrogen and nitrogen adatoms, on the other hand, are strongly bound on many metal surfaces. Therefore, dissociative adsorption is often thermodynamically possible, as will be discussed below.

Molecular adsorption of CO and NO is relatively strong on many metal surfaces. These adsorbates may undergo both dissociative and molecular adsorption on the same surface depending on the experimental conditions.

Figure 4.40 shows schematically three possible forms of potential energy curves for molecular and dissociative adsorption as the molecule approaches the surface. The molecularly adsorbed state can be considered as a precursor state for dissociation. The dotted curves represent molecular adsorption with a heat of adsorption

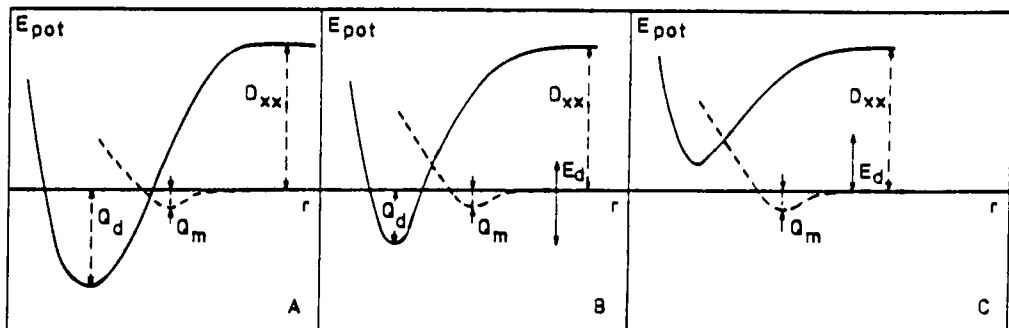


Fig. 4.40. Potential energy plots for dissociative adsorption of a molecule XX. D_{xx} is the dissociation energy of the free molecule, E_d is the activation energy for dissociative adsorption. Q_m is the heat of adsorption in the molecular state. Q_d is the heat of dissociative adsorption, and r is the reaction coordinate.

Q_m at the equilibrium distance r_m . Molecular adsorption is usually a non-activated process. The solid curves represent adsorption of the atoms following dissociation of the molecule in the gas phase, the heat of adsorption is Q_d at the equilibrium distance $r_d < r_m$ corresponding to the short-range chemical interaction.

The crossover point of the two curves determines the activation barrier of the dissociative adsorption. In Fig. 4.40A, which applies, for example, to hydrogen on transition metals, the dissociative adsorption has a zero activation energy. In Fig. 4.40B, dissociation also results in a strong chemisorption bond. However, the dissociative adsorption requires an activation energy. A typical example is hydrogen on a Cu(111) surface [72]. The activation energy for dissociation is much smaller than the dissociation energy of the free molecule. Figure 4.40C shows a typical example of an endothermic, dissociative adsorption. The potential energy of the two adsorbed atoms is higher than that of the free molecule, but lower than that of the two gaseous atoms. Therefore, dissociative adsorption can only take place when the molecule is predissociated in the gas phase and at temperatures where the adsorbed atoms are immobile on the surface. At higher temperatures, when the adsorbed atoms are sufficiently mobile over the surface, the atoms will recombine and desorb as a molecule. A typical example is hydrogen on glass or gold.

It is often observed that molecular adsorption prevails at lower temperatures and that dissociative adsorption occurs at higher temperature. This may be caused by kinetics; the activation energy for dissociative adsorption is then too high for dissociation at lower temperature. It could also have a thermodynamic reason. If the number of surface sites where adsorption can take place is equal for molecular and dissociative adsorption, the surface can accommodate twice as many molecules in the molecular state than in the dissociative state. Hence, molecular adsorption will prevail if the heat of dissociative adsorption is not very much higher than the heat of molecular adsorption. The entropy change upon

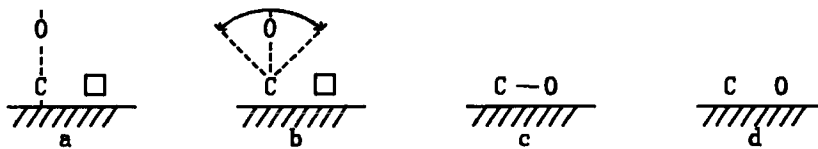


Fig. 4.41. Molecules like CO are bonded in most of the group 8–10 metal surfaces with the molecular axis perpendicular to the surface (a) or slightly tilted. The amplitude of vibration around the surface normal increases with increasing temperature (b). At a certain temperature an oxygen–metal bond is formed (c) and dissociation occurs (d).

adsorption is negative and, consequently, desorption will occur at a sufficiently high temperature. In the case considered above only half the number of molecules can be adsorbed in the dissociative state compared to the molecular state. As a result the entropy of the system will be lower for molecular adsorption and dissociation can occur at higher temperatures.

Dissociative adsorption requires a cluster of several free and contiguous metal atoms in an ensemble on the surface. Therefore it is often found that dissociation occurs only when the surface coverage is low and that molecular adsorption takes place above a certain coverage.

A diatomic molecule has to be adsorbed parallel to the surface in order to dissociate. The more favourable adsorption complex for molecules like CO on a group 8–10 metal surface is that in which the molecular axis stands perpendicular to the surface. It has been demonstrated by ESDIAD (electron stimulated desorption, ion angular dependence) that the molecular axis vibrates with regard to the surface normal and that the amplitude of vibration increases with increasing temperature; this is shown in Fig. 4.41.

At the dissociation temperature the vibration amplitude has become sufficiently large that a bond between the O atom and the metal surface can be formed resulting in dissociation.

Before we present a survey on the adsorption of several simple gases some general aspects of the dissociative adsorption will be treated. Table 4.1 tabulates the dissociation energies of reactants in the gas phase. Table 4.2 shows some examples of the heats of formation of hydrides, nitrides, carbides and oxides.

The following relevant conclusions emerge:

- (1) Dissociation in the gas phase becomes more difficult in the order $\text{H}_2 < \text{O}_2 < \text{NO} < \text{CO}$ and N_2 .
- (2) The order in strength of the metal–X bond ($X = \text{H}, \text{C}, \text{N}$ and O) is $\text{M}-\text{H} < \text{M}-\text{C} < \text{M}-\text{N} < \text{M}-\text{O}$ for the same metal in surface.
- (3) From (1) and (2) it follows that dissociative adsorption on a certain metal surface become more favourable in the order N_2 and $\text{CO} < \text{NO} < \text{O}_2$.
- (4) For the transition metals the M–X bond strength increases for metals further to the left in the periodic table and it decreases on going down from $3d$ to $5d$ metals.

TABLE 4.1

Dissociation energies in the gas phase

d_{298}^0	kJ mole ⁻¹
H ₂	436
O ₂	498
NO	631
N ₂	945
CO	1076

TABLE 4.2

Heats of formation of Ti, Mo, Pd and Ni hydrides, carbides, nitrides and oxides at 198 K, 1 bar. Values in kJ mole⁻¹ of H, C, N, or O

Ti		Ni	
TiH _{1.7}	– 69*		
TiC	–226	Ni ₃ C	+ 46
TiN	–336	Ni ₃ N	+ 1
TiO _{2.2}	–456	NiO	–244
Mo		Pd	
Mo ₂ C	– 23		
Mo ₂ N	– 69		
MoO ₂	–272	PdO	– 85

(All values are taken from Refs. [42–44], except * (from Refs. [45,46].)

The surface structure may have an additional influence on the dissociation. In general, close-packed surfaces are the least active and rough surfaces or surfaces with steps or kinks the most active in dissociation.

4.4.1.2 Elementary theory of dissociation and association reactions on metal surfaces

Let us now analyse dissociation and recombination in detail. As we saw in the previous sections dissociative adsorption is a process consisting of at least two consecutive elementary steps. Molecular adsorption proceeds dissociation. Dissociation occurs when reaction (4.4) is thermodynamically feasible. We learned in Section 4.2.1 that the surface adatom bond energy varies more than the molecular adsorption bond with variation of metal. Adsorption of atoms is favoured by metals with a partially filled *d* valence electron band or metals of a low work function. CO will dissociate on the first row transition metals (except

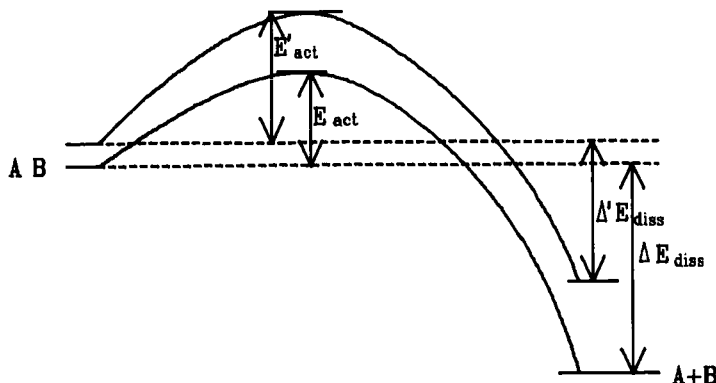


Fig. 4.42. Relation between δE_{act} and δE_{diss} (schematic).

on Cu), it will barely dissociate on Rh, and not at all on Pt or Ir. O₂ will dissociate on all transition metals, including Cu and Ag, but not on Au.

According to the Polanyi relation, the change of the activation energy for dissociation δE_{act} is proportional to the change in dissociation energy $\delta \Delta E_{\text{diss}}$:

$$\delta E_{\text{act}} \approx \frac{1}{2} \delta \Delta E_{\text{diss}} \quad (4.5)$$

On a transition metal surface the dissociating molecule prefers a specific reaction-path [75]. This is sketched in Fig. 4.43 for CO on a (111) surface. The surface atoms generated by dissociation prefer high coordination sites. According to the nomenclature of organometallic chemistry such sites are denoted μ_n sites, n being the number of metal atoms involved in the chemisorptive bond. CO bonded with one molecular atom to the surface is η^1 bonded. Side-on adsorbed CO is η^2 bonded. When the atoms are adsorbed in neighbouring adsorption sites (e.g. a and b, Fig. 4.43) they experience a large repulsive interaction. The effective number of neighbours of the surface metal atom has increased by adsorption, which reduces the bond strength of the atoms that are coordinated to this surface-metal atom. When one of the atoms adsorbs in site a, the other metal surface sites, c or d, are positions where the dissociated atoms share the least number of surface atoms and hence have the smallest repulsive interaction.

The activation energy is least when the CO bond is weakened because of its interaction with the metal surface. Electron transfer from the metal surface into antibonding molecular orbitals weakens the CO bond. This is a very general feature of dissociative adsorption. The dissociation energy of adsorbed molecules decreases when they are adsorbed with considerable electron transfer from the metal surface to the adsorbate.

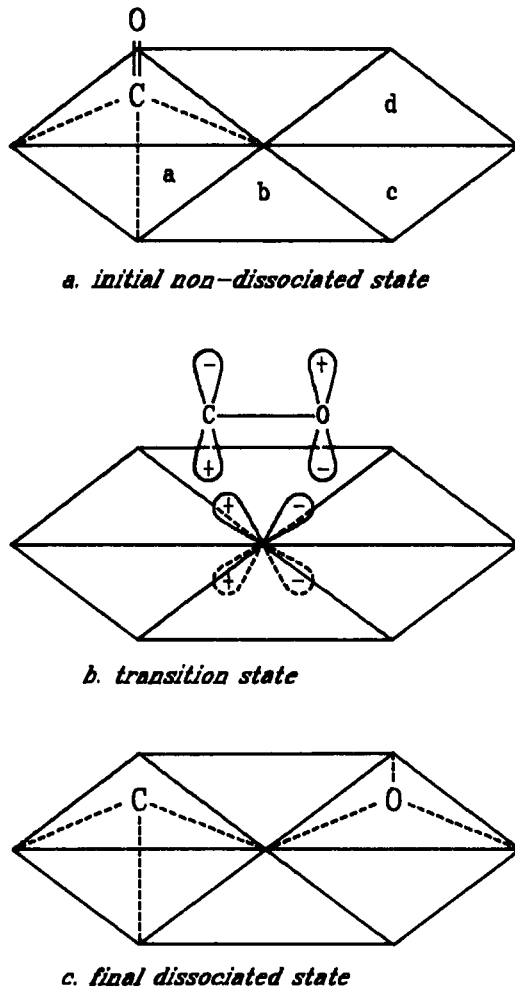


Fig. 4.43. Dissociation of CO (schematic).

For instance, O_2 molecules readily dissociate on the Ag (110) surface. The molecule is adsorbed as O_2 with a charge of the order of ~ 1.6 a.u. [76,77]. Chemisorbed CO undergoes considerable CO bond weakening, because electron donation to CO populates its antibonding $2\pi^*$ orbitals (see Fig. 4.4). The antibonding bond (i.e. weakening orbitals) are usually antisymmetric with respect to a molecule or bond symmetry axis. The dissociating molecule, parallel to the surface, has to interact with surface orbital fragments of proper symmetry in order that electron donation may occur. As sketched in Fig. 4.43 d_{xz} or d_{yz} orbitals have the proper symmetry. So, for a low dissociation energy barrier, interaction with occupied d surface atomic orbitals asymmetric with respect to the surface is essential. Whereas, for a dissociation reaction, electron transfer between surface

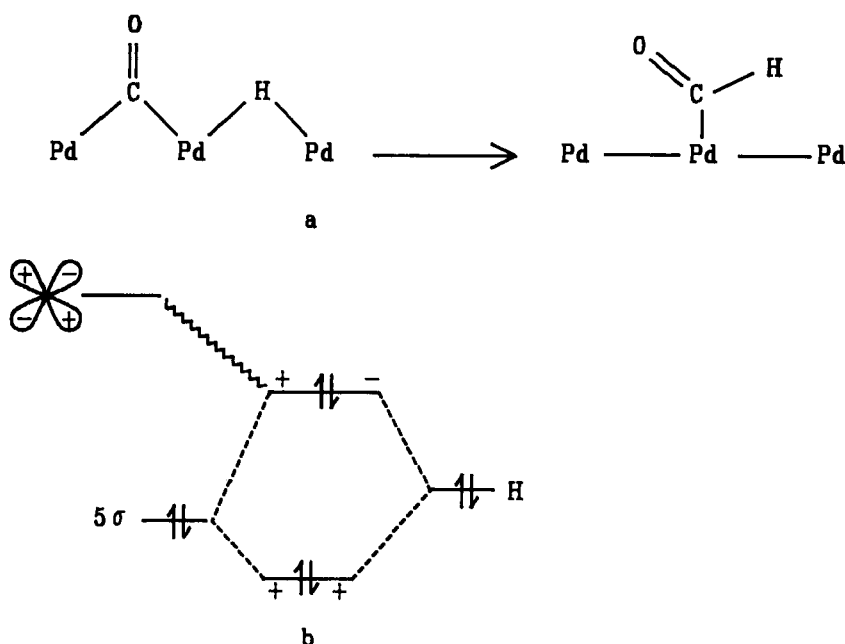


Fig. 4.44. Formyl formation on a palladium surface (schematic). (a) Molecule fragment rearrangement on the metal surface. (b) σ -Orbital interaction scheme.

and adsorbate is favourable, the reverse is the case for the association reaction. This is obvious for diatomic molecules, but it is also valid for more complex reactions. We will analyze this for the formation of a formyl intermediate from adsorbed H and CO. For CO and H chemisorbed to Pd this reaction is sketched in Fig. 4.44.

When the hydrogen atom and CO move together, a repulsive interaction between the doubly occupied CO 5σ orbital and the H s orbital develops [78–80]. This is sketched in Fig. 4.44. A bonding and an antibonding orbital fragment are formed. Both orbitals are doubly occupied, hence they interact repulsively. The repulsive interaction is relieved when electrons from the antibonding orbital can be back-donated to the metal. An empty d_{xz} and d_{yz} orbital has a proper symmetry for that. Therefore formyl formation is expected to occur on metal surfaces with empty, low-lying d valence orbitals. All transition metals, except Cu, Ag and Au, have empty d orbitals. Metals with a high work function, such as Pt and Pd, are particularly suitable. The competitive reaction of CO dissociation will be suppressed on such metals. The formyl formation mechanism described here for a metal surface was first discovered in a theoretical study of a Pd^{2+} organometallic complex [81]. Pd has to be an ion because Pd atoms have no empty d atomic orbitals.

Formyl intermediates are easily hydrogenated to give methanol. Copper based catalysts are very active methanol catalysts. Because Cu has a completely filled d

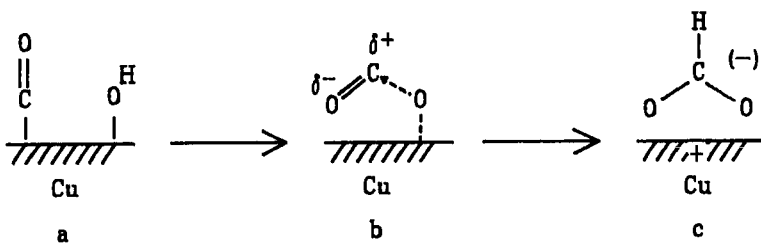


Fig. 4.45. Formate formation from CO and Cu (schematic).

valence electron band, methanol formation cannot proceed on metallic Cu via formyl formation. On a Cu catalyst methanol formation can occur via the formate intermediate, which is subsequently hydrogenated to methanol. Formate formation probably occurs by reaction of a surface hydroxyl with chemisorbed CO. Because of the weak interaction between Cu, Cu⁺ and CO and the charge build-up on the CO oxygen atom, an intermediate, as sketched in Fig. 4.45, is most likely. Methanol formation on Cu occurs most readily by hydrogenation of CO₂. Intermediates like 4.43b and c can now form readily. Below we will discuss a related surface intermediate formed in the Cu-catalysed oxidation of CO.

Another important association reaction is hydrocarbon formation by carbon–carbon bond closure. This occurs with hydrocarbon fragments in the presence of hydrogen or from carbon monoxide (Fischer–Tropsch process). The surface reaction



readily proceeds on the transition metals with *d* valence electron vacancies, but is prohibited on metals with excessively strong M–C or M–H bonds [82,83]. The rate of recombination is expected to be a maximum on Pt, a metal with the weakest M–C bond. Recombination of methyl radicals appears to be prohibited because of repulsive interactions between the methyl hydrogen atoms when the methyl groups approach each other. Steric repulsion decreases when the surface hydrocarbon fragments become less saturated with hydrogen. The interaction of a CH₂ and CH fragment is sketched in Fig. 4.46.

Now a close approach is possible, and interaction of several orbitals can also occur. Besides the repulsive interaction between surface σ bonds, a stabilizing interaction between fragment *p* orbitals also takes place. This results in a relatively low activation energy of recombination that only weakly depends on the metal–carbon bond strength. Competition between C–C chain growth and methanation or termination (CH formation) favours C–C chain growth as the metal–carbon bond energy increases.

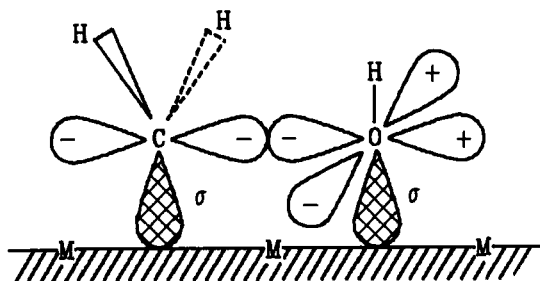
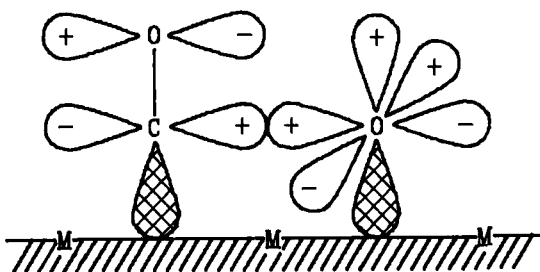
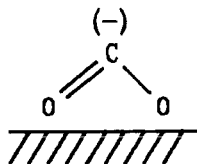
Fig. 4.46. Recombination of CH_2 and CH species.Fig. 4.47. The oxidation of CO by O (schematic).

Fig. 4.48.

The p orbital stabilizing interaction appears to be quite common. It also lowers the activation energy for the O and CO recombination reaction to form linear CO_2 . On a surface that interacts strongly with CO , e.g. a transition metal with partially filled d valence electron orbitals, the reaction proceeds as sketched in Fig. 4.47.

On a low work function metal or one with a filled d valence electron band the bended CO_2 (Fig. 4.48) becomes stabilized and reaction occurs analogously to the $\text{CO}-\text{OH}$ recombination reaction.

As already indicated in the discussion on formyl formation, the transition state on a metal surface may be closely related to that found in the organometallic complexes used in homogeneous catalysis. The p orbital stabilizing interactions have also been shown to play an important role in insertion reactions occurring in organic-metallic complexes [84,85]. It explains, for instance, the higher activa-

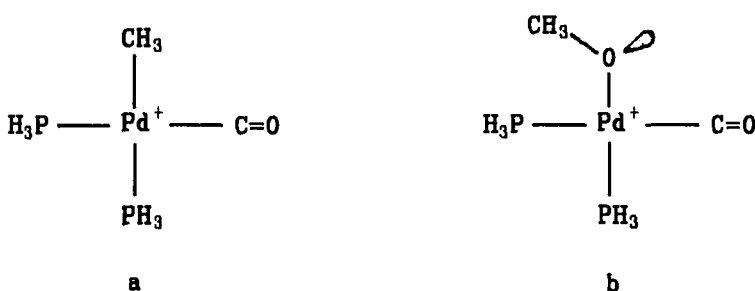


Fig. 4.49. The lone-pair orbital of the methoxy group has a stabilizing interaction with the CO $2\pi^*$ interaction. This interaction is absent with the methyl fragment.

tion energy for insertion of CO in a methyl group compared with a methoxy group in Pd complexes, sketched in Fig. 4.49.

Since dissociation of a molecule requires a certain minimum ensemble of surface atoms, the reactivity of very small metal clusters tends to increase with particle size. Once a cluster with the proper ensemble of atoms has become available the reactivity decreases, because the ensemble acquires an increasing number of metal atom neighbours. These two basic features, illustrated in Fig. 4.50, may explain the frequently observed maximum in cluster reactivity as a function of the number of metal atoms.

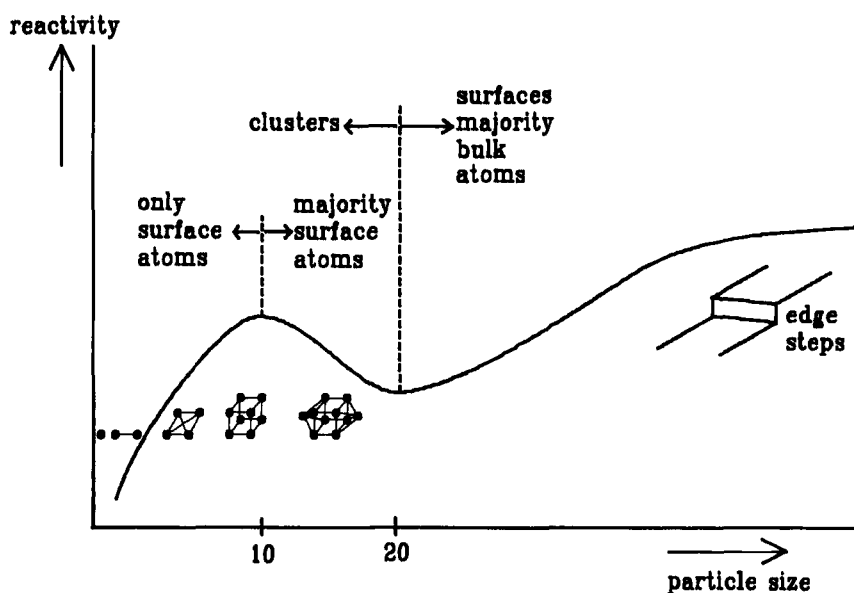


Fig. 4.50. The rate of adsorption as a function of particle size (schematic).

4.4.1.3 CO adsorption

In order to understand the catalytic properties of the various group 8–10 metal surfaces the interactions among neighbouring adsorbed species and their effects on the surface processes should be known, since the surfaces may be covered with different kinds of adsorbates during the reaction. An interesting example is provided by O₂ and CO coadsorption on the Pd (111) surface. Some of the relevant results are summarized here.

Oxygen adsorption is inhibited by pre-adsorbed CO. At coverages below $\theta_{CO} = \frac{1}{3}$, O_{ads} and CO_{ads} form separate domains on the surface. Remarkably, the behaviour is different when O is pre-adsorbed. Then formation of mixed phase of O_{ads} and CO_{ads} occurs (with local coverages of $\theta_O = \theta_{CO} = 0.5$) which are embedded into CO domains. When these mixed phases are present CO₂ is produced even below room temperature. Co-adsorption studies on other noble metal surfaces are consistent with this picture: pre-adsorbed CO inhibits the dissociative adsorption of oxygen whereas CO does adsorb on a surface covered with O. The CO-covered surface is densely packed with CO, but the oxygen atom-covered surface is less densely packed with CO.

The interaction of co-adsorbed H and CO has been studied on a variety of single crystal and polycrystalline surfaces under conditions where reaction does not occur [86]. The following phenomena have been observed: displacement of adsorbed H by CO, blocking of H adsorption by pre-adsorbed CO, segregation of the co-adsorbed species, formation of mixed layers, decreases in the H desorption temperature, but also enhancement in the uptake of CO by the presence of pre-adsorbed H, and formation of new desorption peaks in the TDS. There is no evidence for the formation of directly bonded H–CO from ‘on-top’ sites into bridged sites.

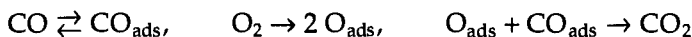
In conclusion, the main effects found for coadsorption are blocking, island formation, displacement by the component with higher heat of adsorption and site conversion. Attractive interactions may occur between the two adsorbates. Hence, the catalytic reactions can be discussed on the basis of the adsorption of the individual reactants in combination with the coadsorption effects mentioned above.

4.4.1.4 Surface reactions of small diatomic and triatomic molecules

The crystal face dependence and the activity of the various group 8–10 metals can be understood in terms of the metal–oxygen bond strength. On an active metal both O₂ and H₂ are dissociatively adsorbed, oxides are not formed under reaction conditions, and the heat of adsorption for O_{ads} is relatively low.

Usually, temperatures of 300–600 K are required for the oxidation of CO over the active metal catalysts Pt, Pd, Ir, Rh, Ru and Ni. It has been established that the

dominant mechanism of the reaction is the Langmuir–Hinshelwood (LH) mechanism:



The activation energy is lower over Pt than over Ir, Rh, Pd and Ru catalysts [87]. CO adsorption inhibits dissociation of O₂ at low temperatures. Because of CO desorption, inhibition becomes less with increased temperatures. The overall rate of oxidation decreases at higher temperatures because of the decrease in surface coverage.

Figure 4.51 shows the rate of CO₂ production over the (111), (100), (410) and (210) surfaces of a Pt-0.25–Rh-0.75 single crystal as a function of temperature using a 2:1 mixture of CO and O₂ for a total pressure of 2×10^{-7} mbar [88]. It shows that the reaction rate increases rapidly between 400 and 500 K up to a temperature T_m where a maximum is reached, after which it slowly decreases with increasing temperature. The temperature at which the maximum occurs increases with increasing the strength of the CO interaction. Similar behaviour has been found on a large number of Pt, Pd, Ir, Rh and Ru surfaces.

In Fig. 4.52 the activity of H₂ oxidation for different metals is plotted as a function of heat of oxygen adsorption. A volcano-type plot is formed. A maximum in rate is found for the metal that can dissociate O₂, but does not bind CO or oxygen too strongly. Gold cannot dissociate O₂, tungsten is inactive because it

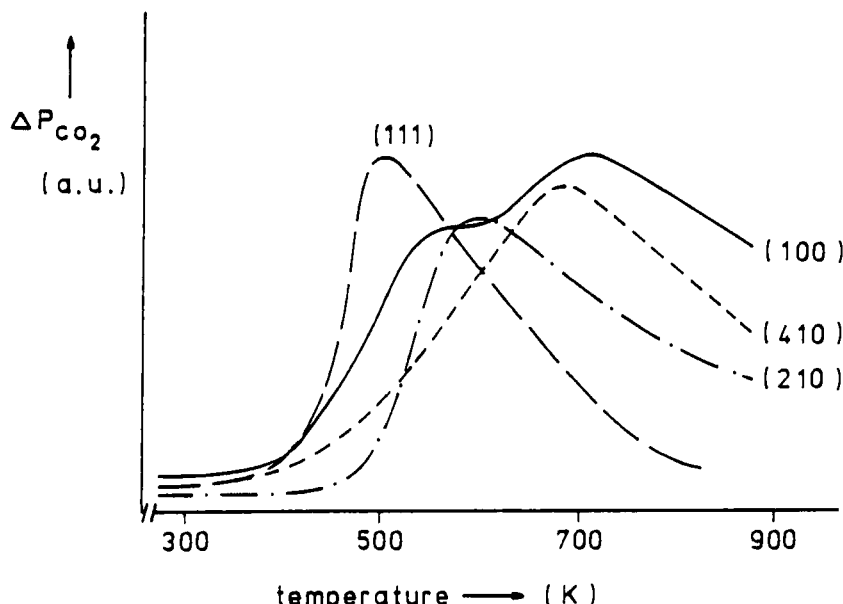


Fig. 4.51. Steady-state rates of CO₂ production for the CO + O₂ reaction over the (111), (100), (410) and (210) surface of a Pt-0.25–Rh-0.75 single crystal (from ref. 88).

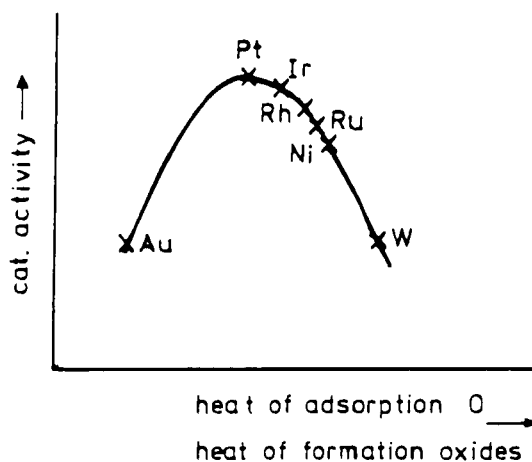


Fig. 4.52. Volcano plot for carbon monoxide oxidation.

forms a stable surface oxide layer. Volcano plots as shown in Fig. 4.52 illustrate the Sabatier principle, stating that optimum activity is obtained when catalysts neither binds intermediates too strongly so as to inhibit adsorption to the surface, nor interacts too weakly so as to cause no initiation of the reaction.

Dissociation is often a crucial step in a catalytic reaction chain. However this is not always the case. Metals active for the $O_2 + H_2$ reaction are the noble metals of group 8–10, especially Pt, a metal with a low O–metal bond strength. The same metals are active for the $CO + O_2$ reaction. The most active metals do not easily break the C–O bond and do not form oxides under reaction conditions. Both reactions are Langmuir–Hinshelwood reactions between adsorbed O and adsorbed H or CO. Desorption of products of the reaction intermediates here is reaction rate controlling.

Active catalysts for the $NO + CO$ reaction must be more active in bond breaking: NO must dissociate, whereas the C–O bond must stay intact. Dissociation is followed by a Langmuir–Hinshelwood reaction of O with adsorbed CO.

For the methanation and NH_3 synthesis reaction the metals must be still more active in bond breaking: the CO and N_2 molecule both must dissociate under reaction conditions and the reaction then proceeds by hydrogenation of C, N and O on the surface. Additional factors that determine the performance of the metal in these reactions are the nature and bond strength of C, N and O on the surface.

4.4.1.5 Adsorption modes and reactivity of hydrocarbons

Hydrocarbons form a variety of species on metal surfaces (shown in Fig. 4.53), which Burwell [89,90] once called “The organometallic zoo” of surface com-

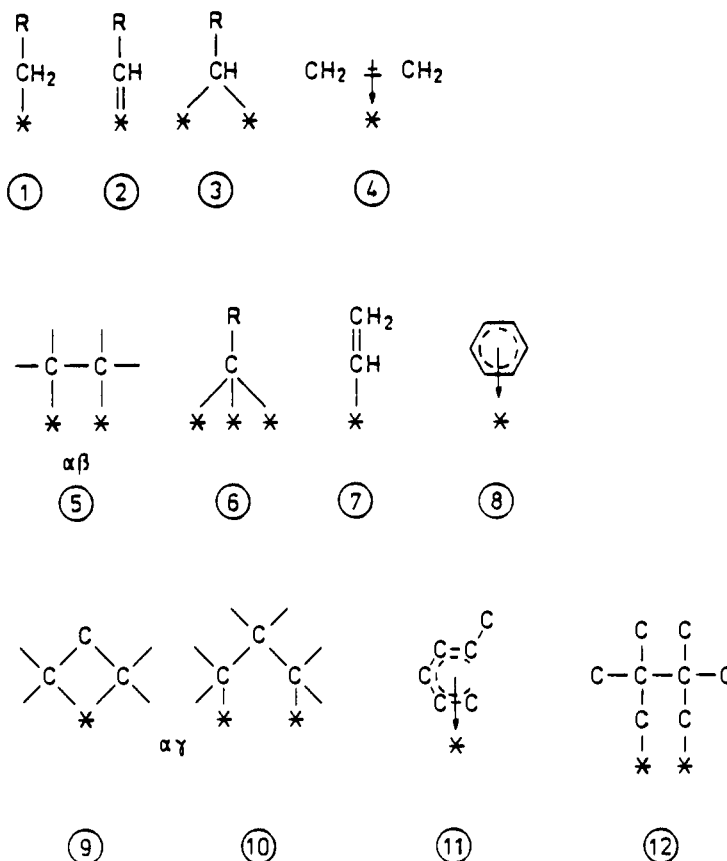
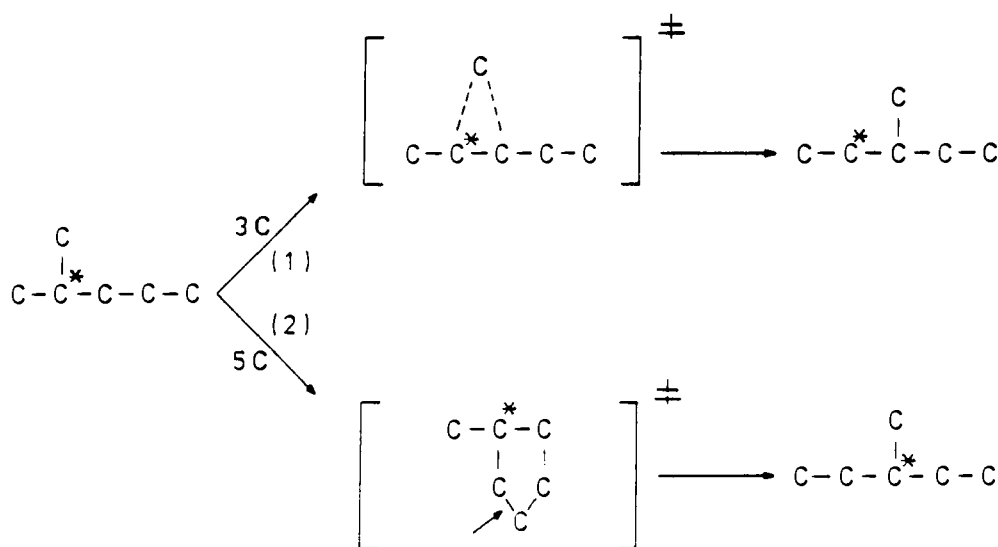


Fig. 4.53. Various organometallic species formed on metal surfaces (only well documented ones are shown — see text).

plexes. Passing over the individual species, we shall discuss what we know about their reactivity in relevant hydrocarbon reactions.

The species (2) or (3), and those from (5) to (7) (all in Fig. 4.53) are supported by both chemical and spectroscopic arguments. It is important to note [91,92] that there are important 'chemical' arguments (exchange reactions) for the presence of multiply-bound species in the presence of hydrogen (or D₂), since the presence of H₂ suppresses the formation of the multiply bound species so much that they are no longer detected at the temperatures at which vibration spectra are monitored [93]. Species (4) and (5) can be considered as alternatives, both originating from the adsorption of ethene on transition metals. Species (4) is preferred on Pd, (5) on Pt [94]. Labelled (C^{*}) isohexanes have been used [95] to show that two mechanisms are operating when, for example, 2-methylpentane is converted into 3-methylpentane [94] (transition state structures are in brackets).



Scheme 4.1.

The required intermediates comprise either 3C atoms (route 1) or 5C atoms (route 2). Isomerisation, as upon (2), is only possible when a *cyclic* intermediate species is formed, such as on the right side of the scheme, which species opens the ring at the place indicated by an arrow. The 3C-cyclic intermediate has to have a form like species (9) or (10) of Fig. 4.53 (possibly with some carbons bound multiply to the metal surface), and with the 5C cyclic intermediate the best indications exist for an intermediate (5).

Intermediates can be converted from one to another. For example, the π -complexed ethene can be converted into ethyldyne species (6) on a hydrogen-lean surface of Pd (100) [96–98].

The reactivity of various species in Fig. 4.53 differs quite a lot. Judging on the grounds of the now available deuterium exchange reaction data, one can say that the singly bound (1) and π -complexed species (4) of Fig. 4.53 are the most reactive forms [99–106], while the multiply-bound species, in particular those like (6), are rather unreactive.

Surface complexes originating from hydrocarbons are those on which the information in the literature is most complete. Oxygen containing molecules have been also studied by the spectroscopic and chemical methods quite intensively.

Figure 4.54 shows schematically the species observed upon adsorption of alcohols (alkoxy species), aldehydes, ketones and carboxylic acids. When alcohols are adsorbed, the methoxy group is always formed very easily with all metal (the evidence for it is from D_2 exchange reactions [107] and various spectroscopic techniques: for the latter see the references below). However, only on Cu and Ag does the stability of this intermediate allow a comfortable study. With the transi-

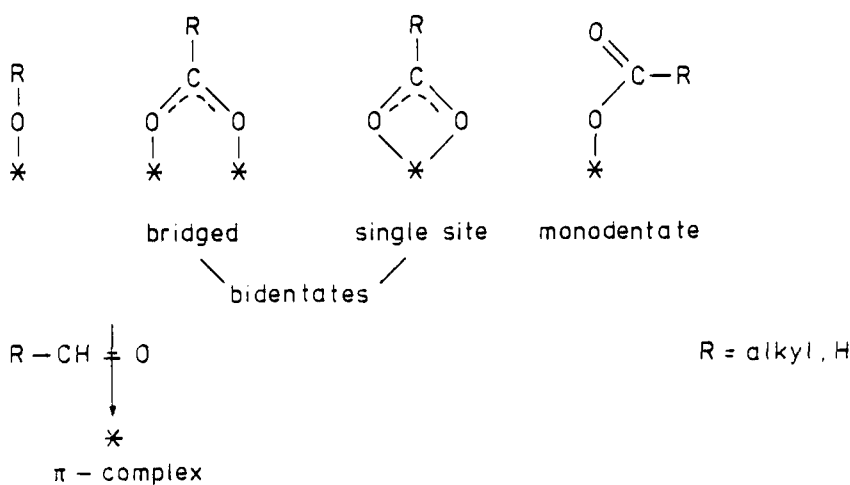


Fig. 4.54. Various surface complexes formed upon adsorption of alcohols, aldehydes or acids, on metals and oxides.

tion metals, the dehydrogenation proceeds very quickly and the authors of Refs. 108–119 collected evidence that the dehydrogenation passes the following stages: molecular methanol → methoxy → formaldehyde → formyl → CO. The reverse order would convert syngas into methanol. Formaldehyde, and probably with it other higher aldehydes and ketones too, is adsorbed by a weak π -complex-like side-on-bond or by an ‘end-on-bond’ [111–115]. The rapid dehydrogenation of methoxy species can be slowed down by modification of the transition metal surfaces by — for example — sulphur deposition or by surface carbide formation. The sites next to the adsorbed methoxy species became occupied, hence preventing activation of the CH bonds.

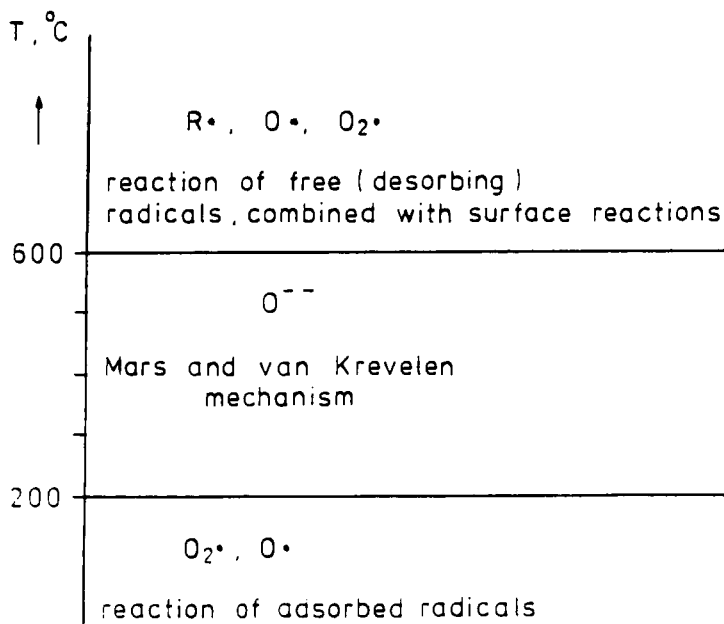
4.4.2 Mechanism of the Reactions on Oxides

4.4.2.1 Reactions related to the oxygen transfer

It is convenient to subdivide the low temperature and medium range temperature oxidation reactions according to the character of the oxygen active species;

- (1) electrophilic oxidations, with species O_2 or O;
- (2) nucleophilic oxidations with a species O (lattice oxygen).

This is related to the temperature range (see Scheme 4.2 [116]) and the type of the catalyst. Type (1) reactions prevail (but are not exclusive to) with ‘early’ transition metal oxides, strongly basic oxides like MgO and rare earth oxides; type (2) reactions prevail on the oxides of the ‘late transition metals’ (group 6 and higher) and on Cu oxides.



Scheme 4.2.

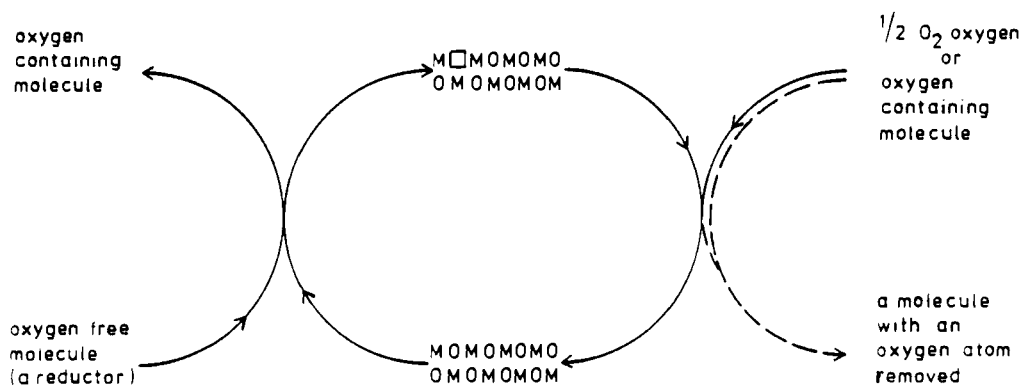


Fig. 4.55. Mars and van Krevelen redox mechanism of the selective oxidation (left side) or selective reduction (right side). Both reactions can also be coupled into a system of two selective reactions running simultaneously.

The type (2) reactions are frequently of a very high selectivity, which is widely exploited by industry (about 20% of all chemicals are produced by oxidation reactions). The type (2) reactions proceed by the so called Mars and Van Krevelen mechanism [117], which is schematically shown for an oxidation reaction in Fig. 4.55.

Two remarks have to be made here. First, the reader should realize that with reactions on metals, the largely prevailing mechanism (perhaps reactions on hydrides or carbides could be the rare exception) is that of Langmuir–Hinshelwood, with a surface reaction among the *adsorbed* species and with rates proportional to the surface coverages θ_s . Upon a reaction running by the Mars and Van Krevelen mechanism, a *lattice component* of the catalyst appears in the product molecules! Second, upon oxidation, lattice oxygen appears in the product and the vacancy is replenished by a dissociative adsorption of dioxygen, which mechanism can be reversed and used for a selective reduction (selective removal of one single oxygen atom) of organic molecules. Then the vacancy is created by a common reductant (CH_4 , H_2) and replenished by oxygen from the organic molecule. In this way, nitrobenzene can be selectively reduced to nitrosobenzene (without undesired reduction to aniline), and aromatic acids (or esters) can be converted into corresponding aldehydes (etc.). It might be practically interesting to combine two selective steps, for example, a selective reduction of nitrobenzene and a selective oxidative dehydrogenation of — say — ethylbenzene [118]. Oxides or mixed oxides call also be used to an advantage for hydrogenation, hydrogenolysis or dehydrogenation (oxidative, or in the absence of oxygen) reactions. Hereby, the heterolytic splitting of the H–H or C–H bonds usually plays the crucial role [119,120].

Oxides are more complicated systems than metals. However, with oxides, too, some information on the molecular level mechanism is available. For example, it has been established that variously coordinated active metal ions posses a different activity [121]. For selective oxidation and reduction, the octahedral oxygen is frequently more reactive than the tetrahedral one. The oxidation reactions are also known to be crystal face sensitive or even specific [122–124].

Oxidation reactions (and the reversed reactions of the selective removal of oxygen, too) are practically very important. In the past, attention was mainly concentrated on oxidation of olefins, but nowadays research is focused on saturated hydrocarbon molecules. Some important reactions are listed in Table 4.3.

Silver is an important metallic catalyst for the selective oxidation of ethylene. The silver catalyst is used to selectively convert ethylene to ethylene epoxide, an important intermediate for antifreeze. Whereas the epoxidation of ethylene proceeds with high selectivity on oxidic silver phases, metallic silver surfaces give only total oxidation of ethylene. Electron-deficient O is created on oxidized silver surfaces and this readily inserts into the electron-rich ethylene bond.

A huge volume of information has been collected on the selective oxidation of olefins, with propene as a typical and most frequently studied molecule. First, it has been established that the reaction is induced by a dissociative adsorption, which — with propene — leads to allyl species [119,120] $\text{CH}_2\text{—CH—CH}_2$. These species are subsequently converted by oxygen of the oxide lattice into the oxygenated product (acroleine, with propene). The frequently used catalysts are com-

TABLE 4.3

Examples of commercialized selective oxidation reactions of organic molecules

Feed	Product
ethylene	ethylene oxide acetaldehyde (liquid phase)
propylene	acrylonitrile (ammonoxidation) propylene oxide (in liquid phase) acrylic acid
isobutene	methyl methacrylate
<i>n</i> -butane	maleic anhydride
naphthalene	anthracinon
methanol	formaldehyde

binations of two oxides, like, for example, $\text{Bi}_2\text{O}_3\text{MoO}_3$. In some cases it appeared to be possible to identify the various functions of individual active sites on the catalysts. For example, Bi sites are known to be mainly responsible for the allyl formation, while the metal–oxygen bond strength is made more suitable for the extraction–addition of oxygen by the formation of mixed Mo–O–Bi bonds. When the feed consists of propene, oxygen and ammonia, acrylonitrile is produced, an important monomer for the production of polymers.

Recently, attention has been shifted to the oxidative functionalisation of saturated molecules. Reactions such as from ethane \rightarrow vinylchloride, propylene \rightarrow methacrylic acid, or butane \rightarrow maleic anhydride, became a target of many research efforts. A catalyst which appeared to be very versatile in such reactions is vanadyl pyrophosphate, $(\text{VO})_2\text{P}_2\text{O}_7$. The mechanism of oxidative functionalisation is not yet known in all details, but there are many indications that it is in some crucial steps different from the mechanism operating with olefins (see also Chapter 5).

4.4.3 Catalysis by Solid Acids

4.4.3.1 General introduction

Oxidic surfaces in particular develop acid or basic properties which are important in catalysis. We will approach this subject first by taking as a starting point the ionic bond model [2]. The lattice is considered to consist of cations and anions held together by electrostatic interactions. Later we will discuss a more balanced theory that also accounts for covalent bonding aspects.

Surface Lewis acidic or basic sites are created on ionic surfaces because surface atoms have a lower coordination number compared to their bulk values. A

condition for surface stability is that the sum of the charges over the surface unit cell is zero and the surface is overall neutral. A useful method to estimate the degree of coordinative unsaturation on an ionic surface is to use Pauling valencies and to compute charge excesses. The Pauling valency, v , is defined as:

$$v = Q/C \quad (4.7)$$

Where Q is the formal ion charge and C its coordination number.

For the Mg^{2+} ion, the Pauling valency equals

$$v^+ = \frac{2}{6} = \frac{1}{3} \quad (4.8a)$$

and for the O^{2-} ion, the valency becomes

$$v^- = -\frac{2}{6} = -\frac{1}{3} \quad (4.8b)$$

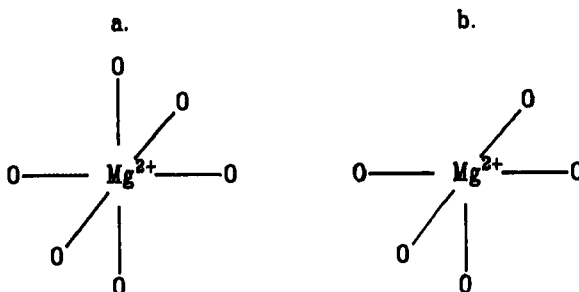


Fig. 4.56. (a) Six-coordinated Mg^{2+} of bulk oxide. (b) Five-coordinated Mg^{2+} on the $MgO(100)$ surface.

On the surface the charge excess of an ion is defined as the formal charge Q of the ion considered plus the sum of the Pauling valencies, computed with respect to the other ion:

$$e^+ = Q^+ + \sum_i v_i^- \quad (4.9)$$

On the $MgO(100)$ surface one finds for e^+

$$e^+ = 2 - \frac{5}{3} = +\frac{1}{3} \quad (4.10)$$

A negative value is computed for e^- on the oxygen anion. A positive charge excess implies Lewis acidity and a negative charge excess implies Lewis basicity. When the surface becomes exposed to NH_3 , ammonia will be adsorbed to the Mg^{2+} ion.

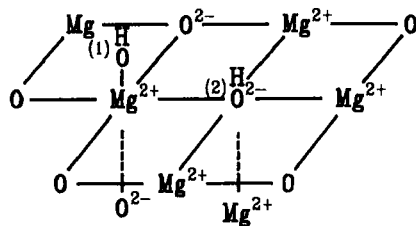


Fig. 4.57. H_2O dissociation on the $\text{MgO}(100)$ surface.

Similarly, H_2O will also bind through its oxygen atom to the surface Mg^{2+} ion.

Brønsted acidity or basicity develop when the H_2O molecule dissociates. Two different hydroxyl coordinations can develop on the MgO surface. As shown in Fig. 4.57, one hydroxyl becomes end-on coordinated to Mg^{2+} , the proton coordinates to the basic bridging oxygen anion.

To determine acidity or basicity it is useful to compute the charge excesses on oxygen atoms O(1) and O(2).

$$e(\text{O}(1)) = -2 + 1 + \frac{1}{3} = -\frac{2}{3} \quad (4.11\text{a})$$

$$e(\text{O}(2)) = -2 + 1 + \frac{5}{3} = +\frac{2}{3} \quad (4.11\text{b})$$

A negative excess charge implies incomplete coordination with positive charge carriers. The end-on hydroxyl group can be considered as being Brønsted basic. Oxygen atom O(2) has excess positive charge, the proton coordinated to this bridging oxygen atom behaves as a Brønsted acid. This is an important and very general conclusion.

When oxidic surfaces become exposed to water, basic hydroxyls, as well as Brønsted acidic protons, are generated upon dissociation of the water. This also occurs on the surfaces of basic oxides. There is an abundance of infrared spectroscopic information confirming the appearance of different OH groups by adsorption of HO on oxidic surfaces. Catalytic reactions induced by Brønsted acidic sites take place on such surfaces. The acidic proton is located on bridging oxygen sites.

Ammonia interacting with a surface, as sketched in Fig. 4.57, will form NH_4^+ ions coordinated to the bridging oxygen atom. Most oxide surfaces behave very similarly to the MgO surfaces. An exception is the surface generated on silica. In SiO_2 the Si cations are tetrahedrally coordinated. This coordination can be restored on the surface when the SiO_2 surface becomes exposed to H_2O . Silanol groups develop, as sketched in Fig. 4.58.

One can easily see that the excess charge on O(1) is zero. So no decision on Brønsted acidity or basicity can be made on the basis of Pauling excess charges. Chemically, the silica-silanol group is slightly acidic, due to the high charge of

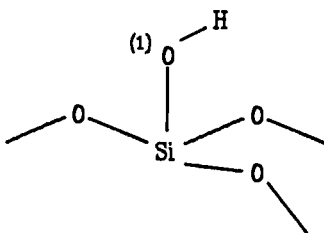


Fig. 4.58. Silanol group.

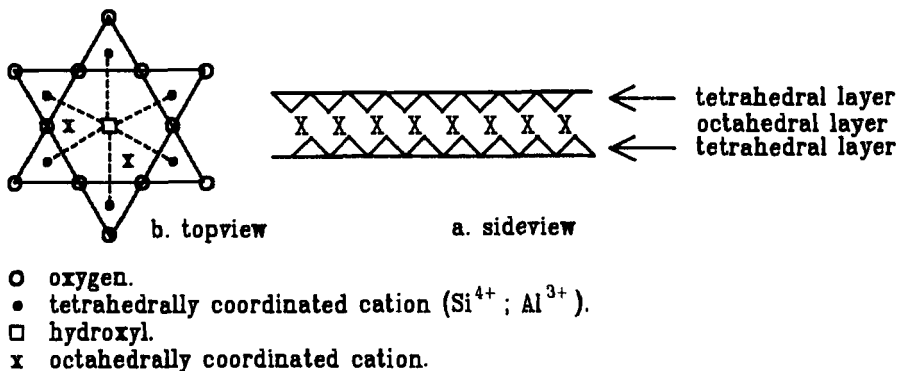


Fig. 4.59. Smectite clay (schematic).

the small Si^{4+} ion to which the hydroxyl is coordinated.

Whereas the surfaces discussed so far have been generated from the bulk by a simple cut, leading to a decrease in the coordination number of the surface atoms, catalytically important acidic surfaces can also be generated in microporous or layered materials by isomorphous substitution of lattice cations. This occurs in zeolites and smectite clays. Zeolites and clays can be considered as aluminosilicates. Their lattice compositions can vary significantly. In zeolites the Al^{3+} ion can be substituted by many other trivalent cations. Si^{4+} can be partially substituted by Ti^{4+} or Ge^{4+} .

In the zeolites each lattice cation is tetrahedrally coordinated to four oxygen anions (see Fig. 4.57). Each oxygen anion shares two lattice cations. In smectite clays an octahedral layer, usually containing Al^{3+} or Mg^{2+} , connects two tetrahedral layers. The tetrahedral layer can be considered neutral when the tetrahedral site contains a four valent cation. This is usually a Si^{4+} ion. A top view and side view are shown in Fig. 4.59.

Isomorphous substitution of Si^{4+} by a trivalent ion (this is often an Al^{3+} ion) results in a negative lattice charge. This negative charge can be compensated by a cation located in the zeolite cage or micropore or on the clay layer. When a

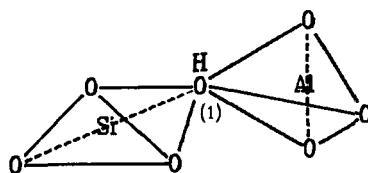


Fig. 4.60. Brønsted acidic proton.

cation is exchanged by an ammonia ion and NH_3 is subsequently desorbed, protons are generated, located on bridging oxygen atoms as sketched in Fig. 4.60.

It is interesting to compute the excess charge on the bridging oxygenation to which the protons are attached:

$$e(\text{O}(1)) = -2 + 1 + \frac{3}{4} + 1 = +\frac{3}{4} \quad (4.12)$$

Compared with (4.8b) this excess charge is quite high and indicates a strong Brønsted acidity of the attached protons.

As we saw earlier when we discussed the acidity of the silanol group, computation of charge excesses provides only a very crude estimate of acidity. As we will see for an explanation of differences in the Brønsted acidity of different zeolites, Pauling's valency rule is too crude.

The tetrahedral unit that forms the basis of the network of the zeolite makes many different structures possible. α -Quartz, the low temperature form of SiO_2 , is one of the dense polymorphs. Many low-density structures can be formed, which are microporous and contain interconnected channels, bound by oxygen atoms that connect the cation-containing lattice tetrahedra. Approximately 60 different structures exist; two examples of are given in Fig. 4.61a and 4.61b. The oxygen atoms are located in the middle of the lines connecting tetrahedrally

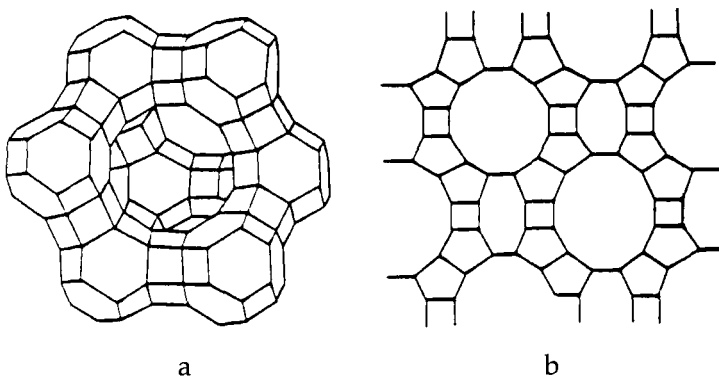


Fig. 4.61. (a) Structure of faujasite. (b) Structure of mordenite.

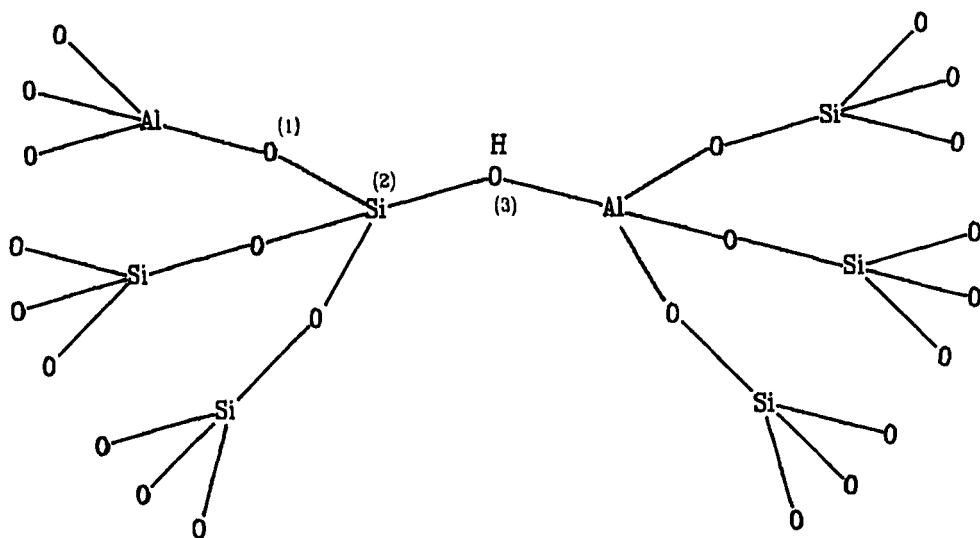


Fig. 4.62. The second coordination shell tetrahedra with respect to a proton in a zeolite.

coordinated atoms. The 12- or 10-ring channel openings enable organic molecules to enter the zeolite cavities.

An important factor that controls the Brønsted acidity of these catalysts is the lattice composition. For a zeolite to be Brønsted acidic, a proton has to connect two tetrahedra containing one tetravalent cation (often Si^{4+}) or a trivalent cation (often Al^{3+}). It appears that within a particular concentration region the deprotonation energy is a strong function of the Al/Si ratio.

To understand this one has to consider the cation composition of tetrahedra in the second coordination shell with respect to the proton in a zeolite (see Fig. 4.59). Because a $[\text{TO}_2]$ tetrahedron containing an Al^{3+} ion carries an overall negative charge, in zeolites no neighbouring tetrahedra can exist which both contain an Al^{3+} ion. For the $[\text{Si}-\text{O}-\text{Al}]$ unit this implies that Al ions can only occupy the three tetrahedra next to a given silicon containing tetrahedron. The deprotonation energy is lower when the occupation by Al of the tetrahedra next to Si decreases, that is when Al is replaced by Si. Once the Al concentration has decreased so that no two $[\text{Si}-\text{O}-\text{Al}]$ dimer pairs occur, the deprotonation energy does not vary any further with the Al content. Because of the lower charge on Al^{3+} its interaction with oxygen atoms as O(1) is less than that of a Si^{4+} ion, so that the Si atom (2) becomes more strongly bound and the bond strength between this Si atom and O(3) decreases. This strengthens the OH bond and hence increases the deprotonation energy. The generally found dependence of proton catalysed reaction on the (Al/Si) content is sketched in Fig. 4.63.

Brønsted acid-catalysed reactions will be proportional to the proton content of a zeolite as long as the intrinsic acidity of a proton remains unchanged, since the

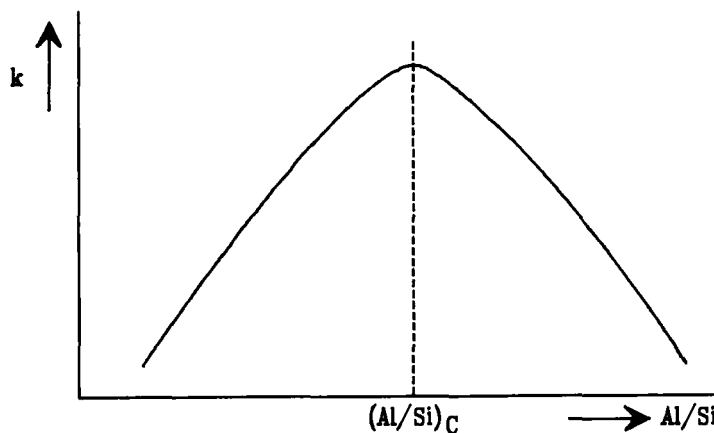
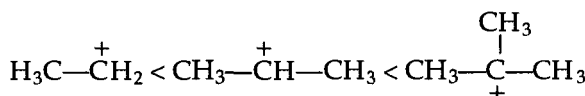


Fig. 4.63. Dependence of acid catalyzed reaction on zeolite Al/Si ratio.

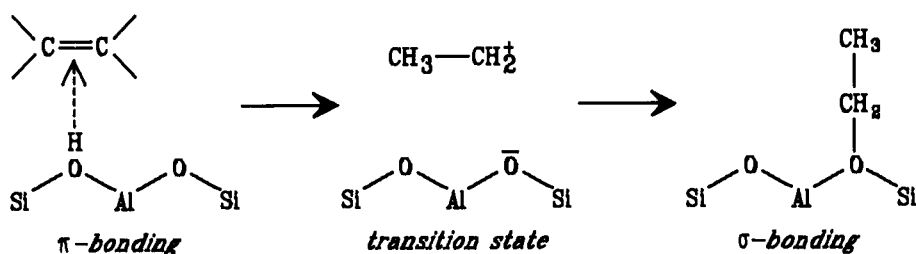
proton concentration is proportional to the Al/Si ratio. Once the Al/Si ratio exceeds a critical value $(\text{Al}/\text{Si})_c$, the intrinsic acidity of a zeolitic proton starts to decrease. This effect dominates over the increased number of protons and, as a consequence, the overall rate of the reaction decreases.

4.4.3.2 Mechanism of protonation

Protonation of a molecule creates charge separation. A positive charge is generated on the protonated molecule and a negative charge on the zeolite lattice. Charge separation is an energy-consuming process, because of the increase in potential energy. In solutions ions become stabilized by hydration or complexation with the solvent molecules. The dielectric constant of a zeolite material is low. In a zeolite the interaction between cation and negatively charged zeolite wall takes over the role of solvation of cations in liquids. The strength of the interaction with the zeolite wall depends on the cation type. The stability of a cation depends on the type of carbon atom that is protonated.



A primary carbenium ion is less stable than a secondary and a tertiary ion is most stable. The interaction of various carbenium ions with the zeolite wall decreases in the same order. A primary carbenium ion forms covalently bonded ethoxy species with the zeolite wall. As illustrated in Fig. 4.64, when an ethylene molecule approaches a proton or weak π hydrogen bond is formed initially. Upon proton transfer a stable σ ethoxy species is formed.

Fig. 4.64. Protonation of ethylene; π - and σ -bonded ethylene [126].

To understand differences in acidity of zeolites one has to consider not only changes in the bond strength of the OH bond, but also zeolite 'solvation' effects on the positively charged carbenium or other ions generated by protonation.

Figure 4.65 illustrates protonation of NH_3 [127,128]. Protonation proceeds via the initial formation of hydrogen-bonded NH_3 , the analogue of the π complex formed with ethylene. Proton transfer only proceeds when the NH_4^+ ion can

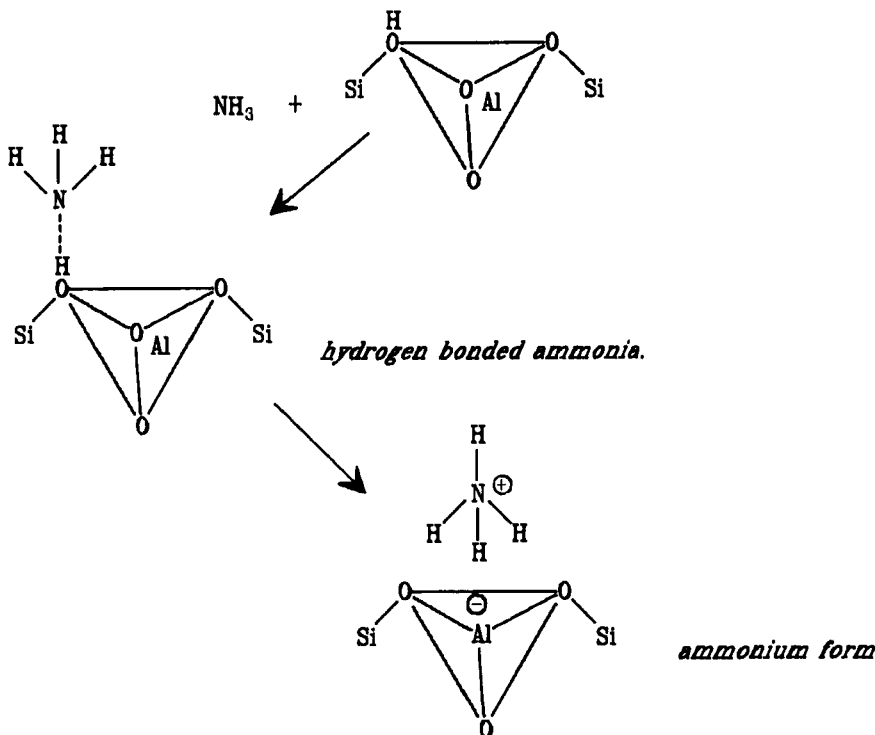


Fig. 5.65. Protonation of ammonia.

become stabilized by the negative charge on the zeolite wall. This occurs when it binds as a tri-dentate to the three negatively charged basic oxygen anion around Al^{3+} .

We also illustrate this for water protonation. The zeolite proton will attach to the water oxygen atom. The proton of water will bind to the basic lattice oxygen anion:

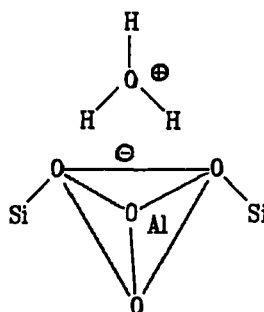


Fig. 4.66. Protonation of water.

Methanol readily gives dimethylether. The mechanism can be considered to proceed as follows:

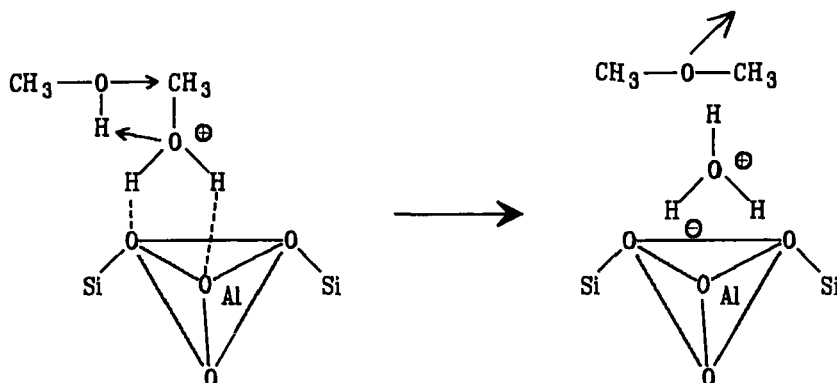


Fig. 4.67. The reaction of methanol to give dimethylether.

A key step is the formation of a stable hydronium ion upon formation of dimethylether. The concept of Brønsted acid–Lewis base catalysis also allows us to understand the formation of ethylene from methanol, as formed in zeolite-catalysed reactions. A possible mechanism is sketched in Fig. 4.68.

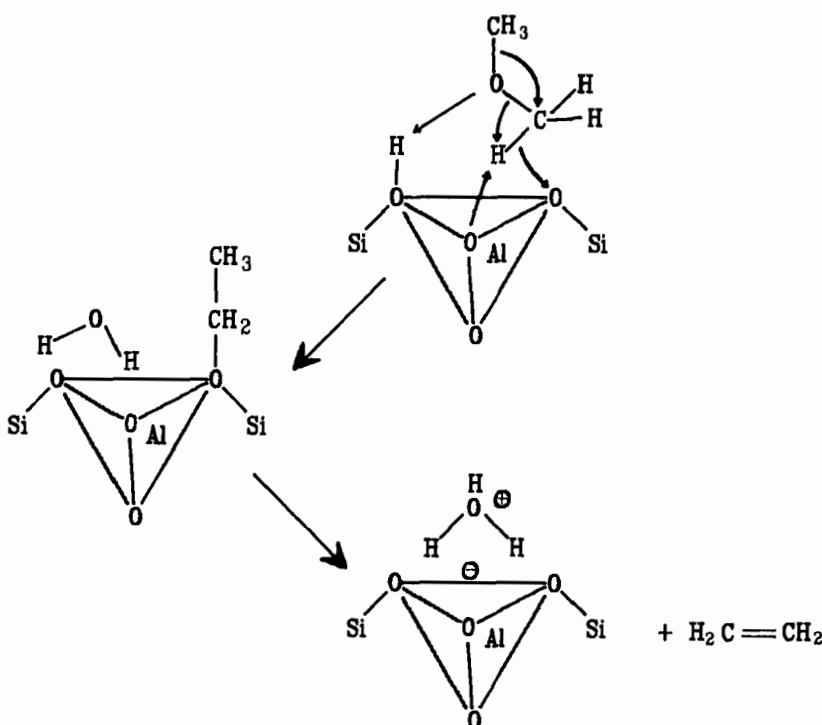


Fig. 4.68. Proton catalysed ethylene formation from methanol.

4.4.8.3 Brønsted acid-catalysed hydrocarbon activation reactions

Activation of unreactive alkanes only occurs at relatively high temperature, even with strong protons, as present in the zeolite [129]. It proceeds via the formation of carbonium ions (Fig. 4.69).

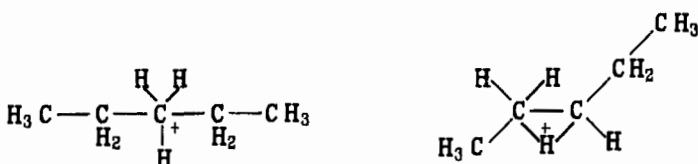


Fig. 4.69. Carbonium ions.

The carbonium ion is a nonclassical molecule, because it contains a pentacoordinated carbon atom. It is very unstable and is therefore difficult to form. It is formed at temperatures of about 500°C . Once formed it readily decomposes to a carbenium ion by H_2 formation or cracking (Fig. 4.70).

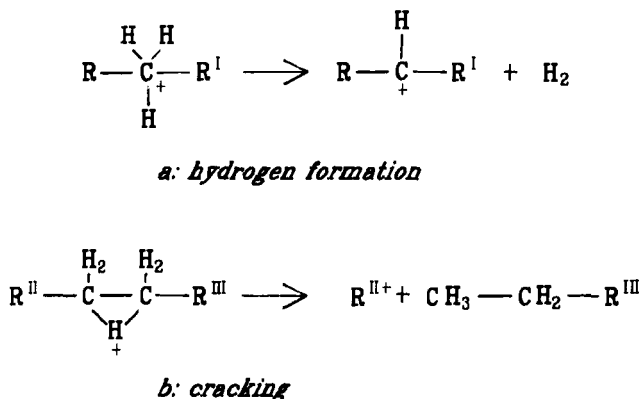


Fig. 4.70. Carbenium ion formation from carbonium ion.

Carbenium ions have been shown to isomerize readily (Fig. 4.71). As long as no primary carbenium ions are involved, isomerization of carbenium ions occurs with low activation energy and at low temperatures. Isoalkane formation occurs by reaction with another alkane and transfer of a hydride ion (Fig. 4.72).

Because the activation energy of the hydride transfer reaction is lower than that of carbonium ion formation, after a short initiation period the hydride transfer reaction will maintain the carbenium ion concentration at a steady-state level. However, secondary reactions occur that give rise to short catalyst lifetimes.

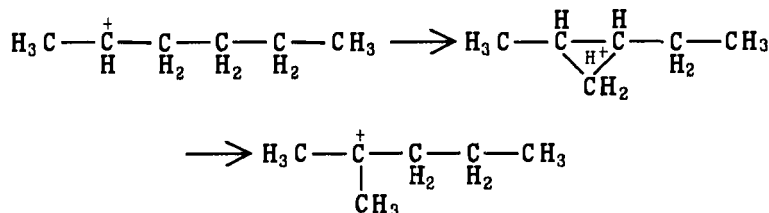


Fig. 4.71. Isomerization of carbenium ions via a triangular intermediate.

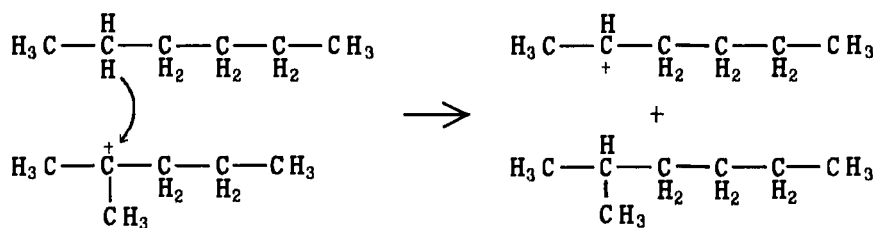


Fig. 4.72. The hydride transfer reaction.

Apart from the hydride transfer reaction the carbenium ion can undergo two other reactions. One is the cracking reaction (Fig. 4.73).

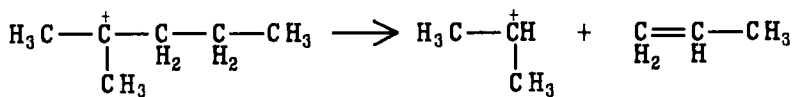


Fig. 4.73. β -Hydrogen transfer leading to cracking.

In the cracking reaction transfer of a hydrogen atom on a β -carbon atom with respect to the ionic atom result in C–C splitting to give a smaller carbenium ion, as well as alkenes. The alkenes can undergo secondary oligomerization and polymerization reactions deactivating the catalysts. When one wishes to reduce the size of hydrocarbon molecules, the cracking reactions of Fig. 4.70 are desired. Catalytic cracking is performed on a large scale using acidic zeolites. Zeolites are preferred because the micropores of the zeolite have a shape-selective effect which prevents the alkenes from polymerizing and forming heavy molecules of large size thus rapidly deactivating the catalyst. Nonetheless the zeolites can also only be applied with short residence times and need to be regenerated frequently.

Whereas catalytic cracking is a useful reaction that requires high temperatures, a low reaction temperature is required in order to produce branched isomers at a high yield in reactions of the type shown in Fig. 4.71). The equilibrium shifts to the *n*-alkanes at high temperature.

In order to reduce the reaction temperature of acid catalysed alkane conversion reactions one can reduce the temperature by replacing carbonium formation by a route via the carbenium ion by protonation of alkenes generated by metal-catalysed (group 8–10 metals, e.g. Pt, Pd) dehydrogenation of alkanes. The metals can be readily dispersed in the micropores of a zeolite. A lowering of the reaction temperature is especially useful for alkane isomerization. A low temperature favours the branched product and inhibits consecutive reactions.

The reaction scheme is shown in Fig. 4.74. The reaction is performed under a high H_2 pressure in order to maintain a low alkene concentration. This is important to reduce the steady-state carbenium ion concentration on the catalyst. Once

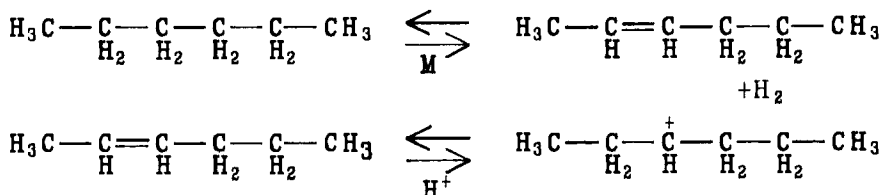


Fig. 4.74. Bifunctional hydroisomerization initiation scheme (see [130]).

the residence time of carbenium ions becomes too long, not only isomerization reaction will occur, but also the now undesirable cracking reaction, which is a consecutive reaction. The low alkene partial pressure reduces the carbenium ion concentration. The catalyst now performs two functions: metal-catalysed CH activation and protonation of alkenes. For this reason the hydroisomerization reaction according to Fig. 4.74 is called a bifunctional reaction.

REFERENCES

For general references to Section 4.2.1 see [1] and [2], to Section (4.2.2) see [12–14].

- 1 R. Hoffmann, *Solids and Surfaces*, VCH, 1988.
- 2 R.A. van Santen, *Theoretical Heterogeneous Catalysis*, World Scientific, 1991.
- 3 R.A. van Santen and A. de Koster, in L. Guczi (Editor), *New Trends in CO Activation. Studies in Surface Science and Catalysis*, Vol. 64, Elsevier, Amsterdam, 1991, p. 1.
- 4 R.A. van Santen, in H.H. Brongersma and R.A. van Santen (Editors), *Fundamental Aspects of Heterogeneous Catalysis Studied by Particle Beams*, NATO ASI series B265, pp. 834–112, Plenum, 1991.
- 5 Y. Schule, P. Siegbahn and U. Wahlgren, *J. Chem. Phys.*, 89 (1988) 6982.
- 6 W. Biemolt, G.J.C.S. van de Kerkhof, P.R. Davies, A.P.J. Jansen and R.A. van Santen, *Chem. Phys. Lett.*, 188 (1992) 477.
- 7 A. de Koster and R.A. van Santen, *J. Catal.*, 127 (1991) 141.
- 8 P. Sautet and J.-F. Paul, *Catal. Lett.*, 9 (1991) 3.
- 9 R.A. van Santen, *Progr. Surf. Sci.*, 25 (1987) 253.
- 10 E. Shustorovich, *Adv. Catal.*, 37 (1990) 101.
- 11 G.J.C. S. van de Kerkhof, W. Biemolt, A.P.J. Janssen, and R.A. van Santen, *Surf. Sci.*, in press.
- 12 H.B. Gray, *Electrons and Chemical Bonding*, Benjamin, New York, 1965.
- 13 M. Elian and R. Hoffmann, *Inorg. Chem.*, 14 (1975) 1058.
- 14 T.A. Albright, J.K. Burdett and M.-H. Whangbo, *Orbital Interactions in Chemistry*, J. Wiley, New York, 1985.
- 15 M.R.A. Blomberg and P.E.M. Siegbahn, *J. Chem. Phys.*, 78 (1983) 5689.
- 16 U.B. Brandemark, M.R.A. Blomberg and P.E.M. Siegbahn, *J. Phys. Chem.*, 88 (1984) 4617.
- 17 J.J. Low and W.A. Goddard, *J. Am. Chem. Soc.*, 106 (1984) 6928.
- 18 J.J. Low and W.A. Goddard, *J. Am. Chem. Soc.*, 106 (1984) 8321.
- 19 J.P. Collmann, L.S. Hegedus, J.R. Norton and R.G. Finke, *Principles and Applications of Organotransition Metal Chemistry*, University Science Books, Mill Valley, 1987.
- 20 P. Powell, *Principles of Organometallic Chemistry*, 2nd Edn., Chapman and Hall, London, 1988.
- 21 A. Yamamoto, *Organotransition Metal Chemistry*, Wiley, New York, 1986.
- 22 R. Crabtree, *The Organometallic Chemistry of the Transition Metals*, 1988.
- 23 C. Elschenbroich and A. Salzer, *Organometallics: A Concise Introduction*, VCH Publishers, New York, 1989.
- 24 J.M. Basset, J.P. Candy, A. Choplin, M. Lecomte, and A. Théolier, in R. Ugo (Editor), *Aspects of Homogeneous Catalysis*, Vol. 7, p. 87, Kluwer Academic Publishers, Dordrecht, 1990.
- 25 J. Falbe (Editor), *New Synthesis with Carbon Monoxide*, Springer Verlag, New York, 1980.
- 26 R.F. Heck and D.S. Breslow, *J. Am. Chem. Soc.*, 83 (1961) 4023.

- 27 F. Basolo and R.G. Pearson, *Mechanisms of Inorganic Reactions*, 2nd Edn., Wiley, New York, 1967.
- 28 K. Noack and F. Calderazzo, *J. Organomet. Chem.*, 10 (1967) 101.
- 29 R.J. Mawby, F. Basolo and R.G. Pearson, *J. Am. Chem. Soc.*, 86 (1964) 5043.
- 30 M.J. Calhorda, J.M. Brown and N.A. Cooley, *Organometallics*, 11 (1991) 1431.
- 31 N. Koga and K. Morokuma, *J. Am. Chem. Soc.*, 108 (1986), 6136.
- 32 J.R. Rogers, O. Kwon, and D.S. Maryneck, *Organometallics*, 10 (1991) 2816.
- 33 M. Brookhart and M.L.H. Green, *J. Organomet. Chem.*, 250 (1983) 395.
- 34 For an example of agostic interaction in the resting state of the catalyst see: M. Brookhart, A.F. Volpe, D.M. Lincoln, I.T. Horváth and J.M. Miller, *J. Am. Chem. Soc.*, 112 (1990) 5634.
- 35 O. Eisenstein and R. Hoffmann, *J. Am. Chem. Soc.*, 103 (1981) 4308.
- 36 J.W. Bruno, T.J. Marks and L.R. Morss, *J. Am. Chem. Soc.*, 105 (1983) 6842.
- 37 H.E. Bryndza, L.K. Fong, R.A. Paciello, W. Tam and J.E. Bercaw, *J. Am. Chem. Soc.*, 109 (1987) 1444.
- 38 T. Ziegler, W. Cheng, E.J. Baerends and W. Ravenek, *Inorg. Chem.*, 27 (1988) 3458.
- 39 L. Vaska, *Acc. Chem. Res.*, 1 (1968) 335.
- 40 J.K. Stille and K.S.Y. Lau, *Acc. Chem. Res.*, 10 (1977) 434.
- 41 C.A. Tolman, *J. Am. Chem. Soc.*, 92 (1970) 4217, 6777, 6785.
- 42 R.H. Crabtree, *Chem. Rev.*, 85 (1985) 245.
- 43 W.D. Jones and F.J. Feher, *Acc. Chem. Res.*, 22 (1989) 91.
- 44 G.W. Parshall, *Acc. Chem. Res.*, 8 (1975) 113.
- 45 G.W. Parshall, *Acc. Chem. Res.*, 3 (1970) 139.
- 46 G.W. Parshall, W.H. Knoth and R.A. Schunn, *J. Am. Chem. Soc.*, 91 (1969) 4990.
- 47 R.R. Schrock, *Acc. Chem. Res.*, 12 (1975) 98.
- 48 R.R. Schrock, *Organometallics*, 9 (1990) 2262.
- 49 T. Ito, H. Tsuchiya and A. Yamamoto, *Bull. Chem. Soc. Jpn.*, 50 (1977) 1319.
- 50 P.W. Jolly and G. Wilke, *The Organic Chemistry of Nickel*, Vol. II, Academic Press, New York, 1975.
- 51 F. Correa, R. Nakamura, R.E. Stimson, R.L. Burwell Jr. and D.F. Shriver, *J. Am. Chem. Soc.*, 102 (1980) 5112.
- 52 P.L. Watson and G.W. Parshall, *Acc. Chem. Res.*, 18 (1985) 51.
- 53 J.E. Bercaw et al. *J. Am. Chem. Soc.*, 109 (1987) 203.
- 54 M.S. Chinn and D.M. Heinekey, *J. Am. Chem. Soc.*, 112 (1990) 5166.
- 55 B.R. James, *Homogeneous Hydrogenation*, Wiley, New York, 1973.
- 56 A.A. Al Ammar and G. Webb, *J. Chem. Soc. Faraday Trans.*, I, 74 (1978) 195, 657; I, 75 (1979) 1900.
- 57 S.J. Thompson and G. Webb, *J. Chem. Soc. Chem. Commun.* (1976) 526.
- 58 D. Godbey, F. Zaera, R. Yates and G.A. Somorjai, *Surf. Sci.*, 167 (1986) 150.
- 59 S.M. Davis, F. Zaera and G.A. Somorjai, *J. Am. Chem. Soc.*, 106 (1984) 2288.
- 60 G.A. Somorjai and M.A. van Hove, *Adsorbate Induced Restructuring of Surfaces*, US Dept. of Energy, Rept. DE-AC03-765 F00098.
- 61 G.A. Boreskov, *Proc. 8th ICC, Berlin*, 1984, Vol. III, p. 231, Verlag Chem., 1984.
- 62 N.J. Kobozev, *Zhur. Fiz. Khim.*, 13 (1939) 1; 14 (1940) 663 and *Acta Phys. Chim. USSR*, 9 (1938) 805.
- 63 D.A. Dowden in *Catalysis, Proc. 5th ICC, Miami Beach*, 1972, Vol. 1, p. 645, North Holland, 1973.
- 64 Y. Soma-Nota and W.M.H. Sachtler, *J. Catal.*, 34 (1974) 162.
- 65 W.M.H. Sachtler, *Catal. Rev. Sci. Eng.*, 14 (1976) 162.

- 66 T.A. Dalmon, M. Primet, G.S. Martin and B. Imelik, *Surf. Sci.*, 50 (1975) 95.
- 67 V. Ponec, *Adv. Catal.*, 32 (1983) 149.
- 68 E.H. van Broekhoven, *Progr. Surf. Sci.*, 19 (1985) 351.
- 69 F.J.C.M. Toolenaar, F. Stoop and V. Ponec, *J. Catal.*, 82 (1983) 1.
- 70 A.G.T.M. Bastein, F.J.C.M. Toolenaar and V. Ponec, *J. Catal.*, 90 (1984) 88.
- 71 M.J. Dees, T. Shido, Y. Iwasawa and V. Ponec, *J. Catal.*, 90 (1984) 88.
- 72 E.M. McCash, S.F. Parker, J. Pritchard and M.A. Chesters, *Surf. Sci.*, 215 (1989) 363.
- 73 J.B. Benzinger, *Appl. Sci.*, 6 (1980) 105.
- 74 M.Th. Karapetyants and M.K. Karapetyants, *Handbook of Thermodynamic Constants*, Ann Arbor, 1970.
- 75 A. de Koster and R.A. van Santen, *Surf. Sci.*, 233 (1990) 366.
- 76 C. Backx, C.P.M. de Groot and P. Biloen, *Surf. Sci.*, 104 (1981) 300.
- 77 M.A. Barteau and R.J. Madix, *Surf. Sci.*, 97 (1980) 101.
- 78 D.L. Thorn and R. Hoffmann, *J. Am. Chem. Soc.*, 100 (1984) 2079.
- 79 H. Berke and R. Hoffmann, *J. Am. Chem. Soc.*, 105 (1983) 427.
- 80 R. Hoffmann, *Solids and Surfaces*, VCH, 1988.
- 81 V. Bonacic-Konicky, J. Konicky, P. Fantuzci and V. Ponec, *J. Catal.*, 111, 409 (1988).
- 82 T. Koerts and R.A. van Santen, *Catal. Lett.*, 6 (1990) 49.
- 83 T. Koerts and R.A. van Santen, *J.C.S., Chem. Comm.*, 18 (1991) 1281.
- 84 M.J. Calhorda, J.M. Brown, N.A. Cooley, *Organometallics*, 10 (1991) 1431.
- 85 R. Postma, personal communication.
- 86 B.E. Nieuwenhuys, *Surf. Sci.*, 126 (1983) 307 and references therein.
- 87 N.W. Cant, P.C. Hicks and B.S. Lennon, *J. Catal.*, 54 (1978) 372.
- 88 J. Siera, F. Rutten and B.E. Nieuwenhuys, *Catal. Today*, 10 (1991) 353.
- 89 R.L. Burwell Jr., *Chem. Eng. News*, 22 (August 1966) 56.
- 90 R.L. Burwell Jr., *Catal. Lett.*, 5 (1990) 237.
- 91 C. Kemball, *Proc. Roy. Soc. (London)*, A207 (1951) 541
- 92 C. Kemball, *Proc. Roy. Soc. (London)*, A217 (1953) 376.
- 93 J.R. Anderson and C. Kemball, *Proc. Roy. Soc. (London)*, A223 (1954) 361.
- 94 S.B. Mohsin, M. Trenary and H.J. Robota, *J. Phys. Chem.*, 92 (1988) 5229.
- 95 M.A. Chesters, C. De La Cruz, P. Gardner, M. Mc Cash, P. Pudney, G. Shahid and N. Sheppard, *J. Chem. Soc. Faraday Trans.*, 86 (1990) 2757.
- 96 F.G. Gault, *Adv. Catal.*, 301 (1989) 1.
- 97 G.H. Atkins and R.I. Masel, *Surf. Sci.*, 185 (1987) 479.
- 98 J.A. Gates and L.L. Kesmodel, *Surf. Sci.*, 124 (1983) 68.
- 99 N.R.M. Sassen, Diss. Thesis, Leiden, 1989.
- 100 G. Leclercq, J. Leclercq and R. Maurel, *J. Catal.*, 50 (1979) 87.
- 101 V. Ponec in D.A. King and D.P. Woodruff (Editors), *Chemical Physics of Solid Surfaces and Heterogeneous Catalysis*, Elsevier, 1982, Vol. 4, p. 365.
- 102 Z. Paal and P. Tetenyi, *React. Kin. Catal. Lett.*, 12 (1979) 131.
- 103 J.R. Anderson and B.G. Baker, *Proc. Roy. Soc. (London)*, A271 (1963) 402.
- 104 J.K.A. Clarke and J.J. Rooney, *Adv. Catal.*, 25 (1976) 125.
- 105 E.H. van Broekhoven and V. Ponec, *Surf. Sci.*, 162 (1985) 731.
- 106 J.R. Anderson and C. Kemball, *Trans. Faraday Soc.*, 51 (1955) 966.
- 107 J.R. Anderson and C. Kemball, *Trans. Faraday Soc.*, 51 (1955) 966.
- 108 G.K. Chuah, N. Kruse, W.A. Schmidt, J.H. Block and G. Abend, *J. Catal.*, 119 (1989) 342.
- 109 G.A. Kok, A. Noordermeer and B.E. Nieuwenhuys, *Surf. Sci.*, 135 (1982) 65.
- 110 R. Ryberg, *J. Chem. Phys.*, 82 (1985) 567.

- 111 C. Houtman and M.A. Bartea, *Langmuir*, 6 (1990) 1558.
- 112 J.L. Davis and M.A. Bartea, *Surf. Sci.*, 208 (1989) 383.
- 113 N.D.S. Canning and R.J. Madix, *J. Phys. Chem.*, 88 (1984) 2437.
- 114 J.B. Benziger and R.J. Madix, *Surf. Sci.*, 79 (1979) 394.
- 115 M.A. Henderson, Y. Zhon, J.M. White and C.A. Mims, *J. Phys. Chem.*, 93 (1989) 3688.
- 116 G.I. Golodets, in G. Centi and F. Trifiró, *New Developments in Selective Oxidation*, Studies in Surface Science and Catalysis, Vol. 55, Elsevier, Amsterdam, 1990, p. 693.
- 117 P. Mars and D.W. van Krevelen, *Chem. Eng. Sci.*, 3 (1954) 41.
- 118 US Patents: 42 37070; 43 39622; 41 63761 to Texaco.
- 119 C.R. Adams and I.J. Jennings, *J. Catal.*, 2 (1963) 63.
- 120 W.M.H. Sachtler and N.H. de Boer, *Proc. 3rd ICC, Amsterdam*, 1964, North Holland Vol. 1, p. 240, 1965.
- 121 T.L.F. Favre, A. Maltha, P.J. Kooyman, A.P. Zuur and V. Ponec, *Proc. XI Symp. Ibero-Am. Catal.*, Guanajuato, 1988, Vol. 2, p. 807.
- 122 J.E. Germain in M. Che and G.C. Bond (Editors), *Absorption and Catalysis on Oxide Surfaces*, Studies in Surface Science and Catalysis, Vol. 21, Elsevier, Amsterdam, 1985, p. 335.
- 123 J. Haber, *Proc. 8th ICC Berlin*, 1984, Chemie Verlag, 1984, Vol. 1, p. 85.
- 124 J.C. Volta and J.L. Portefaix, *Appl. Catal.*, 18 (1985) 1.
- 125 B. Grzybomska, J. Haber and J. Janas, *J. Catal.*, 49 (1977) 150.
- 126 V.B. Kazanskii and I.W. Senchenya, *J. Catal.*, 119 (1989) 108.
- 127 E.H. Teunissen, F.B. van Duyneveldt and R.A. van Santen, *J. Phys. Chem.*, 96 (1992) 366.
- 128 E.H. Teunissen, R.A. van Santen, A.P.J. Jansen and F.B. van Duyneveldt, *J. Phys. Chem.*, 97 (1993) 203.
- 129 D.M. Brouwer in R. Prins and G.C.A Schuit (Editors), *Chemistry and Chemical Engineering of Catalytic Processes*, NATO-ASIE: 39, Sijthoff and Noordholt, Alphen aan de Rijn, 1980, p. 137.
- 130 P.A. Jacobs and J.A. Martens in H. van Bekkum, E.M. Flanigen and J.C. Jansen (Editors), *Introduction to Zeolite Science and Practice*, Studies in Surface Science and Catalysis, Vol. 58, Elsevier, Amsterdam, 1991, p. 445.

Chapter 5

Heterogeneous catalysis

5.1 INTRODUCTION

Three important representative reactions in the field of heterogeneous catalysis have been selected for a more detailed description:

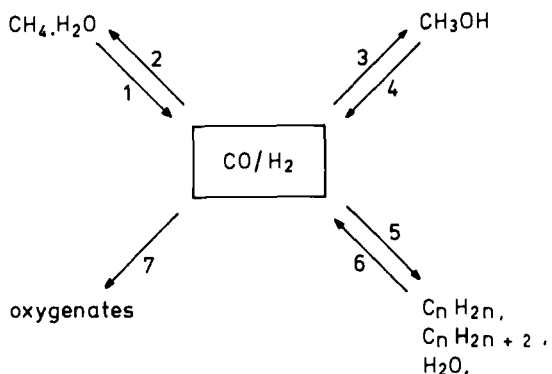
- synthesis gas reactions,
- hydro- and dehydrogenation reactions, and
- catalytic oxidation of ethene to ethylene oxide.

The catalytic reactivity in relation to the position of the catalytic metal in the Periodic Table will be discussed together with the effect of added promoters.

5.2 SYNTHESIS GAS REACTIONS

5.2.1 Introduction

Synthesis gas ($\text{CO} + \text{H}_2$) can be converted into useful products by a network of reactions schematically shown by Scheme 5.1. Synthesis gas is prepared by steam



Scheme 5.1.

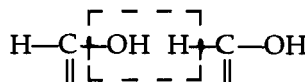
reforming of methane (reaction 1), by partial oxidation of methane or by one of these reactions using heavy oil residues instead of methane (reaction 6). Thermodynamically, production of CH₄ is most favoured, and that of CH₃OH least. Nevertheless, by using a proper catalyst (typically Cu/ZnO/Al₂O₃), selectivity to methanol higher than 98% can be achieved. A promoted Co catalyst allows a high selectivity to higher saturated hydrocarbons to be achieved; with promoted Rh catalysts, a high selectivity to ethanol is found, etc.

Obviously, the reaction network of the synthesis gas is very versatile and only the rather high cost of syngas itself prevents its wide application. When CO conversion was introduced into industrial practice, coal was the main source of CO/H₂. Nowadays, it is mainly CH₄ from remote gas fields. Synthesis gas reactions are also a very suitable subject for courses on catalysis. Many interesting aspects of the mechanism, kinetics and technology can be demonstrated using the data available for this reaction.

5.2.2 Fischer–Tropsch Synthesis of Hydrocarbons

5.2.2.1 The mechanism and its consequences for the technology

Hydrogenation of CO to CH₄ was first observed by Sabatier [1] while Orlov was the first to describe [2] the formation of higher hydrocarbons. Around 1925 Fischer and Tropsch published several patents on industrial processes producing hydrocarbons with a commercially interesting high fraction of C₅–C₁₀ hydrocarbons. Catalysts were promoted iron and cobalt, and the processes ran at medium (or low) pressures [3]. Fischer and Tropsch also suggested a mechanism for the synthesis which nowadays bears their name. Carbon monoxide dissociates and a carbide and an oxide are formed. The oxide is reduced and the carbide, which has the carbon atoms at just the right distances, forms hydrocarbons [3,4]. It appeared later that, in its original form, the suggested mechanism was not correct. First, very few branched hydrocarbons are formed, while a random cross linking in three or two-dimensional carbides should lead to the formation of iso-products. Second, pre-carbidization of the catalysts did not lead to an enhanced rate of synthesis [5]. Therefore, several authors suggested a new mechanism [6]. The initiation step of the synthesis is then the formation of hydroxycarbene:



and the propagation step is dehydrocondensation, as indicated above. This mechanism was generally accepted for more than twenty years.

Pichler and Schulz [7] suggested a third mechanism, which is worth considering and seeking to verify. According to this suggestion, a carbonyl of a metal in question is formed first, which is followed by the formation of formyl (in later

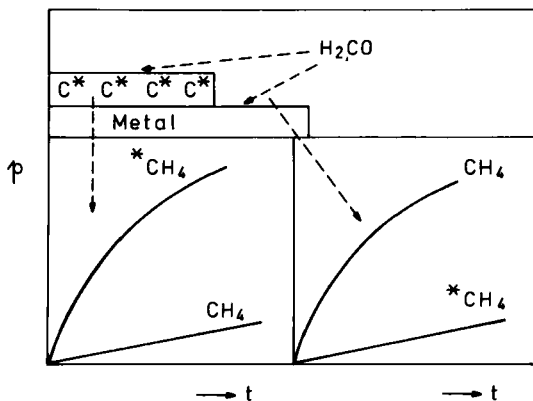


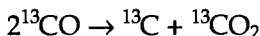
Fig. 5.1. Two possible pathways for the course of methanation. A metal surface partially covered by ^{13}C is offered to the CO/H_2 reaction mixture. Left: The result if C^* ex CO dissociation must be formed first. Right: Reaction runs via oxygen-containing intermediates.

stages, acyl, etc.). Formyl (or a higher analogue) is subsequently hydrogenated, so that hydroxyl containing species are formed which, by a hydrogenolytic splitting, produce methyl or methylene (ethyl, etc.).

There are several other mechanisms to be found in the literature, but the three just mentioned seem to be the most realistic and best supported.

In 1974, the oil supply crisis stimulated research throughout the world on the Fischer-Tropsch Synthesis (FTS) of fuels. Surprisingly, the first result of this was evidence concerning the mechanism: with typical FTS and methanation catalysts — Fe, Co, Ni (Ru) — the initiation step is the dissociation of CO [8] and not the formation of hydroxycarbene.

Let us consider an experiment, shown schematically in Fig. 5.1 [8c]. The surface of a metal is partially covered by disproportionation of ^{13}CO :



This can be done easily with Fe, Co and Ni. Subsequently, this surface is exposed to the $^{12}\text{CO}/\text{H}_2$ mixture. If the reaction sequence is: hydrogenation of CO (to hydroxycarbene or formyl) \rightarrow hydrogenolytic C—O bond splitting, then initially the production of $^{12}\text{CH}_4$ should prevail, as shown on the right-hand side of Fig. 5.1. If the sequence is dissociation \rightarrow hydrogenation of C, $^{13}\text{CH}_4$ would prevail as on the left-hand side of Fig. 5.1. The experiments revealed that the second mechanism operated [8c]. It also appeared that the dissociation of CO requires several contiguous surface metal atoms (large ensemble) to occur [8c]. Since FTS was also found to be a large ensemble reaction, the conclusion could be drawn that the initiation of the FTS and the methanation reaction both comprise a CO dissociation [8c,9].

FTS is a process which is plagued by the self-poisoning of the catalyst, essentially

by coking. A homogeneous catalyst would in principle be free of such troubles and therefore, several years after 1974, an intensive search was conducted for homogeneous FTS catalysts. However, when it appeared that the most efficient synthesis pathway comprised initiation by CO dissociation, which required large ensembles of active atoms [8], the research in this direction was stopped.

The next problem was whether or not the hydrocarbon chain growth requires oxygen-containing intermediates (formyl, acyl, hydrocycarbene, etc.). During a study of this problem, it appeared that the chain growth is promoted when the reaction mixture contains molecules (di-, tri- or tetrachlormethane, azomethane), which can generate CH_x species *in situ* [9–11]. Furthermore, it has been observed that, when a surface of a metal is covered by disproportionation of ^{13}CO , higher hydrocarbons (for example, propane or butane) contain more than one ^{13}C [8d]. In other words, it has been clearly proved that oxygen-free intermediates CH_x can polymerize into longer hydrocarbon chains. Moreover, no oxygen-containing intermediates were ever unambiguously detected (IR, EELS, XPS) on the metal surface of working FTS catalysts.

The FTS mechanism: $\text{CO} \rightarrow \text{C}_{\text{surf}} \rightarrow \text{CH}_x \rightarrow \text{C}_n\text{H}_{2n}$ has also received theoretical support, as is shown in Chapter 4.

The step-by-step growth (adding CH_x groups) implies that the product molecules form a distribution, derived for polymers by Schulz and Flory and for FTS by Harrington, and Anderson et al. [12–14]. The unavoidable consequence of the Schulz–Flory–Anderson distribution is that, of all the hydrocarbons, only CH_4 can be formed with a selectivity nearing 100%. However, when producing fuels (the C_5 – C_{10} fraction) both the low and the very high molecular weight hydrocarbons are undesired products. The Shell middle distillate synthesis (SMDS) solved this selectivity problem in a very ingenious way: the reaction is first driven up to high molecular weight molecules (waxes), by applying conditions most suitable for just that process (promoted Co catalyst, low temperatures). Then, in the second step, waxes are selectively cracked by zeolites, thus producing the optimum yield of hydrocarbons in the desired molecular weight region. The resulting gas-oil (diesel) is free of aromatics and has excellent properties as a fuel. The FTS is less suitable for the production of a high-quality gasoline. This is due to the fact that branched and aromatic compounds are not formed in amounts sufficient to achieve a high octane number in the product.

5.2.2.2 Kinetics of the FTS and methanation reaction

For a reaction of such complexity as methanation (or FTS) an exact kinetic theory is actually out of the question. One has to introduce one or more approximations. The usual assumption made is that one reaction step is rate determining (r.d.s.) and other steps are in equilibrium or steady state. Adsorption equilibria are described by Langmuir formulas (Langmuir–Hinshelwood, Hougen–Watson

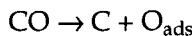
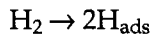
approach) [15] and the approach is sometimes made simpler by using so-called virtual pressures [16] (cf. Chapter 3).

People approaching the mechanism from the kinetic point of view tend to work on the basis of first principles, i.e. ignoring the sometimes already abundant non-kinetic experimental information on the mechanism. Thus, in formulating the kinetic equations, they consider, for example, two alternative pathways as equally possible: (i) the r.d.s. involves an oxygen-containing complex; (ii) the r.d.s. involves C or CH_x ($x = 1-3$), i.e. an oxygen-free complex. Subsequently, they try to describe, on the basis of the kinetics only, which alternative is the correct one. With regard to (i), again three cases can be discerned: (a) r.d.s. is a hydrogen-assisted dissociation of CO [17]; (b) the r.d.s. is the formation of an oxygen-containing intermediate [18]; (c) the r.d.s. is hydrogenolysis of the oxygen-containing intermediate [19]. All the kinetic models just mentioned lead to an approximate power rate law:

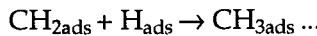
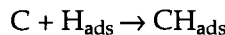
$$\text{rate}(r) = k_{\text{tot}} \cdot p_{\text{H}_2}^{\alpha} p_{\text{CO}}^{\beta}$$

where α is positive and β negative. This has all been done for methanation. However, if the overall FTS has its r.d.s. in one of the above mentioned reactions (a)–(c), it would follow the same kinetics as the methanation. Such an assumption is frequently made.

With the rate determining step involving C or CH_x , the sequence of reaction steps starts with the relevant dissociations



followed by an appropriate number of hydrogenation steps:



Adsorption equilibria of the first two steps lead to the terms

$$\theta_{\text{H}} = \frac{A\sqrt{p_{\text{H}_2}}}{(1 + B\sqrt{p_{\text{H}_2}} + C\sqrt{p_{\text{CO}}} + \dots)}$$

$$\theta_{\text{C}} = \frac{A\sqrt{p_{\text{CO}}}}{(1 + B\sqrt{p_{\text{H}_2}} + C\sqrt{p_{\text{CO}}} + \dots)}$$

The dots represent the terms related to the other products of the reaction which

may potentially be present, or the term related to the assumed steady state of some parallel reaction steps, or some interference terms. Again, this has all been analyzed for methanation, but if in the FTS one of the above reactions is the r.d.s., the kinetics would be the same as for the methanation. If the rate determining step is the reaction $C + H_{ads}$ then in the usual approximation $r = k_{tot} \sqrt{p_{H_2}} \cdot \sqrt{p_{CO}}$, when adsorption of all components is weak. When CO adsorption is much stronger than the adsorption of other species $r = k_{tot} \sqrt{p_{H_2}} / \sqrt{p_{CO}}$. The latter equation gives a better agreement with the experimental data than the first one, but in many cases the value α of the power rate law is found to be $\alpha > 1/2$. To make the agreement better, people make one of two assumptions: (a) the rate determining step is a three-body collision, $C + 2H$ [20]; or (b) the r.d.s. involves CH_x , instead of C and thus, with each equilibrium (steady state) step prior to the r.d.s. hydrogenation step, the rate expression receives one more $\sqrt{p_{H_2}}$ term [21]. For example, in case (b):

$$\theta_{CH} = K \theta_C \theta_H \approx \frac{const \sqrt{p_{H_2}}}{\sqrt{p_{CO}}}$$

For $CH + H_{ads}$ as the r.d.s. $r = k_{tot} p_{H_2} p_{CO}^{-1}$.

An example of kinetic data for methanation, showing the agreement achieved with the theory, is shown in Fig. 5.2.

Another way how to get rid of the problem of too high an α value is to assume an r.d.s. involving an oxygen-containing complex. However, neither of the three suggestions really provides an attractive explanation. With typical FTS and methanation catalysts, oxygen-containing intermediates are not probable, nor is the three-body collision reaction [21]. It is also known that hydrogenation of C is more difficult than that of CH (see hydrocarbon exchange reactions), so that it does not seem reasonable to shift the r.d.s. further in the sequence of the hydrogenation steps. What else, then?

Most likely, one has to consider the following information [22]. A working FTS or methanation catalyst has (at least) three kinds of carbon on its surface: a reactive type, an almost unreactive (C_s) (perhaps carbidic) and coke (C_{graph} , very unreactive). The working (in the FTS) surface is proportional to $(1 - \theta_s - \theta_{graph})$ and the rate of $C + H_{ads}$ is then: $r = k_{tot} (1 - \theta_s - \theta_{graph}) \theta_C \theta_H$.

The θ_s carbon does not contribute noticeably to the FTS but the amount present is a function of p_{H_2} . Hydrogen, when adsorbed, prevents its formation and removes this carbon by a slow reaction up to a certain steady-state concentration, θ_s . This means that the order of α for hydrogen is greater than $1/2$. The situation just described is far from being hypothetical. A group of authors [22a] analyzed the presence of θ_c , θ_s and θ_{graph} on Ni catalysts, a phase diagram has been established and evidence obtained that θ_s and θ_{graph} are functions of temperature and hydrogen pressure [23].

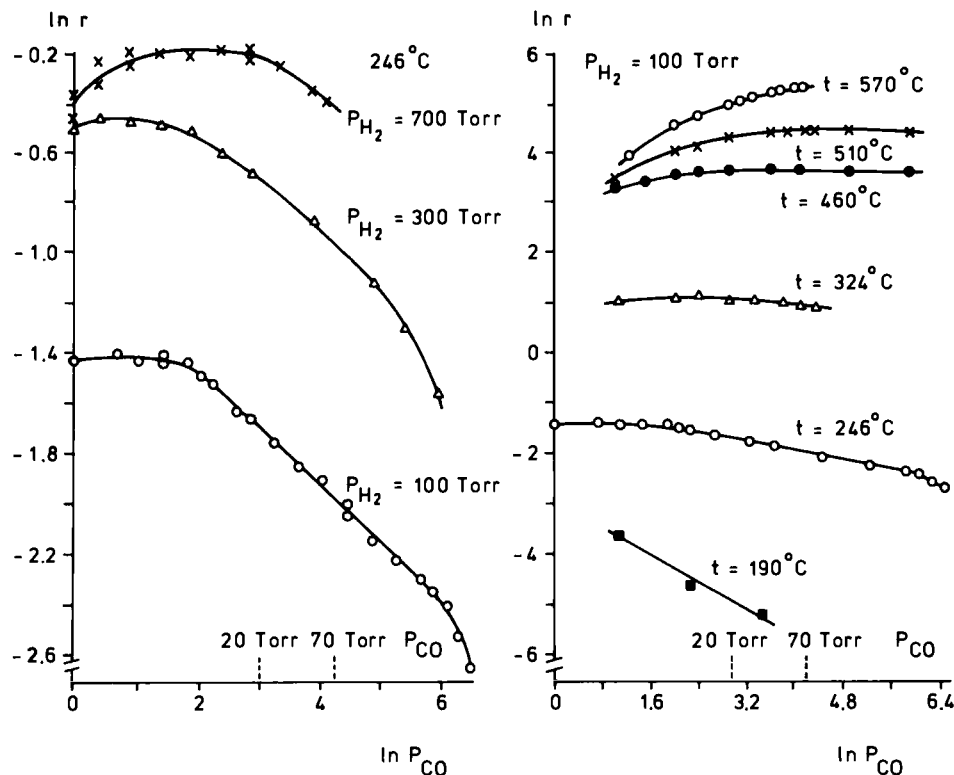


Fig. 5.2. Methanation rate as a function of the $\ln p_{\text{CO}}$. Left: 519 K, three H_2 pressures, as indicated. Right: T , as indicated, $p_{\text{H}_2} = 100 \text{ Torr}$. (From van Meerten et al. [21]).

The distribution of products of a FTS of hydrocarbons can be derived in the following way [12–14]. Let us call a fraction of products with i carbon atoms ϕ_i . Now, if a product with $n\text{C}$ appears in the gas phase, its fraction, Φ_n is a measure of termination of the anchored chain growth (by addition of CH_x units) at the $n\text{C}$ -containing hydrocarbon. At the same time, all products with $i > n$ taken together, are the measure of propagation of the growth. If the probability of growth is α_n and that of termination is $(1 - \alpha_n)$.

$$\frac{\alpha_n}{1 - \alpha_n} = \frac{\sum_{i=n+1}^{\infty} \Phi_i}{\Phi_n}$$

$$\alpha_n = \sum_{i=n+1}^{\infty} \Phi_i / \sum_{i=n}^{\infty} \Phi_i$$

It has been found that $\Phi_{n+1}/\Phi_n \approx \text{const.}$, independent of n , and it can easily be verified that $\text{const.} \approx \alpha = (\alpha_n)$. By repeated substitution $\Phi_{n+1} = \alpha^n \Phi_1$ or $\Phi_n = \alpha^n (\Phi_1/\alpha)$. By plotting $\log \Phi_n$ vs n one can easily determine α .

5.2.3 Modification of the Catalysts by Alloying Metals and by Using Promoters and Supports

5.2.3.1 Metals, alloys, multimetallics

The Periodic Table, and the periods with metals therein, offer the following pattern of activities:

(a) the block of metals between Sc–Cr–La–W contains those metals which dissociate CO at temperatures around and under 300 K. The oxides arising by that process are not easily reduced at temperatures at which the Fischer–Tropsch synthesis can produce sufficiently high hydrocarbons, so that these metals are not good catalysts for FTS.

(b) Mn, Tc, Re probably behave very similarly to the metals under (a).

(c) Fe, Co, Ni, Ru, Rh dissociate CO at slightly elevated temperatures (Fe 300 K, Rh 470 K, Rh) and the oxides of these metals can be reduced by syngas at temperatures around 470 K. Thus, these metals are suitable for the FTS.

(d) Pd, Ir, Pt do not dissociate CO easily enough to be good catalysts for the FTS. However, the surface of these metals, with many defects in the structure, can be active.

(e) Cu, Zn, Ag, Cd, Au, Hg do not adsorb CO strongly enough to be a catalyst for FTS of hydrocarbons. Copper is a component (with ZnO) of the most active catalysts for methanol synthesis.

If one compares the behaviour of the most active FTS catalysts — Fe, Co, Ni and Ru — several things emerge. Unpromoted nickel is probably the most stable catalyst but it produces mainly methane; the other metals, when active in the polymerization of CH_x units, are also susceptible to self-poisoning by inactive carbon deposition. A natural reaction to this is the question: is it not possible to optimize the properties by mixing the metals, by alloying (bimetallic formation, in general)?

In principle, two possibilities exist when two metals form an alloy (a bimetallic system): (i) both metals are active; (ii) A is active, B is inactive in a given reaction (in our case the FTS).

Alloying changes the electron density round A and B and also the distribution of the energy levels over the energy band occupied by the valence electrons. The question is, how important are these changes for catalysis and how much different in its chemisorption properties is an atom A, when it is dispersed in B or forms clusters in B, compared with an atom of a pure metal A? Probably, the most direct answer is given by the X-ray and UV photoemission spectra (integrated over all angles of emission). The results of these techniques state that: (i) there is very

little, if any, electron transfer between the alloy components (A, B); (ii) due to the less suitable conditions in the alloy for the A-A and B-B overlap of atomic orbitals, the dispersion of energy levels is smaller than in pure metals, but the centroid of valency bands does not shift (measurably) upon alloying. Translated into a trivial chemical terminology, both kinds of metal atoms retain their identity in the alloy and, seen from the gas phase, a molecule to be adsorbed 'feels' the difference between A and B atoms (for a more detailed discussion of the problem, see elsewhere [24]).

Even when the solid-state physical methods do not indicate that properties of A-in-B are very different from those of A-in-A, it can still be possible that small changes in the electronic structure (a 'ligand effect' on A) can be important enough for chemisorption and catalysis [25]. This should in principle be seen by: (i) IR spectra of adsorbed molecules; (ii) adsorption calorimetry; (iii) changes in the activation energy of a simple catalytic reaction. There is currently experimental information available on all three points.

With CO as a probe and IR spectra as a detector the following conclusions could be drawn [26]. Carbon monoxide can be adsorbed in several forms, either as single-coordinated (on the top of atoms) or multiply-coordinated (in the valley between 2, 3 and 4 atoms). The multiply-coordinated CO molecules are abundant on Ni and Pd; the single-coordinated form prevails on Ir and Pt. reducing the number of metal particles suppresses the appearance of the multiply-coordinated form. Similarly, alloying of A with an 'inactive' (or a much less active) metal, B, suppresses the appearance of multiply-coordinated CO, too. However, the stretching vibration wave number $\nu(\text{CO})$ of the adsorbed CO does not indicate pronounced changes in the electronic structure of the underlying atom(s). Actually, the maximum possible change in $\nu(\text{CO})$ attributable to the ligand (electronic structure) effects of alloying ($0\text{--}10 \text{ cm}^{-1}$, for most of the catalytically interesting alloys) is considerably lower than the change in the $\nu(\text{CO})$ caused by the maximum CO-CO dipole interaction ($20\text{--}50 \text{ cm}^{-1}$).

Adsorption calorimetry (and analogous information gained by the thermal programmed desorption) of simple gases leads us to the same conclusion [24]. By alloying an active with an inactive metal the distribution of sites with different coordination changes, but not the bonding strength of individual forms.

A word of caution should be added. At this moment only those results can be discussed which were obtained by techniques which have some serious limitations to their power of resolution (such as the IR spectra and calorimetry on powders, etc.). It is possible that future research employing single-crystal IR reflection spectra, single-crystal calorimetry, all combined with surface crystallography, will detect ligand effects of alloying, effects which are made less visible by the integrating character of the research techniques used up to now. However, it seems likely that the essential conclusions regarding the size and importance of the effect will be not changed.

A particularly difficult problem appeared to be the systems of two active metals [27,28]. While, in several cases [27], the product patterns of the catalytic reaction show the presence of both active metals (Pt–Re, Pt–Co, Pt–Ir, Pd–Ni) in the surface, the chemisorption data, such as e.g. IR spectra of adsorbed CO, are less definite on this point. Recently Joyner and Shipiro [28] even speculated that — at least with Pt alloys — it is only Pt which forms the surface. Important information on the last mentioned problem has been supplied by single-crystal experiments, in which one metal (B) is covered by one, two or more monolayers of the second metal (A). It appeared [29] that, to see the bulk properties of a metal A, with regard to XPS and/or CO chemisorption, at least two or three layers of A should be laid down on metal B. This means that an ensemble of three or four contiguous surface A atoms must also have the A atoms underneath (atoms in the next layer, filling the holes of the first layer), to behave like corresponding ensembles of A in bulk metal A. This could be one of the reasons why the size of the necessary ensemble formally derived from the overall kinetic and the top-most layer composition is sometimes unreasonably large.

If we neglect the consequence of (small) ligand effects, alloying of A with B changes mainly the distribution of A ensembles according to the size (ensemble size effect) and, if both metals are active, it creates mixed ensembles (ensemble composition effect). By using such alloys as Ni–Cu or Ru–Cu it has been established that: (a) dissociation of CO is a large ensemble reaction [8b]; (b) FTS is suppressed in a similar way as the CO dissociation alone [8,30]. Some alloy combinations appear to have suitably modified catalytic properties, showing less self-poisoning, a higher production of olefins, a higher sulphur resistance, etc. [30], but no real technological breakthrough has been achieved by using alloys in the industrial practice of the FTS.

5.2.3.2 Supports and promoters

General information

Supports are in most cases used to prevent the sintering of metal particles. This is also the role of the otherwise 'inert' promoters (e.g. Al₂O₃ in Fe). Small metal particles can be prepared as colloids (see e.g. ref. 31) or dispersed on a support. Only the second way and the fused metal technique have been applied to the Fischer–Tropsch synthesis catalysts.

Small metal particles form multiple bonds to the adsorbed species less easily than large particles or continuous planes of single crystals [32]. This is probably the reason why the very small metal particles are less active in FTS of hydrocarbons than the large ones: FTS is initiated by CO dissociation and the products of the dissociation have to be multiply bound. The multiple bonding is probably easier with an ensemble of atoms rather than with single atoms.

An important fact to remember is that an interaction of a metal precursor with an oxide support modifies the support and very often a part of the support dissolves [33]. So, for example, aluminium from Al_2O_3 appears in the liquid phase as chloride, oxychloride, hydroxynitrate, etc. The same holds for oxides of V, Ta, Nb, Ti, Zr and others. On the other hand, silica can be partially dissolved when NH_3 -containing precursors are used. When water or another solvent is removed upon drying, the species formed from the support can appear on the surface of the precursor crystallites and finally, after reduction, on the metal. (Note, a high temperature reduction would remove a volatile AlCl_3 , a low temperature reduction would not.) For certain reactions this could be a way of creating promoters from the support.

Many commercially available support materials contain small amounts of contaminations which can have promoting effects on syngas reactions, as for example, alkali compounds or iron oxide in SiO_2 materials, or TiO_2 in Al_2O_3 , etc. Acidic precursors can leach out these contaminations and actually concentrate them on the metal surface. It has been proved that contaminated commercial silicas can in this way (often unnoticed by the authors) induce methanol synthesis by Cu, or the synthesis of higher alcohols (ethanol, mainly) on rhodium [34].

A separate problem arises when the surface of the support bears non-metallic active centres. Such 'bifunctional' catalysts are widely used in naphtha reforming and it has been suggested that a bifunctional mechanism may also operate in syngas reactions [35].

Possible mechanism of promotion, metallic catalysts in syngas reactions

A theoretically well supported and experimentally well documented phenomenon is a through-the-vacuum influence of a promoter placed on the metal surface (or of the influence of a support, along the lines of contact between the metal and the support). The following is important with regard to this interaction.

(i) This interaction can be strongly localised in space and visualised as a formation of surface complexes from the promoters and coadsorbed molecules (or their fragments). There are known and well proved examples of this type of interaction in coordination chemistry as, for example, a promoted alkyl migration in carbonyls under the influence of Lewis (aprotic) acids [36]. There are indications that such complexes can play a role in heterogeneous catalysis, too [37].

(ii) It is also likely that the effect of the electrostatic field of a promoter or modifier influences the behaviour of molecules (fragments) adsorbed in its neighbourhood. It has been argued [38,39] that the field can enhance or suppress the shifts of electrons (between the metal and adsorbate) accompanying the formation of the chemisorption bond. In particular, the binding through the antibonding LUMOs of adsorbed molecules seems to be influenced strongly, as can be inferred, for example, from the effect of promoters on the IR detected $\nu(\text{CO})$ value. Koutecky et al. [40] calculated the occupation of various orbitals partici-

pating in the bonding of a hypothetical three atomic molecule Pd—C≡O. Promoting ion Na⁺ has been placed against the middle point of the CO bond or on the O side of the molecule. The changes in the occupation of the most relevant orbitals are shown in Table 5.1.

TABLE 5.1
Charge distributions in PdCO and PdCONa⁺ complex

Number of electrons:			
Orbital	CO	PdCO	PdCONa ⁺ *
π(CO)	4	4.0989	4.1684
π(Pd)	—	3.9011	3.8172

*Na⁺ placed against the middle point of the C—O bond.

The second idea to consider is the very popular but very hypothetical '*through-the-metal interaction*', induced by electron transfer, which interaction is supposed to have one of the following forms:

- (i) A massive transfer of electrons between the small particles of the metal and the support/promoter, a transfer which can lead, according to the authors, to the transmutation (Pt behaves like Ir or Au, according to the shift of the electrons) of the catalytic behaviour of the metal [41];
- (ii) Electron transfer is limited, but the field created by this support/promoter interaction somehow influences the whole of the metal particles.

Alternatively, one assumes that the change created by the metal–oxide or metal–H⁺ contact is smeared out over the whole metal particle [42]. The concepts of the through-the-metal interaction enjoy the greatest popularity of all the above-mentioned ideas, among the chemists, but with the support of this idea from the solid state physicists it is just the opposite. For example, the maximum possible charge transfer is very limited (1–2 electrons per 100 atoms in immediate contact with the support/promoters) and even rather small particles show such intensive screening (incomplete but sufficient) [43], that the effect of the field inside the particle, or smearing out of the transferred charge, is in reality hardly possible. Only very small particles which consist of just a few metal atoms can be substantially polarised [44] and influenced in that way. Let us mention that the data which have been often viewed as an experimental evidence (XPS, NEXAFS) of an electron transfer can be better explained in an alternative way. Usually, the claimed 'electron deficiency' of small metal particles may have an alternative, physically better explanation: the shifts in the binding energy are due to the incomplete screening in small particles [26b], or they occur due to the particle-size-dependent absorption probability in the NEXAFS measurements [45].

A massive electron transfer between the metal particles and the supports (or promoters) and the penetration of an electric field into the metal are thus not realistic ideas on the through-the-metal interaction. However, there is one mechanism for such an interaction which is well supported by the quantum theory of chemisorption: when a covalent chemisorption bond is formed, it causes periodic variation (with the distance) in the chemisorption bond strength in its environment. At the nearest site a repulsion is felt, on the next-nearest an attraction, etc. [46a]. However, it is important to realize how strong this interaction is. A realistic estimate, based on observations of the field ion emission images, shows that these interactions are comparable in their strength to the physical (condensation) van der Waals forces [46b].

The reader can find in the literature several calculations showing that in the very closest surroundings of a modifier (sulphur, promoter) the local density of states is dramatically changed, so that a modification of adsorption properties on such sites should be expected. However, the most dramatically changed sites cannot be reached by adsorbing molecules since they are under the van der Waals (repulsive) radius of the modifier atom.

Function of promoters in the hydrocarbon synthesis

It is an old practice [46] to add to metallic catalysts a chemical compound which itself is inactive but which improves the activity/selectivity and/or stability of the metallic catalyst. This is also a common situation in FTS: iron is used in the 'double-promoted' form (Al_2O_3 , alkali carbonate) Co supported, and promoted by alkalis and, for example, ThO_2 , etc. The additives — promoters — have been shown to have the following functions [47]:

- (1) promoters enhance the CO dissociation and the overall rate of synthesis;
- (2) promoters shift the selectivity in the FTS to higher hydrocarbons;
- (3) promoters favour the formation of unsaturated products;
- (4) promoters determine to which extent the FTS of hydrocarbons is accompanied by other reactions (see the next section).

Effect (2) above is most likely a consequence of effect (1). Effect (3) is most likely related to the suppression of the hydrogen adsorption, since a simultaneous hydrogenation of olefins is suppressed when the hydrocarbon-producing catalyst system is promoted by alkalis [48]. Point (4) will be discussed in more detail in the next section. The effect of vanadium promoter (on the Rh/SiO_2 catalyst) on the rate of methane formation from CO preadsorbed at 293K and then subjected to a programmed heating in a flow of hydrogen is shown in Fig. 5.3 [49].

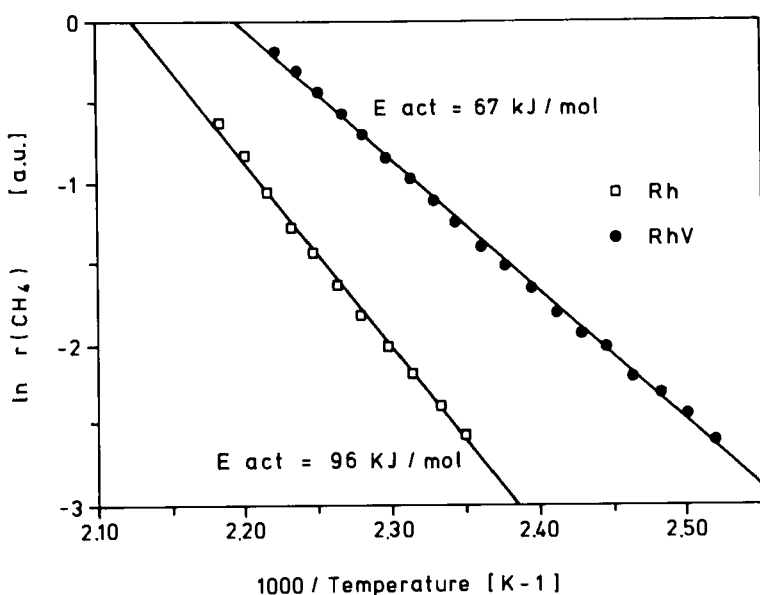


Fig. 5.3. Arrhenius plot for temperature programmed surface reaction: $\ln(\text{rate})$ as a function of $1/T$, for the reaction of a pre-adsorbed CO in the flow of H_2 . Promoted and unpromoted Rh/SiO_2 catalysts [49].

5.2.4 Related Reactions

5.2.4.1 Synthesis of higher oxygenates

It seems that one conclusion can easily be drawn: alcohols are only produced when the catalyst is properly promoted [34]. Actually, all metals of Group VIII (8–10 according to the IUPAC terminology) can be made active in the synthesis of higher alcohols. The most suitable one is Rh (right in the middle) and, while in the right corner of Group VIII the metals have to be promoted to stimulate CO dissociation and CH_x formation, in the left (upper) corner the dissociation has to be suppressed. Since the promoter is inactive as such and the promoter free metal surface is necessary to produce CH_x units and adsorbed hydrogen, the rates, yields and sometimes also selectivities when plotted as a function of the amount of promoter added, often form a curve with a maximum [33], reflecting that the rate r is indeed described by (see Fig. 5.4):

$$r = k(T) \theta_{\text{prom}} \cdot (1 - \theta_{\text{prom}}) \cdot f(p(\text{H}_2), p(\text{CO}))$$

Such an expression is expected to be valid when the promoting action is limited to the perimeter of the promoter patches on the metal surface. Three steps can in principle be influenced by promoters (transition metal oxides):

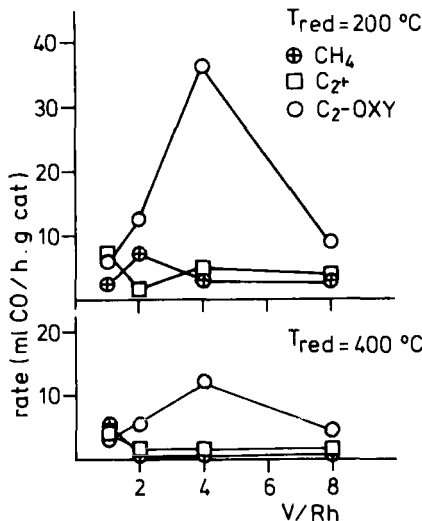


Fig. 5.4. Rate of various product formation, under standard conditions, as a function of the (atomic) promoter/metal ratio, V/Rh catalyst-Rh/SiO₂; promoter introduced as VOCl₂ compound [33].

- (i) Adsorption of CO. It is known that the C–O bond strength is weakened as a consequence of the presence of the promoter, since the latter enhances the population of the antibonding $2\pi\text{CO}$ orbitals (see the foregoing section).
- (ii) Promoters cause the species containing unsaturated C=O bond (potential and most likely intermediates) are hydrogenated to alcohols [49–51].
- (iii) A question still being discussed is whether the promoter also stimulates the formation of the aldehydic intermediates. The latter ones can, in principle, also be formed on an unpromoted surfaces [34,49].

The production of C₂ alcohols is higher on the metals left from the diagonal in Group VIII (Fe, Co, Ru) since these metals tend to accumulate CH_x groups on the whole metallic surface. Rhodium is most suitable for producing ethanol: its CO dissociation activity is weak and thus the CH_x units are preferentially formed on the metal surface round the patches of the promoting oxide.

It is perhaps worthwhile noting that the promoter patches on the metal can be either created during the wet steps of the catalyst preparation, or when a transition metal oxide is used as a support, they can be created by migration of the support material on the metal upon high temperature reduction. The metal surface can be kept almost completely covered *in vacuo* (SMSI effect) [52], but in the presence of CO or of the reaction mixture, the layer of oxide recrystallizes and the metal surface becomes accessible again from the gas phase [33].

5.2.4.2 Synthesis of methanol

This is an important industrial reaction, alone or in combination with others. The CH₃OH production is often coupled to oxidation to formaldehyde, methanol to gasoline (Mobil) process, methanol to olefins process, carbonylation, etc. Due to this, a large volume of information already exists on catalyst preparation, kinetics, reactors and all other aspects of the related chemical technology [53]. However, let us concentrate our attention here on just one selected problem: the role of the promoter and the nature of the active site on the 'metal on oxides' catalysts. Let us mention in passing that pure metals (promoter free) most likely do not catalyze the synthesis.

Ideas suggested in the literature concerning active sites can be subdivided into three main streams:

- (i) The active metal (Cu, Pd, Pt, Ir) is the locus of the reaction. A promoter is possibly necessary to stabilize a certain size, or shape, of metallic particles [54].
- (ii) The surface of the carrier bears the essential intermediates of the synthesis, whereby either the cations (Zn, Cr) are considered to be the active sites, or the OH groups of the support [35,55,56]. In this picture, the metal is just supplying atomic hydrogen by a spill-over.
- (iii) Active sites bearing the essential intermediates are ions of an 'active' metal (Cu, Pd, Co, Cr, Fe) and the zero-valent metallic centres (particles) produce adsorbed hydrogen. The active ions are stabilized by the promoter patches on the metal surface or are localized in the support round the metallic particles. With an oxidizable metal like Cu, additional Cuⁿ⁺ centres can be created by the reaction itself [54].

For a long period of time, the mechanism under (i) was dominant in the literature. One of the main pieces of the support for this mechanism was the finding that with CO/CO₂/H₂ mixtures the activity in the CH₃OH synthesis is a linear function of the Cu⁰ (metallic) surface area [54]. However, it has been overlooked that, in the presence of CO₂, a large fraction of a Cu⁰ surface is covered during a running reaction by oxygen (or oxygen-containing species). This fraction is constant for all catalysts, independent of the Cu⁰ surface area [54]. Thus, it could have been also the Cu⁺ (or Cu²⁺) sites which were responsible for the activity. In the last decade the following well established facts seem to support just that last alternative.

- (1) With Pd catalysts a linear correlation has been found between Pdⁿ⁺ content and synthesis activity [59]. A theory [60] helped to understand why this is so and suggested that also for Cu a (Cu⁺) ion could have a more active centre than a Cu⁰ centre.
- (2) With Cu a slight preoxidation shortens the induction period which otherwise accompanies the reaction with CO/H₂ mixtures on well reduced catalysts [58].

- (3) Anything that stabilizes the presence of Cu^+ indiscriminately enhances the activity of the catalyst; (i) promoters [61]; (ii) CO_2 admixture, up to a certain concentration of CO; (iii) supports (silica treated and impregnated at $\text{pH} > 7$, upon which procedure formation of Cu silicates is stimulated) [62].

Similar observations (but with CO_2) have also been made with Pd, Rh and Pt catalysts [58]. Some relevant information on this point is shown in Fig. 5.5 [59,61]. The hypothesis suggesting that Pd^{n+} or Cu^+ are active sites seems to find strong support in these data (see Fig. 5.5).

The discussion on the active sites and the mechanism is far from closed. The immediate future may bring changes in the picture which is offered above as the most likely one.

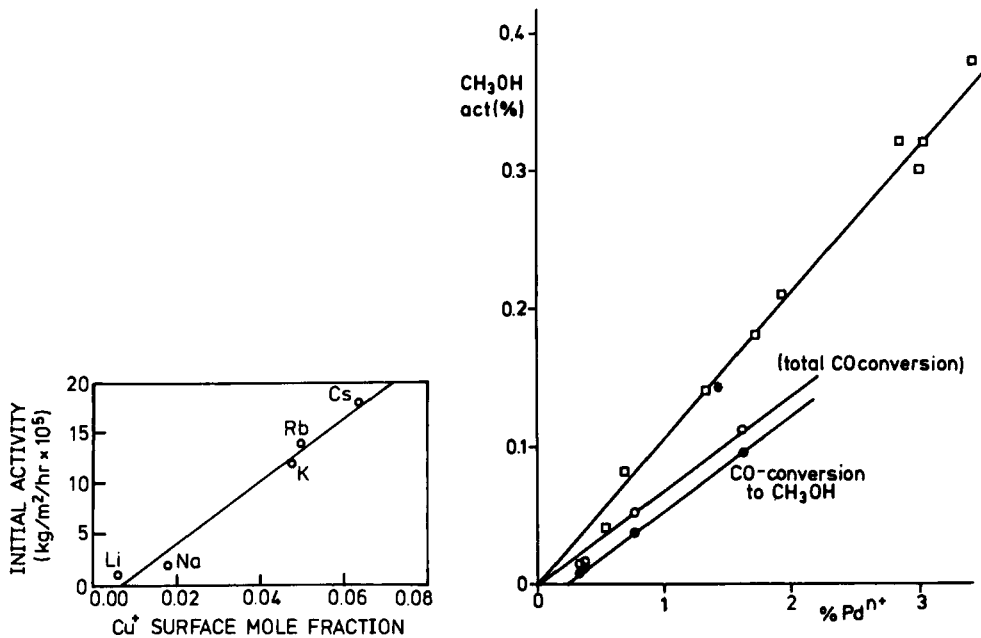


Fig. 5.5. (a) Left: Rate of methanol formation as a function of the Cu^+ concentration (detected by XPS). Catalyst unsupported Cu, promoted by various alkalis [61]. (b) Right: Rate of methanol formation as a function of the Pd^{n+} concentration (detected by chemical extraction and a.a.s.). Catalyst Pd/SiO_2 promoted by MgO/MgCl_2 (various Mg/Pd ratios lead to various Pn^{n+} contents) [59].

5.3 HYDRO-DEHYDROGENATION REACTIONS ON METALS

5.3.1 Introduction

In the beginning of the 20th century Sabatier published a paper which later appeared to be worth a Nobel prize: a paper on the hydrogenation of unsaturated hydrocarbons. Since that time, the hydrogenation of unsaturated hydrocarbons has become the basis of a huge industry (margarine production, the lubricants industry, etc.) as well as a tool for numerous 'fine chemistry' conversions (see Chapter 6, Section 4). In particular, stereoselective hydrogen addition is very important in the pharmaceutical industry. While hydrogenation is favoured at low temperature, dehydrogenation prevails at higher temperatures. Dehydrogenations are also used in the chemical industry, sometimes as *oxygenative* dehydrogenations (methanol to formaldehyde process).

In principle, a catalyst which is good at inducing hydrogenation should be equally good at accelerating the dehydrogenation step. However, this is exactly true only for the particular reaction step on individual active sites and not for the catalyst as a whole. At a high temperature, a very good hydrogenation catalyst can be more poisoned by side reactions (e.g. carbonaceous deposit formation) than a bad one. This can be illustrated by the data in Fig. 5.6 for benzene hydrogenation at low and high temperatures [63].

It can be seen in Fig. 5.6 that, while at low T , pure Ni is more active, at higher T the alloys are better. This is due to a lesser degree of self-poisoning by carbonaceous deposits on Ni–Cu alloys.

5.3.2 Hydrogenation of Olefins

A lot of work has been done with the simplest olefin, ethene. The following points can now be considered as well established.

With all metals from the third to tenth column (Sc to Ni, etc.) of the Periodic Table, a clean metallic surface is too reactive and, at the temperature of freely running hydrogenation, most of the surface is always covered by fragments of ethene. The degree of the C–H and C–C bond dissociation depends on the temperature and pressure (see Chapter 4). The dissociative adsorbed forms can react to give ethane (or methane), but this is a rather slow reaction [64,65], compared with hydrogenation of the weakly adsorbed ethene.

At the remaining surface, where reactive species are adsorbed, a competition takes place between adsorbed hydrogen and ethene. The formal kinetic equation in the form of a power law is then (approx.): rate = $k p_{\text{Et}}^\alpha p_{\text{H}_2}^1$, where α is near to zero or slightly negative. Since adsorption of hydrogen is dissociative, one would expect $\sim p_{\text{H}_2}^2$, if H atoms are added one by one. The reasons why α can be different are discussed elsewhere (see Section 5.2 on syngas reactions). The reactive form

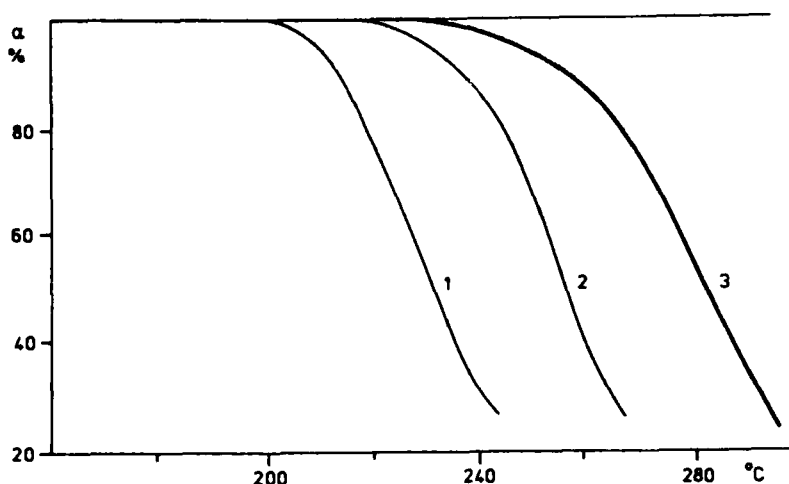
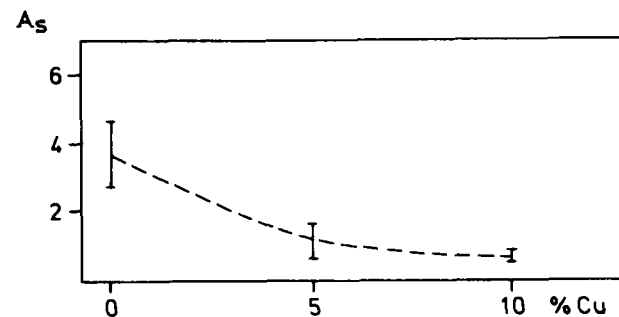


Fig. 5.6. *Above:* Activity in benzene hydrogenation, as % of conversion at 100°C per m² total surface area of unsupported alloys, as a function % Cu in Ni. *Below:* Conversion with a standard amount catalyst as a function of temperature. (1) pure Ni; (2) 10% Cu–Ni alloy; (3) thermodynamic limit at reaction conditions (for other details see [1]).

of ethene is most likely a di- σ -bonded ethene or a π -complexed ethene (see Chapter 4). The role of the various dissociatively adsorbed forms is still a matter of discussion. Some authors suggest that these forms mediate hydrogenation: accepting coadsorbed hydrogen and passing it to the olefin or acetylenic molecules adsorbed on the top of the firmly adsorbed layer [66,67]. However, this is most likely not the prevailing mechanism [68]. The first order reaction in hydrogen could also be explained by the so-called Rideal mechanism: a reaction of H₂ molecules upon collision with the reactive adsorbed ethene species. However, experiments with Au-plated Pd tubes have shown that H₂ has to be adsorbed as atoms before it can react [69].

The order in activity of various metals (with well defined surfaces) in hydrogenation of ethene was first established by Beeck et al. [70] and the data (see

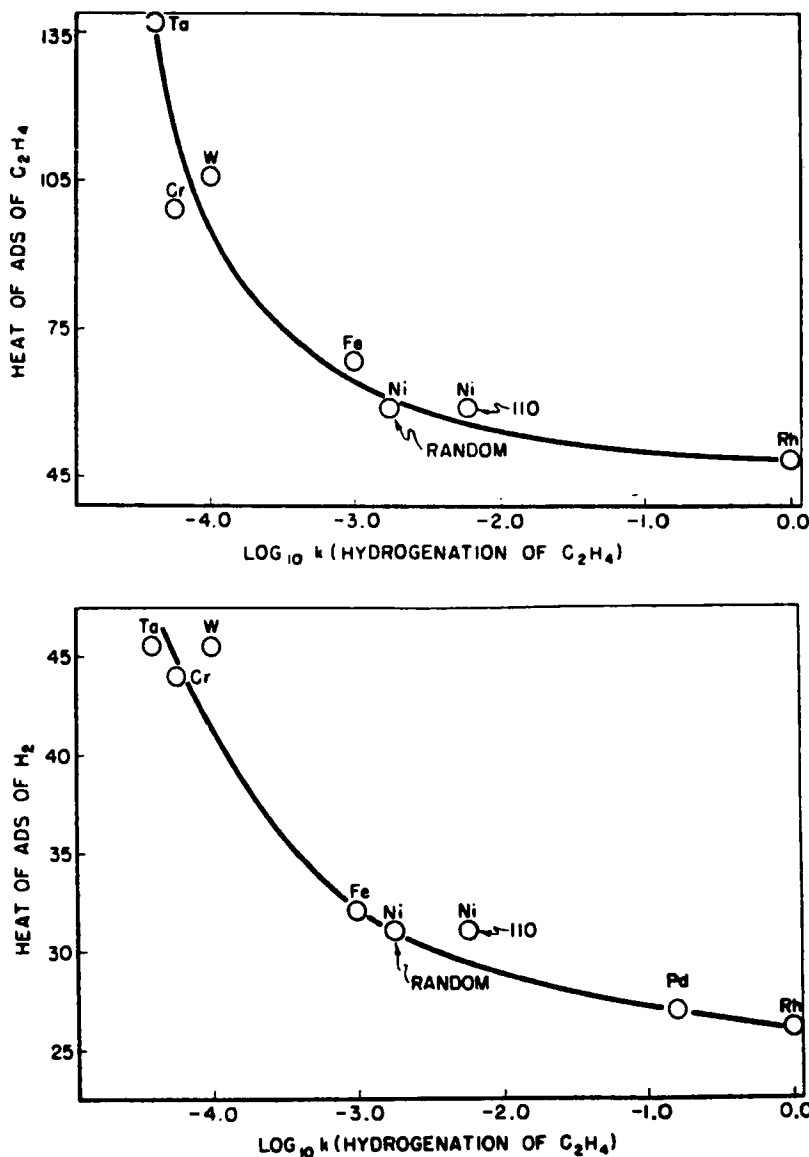


Fig. 5.7. Catalytic activity of metals as a function of heat of adsorption of ethene and hydrogen, respectively.

Fig. 5.7) stimulated a long and ongoing discussion of the problem — what is the relation between the catalytic activity and the electronic structure of metals?

It can be concluded that the most active metals are those that show the lowest heats of adsorption, but which extensively adsorb both reaction components (note: metals like Cu, Ag, Zn, etc. do not do so and are much less active than those shown). Metals in the third to sixth group not only adsorb ethene dissociatively, but in contact

with ethene they also form carbides, which are stable and not very reactive solids.

An interesting question is how many metal atoms are necessary to induce a fast hydrogenation. The simple fact that monomolecular homogeneous catalysts are active in the hydrogenation of olefins indicates that a reaction catalyzed by a single atom (ion) is possible. However, the next question is: when a metal surface offers ensembles of several contiguous surface atoms (multi-atomic adsorption sites), would this enable a much faster reaction? By using alloys in which an active metal was diluted in an inactive one it has been established that with metallic surfaces, too, the hydrogenation/dehydrogenations are likely single-atom-catalyzed reactions [71–73], similar to hydrocarbon–deuterium exchange reactions. In contrast with it, when the surface concentration of an active metal (Ni, Ru, Rh) in a matrix of an ‘inactive’ (much less active) metal decreases and the activity in the reaction in question decreases more than proportionally to the surface concentrations, one can conclude that, for the reaction to occur, one needs simultaneously several contiguous surface metal atoms. The reaction site is thus an ensemble of several atoms. The catalytic effects induced in this way by alloying (bimetallic formation) are called ‘ensemble size effects’. Hydrogenolyses of the C–C, C–O and C–N bonds belong to this group of reactions requiring a large ensemble. This can be sometimes used with advantage to achieve important selectivity effects (ensemble size effects in selectivity) and a practical example of this application is naphtha reforming (see below).

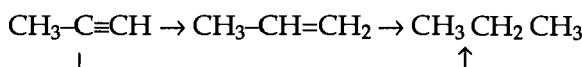
The conclusions just mentioned concerning the catalytic behaviour of the alloys of an active with an inactive metal are only valid if one can safely assume that the adsorption and catalytic properties (electronic structure) of the active atoms do not change significantly upon alloying. Abundant literature information shows that this is a reasonable assumption. The electronic structure effects (also called ligand effects) of alloying are probably always present, but are marginal with respect to the catalytic behaviour and are therefore difficult to prove unambiguously (although easy to claim).

Hydrogenations have been found to be particle-size independent reactions, which rhymes well with the conclusion drawn above that they are single-atom catalyzed. With a molecule like *trans*-di-tertbutyl ethene this is even slightly surprising [74].

Interesting information exists about the crystal-face specificity/reactivity [75]. In ethene hydrogenation the (001) face of Ni is inactive, because this face, under the standard reaction conditions applied, is completely covered by carbonaceous deposits. The (111) and (011) faces are both active and differ by less than a factor of 2 in their activity. The data just mentioned are just another example of a frequently encountered phenomenon: the crystal face specificity or the particle size sensitivity of a reaction is induced by a side reaction and is not caused by the reaction in question [76].

5.3.3 Reactions of Polyenic and Acetylenic Molecules

Many features of these reactions can be illustrated by the data in Fig. 5.8. One can see (left part of Fig. 5.8) that the reaction has a slower phase and a faster one. The first one corresponds to the reaction which runs prevailingly to propene (this happens with a selectivity shown by horizontal lines in the right part of Fig. 5.8). When methylacetylene disappears from the gas phase, a subsequent faster hydrogenation to propane takes place. Such behaviour is explained by the following scheme comprising two parallel reaction pathways:



(and analogously for other acetylenic compounds). In the consecutive pathway (upper line), a high selectivity is achieved by the continuous displacement of propene from the surface by the propyne which is still present (this is a so-called thermodynamically controlled selectivity, since the heats of adsorption play the decisive role [78]). In the 'direct' lower pathway to propane, propyne is more strongly bound to the surface by one or another (possibly dissociative) adsorption forms, which adsorption mode allows hydrogenation into propane without desorption and readsorption of propene. In this picture the constant selectivity on the right side of Fig. 5.8 mainly reflects the extent of this firmly bound adsorption layer.

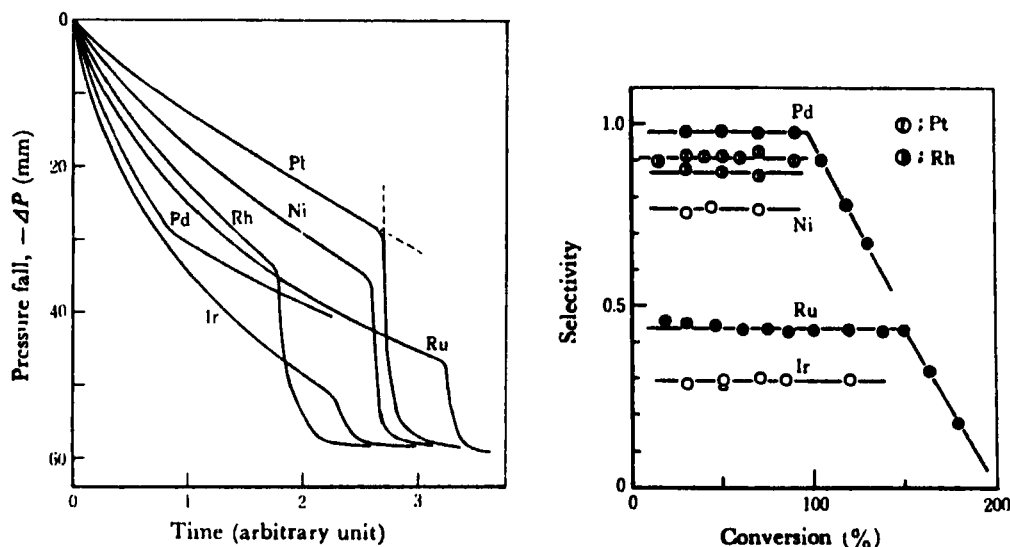


Fig. 5.8. Hydrogenation of methylacetylene in a static closed system with various metals as catalysts. *Left:* Pressure drop as a function of time. *Right:* Selectivity to propene as a function of conversion (100% conversion corresponds with the reaction to propene [15]).

In the hydrogenation of acetylenic compounds the selectivity to olefins is influenced by the 'ensemble size effect' or by the particle size variations. This can be seen from the following information. If, for example, Ir is diluted in its surface by Cu or Au then upon hydrogenation of ethyne, the selectivity to ethene increases with increasing dilution of Ir, i.e. with the diminution of Ir ensembles. With the same metal, smaller particles clearly show a higher selectivity to ethene than the large ones. Both effects — particle size and diminishing and diluting of active sites — are known to suppress the formation of carbon–metal multiple bonds and they both lead to a lower degree of dehydrogenation of adsorbed species [65,76]. Metals like Pd, with an intrinsically high selectivity to ethene, i.e. those where the direct hydrogenation to an alkane does not take place, do not show any significant variation of selectivity with particle size.

Dienes behave in many respects very similarly to acetylenes (see e.g. ref. 78). The consequences of surface modifications for the activity and the selectivity of catalysts also seem to be very similar. Among other things, hydrogenation seems to be faster, per unit of the total metal surface area, with the larger particles [79]. This could be explained by the higher bonding strength of the above-mentioned unsaturated molecules to the coordinatively unsaturated metal atoms [79].

Although the hydrogenation of various acetylenic compounds is industrially very important and scientifically an interesting problem to study, the information gathered up to now is still insufficient to answer all questions. So, for example, the debate is still continuing on the problem whether the hydrogen diluted in metals plays a role or not, or whether the carbonaceous layer (instead of unoccupied metal sites) is the locus of hydrogenation of acetylene or not, etc. (see e.g. the discussion in ref. 80).

5.3.4 Aromatics

A model compound here is benzene. Both the benzene hydrogenation (de-aromatization of oil) as well as the dehydrogenation of cyclohexane into benzene (e.g. upon naphtha reforming) are of practical interest. Hydrogenation of benzene looks similar to the hydrogenation of olefins. For example, in a certain region of reaction conditions, the reaction is near to first order in hydrogen pressure and zero order in benzene pressure [78]. (N.B. A more exact analysis of the kinetics is available too, see ref. 81). However, there also seem to be some important differences.

While it is clear, now, that the C=C bonds can be hydrogenated by homogeneous mononuclear inorganic complexes, an analogous hydrogenation of benzene is most likely not possible. There are some reports in the literature that mononuclear complexes can do it, but a closer inspection of the data reveals that insufficient attention has been paid in the reports to the absolutely necessary exclusion of the formation of small metal particles under reaction conditions. Hydrogenation of polyaromatics might run by a different mechanism and may

be easier [82] and less demanding with regard to the ensemble size. This conclusion seems to be in agreement with the data obtained with Pt–Au alloys: a low-temperature hydrogenation of cyclohexene is also possible on diluted Pt–Au alloys, but hydrogenation of benzene is not [83].

Hydrogenation of benzene is difficult to stop at the level of cyclohexadiene or cyclohexene. *Vice versa*, when cyclohexadiene or cyclohexene are brought into contact with a metal, they disproportionate into benzene and cyclohexane. This reaction has been called ‘Zelinsky irreversible catalysis’. Partial benzene hydrogenation is possible with special catalysts and is of potential importance for the production of cyclohexanone, di-hydroxy-cyclohexane, *exo*-cyclohexene oxide and other important intermediates in the chemical industry. Among the catalysts for this reaction are, for example, metals modified by various promoters, among others by Zn, Cd, Mg or other salts. The function of the promoter here has not yet been definitely established. It can be an electronic effect of cations on the population and, thus, reactivity of the benzene and cyclohexene π^* orbitals, or — as suggested recently — it can be an effect of H_2O accumulation (H_2O stimulates desorption of cyclohexane and prevents its subsequent hydrogenation) near the metal particles due to the hydration of the promoting salt [84].

The order of activities of various metals in benzene hydrogenation recalls that for ethene hydrogenation. According to ref. 85:

benzene:	$Pt > Rh . Ru > Pd > Co > Ni > Fe$	(373 K)
ethene:	$Rh > Ru > Pd > Pt > Ni > Ir > Co > Fe$	($E_a = \text{const.}$)
(all catalysts/metals on silica)		

The sequences are not exactly the same but similar to those obtained with support-free metals (evaporated films).

The activity of all catalysts studied is lower for alkylbenzene than for benzene, and it is also lower for polycondensed aromatic rings. The possible reason for these differences is that the larger molecules make more, different adsorption modes of molecules possible, including those which do not lead to the desired reaction. For example, alkyl substituents in alkylbenzenes react with the metal surface faster than the ring, but only the adsorption through the ring activates the molecules towards its hydrogenation.

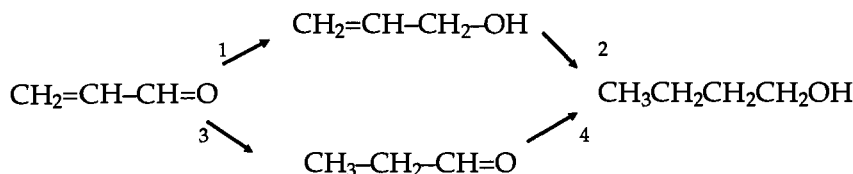
5.3.5 Related Reactions

Hydrogenation of molecules with heteroatoms is also a desirable reaction; for example, in C=O (aldehydes or ketones) —NO₂, C≡N and other bonds. For these hydrogenations, too, transition metals are the most active catalysts and, again, the reaction runs very easily up to the full saturation by hydrogen: from nitro (or nitrile) to amino, and with some metals the undesired hydrogenolytic reactions can also accompany the hydrogenation in the required direction.

Information is already available about the potential intermediates of the above-mentioned hydrogenation reactions (at elevated temperature: this is related to dehydrogenation) and the reader will find it in Chapter 4. Of these species the fast hydrogenation/dehydrogenation likely employs the π -complexed ones, and the α,β -associatively adsorbed species, or the heteroatom coordinated species. The stronger the metal–C and metal–O (or other heteroatom) bonds, the higher will be the tendency to hydrogenolysis (mainly with metals to the left in the periods of the periodic system). When undesired, the hydrogenolytic reaction can sometimes be suppressed by diluting the active atoms in the catalyst surface by inactive (less active) ones (see below).

The knowledge currently available allows us to make useful predictions of which metals (pure or alloyed) and in which form (small or large particle size) have the best chance to be good catalysts for a new reaction with simple (monofunctional) molecules which have not yet been studied. However, much less can be predicted at the moment with regard to the polyfunctional molecules, in which (for example) a C=C bond stands in the neighbourhood of a C=O, C≡N or other bond. The only general theory of selectivity in these reactions is that of Ballandin [86], but this theory does not seem to be satisfactory from the modern point of view. However, useful information is available for some individual reactions. For example, with regard to the α,β -unsaturated aldehydes, of which acrolein is the simplest example. Let us describe this in more detail.

Acrolein is hydrogenated by a network of parallel and consecutive reactions. The main frame of the reaction is:



and accompanying reactions are various hydrogenolytic steps. The most desired product is allyl alcohol, produced with a selectivity S_{al} . In general, hydrogenation of C=O bonds on metals is kinetically more difficult than that of C=C bonds, but thermodynamically the situation is exactly the reverse. It is also thermodynamically more difficult to stop at the stage of step 1 and not to proceed further by step 2. This information underlines the importance of manipulation of the catalyst selectivity and the necessity for the proper choice of the active metal.

The order of activities in the hydrogenation of ketonic bonds is [78]:



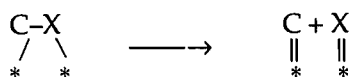
and the main difference in comparison with the C=C bond hydrogenation seems

to be the very low activity of Pd. The activity of metals can be substantially enhanced by using a promoter and for an isolated C=O bond promoters are similar to those used in the syngas reactions (see the section on that topic). However, when the selectivity, S_{al} (or another analogous one), is to be enhanced, the group of potential promoters could be more restricted, since the necessary condition of a good promoter is that the site activating the C=O bond must not bind the C=C bond. The most suitable promoters are then Sn, Ga, Ge, most likely in the ionic form. The selectivity in hydrogenation of α,β -unsaturated aldehydes is strongly influenced by the substitution (steric hindrance) on the bonds (C=C, C=O) in question (for a review, see e.g. ref. 87). Examples of the industrially important reactions of the type just mentioned are hydrogenation of: cinnamic aldehyde (and substituted analogs) to cinnamic alcohol, hydrogenation of furfural to furfuryl alcohol, all-*trans*-retinal to retinol, and some others.

5.3.6 Reactions of Saturated Hydrocarbons

Of the reactions closely related to those discussed above, hydrogenolysis of various bonds (C–C, C–O, C–N) is most important. Upon hydrogenolysis addition of hydrogen is accompanied by splitting of a strong bond (with the molecule in the adsorbed state). Metals are the most active catalysts of these reactions.

On most metals hydrogenolytic reactions are large ensemble reactions (see above). Platinum is most likely an exception and can probably also perform the low-temperature hydrogenolysis by single metal atom catalysis [88]. The reason why a large ensemble is required for a fast reaction at relatively high temperatures is that the splitting of a C–X (X = C, O, N) bond must take place in the adsorbed state of the molecule, in something like the species on the left (the bonds not relevant to the discussion are omitted here):



The C–X can be split thermally, but this step requires a high activation energy. Catalytic splitting is easier. In the latter case, multiple bonding with the surface occurs (see the right side) and for most of the metals of Groups 8–10, this requires that the site * of the scheme above comprises several contiguous metal atoms.

Hydrogenolytic reactions can also be suppressed by carbonaceous layer deposition or by modification of the active surfaces by — for example — sulphur. Suppression of hydrogenolysis gives more chance to a reaction the rate of which decreases only proportionally to the active metal surface concentration, like hydro/dehydrogenation, or some forms of isomerisation (5C cyclic mechanism; see the chapter on elementary steps).

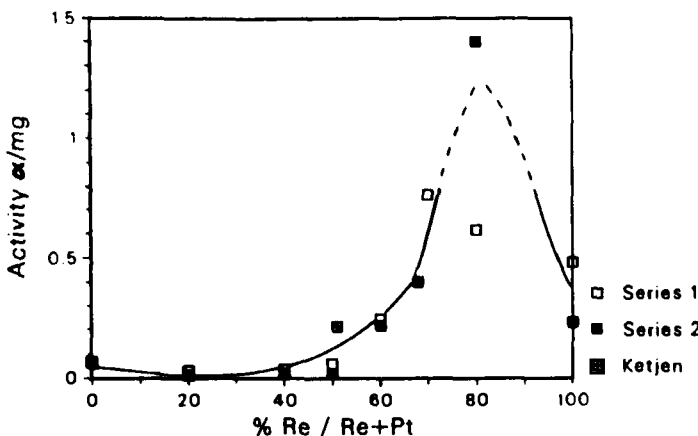


Fig. 5.9. Total activity (conversion per mg/cat) as a function of catalyst composition, in reactions of neohexane on Pt-Re/Al₂O₃ catalysts.

When discussing the practically very important naphtha reforming one must not forget that the various reforming reactions are partially 'bifunctional'. They are initiated by dehydrogenation of saturated hydrocarbons on the metallic surface and they continue, after a lateral migration, as 'carbenium ion' reactions on the surface of the support. Unsaturated intermediates are then easily back-hydrogenated on the metal [89], or desorb as such. Thermodynamically, dehydrogenation and aromatization (all these reactions can be induced by the metal surface) are favoured at higher temperatures and therefore the industrial processes occur at a reaction temperature of 670–770 K. At these temperatures the multiple-site hydrogenolysis occurs freely and must be suppressed by deposited 'C', S or by second inactive elements added to the catalyst, like Sn or Ge. Similarly, Re and Ir as a bulk component and the simultaneously administered 'S' (as surface modifier) can achieve the same goal. It has been shown that, for example, with Pt-Re-S/SiO₂ catalysts the number and quality of acid sites does not change significantly due to the presence of Re and S in the catalysts, but the formation of the most desired intermediates is relatively more favoured than the formation of hydrogenolytic intermediates. Without sulphur Re increases the selectivity and yield to hydrogenolysis and the results indicate that the most active ensembles are the mixed ones, with a composition not far from PtRe₂ [89,90]. This is seen in Fig. 5.9 and 5.10.

Figure 5.9 shows the total activity per mg catalyst in the conversion of neohexane by sulphur-free Pt-Re-Al₂O₃ catalysts. (N.B. Between 20 and 80% Re the metal particle size does not vary significantly.) Figure 5.10 shows schematically how the activities vary in the *n*-hexane reforming reactions on a series of Pt-Re sulphur-free (left) and sulphurized (right) catalysts. With the sulphurized Pt-Re-S/Al₂O₃ catalysts almost all skeletal reactions are induced by the acidic sites. The

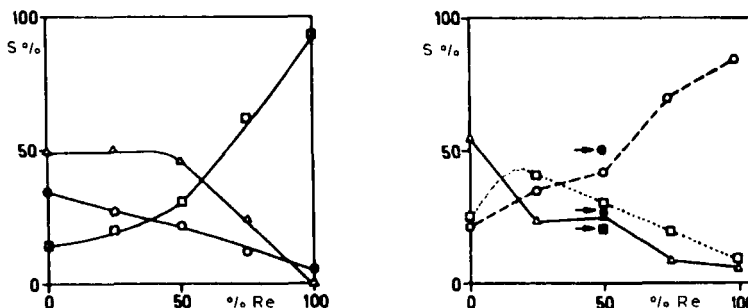


Fig. 5.10. Left: Pt-Re/Al₂O₃ sulphur-free (and Cl-free) catalyst. Selectivities in *n*-hexane conversion. Δ dehydrocyclization (incl. aromatization); \square hydrogenolysis; \circ isomerization. Right: The same catalysts after a standard sulphurization procedure. Arrows show results obtained with a physical mixture of Pt/S/Al₂O₃ and Pt/Re/S/Al₂O₃ catalysts. T = 620 K, 1 bar total pressure.

Pt-Re-S/SiO₂ catalysts under the same conditions are inactive. The Pt-Ir-S/SiO₂ catalysts behave slightly differently: a larger proportion of the total conversion is due to the sulphur-free metallic surface. The catalysts containing Ir are faster than the Re-containing ones but the selectivity to C₅₊ is lower.

5.4 CATALYTIC OXIDATION

5.4.1 Introduction

Oxidation is extremely important both from a scientific and a practical point of view. Without oxidation life would not exist. In the chemical industry, too, oxidation is probably the most important process. A major example is the combustion of fossil fuels. This process is usually uncatalyzed, but sophisticated catalytic processes do exist. Examples in the inorganic industry are the oxidation of sulphur dioxide and ammonia in the manufacture of sulphuric acid and nitric acid, respectively. In the petrochemical industry many catalytic synthesis processes are carried out, for example the production of ethylene and propene epoxide, phthalic acid anhydride. An example which has recently also become important is the catalytic combustion of hydrocarbons in flue gases. Table 5.2 gives a list of examples of oxidation catalysis in industry [93].

In this section we will confine ourselves to the oxidation of hydrocarbons. The addition of oxygen to a hydrocarbon is nearly always thermodynamically favoured. When selective oxidation is aimed at, the reaction has to be kinetically controlled because the most stable situation is the complete combustion into water and carbon dioxide. Usually, the reactivity of intermediate and end products (alcohols, aldehydes, etc.) is higher than that of the starting material. As a consequence, selectivity is difficult to achieve and the catalyst has to be designed carefully: promoters and modifiers are often essential for the success of the

TABLE 5.2
Oxidation catalysis in industry

Processes	Catalysts
1. Inorganic Industry	
Nitric acid by NH ₃ oxidation	Pt–Rh
Sulphuric acid by oxidation of SO ₂	V ₂ O ₅
HCN by oxidation of methane	Pt
HCl to Cl ₂	CuCl ₂
2. Petrochemical Industry	
CH ₄ oxidative coupling	MgO/K ₂ O
Formaldehyde by oxidation of methanol	Fe ₂ (MoO ₄) ₃
Ethylene oxide	Ag / Al ₂ O ₃
Vinyl chloride by ethylene oxychlorination	CuCl ₂ , HgCl ₂
Propene epoxide	Mo, Ti/silica
Acrylonitrile by ammoxidation of propene	Bi ₂ (MoO ₄) ₃
Maleic anhydride from C ₄	(VO) ₂ P ₂ O ₇
Butadiene by C ₄ oxydehydrogenation	(Co,Ni) ₃ (PO ₄) ₂
Caprolactam from cyclohexane	Pd / Al ₂ O ₃
Styrene by oxydehydrogenation of ethylbenzene	Fe ₂ O ₃
Phthalic anhydride from <i>o</i> -xylene	V ₂ O ₅ /TiO ₂
Terephthalic acid from <i>p</i> -xylene	CH ₃ COO(Co,Mn)
3. Fine Chemicals, Biotechnology	
Acetoxylation of ethylene	Pd / support
Hydroquinone-catechol from phenol	Ti–silicalite
Acids from aldehydes	Oxides
Hydroxylation of saturated C–H	Monooxygenase
4. New Energy Sources	
Fuel cells	Pd/ZrO ₂
5. Pollution Control and Environmental Protection	
Catalytic car mufflers	Pt,Pd,Rh / Al ₂ O ₃
Combustion of hydrocarbons in flue gases	CuCo ₂ O ₄ , Pt

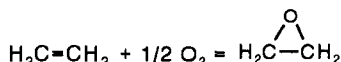
catalytic process. The fact that oxidations are strongly exothermic adds to the problem of achieving a high selectivity. Oxidations are often carried out in the liquid phase since in that case, a relatively good temperature control is possible and the occurrence of 'hot spots' is easier to avoid.

Oxidation can be performed by a large variety of oxidizing compounds. The cheapest and the most important is atmospheric oxygen. However, O₂ is usually less selective and in many cases H₂O₂ or organic peroxides have to be used. Also, especially in fine chemistry, inorganic oxidizing agents are used such as MnO₂, CrO₃, etc. For environmental reasons there is now an imperative to avoid these stoichiometric reactions and to replace them by catalytic reactions. In fine chemistry the price of raw materials is less critical than in bulk chemistry. Hydrogen peroxide is in many respects the ideal oxidizing agent in fine chemistry, mainly because the unpolluting H₂O is the only by-product of the oxidizing agent. In the bulk chemical industry O₂ usually has to be used for economic reasons. An exception to this is formed by processes which use organic peroxides, where the peroxide leads to a valuable by-product (for instance SMPO, Chapter 2). When the overall flow scheme of this process is considered it becomes clear that in this process, too, O₂ is the oxygen donor.

In industry many selective oxidations are carried out in a homogeneously catalyzed process. Heterogeneous catalysts are also applied in a number of processes, e.g. total combustion for emission control, oxidative coupling of methane, the synthesis of maleic acid from butanes, the epoxidation of ethylene. Here we focus upon heterogeneous catalysis and of the many examples we have selected one. We will illustrate the characteristics of catalytic oxidation on the basis of the epoxidation of ethylene. It has been chosen because it illustrates well the underlying chemistry in many selective oxidation processes.

5.4.2 Epoxidation of Ethene

Ethylene epoxide (EO) is an important intermediate in the chemical industry and the mechanism of its formation has been studied in detail [94–98]. For the industrial aspects see Chapter 2. EO is produced by the selective oxidation of ethylene with oxygen:



This reaction is accompanied by complete combustion into water and carbon dioxide. The only selective catalyst known is based on silver. This catalyst was known as early as the 1930s and has been continuously improved since then in a rather empirical way. It has been discovered that the catalyst may be promoted by the addition of alkali metal ions. Moreover, the presence of chlorine has a beneficial effect (cf. Fig. 5.11) [94]. Chlorine has to be added continuously because it disappears from the surface by reacting to give chlorinated ethane. It is sufficient to mix 10–40 ppm chlorine with the feed. The feed consists of a mixture of

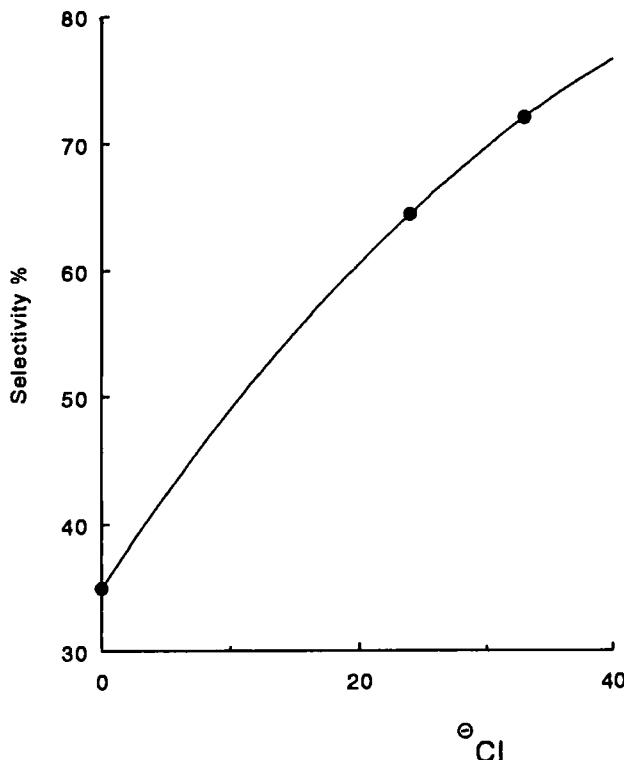


Fig. 5.11. Epoxidation of ethene. Influence of chlorine on selectivity [94].

ethylene (24%), oxygen (8%) and the balance of inert gases. The reaction rate was found to be first order in oxygen and zero order in ethylene in the Shell process.

Usually, the selectivity of the reaction is analyzed on the basis of the following simplified scheme (Fig. 5.12):

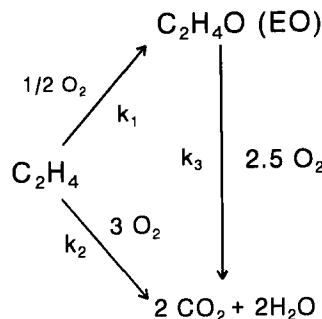


Fig. 5.12. Kinetic scheme of the reactions [94].

The initial selectivity is determined by the ratio k_1/k_2 . At higher conversions k_3 also plays a role.

As catalysts, a low surface area alumina support is used on which large silver particles are present. It is crucial to minimize the consecutive reaction which is enhanced by acid sites of the support. These sites isomerize the epoxide to acetaldehyde which rapidly combusts in a reaction catalyzed by silver.

It is interesting that, until recently, a mechanism was advocated which predicts that the selectivity has a theoretical limit of 86%. This would imply that it does not make sense trying to improve the catalyst much further, because, in practice, plants are already operating at selectivities close to this value. This theory was based on the assumption that the catalyst contains two types of oxygen [95]: molecular O_2 , and atomic oxygen. The productive epoxidation reaction was envisaged as shown in Fig. 5.13.

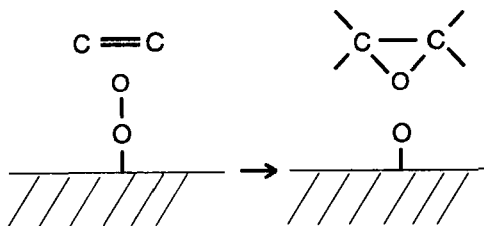


Fig. 5.13. Proposed scheme for selective oxidation of ethylene by preadsorbed molecular oxygen.

According to this mechanism molecular oxygen is adsorbed at the catalyst surface and ethylene reacts with this species to give epoxide, while one oxygen atom remains at the surface. The oxygen atom remaining at the surface has to be removed in order to restore catalytic activity. This, in view of this theory, is only possible by the non-selective complete combustion reaction (Fig. 5.14).

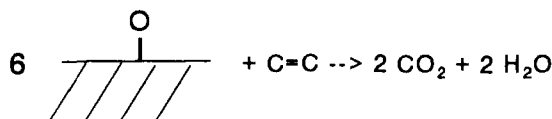


Fig. 5.14. Proposed scheme for complete oxidation of ethylene.

The implication of this mechanism is that the most ideal catalyst under the most optimum conditions would transform six ethylene molecules into EO and one ethylene molecule into water and carbon dioxide. Hence, according to this theory, the selectivity can never exceed 6/7. This theory also explains the favourable influence of chlorine. It was known that chlorine selectively poisons sites on Ag which can adsorb O_2 dissociatively. As atomic oxygen was considered to be

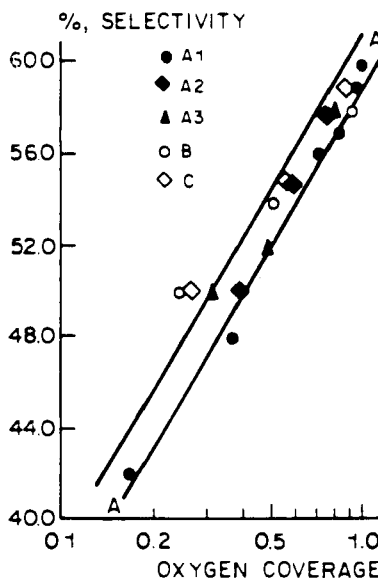


Fig. 5.15. Selectivity versus oxygen coverage of various supported Ag catalysts [94].

the source of complete combustion, its presence should be minimized and the beneficial action of chlorine was explained.

In 1975 another model was proposed [96], in which atomic oxygen was thought to be the source of selective epoxidation. This was later confirmed experimentally [97]. In the following we will outline the basis of this mechanism [98].

There is no doubt that the initial selectivity is governed by the characteristics of the oxygen at the surface. The subsequent reactions also influence the overall selectivity: support acid sites catalyze the isomerization of EO giving acetaldehyde, which is very reactive towards complete combustion. The beneficial influence of alkali promoters is due to the poisoning of the acid sites at the catalyst support.

The selectivity depends strongly on the oxygen coverage. At low oxygen coverages the selectivity is much lower than at high coverages (cf. Fig. 5.15).

According to the current view of the mechanism this is explained as follows. At low coverages the oxygen is very strongly adsorbed, whereas at higher coverages the adsorption is much weaker. From TPD data [99] it was found that, below half monolayer coverage, the binding strength is 50–60 kJ/mol. This contrasts with the data at higher coverages which give only 0–13 kJ/mol. When we consider the reaction enthalpy for the formation of the epoxide from atomic oxygen, the reason why selective epoxidation at low oxygen coverage is slow becomes clear: the reaction enthalpy is only 50–70 kJ/mol. This value barely exceeds the bond strength of oxygen at low coverages. Thus, in this case total

oxidation — a reaction that is much more exothermic — is thermodynamically favoured, whereas epoxidation is hardly possible.

The influence of the promoters and modifiers can be understood from a comparison of the desired reaction, leading to EO, and the undesired reactions, leading to complete combustion. In the desired reaction an electrophilic attack has to take place (Fig. 5.16).

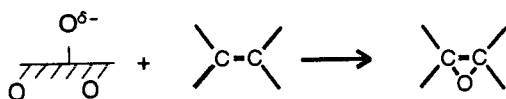


Fig. 5.16. Electrophilic attack of oxygen [94].

In the undesired reaction nucleophilic attack takes place at a C–H bond (Fig. 5.17).

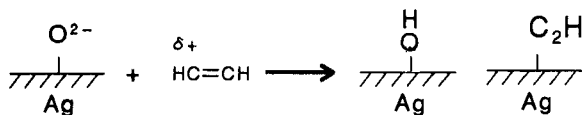


Fig. 5.17. Nucleophilic attack of oxygen [94].

At increasing oxygen coverages the charge on the oxygen atoms will decrease and, as a consequence, the EO production rate increases, whereas the rate of the undesired complete combustion reactions decreases. The influence of Cl is probably to decrease the charge of oxygen. Chlorine is a promoter because, under reaction conditions, it performs this function better than subsurface oxygen atoms. Under reaction conditions the steady-state coverage of oxygen is rather low, whereas chlorine will chlorinate the surface to a higher degree. The influence of the alkali metal might lie in the further stabilization of chlorine. Moreover, alkali metal atoms will poison acidic sites of the weakly acidic alumina support (upon which the silver particles are dispersed) which catalyze the undesired following reactions, increasing the combustion rates.

A summary of the mechanism described above is given in Fig. 5.18.

It is striking that only silver has been found to be a good catalyst. Why is silver unique? The mechanism described here may provide an answer. The key factor might be that silver can dissociate O_2 , but the oxygen atoms are so weakly chemisorbed that epoxidation is possible. Moreover, silver only weakly activates the C–H bonds in ethylene. Definitive answers on the potential and the explanation of promoters and modifiers are waiting for more information.

Up till now it has not been possible to carry out the analogous reaction with propene. Numerous researchers have attempted to develop a process for the

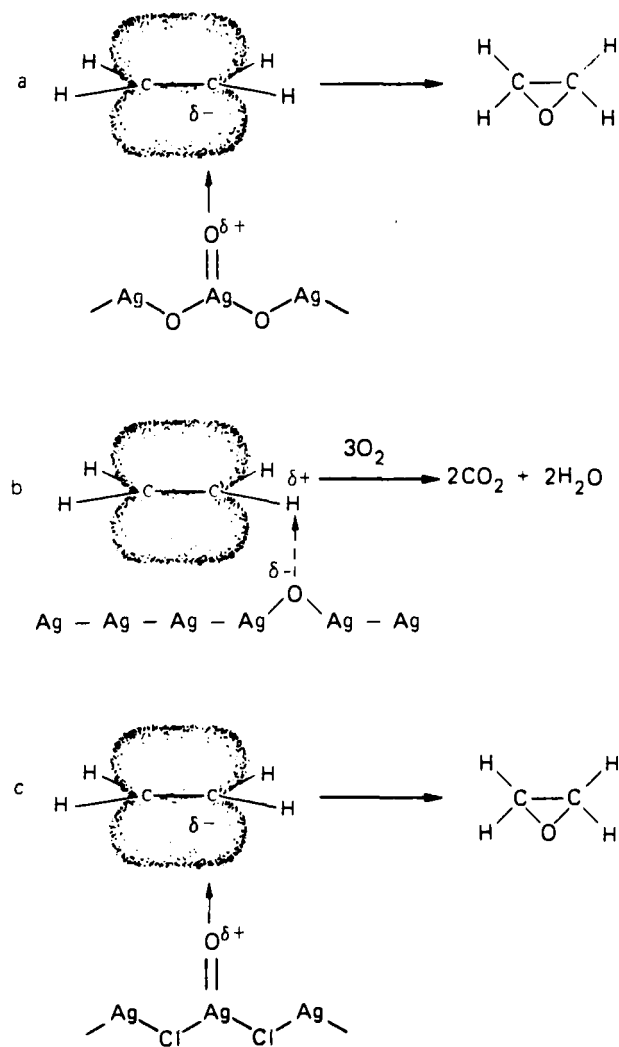


Fig. 5.18. Schematic representation of the proposed transition state leading to epoxidation [94].

direct oxidation of propene into propene epoxide (PO). Only indirect routes have, up to now, been applied in successful selective processes. Those indirect processes involve the use of hydrogen peroxide, organic peroxides and peracids, hypochlorides, etc. (see e.g. SMPO, Chapter 2). The reason that it is difficult to epoxidize propene is the facile formation of an allylic intermediate because the C–H groups in the methyl group become activated.

Because of their success in ethylene epoxidation, it is not surprising that specially modified Ag catalysts have received intense attention. Although promising developments have been reported, there is still no commercial process for the direct oxidation of propene into PO. Here is a real challenge for the scientific community.

REFERENCES

- 1 P. Sabatier and J.B. Sendereras, *C.R. Hebd. Seances Acad. Sci.*, 134 (1902) 514.
- 2 E.J. Orlov, *Zhur. Ross. Khim. Ob-a*, 40 (1908) 1588.
- 3 F. Fischer and H. Tropsch, *Brennst. Chem.*, 4 (1923) 276.
F. Fischer and H. Tropsch, *Ber. Dtsch. Chem. Ges.*, 59 (1926) 830.
F. Fischer and H. Tropsch, *Brennst. Chem.*, 7 (1926) 97.
- 4 M. Ritschel and W. Vielstich, *Chem. Eng. Tech.*, 52 (1980) 327;
D. Kitzelmann and W. Vielstich, *Z. Phys. Chem.*, 112 (1978) 215
- 5 S.R. Craxford and E.K. Rideal, *J. Chem. Soc.*, 1604 (1939).
R.B. Anderson in P.H. Emmett (Editor), *Catalysis*, Reinhold, N.Y., Vol. 4, 1956.
- 6 H.H. Storch, N. Columbic and R.B. Anderson in *The F.T. and Related Synthesis*, Wiley, N.Y., 1951.
H. Pichler, *Adv. Catal.*, 4 (1952) 271.
G. Blyholder and P.H. Emmett, *J. Phys. Chem.*, 64 (1960) 470 and refs. therein.
- 7 H. Pichler and H. Schulz, *Chem. Ing. Tech.*, 42 (1970) 1162.
- 8 (a) P.R. Wentrczek, B.J. Wood and H. Wise, *J. Catal.*, 41 (1976) 363.
(b) M. Araki and V. Ponec, *J. Catal.*, 44 (1976) 439.
J.W.A. Sachtler, J.M. Kool and V. Ponec, *J. Catal.*, 56 (1979) 284.
(c) J.A. Rabo, A.P. Risch and M.L. Poutsma, *J. Catal.*, 53 (1978) 295.
(d) P. Biloen, J.N. Helle and W.M.H. Sachtler, *J. Catal.*, 58 (1979) 95.
- 9 V. Ponec and W.A. van Barneveld, *Ind. Eng. Chem. Prod. Res. Dev.*, 18 (1979) 268.
- 10 N.A. van Barneveld and V. Ponec, *J. Catal.*, 88 (1984) 382.
- 11 R.C. Braddy III and R. Pettit, *J. Am. Chem. Soc.*, 103 (1981) 1287.
- 12 P.J. Flory, *J. Am. Chem. Soc.*, 58 (1936) 1877.
G.V. Schultz, *Z. Phys. Chem.*, 29 (1935) 299.
- 13 E.F.G. Harrington, *Chem. Industry (London)*, (1946) 346.
- 14 R.B. Anderson, R.A. Friedel and H.H. Storch, *J. Chem. Phys.*, 19 (1951) 313.
- 15 O.A. Hougen and K.M. Watson, *Ind. Eng. Chem.*, 35 (1943) 529.
K.H. Yang and O.A. Hougen, *Chem. Eng. Progr.*, 46 (1950) 146.
- 16 J. Ross, *J. Catal.*, 71 (1981) 205.
- 17 S. Van Ho and P. Hariott, *J. Catal.*, 64 (1980) 272.
R.L. Palmer and D.A. Vroom, *J. Catal.*, 50 (1977) 244.
- 18 C.P. Huang and J.T. Richardson, *J. Catal.*, 51 (1978) 1.
V.M. Vlasenko, L.A. Kukhar, M.T. Rusov and N.P. Sachenko, *Kinet. Katal.*, 37 (1972) 762.
- 19 M.A. Vannice, *J. Catal.*, 37 (1975) 462.
D.I. Ollis and M.A. Vannice, *J. Catal.*, 38 (1975) 514.
G.C. Bond and B.D. Turnham, *J. Catal.*, 45 (1976) 128.
- 20 A.O.I. Routavuouma and H.S. van der Baan, *Appl. Catal.*, 1 (1981) 243.
- 21 R.Z.C. van Meerten, J.G. Vollenbroek, M.H. de Croon, P.F. van Nisselroy and J.W.A. Coenen, *Appl. Catal.*, 3 (1982) 29.
- 22 (a) D.W. Goodman, R.D. Kelley, T.E. Madey and J.M. White, *J. Catal.*, 64 (1980) 479.
(b) N.M. Gupta, V.S. Kemble, K.A. Rao and R.M. Jver, *J. Catal.*, 60 (1979) 57.
(c) T.M. Duncan, P. Winslow and A.T. Bell, *J. Catal.*, 93 (1985) 1.
- 23 D.W. Goodman, R.D. Kelley, T.E. Madey and J.T. Yates, *J. Catal.*, 63 (1986) 226.
- 24 V. Ponec, *Adv. Catal.*, 32 (1983) 49.
- 25 W.M.H. Sachtler, *Cat. Rev. Sci. Eng.*, 14 (1976) 193.
W.M.H. Sachtler, *Adv. Catal.*, 26 (1977) 69.

- 26 (a) F.J.G.M. Toolenaar, F. Stoop and V. Ponec, *J. Catal.*, 82 (1983) 1.
A.G.T.M. Bastein, F.J.C.M. Toolenaar and V. Ponec, *J. Catal.*, 90 (1984) 88.
(b) V. Ponec, *J. Quant. Chem.*, 2 (suppl.) (1977) 1.
(c) V. Ponec in *Catalysis*, Spec. Period Repts. Royal Chem. Soc., Vol. 5, p. 48.
- 27 J.A. Rodriguez and D.W. Goodman, *J. Phys. Chem.*, 95 (1991) 4197.
J.A. Rodriguez, R.A. Campbell and D.W. Goodman, *Surf. Sci.*, 244 (1991) 211.
C.T. Campbell, *Ann. Rev. Phys. Chem.*, 41 (1990) 775.
- 28 R.W. Joyner and E.S. Shipiro, *Catal. Lett.*, 9 (1991) 239.
- 29 J.A. Rodriguez, R.A. Campbell and D.W. Goodman, *J. Phys. Chem.* ('Electron donor-electron acceptor interaction in bimetallic surfaces') in press.
- 30 V. Ponec in *Coal Science*, Vol. 3, Academic Press, p.1, 1984.
- 31 G.C. Bond, *Pt Metal Rev.*, 19 (1975) 126.
- 32 E.H. van Broekhoven and V. Ponec, *Surf. Sci.*, 162 (1985) 731.
- 33 A.G.T.M. Bastein, W.J. van der Boogert, G. van der Lee, H. Luo, B. Schuller and V. Ponec, *Appl. Catal.*, 29 (1987) 243.
G. van der Lee and V. Ponec, *Catal. Rev. Sci. Eng.*, 29 (1987) 183.
- 34 L.E.Y. Nonneman, A.G.T.M. Bastein, V. Ponec and R. Burch, *Appl. Catal.*, 68 (1990) L23.
- 35 H.P. Nguyen, P. Meriaudeau and C. Naccache, *Appl. Catal.*, 21 (1986) 337.
- 36 C.P. Horwitz and D.F. Shriver, *Adv. Organometal. Chem.*, 23 (1984) 219.
- 37 W.M.H. Sachtler, D.F. Shriver, W.B. Hollenberg and A.F. Lang, *J. Catal.*, 92 (1985) 429.
- 38 S. Holloway, J.K. Norskov and N.D. Lang, *J. Chem. Soc., Faraday Trans. I*, 83 (1987) 1935.
K.J. Uram, L. Ng and J.T. Yates Jr., *Surf. Sci.*, 177 (1986) 253.
- 39 R.A. van Santen, *Proc. 8th ICC*, Berlin, Springer Verlag, Vol. IV, p. 97, 1984.
R.A. van Santen, *Surf. Sci.*, 251/252 (1991) 6.
- 40 V. Bonacic-Koutecky, J. Koutecky, P. Fantucci and V. Ponec, *J. Catal.*, 11 (1988) 409.
E. Wimmer, C.L. Fu and A. Freeman, *Phys. Rev. Lett.*, 5 (1985) 2618.
- 41 J.R. Katzer, A.W. Sleight, P.Gajardo, J.B. Michel, E.F. Gleason and S. McMillan, *Faraday Disc. Chem. Soc.*, 72 (1981) 121.
G.C. Bond and P. Sermon, *Gold Bull.* (1974) 105.
- 42 L.L. Shen, K. Knozinger and W.M.H. Sachtler, *Catal. Lett.*, 2 (1989) 129.
- 43 G.C.A. Aers and J.E. Inglesfield, *Surf. Sci.*, 217 (1989) 367.
- 44 E. Sanchez Marcos, A.P.J. Jansen and R.A. van Santen, *Chem. Phys. Lett.*, 167 (1990) 399.
- 45 M.J.P. Botman, A.J. den Hartog and V. Ponec in *Structure and Reactivity of surfaces*', Stud. Surf. Sci. Catal., 48 (1989) 179.
- 46 (a) J. Koutecky, *Z. Elektrochem.*, 60 (1956) 835.
T.L. Einstein and J.R. Schrieffer, *Soc. Phys. Rev. B*, 36 (1973) 3629.
(b) J.R. Schrieffer in *Dynamic Aspects of Surface Physics*, Fermi School on Physics, Varena 1974, Editrice Compositori Bologna, p. 25, 1974.
(c) W.D. Mross, *Catal. Rev. Sci. Eng.*, 25 (1983) 591.
(d) W.B. Innes in P.H. Emmett (Editor) *Catalysis*, Reinhold, N.Y., Vol. 1, p.1, 1955.
- 47 R.B. Underwood and A.T. Bell, *Appl. Catal.*, 21 (1986) 157.
J.S. Rieck and A.T. Bell, *J. Catal.*, 96 (1985) 88; 99 (1986) 262.
D.W. Goodman, *Appl. Catal.*, 19 (1984) 1.
G. Broden, G. Haufer and H.P. Bonzel, *Surf. Sci.*, 84 (1979) 295.
T. Okuhara, T. Enomoto, H. Tamari and M. Misono, *Chem. Lett.*, (1984) 1491.
T. Mori, A. Miyamoto, N. Takahishi, M. Fukugaya, M. Miizuma, T. Hattori and Y. Murakami, *Chem. Soc. Chem. Commun.*, (1984) 678.
- 48 D.J. Dwyer and J.H. Aardenbergh, *Appl. Surf. Sci.*, 19 (1984) 14.

- 49 T. Koerts, W. Welters, R.A. van Santen, L.E.Y. Nonneman and V. Ponec in *Natural Gas Conversion*, Stud. in Surf. Sci., 61 (1990) 235.
- 50 H.Y. Luo, A.G.T.M. Bastein, A.A.J.P. Mulder and V. Ponec, *Appl. Catal.*, 38 (1988) 241.
- 51 A.A. Kiennemann, R. Breault, J.P. Hindermann and M. Laurin, *J. Chem. Soc. Faraday Trans I*, 83 (1987) 2119.
- 52 S.J. Tauster, *Acc. Chem. Res.*, 20 (1987) 389.
- 53 M.W. Twigg (Editor) *Catalyst Handbook*, Wolfe, London, 1989.
J. Bart and R.P.A. Sneeden, *Catal. Today*, 2 (1987) 1.
- 54 G.C. Chinchin, M. Spencer, K.C. Waugh and D.A. Whan, *J. Chem. Soc. Faraday Trans I*, 83 (1987) 2193.
G. Chinchin, K.C. Waugh and D.A. Whan, *Appl. Catal.*, 25 (1986) 101.
- 55 Y. Kikuzono, S. Kagami, S. Naito, T. Onishi and K. Tamaru, *J. Chem. Soc. Faraday Disc.*, 72 (1981) 137.
- 56 V. Pitchon, H. Praliaud and G.A. Martin in *Natural Gas Conversion*, Stud. Surf. Sci. Catal., 61 (1990) 265.
- 57 R.G. Herman, K. Klier, G.W. Simmons, B.P. Finn, J.B. Bulko and T.P. Kobylinski, *J. Catal.*, 56 (1979) 407.
K. Klier, *Adv. Catal.*, 31 (1982) 243.
- 58 V. Ponec, *J. Chem. Soc. Faraday Trans I*, 84 (1987) 2244.
V. Ponec and L.E.Y. Nonneman in *Natural Gas Conversion*, Stud. Surf. Sci. Catal., 61 (1990) 225.
- 59 J.M. Driessens, E.K. Poels, J.P. Hindermann and V. Ponec, *J. Catal.*, 82 (1983) 20.
- 60 G. Pacchioni, P. Fantucci, J. Koutecky and V. Ponec, *J. Catal.*, 112 (1988) 34.
- 61 G.R. Sheffer and T.S. King, *J. Catal.*, 115 (1989) 376; 116 (1989) 488.
- 62 M. Amaru, M. Bettahar and D. Olivier, *Appl. Catal.*, 51 (1989) 141.
- 63 W.A.A. van Barneveld and V. Ponec, *Rec. Trav. Chim. Pays-Bas*, 93 (1974) 243.
- 64 G.I. Jenkins and E.K. Rideal, *J. Chem. Soc.* (1955) 2490.
S.J. Stephenson, *J. Phys. Chem.*, 62 (1958) 714.
E.K. Rideal, in *Concepts in Catalysis*, Academic Press, London, 1968.
- 65 S.M. Davis and G.A. Somorjai in D.A. King and D.P. Woodruff (Editors), *The Chemical Physics of Solid Surfaces and Heterogeneous Catalysis*, Vol. 4, Elsevier, Amsterdam, 1982, p. 217.
- 66 A.S. Al Amar and G. Webb, *J. Chem. Soc. Faraday Trans.*, 74 (1978) 195, 657; 75 (1979) 1900.
- 67 D. Godbey, F. Zaera and G.A. Somorjai, *Surf. Sci.*, 167 (1986) 150.
- 68 T. Hattori and R.L. Burwell Jr., *J. Chem. Soc. Chem. Commun.*, (1978) 127.
- 69 R.S. Yolles, B.J. Wood and H. Wise, *J. Catal.*, 21 (1971) 66.
B.J. Wood and H. Wise, *J. Catal.*, 5 (1966) 135.
- 70 O. Beeck, *Disc. Faraday Soc.*, 8 (1950) 118.
- 71 W.M.H. Sachtler and P. van der Planck, *Surf. Sci.*, 18 (1969) 62.
- 72 V. Ponec, *Int. J. Quant. Chem.*, Suppl 12 (2) (1977) 1.
- 73 P. Biloen, F.M. Dautzenberg and W.M.H. Sachtler, *J. Catal.*, 50 (1977) 77.
J.H. Sinfelt, J.L. Carter and D.J.C. Yates, *J. Catal.*, 24 (1972) 283.
- 74 R.L. Burwell, H.H. Kung and R.J. Pellet, *Proc. 6th ICC*, London, Vol. 1, 1976, p. 108.
- 75 G. Dalmai-Imelik and J. Massardier, *ibid*, p. 90.
- 76 E.H. van Broekhoven and V. Ponec, *Surf. Sci.*, 162 (1985) 731.
- 77 N. Yoshida and K. Hirota, *Bull. Chem. Soc. Jpn.*, 48 (1975) 184.
- 78 G.C. Bond in *Catalysis by Metals*, Academic Press, N.Y., 1962.
G.C. Bond and G. Webb, *Adv. Catal.*, 15 (1965) 91.
- 79 J.P. Boitiaux, J. Cosyns and S. Vasudevan, *Appl. Catal.*, 6 (1983) 41.

- 80 Discussion on the paper: Adsorption and reactions on ethyne, *Faraday Disc. Chem. Soc.*, Vol. 8 (1989) 311.
- 81 P. Chou and M.A. Vannice, *J. Catal.*, 107 (1987) 129, 140.
R.Z.C. van Meerten and J.W.E. Coenen, *J. Catal.*, 37 (1975) 37; 46 (1977) 13.
V. Hancil and L. Beranck, *Chem. Eng. Sci.*, 25 (1970) 1121 (phenol hydrogenation).
- 82 R.H. Fish in R. Ugo (Editor), *Aspects of homogeneous Catalysis*, 7, Kluwer, Dordrecht, 1990, p. 65.
- 83 W.A.A. van Barneveld and V. Ponec, *Rec. Trav. Chim. Pays-Bas*, 93 (1974) 243.
V. Ponec, *Proc. 6th ICC*, London, Vol. 2, 1976, p. 851.
- 84 J. Struijk, *Catalytic Routes to Cyclohexene*, Diss. thesis, TU Delft, 1991.
- 85 G.C.A. Schuit and L.L. van Reijen, *Adv. Catal.*, 10 (1958) 242.
- 86 J.A.A. Ballandin, *Adv. Catal.*, 19 (1969) 1.
- 87 T.B.L.W. Marinelli, H. Vleeming and V. Ponec, in L. Guczi et al. (Eds.), *New Frontiers in Catalysis* (Proc. 10th ICC, Budapest, 1992), Stud. Surf. Sci. Catal., 75 (1993) 1211.
- 88 A.J. den Hartog, A.G.T.M. Bastein and V. Ponec, *J. Mol. Catal.*, 52 (1989) 129.
- 89 G. Mills, H. Heinemann, T.H. Milliken and A.G. Oblad, *Ind. Eng. Chem.*, 45 (1953) 134.
- 90 V. Ponec, *Catal. Today*, 10 (1991) 251.
- 91 M.J.P. Botman, C. de Vreugd, H.W. Zandbergen, R. de Block and V. Ponec, *J. Catal.*, 116 (1989) 467.
- 92 P.J.M. Rek, A.J. den Hartog and V. Ponec, *Appl. Catal.*, 46 (1989) 213.
- 93 J. Haber, in P. Ruiz and B. Delmon (Editors), *New Developments in Selective Oxidation by Heterogeneous Catalysis*, Studies in Surface Science and Catalysis, Vol. 72, Elsevier, 1992, pp. 279–304.
- 94 R.A. van Santen and H.P.C.E. Kuipers, The mechanism of ethylene epoxidation, *Adv. Catal.*, 35 (1987) 265–321.
- 95 P.A. Kilty and W.M.H. Sachtler, *Catal. Rev. Sci. Eng.*, 10 (1974) 1.
- 96 E.L. Force and A.T. Bell, *J. Catal.*, 44 (1976) 175.
- 97 R.A. van Santen and C.P.M. de Groot, *J. Catal.*, 98 (1986) 530.
- 98 R.A. van Santen, 'Theoretical Heterogeneous Catalysis', in *World Scientific Lecture and Course Notes in Chemistry*, Vol. 5, World Scientific, Singapore, 1991.
- 99 A.W. Czanderna, *J. Vac. Sci. Technol.*, 14 (1977) 408.

Chapter 6

Homogeneous catalysis with transition metal complexes

6.1 INTRODUCTION

Three topics in homogeneous catalysis with organo-transition metal complexes will be dealt with in this chapter:

- rhodium catalyzed hydroformylation (6.2);
- zirconium catalyzed polymerization of alkenes (6.3); and
- enantioselective hydrogenation (6.4).

Homogeneous catalysis involves a much broader area than will be presented here, but a selection was necessary in order to remain within the scope of this book. The aim of this chapter is to give an impression of the current status of the field of homogeneous catalysis, expectations concerning the future developments of the crucial concepts and techniques, and all this in relation to present and potential industrial applications.

Formally speaking, homogeneous catalysis implies that all reacting partners are present in one phase, usually the liquid phase. A great variety of dissolved homogeneous catalysts are known: Brønsted and Lewis acids and bases, metal complexes, metal ions, organometallic complexes, organic molecules, enzymes, artificial enzymes, etc. Today, 'homogeneous catalysis' is often used in a restricted sense i.e. to refer to catalysis with organometallic and coordination complexes. This is certainly the area that has led to the largest number of industrial applications in the last three decades. From a scientific and application viewpoint the other types of catalysts are equally interesting. In this chapter we will focus on (organo)transition metal complexes as catalysts.

Homogeneous transition metal catalysts are used in such industrial processes as:

- toluene oxidation to benzoic acid;
- xylene oxidation to phthalic acid;
- ester condensation to polyesters;
- carbonylation of methanol to acetic acid;
- carbonylation of methyl acetate to acetic anhydride;
- polymerization of dienes to unsaturated polymers;
- hydroformylation of alkenes to aldehydes (solvents, detergents alcohols, plasticiser alcohols);
- oligomerisation of ethene and propene;
- hydrocyanation of 1,3-butadiene to adiponitrile;
- cyclodi(tri)merization of 1,3-butadiene;
- asymmetric hydrogenation (e.g. L-DOPA);
- codimerization of 1,3-butadiene and ethene;
- oxidation of ethene to ethanal;
- ring opening metathesis polymerization of dicyclopentadiene and norbornene derivatives
- hydrosilylation of alkenes

For further details about these reactions the reader is referred to other works on this topic [1].

In this chapter the reader will be introduced to some of the concepts that are used in the study of homogeneous catalysts and the basic techniques applied to *in-situ* measurements. The study of ligand effects is one of the main themes in homogeneous catalysis [2]: the rate and selectivity of a given process can be optimized to the desired level through proper control of the ligand environment. As will be seen, this initially requires an empirical approach, but once certain trends are known, the variation of ligands can be carried out with some degree of sophistication. It is often clear what factors will influence the optimization process, but the sign of the effect is not always easy to predict. New conversions are most often found by accident; the role of design is still rather modest here.

The three topics described in the following sections have been chosen to be complementary to one another in many senses:

- bulk chemicals vs fine chemicals;
- early-transition metal catalysis vs noble metal catalysis;
- carbonylation vs hydrogenation vs alkene insertions;
- low molecular weight products vs polymers;
- commercialized examples vs a discovery that is just in its infancy.

The three processes have in common that a considerable body of fundamental and detailed knowledge about intermediates and the reaction pathways is already available, a typical feature of homogeneous catalysts.

6.2 RHODIUM CATALYZED HYDROFORMYLATION

6.2.1 Introduction

Functionalization of hydrocarbons from petroleum sources is mainly concerned with the introduction of oxygen into the hydrocarbon molecule. In general, two ways are open to achieve oxygen functionalization: oxidation and carbonylation. Oxidation is commonly encountered in the synthesis of aromatic acids, acrolein, maleic anhydride, ethene oxide, propene oxide, and acetaldehyde. Hydroformylation (CO/H_2) (older literature and the technical literature refer to the 'oxo' reaction) is employed for the large-scale preparation of butanol, 2-ethylhexanol, and detergent alcohols. The main use of 2-ethylhexanol is in phthalate esters which are softeners in PVC. The catalysts applied are based on cobalt and rhodium. (For a general review see ref. 3.)

The hydroformylation of alkenes was accidentally discovered by Roelen [4] while he was studying the Fischer–Tropsch reaction (conversion of syn-gas to liquid fuels with a heterogeneous cobalt catalyst) in the late thirties. In what was probably designed as a mechanistic experiment Roelen examined whether alkenes were intermediates in the 'Aufbau' process for converting syn-gas (from coal, Germany 1938) to fuel. It took more than a decade before the reaction was taken further, but now it was the conversion of petrochemical hydrocarbons into oxygenates that was the driving force. It was discovered that the reaction was not catalyzed by the supported cobalt, but in fact by $\text{HCo}(\text{CO})_4$ which was formed in the liquid state.

A key issue in the hydroformylation reaction is the ratio of 'normal' to 'iso' product (linear and branched product) produced. Figure 6.1 explains this colloquial expression. The linear product is the desired product, since the value of butanal is higher; also because this is the product which can be converted to

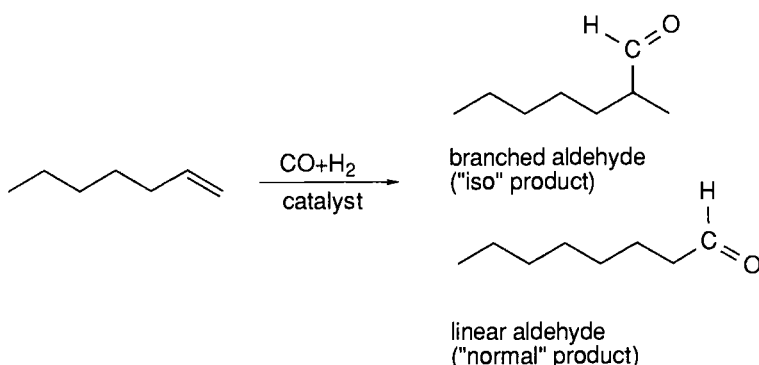


Fig. 6.1. Hydroformylation of terminal alkenes to linear and branched aldehydes.

2-ethylhexanol via base-catalyzed aldol condensation and hydrogenation. Sometimes the aldol condensation reaction is carried out simultaneously with hydroformylation. When butanal is the desired product the condensation reaction is suppressed. The detergent alcohols should preferably be linear because their biodegradability has been reported to be better than that of the branched product. The linearity of the aldehyde product is therefore of great industrial importance. It is an interesting scientific question to see how the linearity can be influenced and maximized.

In the sixties it was recognized that ligand substitution on the cobalt carbonyl might influence the performance of the catalyst. It has been found that aryl phosphines or phosphites have little influence; in fact they may not even coordinate to cobalt under such high CO pressures. Tertiary alkyl phosphines, however, have a profound influence [5]; the reaction is much slower, the selectivity to linear products increases, the carbonyl complex formed, $\text{HCoL}(\text{CO})_3$, is much more stable, and the catalyst acquires activity for hydrogenation. This process has been commercialized by Shell. As a result of the higher stability of the cobalt complex, the Shell process can be operated at lower pressures and higher temperatures (50–100 bar vs 200–300 bar for $\text{HCo}(\text{CO})_4$, 170°C vs 140°C).

6.2.2 Rhodium-based Hydroformylation

With all the characteristics of the cobalt process in mind, it can be seen that there was a sizeable incentive to improve on this performance. Fundamental work by Evans, Osborn and Wilkinson [6,7] demonstrated that rhodium triphenylphosphine catalysts allowed the operation of the hydroformylation reaction at much lower pressure (1 bar) thus offering the prospect of much lower capital and operating costs. The selectivity was also reported to be considerably higher; virtually no hydrogenation was observed and the linearity was in some instances as high as 90%. The rhodium catalysts were reported to be three orders of magnitude faster in rate. The resulting milder reaction conditions would give much less aldol condensation product, if any. In 1971 Union Carbide, Johnson and Matthey, and Davy Powergas joined forces to develop a process based on this new discovery. For a comparison between the hydroformylation catalysts, see Table 6.1.

A convenient catalyst precursor is $\text{RhH}(\text{CO})(\text{PPh}_3)_3$. Under ambient conditions this will slowly convert 1-alkenes into the expected aldehydes, while internal alkenes hardly react. At higher temperatures pressures of 10 bar or more are required. Unless a large excess of ligand is present the catalyst will also have some isomerization activity for 1-alkenes. The internal alkenes thus formed, however, will not be hydroformylated. Accordingly, the 2-alkene concentration will increase while the 1-alkene concentration will decrease; this will slow down the rate of hydroformylation. This makes the rhodium triphenylphosphine catalyst

TABLE 6.1
Summary of hydroformylation catalysts

Catalyst	Co	Co/phosphine	Rh/phosphine
Pressure, bar	200	70	30
Temperature, °C	140	170	120
Substrate alkene	C ₃ internal C ₁₀₊	C ₃ internal C ₁₀₊	C ₃ terminal
Product	aldehyde	alcohol	aldehyde
Linearity, %	60–70	70–90	70–95
Alkane by-product, %	2	10–15	0
Corrosion	+	+	–
Metal deposition	+	+	–
Heavy ends	+	+	–
Catalyst/Co costs	1	2	5000

less suited for the conversion of alkenes other than propene, for which isomerization is immaterial. To date, industrial hydroformylation of higher alkenes is still carried out with cobalt catalysts.

Propene hydroformylation can lead to products with a linearity ranging from 60 to 95%, depending on the phosphine concentration. At very high phosphine concentration the rate is low, but the linearity achieves its maximum value. Low ligand concentrations, with concomitant low linearities, will give turnover frequencies in the order of 10,000 mol mol⁻¹ h⁻¹ at 10 bar and 90°C. In the presence of carbon monoxide this rhodium catalyst has no activity for hydrogenation and the selectivity, based on starting material, is virtually 100%. The butanal produced contains no alcohol and can be converted both to butanol and to other products, as desired.

6.2.3 Ligand Effects

In the last two decades, the key to the successful development of homogeneous catalysts has undoubtedly been the exploitation of the effects that ligands exert on the properties of metal complexes: by tuning the electronic and steric properties of a catalytically active complex, selectivities and rates can be dramatically altered. There are many examples for each metal in the periodic table which show how one and the same metal can catalyze totally different reactions, depending on the surrounding ligands. Ligands that have been utilized to induce changes (by variation of their structure) in the outcome of catalytic reactions include phosphines, amines and imines, alkoxides, and cyclopentadienyl anions. In the following section one group of ligands, the phosphines, will be introduced in

somewhat greater detail; similar approaches have been attempted for the other ligands but our current knowledge in the area of phosphine ligands is most advanced.

6.2.4 Phosphine Ligands

Phosphorus-based ligands have found widespread application not only in organometallic chemistry but also in industrial applications of homogeneous catalysis. Alkyl phosphines are strong bases and as expected they are good σ -donor ligands. Organophosphites are very weak bases but nevertheless they form very stable complexes with (electron-rich) transition metals. The metal-to-phosphorus bonding resembles that described for metal-to-ethene and metal-to-carbon monoxide (see Chapter 4). The σ -donation with the lone pair needs no further explanation. The strong binding of phosphites, especially to low-valent metals, suggests that π -back-bonding should also play a role. This is indeed the case. The current view is that the antibonding σ -orbitals of phosphorus to carbon (in the case of a phosphine) or to oxygen (in the case of a phosphite) play the role of the π -acceptor orbital on phosphorus. The σ -basicity and π -acidity of phosphorus ligands has been studied [2] in an elegant manner by looking at the stretching frequencies of the coordinated carbon monoxide ligands in complexes such as $\text{NiL}(\text{CO})_3$ or $\text{CrL}(\text{CO})_5$ where L is the phosphorus ligand. Strong σ -donor ligands give a high electron density on the metal and hence a substantial back-donation to the CO ligands and lowered IR frequencies result. Strong π -acceptor ligands will compete with CO for the electron back-donation and the CO stretch frequencies will remain high. The IR frequencies represent a reliable measure of the electronic properties of a series of phosphine ligands toward a particular metal. The latter restriction is important because it is clear that a stability series of, e.g., the proton basicity scale is not the same as the metal phosphorus ligand stability series. The electronic parameters of phosphorus ligands may differ somewhat from one metal to another. The electronic parameter for phosphorus centred ligands, as determined for a certain metal becomes more reliable when the catalysis of interest utilizes the same metal complex; i.e. in a study of ligand effects for nickel (zero)-catalyzed reactions the Tolman parameters (see below) represent a good measure, but in a study of ligand effects on rhodium-catalyzed hydroformylation the electronic parameters should preferably be taken from a series of related rhodium complexes. Often the latter data are not available.

Tolman has defined an electronic parameter for phosphorus ligands based upon the vibrational spectra of $\text{NiL}(\text{CO})_3$; with L= $\text{P}(t\text{-Bu})_3$ as the reference, the electronic parameter χ (chi) for the other ligands is simply defined as the difference in the IR frequencies of the symmetric CO stretches of the two complexes. The variability of the phosphorous ligands is nicely reflected in the IR frequencies, which can be measured with sufficient accuracy to give different values for

the relevant substituents. Carbon substituents give χ -values ranging from 0 to 20, phosphites are found in the range from 20 to 40, and halogen substituted compounds are found up to 59 (the unit should be cm^{-1}). For comparison, the ligands at the top of the range, such as PF_3 , are as good electron acceptors as carbon monoxide, or even better. Some typical values have been collected in Table 6.2.

TABLE 6.2

 χ -Value of phosphorus ligands

Ligand PR_3 , R=:	χ -value:
<i>t</i> -Bu	0
<i>n</i> -Bu	4
Ph	13
CH_3O	20
PhO	29
Cl	41
F	55
CF_3	59

Studies have been published aiming at the use of χ -values in a quantitative manner in linear free-energy relationships in the same way as Hammett, Taft, and Kabachnik constants. Since the χ -values stem from IR frequencies rather than stability or chemical kinetic data, it is obvious that such a direct translation is not permissible.

Thus, the electronic parameter for ligands with the same donor atom can be fairly well measured and applied in a qualitative sense. Many attempts have been undertaken to define a reliable *steric* parameter complementary to the electronic parameter. Tolman's parameter θ (theta) is most often used. Tolman proposed measuring the steric bulk of a phosphine ligand from CPK models in the following way. From the metal centre, located at a distance of 2.28 Å from the phosphorus atom in the appropriate direction, a cone is constructed which embraces all the atoms of the substituents on the phosphorus atom (see Fig. 6.2). The cone angle is measured, and these cone angles θ (simply in degrees) are the desired steric parameters. Crystal structure determinations have shown that in practice the angles realized in the structures are smaller than the θ -values would suggest. For example, two *cis* triphenylphosphines may have a P-M-P angle as small as 95° whereas the θ -values would predict 145°. In reality intermeshing of the R substituents leads to smaller effective cone angles.

A complete separation between steric and electronic parameters is not possible; bending the ideal angles may be energetically more favourable for the overall energy of the complex than the 'inflexible' CPK approach, but changing

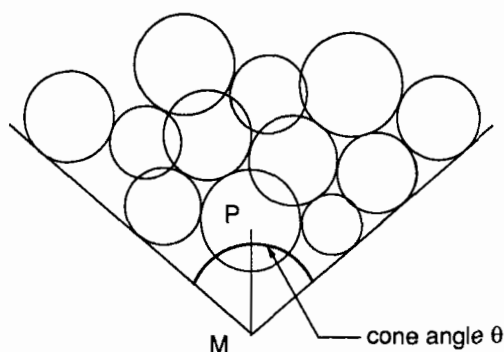


Fig. 6.2. Cone angle as defined by Tolman.

the angles will also change the electronic properties of the phosphine ligand. Bending the alkyl groups away from their ideal angles will destabilize their bonding σ -orbitals and lower the antibonding π^* orbitals, thus enhancing π -back donation. Both the χ - and θ -values should therefore be used with some reservation. Some typical values for the steric parameter are presented in Table 6.3.

TABLE 6.3
 θ -Values of phosphorus ligands, PR_3

$\text{R} = :$	θ -value:
H	87
CH_3O	107
PhO	128
<i>n</i> -Bu	132
Ph	145
<i>i</i> -Pr	160
C_6H_{11}	170
2- <i>t</i> -Bu $\text{C}_6\text{H}_4\text{O}$	175
<i>t</i> -Bu	182
2,6-Me ₂ C ₆ H ₃ O	190
2-MeC ₆ H ₄	194

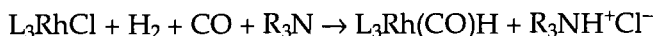
6.2.5 Ligand Effects in Rhodium Catalyzed Hydroformylation

Soon after the initial discovery of the hydroformylation activity of $\text{RhH}(\text{CO})(\text{PPh}_3)_3$ it was found that ligands have a profound influence on the activity and selectivity of the rhodium catalysts. The majority of the numerous

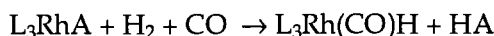
published patents and publications are concerned with the effect of ligands and it is therefore impossible to review this matter here. Instead we have made a choice that includes a study of the electronic and steric effects of phosphines and phosphites and a few examples of bidentate ligands. A few trends will be briefly summarized.

6.2.5.1 Catalyst preparation

The 'catalyst' for hydroformylation is a rhodium(I) hydride species, which is clearly distinct from the species that are active for hydrogenation. The hydrogenation catalysts are cationic $\text{Rh}(\text{I})^+$ or neutral $\text{Rh}(\text{I})\text{Cl}$ species. Carbonylation of alcohols also requires an ionic Rh(I) species, e.g. $[\text{Rh}(\text{CO})_2\text{I}_2]^-$. Often rhodium(I) salts are used as the precursor for hydroformylation catalysts. Under the reaction conditions (H_2 , CO , ligands, temperature $>50^\circ\text{C}$) these salts are converted to a rhodium hydride complex, although there are several papers that seem to invoke cationic rhodium species as the catalysts. Chlorides have a particularly deleterious effect on the activity (i.e. they are not converted into hydrides under mild conditions) and it has been reported that the addition of bases such as amines has a strong 'promoting' effect on such systems:



Rhodium salts of weaker acids are smoothly converted into rhodium hydride without the addition of base:



A = acetate, 2,4-pentanedionate, hydrocarbyl sulphide etc.

6.2.5.2 Phosphites: electronic effects

Aryl phosphites were among the first ligands to be studied extensively. The results obtained with triphenylphosphine and triphenyl phosphite are strikingly similar at low ligand concentrations. At higher ligand:metal ratios phosphites may retard the reaction. The results of the early work by Pruett and Smith [8,9] together with two more recent data [10], are summarized in Table 6.4. We have added the χ - and θ -values in this overview, which were not known at the time the catalytic work was reported.

One general trend that emerges from the table is that ligands with high χ -values give a higher selectivity toward linear products. In addition more isomerization is obtained; unfortunately this is often neglected in the reports. Preferably one would like to have also values for the absolute rates in addition to the selectivities and hence a detailed explanation of the results is not always possible. The trend towards higher linearities breaks down at two instances; one involves a rather bulky ligand with a θ -value of 190° , the other one involves hexafluoroisopropyl phosphite having a very high χ -value. Both give rise to

TABLE 6.4

Hydroformylation with rhodium phosphite and phosphine catalysts

Ligand PR ₃ R=	χ-Value	θ-Value	Linearity of product ^a
n-Bu	4	132	71
n-BuO	20	109	81
Ph	13	145	82
PhO	29	128	86
2,6-Me ₂ C ₆ H ₃ O	28	190	47
4-ClC ₆ H ₄ O	33	128	93
CF ₃ CH ₂ O	39	115	96
(CF ₃) ₂ HCO	51	135	55

^a(conditions: 90°C, 7 bar CO/H₂ = 1:1, substrate 1-heptene, ligand/rhodium varies from 3:1 to 20:1). (From ref. 9; last two entries from ref. 10).

unstable rhodium carbonyl complexes either for steric reasons (see below) or for electronic reasons. The χ-value of the hexafluoroisopropyl phosphite ligand is very high indeed and it is thought that this value of 51 means that electronically it is very similar to CO: i.e. a strong electron acceptor. Hence, the propensity of its mixed carbonyl hydride rhodium complexes to lose CO is likely to be similar to the rather unstable HRh(CO)₄.

6.2.5.3 Phosphites: steric effects

Very bulky phosphite ligands (see Fig. 6.3) also yield unstable rhodium complexes (sterically hindered phosphites are commercially available as antioxidants for polyalkenes). The cone angle of the ligand shown is as high as 175° and the complex formed with rhodium has the formula HRh(CO)₃L; apparently there is not enough space for the coordination of a second phosphite. (In a trigonal bipyramidal complex there is room for two bulky ligands at the two axial positions but this would leave an equatorial position for a σ-bonded hydride

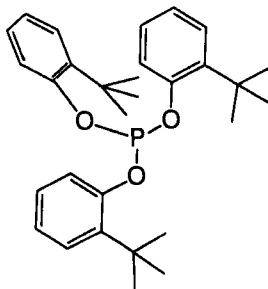


Fig. 6.3. 2-*t*-Butylphenyl phosphite, a convenient bulky phosphite [26].

which is energetically unfavourable.) The monoligand complex cannot be isolated and has only been observed under a pressure of CO and H₂ [11]. This complex easily loses CO which enables coordination of a molecule of alkene. As a result, complexes with bulky phosphite ligands are very reactive towards otherwise unreactive substrates, such as internal or 2,2-dialkyl-1-alkenes. The rate of reaction reaches the same values as those found with the triphenylphosphine catalysts and monosubstituted 1-alkenes, i.e. up to 15,000 mol of product per mol of rhodium complex per hour at 90°C and 10–30 bar. When 1-alkenes are subjected to hydroformylation with these monodentate bulky phosphite catalysts an extremely rapid hydroformylation takes place with turnover frequencies up to 160,000 mole of product per gram of rhodium per hour [12]. A moderate linearity of 65% can be achieved. Due to the very rapid consumption of CO the mass transport of CO can become rate determining, which results in highly unsaturated rhodium complexes giving a rapid isomerization of terminal to internal alkenes. In the extreme situation this means that it makes no difference whether we start with terminal or internal alkenes. Since hydroformylation of internal alkenes is also relatively fast with this catalyst the overall linearity obtained may become rather low (20–30%). This explains the low linearity quoted in Table 6.4 for 2,6-dimethylphenylphosphite.

6.2.5.4 Alkyl phosphines

Phosphorus ligands with low χ -values such as trialkyl phosphines, form very stable complexes in combination with CO and the activity for hydroformylation decreases. The strong binding due to a combination of donor and acceptor ligands inhibits ligand dissociation and no alkene complexation can occur. Mixed alkyl-aryl phosphines give active rhodium hydroformylation catalysts, although higher temperatures are required [13].

6.2.5.5 Diphosphines: electronic effects

Ligand effects of diphosphines have been reported by Unruh and Christensen. They studied the hydroformylation of 1-hexene using substituted ferrocene derived diphosphines Fe(C₅H₄PR₂)₂ (Fig. 6.4).

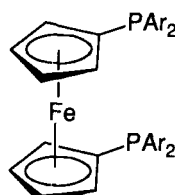


Fig. 6.4. Ferrocene based diphosphine ligands. (Ref. 14; for Ar see Table 6.5).

TABLE 6.5

Hydroformylation with substituted ferrocene based aryl diphosphines (Fig. 6.4)

Ar=	χ_i -Value (Ar)	Linearity %	Relative rate	Isomerization % 2-hexene
Ph	4.3	81	7.2	4
p-Cl-C ₆ H ₄	5.6	87	9.3	5
m-F-C ₆ H ₄	6.0	89	13.7	5
p-CF ₃ -C ₆ H ₄	6.8	92	13.8	6

(Conditions 110°C, 8 bar CO/H₂ = 1:1, 1-hexene, ref. 14, χ_i is defined as the χ -parameter for one substituent in the equation $\chi = \sum \chi_i$ for (R_i)₃P).

The electronic influence of the substituted aryl groups, R, follows a similar trend as that observed for phosphites; higher χ -values lead to higher linearities (Table 6.5). Interestingly, the authors also reported on the rates and selectivities to the isomerization side reaction to 2-hexene. It turns out that under the conditions chosen only a slight increase to isomerized alkene occurs. The rate of hydroformylation increases with increasing π -acceptor capability of the ligand. This study clearly shows that the selectivity to normal products truly increases with increasing χ -values.

The effect can be explained along two lines and, in the absence of complete kinetic data, discrimination between the two is difficult. Firstly, there may be a direct electronic preference for the formation of a higher proportion of the linear alkyl intermediate when the π -back-donation to the phosphine ligand increases. The effectiveness also depends on the kinetics of the catalytic process. Alternatively, but with similar kinetic constraints, the effect of the χ -value may be indirect. It is known from the work with triphenyl phosphine that the linearity of the aldehyde product increases at increasing phosphine concentration. A steric explanation has been accepted [15] for this phenomenon; a more crowded complex will favour a linear alkyl intermediate (see also Figs. 6.7 a-f). Complexes of aryl phosphine ligands with higher χ -values are more stable, leading to the formation of more crowded complexes. If steric effects were dominant one would expect at least a slight decrease of the reaction rate with increasing χ -value and linearity. This certainly holds for the triphenyl phosphine modified catalysts. Since this is not the case here, it is tempting to accept a 'direct' electronic effect on the linearity, be it kinetic in origin (alkene insertion) or thermodynamic (*n*-alkyl-metal vs *i*-alkyl-metal stability).

6.2.5.6 Other bidentates

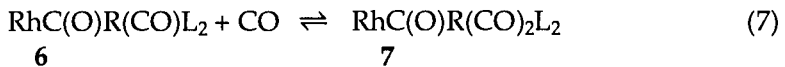
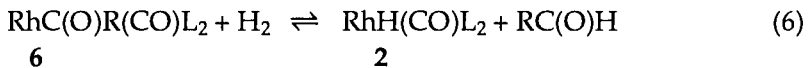
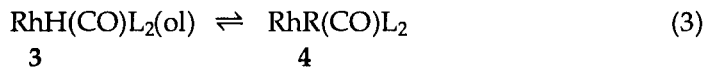
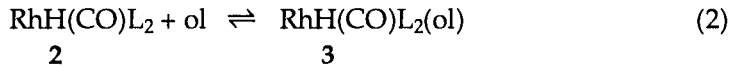
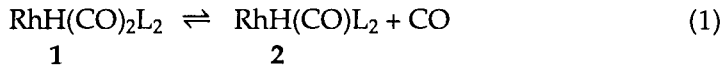
In general bidentate ligands give rise to higher linearities, and a combination of both the effect of bulky ligands and bidentate ligands has been exploited

recently as is outlined in patents reporting on diphosphites [16] and diphosphines [17] with constrained bond angles [18].

6.2.6 Kinetic Studies

In spite of its importance, only very few data have been reported on the kinetics of the hydroformylation reaction. The generally adopted reaction scheme is rather complex and an analytical expression for the rate, even for a system with only one ligand, would be very complicated.

The reaction sequence as proposed by Heck and Breslow [19] is shown in Scheme 6.1.



Scheme 6.1.

In Fig. 6.5 the catalytic cycle is shown in a form that was introduced into this field by Parshall [1].

The scheme reduces to its most simple form when carbon monoxide is the only ligand present in the system, because equilibria of mixed ligand/carbon monoxide complexes do not occur. The kinetics of the hydroformylation reaction using hydrido rhodium carbonyl as the catalyst was studied by Markó [20]. For 1-pentene the rate expression found is:

$$\text{rate} = k[\text{Rh}][\text{H}_2][\text{CO}]^{-1} \quad (6.1)$$

(conditions 75°C, CO pressure 40–170 bar, H₂ pressure 33–126 bar)

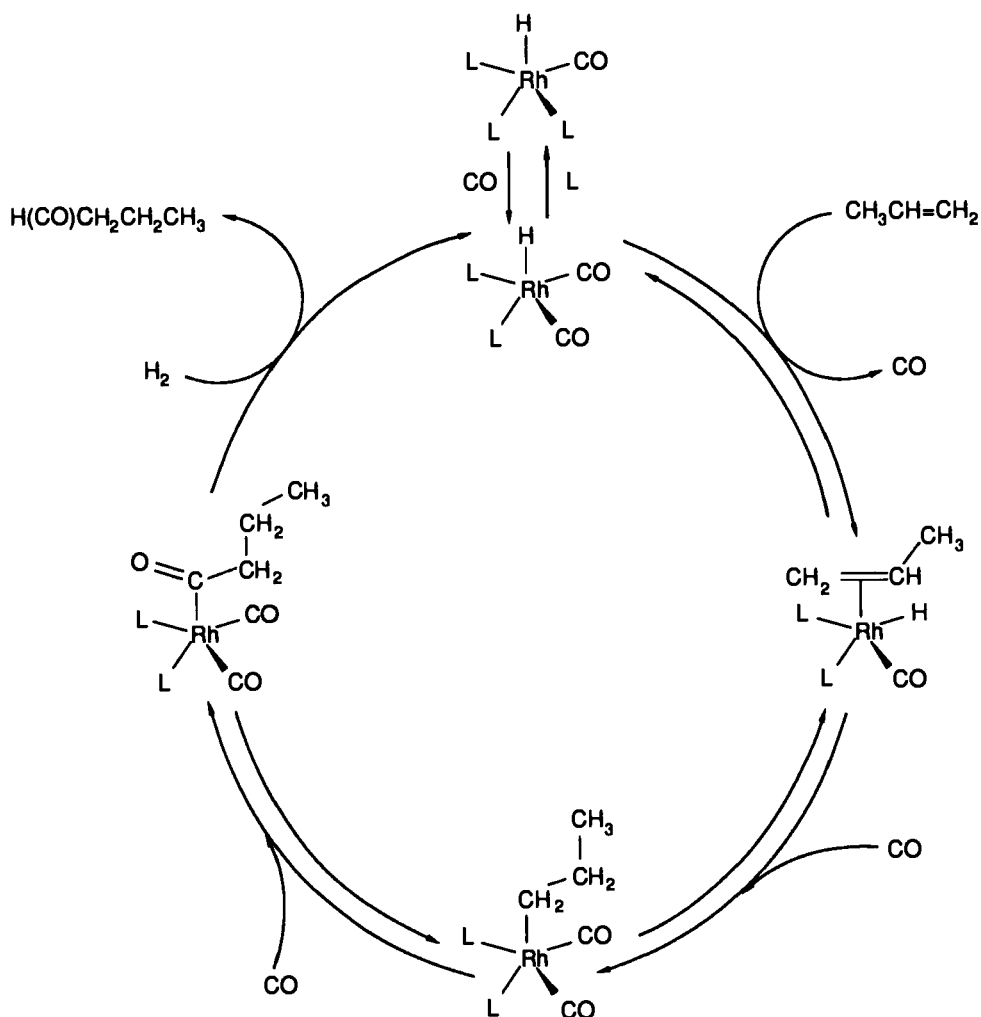
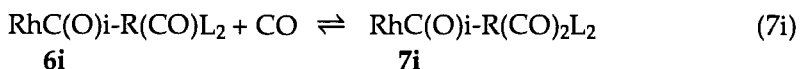
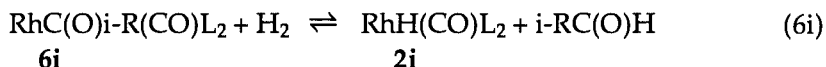
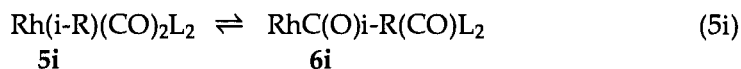
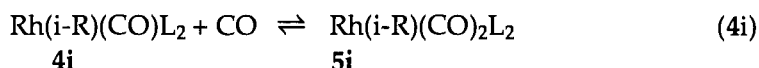
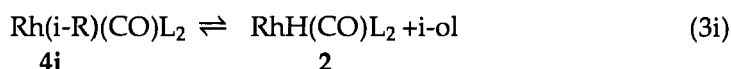
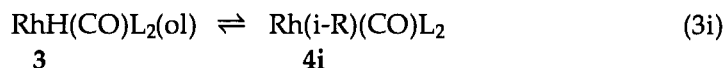


Fig. 6.5. Hydroformylation of propene by $\text{HRh}(\text{CO})\text{L}_3$.

The reaction is first order in rhodium catalyst concentration, first order in dihydrogen pressure and has an order of minus one in carbon monoxide pressure. In our Scheme 6.1 this would be in accord with a rate-determining step at the end of the reaction sequence, e.g. reaction 6. Since the reaction order in substrate is zero, the rhodium catalyst under the reaction conditions predominates as the alkyl or acyl species; any appreciable amount of rhodium hydride occurring under fast pre-equilibria conditions would give rise to a positive dependence of the rate of product formation on the alkene concentration. The minus one order in CO suggests that the acyl species rather than the alkyl species is dominant under the reaction conditions. The negative order in CO is explained [20] by equilibrium

7. The saturated complex loses CO, and subsequently the unsaturated 16-electron species reacts with H₂ to give aldehyde and rhodium hydride (reaction 6).

The hydroformylation of 1-hexene catalyzed by rhodium carbonyl has recently been studied by Lazzaroni and coworkers [21]. They were particularly interested in the influence of reaction parameters on the regioselectivity and the chemoselectivity (to aldehyde and 2-hexene). To understand their results we have to extend Scheme 6.1 by taking account of the formation of linear and branched aldehydes, as well as of isomerization. This is shown in Scheme 6.2.



Scheme 6.2.

The rate constants and R groups with the subscript i represent the pathways and products of the *iso* (or branched) species; the linear products and their rate constants are without subscript, as in Scheme 6.1. Reaction 8i has been added to the scheme to represent the β-hydride elimination from the secondary or iso-alkyl intermediate to give 2-alkene, the isomerization product. They varied the temperature from 15 to 110°C, and the pressure was varied from 40 to 200 bar [21]. Unfortunately the ratio of CO and H₂ was kept constant at 1:1 throughout this study. Chemoselectivity to aldehydes is complete at room temperature, the selectivity to linear aldehyde being about 50%. At higher temperatures and lower pressures the selectivity to aldehyde decreases as a consequence of isomerization to 2-hexenes; the 'escape' step (3i) in Scheme 6.2. As long as 1-hexene is present 2-hexene is not converted. At a later stage, when all 1-hexene is consumed 2-hexene is also converted to branched aldehydes (with formyl groups at the 2- and 3-positions), albeit at a much lower rate. When isomerization occurs the apparent initial linearity of the aldehyde product is much higher than 50%, as is

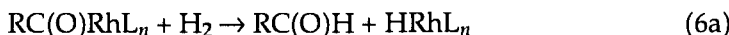
observed in the absence of isomerization. After total conversion of the 1- and 2-alkenes the average linearity is again 50% (rounded figures). Hence the authors conclude that the branched alkyl intermediate $\text{Rh}(i\text{-R})(\text{CO})\text{L}_2$ (in Scheme 6.2) has a tendency to form the isomerized alkene at higher temperatures and lower pressures (particularly CO, reaction 4*i*, must be responsible) instead of reacting further to the acyl species and product. Many studies concerning product linearity have been in error due to the neglect of this phenomenon.

A system kinetically very similar to the phosphine-free rhodium carbonyl catalyst is obtained with bulky phosphites (Fig 6.3). At temperatures from 50 to 80°C, and CO and H₂ partial pressures ranging from 10 to 70 bar, the rate of aldehyde formation is first order in H₂ and approximately minus one order in CO. The reaction rate is independent of the concentration of 1-octene at conversions below 30%. The reaction was found to be first order in rhodium concentration and insensitive to the phosphite/rhodium ratio, provided that the absolute concentration was sufficiently high to generate a hydride complex from the pentanedionate precursor (reaction 9).



In these experiments the isomerization was also recorded and was found to be rather low (6%). The low selectivity to isomerized products has consequences with regard to the mechanism. Let us return the kinetic expression (eqn. 1) which states that the reaction is first order in rhodium and H₂, zeroth order in alkene, and minus one order in CO. In the extreme case of rapid pre-equilibration up to reaction 6 one would expect the system to go back and forth very fast between species **1** and **5**. As we have learned from the work by Lazzaroni this would implicate that the isoalkyl species **3i** would regenerate alkene complex **2** now containing the isomerized alkene. The isomerized alkene, however, is not observed, or only in very minor quantities. This means that backward reactions 3 and 8*i* do not occur. The first reactions of the cycle determining the regio- and chemoselectivity are therefore irreversible while reaction 6 is still rate-determining.

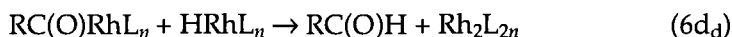
Two mechanisms have been proposed for the last step of the catalytic cycle, reaction 6 (Scheme 6.1), a direct reaction of complex **7** with H₂ and a reaction of the hydride complex **1** and the acyl complex **6** or **7** to give aldehyde plus a rhodium dimer:



Reaction 6a may proceed directly without intermediates as an hydrogenolysis

reaction as has been found experimentally for ruthenium analogues [22] and as has been found to be a likely pathway for cobalt acyl complexes on the basis of ab initio calculations [23]. Alternatively, reaction 6a may proceed via an oxidative addition mechanism followed by reductive elimination. The product of the oxidative addition reaction has been observed in the stepwise hydroformylation cycle of the iridium analogue of this rhodium catalyst [24]. When 6c is fast with respect to 6b the two mechanisms 6a and 6b,c cannot be distinguished experimentally. There are also several experiments in support of mechanism 6d being the last step of the hydroformylation cycle [15, 25, 3 and references therein]. If 6d were operative and rate-determining the rate equation would of course show the bimolecular nature of step 6d; this type of dependency has not been reported for rhodium catalysts. All of the experiments concerning reactions 6a–d, however, refer to model reactions rather than to active catalytic systems, with one exception. During the hydroformylation of cyclohexene or cyclooctene with $\text{HRh}(\text{CO})_3\text{L}$ (L =bulky phosphite) a very rapid exchange of the rhodium bound hydride with the cycloalkene 'sink' occurs, which is an order of magnitude faster than hydroformylation. Hence, when deuteroformylation (i.e. a mixture of D_2 and CO is used) is carried out, a fast exchange of $\text{DRh}(\text{CO})_3\text{L}$ with the solvent hydrogen sink takes place converting the rhodium complex into the hydride, as was confirmed by in-situ IR [11]. The two equations 6a and 6d now read as follows:

Fast exchange with solvent: $\text{DRhLn} \rightarrow \text{HRhLn}$



In this system we can now distinguish between the two pathways. A direct reaction with D_2 will give a deuterium label in the aldehyde product. Due to the fast exchange with excess hydrogen in the alkene solvent, rhodium hydride will carry hydrogen, initially at least, instead of deuterium. Consequently reaction 6d_d will give an undeuterated product aldehyde. In the actual experiment, 60% of the product consisted of the deuterated aldehyde, which proves that reaction 6a is the mechanistic pathway in this active catalytic system. That the degree of deuteration is not quite 100% was ascribed to the production of HD and H_2 during the experiment, kinetic isotope effects, and mass transfer limitations. When a mixture of D_2 and H_2 was used, only hydridoaldehyde was observed. At least for one rhodium catalyst it is now clear that a direct reaction of dihydrogen with the acyl rhodium species concludes the catalytic cycle.

6.2.6.1 Kinetics of the triphenylphosphine catalyst

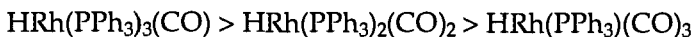
The most detailed published study on the kinetics of the hydroformylation using triphenylphosphine containing rhodium catalysts is by Cavalieri d'Oro et al. [27]. As the overall kinetic equation they found:

$$\text{rate} = k[\text{Rh}][\text{PPh}_3]^{-0.7}[\text{alkene}]^{0.6}[\text{H}_2]^{0.05}[\text{CO}]^{-0.1}$$

(conditions: 90–110°C, 1–25 bar CO, 1–45 bar H₂, PPh₃/Rh ratio 300:1–7:1)

This rate equation tells us that the reaction rate is almost independent of the syn-gas pressure; only a very slight suppression of the rate is observed while raising the CO partial pressure. Triphenyl phosphine retards the reaction within the limits studied (reaction order in PPh₃ –0.7). A positive order is found in alkene substrate concentration, although the order is not quite 1.0 but only 0.6. These results point to a rate-determining step that occurs early in the catalytic cycle. Step (1) as the rate-determining step would lead to a minus one order in CO (or PPh₃ when this is the dissociating ligand) and zero order in alkene. Complexation of alkene to the unsaturated complex (step 2) would give a plus one order in alkene and, depending on the correct kinetics, roughly a minus one order in CO pressure (or PPh₃ concentration). Fast insertion of alkene (step 3), followed by a rate-determining reaction with CO (or PPh₃) (step 4) and / or rate-determining insertion of CO (step 5) would lead to approximately the rate expression found experimentally.

The linearity of the aldehyde product increases with the concentration of triphenyl phosphine. This is being exploited in the Union Carbide process for the hydroformylation of propene in which linearities >90% are obtained. The rate, however, drops to lower values and the most likely explanation for the higher linearities in this system would seem to be the steric congestion around the rhodium atom at high phosphine concentrations, which kinetically and thermodynamically favours the formation of linear alkyl rhodium complexes relative to branched alkyl rhodium complexes. Product linearity decreases with the number of triphenyl phosphines present in the series of precursor complexes:



In this system higher CO pressures lead to lower linearities simply by shifting the complex equilibria to the species containing less phosphine. When isomerization plays a role under the reaction conditions applied, higher CO pressures will also give lower initial linearities by suppression of reaction (8i), the isomerization reaction as outlined above for the carbonyl or phosphite rhodium catalysts. These two effects can be clearly distinguished by monitoring the isomerization reaction when alkenes other than ethene and propene are used.

6.2.7 The Characterization of Intermediates

The intermediates which play a role in a cycle of a homogeneous catalyst can be characterized by various spectroscopic techniques such as NMR, IR, Raman spectroscopy, and UV-vis spectroscopy. Also, intermediates may crystallize from a reaction mixture and the structure can then be solved with a single-crystal X-ray determination. Only on rare occasions do intermediates crystallize from the

reacting systems since their concentrations are low. Often one turns to model compounds of the actual catalyst by changing the ligand or the metal. E.g. iridium complexes show the same catalytic behaviour as the rhodium complexes. Since they are often much slower as catalysts the intermediates can be intercepted (see below). Another common approach is the synthesis of a ligand that simultaneously contains the substrate of the catalytic reaction; this may also lead to the isolation of likely intermediates.

Of the spectroscopic techniques NMR is a particularly useful tool because many of the nuclei of interest in homogeneous catalysts are amenable to NMR studies: ^1H , ^{13}C , ^{15}N , ^{31}P , ^{103}Rh , and ^{107}Pt . Two general drawbacks should be mentioned. First the concentration region that can be studied by NMR (10–100 mmol l⁻¹) is well above the region for active catalysts (<1 mmol l⁻¹). Metal–ligand equilibria may shift considerably with concentration, which makes a direct comparison of NMR data and catalytic runs difficult. The reaction may become very fast at the high concentration used for NMR: too fast for an *in-situ* study. Secondly, when gases are consumed during a reaction it is impossible to run *in-situ* spectra; high-pressure NMR tubes allow the study of complexes under pressure, but when gas is consumed the pressure will drop quickly (high catalyst concentration) and mass transfer may also be a limiting factor in the absence of stirring.

In-situ IR measurements overcome the problems mentioned for *in situ* NMR spectroscopy. The information that we obtain from vibrational spectroscopy is far less detailed, however, than that from NMR. The concentration of the catalyst may be equal to the one used in practical catalytic systems. Secondly, autoclaves have been equipped with IR cells, either as flow cells or via real *in-situ* monitoring in the ‘Moser’ cell (see below), which allows one to work with gaseous reactants. In the following we will mention a (very) few examples of complexes that may be intermediates in the hydroformylation reaction observed with these two techniques.

6.2.7.1 NMR measurements

NMR measurements of ^1H , ^{13}C , and ^{31}P may be very informative about the structure of the complex. The hydride precursor of the catalyst has a trigonal bipyramidal structure in which the two phosphorus ligands present can occupy either two equatorial sites or one axial and one equatorial site (Fig. 6.6).

When ligand exchange is slow on the NMR timescale the structure can indeed easily be deduced from the spectra. A bidentate ligand such as $\text{PPh}_2\text{NMeCH}_2\text{CHPhOPPh}_2$ [28] (we neglect here the asymmetric nature of the ligand), which has two very distinct absorptions for the amino phosphorus and the phosphinite phosphorus nuclei, gives ^1H and ^{31}P spectra that can readily be interpreted. The hydride gives a doublet around -8.7δ with a large coupling constant (116 Hz) with the phosphorus atom *trans* to it and smaller couplings with rhodium (10.1

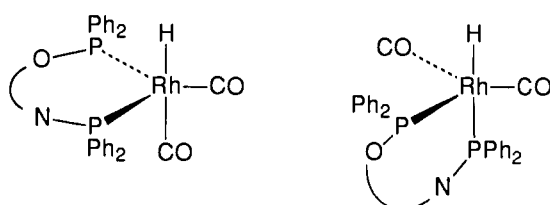


Fig. 6.6. Isomerism in rhodium hydrido carbonyls. The dominant species is the right-hand one (ref. 28).

Hz) and the phosphinite phosphorus nucleus (9.9 Hz). In the phosphorus spectra the expected couplings are with rhodium, the mutual phosphorus coupling; and in the proton coupled spectra the proton coupling for the phosphorus *trans* to it.

Brown and Kent [15] studied the species involved in the hydroformylation of styrene and 1-decene with the catalyst precursor $\text{RhH}(\text{PPh}_3)_3(\text{CO})$ at ambient pressure and temperatures of -80° to 25°C . Under an atmosphere of syn-gas $\text{RhH}(\text{PPh}_3)_3(\text{CO})$ (a) (Fig. 6.7) transforms into $\text{RhH}(\text{PPh}_3)_2(\text{CO})_2$ (b) and (c) and

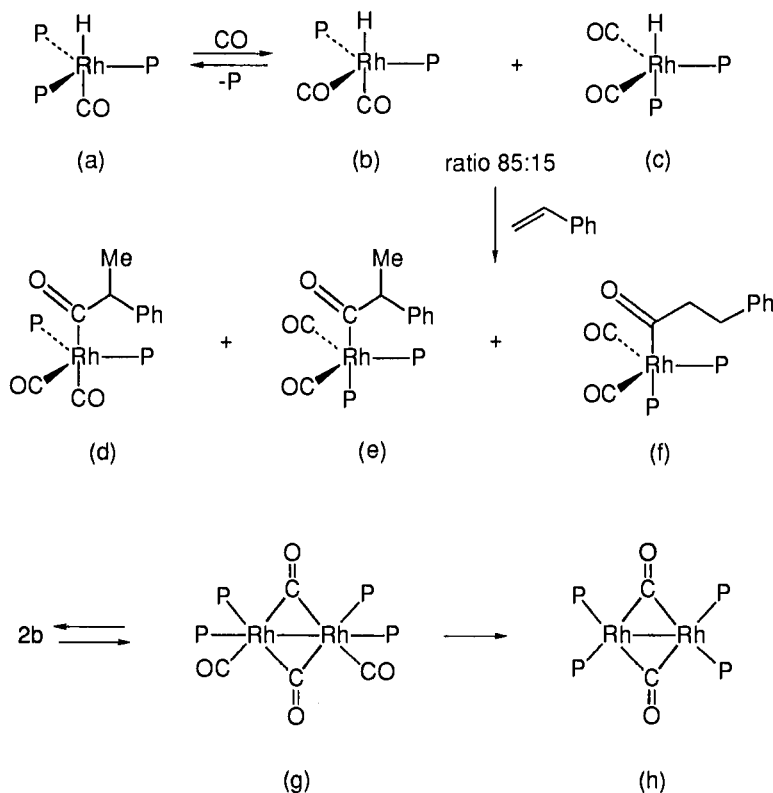


Fig. 6.7. Rhodium complexes found during hydroformylation of styrene ($\text{P}=\text{PPh}_3$) (ref. 15).

free PPh_3 . Typical concentrations are 0.02 mol/l, which is considerably higher than the concentrations used in typical catalytic experiments (<0.5 mmol/l). At room temperature a rapid exchange with free phosphine and CO is observed. Two conformations for $\text{RhH}(\text{PPh}_3)_2(\text{CO})_2$ are observed: isomer (b) has two equatorial phosphines and the other isomer (c) has one equatorial and one axial phosphine. Isomer (b) is the dominant species. When $\text{RhH}(\text{PPh}_3)_2(\text{CO})_2$ is made to react with styrene the branched acyl complex (d) and (e) is formed. Now the isomer (e) is the major species. This is presumably due to steric factors. The branched isomers isomerize slowly to the linear acyl complex (f). This shows that, at low temperature, the kinetic product in the first reaction with styrene is the branched styryl intermediate. With 1-decene only the linear acyl complex is observed. Interestingly, a fast intramolecular exchange of the two distinct phosphines in the complex can be observed. At higher temperatures a rapid exchange with free CO and PPh_3 is also found. Formation of dimeric species (g) and (h) is a general feature of these studies.

The reaction with dihydrogen could not be tracked down in this study. Iridium forms much more stable complexes than rhodium and therefore it has been studied to obtain more details about the complexes and the mechanism of rhodium hydroformylation. Using an iridium complex, Eisenberg and Deutsch [24] succeeded in the identification by NMR of all species involved in the catalytic cycle: the ethyl complex (i) (Fig. 6.8) the propionyl complex (j) (including X-ray structure determination), and, moreover, the dihydride adduct (k). The latter gives the aldehyde product upon decomposition. This series of complexes and their reactions suggests that in the case of iridium the last step in the hydroformylation involves an oxidative addition of dihydrogen. This is the first direct proof of such a mechanism. It is not necessarily true, however, for the rhodium triphenylphosphine modified catalyst, let alone all rhodium catalysts. For instance, when the acyl complexes mentioned above were heated in the Brown and Kent experiments, aldehyde was formed even in the absence of dihydrogen, which would support a bimetallic step for the product formation. The lesson to be learned is that several processes may be very close in activation parameters in

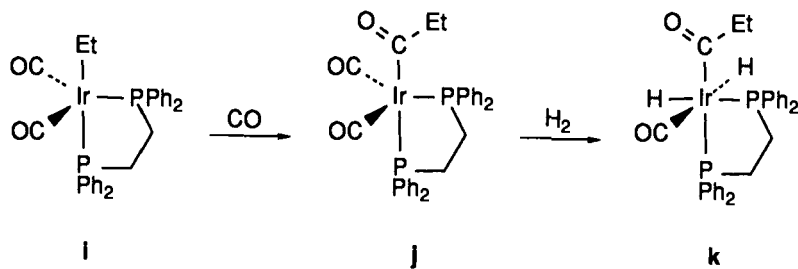


Fig. 6.8. Iridium complexes showing stepwise hydroformylation (ref. 24).

homogeneous catalysis and one has to be aware of the several possibilities rather than one single mechanism.

6.2.7.2 IR studies of ligand-free rhodium carbonyl catalysts

Recently, thorough studies providing great detail on the rhodium carbonyl catalysts have appeared from Pino and Garland [29]. We will refer here to one aspect of their study only; the reaction of 3,3-dimethyl-1-butene, CO, H₂, with Rh₄(CO)₁₂ at 4–14°C. This substrate was chosen because it lacks the possibility to isomerize, while still giving an acceptable rate of hydroformylation. The cluster carbonyl reacts slowly with the syn-gas and alkene to give the monomeric acyl complex RC(O)Rh(CO)₄. The characteristic IR frequencies in the CO stretch region of the latter compound are: 2111, 2065, 2039, 2020, and 1698 cm⁻¹. The latter complex builds up as the dominant intermediate while the catalytic hydroformylation starts. Clearly, the reaction of the acyl complex with dihydrogen is the rate-determining step in this catalytic system. The rate equation for the reaction with hydrogen under the conditions (5–30 bar of H₂ and 10–40 bar of CO) is:

$$\text{rate} = k [\text{RCORh(CO)}_4]^1[\text{CO}]^{-1.1}[\text{H}_2]^1[\text{alkene}]^{0.1}$$

The turnover frequency under these conditions is rather low (<20 mol mol⁻¹ h⁻¹) but the kinetic results, in return, are highly accurate. The minus one order in CO and the plus one order in H₂ agree very well with the results from Markó [20]. The rate of hydroformylation was proportional to the concentration of the acyl complex. The apparent activation parameters were ΔH[‡] = 49.3 kJ/mol and ΔS[‡] = 121 J/mol K. The activation parameters and the reaction order are consistent with reaction 6 and 7 as being rate determining. A low order of 0.1 in alkene was found, which indicates that the 'rate-determining step' is not purely reaction 7 and that either a pre-equilibrium contributes as well or that one of the earlier steps in the cycle is also somewhat slower.

6.2.7.3 IR studies of ligand-modified rhodium carbonyl catalysts

The triphenylphosphine modified rhodium hydroformylation catalyst has been studied with IR under a variety of conditions. As far as high pressure spectra are concerned they are usually measured in cells that are connected via a pump with the autoclave in which the reaction is taking place. The disadvantage is that mass transport limitations of the reacting gas and temperature variations may strongly influence the results. To circumvent these problems Moser introduced a new type of cell which utilizes cylindrical internal reflectance (CIR) through a transmitting crystal that is mounted in the autoclave, submersed in the liquid phase where the reactions are taking place. There is no doubt that one now has the possibility of looking at the catalytic system in operation. The signal-to-

noise ratio of the CIR-FTIR cell is less than that of the common transmission cell. Deposition of solid material onto the crystal may distort the measurements. The difference from the NMR measurements lies in the fact that in the non-reacting, concentrated solution in the NMR tube, the system will have equilibrated to a new composition whereas the in-situ IR measurements give the distribution of the reacting species in the steady state of the catalytic cycle.

Moser studied the $\text{RhH}(\text{PPh}_3)_2(\text{CO})_2$ catalyst at 70°C and pressures of 11–34 bar. First of all it was found that under a pressure of syn-gas the species present also have the formula $\text{RhH}(\text{PPh}_3)_2(\text{CO})_2$ also when an excess of phosphine is present. In the presence of 1-hexene the main species observed is still the hydride $\text{RhH}(\text{PPh}_3)_2(\text{CO})_2$. The absorptions of a minor species are assigned to the corresponding alkyl rhodium complex $\text{Rh}(\text{C}_6\text{H}_{13})(\text{PPh}_3)_2(\text{CO})_2$. This observation is consistent with a slow dissociation of a ligand from the starting hydride, followed by a reaction with the alkene. Such a mechanism leads to an inverse dependence on CO or PPh_3 (or both) and a proportional relation of the rate with the alkene concentration.

In addition, the effect of *para*-substitution of the aryl group in triphenyl phosphine was studied. Substitution influences the IR frequencies of the complexes $\text{RhH}(\text{P}(\text{C}_6\text{H}_4\text{R})_3)_2(\text{CO})_2$, as shown in Table 6.6. Both hydride–metal and C–O stretching frequencies show a regular increase with χ -value. The lower electron density on the metal leads to a decrease in back-donation from rhodium to the carbonyl ligand and hence higher frequencies for the CO stretches are

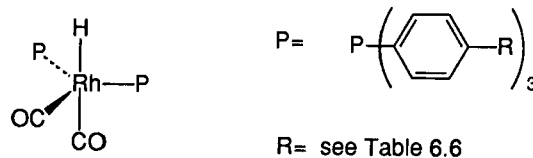


Fig. 6.9. Structure of the complexes [30].

TABLE 6.6
IR frequencies of complexes $\text{RhH}(\text{P}(\text{C}_6\text{H}_4\text{R})_3)_2(\text{CO})_2$ [30]

Substituent R	χ -Value	Metal hydride (cm^{-1})	Carbonyl (cm^{-1})
$\text{N}(\text{CH}_3)_2$		2018	1957, 1918
OCH_3	10.2	2033	1976, 1930
H	12.8	2039	1981, 1937
F	15.0	2041	1988, 1947
Cl	16.8	2042	1991, 1948
CF_3		2050	1997, 1953

observed. The reaction rate increases in the same direction. As was observed for the ferrocene diphosphine complexes by Unruh and Christenson [14], the linearity of the product aldehyde increases with increasing electron withdrawing properties of the ligand.

Interestingly, changes occur in the relative concentrations of the species observed by CIR-FTIR. At low χ -values the hydride $\text{RhHL}_2(\text{CO})_2$ is the major species, but at higher χ -values the alkyl complex $\text{RhRL}_2(\text{CO})_2$ is most abundant. One might conclude that alkene coordination occurs more readily when arylphosphines with higher χ -values are applied. This may be due to a more facile loss of CO and/or a stronger complexation of the alkene donor ligand to more electron deficient rhodium complexes. NMR studies [15] pointed to the presence of acyl complexes as the resting state, albeit in a slightly different operation window. It is unfortunate that kinetic and characterization studies have not yet been conducted on the same system under identical conditions.

6.3 ZIRCONIUM CATALYZED POLYMERIZATION OF ALKENES

6.3.1 *Introduction*

In this section we shall discuss some of the recent advances in the area of alkene polymerizations catalyzed by homogeneous complexes of zirconium and titanium. One of the main research themes for these catalysts has been the polymerization of propene. In less than a decade a completely new family of catalysts has been developed which enables one to synthesize regioselective and stereoselective polymers of a wide variety of monomers. These new catalysts will soon find application on the industrial scale, but as yet only syndiotactic polystyrene has been taken into production. Before outlining the main concepts of this relatively new field a few words will be said about the present heterogeneous titanium catalysts used for the production of polypropylene. For a more extensive review on this matter the reader is referred to the specialist reports [31,32]. The titanium catalyst for the stereoselective polymerization of propene to isotactic polymer was discovered by Ziegler and Natta in the mid fifties. Soon after its discovery it was taken into commercial exploitation and today isotactic polypropene is still one of the most important commodity polymers. As mentioned in Section 2.4, the catalyst and the concomitant technology have undergone drastic changes over the years. Initially the polymer was made in a solution or slurry with moderate selectivity to the isotactic polymer, the atactic material being removed by extraction. Catalyst residues were removed by washing with alcohol. Catalysts with higher activities and selectivities have made separation from catalyst residues and from atactic material superfluous. Two processes are operated today — one in liquid propene and one in the gas phase — which involve only very few process steps compared to the older processes.

6.3.2 Supported Titanium Catalysts

The modern catalyst is a MgCl_2 -supported TiCl_3 complex which replaces the TiCl_3 crystallites used in the older processes. TiCl_3 is bonded to the MgCl_2 support via bridging chloride ions and the titanium site is modified by complexing Lewis bases. Catalyst preparation is a complicated synthetic procedure, although most of the steps are fairly well understood. We will mention briefly here the types of chemical and physicochemical operations involved, without claiming any authenticity for this particular 'recipe'! Small particles of MgCl_2 are prepared by ball milling (other techniques have been reported). The surface of the MgCl_2 is modified by ligands such as alcohols or esters before they are treated with TiCl_4 . Alternatively the support is treated with donor–acceptor complexes of TiCl_4 and esters, ethers or alkoxy silanes. These donor molecules are a prerequisite for obtaining a high isotactic index. Titanium chloride is bonded to the surface via bridging chloro anions. Soluble titanium complexes are removed by washing with hydrocarbons, and excess donor compound may be removed by treatment of the solid particles with liquid TiCl_4 . The titanium is activated by reaction with triethyl aluminum or the Lewis adduct of the latter with the donor compounds applied.

6.3.3 Isotactic Polypropylene

As has already been mentioned in Chapter 2 Section 2.4, the synthesis of the commercial polymer involves regioselective 1,2 insertions of propene in a stereo-regular fashion leading to isotactic polymer, see Figs. 6.10 and 6.11.

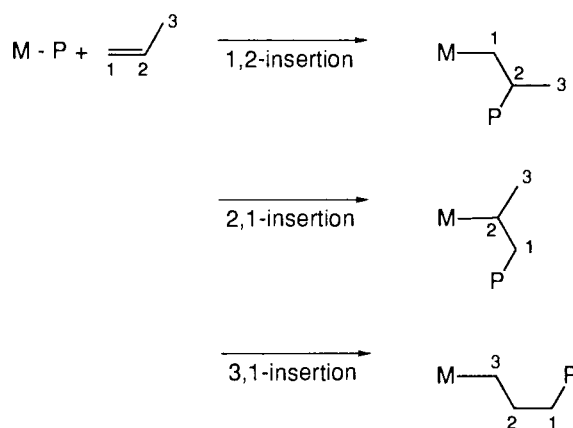


Fig. 6.10. Scheme showing 1,2-insertions, 3,1-insertions and 2,1-insertions.

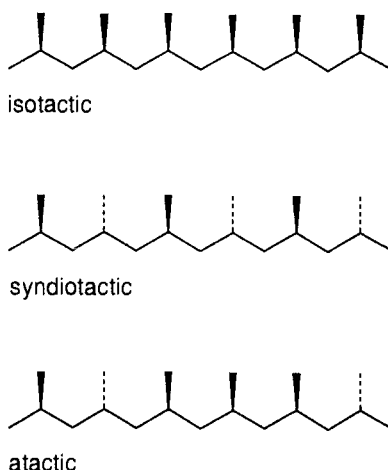


Fig. 6.11. The structure of isotactic, syndiotactic, and atactic polypropene.

Three stereoregularities are distinguished but, in practice more products may be expected, differing in sequences of regularities and mistakes in the chains. Making a polymer is much more complicated than making butanal (see Section 6.2) because the properties of a polymeric material depend on several more molecular properties than those for a low molecular weight product such as butanal. In the catalytic preparation the following properties of the polymer have to be tuned:

- regioselectivity;
- stereoselectivity;
- molecular weight, M_w : weight average molecular weight,
 M_n : number average molecular weight;
- molecular weight distribution, or dispersion ($=M_w/M_n$);
- morphology of the polymer particles.

Physical properties that have to be controlled by these molecular factors include:

- melting point;
- glass transition temperature;
- strength;
- modulus;
- crystallinity; and
- viscosity of the molten polymer.

6.3.4 The Cossee–Arlman Mechanism

The mechanism proposed for the solid titanium chloride catalysts is essentially the same for all catalysts and it is usually referred to as the Cossee–Arlman mechanism [33]. Titanium is hexacoordinated in the $TiCl_3$ or supported catalysts

by four bridging chlorides and one terminal chloride that is replaced by an alkyl from the alkylating agent (Et_2AlCl or Et_3Al), and a vacancy that is available for propene coordination (see Fig. 6.12).

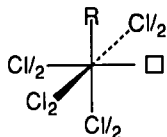


Fig. 6.12. Cossee active site on asymmetric α - TiCl_3 surface (surface not shown).

The asymmetry of the site regulates the mode of coordination of the propene molecule; in other words it steers the direction the methyl group will point to. We will not go into the detail of the mechanism of the heterogeneous reaction as there is, relative to the homogeneous catalysts, a considerable amount of speculation involved. A slightly different mechanism from that of Cossee was proposed by Allegra [34]. In the following we will discuss the homogeneous catalysts and the stereochemistry of the polymerization reaction; for the heterogeneous catalysts and their mechanisms the reader is referred to other texts [31,32].

6.3.5 Homogeneous versus Heterogeneous Catalysts

From the early days on there has been an interest in homogeneous catalysts for the polymerization of propene and ethene with titanium and chromium similar to the vanadium based Ziegler catalysts, which are homogeneous. It was thought that in a homogeneous system all metal atoms (titanium, chromium) could in principle participate in the catalytic process and, activity and other things being equal, this would make removal of the catalyst unnecessary. Also, the molecular weight distribution would be much narrower and could be controlled at will. Drawbacks were also envisaged, such as the morphology of the powder to be formed and stereocontrol. For stereocontrol the TiCl_3 lattice seemed to play an important role and stereocontrol was not considered to be an easy task in a homogeneous catalyst. Polymerization of ethene with homogeneous catalysts has been known for a very long time (1957, Breslow, ref. 35), but these catalysts failed to polymerize propene and only dimerization may be observed. In the seventies the first claims appeared concerning the homogeneous stereospecific polymerization [32] but they received relatively little attention as, during the same years, the first highly active heterogeneous titanium catalysts were reported and the industrial interest in the more risky field of homogeneous catalysts diminished. In the following the general principles of polymerization catalysis will be discussed, with an emphasis on stereocontrol, together with some recent achievements.

6.3.6 Site Control versus Chain-end Control

Over the years two mechanisms have been proposed as being responsible for the stereocontrol of the growing polymer chain; firstly the site-control mechanism and secondly the chain-end control mechanism. In the site-control mechanism the structure of the catalytic site determines the way the molecule of 1-alkene will insert (enantiomeric site-control). Obviously, the Cossee mechanism belongs to this class. In the chain-end control mechanism the last monomer inserted determines how the next molecule of 1-alkene will insert. Several Italian schools have supported the latter mechanism. For heterogeneous catalysts it would seem that site control was strongly gaining preference [32], at least until the more detailed work on homogeneous catalysts became known.

The analysis of the products using high resolution ^{13}C NMR has greatly contributed to the mechanistic insight and distinction between the various catalysts. Two simple examples will serve as an illustration of this point. The relation between two adjacent methyl groups is indicated by *r* (racemic) or *m* (meso), which means that, with respect to the stretched chain, they are on the same side or on opposite sides (see Fig. 6.13). The local connectivities *m* or *r* are somewhat confusing in view of the definition of isotacticity. In an 'isotactic' polymer the same absolute configuration is reproduced at every insertion according to the original proposal by Natta [36] which is indeed the case in sequences of *m* (although 'meso' does not seem to express this). Hence, a syndiotactic polymer consists of a sequence of *r* configurations, whereas the isotactic polymer consists of purely *m* configurations. With two adjacent *m* stereocentres, *mm*, we say that we are dealing with a triad of methyl groups with an isotactic stereochemistry. The chemical shift in the NMR of the ^{13}C atoms depends on the stereochemistry of the substituted carbons in the vicinity; not only can we tell the stereochemical relation with the two nearest neighbours (the *mm*, *mr*, and *rr* triads), but we can also deduce the relation with the two next ones from the chemical shifts observed. In other words, with ^{13}C NMR we are able to distinguish pentads of methyl groups, i.e. we can distinguish from the NMR spectrum, for example, an *rmrrm* sequence from an *mmmm* sequence. We can expect ten different pentads, two of which coincidentally have the same chemical shift and hence, in modern NMR analysis of propene polymers, nine signals are observed. Stereochemical control

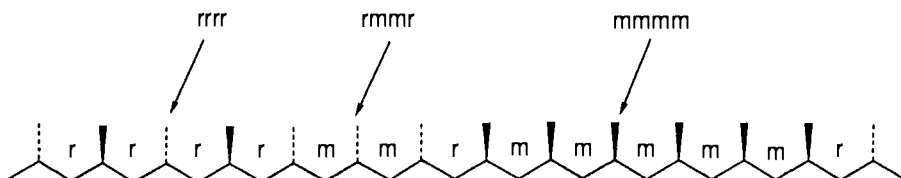


Fig. 6.13. *m* and *r* Relationships in polypropene.

by the catalytic site and control by the growing chain can be easily distinguished from one another by studying the 'mistakes' as they occur in the ^{13}C NMR spectrum. In a system with site control the mistake ideally leads to a single odd insertion in the chain: the site enforces, for instance, the growth of an isotactic chain with all *m* configurations and after one mistake has occurred it will return to producing the same configurations. In the polymer chain this gives a series of *m* relationships interrupted by two *r* configurations. In the NMR spectrum this gives rise to three new peaks belonging to *mmmr*, *mmrr*, and *mrrm* in a 2:2:1 ratio (see Fig. 6.14).

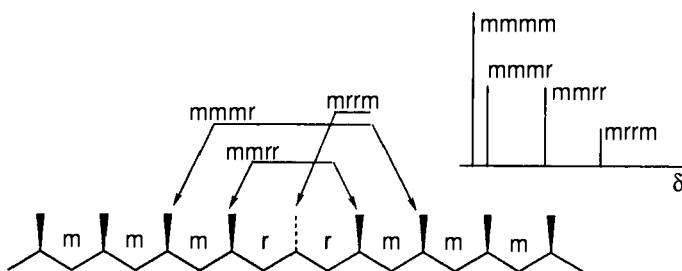


Fig. 6.14. Single mistake during a site-controlled isotactic polymerization and schematic ^{13}C NMR spectrum of the methyl region.

When a chain-end control mechanism is operative the result is different. If one mistake is made in a sequence of isotactic insertions the next propene that comes in will be directed by the previous one and the 'mistake' will propagate in the growing chain. Hence, after a block having all methyl groups pointing to one direction, a block will form having the methyl groups pointing to the other side of the growing chain (Fig. 6.15). An example of polypropene with isotactic stereoblocks was reported in 1984 [37]. Naturally, this achiral catalyst can only give chain-end control as it lacks the necessary chiral centre for site control. In the

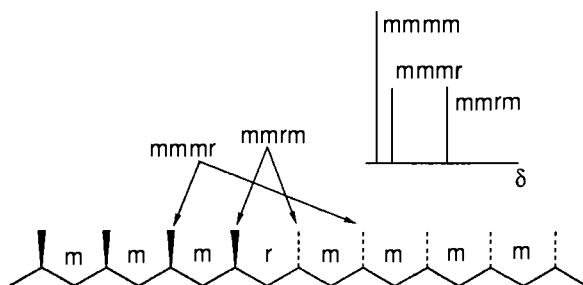


Fig. 6.15. Formation of stereoblocks in a chain-end controlled isoatactic polymerization and schematic ^{13}C NMR spectrum of methyl region.

^{13}C NMR the stereoblocks can be clearly observed as they lead to the typical 1:1 ratio of *mmmr* and *mmrm* absorptions in addition to the main peak of *mmmm* pentads. These are two simple examples showing how the analysis of the ^{13}C NMR spectra can be used for the determination of the most likely mechanism of control of the stereochemistry. Obviously, further details can be obtained from the statistical analysis of the spectra and very neat examples are known [38].

A general difference between the stereochemistry of the products of the homogeneous catalysts on the one hand, and the heterogeneous catalysts on the other, has been noted in the literature. Measurement of the overall isotactic index of the products of the homogeneous catalysts revealed that polymers with isotactic indices as high as 96% still have a melting point of only 140°C, whereas the products of heterogeneous catalysts with such isotactic indices show melting points of 160–166°C. This can be explained as follows. The commercial heterogeneous catalysts, in spite of their high degree of optimization, contain different sites, one group producing polymer with a high isotactic index (99+) and another group of sites producing a small amount, say 4%, of atactic polymer. Hence a mixture of two polymers is formed, the melting point of which is determined by the isotactic component. The homogeneous catalyst, on the other hand, ideally contains only one type of site that produces one polymer with an isotactic index of, say, 96%. While the isotactic index may look very promising, the melting point may be disappointing since all the errors made occur in the main chain of the product, giving a lower melting point. Improved homogeneous catalysts have recently been synthesized that also give polypropene melting points above 160°C and isotactic indices of 99.7% [39].

We now turn to the actual polymerization process and we will try to present a series of pictures that clarifies how chain-end control can be used to obtain either syndiotactic or isotactic polymers. Subsequently we will see how a chiral site can influence the production of syndiotactic or isotactic polymers. Finally, after the separate stories of 'chain-end control' and 'site control', the reader will be confused by introducing the following elements: (1) pure chain-end control can truly occur when the catalyst site does not contain chirality; (2) but since we are making chiral chain ends in all instances, pure site control does not exist. In a polymerization governed by site control there will potentially always be the influence of chain-end control. This does not change our story fundamentally; all we want to show is that stereoregular polymers can indeed be made, and which factors play a role; but their relative importance remains hard to predict.

6.3.7 Chain-End Control: Syndiotactic Polymers

Achiral catalysts derived from $\text{VCl}_4/\text{Al}(\text{C}_2\text{H}_5)_2$ or $\text{V}(\text{acac})_3/\text{Al}(\text{C}_2\text{H}_5)_2$ are the best known examples, giving syndiotactic polymers [40]. Termination experiments have proved that this polymerization involves a 2,1-insertion instead of

the expected 1,2-insertion. This is to say that the intermediate vanadium alkyl contains a branched or secondary alkyl group. Two simple assumptions now explain why a syndiotactic polymer is obtained. Firstly, the growing chain assumes a conformation in which the two largest groups, the polymer chain and the vanadium complex, are *trans* to one another in the chain end formed by the last two carbon atoms (see Fig. 6.16). Secondly, the insertion of propene takes place via a mechanism best described as a 2+2 addition. The methyl group of the propene to be inserted and the one of the previously inserted propene molecule will assume positions leading to a minimum of steric interaction (see Fig. 6.16). Since the two largest groups attached to the last inserted propene are now in mutual *syn* positions, the chain must be rotated in order to obtain the more stable *trans* configurations at both linkages, i.e. the chain being stretched as it is usually represented. When this procedure is repeated a couple of times we see that a syndiotactic microstructure is indeed formed. The most peculiar aspect of this family of catalysts is the apparent formation of a secondary alkyl group at the vanadium centre, where one would normally expect a primary alkyl group. Direct observation has not yet been achieved, but the termination experiments unequivocally prove that the reacting species is a secondary alkyl vanadium complex, both during the fast polymerization reaction with a subsequent molecule of propene, but also, more surprisingly, after presumed equilibration of the living polymer before reacting with, e.g., I₂. There still is the possibility of a very fast equilibrium between the primary and secondary alkyl, the latter being far more reactive.

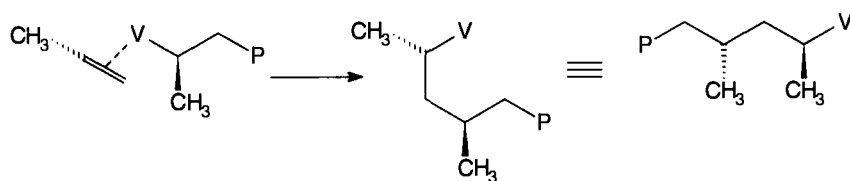


Fig. 6.16. Chain-end control leading to syndiotactic polymer. The polymer chain is arranged in such a way that all carbons of the chain lie in the plane of the figure. The double bond of the propene to be inserted also lies in the plane, with its substituents in a plane perpendicular to the plane of the figure. The methyl groups above or below the plane of the figure are drawn in the usual manner.

6.3.8 Chain-End Control: Isotactic Polymers

By the same token, 1,2-insertion gives an isotactic microstructure. If the methyl group of the previously inserted molecule is upwards, the methyl group of the next molecule will be pointing downwards (see Fig. 6.17). The interaction may not be quite as strong as in the case of 2,1-insertion discussed above, but there will

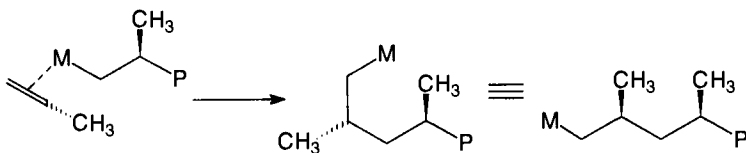


Fig. 6.17. Chain-end control leading to isotactic polymer. The polymer chain is arranged in such a way that it lies in the plane of the figure. The double bond of the propene to be inserted also lies in the plane with its substituents in a plane perpendicular to the plane of the figure. The methyl groups above or below the plane of the figure are drawn in the usual manner.

always be a tendency of the growing chain to arrive at an isotactic stereochemistry when 1,2-insertion occurs. One example of chain-end control leading to isotactic polymer was reported by Ewen [37] using Cp_2TiPh_2 /alumoxane as the catalyst. The stereoregularity increased with lower temperatures; at -45°C the isotactic index as measured on pentads amounted to 52%. As mentioned above, the polymer contains stereoblocks of pentads. At 25°C the polymerization gives almost random 1,2-insertion and an atactic polymer is formed.

6.3.9 Site Control: Recent History

Until 1984 no well-defined homogeneous propene polymerization catalysts were known, based on Group 4 metals. The development of the new family of homogeneous catalysts based on biscyclopentadienyl Group 4 metal complexes for the stereoselective polymerization of alkenes is mainly due to Kaminsky, Ewen and Brintzinger. The first breakthrough came from the laboratory of Sinn and Kaminsky, who had been studying the interaction of zirconium and aluminium alkyls for a few years. In 1980 they reported [42] on an extremely fast homogeneous catalyst for the polymerization of ethene, formed from the interaction of $\text{Cp}_2\text{Zr}(\text{CH}_3)_2$ and $(\text{CH}_3\text{AlO})_n$ [$\text{Cp}=\text{C}_5\text{H}_5$ =cyclopentadienyl, the aluminium compound, alumoxane or aluminoxane, was obtained from the reaction of trimethylaluminium and a hydrated salt, $\text{CuSO}_4 \cdot 5\text{H}_2\text{O}$, as a slow-release source of water]. At 8 bar of ethene and 70°C an average rate of insertion of ethene was reported amounting to 3×10^7 mol of ethene per mol of Zr complex per hour! With propene this catalyst led to completely atactic polymer [43].

Ewen was the first to report the synthesis of stereoregular polymers with soluble Group 4 metal complexes and alumoxane as the co-catalyst [37]. He found that Cp_2TiPh_2 with alumoxane and propene gives isotactic polypropene via chain-end control, see above. The second important breakthrough was how to build a chiral centre into the Group 4 metallocene. Substituted chiral metallocene complexes had already been reported in 1982 by Brintzinger [44]. Using an intrinsically chiral titanium compound (*rac* ethylene-bis-indenyl titanium dichloride) [44] he obtained polypropene that was in part isotactic. Subsequently Kaminsky and Brintzinger showed that highly isotactic polypropene can be

obtained using the racemic zirconium analogue of the ethylene-bis(indenyl) compound [45]. The initial results gave a material with a relatively low molecular weight and a low melting point, 140°C compared to 165° for the material obtained with commercial heterogeneous catalysts. The molecular weight distribution was very narrow, $M_w/M_n=1.8$, as is to be expected from a homogeneous catalyst. The molecular weight may be as high 300,000 [46], strongly decreasing upon raising the temperature. Although the isotactic index is high (>96%) the melting point may be low at 140°C (see above). Modification of the cyclopentadienyl ligands has led to a very rich chemistry and today a great variety of microstructures and combinations thereof can be synthesized as desired, including isotactic polymer with melting points above 160°C, syndiotactic polypropene [47], block polymers, hemiisotactic polymers etc.

Fundamental studies have led to a detailed insight into the mechanism of the polymerization and the control of the microstructure through the substituents on the cyclopentadienyl ligands. For a survey of these studies and the dominant effects playing a role the reader is referred to recent contributions by Ewen [38] and Erker [48]. In the present chapter we will summarize a few of the features that play a role in determining the microstructure; the field is still in development and obviously the definite answer to several questions has not yet been given.

6.3.10 Site Control: Isotactic Polymers

The structure of the catalyst has been proved by Jordan, Turner, and others [49] to be a cationic species, Cp_2M-R^+ ($M = Ti, Zr, Hf$). The basic structure is depicted in Fig. 6.18. Zirconium is tetrahedrally surrounded by two cyclopentadienyl ligands and two chlorides. The latter two ligands are not essential as they are replaced before the polymerization can start by an alkyl group (e.g. CH_3 from methylalumoxane) and by a solvent molecule thus generating the required cationic species. The two cyclopentadienyl anions are linked together by a bridge, here an ethane bridge, and extended with an organic moiety which affords the molecule its chirality. A 1,2-ethane bridged bis(1,1'-tetrahydroindenyl) dianion has been drawn in the example in Fig 6.18. Two compounds are obtained when this complex is synthesized, the *rac*-isomer mixture and the *meso*-isomer. They can often be separated by crystallization. The sterically less hindered *rac*-isomers may be formed in excess. The isomers can only interconvert by breaking a cyclopentadienyl–metal bond and reattaching the metal at the other face of the cyclopentadienyl ligand. This process is very slow compared to the rate of insertion reactions with propene.

The *rac*-isomers have a twofold axis and therefore C_2 symmetry. The *meso*-isomer has a mirror plane as the symmetry element and therefore C_s -symmetry. The racemic mixture can be used for polymerization reactions since the two chains produced by the two enantiomers are identical, if begin and end groups

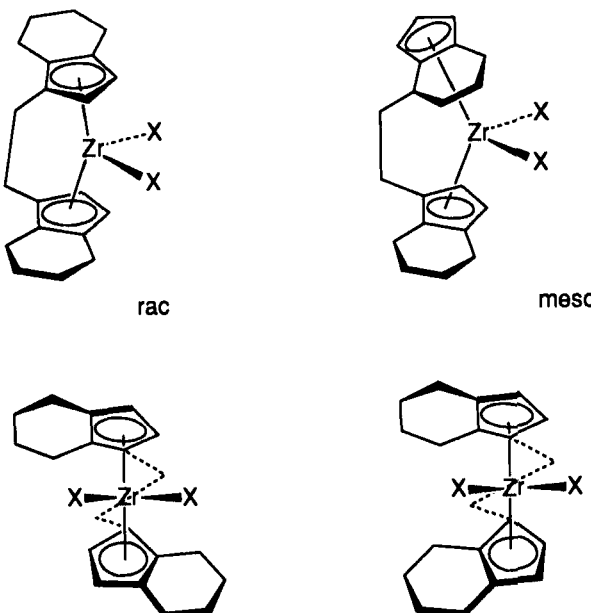


Fig. 6.18. Structure of 1,2-ethanediyl bis(tetrahydroindenyl) MX_2 . Two views of the *rac* and *meso* isomers.

are not considered. The asymmetry possibly introduced initially in the crystal during crystal growth from a chiral catalyst will be removed by melting and crystallization. Note: when catalysts of this type are to be used for asymmetric synthesis, e.g. as Lewis acids in Diels–Alder reactions, separation of the enantiomers is a prerequisite.

For polymerization to occur the X atoms in Fig. 6.18 are replaced by an alkyl chain and a coordinating propene molecule. Coordination of propene introduces a second chiral element and several diastereomers can be envisaged. The step-by-step regulation of the stereochemistry by the site can be most clearly depicted by drawing the molecule as shown in Fig 6.19.

Here we have taken the plane of the paper identical to the plane determined by Zr and the two X atoms of Fig. 6.19 or, in other words, the plane bisecting the two cyclopentadienyl planes. Propene coordinates in a π -fashion to zirconium with the two alkene carbons situated in the plane. The migratory insertion reaction can be described as a 2+2-addition following 1,2-regioselectivity. For the 1,2 insertion two possible structures remain, one with the methyl group pointing up in the present Fig. 6.19.a and one with the methyl group below the plane, Fig. 6.19.b. The tetrahydroindenyl group above the plane (drawn in full) will clearly favour situation 6.19.b. If we accept that the transition state resembles the coordination complex, the stereochemistry of the insertion product follows from structure b \rightarrow c. The alkyl group has migrated to the other coordination site of

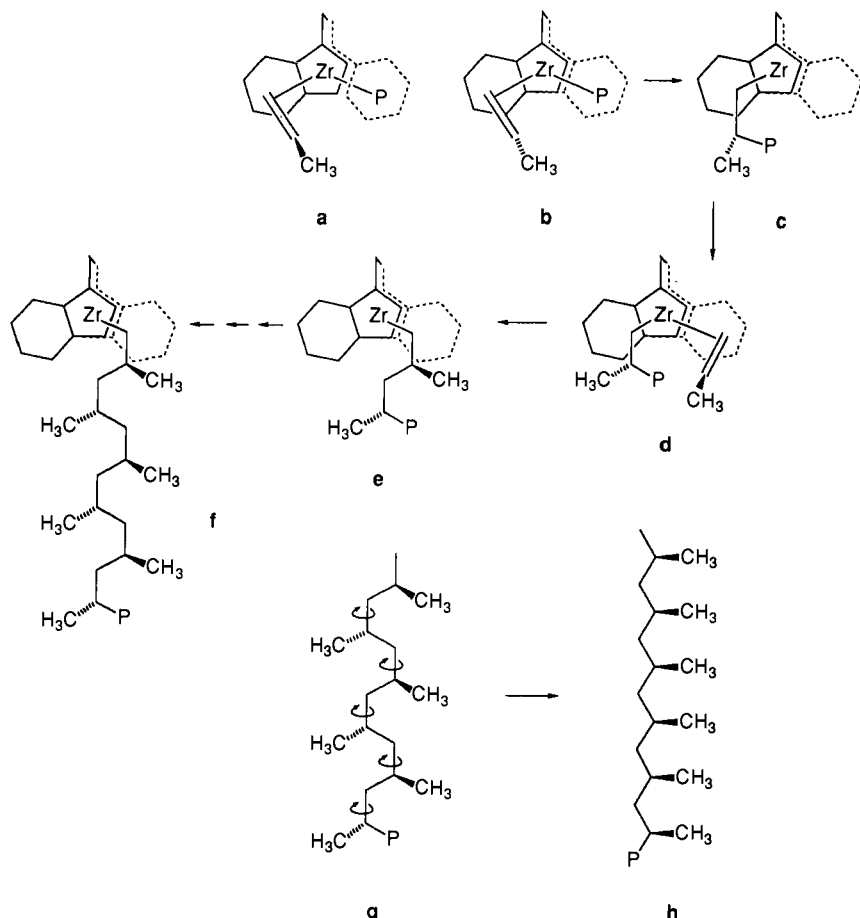


Fig. 6.19. Isotactic polymerization of propene with *rac*-1,2-ethanediyi-bis(indenyl)zirconium complexes. The plane of the drawing coincides with the plane bisecting the two planes of the indenyl ligands. Propene coordination takes place with the alkene π -orbitals in the plane of the drawing. The carbon atoms of the growing chain are depicted in the plane of the figure; in between insertions no rearrangements to more stable conformations have been drawn. Indenyl ligand above the plane drawn in full.

the complex. The question is, what will be the relation between the next insertion and the one that we have just described?

The next molecule of propene will coordinate onto the complex with the methyl group pointing upwards (6.19.d); migration of the new alkyl anion gives e with the stereochemistry shown. When this process is repeated several times, forming the polymer carbon chain in the plane of the figure, structure f is obtained. From this structure we cannot immediately deduce what the microstructure is, since the polymer chain is not stretched as shown before (Fig. 6.11). By rotating

carefully around the bonds indicated we obtain the isotactic stereochemistry, **h**, from **g**. Hence, the experimentally found isotactic stereochemistry with *rac*-bis(indenyl) derived complexes can be explained with a very simple set of pictures.

A series of elegant experiments which support this mechanism involve the use of isopropyl(1-fluorenyl-cyclopentadienyl) ligands [37]. This complex has no chirality (i.e. the dichloride precursor of Fig. 6.20.a) and one might expect no

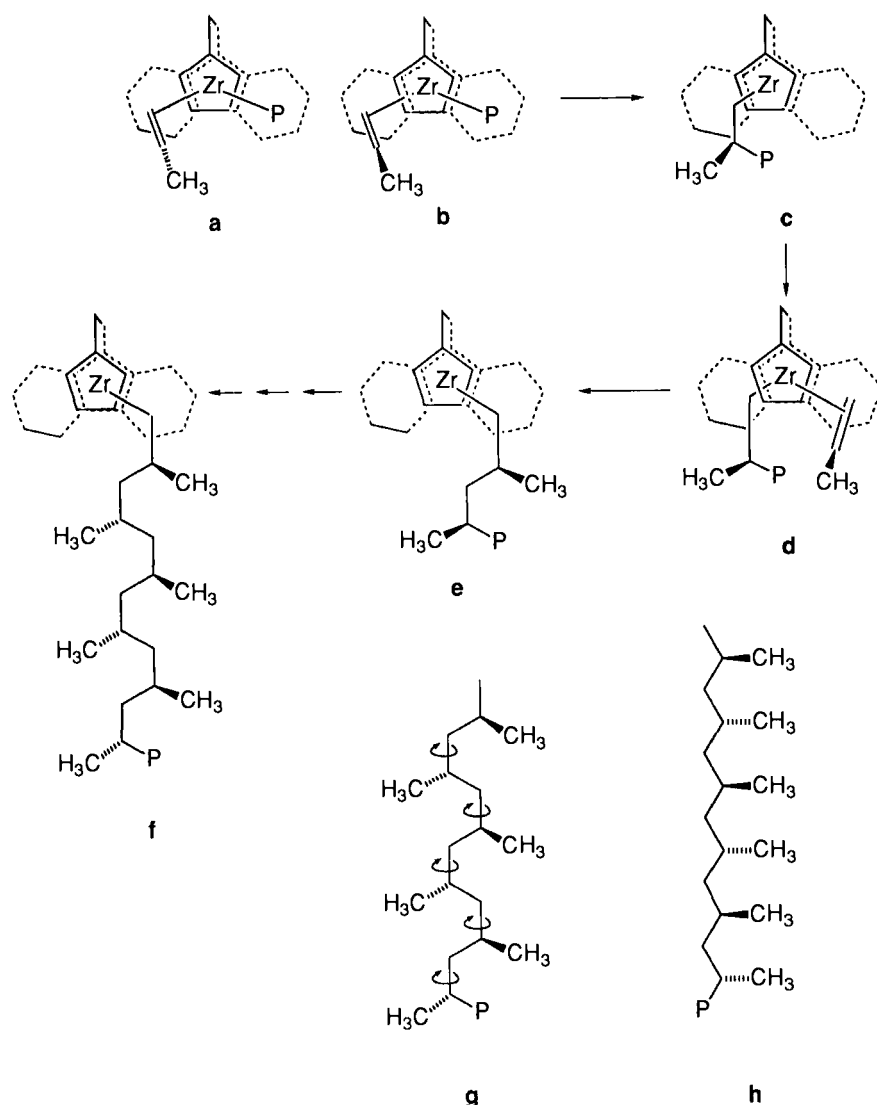


Fig. 6.20. Syndiotactic polymerization of propene with isopropyl(1-fluorenyl-cyclopentadienyl) zirconium complexes. See also Fig. 6.19. The cyclopentadienyl ligand above the plane is drawn in full. The fluorenyl ligand below the plane is drawn with dotted lines.

tacticity in the propene polymer product. The catalyst was found to give syndiotactic polymer. If the fluorenyl group is pointing downwards, propene coordination at both sites will occur with the methyl group above the plane (Fig. 6.20.b). A series of migratory insertions of the alkyl group to propene molecules with their methyl substituents pointing upwards lead to the chain **g**. Stretching the chain leads to structure **h** which clearly has a syndiotactic arrangement of the substituents along the chain. This is an important result, since hitherto it was thought that syndiotactic polymers could only be obtained via 2,1-insertion, controlled by the stereochemistry of the chain end.

Errors can be introduced in several ways, for the indenyl as well as for the fluorenyl complexes:

- 1,2-insertion with the methyl group pointing to the sterically more hindered direction;
- 2,1-insertion (with two orientations);
- 2,1-insertion followed by isomerization (3,1 insertion);
- alkyl migration without insertion; and
- alkyl exchange between metals.

Impurities in the zirconium precursor complex can also lead to lower tacticities. The activities of complexes may differ by several orders of magnitude and therefore the results can be considerably distorted by impurities. With the present knowledge one can estimate the extent to which impurities will distort the results. For example, it has been found that the presence of the *meso*-isomer in a bis(indenyl)ethane-type catalyst may sometimes produce only little of the atactic isomer. The *meso*-isomer containing one alkyl group and a propene coordinated to the vacant site will have no preference for the methyl group pointing up or down, regardless the position of the chain. The two sites, however, will show a great difference towards propene coordination, one being very open and the other being strongly sterically hindered. The hindrance at one site may be such that this site is virtually blocked for propene coordination and as a result the rate of propene polymerization of such a catalyst may be very low.

6.3.11 Double Stereoselection: Chain-End Control and Site Control

So far we have looked at chain-end control and site control if they were independent. As has already been mentioned, a site-control *only* mechanism does not exist; since we are, by definition, making a chiral chain end, site control must be accompanied by chain-end influences. Recent results have shown that this is indeed the case [38,48,41]. The simple explanation given above has to be modified, which may give rise to some confusion. We limit ourselves to two issues: (a) the stereochemistry of the coordinating propene; and (b) reinforcement of the two mechanisms.

(a) Molecular mechanics calculations [50] and a thorough analysis of the substituent effect on the statistical distribution of microstructure defects indicate that, firstly, the polymer chain assumes the energetically most favourable position with respect to the (asymmetric) site. For the fluorenyl-cyclopentadienyl ethane ligand this means that the chain will occupy the empty space at the cyclopentadienyl face. Subsequently, the incoming propene will direct its methyl group into the most favourable direction, which is now the fluorenyl side of the catalyst. This *reverses* the propene orientation given in Fig. 6.20. It does not basically change the explanation because *all* propene molecules will orient themselves in the same direction. For the present purposes Figs. 6.19 and 6.20 are sufficient and we have not attempted to redraw the structures with the polymer chains included; the experts will prefer to treat this problem with molecular mechanics and computer graphics in a more sophisticated manner.

(b) This brings us to double stereoselection and reinforcement of the mechanisms. If the site (a)symmetry were to control the orientation of the chain, and if, then, the orientation of the incoming propene is controlled by both the chain and the site, the highest stereoselection is obtained when the two influences reinforce one another. For 1,2-insertion this can be done most effectively for isotactic polymerization, since chain-end control 'naturally' leads to isotactic polymer and this we can reinforce by site control with ligands of the bis(indenyl)ethane type. The chain-end influence of short chains is smaller than that of longer polymer chain; indeed the isotactic index at the very beginning of the chain was found to be lower than that in the polymer. It may also be inferred that making syndiotactic polymer via a 1,2-insertion mechanism on Ti or Zr complexes is indeed more difficult than making an isotactic polymer, because the two mechanisms now play a counterproductive role.

6.3.12 Further Work

In addition to propene and ethene many other alkenes (higher alkenes, styrenes, cyclic alkenes) have been polymerized with these new catalysts and a great variety of new polymers and oligomers have been synthesized, including plastic materials with melting points as high as 500°C, novel rubber materials etc. Several new polymers can now be made by catalyst design. Basically, the concepts developed by Cossee and his contemporaries have not changed, but today we have the tools to design the catalysts that may give the desired polymer. Stereoselectivity and molecular weight may not be high enough in some instances, but the achievements are impressive with more to follow:

- A cyclopentadienyl, indenyl-ethane ligand undergoes insertion alternatingly in an isotactic and an atactic fashion to give a hemitactic polymer, as is to be expected.

- One could imagine a complex that, at one site, will insert only one certain type of alkene due to high steric constraints (e.g. ethene) and a second alkene at the other site, thus giving an alternating copolymer that may even contain stereoregularity.
- Block polymers can be envisaged in which the tacticity of the blocks alternates via an inversion reaction of the site.
- Block copolymers could be made via sequential polymerization of two monomers at a 'living' catalyst, although the catalyst would produce only one polymer molecule per metal site.

Here we have discussed only very few of the many ligands that have been made. Many variations of substituents at the cyclopentadienyl ligand have been studied, and there are more to come, as well as variation in the structure of the bridge, the anions, the central metal, and replacement of the cyclopentadienyl ligand by other bulky ligands. In summary, the toolbox is quite extensive; prediction of properties of new polymers to be made could guide the catalysis research in the design of new catalysts.

6.4 ASYMMETRIC HYDROGENATION

6.4.1 *Introduction*

To date many examples are known which show that tailor-made chiral metal complexes, comprising a metal atom bound to chiral organic ligands can discriminate with high precision (energy differences in the range of 10 kJ/mol) between enantiotropic atoms or faces of an achiral molecule. Many of these chiral complexes also have an interesting catalytic activity in the production of a broad range of enantiomerically pure compounds. As the chiral complexes can be synthesized in both, in principle, both enantiomers of a compound are accessible. (This is a clear distinction from enzymatically catalyzed reactions, which can produce only one hand of a chiral product.)

The demand for enantiomerically pure compounds in fine chemical synthesis is growing rapidly. An obvious reason for this development is that the opposite hand of a chiral pharmaceutical or chemical with a desired biological activity has at best no activity, or worse, causes side effects.

6.4.2 *Cinnamic Acid Derivatives*

The first industrially interesting production of a chiral pharmaceutical with a chiral metal complex catalyst is the asymmetric hydrogenation of cinnamic acid derivatives to give L-DOPA, see Fig. 6.21.

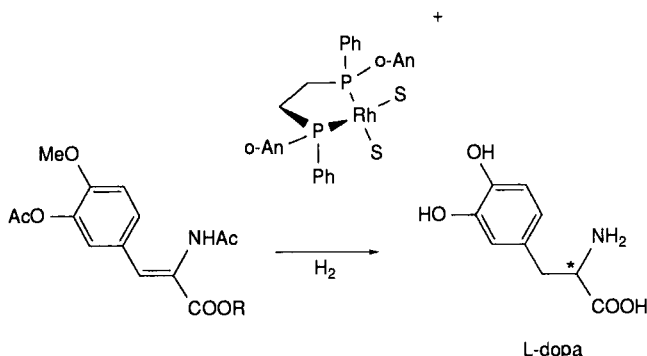


Fig. 6.21. Synthesis of L-DOPA with the cationic Rh-DiPAMP catalyst.

The synthesis of L-DOPA, a drug for the treatment of Parkinson's disease, has been developed by Knowles at Monsanto [51] and was applied on an industrial scale. This kind of enantioselective catalysis became possible when Horner and Knowles in 1968 discovered methods for the synthesis of chiral triorganophosphines. The L-DOPA synthesis is carried out with a cationic rhodium–bisphosphine complex in which the enantioselectivity is induced by the chiral bisphosphine. Surprisingly, the reaction is not very sensitive to the type of chiral bisphosphine used, although it must be added that most ligands tested are bis(diphenylphosphino) derivates and that the enantiomeric excesses obtained do show some variation. On the other hand the reaction is very sensitive to the type of substrate. The presence of polar substituents in these substrates is a prerequisite for a successful asymmetric hydrogenation. This polar substituent, e.g. an acetamido group, is of crucial importance because it functions as a secondary complexation function in addition to the alkene functionality, present in cinnamic acid, that has to be hydrogenated.

In the first step the prochiral alkene entity coordinates to the cationic chiral rhodium centre with either one of the two enantiotopic faces (due to the asymmetry in the diphosphine ligand) which leads to the formation of two possible structures. Only one diastereoisomer of the intermediate alkene–rhodium complex is shown on Fig. 6.22: the second diastereoisomer can be easily imagined by taking the

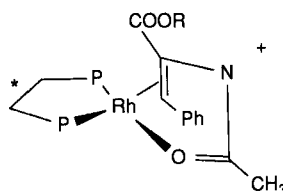


Fig. 6.22. One diastereoisomer of the intermediate alkene–rhodium complex.

mirror image of the complex, however, with retention of the asymmetry of the chelating bisphosphine. Coordination of the auxiliary amide oxygen is of pivotal importance; if it were absent the adduct would have a much less rigid structure (leading to a less-organized transition state during the hydrogenation step) resulting in a lower enantiomeric excess of the product.

Having learned this, Dupont workers [52] have added a temporary auxiliary donor atom to an unsaturated substrate in order to be able to steer adduct formation, and so the enantioselectivity of the hydrogenation. For example, asymmetric hydrogenation of imines or ketones was a reaction that yielded rather low enantiomeric excesses. However, by converting these first into acyl hydrazones the hydrazide oxygen can function as the secondary complexation function and now extremely high enantiomeric excesses can be obtained (Fig. 6.23).

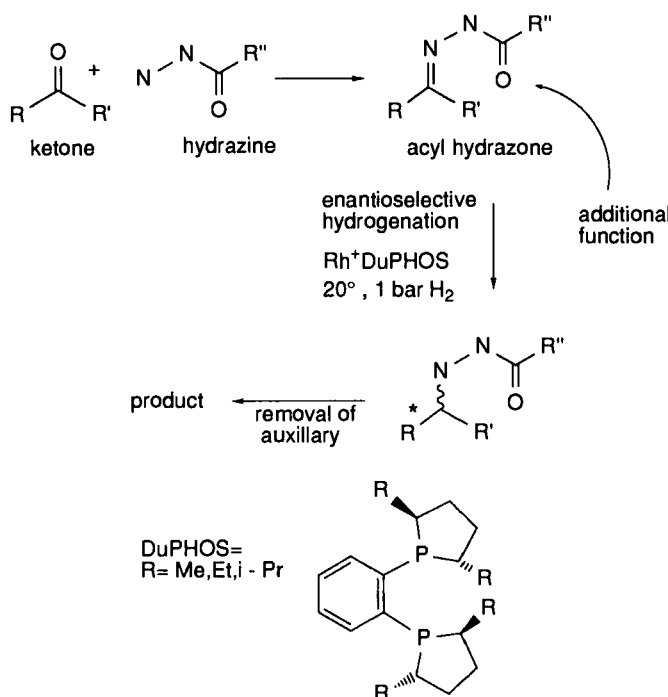


Fig. 6.23. Use of temporary auxiliary in the enantioselective hydrogenation of ketones which enhances the enantiomeric excess to nearly 100% enantiomeric excess.

Detailed studies of the hydrogenation of cinnamic acid derivatives (Fig. 6.22) by Halpern [53] and Brown [54] have revealed that the most stable intermediate of the two alkene adducts is not the one that leads to the major observed enantiomeric product, see Fig. 6.24. This means that the least stable intermediate alkene–rhodium complex reacts faster in the subsequent reaction step involving

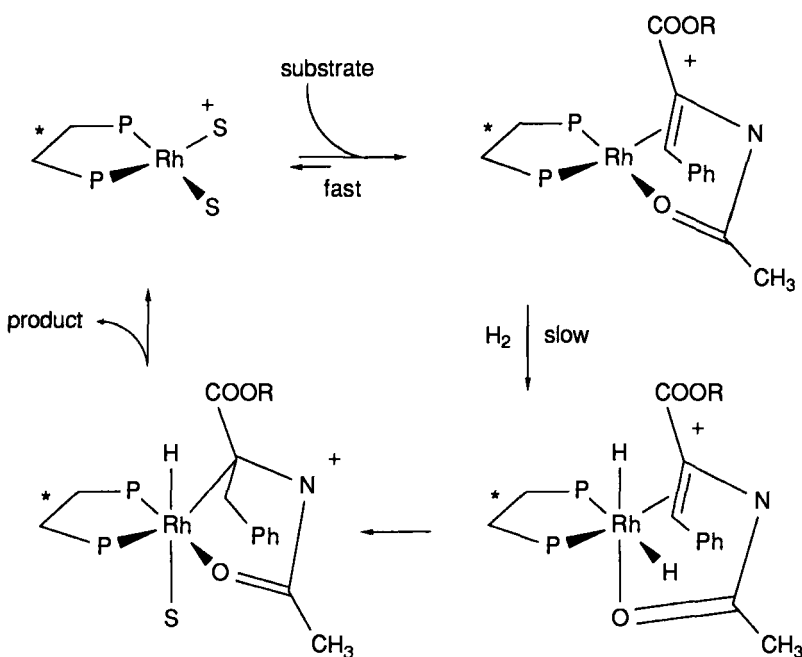


Fig. 6.24. Asymmetric hydrogenation shown for one diastereoisomer.

the oxidative addition of dihydrogen to the alkene–rhodium complex (Fig. 6.24.). The oxidative addition of H₂ is irreversible, the two alkene–rhodium enantiomers are formed in this step. If we assume that no dissociation of the alkene occurs, this step determines the enantioselectivity of the alkene hydrogenation.

Migration of the hydride locks the configuration of the enantiomeric alkene–carbon centre; in general this step is also reversible but probably not in this instance. In the examples studied neither the dihydride intermediates nor the alkyl intermediates have been observed and so it seems reasonable to assume that addition of H₂ is also the rate-determining step. Since the latter is a bimolecular reaction and the other ones are monomolecular rearrangement reactions, one cannot in absolute terms say that oxidative addition is rate-determining.

The example illustrates two points:

1. The intermediate alkene adduct observed in the NMR spectra is not the one leading to the major catalytic pathway, see also Fig. 6.25.
2. Enantioselectivity is determined in the first irreversible step after the stereogenic-centre was formed which is not always the rate-determining step.

The difference of the catalytic system discussed above from that of the Wilkinson catalyst lies in the sequence of the oxidative addition and the alkene complexation. The hydrogenation of the cinnamic acid derivative involves a cationic catalyst of

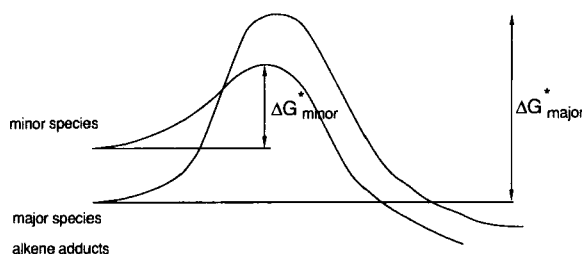


Fig. 6.25. Minor species leading to dominant product route.

which the intermediate alkene (enamide) complex has been spectroscopically observed. In subsequent steps oxidative addition of H_2 and insertion of the alkene occur, followed by reductive elimination of the hydrogenation product. A large series of asymmetric ligands have been developed, most of which have the stereogenic centre(s) in the bridge connecting the phosphorus donor atoms rather than at the phosphorus atoms themselves (cf. DIPAMP in Fig. 6.21). Their synthesis is similar to one developed by Kagan for DIOP (see Fig. 6.26) and starts from asymmetric acids which can be obtained commercially (tartaric acid in the case of DIOP).

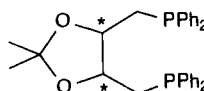


Fig. 6.26. The structure of DIOP.

Crucial to the success of this family of ligands is the C_2 'propeller' type symmetry, which divides the space around rhodium (or any metal) into four quadrants; two relatively empty and two filled (see Fig. 6.27). The two phenyl groups at one face of the chelate ring adopt axial and equatorial positions. This explains the similarity of the effect of this large family of ligands on the enantioselective reactions. Coordination of enamides (see above) will now take place in such a way that the auxiliary donor atom coordinates to one side, and the phenyl

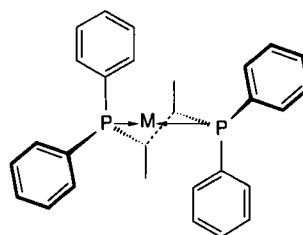


Fig. 6.27. Front view of (*S,S*)-CHIRAPHOS/M showing the C_2 symmetry.

substituted alkene will coordinate to the other side with the face that gives the least interaction of its substituents with the phenyl group of the ligand pointing into the same quadrant. This gives the predominant metal alkene adduct; as we have seen in the above example, this is not to say that the dominant reaction path will arise from this species that is the major component in the equilibrium mixture.

Not all bisphosphine ligands adopt C_2 symmetry with respect to the four phenyl groups. For instance, $\text{Ph}_2\text{P}(\text{CH}_2)_4\text{PPh}_2$ lacks the constraints in the C_4 bridge of the chelate ring that give the unique stereochemistry to the bisphosphine ligands with a C_2 bridge. As a consequence the C_4 bridged bisphosphines do not adopt a C_2 -symmetry but C_s symmetry (Fig. 6.28). In this configuration two phenyl groups are at the side of the chelating ring and will take (more or less) axial positions, while the other two at the opposite face of the ring will assume equatorial positions.

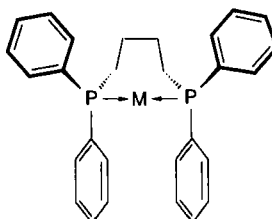


Fig. 6.28. Front view of $\text{Ph}_2\text{P}(\text{CH}_2)_4\text{PPh}_2/\text{M}$ showing the C_s symmetry (simplified).

Even though there may be an asymmetric centre in the backbone of a bisphosphine, if it prefers this C_s 'local' symmetry for the phenyl groups, the enantiomeric character is not optimally passed onto the substrate coordinating to the C_s -diphos ligand–metal complex. Many crystal structures have been determined that support this view and refine it even further, as do molecular graphics (or molecular mechanics) for a broad range of ligands [55].

The practical work-up of the catalyst and product is worthy of some comment. During the reaction the catalyst slowly loses enantioselectivity and at a certain point the reaction is stopped. To recover the rhodium, the mixture is chromatographed over a column containing a complexing phosphine on an organic support. This column material can be burned to give an inorganic rhodium residue. This procedure is only economic if the added value of the product is very high.

6.4.3 Naproxen and Ibuprofen

At present much research is being directed to the development of catalytic routes to a series of asymmetric carboxylic acids that lack the acidamido ligand as additional functionality. Four are listed in Fig. 6.29, which are important as

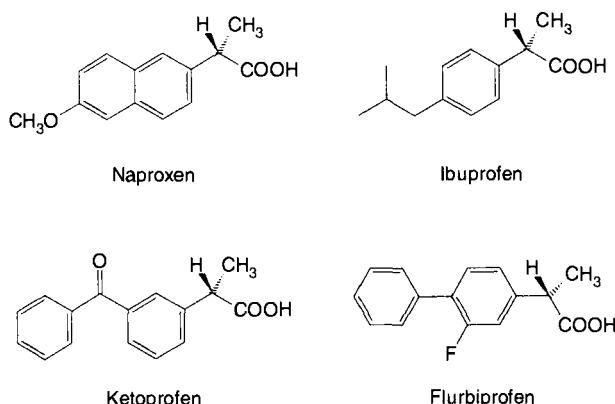


Fig. 6.29. Pharmaceuticals of interest.

anaesthetics for rheumatic diseases. Their turnover in dollars beats many of the bulk chemicals: the turnover of Naproxen in 1990 amounted to \$700 million.

S-Naproxen is now being produced by Syntex by resolution with a chiral auxiliary. The main patents from Syntex will expire in 1993, which represents the main drive for an increase of the efforts to find alternative synthetic routes which may lead directly to an asymmetric carbohydroxylation of the styrene precursor. Asymmetric hydrogenation of molecules of this type has been successfully accomplished by Noyori using ruthenium complexes of the ligand BINAP (Fig. 6.30). With this system a high enantioselectivity can be achieved (97%) albeit at rather high pressures (135 bar). Monsanto [56] claims a similar route with an as yet undefined ligand that operates at a much lower pressure. The starting material is the corresponding acetyl aromatic compound which is reacted with CO₂ via an electrochemical reduction in a divided cell using a lead cathode and a sacrificial aluminum anode in 95% yield.

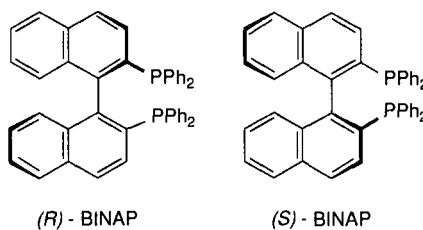


Fig. 6.30. Asymmetric BINAP ligand.

The aluminium salt obtained is acidified and dehydrated to give the unsaturated (atropic type) acid precursor. This can be asymmetrically hydrogenated in methanol under 7 bar of H₂ with an enantiomeric excess of 98.5%. A turnover of 3000 was most efficient. The reaction scheme is shown in Fig. 6.31.

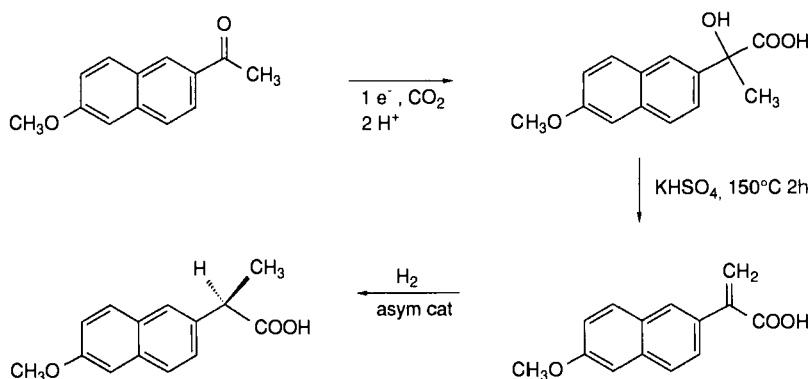
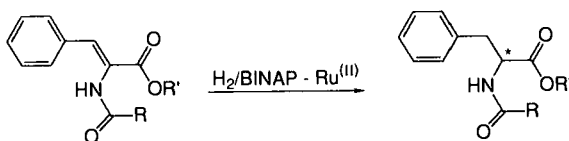


Fig. 6.31. Monsanto route to Naproxen.

6.4.4 BINAP Catalysis

BINAP was first introduced by Noyori [57]. It has been particularly explored for reduction with ruthenium catalysts. BINAP is an atropisomeric ligand because rotation around the central C–C bond is blocked. Accordingly BINAP exists in two enantiomers. Complexes of Ru(II) with BINAP are extremely powerful catalysts for enantioselective hydrogenations of prochiral α,β - and β,γ -unsaturated carboxylic acids, enamides, allylic and homoallylic alcohols, imines etc. In many cases the hydrogenation is quantitative with enantiomeric excesses of over 95%. A wide variety of vitamins, terpenes, β -lactam antibiotics, etc. are accessible by the use of catalysts containing the BINAP stereogenic element. The BINAP-Ru(II) catalysts hydrogenate enamides with high enantiomeric excess provided that the amide substituent and the one substituent at the other carbon are *cis* to one another (Fig. 6.32).

Fig. 6.32. Asymmetric BINAP-ruthenium catalysed hydrogenation of enamide with *cis*-phenyl substituent.

Secondly, the BINAP-Ru(II)(O₂CR)₂ catalyst gives enantioselective hydrogenation of acrylic derivates. See Fig. 6.31 for the synthesis of Naproxen.

Finally, ketones and aldehydes containing another polar group can be hydrogenated. Although the pressures needed for quantitative conversion are high the use of the BINAP-Ru(II) has the advantage that enantiomeric excesses are

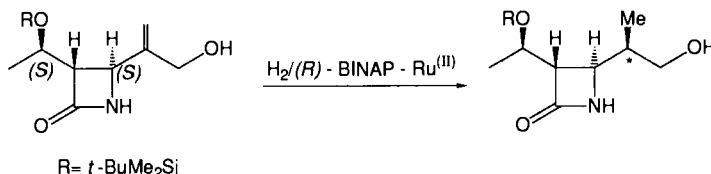


Fig. 6.33. Asymmetric hydrogenation of azetidinone alcohol.

very high. The hydrogenation shown in Fig. 6.33 proceed by enantioface differentiation in prochiral substrates. When the substrate itself is also chiral, the stereoselectivity of the reaction catalysed by a chiral metal complex may be markedly influenced, as in the transition state of the reaction two diastereoisomeric encounter complexes are formed. The hydrogenation of the saturated azetidinone alcohol, which is a key intermediate for the synthesis of carbapenem antibiotics, provides an example for this. The (S),(S)-diastereoisomer is hydrogenated almost quantitatively to the 1 β -methyl isomer with the Ru(II) catalyst of the (R)-BINAP atropisomer. However, the use of the (S)-atropisomeric BINAP-Ru(II) catalyst results in only moderate diastereoselectivity.

Another interesting application is the hydrogenation of a racemic mixture of certain allylic alcohols with the Ru(II)-BINAP catalyst. In this reaction, since the enantiomers of the allylic alcohol are hydrogenated at different rates, a kinetic resolution of the racemate occurs. In the optimal case this may lead to a maximum yield of 50% of one of the enantiomers as the hydrogenated product (100% enantiomeric excess) while the other enantiomer remains unchanged. An interesting and technically important variation is the hydrogenation of a configurationally labile α -substituted β -ketoester which occurs with dynamic kinetic resolution providing one of the four possible diastereoisomeric hydroxy esters in better than 90% yield.

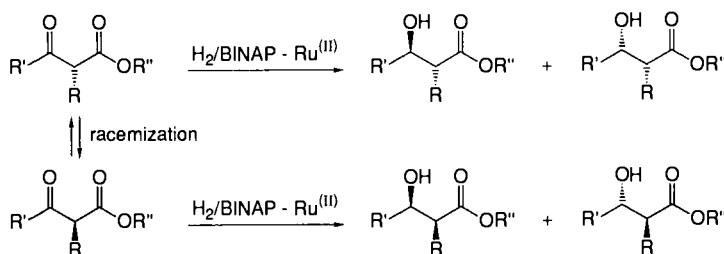


Fig. 6.34. Asymmetric hydrogenation of ketoester racemate.

The success of this so-called second-order stereoselectivity hydrogenation depends on the fact that: (a) the rate of racemization has to be fast with respect to the rate of hydrogenation; (b) the diastereotopic face discrimination by the chiral

BINAP-Ru(II) catalyst must be efficient; and (c) a unique difference between syn- and antidiastereoisomeric transition states must exist in the hydrogenation step.

Finally, another important application of BINAP is found in the Takasago process for the commercial production of (–) menthol from myrcene. The catalyst used is a rhodium complex of BINAP. Figure 6.35 gives the reaction scheme [58]. The key reaction is the enantioselective isomerization of the allylamine to the asymmetric enamine. It is proposed that this reaction proceeds via an allylic intermediate.

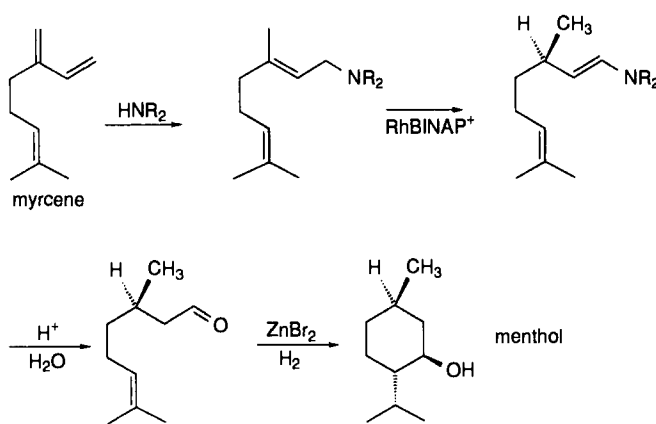


Fig. 6.35. The Takasago process for (–)menthol.

Asymmetric catalysis involving metal catalyzed hydrogenations and isomerizations is becoming increasingly important in the production of pharmaceuticals, agrochemicals and flavours and fragrances. More examples of asymmetric homogeneous catalysts used industrially can be found in the series of articles by Parshall and Nugent [59].

REFERENCES

- 1 G.W. Parshall and S.D. Ittel, *Homogeneous Catalysis. The Applications and Chemistry of Catalysis by Soluble Transition Metal Complexes*, Wiley, New York, 2nd Ed., 1992.
C. Masters, *Homogeneous Transition-Metal Catalysis*, Chapman and Hall, London, 1981.
F.G.A. Stone (Editor), *Advances in Organometallic Chemistry*, Vol. 17, Wiley, New York, 1979.
R. Ugo (Editor), *Aspects of Homogeneous Catalysis*, Vols. 1–7, Kluwer Academic Publishers, Dordrecht, 1990.
- 2 C.A. Tolman, *Chem. Rev.*, 77 (1977) 313.
- 3 R.L. Pruett, *Adv. Organometall. Chem.*, 17 (1979) 1.
- 4 O. Roelen, *Ger. Pat.* 849548 (1938).
- 5 B. Cornils, *Organic Syntheses with Carbon Monoxide*, J. Falbe (Editor), Springer Verlag, Weinheim, 1980, Ch. 1.
L.H. Slaugh and R.D. Mullineaux, *U.S. Pat.* (to Shell) 3 239 569 and 3 239 570 (1969).

- 6 D. Evans, J.A. Osborn and G. Wilkinson, *J. Chem. Soc. (A)*, (1968) 3133.
- 7 G. Wilkinson, *Br. Pat. Appl.* (to Johnson Matthey) 63503 (1969).
- 8 R.L. Pruett and J.A. Smith, *S. African Pat. Appl.* (to Union Carbide) 68/4937 (1968).
- 9 R.L. Pruett and J.A. Smith, *J. Org. Chem.*, 34 (1969) 327.
- 10 P.W.N.M. van Leeuwen and C.F. Roobek, *Br. Pat. Appl.* (to Shell) 2,068,377 (1980).
- 11 T. Jongsma, P.W.N.M. van Leeuwen and G. Challa, *J. Organomet. Chem.*, 421 (1991) 121.
- 12 A. Van Rooy, E.N. Orij, P.C.J. Kamer, F. van den Aardweg and P.W.N.M. van Leeuwen, *J. Chem. Soc. Chem. Commun.*, (1991) 1096.
- 13 A.A. Oswald, D.E. Hendriksen, R.V. Kastrup and E.J. Mozeleski, in *Homogeneous Transition Metal Catalyzed Reactions*, W.R. Moser and D.W. Slocum (Editors), Adv. in Chem. Series 230, ACS, Washington, DC, 1992, p. 395.
- 14 J.D. Unruh and J.R. Christenson, *J. Mol. Catal.*, 14 (1982) 19.
- 15 J.M. Brown and A.G. Kent, *J. Chem. Chem. Soc. Perkin Trans. II*, (1987) 1597.
- 16 E. Billig, A. Abatjoglou and D.R. Bryant, *U.S. Patents* 4,668,651 (1987) and 4,769,498 (1988).
- 17 T.J. Devon, G.W. Philips, T.A. Puckette, J.L. Stavinotha, and J.J. Vanderbilt, *PCT Int. Appl.* WO 87 07,600 (1987), *U.S. Patent* 4,879,416 and 4,694,109 (1989), and *Eur. Pat. Appl.* EP 0 326 286 (1989).
- 18 C.P. Casey, G.T. Whiteker, M.G. Melville, L.M. Petrovich, J.A. Gavney Jr. and D.R. Powell, *J. Am. Chem. Soc.*, 114 (1992) 5535.
- 19 R.F. Heck and D.S. Breslow, *J. Am. Chem. Soc.*, 83 (1961) 4023.
- 20 G. Csontos, B. Heil and L. Markó, *Ann. NY Acad. Sci.*, 239 (1974) 47.
- 21 R. Lazzaroni, P. Pertici and G. Fabrizi, *J. Mol. Catal.*, 58 (1990) 75.
- 22 A.M. Joshi and B.R. James, *Organometallics*, 9 (1990) 199.
- 23 L. Versluis and T. Ziegler, *Organometallics*, 9 (1990) 2985.
- 24 P.P. Deutsch and R.Eisenberg, *Organometallics*, 9 (1990) 709.
- 25 W.D. Jones, J.M. Huggins and R.G. Bergman, *J. Am. Chem. Soc.*, 103 (1981) 4415.
- 26 P.W.N.M. van Leeuwen and C.F. Roobek, *J. Organomet. Chem.*, 258 (1983) 343 and *U.S. Patent* 4,467,116 (1984).
- 27 P. Cavalieri d'Oro, L. Raimondo, G. Pagani, G. Montrasi, G. Gregorio and A. Andreetta, *Chim. Ind. (Milan)*, 62 (1980) 572.
- 28 Y. Pottier, A. Mortreux and F. Petit, *J. Organomet. Chem.*, 370 (1989) 333.
- 29 M. Garland and P. Pino, *Organometallics*, 10 (1991) 1693.
- 30 W.R. Moser, C.J. Papile, D.A. Brannon and S.J. Weiniger, *J. Mol. Catal.*, 41 (1987) 271.
- 31 S. van der Ven, *Polypropylene and Other Polyolefins: Polymerization and Characterization*, Elsevier Science Publishers, New York, 1990.
- 32 B.L. Goodall, "Polypropylene: Catalysts and Polymerization Aspects" in [1], Chapter 1, pp. 1–125.
- 33 P. Cossee, *J. Catal.*, 3 (1964) 80.
E.J. Arlman, *J. Catal.*, 3 (1964) 89.
E.J. Arlman and P. Cossee, *J. Catal.*, 3 (1964) 99.
- 34 G. Allegra, *Makromol. Chem.*, 145 (1971) 235.
- 35 D.S. Breslow and N.R. Newburg, *J. Am. Chem. Soc.*, 82 (1957) 5072.
- 36 G. Natta, P. Pino, P. Corradini, F. Danusso, E. Mantica, G. Mazzanti and G. Moraglio, *J. Am. Chem. Soc.*, 77 (1955) 1708.
- 37 J.A. Ewen, *J. Am. Chem. Soc.*, 106 (1984) 6355.
J.A. Ewen, M.J. Elder, R.L. Jones, S. Curtis, and H.N. Cheng, in *Catalytic Olefin Polymerization*, T. Keii and K. Soga (Editors), Elsevier, Amsterdam, and Kodansha, Tokyo, 1990, p. 439.

- 38 J.A. Ewen, M.J. Elder, R.L. Jones, L. Haspeslagh, J.L. Atwood, S.G. Bott and K. Robinson, *Makromol. Chem., Makromol. Symp.*, 48/49 (1991) 253.
- 39 T. Mise, S. Miya and H. Yamazaki, *Chem. Lett.*, (1989) 1853.
- 40 Y. Takegami and T. Suzuki, *Bull. Chem. Soc. Jpn.*, 42 (1969) 848.
A. Zambelli, G. Natta and I. Pasquon, *J. Polym. Sci.*, C4 (1963) 411.
Y. Doi, S. Suzuki, F. Nozawa, and K. Soga, in *Catalytic Polymerization of Olefins*, T. Keii and K. Soga (Editors), Kodansha, Tokyo, 1986, p. 257
- 41 R. Waymouth and P. Pino, *J. Am. Chem. Soc.*, 112 (1990) 4911.
- 42 H. Sinn, W. Kaminsky, H.-J. Volmer and R. Woldt, *Angew. Chem., Int. Ed. Engl.*, 19 (1980) 390.
- 43 H. Sinn and W. Kaminsky, *Adv. Organometal. Chem.*, 18 (1980) 99.
- 44 F.R.W.P. Wild, L. Zsolnai, G. Huttner and H.H. Brintzinger, *J. Organomet. Chem.*, 232 (1982) 233.
- 45 W. Kaminsky, K. Külper, F.R.W.P. Wild and H.H. Brintzinger, *Angew. Chem. Int. Ed. Engl.*, 24 (1985) 507.
- 46 W. Kaminsky, K. Külper and S.D. Niedoba, *Makromol. Chem., Makromol. Symp.*, 3 (1986) 377.
- 47 J.A. Ewen, *J. Am. Chem. Soc.*, 110, (1988) 6255.
- 48 G. Erker, R. Nolte, R. Aul, S. Wilker, C. Krüger and R. Noe, *J. Am. Chem. Soc.*, 113 (1991) 7594.
- 49 R.F. Jordan, R.E. LaPointe, C.S. Bajgur, S.F. Echols and R. Willett, *J. Am. Chem. Soc.*, 109 (1987) 4111.
G.G. Hlatky, H.W. Turner and R.R. Eckman, *J. Am. Chem. Soc.*, 111, (1989) 2728.
- 50 P. Corradini, G. Guerra, M. Vacatello and V. Villani, *Gazz. Chim. Ital.*, 118 (1988) 173L.
Cavallo, G. Guerra, M. Vacatello and P. Corradini, *Macromolecules*, 24 (1991) 1784.
L. Cavallo, G. Guerra, L. Oliva, M. Vacatello and P. Corradini, *Polym. Commun.*, 30 (1989) 17.
- 51 W.S. Knowles, M.J. Sabacky and B.D. Vineyard, *Adv. Chem. Ser.*, 132 (1974) 274.
- 52 M.J. Burk and J.E. Harlow, *J. Am. Chem. Soc.*, 114 (1992) 6266.
- 53 J. Halpern et al., *Science*, 127 (1982) 401; A.S.C. Chan, J.J. Pluth and J. Halpern, *J. Am. Chem. Soc.*, 102 (1980) 5922.
- 54 J.M. Brown and P.A. Chaloner, *J. Am. Chem. Soc.*, 102 (1980) 3040.
- 55 J.M. Brown and P.L. Evans, *Tetrahedron*, 44 (1988) 4905.
- 56 A.S.C. Chan, *199th National Meeting*, Boston, Am. Chem. Soc., 1990.
- 57 A. Miyashita, A. Yasuda, H. Tanaka, K. Toriumi, T. Ito, T. Souchi and R. Noyori, *J. Am. Chem. Soc.* 102 (1980) 7932.
- 58 K. Tani, T. Yamagata, Y. Tatsuno, Y. Yamagata, K. Tomita, S. Akutagawa, H. Kumabayashi and S. Otsuka, *Angew. Chem. Int. Ed. Engl.*, 24 (1985) 217.
- 59 G.W. Parshall and W.A. Nugent, *ChemTech*, (1988), 184, 314, 376.

Chapter 7

Catalytic reaction engineering

7.1 INTRODUCTION

Catalytic reaction engineering is a scientific discipline which bridges the gap between the fundamentals of catalysis and its industrial application. Starting from insight into reaction mechanisms provided by catalytic chemists and surface scientists, the rate equations are developed which allow a quantitative description of the effects of the reaction conditions on reaction rates and on selectivities for desired products. The study of intrinsic reaction kinetics, i.e. those determined solely by chemical events, belongs to the core of catalytic reaction engineering. Very close to it lies the study of the interaction between physical transport and chemical reaction. Such interactions can have pronounced effects on the rates and selectivities obtained in industrial reactors. They have to be accounted for explicitly when scaling up from laboratory to industrial dimensions.

The present chapter is not meant to be exhaustive. Rather, an attempt has been made to introduce the reader to the major concepts and tools used by catalytic reaction engineers. Section 2 gives a review of the most important reactor types. This is deliberately not done in a narrative way, i.e. by describing the physical appearance of chemical reactors. Emphasis is placed on the way mathematical model equations are constructed for each category of reactor. Basically, this boils down to the application of the conservation laws of mass, energy and possibly momentum. Section 7.3 presents an analysis of the effect of the finite rate at which reaction components and/or heat are supplied to or removed from the locus of reaction, i.e. the catalytic site. Finally, the material developed in Sections 7.2 and 7.3 is applied to the design of laboratory reactors and to the analysis of rate data in Section 7.4.

7.2 MAJOR REACTOR CATEGORIES

7.2.1 Batch Reactor

Reactors which are operated batchwise are called batch reactors. After the loading of the reactor with a batch of reactants, the reaction is started either by increasing the temperature or by adding a catalyst. Both the unconverted reactants and the reaction products are held in the reactor during the reaction. The composition of the reaction mixture thus changes as a function of time. Batch reactors are usually used for the production of high added value products in limited amounts. A typical reactor volume amounts to 10 m^3 and the content is present in the liquid state. Mechanical stirring ensures good mixing as well as a sufficient heat exchange with the surroundings and, if necessary, maintains a solid catalyst in suspension. In the case of perfect mixing both temperature and composition are uniform throughout the reactor. This allows us to write the mass balance for a component A over the complete reactor:

$$\frac{dn_A}{dt} = R_{v,A} V \quad (7.1)$$

where: n_A = the amount of A , mol; t = time, s; $R_{v,A}$ = the volumetric production rate of A , $\text{mol m}^{-3} \text{s}^{-1}$; and V = the reaction volume, m^3 .

The left-hand side of Eqn. 7.1 corresponds to the accumulation of A in the reactor. The right-hand side corresponds to the production of A .

If A is a reactant, its degree of conversion can be defined as:

$$X_A = \frac{n_{A0} - n_A}{n_{A0}} \quad (7.2)$$

i.e. the amount of A which has reacted, $n_{A0} - n_A$, is related to the amount added to the reactor, n_{A0} . Substituting (7.2) into (7.1) leads to:

$$\frac{dX_A}{dt} = - \frac{V}{n_{A0}} R_{v,A} \quad (7.3)$$

7.2.1.1 Single reaction

For a single reaction and known kinetics the balance for A , either Eqn. 7.1 or 7.3, can be integrated at a given temperature to yield a relation between the batch time and the degree of conversion:

$$t = - \int_0^{X_A} \frac{n_{A0}}{R_{v,A} V} dX \quad (7.4)$$

In special cases an analytical expression can be derived for Eqn. 7.4. The assumption of constant density allows us to write:

$$X_A = \frac{C_{A0} - C_A}{C_{A0}} \quad (7.5)$$

and leads for a single irreversible first-order reaction:

$$r_v = k_1 C_A \quad (7.6)$$

or

$$R_{v,A} = v_A r_v = -r_v \quad (7.7)$$

by integration of the balance for A to:

$$X_A = 1 - e^{-k_1 t} \quad (7.8)$$

Table 7.1 lists analytical relations between conversion or concentration and batch time for simple reaction kinetics.

TABLE 7.1

Batch reactor: relations between conversion, X_A , or concentration C_A , and batch time (constant density)

$r_v / \text{mol m}^{-3} \text{s}^{-1}$	$X_A / \text{mol mol}^{-1}$	$C_A / \text{mol m}^{-3}$
k_0	$\frac{k_0 t}{C_{A0}}$	$C_{A0} - k_0 t$
$k_1 C_A$	$1 - e^{-k_1 t}$	$C_{A0} e^{-k_1 t}$
$k_2 C_A^2$	$\frac{k_2 C_{A0} t}{1 + k_2 C_{A0} t}$	$\frac{C_{A0}}{1 + k_2 C_{A0} t}$

7.2.1.2 Multiple reactions

If more than one reaction occurs, it is convenient to define the selectivity for a product Q:

$$S_Q = \frac{n_Q - n_{Q0}}{n_{A0} - n_A} \quad (7.9)$$

as the amount of product Q which has been formed, $n_Q - n_{Q0}$, related to the amount of reactant A which has been converted, $n_{A0} - n_A$. Alternatively, the yield of a product Q relates the amount of Q formed to the amount of A fed:

$$Y_Q = \frac{n_Q - n_{Q0}}{n_{A0}} \quad (7.10)$$

Note that:

$$Y_Q = S_Q X_A \quad (7.11)$$

If the following reactions occur:



a mass balance for Q is required, besides the balance for A :

$$\frac{dn_A}{dt} = V R_{v,A} \quad (7.12)$$

$$\frac{dn_Q}{dt} = V R_{v,Q} \quad (7.13)$$

with the rate of production of Q following from:

$$R_{v,Q} = r_{v,1} - r_{v,2} \quad (7.14)$$

The balance equations (7.12 and 7.13) form a set of coupled ordinary differential equations, which has to be solved numerically. Analytical integration is possible for special cases only.

Assuming first-order reaction kinetics and constant density leads to:

$$\frac{dC_A}{dt} = -k_1 C_A \quad (7.15)$$

$$\frac{dC_Q}{dt} = k_1 C_A - k_2 C_Q \quad (7.16)$$

Integration of (7.15) and (7.16) with:

$$C_A = C_{A0} \quad \text{for} \quad t = 0 \quad (7.17)$$

$$C_Q = 0 \quad \text{for} \quad t = 0 \quad (7.18)$$

as initial conditions, gives following analytical expression for C_A and C_Q as a function of time:

$$C_A = C_{A0} e^{-k_1 t} \quad (7.19)$$

$$C_Q = \frac{C_{A0} k_1}{k_2 - k_1} \left(e^{-k_1 t} - e^{-k_2 t} \right) \quad (7.20)$$

Note that the concentration of P follows from the total mass balance:

$$C_P(t) = C_A - C_A(t) - C_Q(t) \quad (7.21)$$

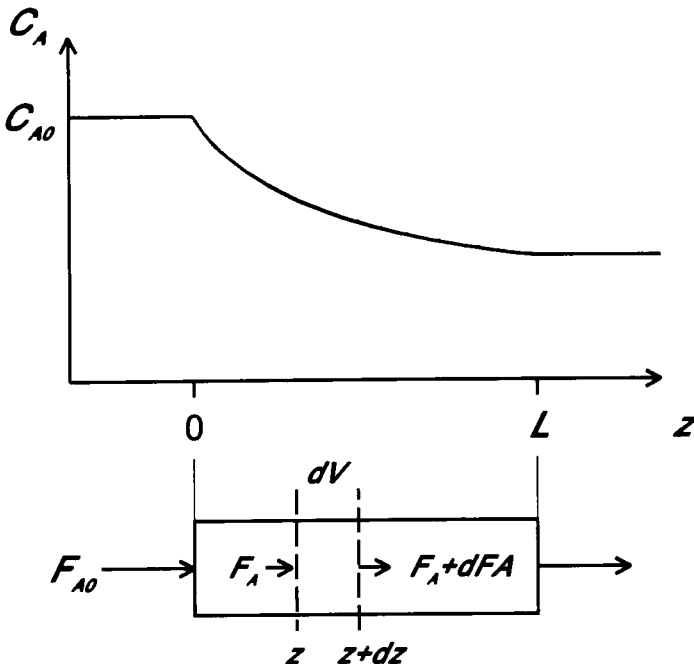


Fig. 7.1. Reactant concentration versus reactor length in a tubular reactor.

7.2.2 Plug Flow Reactor

Numerous reactions are performed by feeding the reactants continuously to cylindrical tubes, either empty or packed with catalyst, with a length which is 10 to 1000 times larger than the diameter. The mixture of unconverted reactants and reaction products is continuously withdrawn at the reactor exit. Hence, constant concentration profiles of reactants and products, as well as a temperature profile are established between the inlet and the outlet of the tubular reactor, see Fig. 7.1. This requires, in contrast to the batch reactor, the application of the law of conservation of mass over an infinitesimal volume element, dV , of the reactor. In contrast to a batch reactor the existence of a temperature profile does not allow us to consider the mass balances for the reacting components and the energy balance separately. Such a separation can only be performed for isothermal tubular reactors.

In view of the high length-to-diameter ratio of most tubular reactors the flow through them can in most cases be described adequately as a so-called plug flow. It is assumed that:

- flow occurs in one direction only, i.e. parallel to the axis of the tube;
- radial, i.e. perpendicular on the axis, non-uniformities can be neglected;
- flow occurs by forced convection only.

These assumptions lead to the picture of the flow as that of a plug of fluidum with uniform properties being pushed through the tube. In a plug flow reactor the mass balance for a component A over an infinitesimal reactor element, as defined in Figure 7.1, gives:

$$(F_A + dF_A) - F_A = R_{v,A} dV \quad (7.22)$$

The left-hand side of Eqn. (7.22) corresponds to the net flow of A out of the reactor element which, in the steady state, has to equal the net production rate of A, i.e. the right-hand side of (7.22). For a tubular reactor with a fixed catalytic bed, it is more convenient to relate the production rates to the catalyst mass, rather than to the reactor volume. Hence, the right-hand side of Eqn. 7.22 becomes:

$$R_{w,A} dW \quad (7.23)$$

where $R_{w,A}$ = the specific production rate of A, mol kg⁻¹_{cat} s⁻¹, and dW = the catalyst mass in the reactor element dV , kg_{cat}.

Analogous to the batch reactor, a fractional conversion of a reactant A can be defined as:

$$X_A = \frac{F_{A0} - F_A}{F_{A0}} \quad (7.24)$$

with F_{A0} being the molar flow rate of A at the reactor inlet, mol s⁻¹.

This leads to:

$$\frac{dX_A}{d(V/F_{A0})} = -R_{v,A} \quad (7.25)$$

or:

$$\frac{dX_A}{d(W/F_{A0})} = -R_{w,A} \quad (7.26)$$

Equations (7.25) or (7.26) are so-called continuity equations for A. Integration results in:

$$\frac{V}{F_{A0}} = - \int_0^{X_A} \frac{1}{R_{v,A}} dX \quad (7.27)$$

or:

$$\frac{W}{F_{A0}} = - \int_0^{X_A} \frac{1}{R_{w,A}} dX \quad (7.28)$$

Comparison with the corresponding Eqn. 7.4 for a batch reactor shows the

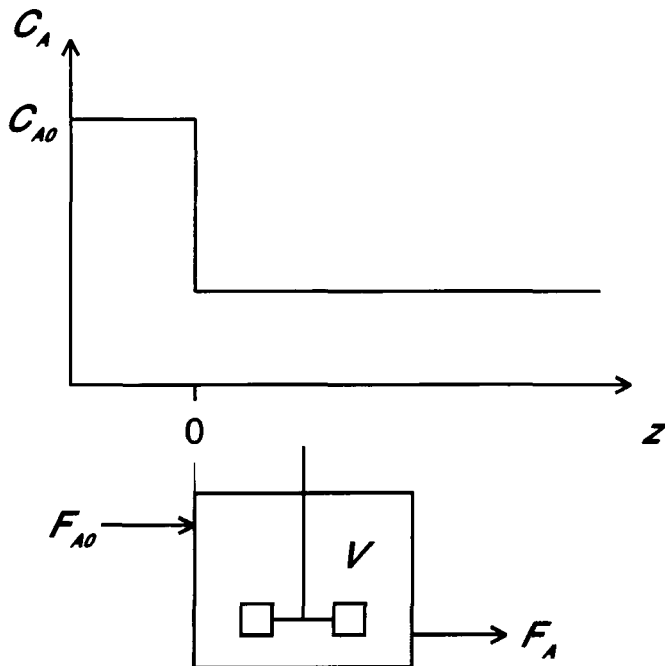


Fig. 7.2. Reactant concentration versus position in a CSTR.

mathematical analogy between a plug flow reactor and a batch reactor. The results obtained in the preceding paragraph can be transposed to the plug flow reactor, provided that a space time τ_0 is defined for the plug flow reactor by:

$$\tau_0 = \frac{VC_{A0}}{F_{A0}} \quad (7.29)$$

in s; or:

$$\tau_0 = \frac{WC_{A0}}{F_{A0}} \quad (7.30)$$

in $\text{kg}_{\text{cat}} \text{m}^{-3} \text{s}$.

7.2.3 Continuous Flow Stirred Tank Reactor (CSTR)

Another type of continuous flow reactor is found in industry: the continuous flow stirred tank reactor (CSTR), Fig. 7.2. Stirring of the reactor content might be necessary to increase the heat exchange with the surroundings or to maintain a heterogeneous catalyst in suspension. If more than one fluid phase is present in the reactor, stirring increases the contact surface area and, hence, the rate of mass transfer between these phases.

Mixing can be considered at two length scales. Macromixing relates to the mixing of fluid elements at the scale of the reactor. Ideal macromixing requires that the time scale at which the fluid elements are mixed can be neglected with respect to the time scale at which these elements flow through the reactor. Ideal micromixing requires that the time scale at which reacting molecules are mixed can be neglected when compared to the time scale at which they react. In a perfectly mixed flow reactor (CSTR) the reactor content is uniform at both length scales, both with respect to composition and to temperature. Hence, the mass balance for a component can be taken over the complete reactor, Fig. 7.2. At steady state this leads to:

$$F_A - F_{A0} = R_{v,A} V \quad (7.31)$$

Or, after introduction of the fractional conversion of A, Eqn. 7.24):

$$X_A = -R_{v,A} V/F_{A0} \quad (7.32)$$

Note that the uniform conditions in the reactor equal those at the reactor outlet, which implies that the production rate of A is also determined by the outlet conditions. The mass balance for a component in a CSTR is an algebraic equation, in contrast to the case of reactions in a batch or a plug flow reactor. For a single, irreversible first-order reaction and constant density, Eqn. 7.32 becomes:

$$X_A = k_1 C_{A0} (1 - X_A) V/F_{A0} \quad (7.33)$$

or, after substitution of Eqn. 7.29 and solving for X_A :

$$X_A = \frac{k_1 \tau_0}{1 + k_1 \tau_0} \quad (7.34)$$

Table 7.2 lists analytical relations between conversion or concentration for some simple reaction kinetics.

TABLE 7.2

CSTR: relations between conversion, X_A , or concentration, C_A , and $\tau_0 = VC_{A0}/F_{A0}$ (constant density) for simple reaction kinetics

$r_v/\text{mol m}^{-3} \text{s}^{-1}$	$X_A/\text{mol mol}^{-1}$	$C_A/\text{mol m}^{-3}$
k_0	$\frac{k_0 \tau_0}{C_{A0}}$	$C_{A0} - k_0 \tau_0$
$k_1 C_A$	$\frac{k_1 \tau_0}{1 + k_1 \tau_0}$	$\frac{C_{A0}}{1 + k_1 \tau_0}$
$k_2 C_A^2$	$\frac{1 - \sqrt{1 + 4k_2 C_{A0} \tau_0}}{2k_2 C_{A0} \tau_0}$	$\frac{-1 + \sqrt{1 + 4k_2 C_{A0} \tau_0}}{2k_2 \tau_0}$

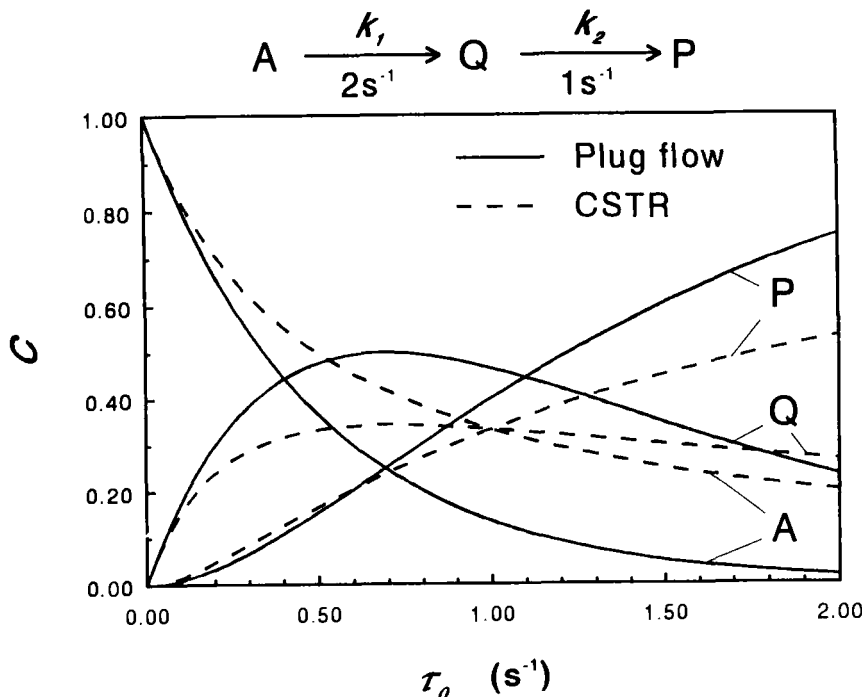


Fig. 7.3. Reactant and product concentrations for $A \rightarrow Q \rightarrow P$ ($k_1 = 2k_2$, constant density) versus batch time of τ_0 in a batch of plug flow reactor (solid lines) or in a CSTR (dashed lines).

It is worthwhile to compare the conversion obtained in an isothermal plug flow reactor with that obtained in a CSTR for given reaction kinetics. A fair comparison is given in Fig. 7.3 for irreversible first-order kinetics by showing the conversion obtained in both reactors as a function of τ_0 . The conversion of A obtained in a plug flow reactor is higher than that obtained in a CSTR. This holds for every positive partial reaction order with respect to A . For multiple reactions selectivities and yield enter into the picture.

$$S_Q = \frac{F_Q - F_{Q0}}{F_{A0} - F_A} \quad (7.35)$$

$$Y_Q = \frac{F_Q - F_{Q0}}{F_{A0}} \quad (7.36)$$

Figure 7.3 also compares the evolution of the concentrations of the intermediate Q and the product in case of two first-order reactions in series in a CSTR with that in a batch or plug flow reactor. For constant density, the mass balance for the reaction components in a CSTR are:

$$C_A = \frac{C_{A0}}{1 + k_1 \tau_0} \quad (7.37)$$

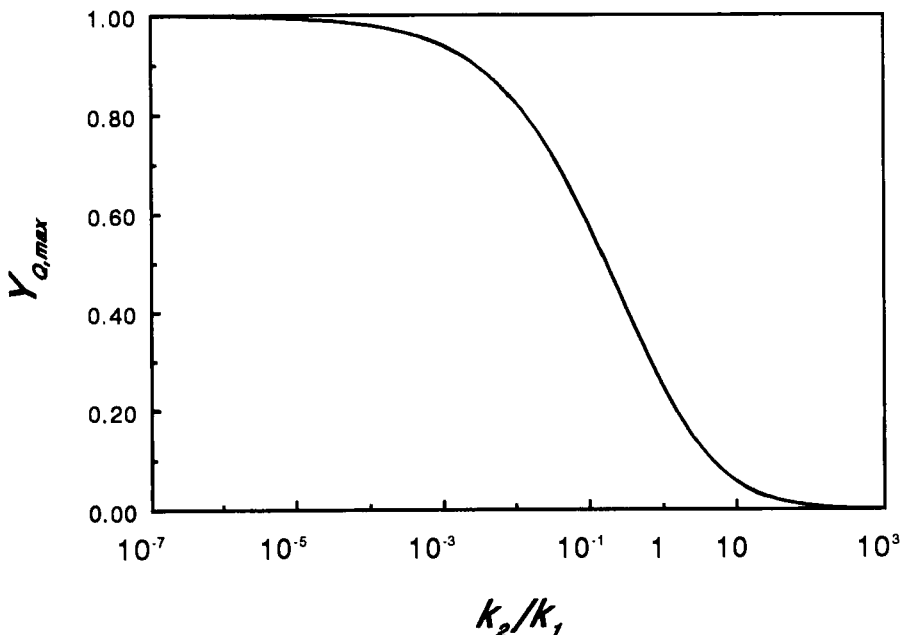


Fig. 7.4. Maximum yield of intermediate in a CSTR as a function of $\lambda_2 = k_2 / k_1$.

$$C_Q = \frac{k_1 C_{A0} \tau_0}{(1 + k_1 \tau_0)(1 + k_2 \tau_0)} \quad (7.38)$$

$$C_P = C_{A0} - C_A - C_Q \quad (7.39)$$

For positive reaction orders with respect to the reactants the intermediate yields obtained in a CSTR are lower than those obtained in a batch or a plug flow reactor.

The maximum yield for the intermediate Q is a function of k_2/k_1 only:

$$Y_{Q,\max} = \left(\sqrt{\frac{k_2}{k_1}} + 1 \right)^{-2} \quad (7.40)$$

This relationship is shown in Fig. 7.4.

7.2.4 Nonisothermal Reactors

In practice the heat effects associated with chemical reactions result in non-isothermal conditions. In the case of a batch reactor the temperature changes as a function of time, whereas an axial temperature profile is established in a plug flow reactor. The application of the law of conservation of energy, in a similar

way as the law of conservation of mass in the preceding paragraphs, leads to the so-called energy equation.

For a batch reactor, the accumulation of enthalpy results from the production of enthalpy and the transfer of heat from the surroundings:

$$mc_p \frac{dT}{dt} = (-\Delta_r H) r_v V - A_k U (T - T_u) \quad (7.41)$$

with m = mass of the reaction mixture, kg; c_p = specific heat capacity, $\text{J kg}^{-1} \text{K}^{-1}$; $\Delta_r H$ = reaction enthalpy, J mol^{-1} ; r_v = volumetric reaction rate, $\text{mol m}^{-3} \text{s}^{-1}$; V = volume of the reaction mixture, m^3 ; A_k = heat exchange surface area, m^2 ; U = global heat transfer coefficient, $\text{W m}^{-2} \text{K}^{-1}$; and T_u = temperature of the surroundings, K.

For a steady-state plug flow reactor, the increase of enthalpy over an infinitesimal reactor element results from the enthalpy production by reaction and the transfer of heat from the surroundings, leading to:

$$Gc_p \frac{dT}{dV} = (-\Delta_r H) r_v - \frac{4U}{d_t} (T - T_u) \quad (7.42)$$

with G = mass flow rate, kg s^{-1} , and d_t = tube diameter, m.

Note that:

$$dV = \frac{1}{4} \pi d_t^2 dz \quad (7.43)$$

For a steady-state perfectly mixed flow reactor the energy balance can be made over the complete reactor:

$$Gc_p(T - T_0) = (-\Delta_r H) r_v V - A_k U (T - T_u) \quad (7.44)$$

with T_0 = inlet temperature, K.

If more than one reaction occurs, the enthalpy production terms in Eqns. 7.41, 7.42 and 7.44 have to be obtained from a summation.

Note that the reaction kinetics depend on both the composition and the temperature, i.e. for a single reaction:

$$r_v = r_v(X_A, T) \quad (7.45)$$

Hence, the energy equation has always to be considered simultaneously with the corresponding continuity equation. This results in a set of ordinary differential equations, with as initial conditions:

$$X_A = 0 \quad \text{at} \quad t = 0 \quad (7.46)$$

$$T = T_0 \quad \text{at} \quad t = 0 \quad (7.47)$$

for a batch reactor, and:

$$X_A = 0 \quad \text{at} \quad z = 0 \quad (7.48)$$

$$T = T_0 \quad \text{at} \quad z = 0 \quad (7.49)$$

for a plug flow reactor. In general, a numerical integration is required to obtain the conversion and temperature as a function of batch time, t , or reactor length, z . For a perfectly mixed flow reactor, however, the conversion and the temperature follow from the solution of the set of algebraic Eqns. 7.32 and 7.44.

7.3 REACTION COMBINED WITH TRANSPORT

Up to this point it has been assumed that the composition and the temperature were uniform throughout the complete reactor for perfect mixing, or within an infinitesimal volume element for plug flow. These assumptions usually hold for homogeneously catalysed reactions involving a single phase. If the reactants are present in more than one phase, as in so-called gas–liquid reactions, or if a heterogeneous catalyst is involved, it is often necessary to relax the hypothesis of uniformity. Indeed, the presence of several phases requires transport in and/or transfer between these phases to allow reaction to take place. Since the driving force for transport and transfer of mass or heat is provided by concentration or temperature gradients, the latter cannot always be neglected. Consequently, the mass or enthalpy production terms in the reactor equations of the preceding paragraph are not always determined by the chemical (so-called intrinsic) kinetics only, but also by the rates of the physical transport and transfer phenomena. In such a situation the reaction is said to be transport limited.

7.3.1 Heterogeneous Catalysis

Figure 7.5 illustrates the possible different physical and chemical steps starting from a reactant A and ending in a reaction product B via a heterogeneously catalysed reaction path. There are seven steps:

1. Transfer of A from the fluid phase surrounding the catalyst pellet, the so-called bulk fluid phase, to the external surface of the pellet.
2. Transport from the external surface of the pellet through the pores towards the active sites on the interior surface.
3. Chemisorption of A on an active site * as A^* .
4. Surface reaction of A^* into B^* .
5. Desorption of B^* .
6. Transport of B through the pores towards the external surface of the pellet.
7. Transfer of B from the external surface of the pellet to the bulk fluid phase.

Steps 3–5 are strictly chemical and consecutive to each other: Hougen–Watson–Langmuir–Hinshelwood rate equations describing the rate of the purely chemical phenomenon consisting of steps (3)–(5) have been derived in the chapter on the

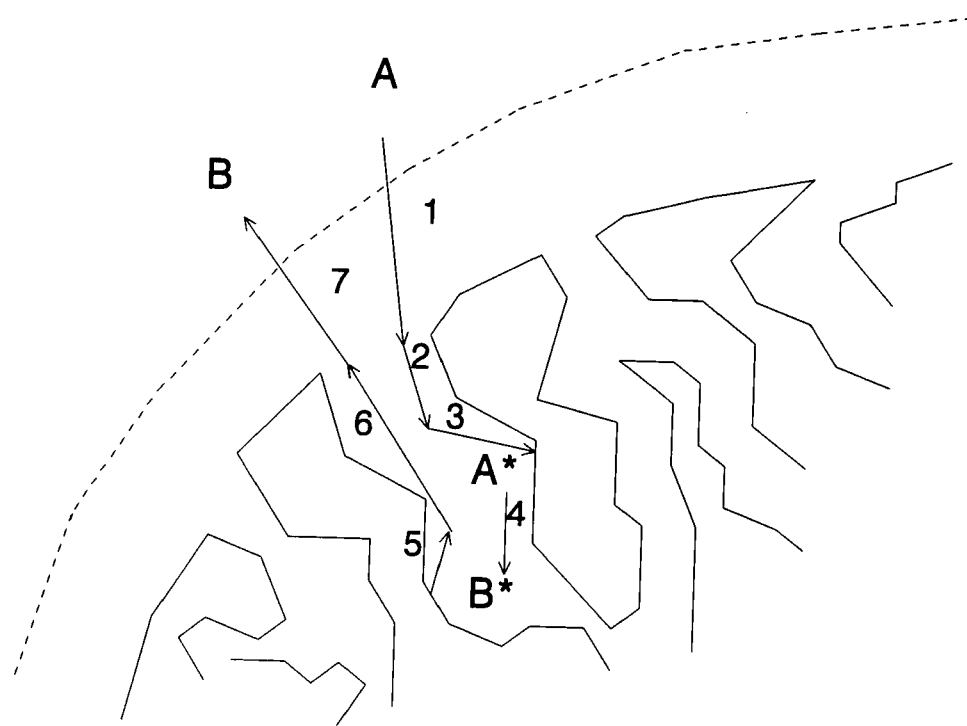


Fig. 7.5. Chemical and physical steps involved in the heterogeneously catalysed reaction $A \rightarrow B$ (*: active site).

kinetics of catalysed reactions. In the transport limited situation the supply of reactant and/or the removal of reaction product will not be sufficiently fast to keep pace with the potential intrinsic rate, and the concentrations of A and B inside the pores will be different from the corresponding concentrations in the bulk of the fluid phase.

The transfer steps 1 and 7 are strictly physical and in series with steps 3–5: the transfer occurs separately from the chemical reaction. The transport steps 2 and 6, however, cannot be separated from the chemical steps 3–5: the transport inside the pores occurs simultaneously with the chemical reaction. In the next sections these two situations are analyzed quantitatively.

7.3.1.1 Transport and reaction in series

External mass transfer

The transfer of mass from the bulk of a fluid phase to the external surroundings can be described by the so-called film model, see Fig. 7.6. The film model assumes the existence of a stagnant layer of thickness δ along the external surface of the

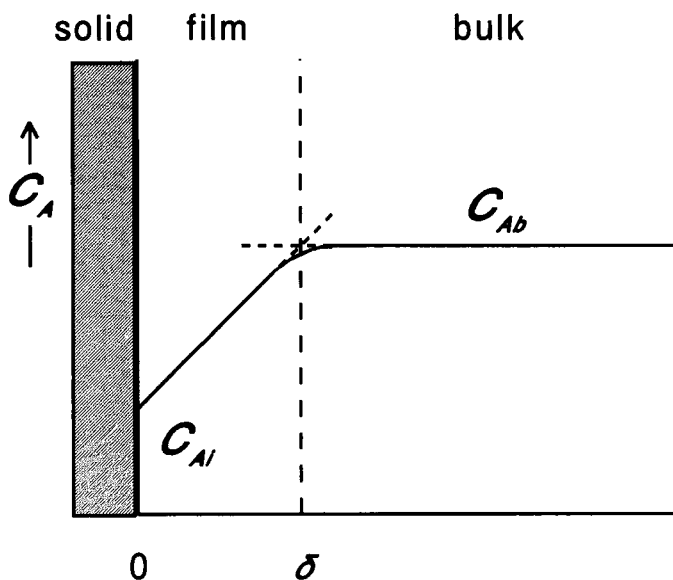


Fig. 7.6. External concentration profile. Solid line: existing profile; dashed line: profile according to the film model.

catalyst. The complete resistance to mass transfer is located in this layer. The concentration gradient allowing the transfer is thus also confined to this layer.

The rate of transfer, expressed as a molar flux N_A ($\text{mol m}^{-2} \text{s}^{-1}$), is proportional to the driving force, which with the film model gives:

$$N_A = k_{fA} (C_A - C_{Ai}) \quad (7.50)$$

with k_{fA} being the mass transfer coefficient for A , $\text{m}_i^3 \text{ m}_i^{-2} \text{ s}^{-1}$.

It can be shown (see Appendix A) that, if molecular diffusion towards the external surface is the only transport mechanism, the following relation holds:

$$k_{fA} = \frac{D_{Am}}{\delta y_{fA}} \quad (7.51)$$

where D_{Am} = the effective binary diffusion coefficient of A in the stagnant layer, $\text{m}_i^3 \text{ m}_i^{-1} \text{ s}^{-1}$, and y_{fA} = the film factor relative to equimolar counterdiffusion.

For ideal gases the effective binary diffusion coefficient can be calculated from molecular properties (see Appendix A). The film thickness, δ , is determined by hydrodynamics. Correlations are given in the literature which allow the calculation of the transfer coefficient in the case of equimolar counterdiffusion, k_f , rather than the film thickness, δ :

$$k_f = \frac{D_{Am}}{\delta} \quad (7.52)$$

At the steady state the flux of A towards the external surface of the catalyst pellet has to be equal to the rate of disappearance of A , expressed per unit external surface area:

$$N_A = r_{v,p} \frac{V_p}{A_p} \quad (7.53)$$

with $r_{v,p}$ = reaction rate per unit pellet volume mol $m_p^{-3} s^{-1}$; V_p = volume of a catalyst pellet, m_p^3 ; A_p = external surface area of a catalyst pellet, m_i^2 .

Note that the following relations hold:

$$r_{v,p} = r_w / \rho_p \quad (7.54)$$

$$r_w = a_s r_a \quad (7.55)$$

where r_w = specific reaction rate, mol $kg_{cat}^{-1} s^{-1}$; r_a = areal reaction rate i.e. per unit *internal* surface area, mol $m_p^{-2} s^{-1}$; a_s = specific *internal* surface area, $m_p^2 kg_{cat}^{-1}$; and ρ_p = pellet density, $m_p^3 kg_{cat}^{-1}$.

For an irreversible first-order reaction:

$$r_{v,p} = k_{v,p} C_{Ai} \quad (7.56)$$

Eqn. 7.53 becomes:

$$k_{fA} (C_A - C_{Ai}) = \frac{1}{a'_v} k_{v,p} C_{Ai} \quad (7.57)$$

where

$$a'_v = \frac{A_p}{V_p} \quad (7.58)$$

is the volumetric external surface area in $m_i^2 m_p^{-3}$.

Note that it is the concentration of A at the external surface which appears in the first-order rate expression and not the concentration of A in the bulk of the fluid phase. Solving Eqn. 7.57 for the concentration of A at the external surface gives:

$$C_{Ai} = \frac{k_{fA} a'_v}{k_{v,p} + k_{fA} a'_v} C_A \quad (7.59)$$

and for the observed reaction rate:

$$r_{v,p}^{obs} = \left(\frac{1}{k_{fA} a'_v} + \frac{1}{k_v} \right)^{-1} C_A \quad (7.60)$$

which shows that the observed rate is determined by a physical resistance:

$$\tau_D = \frac{1}{k_{fA} a'_v} \quad (7.61)$$

and by a chemical resistance:

$$\tau_R = \frac{1}{k_v} \quad (7.62)$$

τ_D and τ_R can be looked upon as the time scales for transfer and reaction, respectively. The observed rate can also be written as:

$$r_{v,p}^{\text{obs}} = \frac{k_v}{1 + Da_{II}} C_A \quad (7.63)$$

with

$$Da_{II} = \frac{\tau_D}{\tau_R} = \frac{k_v}{k_{fA}} a_v \quad (7.64)$$

The importance of external mass transfer limitations can now be discussed in terms of Da_{II} , the Damköhler number.

Figure 7.7 shows the concentration profiles which are established at the steady-state for different values of Da_{II} . Large values for Da_{II} correspond to strong mass transfer limitations, in which case the observed reaction rate becomes:

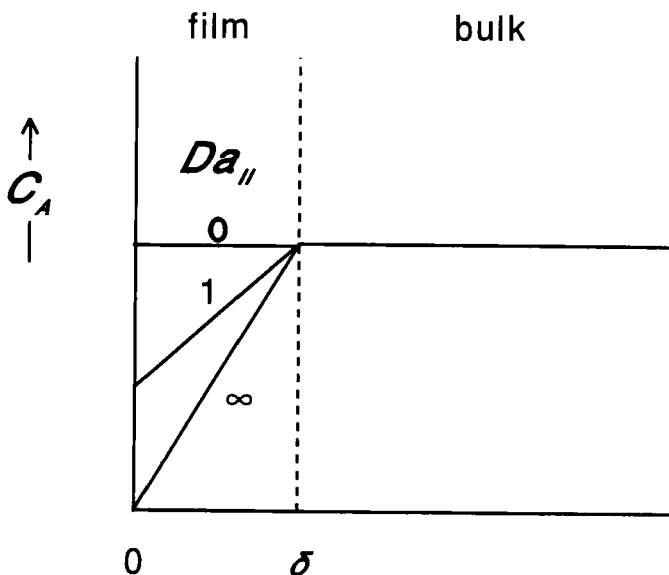


Fig. 7.7. External profiles according to film model for different values of Da_{II} .

$$r_{v,p}^{\text{obs}} = k_{fA} a'_v C_A \quad (7.65)$$

i.e. the observed reaction kinetics depend only on the mass transfer and hence are first order. The observed first-order kinetics are obtained independently of the intrinsically reaction kinetics, i.e. even for intrinsically higher reaction orders.

It should also be noted that in this regime the amount of A converted per unit time is proportional to be the external surface area and not to the catalyst volume, weight or internal surface area.

Low values for Da_{II} correspond to a situation where mass transfer limitations can be neglected:

$$r_{v,p}^{\text{obs}} = k_{v,p} C_A \quad (7.66)$$

i.e. the observed kinetics (Eqn. 7.66) agree with the intrinsic kinetics as the difference between the concentration in the bulk and at the external surface can be neglected.

Figure 7.8 shows the temperature dependence of:

$$k^{\text{obs}} = \left(\frac{1}{k_{fA} a'_v} + \frac{1}{k_v} \right)^{-1} \quad (7.67)$$

Increasing the temperature always leads to a strongly transfer limited regime, as the mass transfer coefficient is almost independent of temperature.

For positive reaction orders the existence of significant concentration differences between the bulk of the fluid phase and the external surface of the catalyst pellet leads to lower reaction rates. This can be expressed by the external effectiveness factor, η_e :

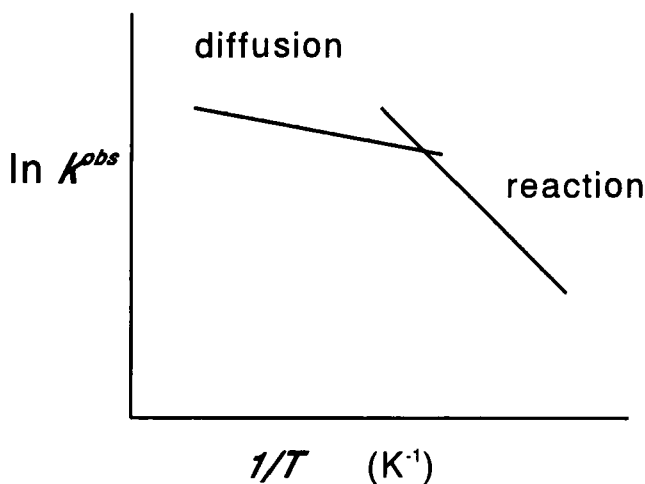


Fig. 7.8. The observed rate coefficient as a function of temperature for transport and reaction in series (first-order kinetics).

$$\eta_e = \frac{r_{v,p}^{\text{obs}}}{r_{v,p}(C_A)} \quad (7.68)$$

or:

$$\eta_e = \frac{r_{v,p}(C_{Ai})}{r_{v,p}(C_A)} \quad (7.69)$$

For intrinsic first-order kinetics Eqn. 7.69 becomes:

$$\eta_e = \frac{1}{1 + Da_{II}} \quad (7.70)$$

Equation 7.70 also holds for general reaction kinetics, provided the Da_{II} number is generalized to:

$$Da_{II} = \frac{\text{reaction rate}}{\text{maximum transfer rate}} \quad (7.71)$$

both numerator and denominator being calculated for the bulk conditions:

$$Da_{II} = \frac{r_{v,p}(C_A)}{k_{fA} a'_v C_A} \quad (7.72)$$

Both the calculation of the external effectiveness factor and of the Da_{II} number require the knowledge of the intrinsic rate expression, $r_{v,p}(C_A)$. The Carberry number [1]:

$$Ca = \eta_e Da_{II} \quad (7.73)$$

does not require this knowledge, but only the observation of the rate. Indeed, substitution of Eqns. 7.68 and 7.72 into Eqn. 7.73 gives:

$$Ca = \frac{r_{v,p}^{\text{obs}}}{k_{fA} a'_v C_A} \quad (7.74)$$

also:

$$Ca = \frac{C_A - C_{Ai}}{C_A} \quad (7.75)$$

Hence, low values of Ca correspond to the kinetic regime, whereas values of Ca close to one correspond to the transfer limited regime.

External heat transfer

In practice the effects of heat transfer from the bulk of a fluid phase to the external surface of a solid catalyst are more important than the effects of mass transfer. An approach analogous to that of mass transfer leads, for a single reactant, to:

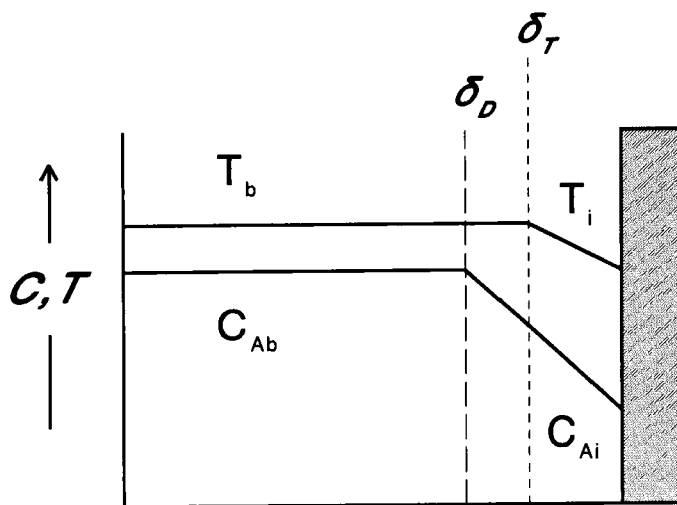


Fig. 7.9. Temperature and concentration profiles for an endothermic reaction.

$$\alpha a'_{\text{v}} (T - T_i) = \Delta_r H r_{\text{v},p} \quad (7.76)$$

where $\Delta_r H$ = reaction enthalpy, J mol^{-1} , and α = heat transfer coefficient, $\text{W m}^{-2} \text{K}^{-1}$.

Figure 7.9 shows the temperature and concentration profiles caused by transfer limitations in the case of an endothermic reaction. For an exothermic reaction the temperature at the external surface, T_i , increases with increasing transfer limitations. Hence the external effectiveness factor, η_e , becomes greater than 1 as soon as the decrease of the reactant concentration is compensated by the increase of the temperature.

Combination of Eqn. 7.76 with Eqns. 7.50 and 7.53 leads to:

$$\frac{\alpha(T_b - T_i)}{k_{fA}(C_{Ab} - C_{Ai})} = \Delta_r H \quad (7.77)$$

or, substituting expression 7.75 for the Carberry number in 7.77:

$$\frac{T_b - T_i}{T_b} = \frac{k_{fA} \Delta_r H C_{Ab}}{\alpha T_b} Ca = \beta_e Ca \quad (7.78)$$

which allows us to calculate the temperature difference from an observed rate.

The maximum relative temperature difference (external Prater number) is given by:

$$\frac{|\Delta T_{\max}|}{T_b} = \frac{k_{fA} |\Delta_r H| C_{Ab}}{\alpha T_b} = |\beta_e| \quad (7.79)$$

and may reach values up to 3 (corresponding to 100–1000 K) for a gaseous fluid phase.

7.3.1.2 Transport simultaneous with reaction

Mass transport

(a) Effective diffusivity

For most catalysts the fraction of active sites located on the external surface of the catalyst pellet can be neglected. The reactant has to be transported through the pores inside the pellet to reach the active sites.

The driving force for the transport is provided by a concentration gradient: as the reactant moves further towards the center of the pellet its concentration is decreased by reaction. The resistance to the transport mainly originates from collisions of the molecules, either with each other or with the pore walls. The latter dominate when the mean free path of the molecules is larger than the pore diameter. Usually both type of collisions are totally random, which amounts to saying that the transport mechanism is of the diffusion type. Hence the rate of transport, expressed as a molar flux in $\text{mol m}_p^{-2} \text{s}^{-1}$, in the case of equimolar counterdiffusion can be written as:

$$N_A = -D_{eA} \frac{dC_A}{dz} \quad (7.80)$$

where z = the pellet coordinate, defined as the perpendicular distance from the external surface, m_p , and D_{eA} = the effective diffusion coefficient of A in the pellet, $\text{m}_f^3 \text{m}_p^{-1} \text{s}^{-1}$.

Equation 7.80 is analogous to Fick's law. However, the effective diffusion coefficient has to take account of the fact that the diffusion does not occur in a homogeneous medium, but only through the pores of the pellet. This has two consequences. First, only a fraction, ϵ_p , of the pellet volume is occupied by pores. For an isotropic pore structure it can easily be shown that ϵ_p also equals the fraction of the area available for the diffusion towards the centre of the pellet. Second, the driving force for diffusion, according to Eqn. 7.80, is based on the concentration difference between a distance z and $(z + dz)$. In fact the orientation of pores deviates from the direction perpendicular to the external pellet surface. This results in a diffusion path along the pores which is longer than dz and hence a smaller driving force. This is accounted for by introducing a tortuosity factor, τ_p . Both corrections lead to the following expression for the effective diffusion coefficient:

$$D_{eA} = \frac{\epsilon_p D_A}{\tau_p} \quad (7.81)$$

Typical values for ε_p lie between 0.3 and 0.6, and for τ_p between 2 and 5. In the case of equimolar counterdiffusion D_A is given by the Bosanquet formula:

$$\frac{1}{D_A} = \frac{1}{D_{A\text{m}}} + \frac{1}{D_{A\text{k}}} \quad (7.82)$$

where $D_{A\text{m}}$ = the molecular diffusion coefficient corresponding to the intermolecular collisions, $\text{m}^2 \text{s}^{-1}$, and $D_{A\text{k}}$ = the Knudsen diffusion coefficient corresponding to collisions of the molecules with the pore walls, $\text{m}^2 \text{s}^{-1}$.

The calculation of $D_{A\text{m}}$ is outlined in Appendix A. For ideal gases the Knudsen diffusion coefficient is given by:

$$vcx d \propto D_{A\text{k}} = \frac{2}{3} \bar{r} \sqrt{\frac{8RT}{\pi M_A}} \quad (7.83)$$

where \bar{r} = average pore radius for a unimodal pore radius distribution, m.

(b) Effectiveness factor and Thiele modulus

When the diffusion of a reactant inside the pellet is not fast enough to compensate for its disappearance by reaction a decreasing concentration profile is established in the pellet. For positive partial reaction orders with respect to the reactant this leads to lower reaction rates at positions away from the external surface and hence to a lower reaction rate when averaged over the complete pellet volume. A measure for the degree of internal diffusion limitations is given by the internal effectiveness factor, η , defined as:

$$\eta = \frac{\text{reaction rate with internal diffusion limitation}}{\text{reaction rate at external surface conditions}} \quad (7.84)$$

or:

$$\eta = \frac{\frac{1}{V_p} \int r_{v,p}(C_A) dV}{r_{v,p}(C_{A_i})} \quad (7.85)$$

The observed reaction rate is given by:

$$r_{v,p}^{\text{obs}} = r_{v,p}(C_{A_i}) \eta \quad (7.86)$$

It also follows from the above definition that the effectiveness can be conveniently calculated from the ratio of fluxes through the external surface:

$$\eta = \frac{N_A|_{z=0}}{r_{v,p}(C_{A_i}) / a'_v} \quad (7.87)$$

Obviously the effectiveness factor, η , depends upon the effective diffusion coefficient, D_{eA} , and kinetic parameters such as a first-order rate coefficient, $k_{v,p}$, as well as on the shape of the catalyst pellet.

Consider, by way of example, an irreversible first-order reaction, $A \rightarrow B$, occurring in a pellet with slab geometry. As a result of the concentration profile, the reaction rate depends on the position within the catalyst pellet. Hence, a mass balance for the reactant has to be taken over an infinitesimal slice of the slab. At the steady state this leads to:

$$N_{A,z+dz} - N_{A,z} = -k_{v,p} C_A dz \quad (7.88)$$

or

$$\frac{dN_A}{dz} = -k_{v,p} C_A \quad (7.89)$$

or, after substitution of Eqn. 7.80 and assuming a constant effective diffusivity:

$$D_{eA} \frac{d^2 C_A}{dz^2} = k_{v,p} C_A \quad (7.90)$$

with as boundary conditions:

$$C_A = C_{A_i} \text{ at } z = 0 \quad (7.91)$$

$$\frac{dC_A}{dz} = 0 \text{ at } z = L \quad (7.92)$$

if the slab thickness equals $2L$.

Introduction of the dimensionless variables:

$$C_A^* = \frac{C_A}{C_{A_i}} \quad (7.93)$$

and

$$z^* = \frac{z}{L} \quad (7.94)$$

transforms Eqn. 7.90 into:

$$\frac{d^2 C_A^*}{dz^{*2}} = \frac{L^2 k_{v,p}}{D_{eA}} C_A^* \quad (7.95)$$

with, as boundary conditions:

$$C_A^* = 1 \text{ at } z^* = 0 \quad (7.96)$$

$$\frac{dC_A^*}{dz^*} = 0 \text{ at } z^* = 1 \quad (7.97)$$

It follows from Eqn. 7.95 that the concentration profile depends on a single dimensionless number which is equal to the ratio of the time scale for internal diffusion:

$$\tau_D = \frac{L^2}{D_{eA}} \quad (7.98)$$

to the time scale for reaction:

$$\tau_R = \frac{1}{k_{v,p}} \quad (7.99)$$

and, hence, can be called, after Damköhler:

$$Da_{II} = \frac{L^2 k_{v,p}}{D_{eA}} \quad (7.100)$$

Low values of Da_{II} corresponds to a situation where internal diffusion limitations, and hence internal concentration gradients, can be neglected, i.e. the observed rate agrees with that expected from the intrinsic reaction kinetics. Low values of Da_{II} lead to an effectiveness factor, η , close to 1. Large values of Da_{II} correspond to strong internal diffusion limitations. In the limit the internal diffusion is potentially so slow that the reactants do not penetrate the pellet at all. In this case the reaction is limited to the external surface of the pellet. Large values of Da_{II} lead to an effectiveness factor, η , close to 0.

The exact shape of the concentration profile follows from the integration of the corresponding continuity Eqn. 7.95:

$$C_A = \frac{\cosh \phi (z^* - 1)}{\cosh \phi} \quad (7.101)$$

with:

$$\phi = L \sqrt{\frac{k_{v,p}}{D_{eA}}} \quad (7.102)$$

ϕ is referred to as the Thiele modulus. From Eqn. 7.100 it follows that:

$$Da_{II} = \phi^2 \quad (7.103)$$

Figure 7.10 shows the internal concentration profiles calculated according to Eqn. 7.101 for different values of the Thiele modulus. Knowing the exact internal concentration profile, Eqn. 7.101, allows us to calculate the molar flux through the external surface of the slab from Eqn. 7.80):

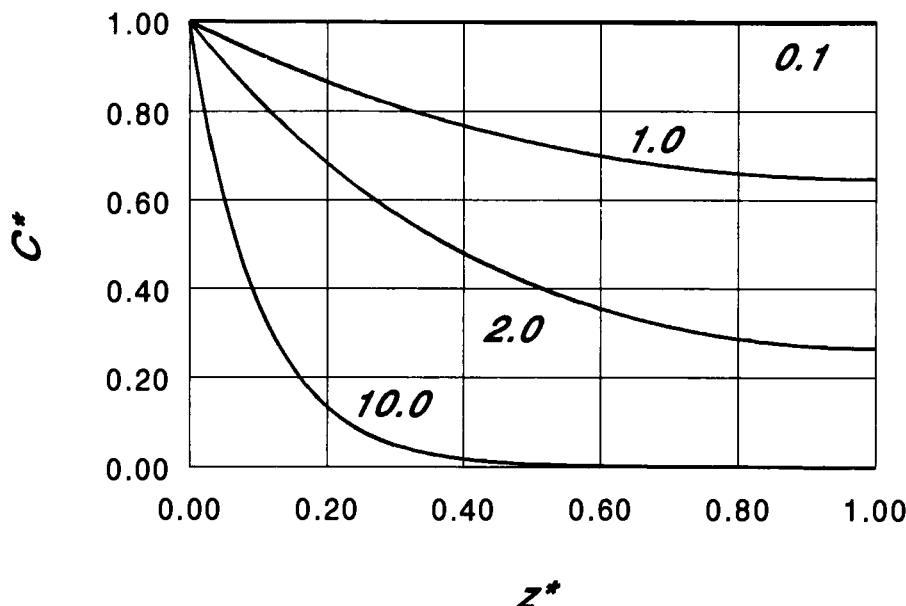


Fig. 7.10. Reactant concentration profiles within a catalyst slab for an irreversible first-order reaction, at different values of the Thiele modulus.

$$N_A|_{z=0} = -D_{eA} \frac{dC_A}{dz} \Big|_{z=0} \quad (7.104)$$

which gives:

$$N_A|_{z=0} = k_{v,p} C_{Ai} L \frac{\tanh \phi}{\phi} \quad (7.105)$$

The flux that would be established in the absence of internal diffusion limitations is given by:

$$N_A^{\text{intr}} = k_{v,p} C_{Ai} L \quad (7.106)$$

which, according to Eqn. 7.87, leads to the following expression for the effectiveness factor:

$$\eta = \frac{\tanh \phi}{\phi} \quad (7.107)$$

Figure 7.11 shows relation 7.107 on a double logarithmic scale. Two asymptotes can be distinguished:

$$\lim_{\phi \rightarrow 0} \eta = 1 \quad (7.108)$$

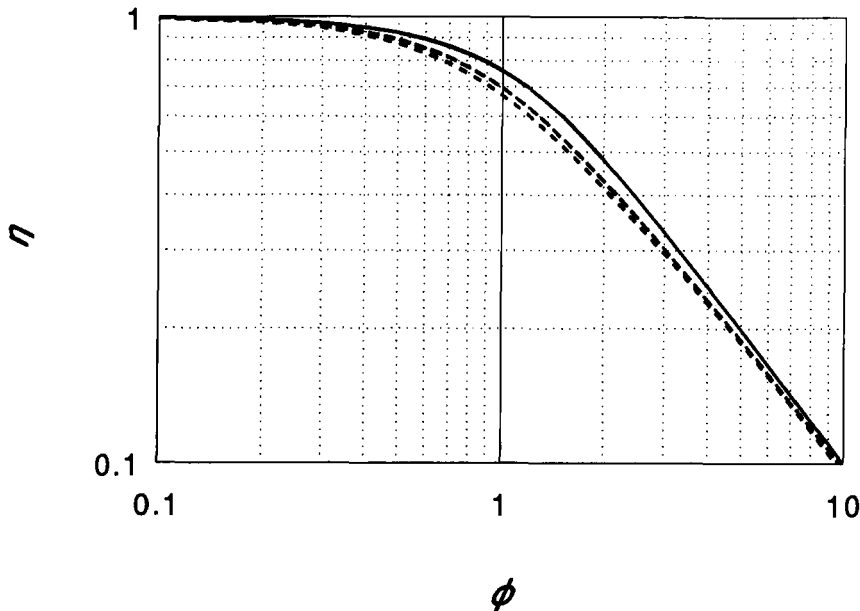


Fig. 7.11. Effectiveness factor for slab (—), cylinder (---) and sphere (- - -) geometry as function of the generalised Thiele modulus.

and:

$$\lim_{\phi \rightarrow \infty} \eta = \frac{1}{\phi} \quad (7.109)$$

For a pellet shape such as a sphere or a cylinder, expressions analogous to 7.107 can be derived along the same lines as for a slab geometry.

Figure 7.11 also shows the relationship between the effectiveness factor and the Thiele modulus for other pellet shapes. In general the linear dimension L of the slab is replaced by:

$$L = \frac{1}{a'_v} = \frac{V_p}{A_p} \quad (7.110)$$

which leads to a Thiele modulus generalized for particle geometry:

$$\phi = \frac{1}{a'_v} \sqrt{\frac{k_{v,p}}{D_{eA}}} \quad (7.111)$$

For spherical pellets a'_v is given by:

$$a'_v = \frac{6}{d_p} \quad (7.111)$$

Note that the asymptotic behaviour, Eqns. 7.108 and 7.109, is not affected by the pellet shape due to the choice of L .

The above analytical relations have been derived for irreversible first-order kinetics. Arbitrary kinetics do not generally allow an analytical solution. The continuity equation for A , written again for a slab geometry:

$$\frac{d}{dz} \left(D_{eA} \frac{dC_A}{dz} \right) = r_{v,p} \quad (7.113)$$

has to be integrated numerically to obtain the internal concentration profile and the exact value of the effectiveness factor. Further generalisation of the Thiele modulus in such a way that the relation between the effectiveness factor and this modulus remains, at least approximately, as given in Figure 7.11 is possible [2]. Indeed, a first integration of the continuity equation for A , starting from the centre plane of the slab, leads to:

$$D_{eA} \frac{dC_A}{dz} = \left[2 \int_{C_{Ai}|_{z=L}}^{C_A} D_{eA} r_{v,p} dC \right]^{1/2} \quad (7.114)$$

taking account of the boundary condition (7.92) at the centre plane. The effectiveness factor is given by:

$$\eta = \frac{D_{eA} \frac{dC_A}{dz}|_{z=0}}{r_{v,p} (C_{Ai}) L} \quad (7.115)$$

or, substituting Eqn. 7.114:

$$\eta = \frac{\left[2 \int_{C_{Ai}|_{z=L}}^{C_{Ai}} D_{eA} r_{v,p} dC \right]^{1/2}}{r_{v,p} (C_{Ai}) L} \quad (7.116)$$

At the centre plane and for strong internal diffusion limitations the concentration of A either vanishes or equals the equilibrium concentration, leading to:

$$\eta = \frac{a'_v \left[2 \int_{C_{A,\text{eq}}}^{C_{Ai}} D_{eA} r_{v,p} dC \right]^{1/2}}{r_{v,p} (C_{Ai})} \quad (7.117)$$

for strong internal diffusion limitations.

To generalize the asymptotic behaviour of η shown in Fig. 7.11 to arbitrary kinetics, it then suffices to define the generalised Thiele modulus as:

$$\phi = \frac{r_{v,p}(C_{Ai})}{a'_v \left[2 \int_{C_{A,eq}}^{C_{Ai}} D_{eA} r_{v,p} dC \right]^{1/2}} \quad (7.118)$$

Substituting Eqn. 7.118 into 7.117, indeed, also gives:

$$\eta = \frac{1}{\phi} \quad (7.119)$$

for strong internal diffusion limitations. From Eqns. 7.112, 7.117 and 7.119 it follows that, for strong internal diffusion limitations, the effectiveness factor is inversely proportional to the pellet diameter.

It is easily shown that, for irreversible first-order kinetics, Eqn. 7.118 reduces to 7.111.

Obviously, the use of Fig. 7.11 with the generalized Thiele modulus as defined by 7.118 requires a knowledge of the rate equation in order to be able to calculate the integral in the denominator. For partial reaction orders varying from one-half to three the deviations from the exact numerical solution are limited to 15%. These deviations are highest at Thiele moduli around one.

If, under experimental conditions internal mass transfer limitations are present then for an n th-order irreversible reaction the observed reaction rate can be written as:

$$r_{v,p}(\text{obs}) = \eta r_{v,p}(C_{Ai}) = \frac{r_{v,p}(C_{Ai})}{\phi} = a'_v \left(\frac{2}{n+1} \right)^{1/2} \left(\frac{k_{v,p}}{D_{eA}} \right)^{1/2} C_{Ai}^{\frac{(n+1)}{2}} \quad (7.120)$$

This result implies that it is not the intrinsic kinetics that are observed, but the so-called disguised or false kinetics. This has as consequences that:

- the observed rate is inversely proportional to d_p ;
- the observed reaction order is now $(n+1)/2$;
- the observed activation energy equals $(E_a + E_D)/2$, with E_D being the ‘activation’ energy for diffusion.

Heat transport

When heat effects are important, one has to account simultaneously for heat transport, mass transport, and reaction. Heat transport through a catalyst pellet can be described by the Fourier law:

$$q = -\lambda_e \frac{dT}{dz} \quad (7.121)$$

with λ_e being the effective conduction coefficient in the pellet, $\text{W m}^{-1} \text{K}^{-1}$.

The steady-state enthalpy balance for a slab with thickness $2L$ is then given by:

$$\lambda_e \frac{d^2T}{dz^2} = \Delta_r H r_{v,p}(C_A, T) \quad (7.122)$$

As the rate expression also depends on the concentrations of the reaction components, a continuity equation has to be considered simultaneously with the energy equation (7.122):

$$D_{eA} \frac{d^2C_A}{dz^2} = r_{v,p}(C_A, T) \quad (7.123)$$

The boundary conditions are:

$$T = T_i, C_A = C_{Ai} \text{ at } z = 0 \quad (7.124)$$

$$\frac{dT}{dz} = 0, \frac{dC_A}{dz} = 0 \text{ at } z = L \quad (7.125)$$

Elimination of $r_{v,p}(C_A, T)$ from Eqns. 7.122 and 7.123 leads to:

$$\frac{\lambda_e}{\Delta_r H} \frac{d^2T}{dz^2} = D_{eA} \frac{d^2C_A}{dz^2} \quad (7.126)$$

Integration of Eqn. 7.126 taking account of the boundary conditions Eqn. 7.124 and 7.125 gives an algebraic relation between the temperature and the concentration:

$$T - T_i = \frac{D_{eA} \Delta_r H}{\lambda_e} (C_A - C_{Ai}) \quad (7.127)$$

and allows us to calculate the temperature difference between the external surface and the position in the pellet where $C_A = 0$. The maximum relative temperature difference can be written as:

$$\frac{|T - T_i|_{\max}}{T_i} = \frac{D_{eA} |\Delta_r H| C_{Ai}}{\lambda_e T_i} = |\beta_i| \quad (7.128)$$

where β_i represents the internal Prater number.

Equations 7.127 and 7.128 hold for any pellet geometry. Substituting typical values for the quantities appearing in the right-hand side of 7.128 leads to the conclusion that, for most practical purposes, the internal temperature differences can be neglected.

7.3.2 Homogeneous Catalysis

Several important homogeneously catalysed reactions involve more than one phase. Examples are found in carbonylations, hydroformylations, hydrogenations, hydrocyanation, oxidations and polymerisations. Typically reactant(s) such as oxygen, hydrogen and / or carbon monoxide have to be transferred from the gas phase to the liquid phase, where reaction occurs. The liquid phase contains the homogeneous catalyst together with a liquid reactant and often a solvent. The transport from one phase to the other again requires a driving force in the form of concentration or temperature gradients. The latter can usually be neglected. Figure 7.12 shows the concentration profiles which are established in a direction perpendicular to the gas–liquid interface.

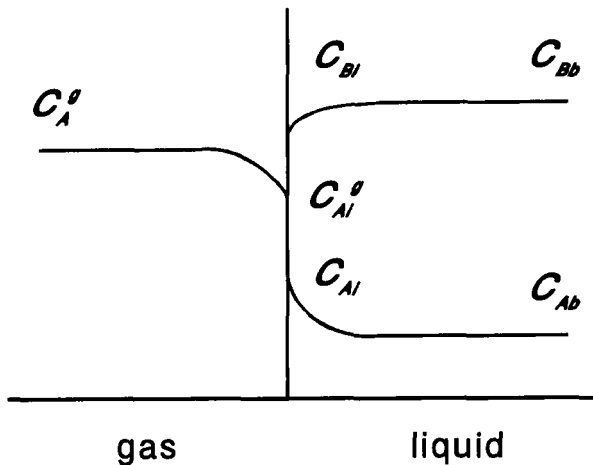


Fig. 7.12. Concentration profile of a reactant in the neighbourhood of a gas–liquid interface with a homogeneously catalysed reaction in the liquid phase.

Several steps can be distinguished:

1. transport of A from the bulk of the gas phase to the gas–liquid interface.
2. transfer of A at the interface from the gas to the liquid phase.
3. transport of A towards the bulk of the liquid.
4. reaction of A in the liquid.

Steps 1 and 2 are strictly physical and consecutive to each other. In most cases the resistances corresponding to steps 1 and 2 can be neglected when compared to those corresponding to steps 3 and 4. This means that the liquid phase concentration of A, C_{Ai}^1 , can be calculated from:

$$C_{Ai}^1 = \frac{p_A}{H_A} \quad (7.129)$$

where H_A = the Henry coefficient of A , Pa m 3 mol $^{-1}$, and p_A = partial pressure of A in the bulk of the gas phase, Pa.

Steps 3 and 4 cannot, in general, be separated from each other: the transport away from the interface occurs simultaneously with the chemical reaction. In the next section this will be analyzed quantitatively in a way analogous to Section 7.3.1.

7.3.2.1 Transport simultaneous with reaction

Utilization factor

For positive partial reaction orders with respect to the reactant which has to be transferred, the existence of a concentration profile leads to a reaction rate per unit reaction volume, i.e. liquid volume, which is lower than the volumetric rate that would be obtained in the absence of concentration gradients. The extent of this slowing down of the reaction can be expressed by the effectiveness factor, also called liquid utilization factor in this context, defined for a single reaction as:

$$\eta_L = \frac{\text{reaction rate with transport limitations}}{\text{reaction rate at the conditions prevailing at the liquid side of the interface}} \quad (7.130)$$

It follows from the above definition that for an irreversible first-order reaction, the utilization factor is given by:

$$\eta_L = \frac{N_A|_{y=0} a_v}{k_v C_{Ai}} \quad (7.131)$$

where the superscript, l, has been omitted for convenience of notation, and with k_v = the volumetric first-order rate coefficient, s $^{-1}$, and $a_v = A_L / V_L$ the volumetric interface surface area, m 2 m $^{-3}$.

The calculation of the molar flux of A at the interface, $N_A|_{y=0}$, follows from the film theory.

Film theory

In the film theory the complete resistance to mass transfer from the interface to the bulk of the liquid is confined to a fictitious film along the interface. The bulk of the fluid is considered to be perfectly mixed in the direction perpendicular to the interface, i.e. the concentration of A is uniform beyond the film. Figure 7.13 shows the concentration profile of A according to the film theory.

Furthermore, the only transport mechanism considered in the film is that of molecular diffusion perpendicular to the interface. The diffusion of A in the fictitious liquid film obeys Fick's law:

$$N_A = -D_A \frac{dC_A}{dy} \quad (7.132)$$

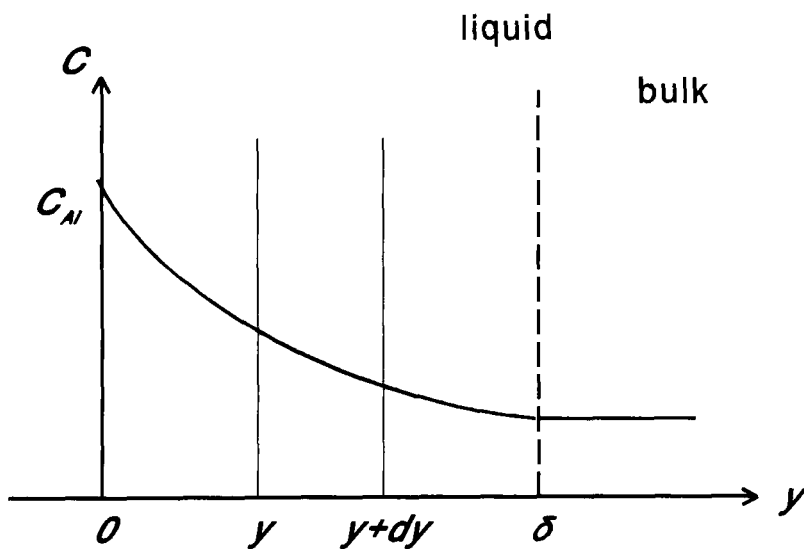


Fig. 7.13. Concentration profile of a reactant A in the liquid phase according to the film theory (δ = film thickness).

with D_A being the molecular diffusion coefficient of A , $\text{m}_\text{L}^2 \text{ m}^{-1} \text{ s}^{-1}$.

In the absence of reaction — i.e. for purely physical transfer of A from gas to liquid — the flux is independent of y and Eqn. 7.132 can be integrated to:

$$N_A = \frac{D_A}{\delta} (C_{Ai} - C_{Ab}) \quad (7.133)$$

for a constant diffusion coefficient. The film thickness, δ , is an unknown. But the mass transfer coefficient, k_L :

$$k_\text{L} = \frac{D_A}{\delta} \quad (7.134)$$

can be calculated from correlations available in the literature.

In the presence of reaction, the molar flux of A at a position y within the film follows from the derivative of the concentration profile at that position. The latter follows from a balance for A over an infinitesimal volume element, between y and $y + dy$, of the fictitious film:

$$D_A \frac{d^2 C_A}{dy^2} = -R_{v,A} \quad (7.135)$$

or, for an irreversible first-order reaction, and after introducing dimensionless variables:

$$\frac{d^2 C_A^*}{dy^*{}^2} = \frac{\delta^2 k_v}{D_A} C_A^* \quad (7.136)$$

with:

$$C_A^* = \frac{C_A}{C_{Ai}} \quad (7.137)$$

$$y^* = \frac{y}{\delta} \quad (7.138)$$

and as boundary conditions:

$$C_A^* = 1 \quad \text{at } y^* = 0 \quad (7.139)$$

$$C_A^* = C_{Ab}^* \quad \text{at } y^* = 1 \quad (7.140)$$

The concentrations which define the boundary conditions, i.e. C_{Ai} and C_{Ab} , follow from mass balances for A in the bulk of the gas and the liquid phase. Only if these phases are perfectly mixed do C_{Ai} nor C_{Ab} depend on the position in the reactor.

From 7.136 it is clear that the concentration profile within the film depends on a dimensionless number, completely analogous to the Damköhler number (7.100) of Section 7.3.1.2:

$$Da_{II} = \frac{\delta^2 k_v}{D_A} \quad (7.141)$$

and which equals the ratio of the time scale for mass transfer to that for chemical reaction. Integration of 7.136 with the boundary conditions 7.139 and 7.140 leads to:

$$C_A^* = \frac{\sinh [\gamma(1 - y^*)] + C_{Ab}^* \sinh \gamma y^*}{\sinh \gamma} \quad (7.142)$$

with:

$$\gamma = \delta \sqrt{\frac{k_v}{D_A}} = Da_{II}^{1/2} \quad (7.143)$$

the so-called Hatta number, completely analogous to the Thiele modulus of Section 7.3.1.2.

It follows from Eqn. 7.134 that for irreversible first-order kinetics the Hatta number, γ , can be calculated from:

$$\gamma = \frac{\sqrt{k_v D_A}}{k_L} \quad (7.144)$$

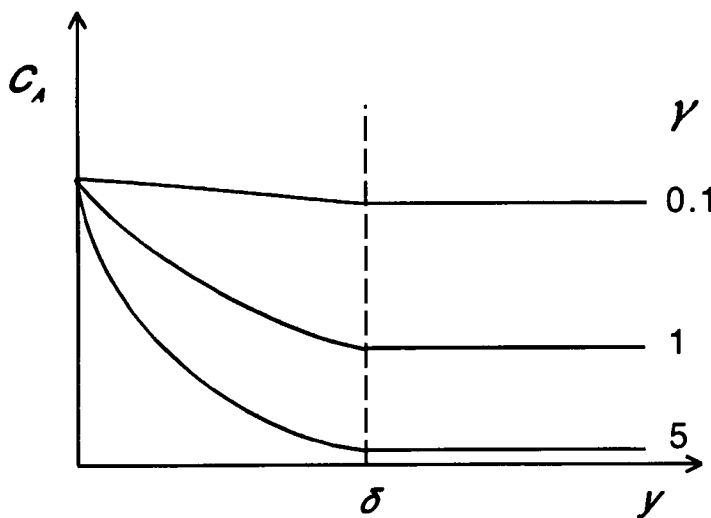


Fig. 7.14. Concentration profiles in a liquid phase with a homogeneous catalyst for irreversible first-order kinetics at different values of the Hatta number. Reactant A has to be transferred from the gas phase.

Figure 7.14 shows the concentration profiles of the reactant A calculated with Eqn. 7.142 for different values of the Hatta number.

Application of Fick's law (7.132) allows us to calculate the corresponding molar fluxes, e.g. at the gas–liquid interface:

$$N_A|_{y=0} = \frac{\gamma}{\tanh \gamma} \left(1 - \frac{C_{Ab}}{C_{Ai} \cosh \gamma} \right) k_L C_{Ai} \quad (7.145)$$

Hence, for an irreversible first-order reaction, the utilization factor of the liquid phase follows from Eqn. 7.131 as:

$$\eta_L = \frac{1}{Sh_m \gamma \tanh \gamma} \left(1 - \frac{C_{Ab}}{C_{Ai} \cosh \gamma} \right) \quad (7.146)$$

with:

$$Sh_m = \frac{k_L}{a_v D_A} \quad (7.147)$$

the dimensionless Sherwood number, the general physical meaning of which is the ratio of the time scale for molecular diffusion to that for the global mass transfer. In this particular situation the Sherwood number also equals the ratio of the total liquid volume (i.e. of the liquid present in the bulk and in the film) to the volume of the liquid in the film. Indeed substitution of 7.134 in 7.147 leads to:

$$Sh_m = \frac{1}{a_v \delta} \quad (7.148)$$

or:

$$Sh_m = \frac{V_L}{A_L \delta} \quad (7.149)$$

Equation 7.146 for the utilization factor corresponds to 7.107 for the case of heterogeneous catalysis with diffusional limitations. The analogy between 7.146 and 7.107 is complete when $Sh_m = 1$, i.e. when the reaction occurs simultaneously with diffusion throughout the complete liquid volume. The presence of a Sherwood number, besides the Hatta number, is needed to describe situations where a significant part of the reaction occurs in the bulk of the liquid, i.e. in series with the transport through the film. Such a situation is often encountered. Typical values for the Sherwood number are:

$$10 < Sh_m < 5000 \quad (7.150)$$

as can be concluded from the values for k_L , a_v and D_A given in Table 7.3.

TABLE 7.3

Typical values for the parameters involved in mass transfer from gas to liquid [3]

$k_L / m_f^3 m_i^{-2} s^{-1}$	$5 \times 10^{-5} - 5 \times 10^{-4}$
$a_v / m_f^2 m_i^{-3}$	$10^2 - 10^3$
$D_A / m_f^3 m_i^{-1} s^{-1}$	$10^{-9} - 10^{-8}$

Typical values for the Hatta number of industrial reaction involving homogeneous catalysts are:

$$10^{-2} < \gamma < 1 \quad (7.151)$$

Following Weisz, a criterion featuring only observable quantities can be applied to assess the degree of slowing down by mass transfer of a homogeneously catalysed reaction:

$$\Phi_L = \eta_L \gamma^2 \quad (7.152)$$

Indeed, substitution of Eqns. 7.131 and 7.144 into 7.152 leads, for irreversible first-order kinetics, to:

$$\Phi_L = \frac{N_A|_{y=0} a_v D_A}{k_L^2 C_{Ai}} \quad (7.153)$$

where $N_A|_{y=0}$, a_v and C_{Ai} can be observed and D_A and k_L calculated.

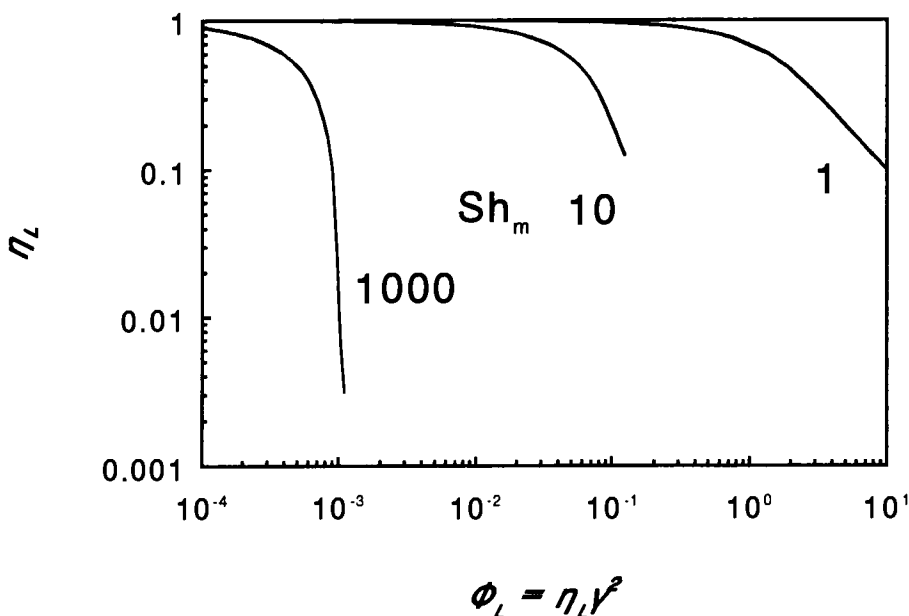


Fig. 7.15. Liquid utilization factor versus Φ_L for an irreversible first-order reaction at different values of the modified Sherwood number.

Figure 7.15 shows the utilization factor versus the observable Φ_L for the different values of Sh_m .

In most practical situations a utilization factor tending towards 1 can be achieved. There is practically no reaction in the film. The reaction essentially occurs in the bulk of the liquid phase. Hence, homogeneously catalysed reactions are performed in reactors with a continuous liquid phase and a dispersed gas phase. The gas transfer rate can often be kept sufficiently high by simply bubbling the gas through the liquid. For highly exothermic reactions mechanical stirring may be used to improve the heat transfer from the reactor toward the internal heat exchangers or the cooling jacket.

Multiple reactions

In case of multiple reactions one has to account not only for slowing down of the reaction rates but also the effects on selectivity and yield.

If the following reactions are considered:



with first-order kinetics, it was shown in Section 7.2.3 that in an ideal (i.e. homogeneous) continuous stirred tank reactor the maximum yield of Q is given by:

$$\gamma_{Q,\max} = \left(\sqrt{\frac{k_2}{k_1}} + 1 \right)^{-2} \quad (7.40)$$

This section treats a situation typical of homogeneously catalysed reactions. A is absorbed from the fluid phase 1 and reacts to give Q in the fluid phase 2. Q may then either desorb into the gas phase or react further to P . The application of the film model leads to the concentration profiles shown in Fig. 7.16.

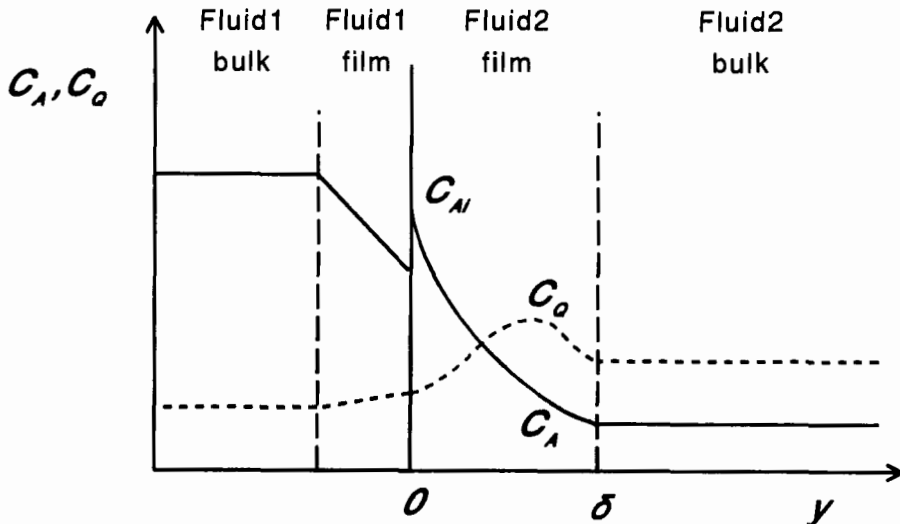


Fig. 7.16. Concentration profiles corresponding to $A \rightarrow Q \rightarrow P$ according to the film model as applied by Bridgwater [4].

Analytical expressions for the concentration profiles shown can be obtained by integrating the continuity equations for A and Q with the boundary conditions corresponding to Fig. 7.16 without terms for transport by convection or any other mechanism. The yield of Q then follows from:

$$\gamma_Q = \frac{D_Q \frac{dC_Q}{dy} \Big|_{y=0}}{-D_A \frac{dC_A}{dy} \Big|_{y=0}} \quad (7.154)$$

and can be shown to be determined not only by:

$$\gamma_A = \frac{\sqrt{k_{v1} D_A}}{k_L} \quad (7.155)$$

and:

$$Sh_m = \frac{V_L}{A_L \delta} \quad (7.149)$$

i.e. by the dimensionless groups characterizing the absorption-reaction of A , but also by:

$$\lambda_1 = \frac{k_L D_Q}{k_g H_Q D_A} \quad (7.156)$$

which, for $D_Q \approx D_A$, equals the ratio of the liquid-side mass transfer coefficient to the gas-side mass transfer coefficient of Q , and:

$$C_Q^* = \frac{p_Q|_{y=0}}{H_Q C_A} \quad (7.157)$$

i.e. the concentration of Q on the liquid side of the interface in equilibrium with the gas phase relative to the concentration of A , and finally by:

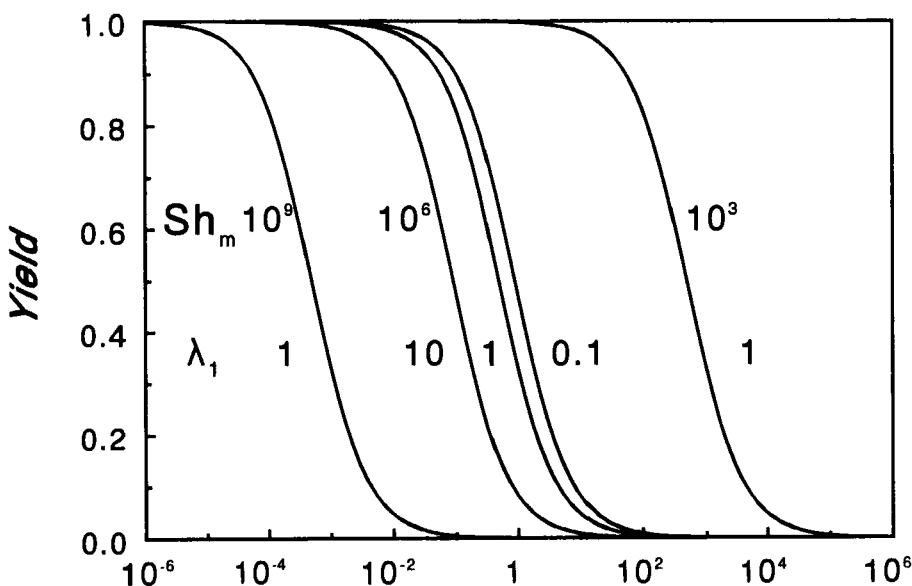
$$\lambda_2 = \frac{k_{v2} / D_Q}{k_{v1} / D_A} \quad (7.158)$$

which, for $D_Q \approx D_A$, determines the intrinsic chemical yield that can be obtained, viz. 7.40. Bridgwater calculated the yield of Q for different combinations of the numbers enumerated above. Figure 7.17 shows results obtained for a situation not unlikely to be encountered in homogeneously catalysed reactions involving two fluid phases.

The lower values of Sh_m correspond to a relatively high interfacial surface area a_v . Q is able to diffuse back into the gas before it undergoes further reaction. Under such conditions the yield of Q can be good even for λ_2 much greater than 1. Also, a comparison of Figs. 7.17 and 7.4 reveals a much better yield than the yield obtained in a continuous stirred tank reactor.

For larger values of Sh_m this advantage disappears as B now reacts further before it can desorb into the gas phase.

Although $\gamma_A = 10^{-3}$ corresponds to negligible conversion of A in the film, the yield of Q is significantly affected by λ_1 , i.e. the relative rate at which Q diffuses from the film to the bulk. This is shown in Fig. 7.17 for $Sh_m = 10^6$. Low values of λ_1 favour high yields of Q . Evidently, the same holds for C_Q^* : the lower the solubility of Q in the liquid the higher the maximum yield of Q .



$$\lambda_2 = k_{v2}/k_{v1}$$

Fig. 7.17. Yield of Q versus $\lambda_2 = k_{v2}/k_{v1}$ ($A \xrightarrow{1} Q \xrightarrow{2} P$, first-order kinetics: $\gamma_A = 10^{-3}$, $C_Q^* = 0$, $D_Q/D_A = 1$) for different values of Sh_m and λ_1 . A is transferred from gas to liquid phase [4].

7.4 EXPERIMENTAL DETERMINATION OF REACTION KINETICS

7.4.1 Scope

The ultimate goal of catalysis, and catalyst development in particular, is the maximization of the rate of a desired reaction. Despite considerable progress during the last years, the formulation of new catalysts is still very much a matter of trial and error, requiring substantial experimental effort. An initial screening of candidate catalysts should lead to a reliable preliminary selection. The most promising formulations should be investigated in greater detail. Finally, the scaling up of the catalytic reaction towards the industrial application should be envisioned. Such a scale-up starts from the knowledge of detailed reaction kinetics, i.e. rate equation(s) describing the effects of process conditions, such as temperature and concentrations, on the reaction rate(s). Detailed reaction kinetics also allow the optimization of existing processes. From a more fundamental point of view, experimental rate data can provide information which, combined with spectroscopic techniques, improves insight in the catalytic reaction mechanisms and hence provides guidelines for further improvement.

The principles underlying kinetic experiments do not depend upon the specific objectives aimed at. No matter what the purpose, accurate are required, which can easily be interpreted. Hence this section relates to catalyst screening and development, as well as to detailed reaction kinetics either for design or for fundamental purposes.

7.4.2 Reactors

The selection and design of a reactor for bench-scale kinetic experiments should be considered case by case. It is important to stress, however, that one should not try to build a bench scale replica of what is believed to be or is the industrial reactor. Industrial reactors are designed to operate a process in a profitable way, which is not the case for experimental reactors. In industrial reactors heat, mass and momentum transport has to occur in an economically justifiable way, leading in general to temperature, concentration and/or pressure gradients inside the reactor. Also, the hydrodynamics can be rather complicated. Fluidised beds, bubble columns and trickle flow reactors require model equations which involve several physical parameters, besides the intrinsic kinetic parameters. Empirical correlations allowing the calculation of these physical parameters are available. The validity region of these correlations is often limited to the hydrodynamic conditions prevailing during industrial operation, however. Hence, the only straightforward and accurate access to rate data is provided by laboratory reactors where care has been taken that the effects of transport phenomena on the measured rates can be neglected. The means to ascertain this on the scale of the catalyst pellet are given in Section 7.4.2.3. Also, the hydrodynamics should be ideal in laboratory reactors: either plug flow or perfect mixing should be established. Laboratory reactors should be operated isothermally and isobarically. If this cannot be achieved, at least the temperature profiles in the reactor have to be measured. Finally, operating with continuous flow allows, in contrast to batch operation, the variation of the conversion in an independent way, with proper account being taken of catalyst deactivation.

In the following section the two commonly preferred laboratory reactors — the plug flow reactor and the continuous stirred tank reactor (CSTR) — are discussed.

7.4.2.1 Plug flow reactor

Plug flow reactors are often used to investigate heterogeneously catalysed reactions. Typically 0.1–10 g of catalyst with a pellet diameter smaller than 1 mm is loaded into a tube of 1 cm diameter and a few dm long. A central thermocouple well allows the measurement of the temperature inside the catalytic bed.

The assumptions underlying plug flow and the corresponding continuity equations have been given previously in Section 7.2.2.

For a catalytic reaction the continuity equation for a reactant provides access to the corresponding net production rate through the measurement of the reactant conversion versus the space-time W/F_{A0} followed by differentiation:

$$R_{w,A} = - \frac{d X_A}{d(W / F_{A0})} \quad (7.159)$$

The conversion can be determined by a measurement of the flow rates, Eqn. 7.24. This usually involves a chromatographic analysis of the reactor outlet stream. A complete kinetic analysis requires the determination of X_A versus W/F_{A0} curves over the range of temperatures, total pressures and inlet compositions y_0 , of interest. The production rates obtained after differentiation are then regressed by a postulated rate equation on featuring parameters, such as preexponential factors, A_0 , and activation energies, E_a :

$$\hat{R}_{w,A} = \hat{R}_{w,A}(T, p_t, y_0; A_0, E_a, \dots) \quad (7.160)$$

The regression consists of the minimization of the sum of squares of the residuals between the observed and the calculated production rates by adjusting the unknown kinetic parameters [5]:

$$S(\beta) = \sum_{i=1}^n (R_i - \hat{R}_i)^2 \rightarrow \text{Min} \quad (7.161)$$

where β = adjustable parameters such as A_0 , E_a ; i = experiment index; and n = total number of experiments.

Such a method of kinetic analysis is termed the differential method since the residual sum of squares is based on rates. The required differentiation of X_A versus W/F_{A0} data can be a source of errors, however. To avoid this, the same set of data can be analyzed by the so-called integral method, which consists of minimizing a residual sum of squares based on the directly observed conversions:

$$S(\beta) = \sum_{i=1}^n (X_{Ai} - \hat{X}_{Ai})^2 \rightarrow \text{Min} \quad (7.162)$$

The calculated conversions, \hat{X}_{Ai} , are obtained by integration of the continuity equation (7.159) for A for each of the investigated conditions i .

In some cases it is possible to perform experiments at conversions low enough to allow neglect of the effect of conversion on the rate. In other words: the rate is constant throughout the plug flow reactor. Equation (7.159) can then be integrated to:

$$R_{w,A} = - \frac{X_A}{W/F_{A0}} \quad (7.163)$$

which shows that the measurement of the conversion can give direct access to the rate. A plug flow reactor operated in such a way that Eqn. 7.163 holds, is called a differential plug flow reactor.

The plug flow reactor has the following advantages:

- simple set-up, basically a tube with packed catalytic bed;
- variation of W/F_{A0} by changing the amount of catalyst W or F_{A0} allows a broad range of conversions to be covered.

And the following disadvantages:

- low flow rates can lead to concentration and temperature gradients over the stagnant layer surrounding the catalyst pellets;
- conversions are measured rather than rates;
- care must be taken to ensure plug flow;
- isothermicity is hard to realize for reactions with strong heat effects.

Concerning the plug flow requirement, the following rules of thumb can be applied for $Re_p > 10$:

$$\frac{d_t}{d_p} > 10 \quad (7.164)$$

with d_t being the inner tube diameter, m_r

$$\frac{L}{d_p} > 50 \quad (7.165)$$

with L being the length of the bed, m_r

If Eqn. 7.164 is fulfilled, the effect of the reactor wall on the flow pattern can be neglected. Deviation from plug flow can also occur by superposition on the plug flow of a diffusion like transport mechanism in the axial direction. This can be neglected provided Eqn. 7.165 is satisfied. A more detailed analysis is necessary for $Re_p < 10$.

Deviations from isothermicity can be suppressed by diluting the catalyst bed with inert particles up to volumetric ratios of inert to catalytical material of 20 to 1. Higher dilutions can cause deviations from plug flow because all the catalyst pellets are no longer contacted by the reactant to the same extent. Radial temperature gradients are more critical than axial gradients. In order to limit the effects of heat transport limitations on the observed rates to 5% it is sufficient that for a single reaction with the following kinetics:

$$r_{v,p} = A_0 e^{-E_a/RT} f(C_A) \quad (7.166)$$

the following criterion holds [6]:

$$\frac{|\Delta_r H| r_{v,p}^{obs} (1 - \epsilon_b) (1 - b) d_t^2}{\lambda_{er} T_w} < \frac{1.6 RT_w / E_a}{1 + 8 \frac{d_p}{d_t Bi_w}} \quad (7.167)$$

where $1 - \epsilon_b$ = bed fraction of the reactor volume, $m_b^3 m_r^{-3}$; $1 - b$ = catalyst pellet fraction of the bed, $m_p^3 m_b^{-3}$; T_w = internal wall temperature, K; and:

$$Bi_w = \frac{\alpha_w d_p}{\lambda_{er}} \quad (7.168)$$

is the thermal Biot number, the ratio of the radial heat transport resistance through the bed to the heat transfer resistance at the wall, where: α_w = heat transfer resistance at the wall, $W m^{-2} K^{-1}$; and λ_{er} = effective radial thermal conductivity of the bed, $W m^{-1} K^{-1}$.

A complete derivation of Eqn. 7.167 would take us too far from the central theme of this chapter. Basically, a perturbation approach is followed, i.e. the rate equation is linearized with respect to the temperature in the vicinity of the inner wall temperature T_w by a Taylor expansion, neglecting the higher order terms:

$$r_{v,p}(T) = r_{v,p}(T_w) \left(1 + \frac{T - T_w}{T_w} \frac{E_a}{RT_w} \right) \quad (7.169)$$

Correlations for α_w and λ_{er} are found in the literature. Values of $10^3 W m^{-2} K^{-1}$ for α_w and of $1 W m^{-1} K^{-1}$ for λ_{er} are typical. Biot numbers lie around 1. It follows from Eqn. 7.167 that high dilutions with inert and small tube diameters favour radial isothermicity. Also an inert with high thermal conductivity should be used, whenever possible.

7.4.2.2 Continuous flow stirred tank reactor (CSTR)

Perfectly mixed flow reactors are often used for kinetic studies when a liquid phase is involved. The perfect mixing, as defined in Section 7.2.1, is obtained by mechanical stirring. Homogeneous catalysts are continuously fed in parallel with the reactants. Catalyst recovery is not a concern during kinetic studies. Heterogeneously catalyzed reactions can be investigated by having the catalyst pellets suspended in the liquid phase of so-called slurry reactors. The pellets with a diameter usually lower than $100 \mu m$ can be maintained in the reactor by membrane filters. The heterogeneous catalyst can also be packed in a fixed bed over which the fluid stream is internally recirculated, as shown schematically in Figure 7.18.

External recirculation, also represented schematically in Fig. 7.18, is an alternative to achieve perfect mixing, which is convenient when only gas streams are involved. The minimum external recirculation ratio depends on the reaction

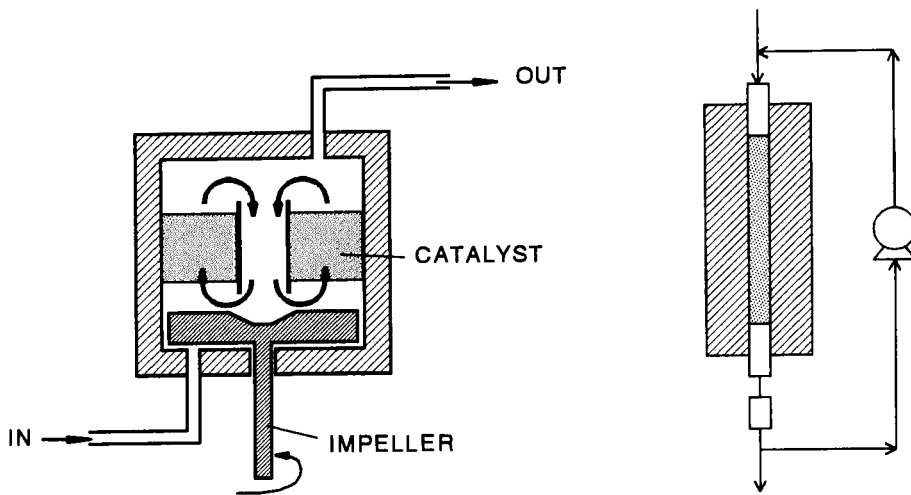


Fig. 7.18. CSTR with fixed bed and internal (Berty reactor) or external recirculation.

kinetics, but typically ratios higher than 10 are required to achieve perfect mixing. Experiments performed with a CSTR give direct access to the net production rates of components by writing down the corresponding mass balances:

$$R_{w,A} = - \frac{X_A}{W/F_{A0}} \quad (7.170)$$

Hence, the differential method of kinetic analysis can be applied.

The CSTR presents the following advantages:

- isothermicity is easily achieved;
- concentration and temperature gradients over the stagnant film surrounding the catalyst pellets can be neglected;
- rates are directly measured.

And the following disadvantages:

- rates are measured at outlet conditions, cf. Fig. 7.2, which cannot be set in a straightforward way;
- dead volumes in the reactor or the external recirculation lines can lead to blank effects, i.e. conversion in the absence of catalyst.

7.4.2.3 Transport disguises at pellet scale

In order to obtain accurate and easily interpretable rate data it is not sufficient to ensure either plug flow or perfect mixing i.e. ideality at reactor scale. For heterogeneously catalyzed reactions in particular, care has to be taken that heat

and/or mass transport to or from the catalytically active site does not interfere with the intrinsic rate measurement. The transport phenomena involved have been analyzed in Section 7.6.3.1. This section provides criteria to assess whether or not transport disguises occur and discusses how to avoid them.

External transfer

Assessment of external transfer effects on measured rates requires the knowledge of the corresponding transfer coefficients.

(a) Slurry reactors

For laboratory slurry reactors the following correlation can be used to calculate the mass transfer coefficient [7]:

$$Sh = 2 + 0.4 Re^{1/4} Sc^{1/3} \quad (7.171)$$

with:

$$Sh = \frac{k_{LS} d_p}{D_A}$$

the Sherwood number characteristic for ratio of the total mass transfer to the diffusive mass transfer.

$$Sc = \frac{\mu}{\rho D_A} \quad (7.172)$$

$$Re = \frac{N_p d_I^5 N_I^3 d_p^4 \rho^3}{\mu^3 V_L} \quad (7.173)$$

the Reynolds number, where: d_I = diameter of stirring blade, m; N_I = stirring frequency, s^{-1} ; V_L = liquid volume, m^3 ; N_p = power number, typically 5 in laboratory slurry reactors; and d_p = catalyst pellet diameter, $6 \cdot 10^{-5} \text{ m} < d_p < 10^{-3} \text{ m}$.

Typical values for the mass transfer coefficient lie around $10^{-3} \text{ m}^3 \text{ m}^{-2} \text{ s}^{-1}$ which is sufficiently high to allow neglect of the effects of mass transfer from the bulk of the liquid to the external pellet surface on the measured rates. In order to verify this it is sufficient to substitute the calculated mass transfer coefficient in Eqn. 7.74 for the Carberry number, bearing Eqn. 7.75 in mind.

The heat transfer coefficient can be calculated from the mass transfer coefficient by means of the Chilton–Colburn analogy, also called the j factor analogy. The j factors are defined as:

$$j_D = Sh Re^{-1} Sc^{-1/3} \quad (7.174)$$

$$j_H = Nu Re^{-1} Pr^{-1/3} \quad (7.175)$$

with:

$$Nu = \frac{\alpha_{LS} d_p}{\lambda_f} \quad (7.176)$$

the Nusselt number, characteristic for the ratio of the total heat transfer to the conductive heat transfer; and:

$$Pr = \frac{c_p \mu}{\lambda_f} \quad (7.177)$$

In case of perfect Chilton–Colburn analogy, both factors are equal:

$$j_D = j_H \quad (7.178)$$

and α_{LS} follows from k_{LS} :

$$\alpha_{LS} = \rho c_p \left(\frac{Sc}{Pr} \right)^{2/3} k_{LS} \quad (7.179)$$

Typical values for the heat transfer coefficient lie around $10^4 \text{ W m}^{-2} \text{ K}^{-1}$. Heat transfer effects rarely affect rates measured in slurry reactors.

When one or more reactants are fed as a gas, the possible effects of the transfer from gas to liquid have also to be considered, of course. Here, too, correlations allowing the calculation of the corresponding transfer coefficients are available. Gas–liquid transfer effects can be easily diagnosed experimentally, however. The absence of gas–liquid transfer effects can be assumed if the observed specific rate is independent of the stirring frequency and/or of the catalyst concentration over the range of conditions investigated.

(b) Fixed bed reactors

In laboratory fixed bed reactors, Reynolds numbers based on the pellet diameter can be as low as one, leading to a relatively thick stagnant fluid film around the pellet. The following correlations can be used to calculate the transfer coefficients [8]:

$$j_D = 1.66 Re_p^{-0.51} \quad (7.180)$$

for $10^{-2} < Re_p < 50$ and [9]:

$$j_H = 1.10 (Re_p^{0.41} - 0.15)^{-1} \quad (7.181)$$

for $13 < Re_p < 2136$ with:

$$Re_p = \frac{4G d_p}{\pi d_t^2 \mu} \quad (7.182)$$

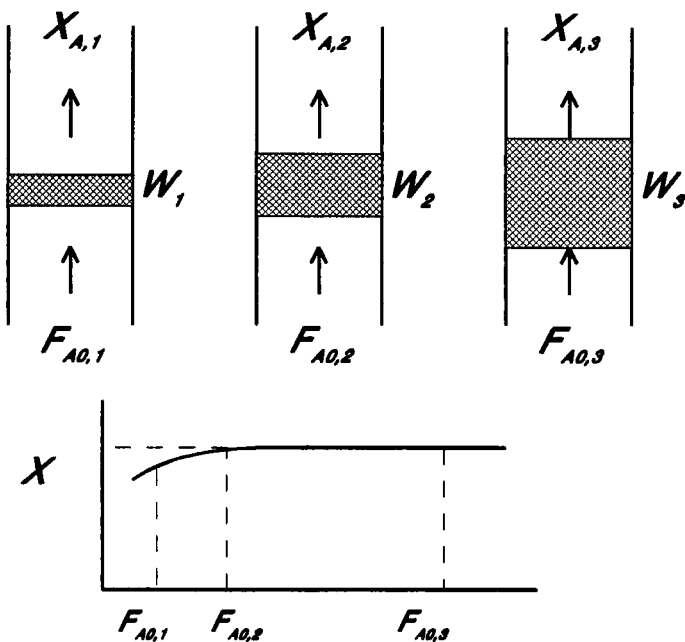


Fig. 7.19. Experimental tests to diagnose external mass transfer effects.

Correlation 7.181 should be used with care at low Reynolds numbers. Typical values for gas–solid transfer are $1 \text{ m}_f^3 \text{ m}_i^{-2} \text{ s}^{-1}$ for the mass transfer coefficient and $10^2 \text{ W m}^{-2} \text{ K}^{-1}$ for the heat transfer coefficient.

Substitution of the calculated value for the mass transfer coefficient, k_{fA} , in expression 7.74 for the Carberry number again allows us to assess whether or not mass transfer effects can be neglected.

Figure 7.19 represents schematically a way to determine experimentally whether external mass transfer can be neglected. Transfer effects do not occur when the conversion for a given space-time does not depend on the flow rate. The test is not very sensitive, however. This is caused by the small dependence of the mass transfer coefficient on the flow rate at the low Reynolds numbers prevailing in laboratory fixed bed reactors.

The assessment of the heat transfer effects requires a linearisation of rate expression (7.166) around the bulk temperature T_b :

$$r_{v,p}^{\text{obs}} = r_{v,p}(T_b) \left(1 + \frac{T_i - T_b}{T_b} \frac{E_a}{RT_b} \right) \quad (7.183)$$

Combination of Eqn. 7.183 with the energy balance for a spherical pellet:

$$\alpha \frac{6}{d_p} (T_b - T_i) = \Delta_r H r_{v,p}^{\text{obs}} \quad (7.184)$$

gives:

$$r_{v,p}^{\text{obs}} = r_{v,p}(T_b) \left(1 - \frac{d_p \Delta_r H r_{v,p}^{\text{obs}}}{6\alpha T_b} \frac{E_a}{RT_b} \right) = r_{v,p}(T_b) (1 - Ca \beta_e \gamma) \quad (7.185)$$

If the deviation between the observed rate and the rate corresponding to the bulk temperature has to be less than 5%, the following criterion is obtained:

$$\frac{d_p |\Delta_r H| r_{v,p}^{\text{obs}}}{\alpha T_b} < 0.3 \frac{RT_b}{E_a} \quad (7.186)$$

Note that criterion 7.186 requires a knowledge of the apparent activation energy for the reaction. Criterion 7.186 holds whether internal diffusion limitations exist or not. When the criterion concerning external heat transfer is compared to criterion 7.167 concerning radial heat transport limitations through the bed, it can been seen that the latter are more critical unless:

$$\frac{\alpha}{\lambda_{er}} (1 - \epsilon_b) (1 - b) d_t < 5.3 \quad (7.187)$$

which is rather unusual.

Internal diffusion

Internal diffusion limitations can generally be easily avoided in laboratory slurry reactors as the minimum of the pellet diameter is determined by the maximum of the pore size of the membrane filter used to maintain the catalyst in the reactor. Membrane filters allowing the use of pellets with a diameter of 1 μm are commercially available.

In fixed bed reactors, however, the catalyst pellet diameter has to be at least 0.1 mm in order to avoid an excessive pressure drop over the bed. With such a diameter internal diffusion effects can be important.

Introduction of the Weisz modulus:

$$\Phi = \eta \phi^2 \quad (7.188)$$

leads to the so-called Weisz criterion to assess the importance of internal diffusion:

$$\Phi >> 1 \quad (7.189)$$

corresponds to strong internal diffusion limitations. Indeed large values of the Weisz modulus can only correspond to large values of the generalized Thiele modulus, and, hence, to strong internal diffusion limitations.

Substituting Eqns. 7.86 and 7.118 into 7.188 leads, for spherical pellets, to [10]:

$$\Phi = \frac{r_{v,p}^{\text{obs}}}{r_{v,p}(C_{Ai})} - \frac{r_{v,p}^2(C_{Ai})}{a_v^2 \left[2 \int_{C_{A,\text{eq}}}^{C_{Ai}} D_{eA} r_{v,p}(C) dC \right]} \quad (7.190)$$

or, assuming a constant D_{eA} :

$$\Phi = \frac{r_{v,p}^{\text{obs}} d_p^2}{2 D_{eA} 36} \frac{r_{v,p}(C_{Ai})}{\int_{C_{A,\text{eq}}}^{C_{Ai}} r_{v,p}(C) dC} \quad (7.191)$$

Hence, the application of the Weisz criterion requires the knowledge of the rate equation. For an irreversible n th order reaction, Eqn. 7.191 reduces to:

$$\Phi = \frac{(n+1)}{2} \frac{r_{v,p}^{\text{obs}} d_p^2}{D_{eA} C_{Ai} 36} \quad (7.192)$$

In this case the experimental determination of the rate and the knowledge of the reaction order is sufficient to assess the importance of internal diffusion limitations. Note that only $n > -1$ is meaningful.

An experimental test to verify the absence of significant concentration gradients inside the catalyst pellet is based on the inverse proportional relation between the effectiveness factor and the pellet diameter for strong internal diffusion limitations. Hence, a measured rate which is independent of the pellet size indicates that internal diffusion limitations can be neglected. Care should be taken to avoid artifacts. External heat transfer effects also depend on pellet size and for exothermic reactions might compensate the internal diffusion limitations. If the catalyst pellet consists of a support with an non-uniformly distributed active phase, crushing and sieving to obtain smaller pellets is hazardous.

Concerning internal temperature gradients, a criterion which guarantees that the deviation of the observed volumetric rate from the isothermal rate is less than 5% is given in an analogous way by [11]:

$$r_{v,p} \frac{|\Delta_r H| d_p^2}{\lambda_p T_i} < 3 \frac{RT_i}{E_a} \quad (7.193)$$

or:

$$(\eta \phi^2) |\beta_i| \gamma_i < 0.05 \quad (7.194)$$

For all practical purposes internal temperature gradients can be neglected in laboratory reactors.

APPENDIX 7.A: MULTICOMPONENT DIFFUSION IN THE PRESENCE OF REACTION

For a single reaction:

$$\sum v_j A_j = 0$$

with v_j = stoichiometric coefficient of A_j , negative for reactants, positive for products; it can be shown that:

$$k_{fj} = \frac{D_{jm}}{y_{fj} \delta} \quad (7.A1)$$

with δ = thickness of the fictitious stagnant layer, m_i ; D_{jm} = effective binary diffusion coefficient of j in the reaction mixture, $m_i^3 m_i^{-1} s^{-1}$; y_{fj} = film factor relative to equimolar counterdiffusion; if molecular diffusion towards the external surface is the only transport mechanism.

Equimolar counterdiffusion occurs when:

$$\sum v_j = 0 \quad (7.A2)$$

of which the most simple example is provided by:



and is described by Fick's law:

$$N_A = -D_{AB} \frac{dC_A}{dz} \quad (7.A3)$$

Integration, for constant N_A and D_{AB} , leads to:

$$N_A = \frac{D_{AB}}{\delta} (C_A - C_{Ai}) \quad (7.A4)$$

The binary molecular diffusion coefficient, D_{AB} , can be derived from the kinetic gas theory. A more accurate empirical correlation is given by:

$$D_{AB} = \frac{3.2 \cdot 10^{-8} T^{1.75}}{p_t (v_A^{1/3} + v_B^{1/3})^2} \left(\frac{1}{M_A} + \frac{1}{M_B} \right)^{1/2} \quad (7.A5)$$

with v = diffusion volume, $m^3 mol^{-1}$.

In general, however, reaction is accompanied with expansion or contraction:

$$\sum v_j \neq 0 \quad (7.A6)$$

For ideal gases, the flux of a reactant A is now given by:

$$N_A = y_A \sum N_j - \sum D_{Aj} \frac{dC_A}{dz} \quad (7.A7)$$

with y_A = mole fraction of A in the mixture; i.e. the flux of A not only depends on the concentration gradient of A , which would be convenient, but on the concentration gradients of all the reacting components.

Hence the so-called effective binary diffusion coefficient, D_{Am} is introduced. The latter is *defined* as:

$$N_A = y_A \sum N_j - D_{Am} \frac{dC_A}{dz} \quad (7.A8)$$

For ideal gases an expression for the effective binary diffusion coefficient, D_{Am} , as a function of the binary diffusion coefficient, D_{Aj} , can be derived as in this case the Stefan–Maxwell equation holds:

$$\frac{dC_A}{dz} = \sum_{j \neq A} \frac{1}{D_{Aj}} (y_j N_A - y_A N_j) \quad (7.A9)$$

Solving 7.A8 for dC_A/dz and equating the result to the right-hand side of 7.A9 leads to:

$$\frac{1}{D_{Am}} = \frac{\sum_{j \neq A} \frac{1}{D_{Aj}} \left(y_j - y_A \frac{N_j}{N_A} \right)}{1 - y_A \sum N_j / N_A} \quad (7.A10)$$

Taking into account the stoichiometry of the reaction:

$$\frac{N_j}{v_j} = \text{constant} \quad (7.A11)$$

Equation 7.A10 becomes:

$$\frac{1}{D_{Am}} = \frac{\sum_{j \neq A} \frac{1}{D_{Aj}} \left(y_j - y_A \frac{v_j}{v_A} \right)}{1 - y_A \sum \frac{v_j}{v_A}} \quad (7.A12)$$

and Eqn. 7.A8 becomes:

$$N_A = - \frac{D_{Am}}{1 - y_A \sum \frac{v_j}{v_A}} \frac{dC_A}{dz} \quad (7.A13)$$

which, for equimolar counterdiffusion reduces to 7.A3. Integration of 7.A13 for constant N_A , D_{Am} and total molar concentration leads to:

$$N_A = -\frac{D_{Am} C_t}{\delta \sum \frac{v_j}{v_A}} \ln \frac{1 - y_A \sum \frac{v_j}{v_A}}{1 - y_{Ai} \sum \frac{v_j}{v_A}} \quad (7.A14)$$

with: C_t = total molar concentration, mol m⁻³, which can be rewritten as:

$$N_A = \frac{D_{Am}}{y_{fA} \delta} (C_A - C_{Ai}) \quad (7.A15)$$

if the so-called film factor, y_{fA} , is given by the logarithmic mean of $(1 - y_A \sum v_j/v_A)$ over the film:

$$y_{fA} = \frac{\sum \frac{v_j}{v_A} (y_{Ai} - y_A)}{\ln \left\{ \frac{1 - y_A \sum \frac{v_j}{v_A}}{1 - y_{Ai} \sum \frac{v_j}{v_A}} \right\}} \quad (7.A16)$$

For equimolar counterdiffusion, the film factor reduces to one.

Combination of (7.A15) and:

$$N_A = k_{fA} (C_A - C_{Ai}) \quad (7.A17)$$

leads to expression 7.A1 for the transfer coefficient of A. Actually, 7.A1 can also be written as:

$$k_{fA} = \frac{k_{fA}^0}{y_{fA}} \quad (7.A18)$$

with:

$$k_{fA}^0 = \frac{D_{Am}}{\delta} \quad (7.A19)$$

The literature provides correlations for k_f^0 .

NOTATION

a_s	specific internal surface area	$\text{m}_p^2 \text{ kg}_{\text{cat}}^{-1}$
a_v	volumetric interface surface area	$\text{m}_i^2 \text{ m}_L^{-3}$
a'_v	volumetric external surface area	$\text{m}_i^2 \text{ m}_p^{-3}$
A_k	heat exchange surface area	m^2
A_p	external surface area of a catalyst pellet	m_i^2
A_0	preexponential factor	depending on reaction
b	void catalyst pellet fraction of the bed	$\text{m}_p^3 \text{ m}_f^{-3}$
Bi	Biot number ($= \frac{\alpha d}{\lambda_e}$)	
c_p	specific heat capacity	$\text{J kg}^{-1} \text{ K}^{-1}$
C_A	molar concentration of A	mol m_f^{-3}
C_A^*	dimensionless molar concentration of A	
Ca	Carberry number ($= \eta_e D_{eA}^{1/2}$)	
d	diameter	m
d_p	catalyst pellet diameter	m
d_t	inner tube diameter	m
d_l	diameter of stirring blade	m
D_A	equimolar diffusion coefficient	$\text{m}_i^2 \text{ m}^{-1} \text{ s}^{-1}$
D_{Ak}	Knudsen diffusion coefficient	$\text{m}_i^2 \text{ s}^{-1}$
D_{Am}	molecular diffusion coefficient	$\text{m}_i^2 \text{ s}^{-1}$
D_{eA}	effective diffusion coefficient	$\text{m}_i^2 \text{ m}_p^{-1} \text{ s}^{-1}$
Da_{II}	Dahmköhler II number ($= \frac{\tau_D}{\tau_R} = \frac{L^2 k_{v,p}}{D_{eA}}$)	
E_a	activation energy	J mol^{-1}
F_A	molar flow rate	mol s^{-1}
G	mass flow rate	kg s^{-1}
H_A	Henry coefficient	$\text{Pa m}_L^3 \text{ mol}^{-1}$
$\Delta_r H$	reaction enthalpy	J mol^{-1}
i	experiment index	
j	number of components	
j_D	j -factor for mass transfer Chilton–Colburn ($= Sh Re^{-1} Sc^{-1/3}$)	
j_H	j -factor for heat transfer Chilton–Colburn ($= Nu Re^{-1} Pr^{-1/3}$)	
k	reaction rate coefficient	depending on reaction
$k_{f,A}$	mass transfer coefficient	$\text{m}_f^3 \text{ m}_i^{-2} \text{ s}^{-1}$

k_G	mass transfer coefficient in gas	$\text{mol m}_i^{-2} \text{s}^{-1} \text{Pa}^{-1}$
k_L	mass transfer coefficient in liquid	$\text{m}_L^3 \text{m}_i^{-2} \text{s}^{-1}$
k_v	volumetric first order rate coefficient	s^{-1}
L	length	m
m	mass	kg
M_A	molar mass of A	kg mol^{-1}
n	total number of experiments or reaction order	
n_A	amount	mol
N_A	molar flux	$\text{mol m}^{-2} \text{s}^{-1}$
N_p	power number	
N_I	stirring frequency	s^{-1}
Nu	Nusselt number ($= \alpha d / \lambda$)	
P_A	partial pressure	Pa
P_t	total pressure	Pa
Pr	Prandtl number ($= c_p \mu / \lambda$)	
q	heat flux	W m^{-2}
r	pore radius	m
r_a	areal reaction rate (per unit internal surface area)	$\text{mol m}_p^{-2} \text{s}^{-1}$
r_v	volumetric reaction rate	$\text{mol m}^{-3} \text{s}^{-1}$
$r_{v,p}$	reaction rate per unit pellet volume	$\text{mol m}_p^{-3} \text{s}^{-1}$
r_w	specific reaction rate	$\text{mol kg}_{\text{cat}}^{-1} \text{s}^{-1}$
R	gas constant	$\text{J mol}^{-1} \text{K}^{-1}$
$R_{v,A}$	volumetric production rate of A	$\text{mol m}^{-3} \text{s}^{-1}$
$R_{w,A}$	specific production rate of A	$\text{mol kg}_{\text{cat}}^{-1} \text{s}^{-1}$
Re	Reynolds number ($= \frac{N_p d_5^5 N_I^3 d_p^4 \rho^3}{\mu^3 V_L}$)	
Re_p	Reynolds number based on pellet diameter $(= \frac{4 G d_p}{\pi d_t^2 \mu})$	
S	objective function	
S_A	selectivity	
Sc	Schmidt number ($= \mu / \rho D_A$)	
Sh	Sherwood number ($= k_{LS} d_p / D_A$)	
Sh_m	modified Sherwood number ($= k_L / a_v D_A$)	
t	time	s
T	temperature	K

T_w	internal wall temperature	K
U	global heat transfer coefficient	$\text{W m}^{-2} \text{K}^{-1}$
v	diffusion volume	$\text{m}^3 \text{mol}^{-1}$
V	volume	m^3
V_L	liquid volume	m_L^3
W	catalyst mass	kg_{cat}
X_A	conversion of A	
y	coordinate perpendicular to gas–liquid interface	$\text{m}_L^3 \text{m}_i^{-2} \text{s}^{-1}$
y^*	dimensionless coordinate perpendicular to gas–liquid interface	
y_A	mole fraction of A in gas	
y_{fA}	film factor relative to equimolar counter diffusion	
y_0	inlet composition	mol mol^{-1}
Y_A	yield	mol mol^{-1}
z	distance coordinate in 1 direction	m
z^*	dimensionless place coordinate	

Greek symbols:

α	heat transfer coefficient	$\text{W m}^{-2} \text{K}^{-1}$
β	adjustable parameter such as $A_0, E_a\dots$	
β_e	external Prater number	
β_i	internal Prater number	
γ	dimensionless activation energy ($= E_a / (RT)$)	
γ_A	Hatta number ($= Da^{1/2} = \delta \sqrt{\frac{k_v}{D_a}}$)	
δ	film thickness	m
ε_b	void bed fraction	$\text{m}_b^3 \text{m}_i^{-3}$
ε_p	void fraction	$\text{m}_p^3 \text{m}^{-3}$
η	internal catalyst effectiveness factor	
η_e	external catalyst effectiveness factor	
λ_e	effective conduction coefficient	$\text{W m}^{-1} \text{K}^{-1}$
λ_1	ratio of the liquid side mass transfer coefficient to the gas side mass transfer coefficient of Q for $D_Q \approx D_A$	
λ_2	rate constant ratio for $D_Q \approx D_A$	

μ	dynamic viscosity	$\text{kg m}^{-1} \text{s}^{-1}$
v_A	stoichiometric coefficient of A	
ρ	density	kg m^{-3}
τ	characteristic time	$\text{s}, \text{kg}_{\text{cat}} \text{m}^{-3} \text{s}$
τ_D	characteristic time for diffusion	s
τ_R	characteristic time for reaction	s
ϕ	Thiele modulus ($= L \sqrt{\frac{k_{v,p}}{D_{eA}}}$)	
Φ	Weisz modulus ($= \eta \phi^2$)	

Subscripts:

A, B, \dots	with respect to A, B, \dots
b	bulk; also bed
e	external; also effective
f	fluid; also film
G	gas
i	interface
i	also experiment index
j	component index
L	liquid
p	pellet; also particle
r	reactor; also radial
s	solid
t	tube; also total
u	surrounding
v	volume
w	wall
W	specific
o	initial or inlet condition
$0, 1, 2, \dots$	order of reaction
$-$	vector

Superscripts:

o	initial; also standard
*	calculated

REFERENCES

- 1 J.J. Carberry, *Chemical and Catalytic Reaction Engineering*, McGraw-Hill, New York, 1976, pp. 205–208.
- 2 K.B. Bischoff, *A.I.Ch.E.J.*, 11 (1965) 351–355.
- 3 P. Trambouze, H. van Landeghem and J.-P. Wauquier, *Chemical Reactors Design/Engineering/Operation*, Editions Technip, Paris, 1988, p. 195.
- 4 J. Bridgwater, *Chem. Eng. Sci.*, 22 (1967) 185–191.
- 5 G.F. Froment and K.B. Bischoff, *Chemical Reactor Analysis and Design*, Second Edition, Wiley, New York, 1990, pp. 87–114.
- 6 D.E. Mears, *J. Catal.*, 20 (1971) 127–131.
- 7 Y. Sano, N. Yamaguchi and T. Adachi, *J. Chem. Eng. Jpn.*, 7 (1974) 255–261.
- 8 O.A. Hougen, *Ind. Eng. Chem.*, 53 (1961) 509–528.
- 9 J. De Acetis and G. Thodos, *Ind. Eng. Chem.*, 52 (1960) 1003–1006.
- 10 G.F. Froment and K.B. Bischoff, *Chemical Reactor Analysis and Design*, Second Edition, Wiley, New York, 1990, pp. 166–171.
- 11 J.A. Moulijn, A. Tarfaoui and F. Kapteijn, *Appl. Catal.*, 12 (1991) 1–12.

Chapter 8

Preparation of catalyst supports and zeolites

8.1 INTRODUCTION

Catalysts usually consist of two or more components: the support and one or more active phase(s). The term active phase needs little explanation: it is the phase that is principally responsible for the catalytic activity. The support is the vehicle for the active phase. It exercises several functions, among which are the maximization of the surface area of the active phase by providing a large area over which it may be spread and allowing the active phase to be cast into the form of coarse particles suitable for use in technical reactors. The active phase usually constitutes between 0.1 and 20% of the total catalyst and is normally in the form of very small crystallites (1–50 nm). The support is usually supposed to be catalytically inactive by itself; however in partnership with the active phase it can participate in the total reaction in important ways.

Typical substances that find wide use as high-area supports include silica gel and γ -alumina, which can be obtained with surface areas in the range 100–800 m^2/g . Materials used as low-area supports ($\sim 1 \text{ m}^2/\text{g}$) include α -alumina and mullite (alumina-silica). It is not easy to make general statements about the preparation of industrial catalysts because of the great variety of forms they take, but in many cases one can distinguish between the chemical operations in which the various components are assembled in the desired form, and the fabrication step in which they are made into the desired shape. The first step will be illustrated by a description of the method of preparing of silica gel and γ -alumina support material [1].

8.2 PREPARATION OF SILICA GEL CATALYST SUPPORTS

8.2.1 Preparation of Silica Gel

Soluble silicates are commonly used as starting material. The key variables in these solutions are:

1. the alkali metal;
2. the ratio of SiO₂ to alkali metal oxide expressed as a molar ratio;
3. the concentration of solids.

Sodium silicates are produced as glasses having SiO₂:Na₂O molar ratios between 1.6 and 3.9. These are sold in lump or pulverized form, partly hydrated powders and as concentrated solutions. For the production of precipitated silicas a solution of sodium silicate with a ratio of about 3.25 is usually used, rather than lower ratios, since less acid is required for the neutralization of alkali per unit of silica, and this ratio is available at low cost [2]. In aqueous solution this sodium silicate not only contains monomeric silicate species (SiO₄⁴⁻) but also dimeric (Si₂O₇⁶⁻), trimeric (Si₃O₁₀⁸⁻) tetrameric (Si₄O₁₂⁸⁻) and higher oligomeric species, as for example, the double-four ring octameric species (Si₈O₂₀⁸⁻), see Scheme 8.1.

A powerful technique for investigating these different species is ²⁹Si-NMR (see Fig. 8.1). Different lines can be observed in the ²⁹Si-NMR spectrum of a silicate solution corresponding to the differently positioned ²⁹Si nuclei in the (poly)silicate ions. The highest values for the chemical shift ($\delta = -71.5$ ppm with respect to tetra methyl silane) are found for the monomeric silicate units while the resonances of fully condensed silicon atoms (i.e. Si-(O-Si)₄: tetrasiloxo silane) are to be found at the lowest values for the chemical shift ($\delta = -110$ ppm).

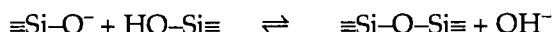
In order to distinguish between the different signals a nomenclature based on the number, n , of siloxane bridges (Si-(O-Si)_n: $n = 0, 1, 2, 3$, or 4) is introduced (Q₀, Q₁, Q₂, Q₃ and Q₄, respectively).

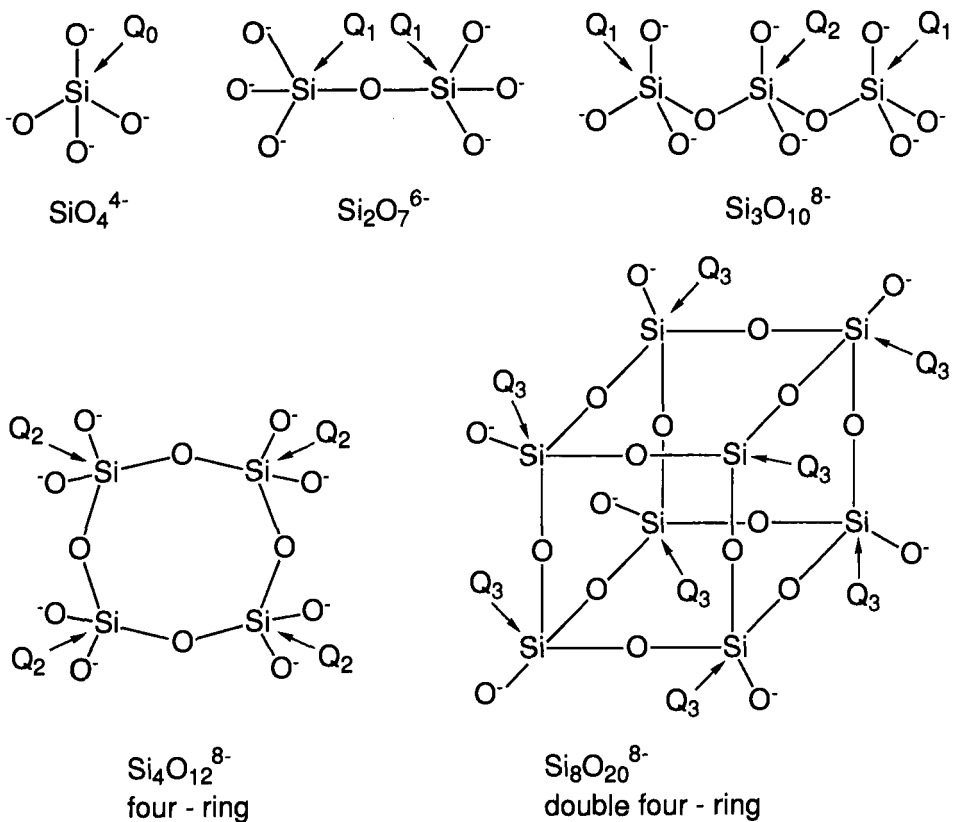
The formation of silica gel from these silicate solutions proceeds according to the following steps:

- Firstly, when lowering the pH of the solution by addition of an acid (usually H₂SO₄), silanol groups are formed according to the following equilibrium



- The silanol groups so formed have a strong tendency to polymerize in such a way that polymers are formed with a maximum of siloxane (Si-O-Si) bonds and a minimum of uncondensed Si-OH groups. The main polymerization reaction is:





- At the earliest stage of polymerization this leads to the formation of ring structures, the cyclic tetramer, for example, followed by addition of monomers to these and linking together of the cyclic oligomers to larger three-dimensional molecules. These condense internally to the most compact state with $\equiv\text{Si}-\text{OH}$ groups remaining on the outside.
- The resulting spherical units are, in effect, the nuclei that develop into larger particles. Because small particles are more soluble than larger ones, and since not all particles have the same size, the particles grow in average size and diminish in numbers as the smaller ones dissolve and the silica is deposited upon the larger ones (Ostwald ripening).
- Above pH 6 or 7 and up to pH 10.5, where silica begins to dissolve as silicate, the silica particles are negatively charged and repel each other. Therefore they do not collide, so that particle growth continues without aggregation. However, if salt is present at a concentration greater than 0.2–0.3 molar, as when sodium silicate is neutralized with sulphuric acid, the charge repulsion is reduced and aggregation and gelling occur.

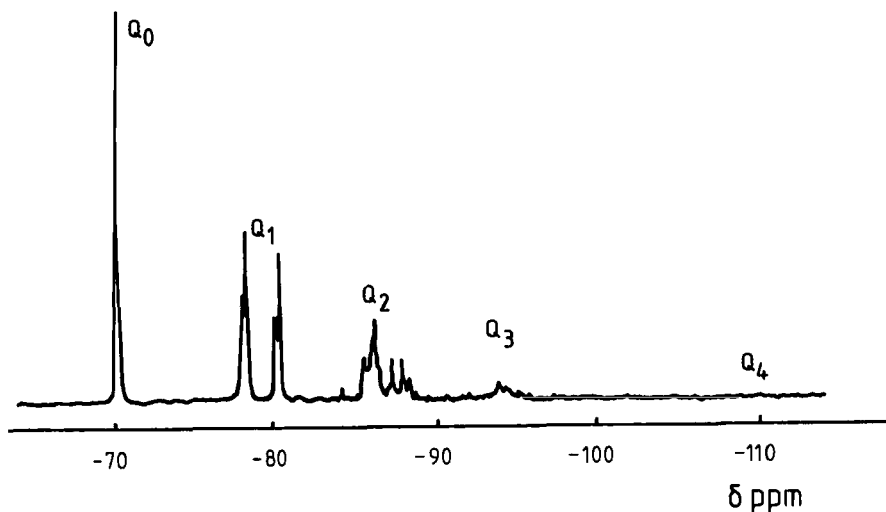


Fig. 8.1. Typical ^{29}Si -NMR spectrum of a potassium silicate solution $\text{SiO}_2/\text{K}_2\text{O} = 1.0$ [3].

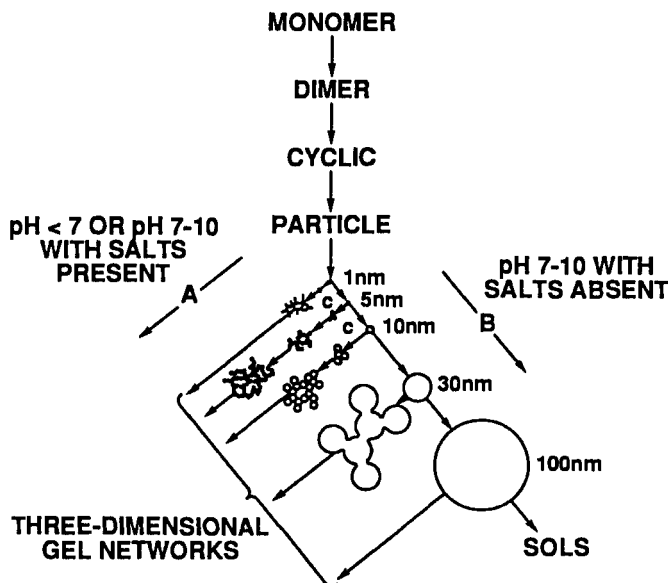


Fig. 8.2. Schematic representation of the formation of silica gel.

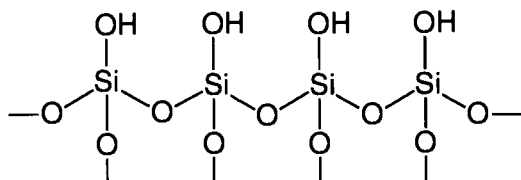
- At low pH the silica particles bear very little ionic charge and thus can collide and aggregate into chains and then gel networks.

The successive steps in polymerization from monomer to large particles and gels have been represented schematically by Iler as in Fig. 8.2.

The silica gels obtained in this way are mixed with a solution of the salts formed by the neutralization of the alkali by the acid (usually a sodium sulphate solution). These salts can be removed by filtering and washing the gel. The silica gel obtained in this way, in which the pores are filled with water, is called the *aquagel*. From this a *xerogel* is obtained when the water is removed by evaporation.

The structure of the xerogel will be compressed and the porosity reduced at least to some degree by the surface tension forces as the water is removed. An *aerogel* is a special type of xerogel from which the liquid has been removed in such a way as to prevent any collapse or change in the structure as liquid is removed. Specifically, this is done by heating the liquid-filled gel, usually an *alcogel*, in an autoclave to above the critical point of the liquid, so that there is no liquid-vapour interface, and releasing the vapour.

All silicas dried from water at less than 150°C have a fully hydroxylated surface in which the surface structure terminates in silanol groups. This is readily wettable by water and water-soluble organic molecules.



According to Böhm the concentration of $\equiv\text{Si}-\text{OH}$ groups on the silica surface is rather constant, at a value of 6.6 OH groups per nm² [4].

Commercial silica gels for use as catalyst bases are, for example, produced by Akzochemie and Davison, having specific surface areas between 100 and 800 m²/g and pore volumes between 0.3 and 2.0 ml/g. These silica gels contain as main impurities S (sulphate), Na, Al, Fe and Ti.

8.2.2 Silica Precipitation from Vapour: Pyrogenic Silica

Very pure silica can be obtained by the oxidation or hydroxylation of purified SiCl₄ at high temperature.



SiCl₄ can be burned in oxygen to yield SiO₂ and Cl₂, but simpler equipment can be used when SiCl₄ is mixed with CH₄ and burned to produce fine SiO₂ and HCl.



The silicas made by this process are commonly known by their trademarks, 'Aerosil' produced by Degussa in Europe, and 'Cabosil' produced by Cabot in America.

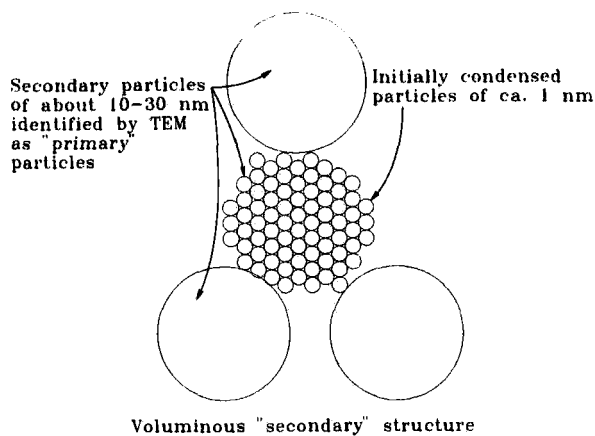


Fig. 8.3. Schematic representation of the structure of pyrogenic silica.

The structure of these pyrogenic silicas has been discussed by Barby [5], particularly with reference to their specific surface area. It was concluded that the initially condensed particles are only about 1 nm in diameter and that these are so closely packed (high coordination number) to secondary particles of 10 to 30 nm that only a small amount of nitrogen can penetrate the micropores between them. Thus the secondary particles are the ones that are commonly identified in electron micrographs and which determine the specific surface area. They are the 'primary' particles in the voluminous aggregate structure and have a low coordination number of about 3 (see Fig. 8.3). Because of the low level of impurities this type of silica is often used as catalyst support in fundamental studies.

8.3. PREPARATION OF ALUMINA CATALYST SUPPORTS

8.3.1 Preparation of $\gamma\text{-Al}_2\text{O}_3$ and $\eta\text{-Al}_2\text{O}_3$

Because of the amphoteric character of aluminium, it is soluble in both acidic and basic solvents. In acidic solutions below pH = 2 aluminium will be present as solvated Al^{3+} ions, while in basic solutions above pH = 12 it is present in the form of aluminate ions (AlO_4^{5-}).

Starting from an aqueous acidic Al^{3+} solution (for example an aluminium sulphate solution) precipitation occurs if the pH of the solution is increased above about pH = 3 by addition of a base. The first precipitate is a gel-like substance in which minute crystals of boehmite (AlO(OH)) are present. If this is filtered without aging and then calcined at temperatures up to 600°C an X-ray amorphous material is obtained. The material remains amorphous until after firing to temperatures greater than 1100°C. $\alpha\text{-Al}_2\text{O}_3$ is formed at higher temperatures.

If the initial microcrystalline boehmite gel slurry is aged at 40°C it is converted

into bayerite, a crystalline form of $\text{Al}(\text{OH})_3$. If this product is filtered, dried and then calcined, a compound designated as $\eta\text{-Al}_2\text{O}_3$ is formed. Calcination at yet higher temperatures produces another compound $\theta\text{-Al}_2\text{O}_3$, which is converted into $\alpha\text{-Al}_2\text{O}_3$ at temperatures exceeding 1100°C .

The bayerite may also be converted by further aging of the slurry at higher temperatures (80°C) and pH about 8 into a much more crystalline form of boehmite, referred to as crystalline boehmite. When this precipitate is heated, after filtration and washing, it becomes another set of compounds, $\gamma\text{-Al}_2\text{O}_3$ and $\delta\text{-Al}_2\text{O}_3$, which are very similar but not identical to $\eta\text{-Al}_2\text{O}_3$ and $\theta\text{-Al}_2\text{O}_3$. Upon heating to temperatures higher than 1100°C , the compound $\gamma\text{-Al}_2\text{O}_3$ becomes $\alpha\text{-Al}_2\text{O}_3$. If the bayerite is aged at high pH, gibbsite is formed. This is converted to $\chi\text{-Al}_2\text{O}_3$ and $\kappa\text{-Al}_2\text{O}_3$ as its dehydrated forms, materials that are less important for the use as catalyst supports.

It is also possible to start the precipitation from a basic AlO_4^{5-} solution by addition of an acid. At pH below about 11 precipitation of a gel-like bayerite occurs, which can be treated as indicated above.

Finally it is also possible to obtain a crystalline boehmite precipitate directly, by simultaneous addition of a basic and an acidic solution to a reactor to obtain precipitation in the pH range between 6 and 8.

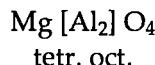
The different routes for the formation of the various aluminas are shown schematically in Fig. 8.4.

The important compounds for use as catalyst supports are $\gamma\text{-Al}_2\text{O}_3$ and $\eta\text{-Al}_2\text{O}_3$, particularly the former. They represent supports with high surface area ($15\text{--}300 \text{ m}^2/\text{g}$) and high thermal stability from which the surface acidity can be controlled.

8.3.2 Structure of $\gamma\text{-Al}_2\text{O}_3$ and $\eta\text{-Al}_2\text{O}_3$

Both $\gamma\text{-Al}_2\text{O}_3$ and $\eta\text{-Al}_2\text{O}_3$ are members of a class of binary oxides in which the oxygen packing is of the cubic close packing type, with the cations situated partly in tetrahedral and partly in octahedral positions. These compounds are called spinels after the mineral spinel which has the composition MgAl_2O_4 . In spinel Mg^{2+} occupies tetrahedral and Al^{3+} occupies octahedral positions. The unit cell of a cubic close packed structure is shown in Fig. 8.5.

The O^{2-} ions form a face centred cube (fcc) containing 4O^{2-} ions. As indicated in the figure, each cube contains four octahedral positions, from which two are occupied by Al^{3+} and eight tetrahedral positions, from which one is occupied by Mg^{2+} . Schematically this can be indicated by the formula



in which the cations in octahedral positions are placed between brackets.

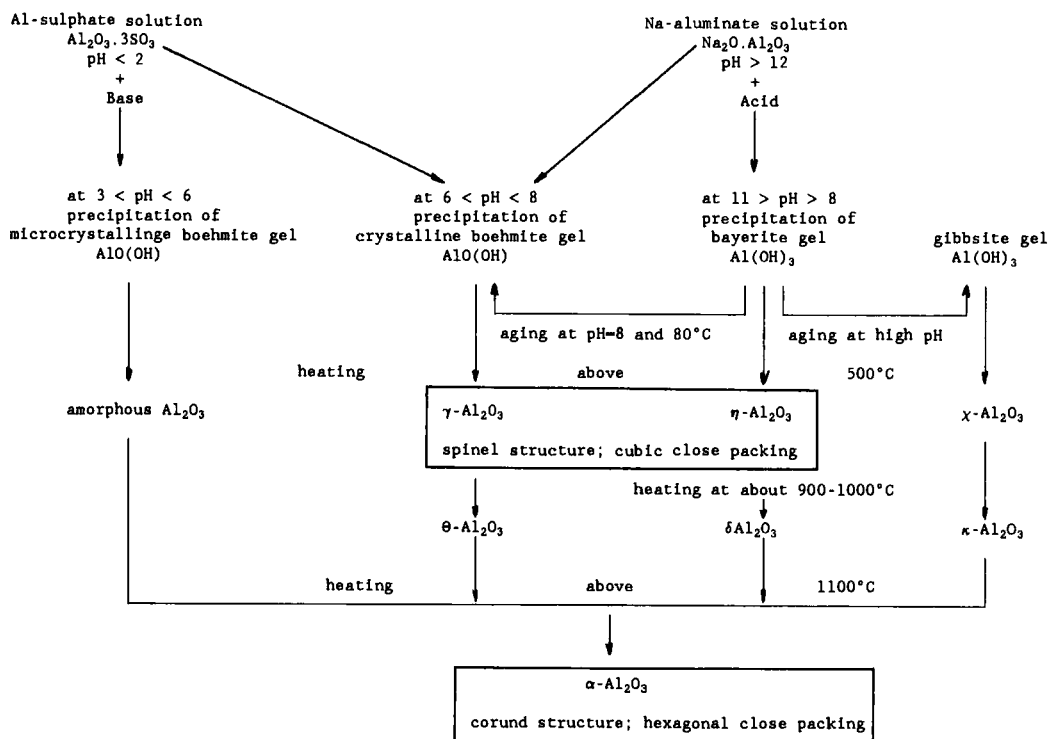
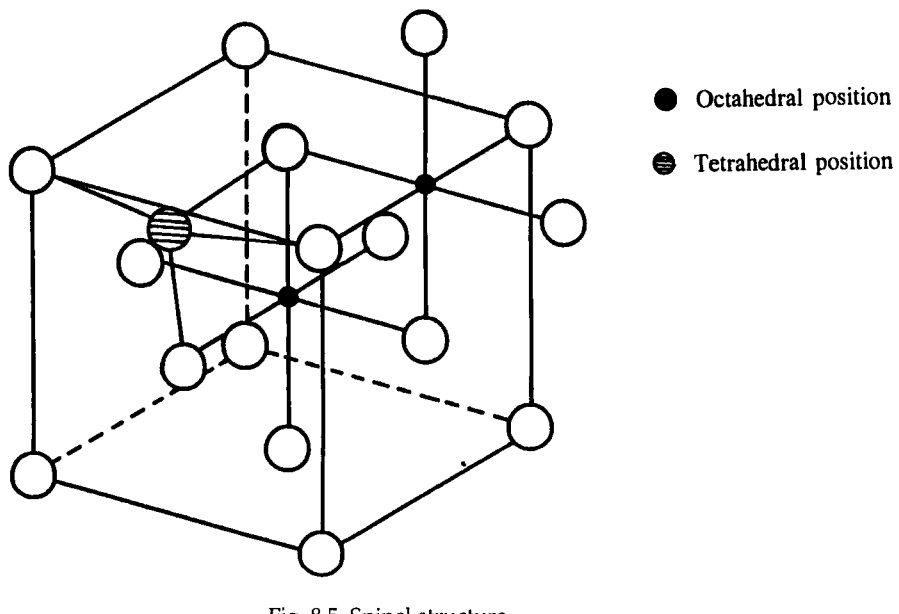
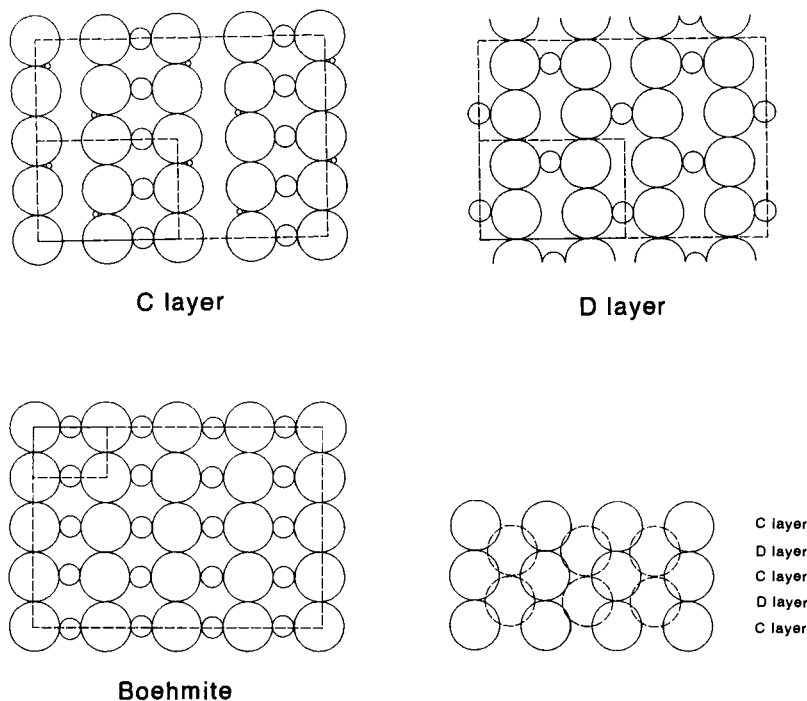
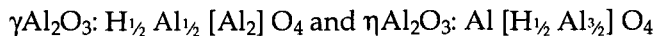


Fig. 8.4. Schematic representation of the formation of the different forms of alumina.



Fig. 8.6. Structure of $\gamma\text{-Al}_2\text{O}_3$.

The X-ray diagrams of $\gamma\text{-Al}_2\text{O}_3$ and $\eta\text{-Al}_2\text{O}_3$ are similar to that of spinel. Because of this similarity and the presence of H atoms in the structures the formulas of the two aluminas are given formally as:



in which some of the Al^{3+} ions occur in tetrahedral positions. In all probability the protons are not located in tetrahedral or octahedral positions, as suggested here, but at the surface in OH groups. One in every eight O^{2-} ions is therefore at the surface as OH^- , which means that the crystals are small and their surfaces consist largely of OH^- groups. These conclusions are in good agreement with the observation that the surface areas of $\gamma\text{-Al}_2\text{O}_3$ and $\eta\text{-Al}_2\text{O}_3$ are high ($\sim 250 \text{ m}^2/\text{g}$) and that these structures contain a relatively large amount of 'bonded water'.

$\eta\text{-Al}_2\text{O}_3$ contains relatively more tetrahedrally coordinated Al^{3+} ions than $\gamma\text{-Al}_2\text{O}_3$. Lippens [6] proposed the models of $\eta\text{-Al}_2\text{O}_3$ and $\gamma\text{-Al}_2\text{O}_3$ shown in Figs. 8.6 and 8.7, respectively.

For $\eta\text{-Al}_2\text{O}_3$ we start with the close-packed oxygen layer shown in Fig. 8.7. This forms the (111) plane in cubic close packing. There are now two types of arrange-

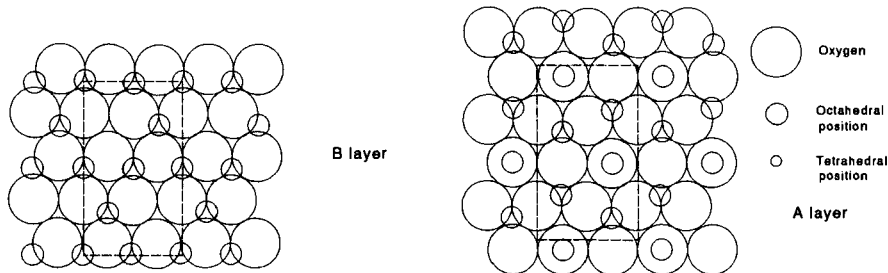


Fig. 8.7. Structure of $\eta\text{-Al}_2\text{O}_3$.

ments of the Al^{3+} ions. One (the β layer) has Al^{3+} ions located in octahedral positions only. The other (the A layer) is obtained from this by transferring two-thirds of the cations from octahedral to tetrahedral positions. The resultant structure is a stacking of the layers ABAB....

The $\gamma\text{-Al}_2\text{O}_3$ structure is more easily visualized by considering the (110) crystal plane. Again we have two types of layers, designated here as C and D layers. The D layer has only octahedrally located Al^{3+} ions, and the C layer has as many tetrahedral as octahedral sites. The packing of the structure is CD₂C....

The important structural characteristic of alumina in catalysis is the surface, and since alumina occurs in the form of lamellae it is most probable that only one type of surface plane is predominant. According to Lippens, this is the (111) plane for $\eta\text{-Al}_2\text{O}_3$ and the (110) plane for $\gamma\text{-Al}_2\text{O}_3$. These differences are important to the applicability of the alumina in catalytic processes; $\gamma\text{-Al}_2\text{O}_3$ appears better suited to hydrodesulphurization catalysts, whereas $\eta\text{-Al}_2\text{O}_3$ appears better suited to reforming catalysts. The $\eta\text{-Al}_2\text{O}_3$ is the more acidic of the two because of the higher density of Al^{3+} in tetrahedral sites.

8.4 ZEOLITE SYNTHESIS

8.4.1 Introduction

As zeolite structures are built from SiO_4^{4-} and AlO_4^{5-} tetrahedra these primary building blocks must also be present in the synthesis mixture and, because aluminate ions are only stable at high pH values, zeolite synthesis always takes place from basic solutions. An important factor determining the synthesis conditions is the Si/Al ratio of the zeolite to be synthesized. The higher the Si/Al ratio and so the lower the Al content the more difficult is the synthesis and the more severe the conditions that are needed. Therefore, to illustrate the different aspects of zeolite synthesis the preparation of four types of zeolites with increasing Si/Al will be described in this chapter.

Successively, these will be:

zeolite A	or	LTA	with	Si/Al = 1
zeolite Y	or	FAU	with	Si/Al \approx 2.5
Mordenite	or	MOR	with	Si/Al \approx 5 and
zeolite ZSM-5	or	MFI	with	Si/Al > 12

However, before these specific preparation methods are described, we first discuss the subsequent events occurring in the course of a zeolite synthesis.

Generally the first step is the preparation of the reaction mixture at low temperature (< 60°C). The different ingredients are mixed in this step, which in most cases results in the formation of the so-called synthesis gel. In this gel silicate and aluminate monomers and oligomers in solution are in equilibrium with condensed silicate and aluminate units in the gel phase. In some cases a digestion period is necessary to reach this equilibrium.

In the second step the temperature of the synthesis mixture is raised to the crystallisation temperature (generally between 100 and 200°C). During this process continued dissociation of silicate and aluminate oligomers occurs, resulting in an increasing concentration of monomeric silicate and aluminatespecies in the solution.

Once the high crystallization temperature is reached, zeolite crystallization will start after an induction period. During this induction period the dissolution of the gel phase continues, leading to the formation of clusters of polysilicates or aluminosilicates that become stable above a certain critical dimension (e.g. about 10 Å for zeolite A and about 20 Å for zeolite ZSM-5), and crystallization commences. The course of nucleation and crystallization of zeolites can generally be described by a characteristic S-shaped crystallization curve, in which the amount of crystalline material is plotted against crystallization time. Depending on the type of zeolite, crystallization will be completed after several hours to several days. The crystals must then be separated from the mother liquor by decantation, filtration or centrifugation, followed by washing with water. The final step in zeolite preparation is the drying and calcination procedure, after which the zeolite void volume is free for the different applications.

8.4.2 Synthesis of Zeolite A

Zeolite A or LTA (Linde Type A) with a chemical composition of $\text{Na}_2\text{O} \cdot \text{Al}_2\text{O}_3 \cdot 2\text{SiO}_2$ can be synthesized from sodium aluminate–sodium silicate gels. Typical gels are prepared from aqueous solutions of $\text{Na}_2\text{O} \cdot \text{Al}_2\text{O}_3$, $\text{Na}_2\text{O} \cdot 3.25\text{SiO}_2$ (water-glass) and NaOH. The starting reactant mixture composition can be illustrated by diagrams of the type given in Fig. 8.8. The anhydrous composition of the gel is plotted on a mole percent basis in triangular coordinates. The concentration (H_2O content) of the gel, which cannot be shown in this type of diagram, is also important, as is the nature of the starting materials.

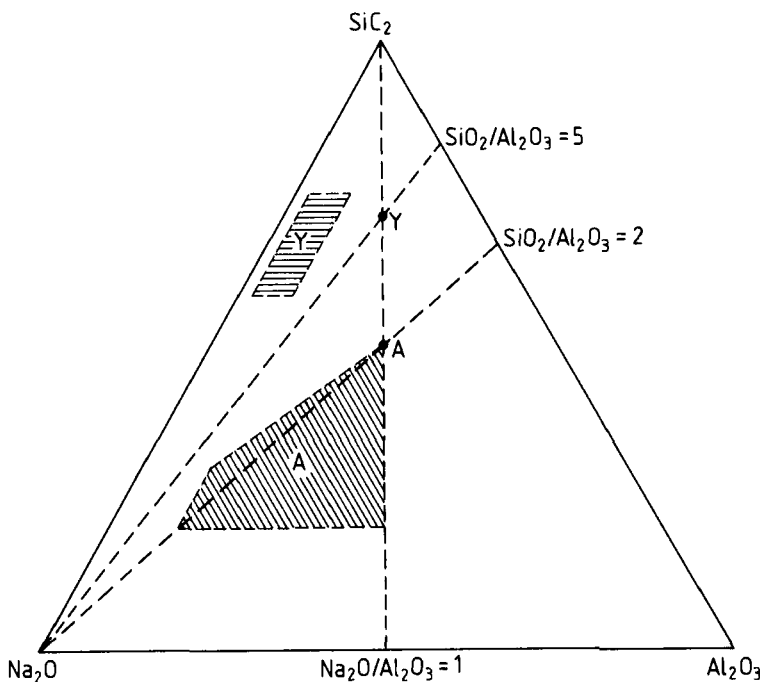


Fig. 8.8. Reaction composition diagram for the synthesis of zeolite A and zeolite Y.

A typical gel composition, taken from ref. 9, is:

mol ratio

$$\text{Na}_2\text{O} : \text{Al}_2\text{O}_3 : \text{SiO}_2 : \text{H}_2\text{O} = 2.50 : 1.00 : 1.95 : 170$$

weight ratio

$$2.5 \times 62 : 1.0 \times 102 : 1.95 \times 60 : 170 \times 18 = 155 : 102 : 117 : 3060$$

corresponding to a solids concentration of about 11%.

Crystallization is performed at 80–100°C and takes about 4–24 h, after which the zeolite can be obtained by filtering and washing with water. Typical crystallite sizes obtained by this method are between 1 and 10 µm.

8.4.3 Synthesis of Zeolite Y

For the synthesis of zeolite Y it is necessary to add extra SiO₂ in the form of a reactive silica gel or silica sol to the synthesis mixture [10] to obtain the right composition. A typical gel composition in this case is:

mol ratio

$$\text{Na}_2\text{O} : \text{Al}_2\text{O}_3 : \text{SiO}_2 : \text{H}_2\text{O} = 4.00 : 1.00 : 10.0 : 160$$

weight ratio

$$4 \times 62 : 1 \times 102 : 10 \times 60 : 160 \times 18 = 248 : 102 : 600 : 2880$$

corresponding to a solids concentration of about 25%.

The gel prepared from colloidal silica is heterogeneous on a molecular scale, containing relatively large units of silica particles with molecular weights of 1,000,000 to 500,000 and ranging in size from 10 to 20 nm. Therefore, room temperature equilibration or aging of the gel is necessary before the crystallization at 100–120°C can be started. In 2–4 days a highly crystallized product can be obtained which, after filtering and washing, can be transformed into the acidic form by ion exchange.

As zeolite Y is not stable in low pH solutions, however, it is not possible to introduce H⁺ by direct exchange with Na⁺ using mineral acid solutions. Generally two methods can be considered to solve this problem:

- (i) Ion exchange with NH₄⁺ followed by decomposition of NH₄⁺ into H⁺ and NH₃ by heating above about 350°C; or
- (ii) Ion exchange by divalent or trivalent metal ions followed by a heat treatment to obtain hydrolysis. For this purpose rare earth ions (RE³⁺) are usually used.

8.4.4 Synthesis of Mordenite

Synthesis of low silica mordenite is possible from alkaline mixtures, but in order to obtain high silica mordenite with a chemical composition of Na₂O·Al₂O₃·10SiO₂ it is necessary to add an organic modifier. Because of the low Al content, the zeolite framework loses its polar properties and can no longer be stabilized by the adsorption of hydrated alkali ions. Instead, positively charged organic molecules are needed which, besides charge compensation, also have nonpolar interactions with the zeolite framework. Amines are often used for this purpose, and for mordenite synthesis diethylamine (DEA) is used in particular.

A typical gel composition is:

mol ratio

$$\text{Na}_2\text{O} : \text{Al}_2\text{O}_3 : \text{SiO}_2 : \text{DEA} : \text{H}_2\text{O} = 1.00 : 1.00 : 6.60 : 20 : 300$$

weight ratio

$$1 \times 62 : 1 \times 102 : 6.6 \times 60 : 20 \times 73 : 300 \times 18 = 62 : 102 : 396 : 1400 : 5400$$

corresponding to a solids concentration of about 7.5%. Crystallization is performed at 175°C under autogenous pressure and takes 2–4 days. After filtering and washing, the mordenite in its sodium form is obtained, which can be transformed in the acidic form by ion exchange of Na⁺ with H⁺, which is usually done via ammonium exchange and subsequent heating.

8.4.5 *Synthesis of ZSM-5*

The synthesis of ZSM-5 and other (very) high silica zeolites becomes possible when, instead of alkali hydroxides, tetraalkylammonium hydroxides are used to obtain the high pH necessary for zeolite synthesis. In the case of ZSM-5 tetrapropylammonium hydroxide must be used [11].

A typical gel composition is

mol ratio



weight ratio

$$1.25 \times 62 : 1 \times 102 : 30 \times 60 : 18 \times 203 : 800 \times 18 = 77.5 : 102 : 1800 : 3654 : 14400$$

corresponding to a solid concentration of about 10%. Crystallization is performed at 150–175°C under autogenous pressure and takes 2–5 days. After filtering and washing the zeolite is obtained with the tetrapropylammonium ion still present in the zeolite framework (1 TPA per pore intersection). It is for this reason that the tetrapropylammonium ion is also indicated as template for this particular zeolite.

To remove the template it is necessary to decompose it, which can be done by heating it above about 550°C. What is obtained is ZSM-5 in which some Na^+ is still present. Because of the low alumina content the acid stability is so good that this can be exchanged in mineral acid solution to obtain H-ZSM-5. The synthesis mentioned above can also be performed in the absence of Na_2O and Al_2O_3 . In that case a purely silica form of ZSM-5 is obtained which is also called silicalite 1.

8.5 CATALYST SHAPING

8.5.1 *Introduction*

Forming or shaping of supports and catalysts is an important step in the preparation procedure of a commercial catalyst. The catalyst must have a prescribed shape and size for the given chemical reactor. This shape and size is determined by the application of the catalyst and the type of the reactor in which it will be used. Table 1 gives a rough survey of the different shapes and the reactors in which they are used.

For a fixed bed reactor it is very important that the pressure drop over the bed is as low as possible. This condition is usually fulfilled by using pellets, extrudates or spheres with a diameter greater than 3 mm. A fixed bed can have a height of ten meters or more. For this reason the catalyst particles in a fixed bed must have a high mechanical strength, otherwise the particles in the lower part of the bed will break under the weight of the upper half of the catalyst bed. In the riser reactor there is a continuous transport of catalyst pellets. Here it is necessary that

TABLE 8.1

Different types of catalyst shapes

Shape	Size	Type of reactor
Extrudate	$d = 1\text{--}50 \text{ mm}$ $l = 3\text{--}30 \text{ mm}$	Fixed bed reactor
Pellet	$d = 3\text{--}10 \text{ mm}$ $h = 3\text{--}10 \text{ mm}$	Fixed bed reactor
Granule	$d = 1\text{--}20 \text{ mm}$	Fixed bed reactor
Bead	$d = 1\text{--}5 \text{ mm}$	
Sphere	$d = 1\text{--}5 \text{ mm}$	Fixed bed reactor Riser reactor
Sphere	$d = 20\text{--}100 \mu\text{m}$	Fluid bed reactor Slurry reactor

these catalyst particles are as smooth and strong as possible because the constant movement can degrade the catalyst very rapidly. In the fluidized bed reactor the catalyst bed is fluidized and the catalyst particles are in constant vigorous movement during which the particles constantly impinge on each other. These particles must thus have a very high attrition resistance, otherwise fines will be formed and blown out of the reactor. Different techniques are used for shaping the catalysts into the shapes mentioned in Table 8.1. In the following paragraphs we will deal with these techniques in more detail [12–14].

8.5.2 Spray Drying

Spray drying is a technique which is used to produce spherical materials. It can be used as an intermediate process for drying and producing free-flowing powders, or as a real shaping technique producing attrition-resistant spherical particles with a diameter between 10 and 100 μm .

These particles are used in fluidized beds. Different types of spray dryers are used. (The difference is the way in which the solution is sprayed or atomized.) In a spray dryer a hydrogel or sol solution is sprayed through nozzles into a heated zone. Depending on the temperature, either drying or both drying and calcination occur as the drops fall. Two different types of a spray dryers are shown in Fig. 8.9. The difference between the two types is the way in which the small droplets are formed or atomized. For example, the nozzle through which the liquid is blown may have very small holes or may be a rapidly rotating wheel. There are also spray dryers with a nozzle blowing upwards, like a fountain. The type of liquid atomizer is very important for the maximum attainable particle size and the broadness of the particle size distribution. Some general characteristics

TABLE 8.2

Advantages and disadvantages of different spray drying atomization systems

Atomisation system	Advantages	Disadvantages
Rotating disc	High feed rates Less downtime Low pressure pumps can be used	Larger diameter dryer required Coarse particle size not obtainable
Pressure nozzle	Large agglomerate capability Smaller dryers can be used	Downtime due to part wear and plugging High pressure pumps required

are given in Table 8.2. If an abrasive material is being processed, the openings in the nozzle or the surface of the wheel may be eroded which can influence the droplet size and change the character of the produced material.

The spray of spherical droplets consisting of sol or gel particles will grow together, forming agglomerates as the liquid in the droplets evaporates during the process. Spray drying for the production of fluid bed catalyst will start with gel forming materials. These are materials which shrink and coalesce on drying or which are film-forming materials. After drying and calcination these materials form good attrition-resistant spheres. If non-gel-forming or non-coalescing-type materials are spray dried, gels or film formers may be used as matrices for the more crystalline materials. For example, bismuth molybdate can be included in silica gel and then spray dried. This silica gel is added in the form of colloidal silica. Another example is zeolites in a matrix of alumina gel.

The process itself is more art than science. There is hardly any information in the open scientific literature. Most publications have to do with spray drying of ceramic powders (ref. 15 and references therein, ref. 16). There are also some standard books about spray drying [17]. Important process parameters are the viscosity of the liquid, the solids content of the suspension, the film-forming characteristics, the type of atomizer, the temperature, the rotation speed of the wheel, gas velocity, etc.

8.5.3 Granulation

Granules are particles with a more or less spherical shape. The diameter of these particles can be between 2–30 mm. Granulation is widely used in other fields of technology, if spherical particles are needed. The principle of the shaping method is best described by the snowball effect. A round dish (see Fig. 8.10) is used, which is rotating about an inclined axis, the angle of inclination of which is variable. Small particles are fed into the dish. At the same time a cohesive slurry

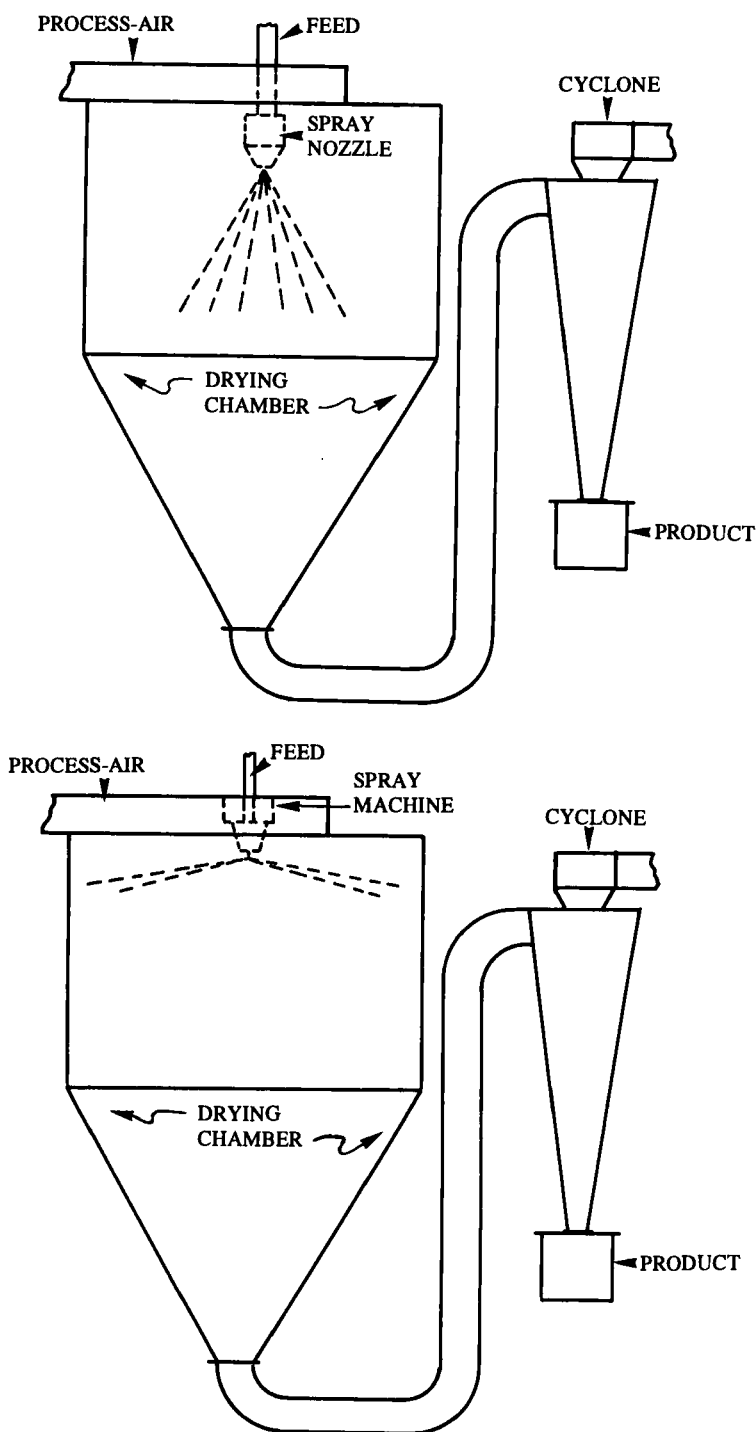


Fig. 8.9. Two different spray dryers [12]. Top: with a spray nozzle. Bottom: with a rotating wheel.

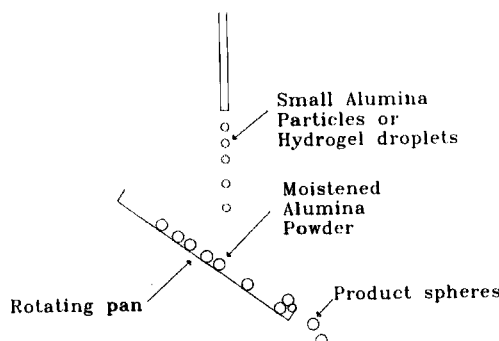


Fig. 8.10. Production of spheres using the rotating dish method [13].

is sprayed onto the small particles. The particle surface becomes wet and granules begin to grow. There are many mechanisms for growth and which mechanism predominates will depend on many factors, such as the size, strength, plasticity and surface wetting of the granules, the degree of agitation and the amount of fines in the powder bed. The basic mechanisms are:

- nuclei creation
- nuclei growth
- coalescence of nuclei
- crushing of smaller granules
- layering of fragments onto larger granules

As a result of all these mechanisms the small particles rotating in the dish grow layer by layer and become larger, more or less spherical particles. As the process is moisture dependent, the size and strength can be controlled by controlling the rate of liquid input and by the fineness of the spray. By adjusting the inclination, granules of the desired size automatically leave the granulator dish.

There is a lot of art in this technique, too, but there are also several publications in the open literature about the principles of this shaping process. The basic mechanisms which play a role are described in the classic review by Rumpf [18]. Newitt and Conway-Jones [19] identified four types of liquid bonding mechanisms which depend on the relative amount of liquid present in the wetted powder. Rumpf calculated the strength of the bond between the particles in the wetted powder.

After drying, the green spheres are calcined to obtain a higher mechanical strength. It is most important in the process to control the parameters which are responsible for making spherical particles. Since the spheres grow layer by layer, it is important to prevent the formation of onion-like material, the layers of which can be peeled away very easily. To prevent this, binders are used to improve the adherence of the layers after calcination. In other fields of application, e.g. the production of iron ore pellets, cement is used to give a very strong bonding. In

in the case of catalysts the use of binders is restricted. If there is poor adherence the spheres are very weak and it will also be impossible to impregnate these spheres with a water-soluble salt.

8.5.4 Pelletization

In this shaping process a powder is pressed between two punches in a pelletizing press. The three different steps in the process are presented in Fig. 8.11. In step I the free-flowing powder is poured into the cylindrical hole. In step II the lower punch and the upper punch are moving towards each other and the powder is pressed at a pressure of about $10^2 - 5 \times 10^3$ atm and a pellet is formed. In step III the upper punch moves upwards and the lower punch pushes the pellet out of the hole. In the next step the pellet is moved away, the lower punch moves downwards and the hole is filled again.

The schematic diagram shows that it is obvious that it is very important to use a free-flowing powder. The catalyst manufacturers use machines containing about 50 punches mounted in a circle. They produce 50,000 to 100,000 pellets/h. Because of the very rapid processing the hole must be filled in a reproducible way in less than one second. The filling of the hole determines the weight of the pellet. The grains of the free-flowing powder must be deformable during the pelleting process to form good pellets. Wear is an important problem and lubricants like graphite, stearic acid, aluminium stearate and talc are used to reduce this wear problem. These lubricants or plasticizers also act as a lubricant between the powder particles and improve the compacting of the powder and the formation of the pellet.

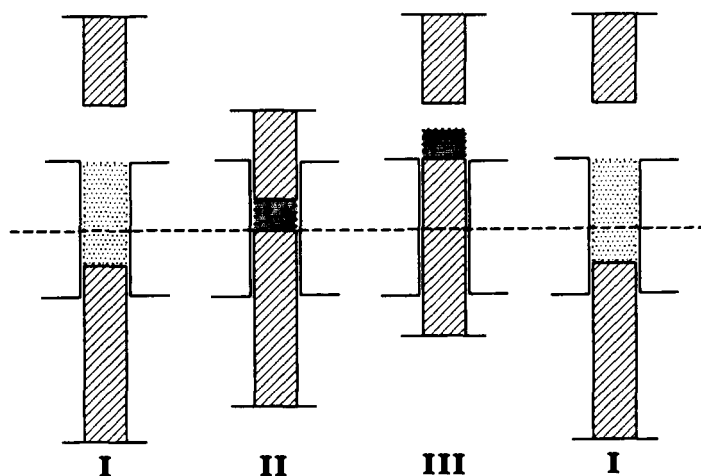


Fig. 8.11. Three steps of the pelletization process.

The pellets are very uniform in size and shape and are mostly cylindrical. They have a high mechanical strength with a reasonable porosity. To increase the macroporosity one adds e.g. sawdust and (bio)polymers. After the pelletization process the pellets are calcined to burn out the lubricants and other combustible additives.

It is also possible to make other shapes than just cylindrical ones. By using special dies one can make cylindrical pellets with a hole in the centre, corrugated cylinders, and even spheres.

Pelletization is a rather expensive method as compared to the other shaping methods [3]. The modern machines with a very high pelletization speed have high maintenance costs.

8.5.5 Extrusion

Extrusion is the most commonly applied shaping technique for catalysts or catalyst supports. Many types of extrusion equipment are used, some of which are very sophisticated, but the process is in principle very simple. A wet paste of the catalyst is fed to a screw transport system and the screw forces the paste through small holes in a die plate at the end of the extruder (see Fig. 8.12). This die can have holes in the form of a circle, rings, ovals, stars, three-lobed joined rings and many other shapes, so extrudates of different shapes and sizes can be made. As the ribbon of the extruded paste emerges from the hole in the die plate it begins to dry and harden sufficiently to maintain its shape. The ribbon is either cut into prescribed lengths by a knife rotating outside the end plate or allowed to break up in small pieces of irregular length when the material is dried and calcined in a drier or calciner.

The extruder can be fed with a paste or a dry powder. In the case of a dry powder the extruder will have a kneading section where a liquid is added to the powder and the powder is kneaded to a paste. In the other case the paste is made in a separate kneader before feeding it into the extruder. The rheological properties of the paste are very important, so the formulation of the paste is the most

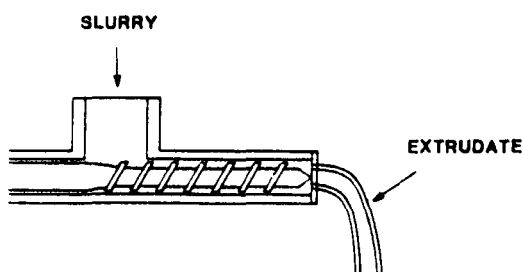


Fig. 8.12. Production of extrudates [13].

important part of this shaping process. Peptizing agents such as nitric acid are used to deagglomerate the particles in the powder. This step also helps to govern the mesoporosity of the end product [21–23]. The peptization influences the flow behaviour of the paste. The porosity of the starting powder and the end product determine the quantity of fluid which must be added to the powder. The high pressure in the extruder will diminish the pore volume of the extrudate during the extrusion process, so the pore volume of the extrudate will be less than the pore volume of the starting powder. The volume of fluid/gram of powder which is added to the powder must be equal to or slightly more than the pore volume of the end product. If it is much more there will be no ribbon coming out of the extruder but a fluid. If it is much less the paste will stick in the extruder and it will not be easy to get the dry paste out.

The shape of the holes in the die, and especially the shape of the entrance of these holes is also very important in this shaping process [15,16]. The material used for the die plate like teflon, nylon, stainless steel, etc. [17], can also play an important role in the extrusion process.

Sometimes additives are used, e.g.

- compounds for improving the rheological behaviour of the paste;
- deflocculants to improve the peptization and to increase the content of solids;
- compounds to bind the water coming out of the pores during the extrusion;
- combustible material to increase the macroporosity.

This type of shaping is also an art and is the proprietary technology of the catalyst manufacturer. Thus little is known in the open literature [21–26]. However, there are more publications about the extrusion of ceramics and clays [27,28].

If the extrusion is performing well the particles formed are very regular, hard and uniform. The extruder can produce great quantities of variously shaped products and, as a consequence, the extrusion process is relatively cheap in comparison with the pelletization method of making catalyst shapes. The mechanical strength is less than that of the pellets so the extrudates are less resistant to abrasion, but they do have better characteristics from the standpoint of porosity and freedom from lubricant. Furthermore, many different shapes and sizes are possible.

8.5.6 Oil-Drop Method/Sol-Gel Method

Spheronizing processes for particles in the millimetre range may be classified into methods which rely on the build-up of smaller particles into spheres by means of a rolling, or ‘snowball’ technique (see granulation), and those which form spheres by individually shaping particles. The production costs are low for the first technique, but the spheres are irregular and there is a broad particle size distribution. The spheres manufactured by individual shaping are more expensive,

but their shape and particle size are very regular and they have a higher mechanical strength. In general, catalysts or supports of this type are produced by the so-called 'oil-drop' or 'sol-gel' method; i.e. by suspending drops of an aqueous liquid in a water-immiscible liquid such as silanol or another oil so as to form spherical drops. The gelation of the drops is brought about by a change in pH. The spheres are then aged for a sufficient time so that the drops can be withdrawn, washed, dried and calcined.

The principle of the sol-gel process is as follows. A sol is prepared by peptizing a well suited alumina powder with an acid. The powder particles or agglomerates are stabilized by a positively charged layer on the surface of these particles. An increase in pH allows the hydroxyl ions to neutralize the positive ions on the surface of the particles. These particles will grow together to larger particles and gelation will occur. The sol-gel process can be carried out in several ways:

- For small spheres the sol in the spheres is gelated by an external ammonia solution through which the sol droplets fall after passing the oil layer. The gelating process in the droplets continues during the aging step to confer sufficient rigidity on the spheres [29–31].
- For larger spheres the sol itself contains compounds like urea or hexamethylenetetramine which decompose in the heated oil (ca 90°C) giving hydroxyl ions which will increase the pH [29–32] and cause gelation.
- Another method has been developed by Labofina [33] in which organic monomers are used which polymerize in the heated oil, giving sufficient rigidity to the spheres so that they may be handled with ease during the ensuing steps.

Sol-gel processes have been used for the preparation of silica [34] and alumina supports [30,35].

A description is given of a sol-gel process in Fig. 8.13 [31,32]. This equipment can also be used for *in-situ* impregnation of the gelated spheres. In that case the salt which is used for impregnation will be dissolved in the ammonia solution [31].

The procedure for the preparation of alumina spheres is as follows. Pseudoboehmite powder ($\text{AlOOH} \cdot x\text{H}_2\text{O}$) is dispersed in an aqueous solution of urea and a monovalent inorganic acid, e.g. HNO_3 . The type of powder or powder mixture may exert considerable influence on the properties of the sol and the end product [12]. The type of acid which is used for the peptization of the pseudoboehmite powder is not very important [12], so nitric acid is used, being the most suitable one.

The viscosity of the sol, which is very important in relation with the dropping, will be controlled by the concentration of the powder, urea and nitric acid. Pseudoboehmite concentrations as high as 33 wt.% are possible. Urea addition lowers the viscosity of the sol and there is an optimum viscosity, depending on the amount of acid added. To obtain a good dispersion of the alumina particles in the sol, the sol must be made by using a high shear mixer. The sol of the correct viscosity is pumped through the orifices and the droplets will fall into the oil

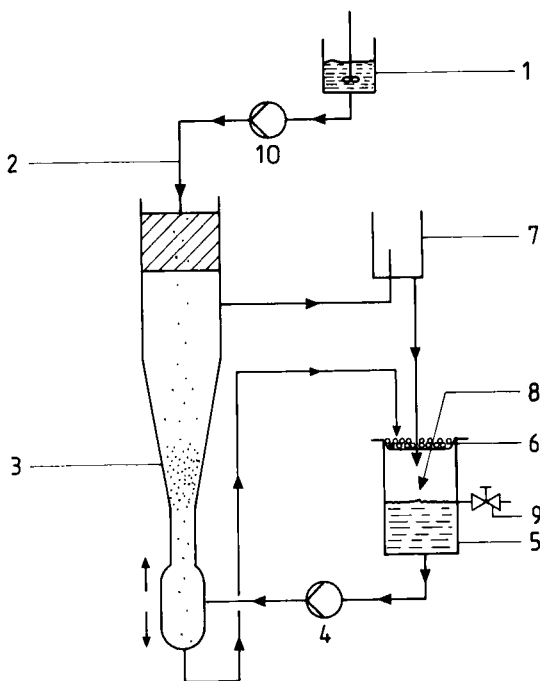


Fig. 8.13. Diagram of a set up for continuous sol-gel preparation of alumina spheres. (1) sol preparaton; (2) dropping of sol into layer of petrol ether; (3) gelation reactor filled with a NH_4OH solution; (4) circulation pump; (5) supply vessel for the gelation fluid; (6) particle separation; (7) overflow, maintaining a certain level in (3); (8) addition of fresh NH_4OH solution; (9) purge; (10) sol pump.

layer (petroleum ether, b.p. 40–60°C) with a layer thickness of 20 cm. Some ionic surfactant is added to the oil to ensure that the droplets easily pass the oil/water interface. Gelation of the sol droplets will occur in the ammonia solution and round spheres will be formed. The residence time in the gelating fluid will be influenced by the density of the droplets and the fluid and the flow velocity of the fluid. For a complete gelation a residence time of about 30 minutes for spheres with a diameter of 5 mm is sufficient [20]. The gelated spheres are sieved, washed with water and ethanol and dried at about 80°C. The spheres are calcined after drying. After calcination, alumina spheres will be produced all with the same diameter of about 3 mm and a high mechanical stability.

The preparation parameters during the sol-gel process are of great influence on properties like pore distribution, pore volume, strength etc. of the end product. It is possible to enlarge the pores in the gelated spheres by applying a hydrothermal treatment after the gelating step [36]. All these parameters can be controlled. So this method makes it is possible to prepare 'tailor-made' supports for catalysts in a reproducible way.

REFERENCES

- 1 G.C. Bond, *Heterogeneous Catalysis; Principles and Applications* (2nd edn.), Oxford Science Publications, 1987.
- 2 R.K. Iler, *The Chemistry of Silica*, Wiley, 1979.
- 3 P.W.J.G. Wijnen, A spectroscopic study of silica gel formation from aqueous silicate solutions, Ph.D. Thesis, TU Eindhoven, 1990.
- 4 H.P. Böhm, *Adv. Catal.*, 16 (1966) 220.
- 5 D. Barby, Silicas, in: G.D. Parfitt and K.S.W. King (Editors), *Characterization of Powder Surfaces*, Academic Press, New York, 1976.
- 6 B.C. Lippens, Ph.D. Thesis, TU Delft, 1961.
- 7 D.W. Breck, *Zeolite Molecular Sieves*, Wiley, 1974.
- 8 J.C. Jansen, The synthesis of zeolites, in: H. van Bekkum, E.M. Flanigen and J.C. Jansen (Editors), *Introduction of Zeolite Science and Practice*, Studies in Surface Science and Catalysis, Vol. 58, Elsevier, Amsterdam, 1991, pp. 77–136.
- 9 Henkel GmbH, Dutch Patent Application 74 06306 (1974).
- 10 D.W. Breck, U.S. Patent 3,130,007 (1964).
- 11 R.J. Argauer and G.R. Landolt, U.S. Patent 3,702,886 (1972).
- 12 A.B. Stiles, *Catalyst Manufacture*, Chemical Industries 14, Marcel Dekker, New York, 1983.
- 13 J.T. Richardson, *Principles of Catalyst Development*, Plenum Press, New York, 1989.
- 14 'Compaction of Particulate Solids', Course Manual, University of Bradford, 9–11 April 1980.
- 15 S.J. Lukasiewicz, *J. Am. Ceram. Soc.*, 72 (4) (1989) 617–624.
- 16 D. Kumar, R. Ladisch, E. Lutz and N. Clausen, *Ber. DKG* 5/88, 141–144.
- 17 K. Masters, *Spray Drying* (4th edn.), Wiley, New York, 1985.
- 18 H. Rumpf, in: W.A. Knepper (Editor), *Agglomoration*, Interscience, 1962.
- 19 D.M. Newitt and J.H. Conway-Jones, *Trans. Inst. Chem. Eng.*, 36 (1958) 422.
- 20 H. Rumpf, *Chem. Eng. Techn.*, 30 (1958) 144.
- 21 W. Stoepler and K.K. Unger, in: G. Poncelet, P. Grange and P.A. Jacobs (Editors), *Preparation of Catalysis III*, Studies in Surface Science and Catalysis Vol. 16, Elsevier, Amsterdam, 1983, pp. 643–651.
- 22 K. Jiratova, L. Janácek and P. Schneider, *ibid.* pp. 653–663.
- 23 A. Damme and K.K. Unger, in: B. Delmon, P. Grange, P.A. Jacobs and G. Poncelet (Editors), *Preparation of Catalysts IV*, Studies in Surface Science and Catalysis Vol. 31, Elsevier, Amsterdam 1987, pp. 343–351.
- 24 A. Ovenston and J.J. Benbow, *Trans. Br. Ceram. Soc.*, 67 (1968) 543–567.
- 25 J.J. Benbow, *Chem. Eng. Sci.*, 26 (1971) 1497–1473.
- 26 R.M. Griffith, *Can. J. Chem. Eng.*, (1966), 108–110.
- 27 J.J. Benbow, S.H. Jazayeri and J. Bridgewater, in: G.J. Messing, E.R. Fuller and H. Hauser (Editors), *Cer. Trans.*, Vol. IIB, Am. Cer. Soc., pp. 624–634.
- 28 ibid., Proc. 2nd Int. Conf. on Ceramic Powder Processing Science, Berchtesgaden, 1988. H. Hausner, G.L. Messing and S. Hirano (Editors), Deutsche Ker. Gesellschaft, Köln, 1990, pp. 581–587.
- 29 M.E.A. Hermans, *Sc. of Cer.*, 5 (1970) 523–538.
- 30 A. Meyer and K. Noweck, Eur. Pat. 0090994 (1987)
- 31 A.E. Duisterwinkel, Ph.D. Thesis, Delft University Press, Delft 1991.
A.E. Duisterwinkel, Dutch Patent Application 90.01093, May 1990.
- 32 H. Barton *et al.*, in: B. Delmon, P.A. Grange and G. Poncelet (Editors), *Preparation of*

- Catalysts IV, Studies in Surface Science and Catalysis Vol. 31, Elsevier, Amsterdam, 1987,*
pp. 103–111.
- 33 R.M. Cahen, J.M. Andre and H.R. Debus, in: B. Delmon, P. Grange, P. Jacobs and G. Poncelet (Editors), *Preparation of Catalysts II, Studies in Surface Science and Catalysis Vol. 3, Elsevier, Amsterdam, 1979*, pp. 585–594.
 - 34 T.G. Spek, Eur. Patent 0067459 (1982).
 - 35 M.A. Day, Eur. Patent 0115927 (1984).
 - 36 C.J.G. van der Grift, Ph.D. Thesis, University of Utrecht, May 1990.

Chapter 9

Preparation of supported catalysts

9.1 INTRODUCTION

The preparation of supported catalysts is, as the saying goes, still much more an art than a science. Usually, after the catalyst for a particular purpose has been identified, its manufacture is optimized through varying experimentally easily accessible parameters (pH , T , loading of the active phase, additives) in a previously established basic recipe. It is not that the fundamental chemistry involved is not known, but the best catalyst-preparation recipes are generally so complicated, chemically speaking, that no precise description of the reactions taking place during the manufacturing process can be given. Nevertheless, the scientific basis of catalyst preparation has received quite a lot of attention in recent years, and in a few cases a rather detailed understanding of the various steps in the preparation procedure has been achieved. Since the aim of the present work is to emphasize molecular aspects wherever possible, it is these cases that will receive most attention, more than perhaps would be warranted on the basis of their (industrial) importance.

It is worth mentioning again that supported catalysts are often applied, because they combine a relatively high dispersion (amount of active surface) with a high degree of thermostability of the catalytic component, cf. Fig. 9.1. The support, which is itself usually not catalytically active (but it may be), is a thermostable, highly porous material onto which the active component is applied. Frequently used support materials are $\gamma\text{-Al}_2\text{O}_3$, SiO_2 , active C, and, to a lesser extent, TiO_2 . Supported catalysts can be prepared basically in two ways: (i) selective removal of a component from a non-porous phase containing (a precursor of) the active component(s) and the support, e.g. a coprecipitate; and (ii) separate application of (a precursor of) the catalytically active material(s) onto a pre-existing support, e.g. by impregnation or precipitation. Which one will be

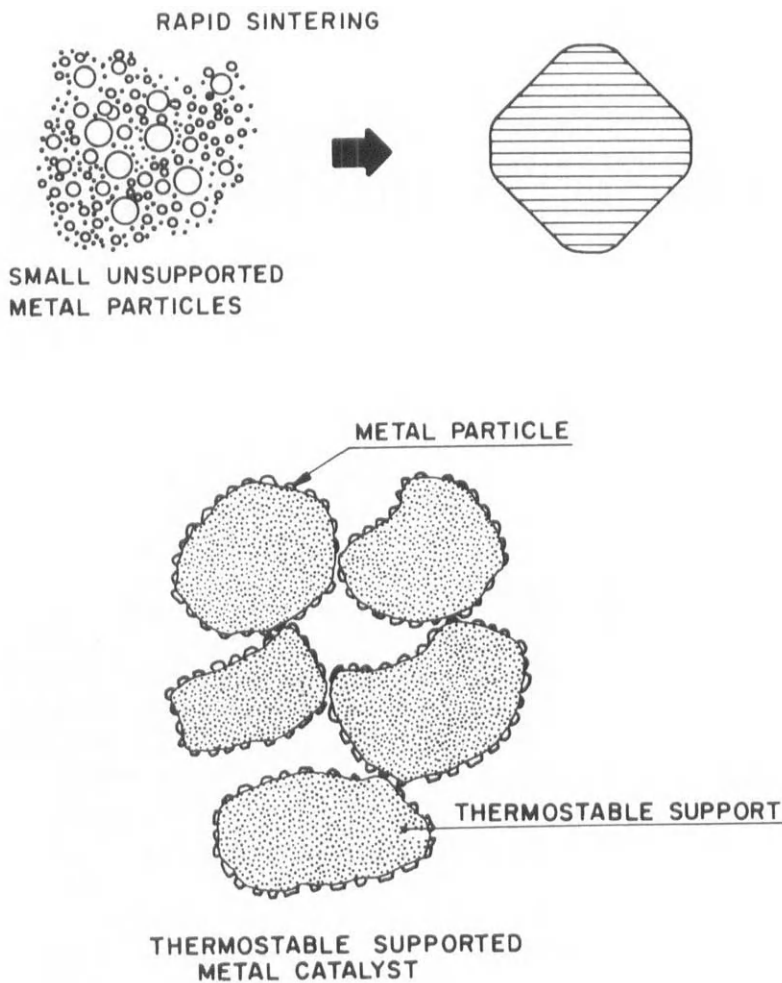


Fig. 9.1. A thermostable carrier prevents sintering of the active material.

chosen in a particular case depends, among other things, on the loading one wants to achieve: when applying cheap metals and oxides one typically strives for maximum active surface area per unit volume, in which case the selective removal strategy may well be advantageous; however, the very expensive noble metals are employed only at low loadings, where the aim is to prepare very small particles having almost all their atoms at the surface (maximum utilization), and impregnation is then the method of choice. In this chapter, we will first discuss route (i), and then go on to discuss route (ii). In the latter case, the interaction of the catalyst precursor and the support surface turns out to be of crucial importance. To understand this interaction one needs some understanding of the surface chemistry of support materials, and this is provided in Section 9.3.1.

9.2 SELECTIVE REMOVAL

Many industrially used, high-loading supported catalysts are produced by selective removal of mainly water and oxygen, and, sometimes, carbon dioxide, from a non-porous precursor material. An old, but still very important example is the ammonia synthesis catalyst. The starting material of this catalyst is a melt of magnetite (Fe_3O_4), alumina, and potassium oxide produced in an electric furnace in a non-oxidizing atmosphere at about 1500°C. Utilization of magnetite, or a corresponding mixture of iron (II) and iron (III) oxides, is required to dissolve the alumina. The alumina and potassium oxide content is low, viz. of the order of 2 to 5 wt.%. After a (difficult) crushing to particles (granules) of the required size, the catalyst is reduced and passivated. The selective removal of oxygen during reduction leads to highly porous, mechanically strong particles. The high iron content causes the iron surface area per unit volume to be high; but the relatively narrow pores in the resulting catalyst lead to diffusion limitations. Collapse of the structure during reduction and at reaction temperatures (400–500°C) is prevented by the alumina acting as a spacer. Here, the alumina, due to its minor presence, is not referred to as a support, but as a structural promoter. The K_2O mainly acts as an electronic promoter, facilitating the dissociative chemisorption of N_2 . Although the production of this catalyst is rather expensive, its excellent properties have ensured it a dominant position ever since its invention in about 1910.

Other catalysts used in large-scale processes are produced starting from coprecipitates. Instances are the Ni/alumina (methane) steam reforming catalyst and Cu(oxide)-Zn oxide/alumina catalysts applied in the low-temperature CO shift reaction and in methanol synthesis. The ions of the active component(s) and of the support are precipitated together as hydroxides or hydroxy salts (e.g. hydroxy carbonates), using NaOH or NaHCO_3 as the precipitating agent. After filtering and drying, the solid is processed into pellets, calcined and reduced (alternatively the solids are pelletized after calcination). It is essential that the ions of the active material and the support are intimately mixed already in the precipitation step to achieve a homogeneous distribution of the active particles in the final catalyst, i.e. they have to precipitate simultaneously. Usually this requires variations of pH to be prevented, since this would result in the preferential precipitation of one component. Interestingly, with nickel and aluminium ions coprecipitation can result in a mixed basic carbonate, while copper and zinc ions can also react to form a mixed basic salt. Indeed, strictly speaking, real coprecipitation only occurs when a ‘double salt’, i.e. a material with fixed stoichiometry and characterized by a single solubility product, is produced; most often one has simultaneous precipitation and co-aggregation. Removal of CO_2 and water during calcination and of oxygen during reduction leads to the porous catalyst. In the $\text{Ni}/\text{Al}_2\text{O}_3$ case the calcination temperature should not be too high

to prevent spinel formation, which would reduce the reducibility of the nickel component drastically.

It is fair to say, however, that this manufacturing route is not easy to control. The extent of mixing of the constituents depends on the details of the precipitation procedure (order and mode of addition of the different solutions, temperature, aging period of precipitate in the mother liquor, filtering and washing procedures). The size of the active particles, their distribution, as well as the porous structure and the mechanical strength of the finished (reduced) catalyst pellets vary considerably with the extent of mixing of the components established in the precipitation step. Scaling-up of the coprecipitation reaction, asking for the efficient mixing of large volumes of solutions, is hard. Also, the structure of the solid is profoundly changed during calcination and reduction. The properties of the resulting catalyst depends on variables such as water vapour pressure and the local thermal history. With large volumes of catalyst to be thermally treated, it is difficult to control these variables and to prevent considerable variations over the catalyst bed. Production of supported catalysts by coprecipitation is analogous to building and pushing over a brick wall, the pushing over being a metaphor for the drastic change in the structure of the solid during the removal of water, carbon dioxide and oxygen. While it is already difficult to build the wall reproducibly by coprecipitation, it is well nigh impossible to push it over in an entirely controlled way. Nevertheless, it is often not possible to establish a reasonably uniform, dense distribution of active particles by other methods, while the intimate interactions fostered during coprecipitation may result in higher activity and/or stability of the active metal crystallites, and several industrially important catalysts are still produced from coprecipitates.

9.3 APPLICATION ON A SEPARATELY PRODUCED SUPPORT

In this section we will discuss extensively the processes of precipitation and impregnation. The phenomena of adsorption and ion-exchange will be subsumed under the latter heading. Each preparation route has its advantages and disadvantages, and often a preference for one technique over the other is a matter of compromise. The active component can be applied on powder supports or on preshaped porous carrier bodies, e.g. extrudates. In the former case, pore-diffusion limitations that would give uneven active-phase distributions are virtually absent, but in the latter case one has better control of pore-size distribution and handling is easier. Active components deposited in large amounts onto powders change their mechanical and surface properties, so that subsequent pelleting or extrusion may be more difficult. In the laboratory, deposition onto powders is often practised, but commercial manufacturers find preshaping on the whole more practical.

9.3.1 Support Surface Chemistry

9.3.1.1 Oxides

The surface of an oxide offers an approaching active-phase precursor various sites with which to interact, viz. different types of hydroxyl groups, roughly classified as acidic, neutral and basic, and coordinatively unsaturated (c.u.s.) metal sites (Lewis-acid centres). The OH groups can be distinguished with IR spectroscopy: the lower its OH stretching frequency, for a given oxide, the more acidic its character. Some representative IR spectra (O–H stretch region) of the more important oxidic support materials $\gamma\text{-Al}_2\text{O}_3$, SiO_2 and TiO_2 , are shown in Fig. 9.2. Roughly speaking, one can distinguish in the $\gamma\text{-Al}_2\text{O}_3$ OH spectrum three

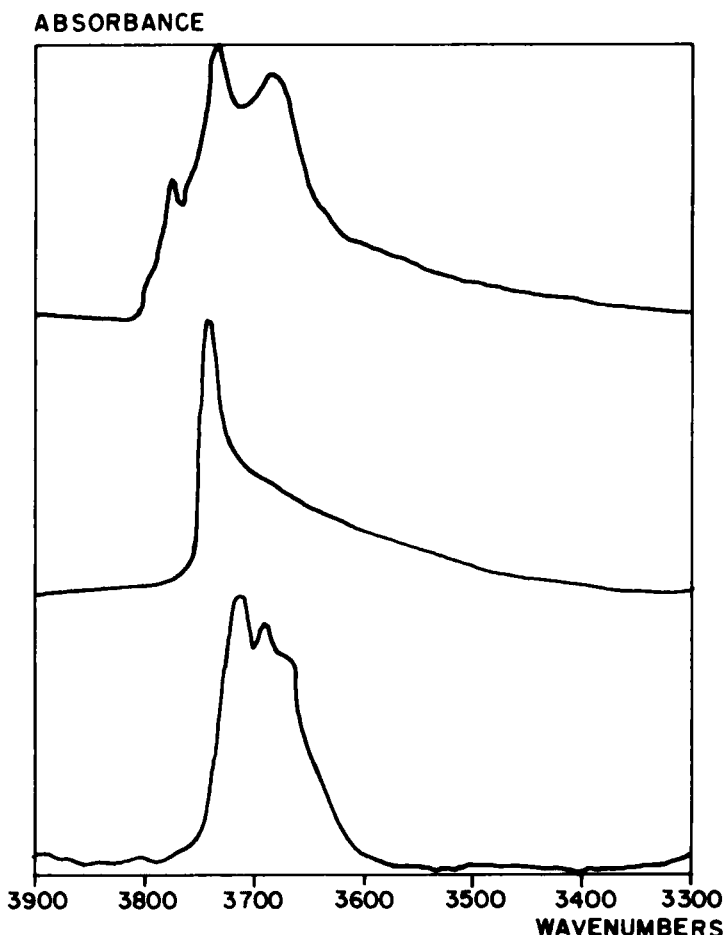
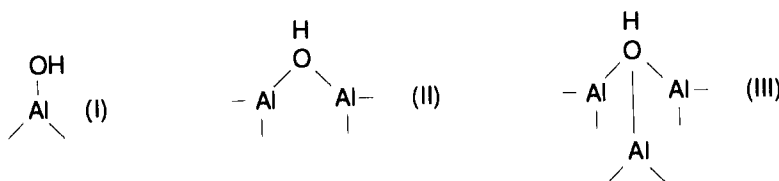
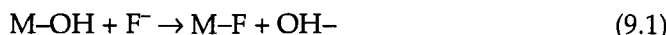


Fig. 9.2. IR spectra (OH stretch region) of, from top to bottom, $\gamma\text{-Al}_2\text{O}_3$, SiO_2 and TiO_2 .

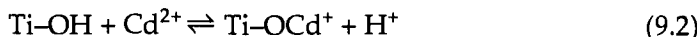
band systems, which can be assigned to specific surface OH configurations: The high-frequency band is due to structures of type I, while the middle and low-frequency bands are due to structures of types II and III, respectively.



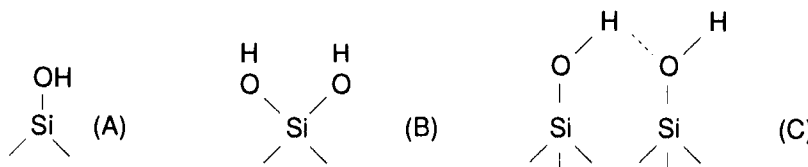
Similarly, for TiO_2 , whose spectrum consists of two band systems, the high-frequency one corresponds to basic, i.e. single-bonded, hydroxyl groups, while the other corresponds to more acidic bridged hydroxyls. The anionic character of the type I hydroxyls on alumina and titania is exemplified by the fact that they preferentially exchange with fluoride ions:



In their turn, the acidic hydroxyl groups on TiO_2 are preferentially methylated using such agents as methyl iodide and p-toluenesulphonic acid. The exchange of Cd^{2+} ions also involves primarily these groups, as one would expect:

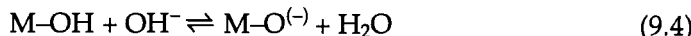


The OH stretch region of the IR spectrum of SiO_2 typically consists of a strong sharp band at about 3740 cm^{-1} and a broader feature at lower wavenumbers (cf. Fig. 9.2b). The sharp band can be ascribed to isolated (A), and presumably also to geminal (B) hydroxyls, while the broader feature is due to vicinal (C) hydroxyl groups, which show internal hydrogen bonding:

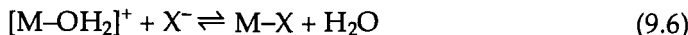
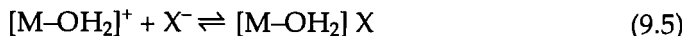


Chemically speaking, however, these $\text{Si}-\text{OH}$ groups are difficult to distinguish, and for most purposes one can regard them as forming a homogeneous population. We note in passing that 'internal' hydroxyls (i.e. existing in the bulk, rather than on the surface of the silica) are sometimes present and contribute to the broad feature in the IR spectrum.

When an oxide is brought into contact with an aqueous solution, the surface hydroxyl groups enter into the following equilibria:



where the basic OH groups will be primarily involved in reaction 9.3 and acidic ones in reaction 9.4. The extent of surface charging, and its sign, obviously depends on the pH of the solution with which the surface is in contact. The pH at which the net surface charge is zero is called the pzc (= point of zero charge). Of the oxides discussed here, $\gamma\text{-Al}_2\text{O}_3$ is the most basic and has a pzc of about 8, TiO_2 is intermediate with a pzc of 5–6, while SiO_2 is the most acidic with a pzc near 2. Above the pzc, the surface of a particular oxide is negatively charged, and will attract cations, while below the pzc it is positively charged, and anionic species will be able to adsorb, under formation of an outer-sphere (reaction 9.5), or an inner-sphere (reaction 9.6) complex:



A good example of outer-sphere complex formation is the adsorption of $\text{Co}(\text{CN})_6^{3-}$ ions on $\gamma\text{-Al}_2\text{O}_3$. As can be seen from Fig. 9.3, lowering the pH leads to a concomitant increase in the amount of anion adsorbed, while neutralizing the solution again induces the $\text{Co}(\text{CN})_6^{3-}$ ions to desorb again. The process is perfectly reversible, which is not usually the case for inner-sphere complex formation.

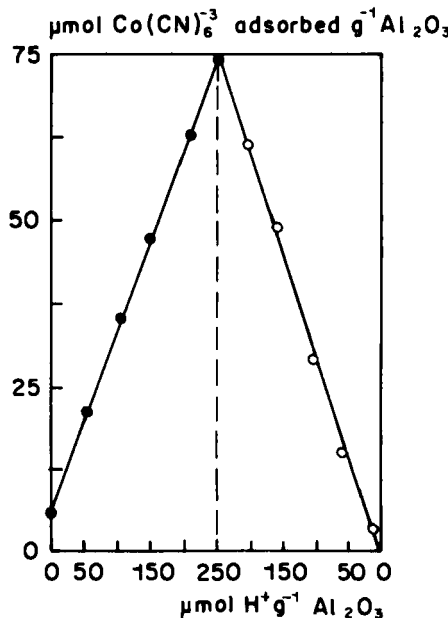


Fig. 9.3. Adsorption of cobalt cyanide ions on $\gamma\text{-Al}_2\text{O}_3$ as a function of surface protonation.

●, addition of HNO_3 ; ○, addition of KOH .

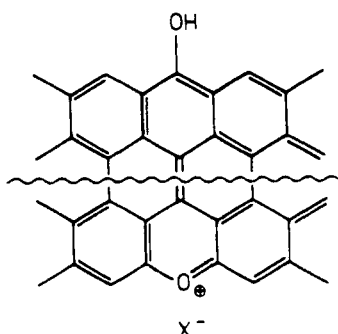


Fig. 9.4. Model of basic surface oxides on carbon. The wave line indicates that the two oxygen functions can be separated by some distance; it is only necessary that a suitable resonance structure can be constructed. X^- symbolizes an exchangeable anion. (Reproduced by permission from H.P. Boehm and H. Knozinger, *Catalysis*, Vol. 4, Ch. 2, Springer-Verlag, Berlin, 1983.)

9.3.1.2 Active carbon

The surface of active carbons contains a rather wide variety of oxygen-containing groups, which have not yet been completely analyzed. Such acidic surface groups as carboxylic acid and phenolic hydroxyl groups are often present. However, the main feature of (active) carbons is that they have weak anionic-exchange properties. The structure of the site responsible for this feature has not been elucidated until now; a recent suggestion is presented in Fig. 9.4. Another important property of (active) carbons is that they can fairly strongly adsorb aromatic molecules, a property that in catalyst preparation is sometimes made use of when cations complexed with (an) aromatic ligand(s) are employed as catalyst precursors. Carbon-supported transition-metal porphyrins, catalysts for the electrochemical reduction of dioxygen, for example, can be simply prepared by letting the chelate adsorb onto the carbon from a suitable solvent.

9.3.2 Impregnation

In impregnation, a solution of a metal salt of sufficient concentration to give the desired loading is added to the support, after which the system is aged, usually for a short time only, dried, and calcined. With a preshaped support an 'incipient wetness' (also called 'dry' or 'pore volume') impregnation is generally used, in which an amount of solution is added which is just sufficient to fill up the pore volume of the support particles, or slightly less. With powdered supports a volume of solution substantially larger than the pore volume can, and often is, applied ('wet' impregnation). Unless the catalyst precursor is strongly adsorbed on the support, it is important to stir the slurry continuously during drying in order to get a homogeneous distribution of the precursor over the support.

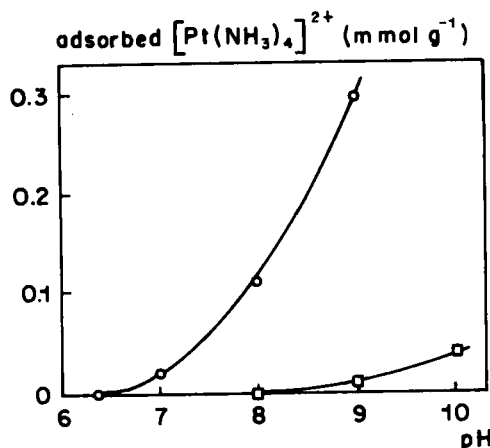


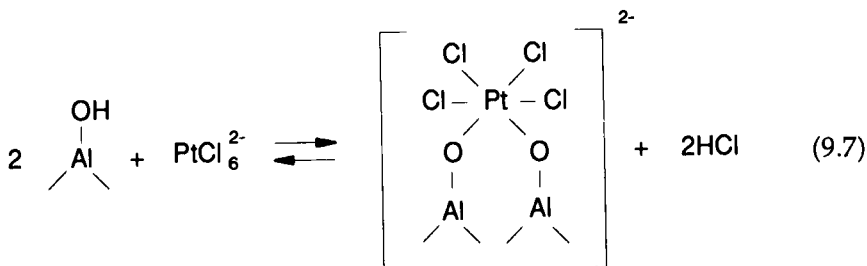
Fig. 9.5. Adsorption from solution containing $[Pt(NH_3)_4]^{2+}$ (as chloride) onto silica gel (Davison 70, $370 \text{ m}^2 \text{ g}^{-1}$) and γ -alumina (Aloca F-20, $204 \text{ m}^2 \text{ g}^{-1}$) as a function of pH. Room temperature. ○, silica gel; □, γ -alumina. After H.A. Benesi, R.M. Curtis and H.P. Studer, *J. Catal.*, 10 (1968) 328.

Adsorption effects in wet impregnation can usually be described in terms of the surface charging model, Eqns. 9.5 and 9.6. As an example, Fig. 9.5 shows the adsorption of the tetraamine Pt cation on silica and alumina as a function of pH; this is a classical route to highly dispersed Pt-on-silica. As expected, in view of its lower pzc, the extent of adsorption is higher for silica, and the adsorption increases with increasing pH. A pH of about 9 is the practical limit, since above that value the silica and alumina supports start to dissolve appreciably. In the case of zeolites, one introduces the catalyst precursor by ion exchange if at all possible. The problem here is, to keep the metal particles inside the crystallites during calcination and reduction. Various detailed procedures have been developed to deal with this problem. In the remainder of this section we will focus on dry impregnation of preshaped carriers — we will first have a look at three examples in which adsorption plays an important role, and then go on to discuss what can happen if the precursor-support interaction is weak or absent, and what tricks there are to counteract any undesirable effects.

9.3.2.1 Supported noble-metal catalysts

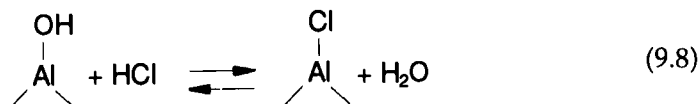
As there are no qualitative differences between the various noble metals as far as the chemistry involved in placing them on the various supports is concerned, we will limit our discussion to just one of them, viz. platinum.

Alumina-supported Pt catalyst are conventionally made via impregnation of $\gamma\text{-Al}_2\text{O}_3$ extrudates with an aqueous solution of chloroplatinic acid, H_2PtCl_6 . The acid adsorbs strongly on the alumina surface and, in view of its being relatively irreversible, can be described as involving an inner sphere complex according to:

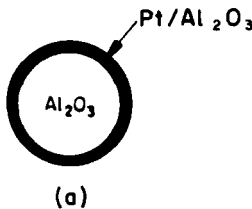


The Al-OH groups involved in this reaction are likely to be the basic ones, since the adsorption reaction is probably to be thought of as analogous to the hydrolysis of the PtCl_6^{2-} species that occurs in aqueous solution at higher pH values. The fact that the platinum adsorption capacity of a typical γ -alumina is of the order of $1.5 \mu\text{mol}/\text{m}^2$, while the amount of basic OH groups is typically 3 to $3.5 \mu\text{mol}/\text{m}^2$, as determined by titration with $\text{MoO}_2(\text{acetylacetone})_2$, fits in nicely with this idea.

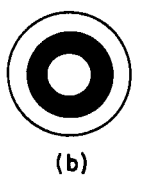
Usually, one aims at a Pt loading considerably lower than that corresponding to saturation, viz. 1 wt.% or less, which corresponds, with the surface area of alumina being typically around $250 \text{ m}^2/\text{g}$, to $0.2 \mu\text{mol}/\text{m}^2$ or less. Impregnation with an aqueous solution containing the required amount of H_2PtCl_6 , however, does not lead to a homogeneous Pt distribution: because of the strong interaction between PtCl_6^{2-} ions and the alumina surface, and since the adsorption reaction is very fast, Pt will be deposited on all the adsorption sites these ions encounter on their way in from the outer surface of the extrudate, until the solution is completely depleted. This results in supported catalyst bodies with the platinum concentrated in the outer rim, as visualized in Fig. 9.6 (egg-shell distribution). Sometimes one wants such a distribution, to be sure, e.g. when the reaction to be catalysed is severely diffusion limited, but more often a homogeneous distribution is desired. This can be achieved by adding HCl to the impregnation solution, which adsorbs on the same sites as the chloroplatinic species according to



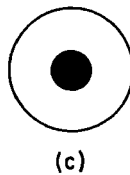
This competitive adsorption drives the platinum deeper into the extrudates, and when sufficient HCl is added, the PtCl_6^{2-} adsorption reaction is moderated to such an extent that a reasonably homogeneous distribution is obtained. One can also add acids that adsorb even more strongly than chloroplatinic acid, e.g. oxalic or citric acid, with which Pt profiles such as shown in Fig. 9.6 can be prepared. Profile (b) can be useful when a strongly adsorbing poison is present in the stream



(a)

SHELL ADSORPTION OF CHLOROPLATINIC ACID.

(b)



(c)



(d)

INCREASING ACID STRENGTH

Fig. 9.6. Pellet concentration profiles with adsorbing acids. (b)–(d): see text.

to be treated, e.g. Pb in automobile exhaust gas, while profiles (c) and (d) could be advantageous e.g. in diffusion-limited consecutive reactions.

After impregnation a $\text{Pt}/\text{Al}_2\text{O}_3$ catalyst is dried and calcined to produce supported Pt-oxide species (some Cl is retained on the alumina), which can then be reduced, usually at relatively mild temperatures (about 300–350°C) in hydrogen to produce small Pt particles (about 10 Å).

In certain applications, e.g. liquid-phase hydrogenations and H_2/O_2 fuel cells, one prefers carbons (active carbon or carbon black) as support material, because they are chemically rather inert (not attacked by strongly acidic or caustic solutions) and, important for fuel cells, electrically conducting. Carbon-supported Pt catalysts are normally prepared in the same way as their alumina-supported counterparts, i.e. via impregnation with an aqueous solution of chloroplatinic acid. Because of the anion-exchange capacity of carbons, there is an interaction, albeit rather weak, between the $\text{PtCl}_6^{(2-)}$ ions and the support which is sufficient to largely prevent migration of the Pt species during drying (see below), but not strong enough to induce large inhomogeneities in Pt distribution, obviating the addition of HCl to the impregnation solution. Alternatively, the carbon can be mildly oxidised to produce surface carboxyl groups and the Pt brought on through ion-exchange.

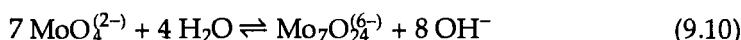
9.3.2.2 Disproportionation catalysts

In the disproportionation (metathesis) of olefins, i.e. the reaction $2R_1-CH=CH-R_2 \rightleftharpoons R_1-CH=CH-R_1 + R_2-CH=CH-R_2$, a MoO_3/Al_2O_3 catalyst is often applied. Its preparation involves impregnation of $\gamma-Al_2O_3$ extrudates with an aqueous solution of ammonium heptamolybdate (AHM) or an ammoniacal solution of ammonium dimolybdate (ADM).

The interaction between AHM and an $\gamma-Al_2O_3$ surface has been extensively studied. Two adsorption reactions take place. In the first instance, HM ions react with the basic OH groups according to



That only the basic OH groups are involved here follows from FTIR measurements: only the high-frequency OH band (Cf. Fig. 9.2a) disappears from the IR spectrum of the alumina support. The tetrahedral coordination of Mo in the adsorbed phase has been verified by EXAFS and Raman spectroscopies (Mo is octahedrally coordinated in AHM). Reaction 9.9 is followed by a (reversible) physisorption of AHM molecules on the c.u.s. Al sites in the alumina surface. When the impregnation is effected with the ammoniacal molybdate solution, which contains only $MoO_4^{(2-)}$ ions at a pH of 9–10, no interaction initially occurs between the solute and the alumina surface: the pH being appreciably higher than the pzc, the basic OH groups are unreactive and the molybdate ions are not attracted to the negatively charged surface. Upon drying, however, the ammonia escapes in preference to water, so that the pH inside the pores drops, which in turn leads to the formation of HM ions according to



this equilibrium starting to shift to the right hand side at pH around 7. The occurrence of this process in the catalyst pores has been verified with Raman spectroscopy (Fig. 9.7). The HM ions, thus formed, then engage in the same adsorption reactions as described above, with this difference that at the drying temperature (70–110°C) the physisorption reaction takes precedence over reaction 9.9.

It has been found that maximum performance is reached at just that loading which corresponds to the adsorption capacity of the alumina carrier employed.

In the case of functionalized olefins, i.e. where R_1 and/or R_2 are not simple alkyl chains, it is better to use a Re_2O_7/Al_2O_3 catalyst. Such catalysts can be prepared by pore-volume impregnation with an aqueous solution of ammonium perrhenate. It is observed that the turnover frequency, i.e. the activity per Re atom, increases considerably with Re_2O_7 loading up to monolayer coverage of the alumina surface (about 18 wt.% Re_2O_7 for an alumina of $200\text{ m}^2/\text{g}$). A theory

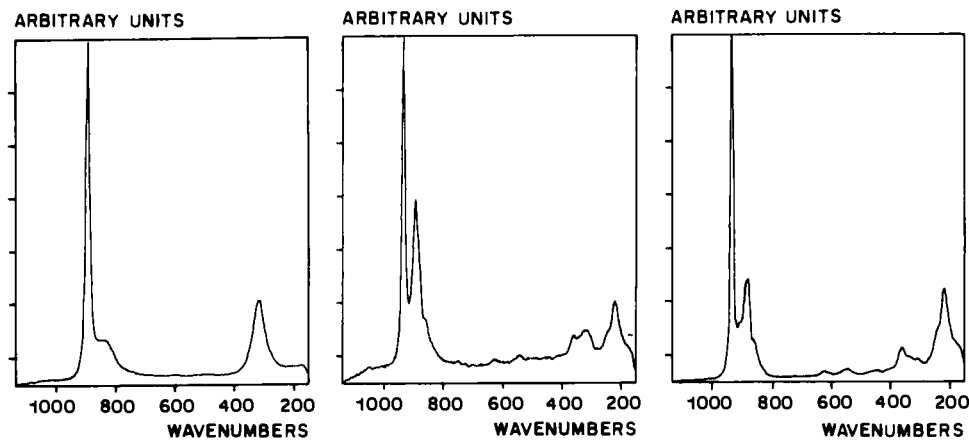


Fig. 9.7A. Ammoniacal Mo solution, after evaporation of (a) 1/3, (b) 2/3, and (c) all of the solution. Raman *in-situ* cell. Spectrum (a) is identical to $(\text{NH}_4)_2\text{MoO}_4$ aq. Spectrum (c) is identical to that of solid AHM.

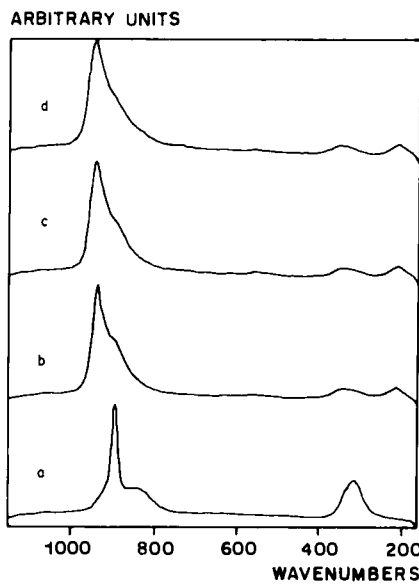


Fig. 9.7B. In-situ Raman spectrum of $\gamma\text{-Al}_2\text{O}_3$ impregnated with ammoniacal Mo solution ($\rightarrow 10.5\text{ \%w Mo}$). (a) Wet catalyst, and after (b) 20, (c) 40, and (d) 60 min drying at 120°C. Spectrum (d) is identical to that of dried AHM/ $\gamma\text{-Al}_2\text{O}_3$ of the same Mo loading.

explaining this behaviour has been proposed, postulating that at low loadings the ReO_4^- ions react with the basic OH groups, and at higher loadings with neutral and acidic ones, only in the last case leading to active, because electron-deficient, Re centres capable of complexing a double bond.

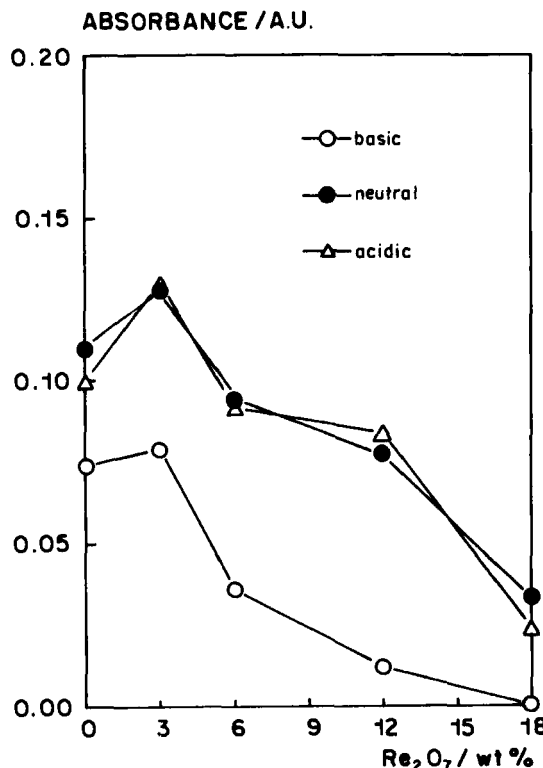


Fig. 9.8. The absorbances of the three different types of OH groups as a function of the Re₂O₇ loading of Re₂O₇/γ-Al₂O₃ catalysts.

In the dried catalyst Re is mainly present as small (NH₄)ReO₄ crystallites, which upon calcination spread over the alumina surface to form isolated ReO₄ units, as has been established by Raman spectroscopy. Studying the evolution of the alumina OH bands with IR, Fig. 9.8, shows that up to 3 wt.% Re₂O₇ the OH groups are not too much affected, the ReO₄⁻ ions presumably reacting with the c.u.s. Al sites, leading to totally inactive sites. With increasing Re₂O₇ loading, it is indeed the high-frequency band that is preferentially reacted away, thus verifying the above postulate.

9.3.2.3 Supported Co(Ni)Mo hydrotreating catalysts

Alumina-supported Co- and Ni-promoted molybdenum sulphide hydrotreating catalysts are the main workhorses in many refineries and have, therefore, attracted a lot of attention from catalytic chemists. They are usually prepared via co-impregnation, i.e. pore-volume impregnation with both Mo and the promoter atom present in solution. After drying and calcining, the catalyst manufacture is complete, but it has to be sulphided before use. Traditionally, this is done *in situ*

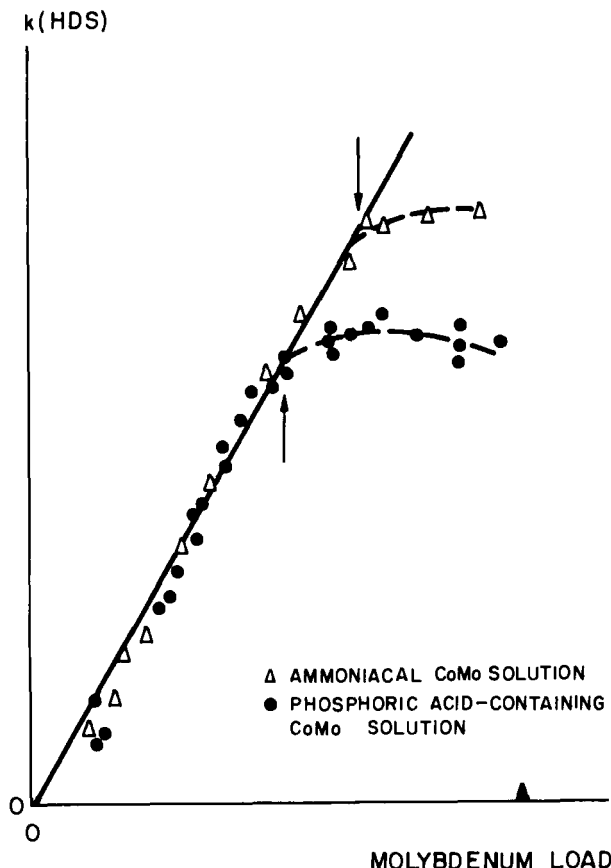


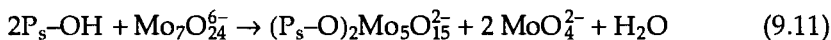
Fig. 9.9. Relationship between HDS activity and CoMo loading. Fixed $\gamma\text{-Al}_2\text{O}_3$ support, fixed Co/Mo atomic ratio. ▲ indicates monolayer coverage of the support by Mo; → indicates Mo-adsorption capacity of the $\gamma\text{-Al}_2\text{O}_3$ applied when using the impregnation solutions indicated.

with the feed to be treated, spiked with some extra sulphur (as, e.g., CS_2), but nowadays one can buy presulphided catalysts, which can be converted into the active form much faster, thus limiting the loss of production days of the hydro-treatment unit. The active phase consists of small MoS_2 particles, 10–15 Å in diameter, with promoter atoms decorating their edges. It is generated from the molybdenum species that adsorb on the alumina carrier during impregnation and drying, as Fig. 9.9 makes plausible — the details of the adsorption reactions will be discussed below. The problem with non-adsorbed Mo is that during calcination it tends to react with the promoter atoms present to form $\text{Co}(\text{Ni})\text{MoO}_4$, which unfortunately is not a good precursor to the active phase. Interacting with the subjacent alumina stabilizes the $\text{Mo}-\text{O}_x$ species against this reaction, leading to a two-dimensional surface phase from which highly dispersed MoS_2 can be generated. The promoter atoms should also be present in this

surface phase, but in the absence of long-range ordering it has been impossible to locate them precisely.

There are two main co-impregnation solutions, one being ammoniacal and the other containing phosphoric acid. The chemistry involved when applying the former is quite similar to that described above for the $\text{MoO}_3/\text{Al}_2\text{O}_3$ disproportionation catalyst. The point is that the presence of Co or Ni ions does not appear to influence the molybdate equilibria and adsorption reactions to any great extent. On the other hand, the concentration profiles of Co/Ni and Mo over the alumina extrudates are always identical, indicating that adsorption or precipitation of the molybdate species entrains adsorption or precipitation of the Co/Ni species. Indeed, when a precipitate develops in an ammoniacal impregnation solution, it does contain both promoter and Mo ions. The precise chemistry involved is as yet obscure, however.

In general, concentrated Mo solutions are difficult to handle, especially when they also contain Co or Ni ions, as they tend to be rather unstable. The situation can be much improved by adding phosphoric acid, because it reacts with molybdate to form a variety of, usually extremely soluble, molybdophosphates, such as $\text{H}_6\text{P}_2\text{Mo}_5\text{O}_{23}$ and $\text{H}_3\text{PMo}_{12}\text{O}_{40}$. The other side of the coin is that the presence of phosphate ions considerably complicates the Mo adsorption chemistry. As far as it is known today, what happens when an alumina is impregnated with a phosphoric acid-containing co-impregnation solution is that part of the alumina surface is converted into an AlPO_4 surface phase. The formation of this phase does not start with the exchange of a basic hydroxyl group for a H_2PO_4^- ion, as might have been expected, but rather with the exchange of a bridging OH. Aluminium-phosphate formation has the following consequences: (i) some loss in support surface area, and (ii) a decrease in the Mo-adsorption capacity of the support. Polyoxomolybdates do adsorb on AlPO_4 via its P-OH groups, e.g. according to



but the level of adsorption is lower than on the original alumina. Moreover, the patches of alumina left in the impregnated particles are somewhat less reactive than in the absence of neighbouring AlPO_4 patches, perhaps for steric reasons.

The Mo adsorption capacity for both the ammoniacal and the phosphoric acid routes of a particular alumina can be estimated on the basis of the adsorption reactions found to obtain in the two cases, and the numbers derived for the alumina used as a support for the catalysts figuring in Fig. 9.9 are indicated in that figure by arrows.

Since a somewhat higher active phase loading can be achieved in the ammoniacal as against the phosphoric acid route, one may wonder why P-containing catalysts are still in use. Well, here we have to draw a distinction between hydrodesulphurization (HDS) and hydrodenitrogenation (HDN). In the former

process phosphorus has no catalytic role to play, so that its presence is of no advantage, and indeed, as the handling of non-P impregnation solutions has improved, we have witnessed a gradual replacement of CoMoP/Al₂O₃ HDS catalysts by their CoMo/Al₂O₃ counterparts. In HDN, however, P acts as a promoter, which more than offsets the slight loss in the amount of active phase, and for this application NiMoP/Al₂O₃ remains the catalyst of choice.

As to calcination temperatures, it is advisable to keep them relatively low, say about 723 K. At significantly higher *T*, the promoter ions tend to go subsurface (incipient spinel formation) and so are lost from the surface, and eventually from the active phase. Also, in the case of a P-containing catalyst, further surface-area loss may occur due to migration of the phosphate anions into the bulk of the alumina.

Although most attention has been paid, naturally, to alumina-supported Co(Ni)Mo catalysts, other supports have been looked at as well. The adsorption of polyoxo molybdates on titania can be described in the same terms as that on alumina: a reaction with basic surface OH groups, followed by physisorption on c.u.s. Ti sites. Since freshly calcined titania contains a relatively small amount of surface hydroxyls, practically a full monolayer coverage can be achieved via the latter adsorption reaction. Classical impregnation routes have not been very successful in the case of silica, however, as adsorption of molybdates occurs only to a limited extent owing to a lack of basic OH groups and Lewis-acid sites on the silica surface. Reasonable Mo loadings at reasonable dispersions can be prepared on active carbon carriers, making use again of their weak anion-exchange capacity; such catalysts should not be calcined, however.

9.3.2.4 Consequences of the absence of precursor–support interaction

In the case where there is no interaction between the catalyst precursor and the support surface to fix the former to the latter, the dynamics of drying become of prime importance. Briefly, upon drying impregnated porous particles (extrudates, pellets, spheres), evaporation of the solvent (almost always water), starts at the external surface, resulting in menisci at the pore mouths and setting up a suction pressure. At normal drying rates, and employing simple aqueous solutions, the liquid lost by vaporization in smaller pores is supplied from the connecting larger pores due to the capillary pressure difference. Thus, the evaporation takes place mainly at the pore mouths of the smaller pores while solution flows from the interior of the particle towards them. The impregnation liquid is by this means concentrated near the mouths of the small pores at the outer surface, until (super)saturation occurs and the catalyst precursor crystallizes or precipitates, which results in the pore-mouths becoming even smaller and so remaining preferentially wetted, etc.. The end result is a segregation of the catalyst precursor at the particle periphery (egg-shell distribution). Here it is assumed, that the concentration differences, caused by the localized evaporation,

are not counterbalanced by diffusion, in which case (super)saturation and crystallization would occur in all still solution-filled pores simultaneously. This is a safe assumption, diffusion being a rather slow process, unless the drying rate is extremely low. Nevertheless, the picture given here is somewhat simplified, and part of the catalyst precursor does usually remain in the interior of the support particle, especially when the pore-size distribution is very sharp (entailing small capillary pressure differences, i.e. relatively little liquid movement). It is further noted that not only is the distribution of the catalyst precursor over the support body inhomogeneous, its particle-size distribution is also often very broad.

As is implicit in the above, the transport of the catalyst precursor to the outer rim of the support body can be suppressed by (i) using very high drying rates, e.g. through applying micro-wave heating, and (ii) increasing the viscosity of the impregnation solution, e.g. by adding a polymeric substance (preferably one that does not increase the viscosity so much at room temperature, so that the impregnation rate is not seriously affected, but only at temperatures in the drying regime). In either case, the rate of removal of water is made higher than the rate of liquid capillary flow, so that the evaporation front moves smoothly inward into the particle, and the solute precipitates concomitantly. It is to be borne in mind, however, that the use of polymeric additives may affect the morphology of the precipitated active phase.

It has also been observed that employing, at near-saturation, a catalyst precursor that does not crystallize at all but rather forms a coating on the support surface, can lead to a homogeneous distribution of small particles — a case in point being the application of an iron EDTA complex at alkaline pH to produce, after calcination, small (2–5 nm) Fe_2O_3 particles homogeneously distributed through SiO_2 extrudates.

9.3.3 Deposition–Precipitation

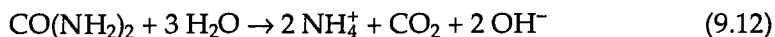
As coprecipitation methods are not easy to control and reproduce, and impregnation techniques can not always be made to yield the desired active-phase distribution, loading and/or dispersion, it is worthwhile considering alternative methods. One of these is deposition–precipitation, which will be discussed in this section.

9.3.3.1 Basics of the method

Traditionally, the objective of precipitation is to obtain a well-dispersed metal hydroxide (or carbonate) phase on a support through its precipitation from an aqueous metal solution onto a support powder by adding a base. The support powder is suspended in the metal salt solution. Upon addition of, say, NaOH , the pH increases strongly and metal hydroxide species are generated. When their concentration exceeds the (super)solubility limit, metal hydroxide particles can

nucleate and grow. The trick is to let the nucleation happen on the support surface rather than in the solution, which would result in large crystallites and an inhomogeneous metal distribution. To prevent rapid nucleation and growth in the bulk of the solution, the precipitant has to be added slowly and under vigorous mixing conditions to prevent the formation of regions of high local pH. The best strategy would appear to be to inject the alkali solution slowly through a hypodermic syringe below the surface of the liquid, while the suspension is vigorously agitated. Highly efficient mixing is difficult to achieve on a large scale, however, so this condition poses an up-scaling problem.

To establish a very uniform distribution of small active particles over a support, and to get around the mixing problem, the procedure of deposition-precipitation was developed. For the method to work well it is essential, as for precipitation in general, that the support facilitates the nucleation of an active precursor (cf. below). In the classical embodiment of the method, a metal salt solution containing urea is well mixed with the support powder at room temperature. Then, the temperature is raised to 70–90°C, where the urea slowly hydrolyses according to



The hydroxyl ions are produced homogeneously throughout the solution, thus obviating the need for strong mixing. Since, in the presence of an active precursor-support interaction, nucleation of the catalyst precursor (metal hydroxide species in the present example) at the surface of the support proceeds at lower concentrations than those needed for precipitation in the bulk of the solution, precipitation exclusively on the support surface can be achieved. This procedure has been used with success to produce a number of different catalysts. An example to illustrate the basics of the method is shown in Fig. 9.10: precipitation of manganese(II) from a homogeneous solution by raising the hydroxyl ion concentration is represented by the evolution of the pH as a function of time during the hydrolysis of urea. Without suspended silica, the pH of the manganese nitrate solution passes through a maximum. Before nucleation in the bulk of the solution can proceed, the concentration has to be increased above the concentration corresponding to the solubility of larger crystallites (supersaturation limit). After nucleation, the pH level drops to that corresponding to the solubility product of manganese(II) hydroxide. With suspended silica, on the other hand, the nucleation barrier is absent, and the precipitation on the silica surface proceeds smoothly.

Apart from raising the pH level, precipitation can be induced in a variety of other ways. Anionic species, for example, can be deposited on the surface of suspended carriers by decreasing the pH level. This procedure has been used for vanadium(V) and Mo(VI). Oxidation at a pH level where the ions of the lower valency are soluble and the oxidized species insoluble, can also be utilized to precipitate from a homogeneous solution. Iron(II/III) and Mn(III/IV) are cases in point. Oxidation can be

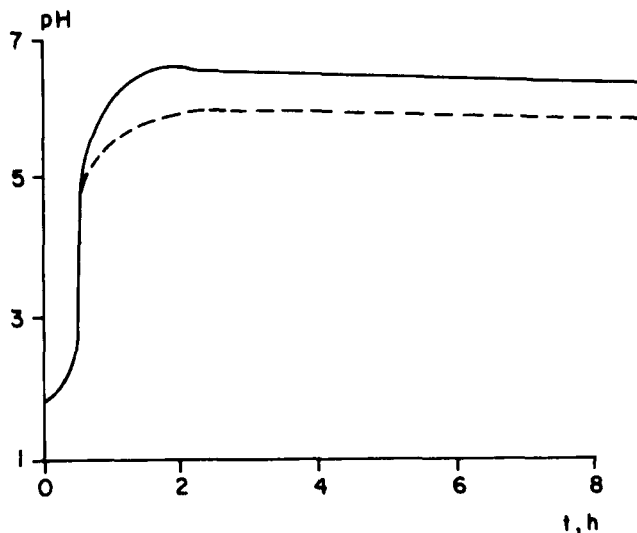


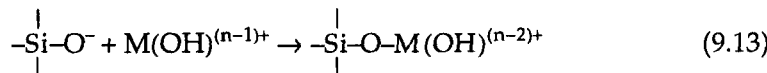
Fig. 9.10. Records of pH as a function of time in the absence (—) and presence (---) of silica during the precipitation of Mn(II).

effected by dissolved agents like nitrate, or electrochemically. Reduction to insoluble ionic compounds has been applied with Cr, Cu, and Mo. Reduction to the metal has also been practised, and appears to work especially well with noble metals. Decomplexing is another possibility: e.g. destruction of complexing EDTA by hydrogen peroxide has been employed to produce supported catalysts.

After the deposition-precipitation step has been completed, the solid is filtered, washed and dried. Before activation and use, it has to be shaped (e.g. pelleted), and, in most cases, calcined.

9.3.3.2 Deposition-precipitation on silica powders

Deposition-precipitation is often practised with silica as the support. Especially suitable is aerosil silica, which consists of very small non-porous spheres, so that the precipitation process is not affected in any way by diffusion processes. It is well known that most hydrolysed metal species have a high affinity for the silica surface, thus fulfilling the condition for obtaining surface precipitation only. In the colloid-chemical literature, the initial adsorption of the (partially) hydrolysed metal ions with a silica surface is often described in terms of a surface-complexation model, involving negatively charged surface sites, which exist on silica at pH above 2 (= pzc of silica), and positively charged metal species:



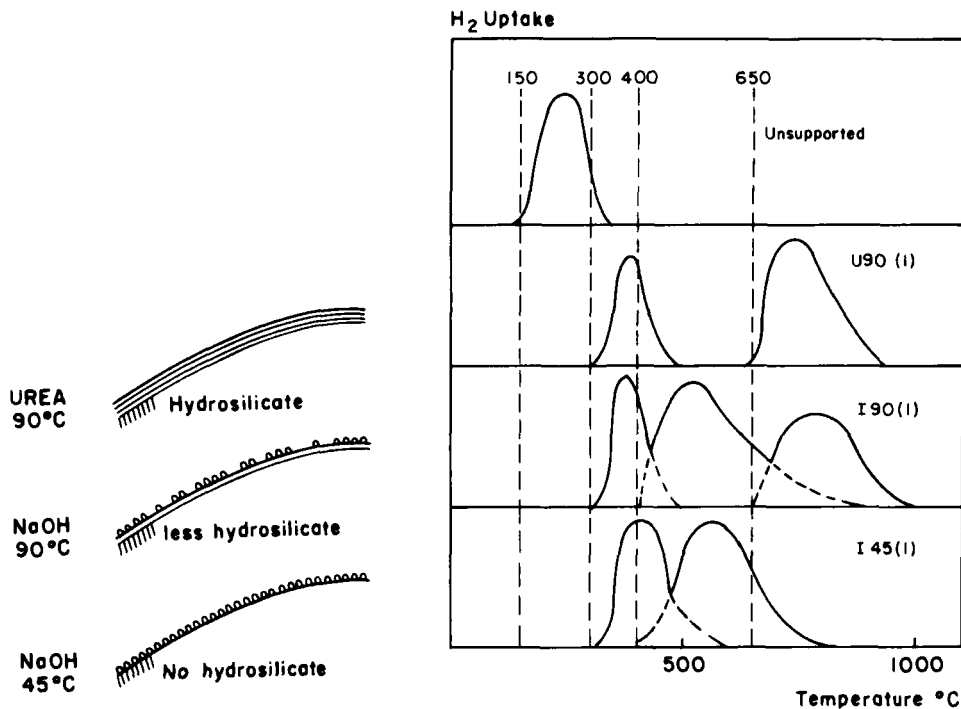
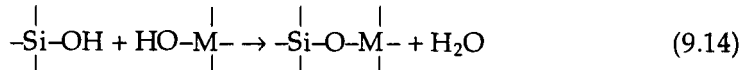


Fig. 9.11. Left: structures resulting from deposition-precipitation of Fe(II) by different procedures. Right: temperature-programmed reduction of Fe oxide deposited on silica by hydrolysis of urea (U 90(1)), injection at 90°C (I 90(1)), and injection at 45°C. For comparison bulk Fe oxide is included.

On the other hand, there is evidence that the pH may affect the reactivity of the hydroxyl groups, in that OH⁻ ions have been found to catalyse the condensation of two hydroxyl groups on different silica particles to water and an oxygen bridge. In analogy, an alternative description of the initial reaction between a hydrolysed metal species and the silica surface would be



A careful study of Cu(II) precipitation on SiO₂ from different salts has shown that the latter description is in fact quite satisfactory.

It has been established that the pH needs to be above about 4 for reaction 9.14 to proceed. Thus, in the case of Fe(III), where nucleation already starts at pH around 2, the silica surface is not able to compete, and Fe(OH)₃ particles are generated in solution. These particles do not subsequently react with the silica surface upon further increasing the pH, resulting eventually in a separate, rather than supported, iron (hydr)oxide phase. However, iron(III) can be deposited on SiO₂ by injecting a weakly acidic Fe(III) solution into a silica suspension, whose pH is kept above 5.

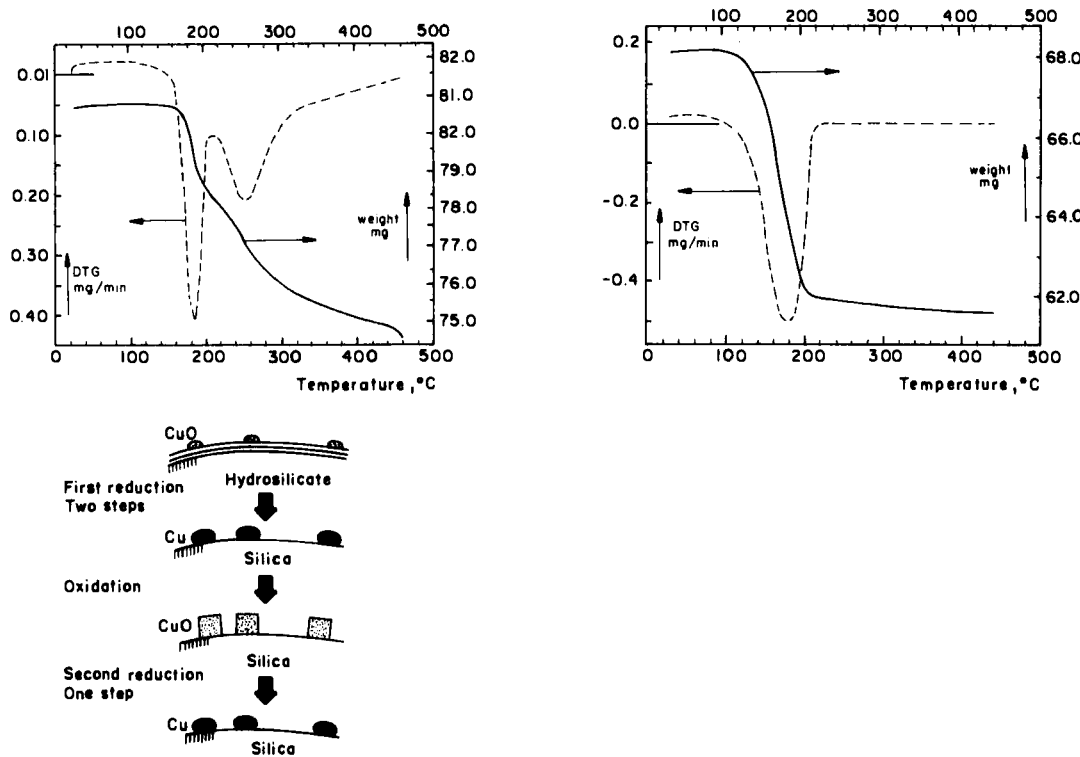


Fig. 9.12. Thermogravimetric reduction of Cu deposited on silica from basic Cu nitrate. Both the weight and the rate of the decrease in weight are represented. Top left: first reduction. Top right: second reduction. Bottom: structure of catalyst before and after reduction, reoxidation and second reduction.

To produce Fe(oxide)/ SiO_2 particles one could use a solution of Fe(II), in which case air has to be excluded to prevent its oxidation to Fe(III). Iron (II) starts to react markedly above $\text{pH} = 4.8$ (urea, 90°C). In this case, the reaction is not limited to Eqn. 9.14, but a bulk hydrosilicate is formed. Upon performing an injection experiment at 45°C , it is observed that the reaction with the support is less extensive at that temperature. As the slightly higher pH at the injection point brings about the formation of a less reactive iron species, attack of the support is less marked than in the urea case even at 90°C . The structures obtained in the three different experiments are indicated in Fig. 9.11. The different extents of hydrosilicate formation are reflected in the temperature-programmed reduction (TPR) experiments, as can be seen in Fig. 9.11. Previous air-drying partially oxidizes the Fe(II). As interaction with silica stabilizes Fe(II), the supported Fe samples show a separate reduction step to Fe(II), which is not displayed by bulk Fe oxide. The iron hydrosilicate obtained in urea precipitation at 90°C is fairly stable and is reduced only above 650°C . The Fe(II) precipitated at 45°C is more

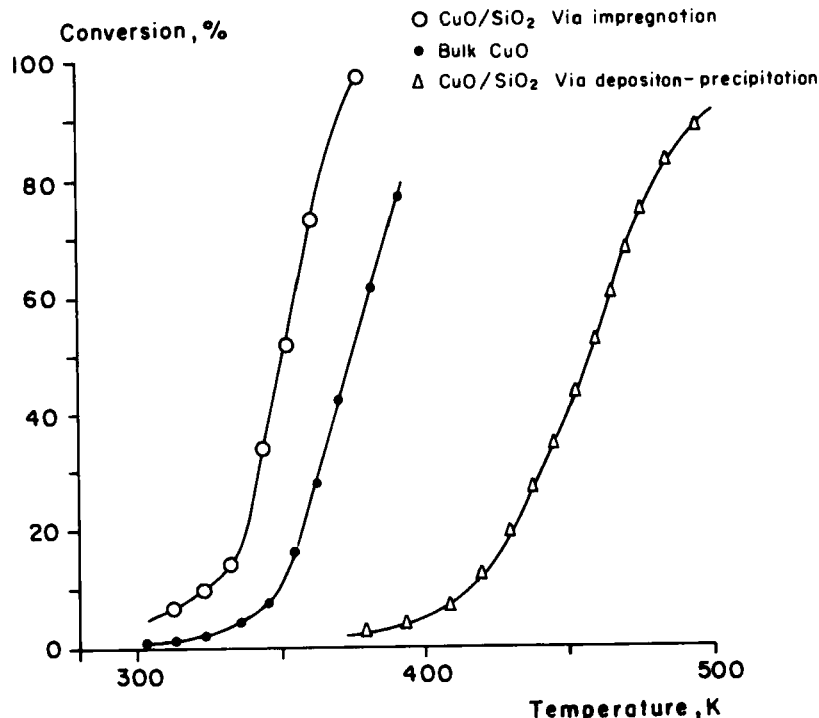


Fig. 9.13. Co-oxidation activity of freshly calcined Cu(II)-oxide catalysts. CuO loading in the SiO₂-supported catalysts is about 28 wt.%.

loosely bonded and its reduction starts already at 450°C, and injection at 90°C leads to an intermediate situation. The different extents of reaction of the support can also be visualized through transmission electron microscopy: the carrier loaded at 45°C shows the silica particles covered by very small Fe oxide particles, while the carrier has reacted to thin hydrosilicate platelets at 90°C (urea).

Hydrosilicate formation is also in evidence in the Cu(II)-SiO₂ system. Via precipitation from a homogeneous solution one can obtain highly dispersed copper oxide on silica (cf. above, Fig. 9.10, where it should be noted that the Cu case is more complicated than the Mn one in that intermediate precipitation of basic salts can occur). Reaction to copper hydrosilicate is evident from temperature-programmed reduction. As shown in Fig. 9.12 the freshly dried catalyst exhibits reduction in two peaks, one due to Cu(II) (hydr)oxide and the other, at higher temperature, to Cu(II) hydrosilicate. Reoxidation of the metallic copper particles leads to Cu(II) oxide, and subsequent reduction proceeds therefore in one step. The water resulting from the reduction of the oxide does not produce significant amounts of copper hydrosilicate, in contrast to what usually happens in the case of nickel.

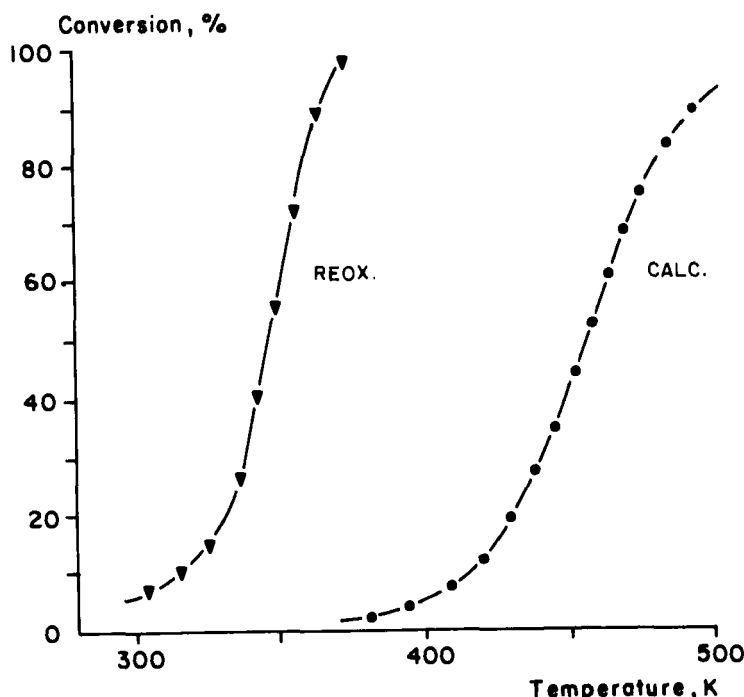


Fig. 9.14. Effect of reduction and reoxidation on the CO-oxidation activity of a CuO/SiO_2 catalyst prepared by deposition-precipitation.

The activity of the thus prepared $\text{Cu}(\text{oxide})/\text{SiO}_2$ catalyst in the oxidation of carbon monoxide is represented in Fig. 9.13. It can be seen that the activity of the fresh catalyst before reduction is rather low. In spite of the very good dispersion (high surface area), the conversion at e.g. 180°C is much lower than that of unsupported copper oxide and the less well dispersed copper oxide. However, reduction and reoxidation leads to a much higher activity, cf. Fig. 9.14. Apparently, then, the activity of copper ions in a copper hydrosilicate is much lower than that of those in an oxide. As the dispersion remains very high in the transformation of the one phase into the other, a high catalytic activity can therefore be achieved.

Nickel reacts even more strongly than copper with silica; indeed, silica completely reacts with nickel(II) ions precipitating at 90°C to nickel hydrosilicate, provided sufficient nickel is supplied. As a result, the structure or the support completely disappears from the electron micrographs, only the hydrosilicate platelets being in evidence.

The technique of deposition-precipitation has been continuously improved. One of the latest improvements has been the use of electrochemical procedures both to dissolve and to precipitate the active precursor. The adjustment of the

valency of the element to be applied on the support to establish a sufficiently strong interaction with it has continued to broaden the range of application of the deposition-precipitation procedure considerably. Recent instances are the application of vanadium(III) and molybdenum(IV) on silica.

9.3.3.3 Deposition-precipitation onto preshaped carrier bodies

As remarked above, it is often desirable to apply a catalyst precursor directly onto a preshaped support. An obvious way to proceed would be to pore-volume impregnate the carrier bodies with the required amounts of metal salt and urea (or, alternatively, nitrite) in an aqueous solution and heat the impregnated particles to 70–90°C. This can actually be made to work, as has been shown recently in the case of Ni/ γ -Al₂O₃, but the preparation of highly loaded catalysts would appear to be problematic with this route.

The deposition on about 1 mm porous SiO₂ granules via urea hydrolysis has been studied for Mn⁽²⁺⁾. As expected, the rate determining step is the urea hydrolysis step itself. In these conditions, the metal profile over the granules is determined by the relative rates of diffusion of hydrolysed Mn species in the pores and of reaction of these species with the SiO₂ surface. This is relatively well described with the Thiele concept, as is evident from Fig. 9.15. The rate of the surface reaction is lower for Rh⁽³⁺⁾ and Ni⁽²⁺⁾ than for Mn⁽²⁺⁾, which should lead

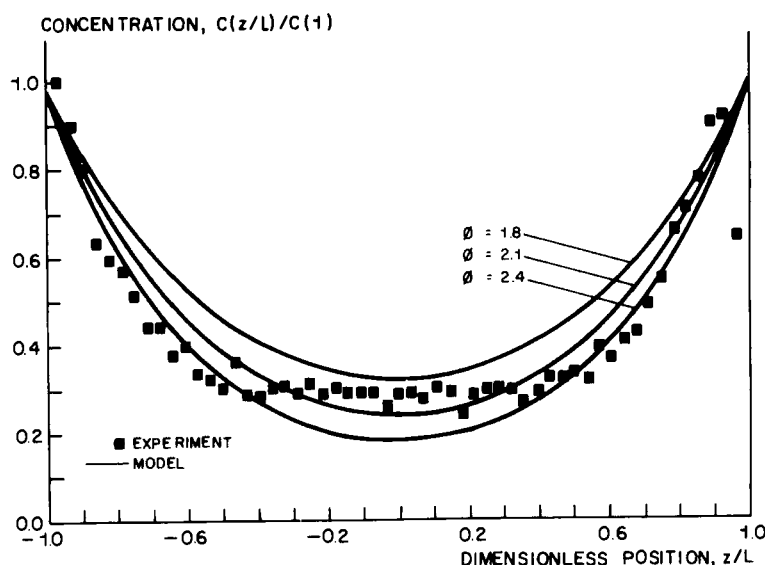


Fig. 9.15. Distribution of manganese over a representative silica granule from experiment U34.

The drawn lines have been calculated for different values for the Thiele modulus (Φ).

(Courtesy K.P. de Jong.)

to flatter metal profiles. However, a certain concentration gradient inside the carrier body cannot be avoided when applying this preparation method to larger support particles. Whether these concentration gradients are acceptable or not will depend on the catalyst and its specific application.

FURTHER READING

- James T. Richardson, *Principles of Catalyst Development*, Plenum Press, New York, 1989, Ch. 6.
- C. Marcilly (and J.P. Franck), La préparation des catalyseurs, *Rev. Inst. Fr. Petrole*, 39 (1984) 189–208, 337–364.
- H.P. Boehm and H. Knozinger, Nature and estimation of functional groups on solid surfaces, in: *Catalysis*, Vol. 4, Springer-Verlag, Berlin etc., 1983, pp. 39–207.
- J.A.R. van Veen, A method for the quantitative determination of the basic OH groups on an alumina surface, *J. Coll. Interf. Sci.*, 121 (1988) 214–219.
- J.A.R. van Veen, An enquiry into the surface chemistry of TiO₂(anatase), *Z. Phys. Chem. NF*, 162 (1989) 215–229.
- A.V. Neimark, L.I. Kheifetz and V.B. Fenelonov, Theory of preparation of supported catalysts, *Ind. Eng. Chem. Prod. Res. Dev.*, 20 (1981) 439–450.
- M. Kotter, Herstellung von Trankkatalysatoren als Verfahrenstechnische Aufgabe, *Chem.-Ing.-Tech.*, 55 (1983) 179–185.
- S.-Y. Lee and R. Aris, The distribution of active ingredients in supported catalysts prepared by impregnation, *Catal. Rev.-Sci. Eng.*, 27 (1985) 207–340.
- M. Komiyama, Design and preparation of impregnated catalysts, *ibid.*, 341–372.
- O.A. Sceiza, A.A. Castro, D.R. Ardiles and J.M. Parera, Modeling of the impregnation step to prepare supported Pt/Al₂O₃ catalysts, *Ind. Eng. Chem. Fundam.*, 25 (1986) 84–88.
- M. Sibeijn, R. Spronk, J.A.R. van Veen, and J.C. Mol, IR studies of Re₂O₇ metathesis catalysts supported on (phosphated) alumina, *Catal. Lett.*, 8 (1991) 201–208.
- J.A.R. van Veen *et al.*, Chemistry of (phospho-)molybdate adsorption on alumina surfaces, *J. Phys. Chem.*, 94 (1990) 5275–5285.
- J.W. Geus, Production and Thermal Pretreatment of Supported Catalysts, *Preparation of Catalysts III*, Elsevier, Amsterdam, 1983, pp. 1–32.
- L.M. Knijff, P.H. Bolt, R. van Yperen, A.J. van Dillen, J.W. Geus, Production of nickel-on-alumina catalysts from preshaped bodies; K.P. de Jong, Deposition-precipitation onto pre-shaped carrier bodies — possibilities and limitations; P.J. van den Brink, A. Scholten, A. van Wageningen, M.D.A. Lamers, A.J. van Dillen, J.W. Geus, The use of chelating agents for the preparation of iron oxide catalysts for the selective oxidation of hydrogen sulfide, all in *Preparation of Catalysts V*, Elsevier, Amsterdam, 1991.

Chapter 10

Catalyst characterization with spectroscopic techniques

10.1 INTRODUCTION

Catalyst characterization plays an important role in catalysis. No fewer than 78% of the roughly 250 papers presented at the Ninth International Congress on Catalysis (Calgary, Canada, 1988) contained at least some results on the catalyst(s) obtained by characterization techniques. The remaining 22% of the papers dealt with reactions over essentially uncharacterized catalysts [1]. Figure 10.1 shows which techniques are often used in catalysis.

This chapter briefly describes the concepts of the techniques that are most frequently used for catalyst characterization. The intention is to give the newcomer an idea of what these methods tell about a catalyst. References to more extensive treatments are given at the end of this chapter [2–7]. Physisorption is dealt with in a separate chapter (Chapter 12) and two examples of temperature programmed techniques are treated in some detail in Chapter 11.

10.1.1 Aim of Catalyst Characterization

The catalytic properties of a surface are determined by its composition and structure *on the atomic scale*. Thus, it is not sufficient to know that a surface consists of a metal and a promoter, say iron and potassium, but it is essential to know the exact structure of the iron surface, including defects, steps, etc., as well as the exact location of the promotor atoms. Thus, from a fundamental point of view, the ultimate goal of catalyst characterization should be to look at the surface atom by atom, and under reaction conditions. At present, this is only occasionally possible in highly simplified model systems such as the well defined surfaces of single crystals, or the needle shaped tips used in field emission studies [8].

The industrial point of view of catalyst characterization is different. Here the main interest is to optimize or produce an active, selective, stable and mechani-

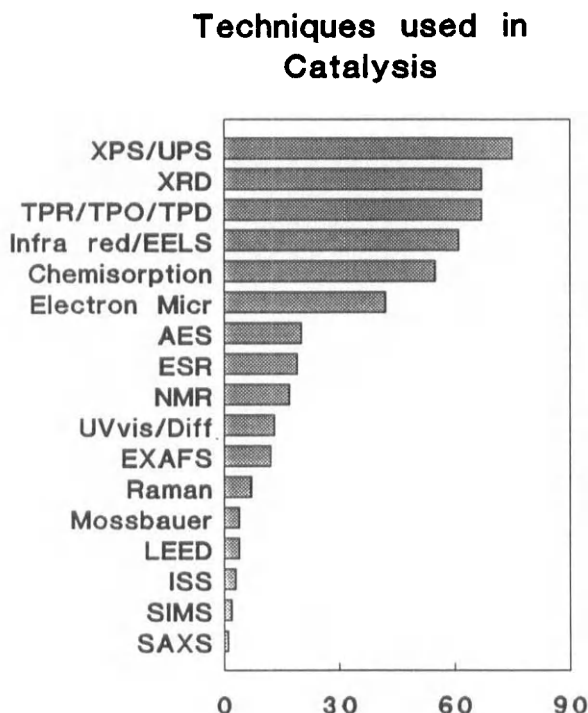


Fig. 10.1. Bar diagram showing how often certain techniques have been used in the papers at the Ninth International Congress on Catalysis [1].

cally robust catalyst. In order to accomplish this, tools are needed which identify those structural properties that discriminate efficient from less efficient catalysts. In principle, all spectroscopic information that helps to achieve this is welcome. Empirical relations between the factors that govern catalyst composition, particle size and shape, and pore dimensions on one side, and catalytic performance on the other can be extremely useful in developing catalysts.

Simplifying, one could say that catalyst characterization in industrial research deals with the materials science of catalysts on a more or less mesoscopic scale, whereas the ultimate goal of fundamental catalytic research is to characterize the surface of a catalyst on the *atomic* scale.

10.2 TECHNIQUES

There are many ways to obtain information on the physico chemical properties of materials. Figure 10.2 presents a scheme from which almost all techniques can be derived. Spectroscopies are based on some type of excitation, represented by the ingoing arrow in Fig. 10.2, to which the catalyst responds, symbolized by the

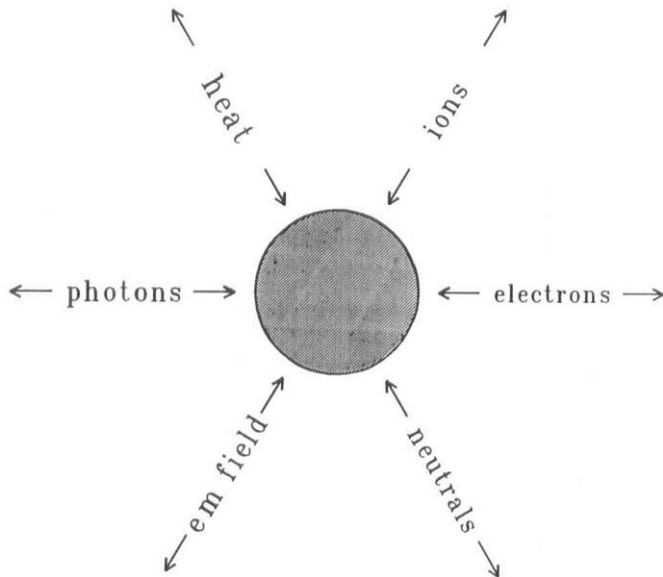


Fig. 10.2. Possibilities for catalyst investigations, each inward arrow stands for an excitation, each outward arrow indicates how the information is to be detected.

outgoing arrow. For example, one can irradiate a catalyst with X-rays and study how the X-rays are diffracted (X-ray diffraction, XRD), or one may study the energy distribution of electrons that are emitted from the catalyst due to the photoelectric effect (X-ray photoelectron spectroscopy, XPS). One can also heat up a spent catalyst and look at what temperatures reaction intermediates and products desorb from the surface (temperature programmed desorption, TPD). We will now discuss some of the most important techniques for investigating catalysts.

10.2.1 X-Ray Diffraction (XRD)

According to Fig. 10.1, XRD is one of the most frequently applied techniques in catalyst characterization. X-rays have wavelengths in the Å range, are sufficiently energetic to penetrate solids and are well suited to probe their internal structure. XRD is used to identify bulk phases and to estimate particle sizes [9].

An X-ray source consists of a target which is bombarded with high energy electrons. The emitted X-rays arise from two processes. Electrons slowed down by the target emit a continuous background spectrum of Bremsstrahlung. Superimposed on this are characteristic, narrow lines. The Cu K α line, for example, arises because a primary electron creates a core hole in the K shell, which is filled by an electron from the L shell (K β : the K-hole is filled from the M-shell, etc.) under emission of an X-ray quantum. The process is called X-ray fluorescence. It

is not only the basis for X-ray sources but is also encountered in electron microscopy, EXAFS and XPS.

X-ray diffraction is the elastic scattering of X-ray photons by atoms in a periodic lattice. The scattered monochromatic X-rays that are in phase give constructive interference. Figure 10.3a illustrates how diffraction of X-rays by crystal planes allows one to derive lattice spacings, d , by measuring the angles, 2θ , under which constructively interfering X-rays with wave length, λ , leave the crystal, by using the Bragg relation:

$$n \lambda = 2d \sin \theta; \quad n = 1, 2, \dots \quad (10.1)$$

The XRD pattern of a powdered sample is measured with a stationary X-ray source (usually Cu K α) and a movable detector, which scans the intensity of the diffracted radiation as a function of the angle 2θ between the incoming and the diffracted beams. When working with powdered samples, an image of diffraction lines occurs because a small fraction of the powder particles will be oriented such that by chance a certain crystal plane (hkl) is at the right angle with the incident beam for constructive interference.

Diffraction patterns can be used to identify the various phases in a catalyst. An example is given in Fig. 10.3b, where XRD is used to follow the reduction of alumina-supported iron oxide at 675 K as a function of time. The initially present $\alpha\text{-Fe}_2\text{O}_3$ (haematite) is partially reduced to metallic iron, with Fe_3O_4 (magnetite) as the intermediate. The diffraction lines from platinum are due to the sample holder [10].

The width of diffraction peaks carries information on the dimensions of the reflecting planes. Diffraction lines from perfect crystals are very narrow. For crystallite sizes below 100 nm, however, line broadening occurs due to incomplete destructive interference in scattering directions where the X-rays are out of phase. The Scherrer formula relates crystal size to line width:

$$\langle L \rangle = \frac{K\lambda}{\beta \cos \theta} \quad (10.2)$$

in which β is the peak width and K a constant (often taken unity). The linear dimension $\langle L \rangle$ is a volume-averaged thickness of the crystallites, measured in a direction normal to the reflecting planes.

X-ray line broadening provides a quick but not always reliable estimate of the particle size. Better procedures are based on line-profile analysis with Fourier transform methods. The average size is obtained from the first derivative of the cosine coefficients and the distribution of particle sizes from the second derivative. The reader is referred to Cohen and Schwartz [9] for more details.

XRD may be very common in catalysis, but it does have disadvantages. Because XRD is based on interference between reflecting X-rays from lattice

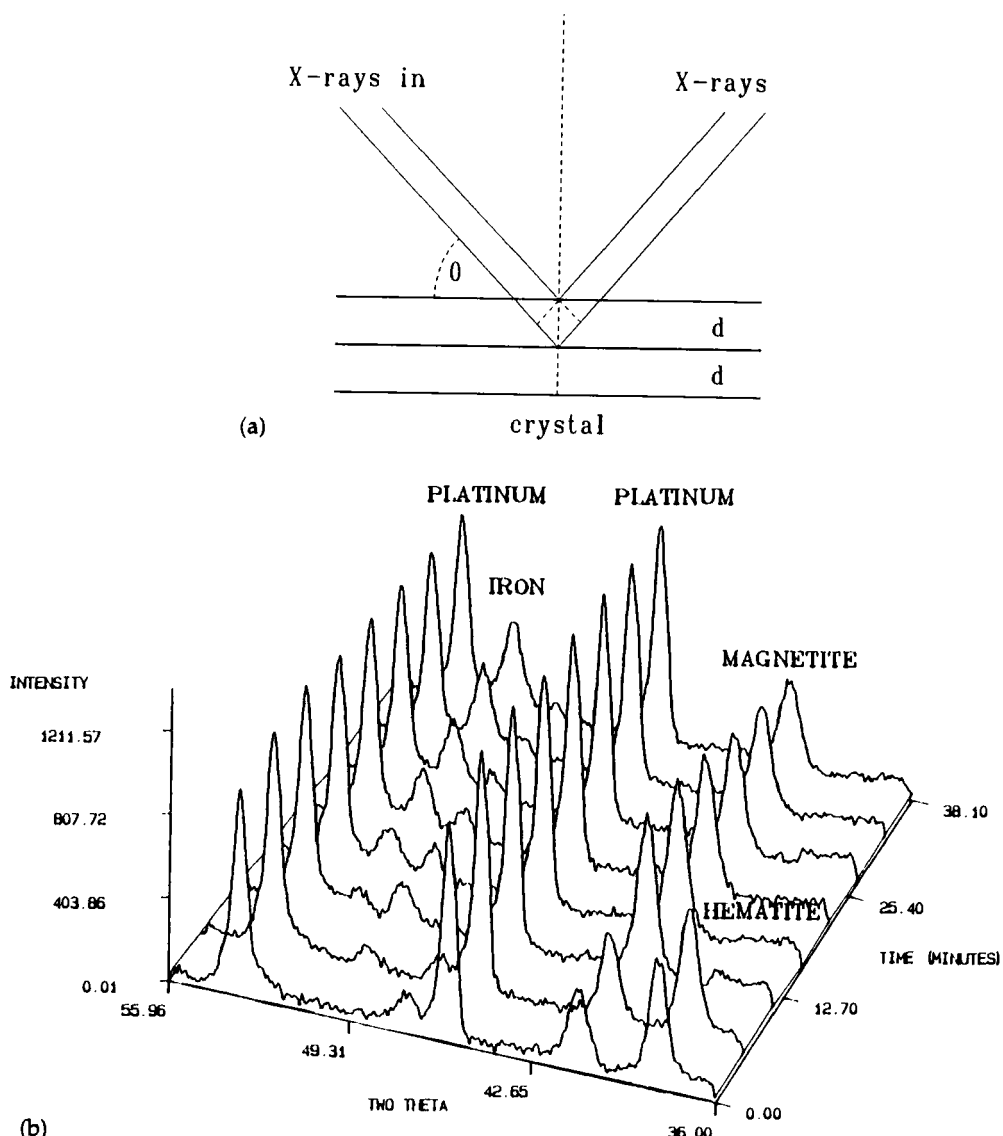


Fig. 10.3. Top: X-rays reflected by a series of atoms in a lattice plane interfere constructively in directions given by Bragg's Law. Bottom: XRD shows the reduction of alumina-supported iron oxide at 675 K (from Jung and Thomson [10]).

planes, the technique requires samples which possess sufficient long range order. Amorphous phases and small particles give either broad and weak diffraction lines or no diffraction at all, with the consequence that if catalysts contain particles with a size distribution, XRD may only detect the larger ones. In unfortunate cases, the diffraction lines from the metal may overlap with those

from the support. Finally, the surface region is where catalytic activity resides, but this part of the catalyst is virtually invisible for XRD.

10.2.2 Electron Microscopy

Electron microscopy is a rather straightforward technique to determine the size and shape of supported particles. It can also reveal information on the composition of the particles, for example by detecting the X-rays which are produced by the interaction of the electrons with matter, or by analyzing the way how the electrons are diffracted [11].

Electrons have characteristic wavelengths in the range 0.1–1 nm (visible light: 400–700 nm), and come close to seeing atomic detail. Figure 10.4 summarizes what happens with the high energy (100–400 keV) electrons when the primary beam hits the sample.

- Depending on sample thickness a fraction of the electrons passes through the sample without suffering energy loss. As discussed later, these electrons are used in transmission electron microscopy (TEM).

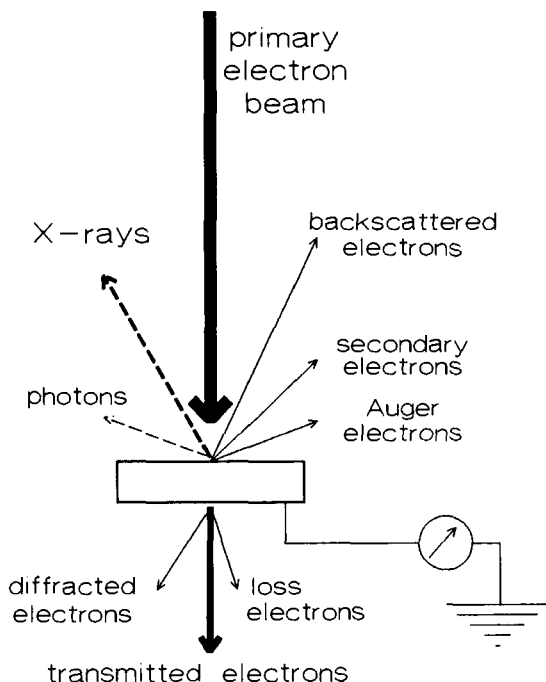


Fig. 10.4. The interaction of the primary electron beam with a sample in electron microscopy produces a wealth of detectable signals.

- Electrons are diffracted by particles with the favourable orientation towards the beam, enabling one to obtain crystallographic information.
- Electrons can collide with atoms in the sample and be scattered back; back scattering is more effective when the mass of the atom increases.
- X-rays and Auger electrons are formed in the relaxation of core-ionized atoms, as discussed in the sections on AES and XPS.
- Electrons excite characteristic vibrations in the sample which can be studied by analyzing the energy loss suffered by the primary electrons.
- Many electrons loose energy in a cascade of consecutive inelastic collisions. These are called secondary electrons; most of these had their last loss process in the surface region just before leaving the sample.
- The emission of a range of photons from UV to infrared is called cathodoluminescence and is caused by the recombination of electron-hole pairs. Thus, the interaction of the primary beam with the sample provides a wealth of information on morphology, crystallography and chemical composition.

Transmission electron microscopy (TEM) uses transmitted and diffracted electrons. A TEM instrument is very similar to an optical microscope, if one replaces optical by electromagnetic lenses. In TEM, a high intensity primary electron beam passes through a condenser to produce parallel rays which impinge on the sample. As the attenuation of the beam depends on the density and the thickness, the transmitted electrons form a two-dimensional projection of the sample mass, which is subsequently magnified by the electron optics to produce a so-called bright field image. The dark field image is obtained from the diffracted electron beams, which are slightly off angle from the transmitted beam. For supported catalysts, dark field pictures show enhanced contrast for supported metals. Typical operating conditions of a conventional TEM instrument are 100 keV electrons, 10^{-6} mbar vacuum, 0.5 nm resolution and a magnification of 300,000. High resolution microscopes show atomic resolution and magnifications of 1,000,000.

Scanning electron microscopy (SEM) is carried out by rastering a narrow electron beam over the surface and detecting the yield of either secondary or back-scattered electrons as a function of the position of the primary beam. Contrast is caused by the orientation: parts of the surface facing the detector appear brighter than parts of the surface with their surface normal pointing away from the detector. The secondary electrons have low energies (10–50 eV) and originate from the surface region of the sample. Back-scattered electrons come from deeper and carry information on the composition of the sample, because heavy elements are more efficient scatterers and appear brighter in the image. Dedicated SEM instruments have resolutions of about 5 nm. Simple versions of SEM with micron resolution are often available on Auger electron spectrometers, for the purpose of sample positioning. The main difference between SEM and TEM is that SEM sees contrast due to the topology of a surface, whereas TEM projects all information in a two-dimensional image, which, however, is of sub

nanometer resolution. A STEM instrument combines the two modes of electron microscopy.

As illustrated by Fig. 10.4, an electron microscope offers additional possibilities for analyzing the sample. Diffraction patterns (spots from a single-crystal particle and rings from a collection of randomly oriented particles) enable one to identify crystallographic phases as in XRD. Emitted X-rays are characteristic for an element and allow for a determination of the chemical composition of a selected part of the sample (typical dimension 10 nm). This technique is called electron microprobe analysis (EMA, EPMA) or, referring to the usual mode of detection, energy dispersive analysis of X-rays (EDAX or EDX). Also the Auger electrons carry information on sample composition, as do the loss electrons. The latter are potentially informative on the low Z elements, which have a low efficiency for X-ray fluorescence.

For studying supported catalysts, TEM is the commonly applied form of electron microscopy. Detection of supported particles is possible provided that there is sufficient contrast between particles and support. This may impede applications of TEM on supported oxides. Determination of particle sizes or of distributions therein rests on the assumption that the size of the imaged particle is truly proportional to the size of the actual particle and that the detection probability is the same for all particles, independent of their dimensions. Semi *in situ* studies of catalysts are possible by coupling the instrument to an external reactor. After evacuation of the reactor, the catalyst can be transferred directly into the analysis position, without seeing air [12]. For reviews of TEM on catalysts we refer to refs. [11,12].

10.2.3 Temperature Programmed Techniques

Temperature programmed reduction (TPR), oxidation (TPO), desorption (TPD), sulphidation (TPS) and reaction spectroscopy (TPRS) form a class of techniques in which a chemical reaction is monitored while the temperature increases linearly in time. These techniques are applicable to real catalysts and single crystals and have the advantage that they are experimentally simple and inexpensive in comparison to many other spectroscopies. Interpretation on a qualitative base is rather straightforward [13].

The basic set up for TPR, TPO and TPD consists of a reactor and a thermal conductivity detector to measure the hydrogen content in TPR/TPD or the oxygen content in TPO, of the gas mixture before and after reaction. More sophisticated TP equipment contains a mass spectrometer for the detection of reaction products.

TPR and TPO patterns of silica-supported rhodium, iron, and iron–rhodium catalysts are shown in Fig. 10.5 [14]. These catalysts were prepared by pore volume impregnation from aqueous solutions of iron nitrate and rhodium

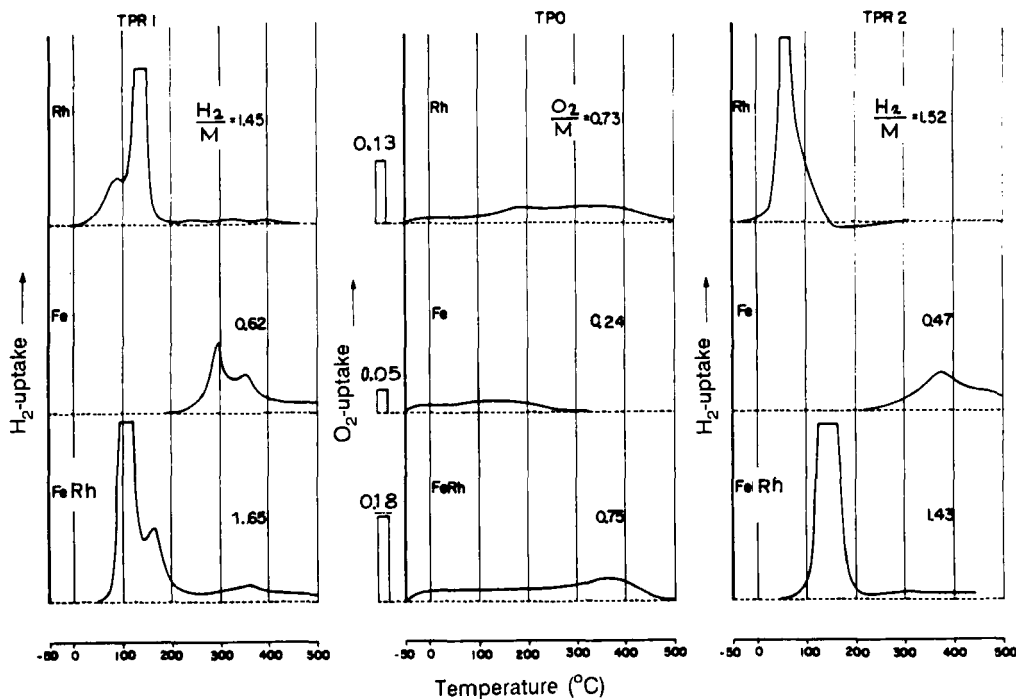


Fig. 10.5. TPR/TPO of silica-supported Rh, Fe, and Fe-Rh catalysts. The left TPR curves have been measured from freshly impregnated catalysts, the right ones after complete oxidation in the TPO experiment (from van't Blik and Niemantsverdriet [14]).

chloride. Note the difference in reduction temperature between the noble metal rhodium and the non-noble metal iron. The bimetallic combination reduces largely in the same temperature range as the rhodium catalyst does, indicating that rhodium catalyzes the reduction of the iron. This forms evidence that rhodium and iron are well mixed in the fresh catalyst. The TPR patterns of the freshly prepared catalysts consist of two peaks, one coincides with that of the TPR pattern of the fully oxidized catalyst (right panel of Fig. 10.5) and can thus be assigned to the reduction of the metal oxide. The remaining peak of the first TPR is assigned to the reduction of the metal salt precursors, iron nitrate and rhodium chloride.

The area under a TPR or TPO curve represents the total hydrogen consumption, and is commonly expressed in terms of moles of H_2 consumed per mol of metal atoms, H_2/M . The ratios of almost 1.5 for rhodium in Fig. 10.5 indicate that rhodium was present in the form of Rh^{3+} . For iron, the H_2/M ratios are significantly lower, indicating that this metal is only partially reduced.

TPR provides a quick characterization of metallic catalysts. It gives information on the phases present after impregnation and on the eventual degree of reduction. For bimetallic catalysts, TPR patterns often indicate if the two components are mixed or not. A more detailed description of TPR and TPS is given in

Chapter 11. Temperature programmed desorption (TPD) is popular for determining concentrations of species adsorbed on the surfaces of single crystals and of real catalysts. In principle one can also determine the energy of the adsorption bond, however, only after applying rather involved computations [15]. We refer to Ref. [16] for a critical evaluation of TDS analysis.

10.2.4 Surface Spectroscopy

A technique becomes surface sensitive if the radiation or particles to be detected can travel no more than a few atomic distances through the solid. Low energy electrons and ions are particularly suitable for investigating the surface region. The consequence of working with electrons and ions is that experiments have to be done in vacuum (at least 10^{-6} mbar) otherwise the particles leaving the surface would not be able to reach a detector. The reason that surface spectroscopies are preferably applied under ultra high vacuum (pressures in the 10^{-10} mbar range) is that, in order to obtain meaningful results on the intrinsic properties of a clean surface, or of the surface with a certain adsorbed gas, contamination by residual gases in the measurement chamber should be prevented. For the characterization of catalysts the requirements on vacuum are less stringent and pressures on the order of 10^{-8} mbar are quite acceptable.

10.2.4.1 The electron spectroscopies: XPS, UPS, AES [17,18]

X-ray photoelectron spectroscopy (XPS) is based on the photoelectric effect: an atom absorbs a photon of energy $h\nu$; next, a core or valence electron with binding energy E_b is ejected with kinetic energy (Fig. 10.6):

$$E_k = h\nu - E_b \quad (10.3)$$

Routinely used X-ray sources are Mg K α ($h\nu = 1253.6$ eV) and Al K α ($h\nu = 1486.3$ eV). In XPS one measures the intensity of photoelectrons $N(E)$ as a function of their kinetic energy E_k . The XPS spectrum is a plot of $N(E)$ versus E_k , or, more often, versus binding energy E_b . Figure 10.7a shows the XPS spectrum of a freshly impregnated alumina-supported rhodium catalyst.

Photoelectron peaks are labelled according to the quantum numbers of the level from which the electron originates. An electron coming from an orbital with main quantum number n , orbital momentum l (0,1,2,3,...indicated as $s, p, d, f, ..$) and spin momentum s (+1/2 or -1/2) is indicated as nl_{l+s} . Examples are Rh 3d_{5/2}, Rh 3d_{3/2}, O 1s, Fe 2p_{3/2}, Pt 4f_{7/2}. For every orbital momentum $l > 0$ there are two values of the total momentum: $j = l + 1/2$ and $j = l - 1/2$, each state filled with $2j + 1$ electrons. Hence, most XPS peaks come in doublets and the intensity ratio of the components is $(l + 1)/l$. In case the doublet splitting is too small to be observed (as in practice with Si 2p, Al 2p, Cl 2p), the subscript $l + s$ is omitted.

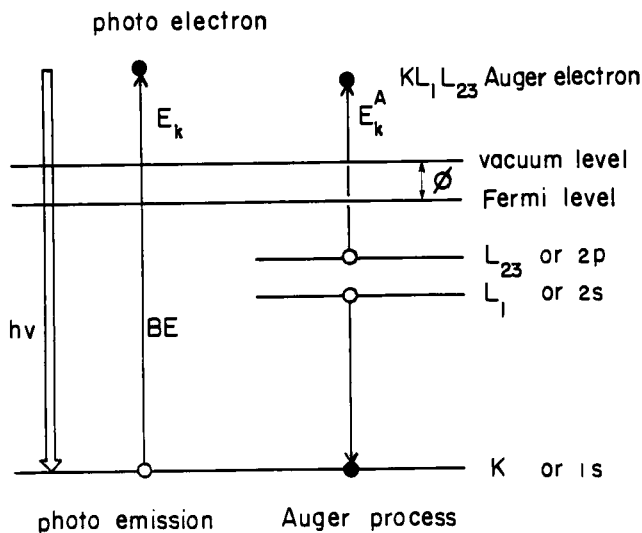
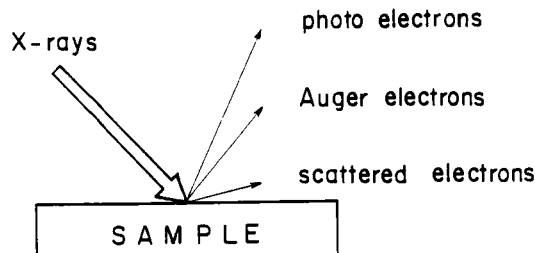


Fig. 10.6. Photoemission and Auger decay: an atom absorbs an incident X-ray photon with energy $h\nu$ and emits a photoelectron with kinetic energy $E_k = h\nu - E_b$. The excited ion decays either by the indicated Auger process or by X-ray fluorescence.

Because a set of binding energies is characteristic for an element, XPS can be used to analyze the composition of samples. Almost all photoelectrons used in laboratory XPS have kinetic energies in the range of 0.2 to 1.5 keV, and probe the outer layers of the catalyst. The mean free path of electrons in elemental solids depends on the kinetic energy. Optimum surface sensitivity is achieved with electrons at kinetic energies of 50–250 eV, where about 50% of the electrons come from the outermost layer.

Binding energies are not only element specific but contain chemical information as well: the energy levels of core electrons depend on the chemical state of the atom. Chemical shifts are typically in the range 0–3 eV. Figure 10.7b shows that the binding energy of the Rh 3d_{5/2} peak of RhCl₃ in the XPS spectrum of a freshly impregnated catalyst is some 2.5 eV higher than that of rhodium metal in

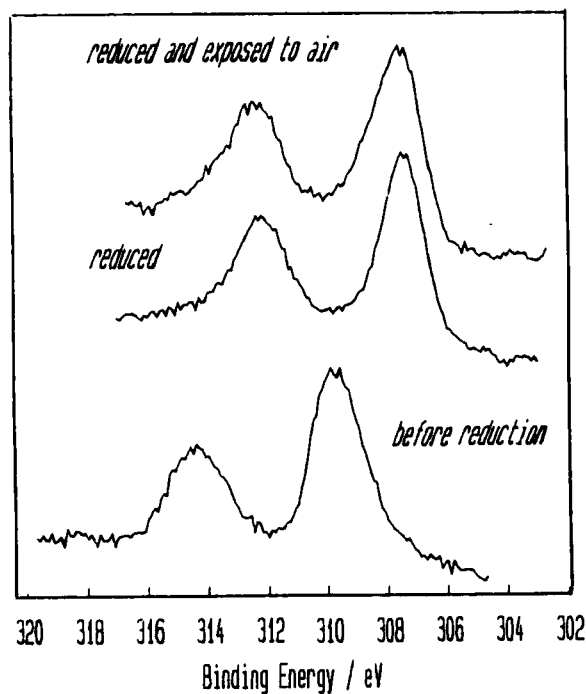
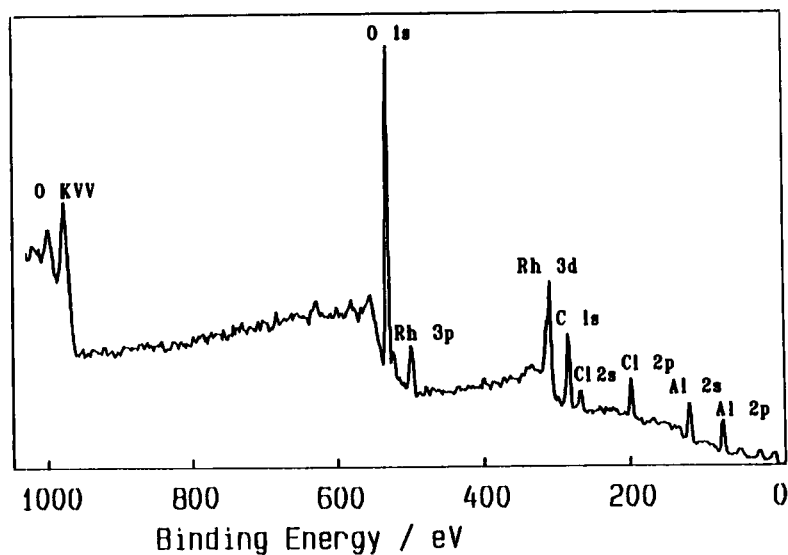


Fig. 10.7. XPS spectra of Rh/Al₂O₃ prepared by impregnation from a RhCl₃ solution, (a) survey spectrum of low resolution, (b) Rh 3d spectra at high resolution (from Borg et al. [19]).

the spectrum of the reduced catalyst [19]. The reason is that the electrons of the Rh³⁺ ion feel a higher attractive force from the nucleus than those of the neutral atom. In general, the binding energy increases with increasing oxidation state and, for a fixed oxidation state, with the electronegativity of the ligands, as the series FeBr₃, FeCl₃, FeF₃ in Table 10.1 illustrates.

TABLE 10.1
Binding energies of Fe 2p_{3/2} electrons in several components [20]

compound	E _b (eV)
iron metal	706.7
FeO	710.0
Fe ₂ O ₃	710.7
Fe(CO) ₅	709.4
FeBr ₃	710.0
FeCl ₃	711.1
FeF ₃	714.0

Note that XPS measures *binding energies*. These are not necessarily equal to the energies of the orbitals from which the photoelectron is emitted. The difference is caused by the reorganization of the remaining electrons when an electron is removed from an inner shell. Thus the binding energy of the photoelectron contains both information on the state of the atom before photoionization (the initial state) and on the core-ionized atom left behind after the emission of an electron (the final state). Fortunately, it is often correct to interpret binding energy shifts as those in Fig. 10.7b in terms of initial state effects. The charge potential model elegantly explains the physics behind such binding energy shifts, by means of the formula:

$$E_b^i = kq_i + \sum_j \frac{q_j}{r_{ij}} + E_b^{\text{ref}} \quad (10.4)$$

in which E_b^i is the binding energy of an electron from an atom i , q_i the charge on the atom, k a constant, q_j the charge on a neighbouring atom j at distance r_{ij} from

atom i , and E_b^{ref} a suitable reference. The first term indicates that the binding energy goes up with increasing positive charge on the atom from which the photoelectron originates. In ionic solids, the second term counteracts the first, because the charge on a neighbouring atom will have the opposite sign. Because of its similarity to the lattice potential in ionic solids, the second term is often referred to as the Madelung sum.

Although XPS is predominantly used for studying surface compositions and oxidation states, the technique can also yield information on the dispersion of supported catalysts, as illustrated by the example on $\text{ZrO}_2/\text{SiO}_2$ catalysts, see Fig. 10.8a. [21]. The spectrum of a catalyst made by a new preparation process starting from zirconium ethoxide exhibits a significantly higher Zr intensity than those of catalysts prepared by the usual impregnation from a zirconium nitrate solution. Because the escape depth of the electrons in XPS is limited to a few nanometers, a higher Zr/Si intensity ratio (at the same zirconium content) indicates that the ZrO_2 phase is better dispersed.

One can use the Zr/Si intensity ratio to investigate the thermal stability of the catalysts. As Fig. 10.8b shows, the impregnated catalysts show a decrease in Zr/Si ratio at relatively low calcination temperatures, indicating that the zirconium phase loses dispersion. The catalyst prepared via the new ethoxide route is much better resistant to sintering. Dispersion values can be calculated from the

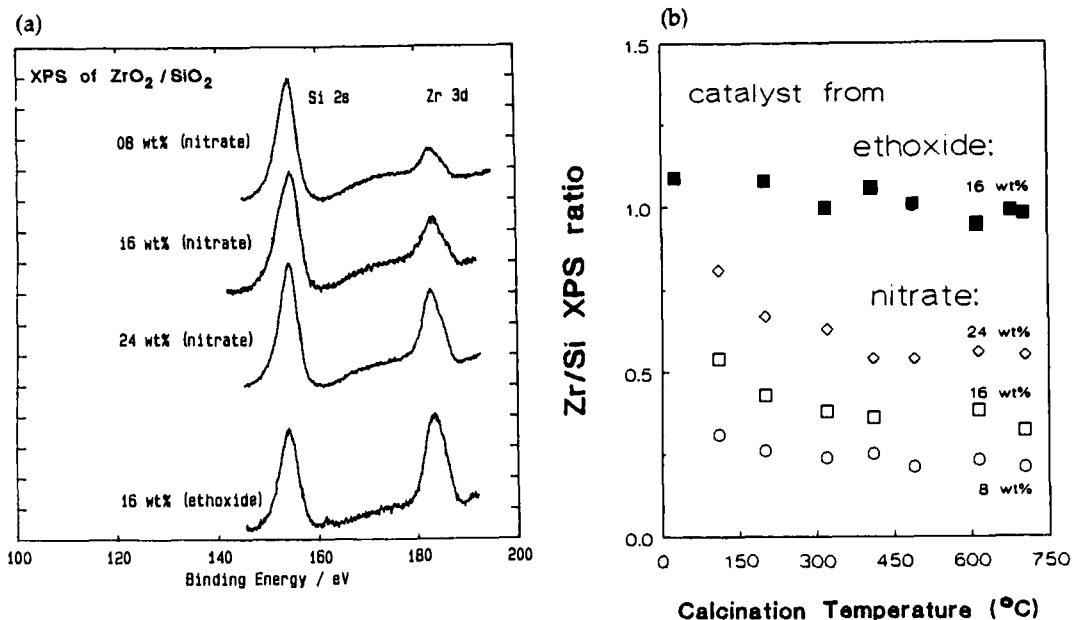


Fig. 10.8. Left: XPS spectra of calcined $\text{ZrO}_2/\text{SiO}_2$ catalysts; right: Zr/Si intensity ratios indicate that the catalyst prepared from zirconium ethoxide is much better dispersed than the ones from nitrate (from Meijers et al. [21]).

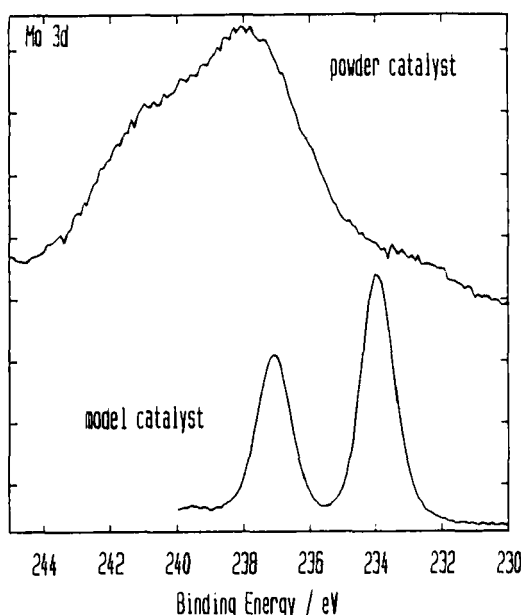


Fig. 10.9. Effect of charging on the Mo 3d signal in the XPS spectrum of a $\text{MoO}_3/\text{SiO}_2$ catalyst.
Charging is absent in a conducting model catalyst [23].

Zr/Si ratio, by using a model, for example the one published by Kuipers et al. [22]. When applied to the spectra of Fig. 10.8, Kuipers' model indicates that the ZrO_2 dispersion of the three impregnated and calcined catalysts is 5 to 15%, whereas the dispersion of the catalyst from ethoxide is around 75%.

An experimental problem in XPS (and in other electron or ion spectroscopies as well) is that electrically insulating samples may charge up during measurement, because photoelectrons leave the sample. The potential which the sample acquires is determined by the photoelectric current of electrons leaving the sample, the current through the sample holder (usually grounded) towards the sample and the flow of Auger and secondary electrons from the source window onto the sample. Due to the positive charge on the sample, all XPS peaks in the spectrum shift by the same amount to higher binding energies. More serious than the shift itself is that different parts of the catalysts may acquire slightly different amounts of charge. This phenomenon, called differential charging, gives rise to broadening of the peaks, which leads to less resolution, see Fig. 10.9. In fact, the broad Zr 3d signal in the spectra of Fig. 10.8 is actually a doublet (similar to the Rh 3d signal in Fig. 10.7b) but is not measured as such due to differential charging.

Correcting for charge shifts is done by using the binding energy of a known compound. In SiO_2 -supported catalysts one uses the binding energy of the Si 2p electrons which should be 103.4 eV. If nothing else is available, one can use the always present carbon contamination with a C 1s binding energy of 284.4 eV. The

use of a floodgun, which sprays low energy electrons onto the sample, and special sample mounting techniques in which powders are pressed in a conducting indium foil, may alleviate the charging problems to some extent.

Sensitive materials, such as metal salts or organometallic compounds used as catalyst precursors, may decompose during XPS analysis, particularly when a standard X-ray source is used. Heat and electrons from the source may cause damage to samples. In such cases a monochromatic XPS offers a solution [24].

Ultraviolet photoelectron spectroscopy (UPS) differs from XPS in that UV light (He I, 21.2 eV; He II 40.8 eV) is used. At these low exciting energies, photoemission is limited to valence electrons. Hence, UPS spectra contain important chemical information. At low binding energies UPS probes the density of states (DOS) of the valence band (but images it in a distorted way in a convolution with the unoccupied states). At slightly higher binding energies (5–15 eV), occupied molecular orbitals of adsorbed gases may become detectable. UPS also provides a quick measure of the macroscopic work function, ϕ , the energy separation between the Fermi and the vacuum level: $\phi = h\nu - W$, where W is the width of the spectrum. UPS is a typical single crystal technique applied in surface science, but is rarely used on catalysts. The main reason is that all elements contribute peaks to the valence band region. As a result, the UPS spectra of supported catalysts, which contain at least three elements and often more, are rather complicated.

After the emission of a photoelectron in XPS, the atom is left behind as an ion with a hole in one of its core levels. This is an unstable state. Deexcitation of the excited ion occurs via X-ray fluorescence or via an Auger transition (Fig. 10.6). Therefore, XPS spectra contain peaks due to Auger electrons, which have the characteristic property that they occur at fixed kinetic energies, characteristic of the element from which they are emitted.

In Auger electron spectroscopy (AES), core holes are created by exciting the sample with a beam of electrons (1–5 keV). The Auger electrons appear as small peaks on a high background of secondary electrons scattered by the sample from the incident beam. To enhance the visibility of the Auger peaks, spectra are usually presented in the derivative dN/dE mode. Figure 10.10 shows the Auger spectra measured from a flat, conducting model for a SiO_2 -supported ZrO_2 catalyst, in which the signals of Zr, Si, O and C are clearly visible [25]. Note the decrease in intensity of the carbon impurity upon oxidation, as well as the appearance of a new impurity, chlorine, visible in the spectrum at about 180 eV.

The strong point of AES is that it provides a quick measurement of the surface region of conducting samples. For many catalytically relevant elements (C, Cl, S, Pt, Ir, Rh) the corresponding Auger electrons have energies in the range of 100–300 eV where the mean free path of the electrons is close to its minimum. For those elements, AES is considerably more surface sensitive than XPS. A disadvantage of AES is that the intense electron beam easily causes damage to sensitive materials (polymers, insulators, adsorbate layers). Charging of isolating samples

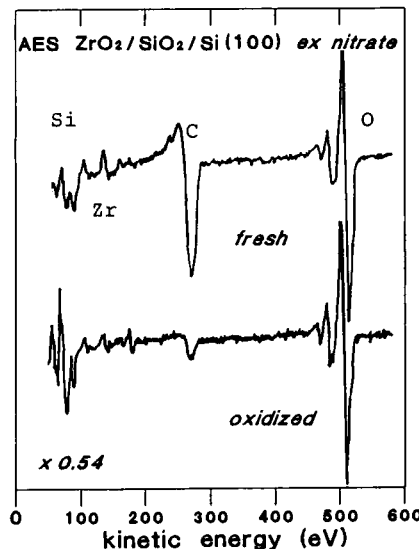


Fig. 10.10. Auger spectra of a conducting $\text{ZrO}_2/\text{SiO}_2/\text{Si}(100)$ model catalyst after impregnation and calcination (from Eshelman et al. [25]).

also presents serious problems. This is the main reason that AES, although of great importance in surface science and materials science, is not often used on supported catalysts.

In conclusion, XPS is among the most frequently used techniques in catalysis. The advantages of XPS are that it readily provides the composition of the surface region and that it can also distinguish between chemical states of one element. XPS is becoming an important tool for studying the dispersion of active phases over the support. The related techniques UPS and AES are very useful in surface science but, with a few exceptions for AES, less suitable for the characterization of catalysts.

10.2.4.2 The ion spectroscopies: SIMS, LEIS, RBS

When a beam of low energy (≤ 5 keV) ions impinges on a surface, the ions can penetrate the sample and lose their energy in a series of inelastic collisions with the target atoms. This may lead to the emission of secondary ions and neutrals from the surface (SIMS, SNMS). Another possibility is that the ions scatter elastically from the surface atoms (low energy ion scattering) or, when high energy ions are used, from atoms deeper in the sample (Rutherford back scattering). In addition to this, ions can be neutralized by taking up an electron from the sample.

Secondary ion mass spectrometry (SIMS) is by far the most sensitive surface technique, but also the most difficult to quantify [26,27]. When a surface is exposed to a beam of ions (Ar^+ , 0.5–5 keV), energy is deposited in the surface

region of the sample by a collisional cascade. Some of the energy will return to the surface and stimulate the ejection (desorption) of atoms, ions, and multi atomic clusters. In SIMS, positive or negative secondary ions are detected directly with a quadrupole mass spectrometer. In the more recently developed SNMS, the secondary neutrals are ionized, for example by electron impact ionisation, before they enter the mass spectrometer.

Figure 10.11 shows the positive SIMS spectrum of a silica-supported zirconium oxide catalyst precursor, freshly prepared by a condensation reaction between zirconium ethoxide and the hydroxyl groups of the support [21]. Note the simultaneous occurrence of single ions (H^+ , Si^+ , Zr^+) and molecular ions (SiO^+ , $SiOH^+$, ZrO^+ , $ZrOH^+$, ZrO_2^+). Also the isotope pattern of zirconium is clearly visible. Isotopes are important in the identification of peaks, because all peak intensity ratios must agree with the natural abundances. In addition to the peaks expected from zirconia on silica mounted on an indium foil, the spectrum of Figure 10.11a also contains peaks from Na^+ , K^+ , and Ca^+ . This is typical for SIMS: sensitivities vary over several orders of magnitude and elements such as the alkalis are already detected when present in trace amounts.

SIMS is strictly speaking a destructive technique. In the dynamic mode, used for making concentration depth profiles, several tens of monolayers are removed per minute. In static SIMS, however, the rate of removal corresponds to one

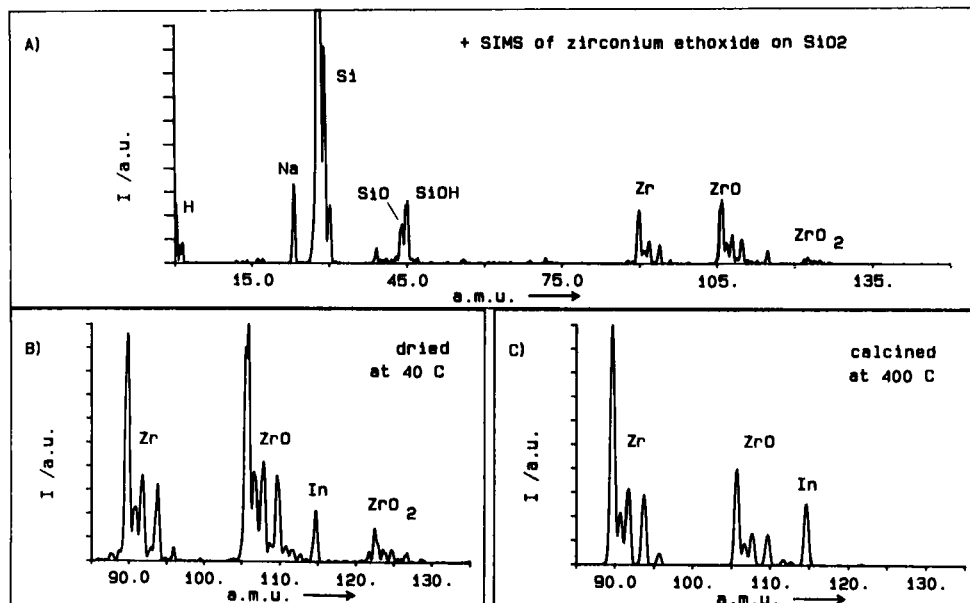


Fig. 10.11. Positive SIMS spectra of a ZrO_2/SiO_2 catalyst, (A,B) after preparation from $Zr(OC_2H_5)$ and (C) after calcination in air at 775 K (from Meijers et al. [21]).

monolayer per hour or more, implying that the surface structure does not change during the measurement (between seconds and minutes). In this case one can be sure that the molecular ion fragments are truly indicative of the chemical structure on the surface.

The advantages of SIMS are its high sensitivity (detection limit of ppm for certain elements), its ability to detect hydrogen and the emission of molecular fragments which often bear tractable relationships with the parent structure on the surface. Disadvantages are that secondary ion formation is a poorly understood phenomenon and that quantisation is often difficult. A major drawback is the matrix effect: secondary ion yields of one element can vary tremendously with its chemical environment. This matrix effect and the elemental sensitivity variation of five orders of magnitude across the periodic table make quantitative interpretation of SIMS spectra of technical catalysts extremely difficult.

In spite of quantisation problems, SIMS can give useful information if one uses appropriate reference materials. The spectra in Fig. 10.11b and c indicate that the relative intensities of the ZrO_2^+ , ZrO^+ and Zr^+ , contain information on the chemical environment of the zirconium: Spectrum 11b of the zirconium ethoxide ($\text{O:Zr} = 4:1$) shows higher intensities of the ZrO_2^+ and ZrO^+ signals than the calcined ZrO_2 ($\text{O:Zr} = 2:1$) does. The way to interpret this information is to compare the spectra of the catalysts with reference spectra of ZrO_2 and zirconium ethoxide [21].

For single crystals, matrix effects are largely ruled out and excellent quantisation has been achieved by calibrating SIMS yields by means of other techniques such as electron energy loss spectroscopy or thermal desorption spectroscopy [26]. Here SIMS offers the challenging perspective to monitor reactants, intermediates and products of catalytic reactions in real time while the reaction is in progress.

SNMS does not suffer from the matrix effects that are associated with ionization. Here the sensitivity for a certain element is mainly determined by its sputter yield. Sputtering is relatively well understood, and consequently, excellent quantisation of SNMS has been demonstrated. SNMS is a relatively new technique; it has not yet been fully exploited on catalysts.

In low energy ion scattering (LEIS, also called ion scattering spectroscopy, ISS) a beam of noble gas ions with energy of a few keV scatters elastically from a solid surface. The energy of the outgoing ion is determined by energy and momentum conservation and reveals the mass of the target atom from which it scattered. When the ion energy detector is placed at an angle of 90° with respect to the incident beam, one has:

$$\frac{E}{E_0} = \frac{M_{\text{at}} - M_{\text{ion}}}{M_{\text{at}} + M_{\text{ion}}} \quad (10.5)$$

in which E_0 is the energy of the incident ion, E its energy after scattering, M_{ion} the mass of the incident ion and M_{at} the mass of the atom with which the ion collides. Hence, the energy spectrum of the back-scattered ions is equivalent to a mass

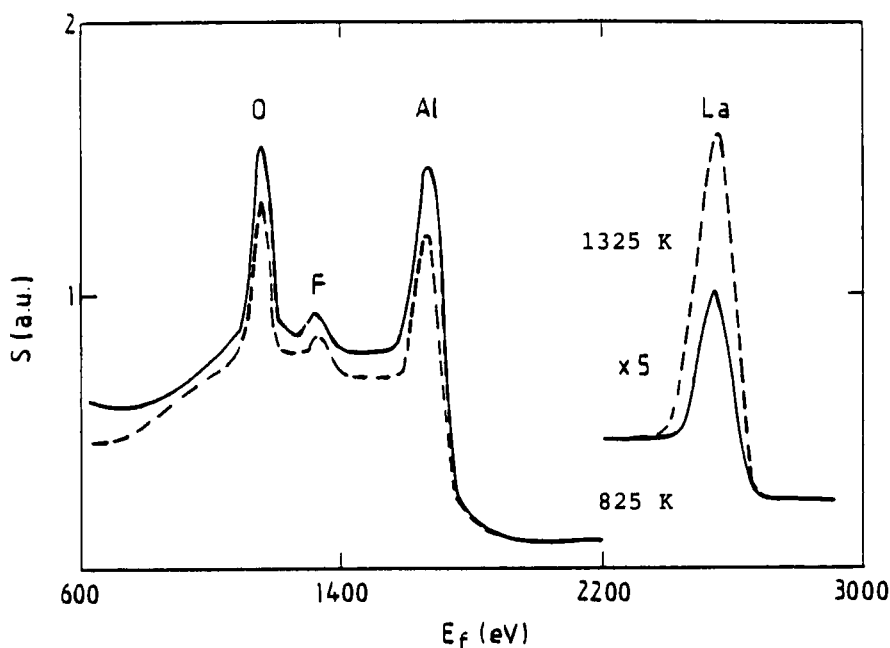


Fig. 10.12. LEIS spectra of $\text{La}_2\text{O}_3/\text{Al}_2\text{O}_3$ catalysts after calcination at 825 and 1325 K, taken with a 3 keV He^+ beam indicate that lanthanum oxide spreads over alumina at high temperatures (from van Leerdam et al. [28]).

spectrum of the surface atoms [7]. Figure 10.12 shows LEIS spectra of an alumina-supported lanthanum oxide catalyst. In agreement with the expression for the energy, Figure 10.12 illustrates that the primary ions loose less energy to heavy atoms than to light atoms. The La dispersion is reflected by the intensity ratio La/Al of the corresponding peaks in the LEIS spectrum: the La/Al ratio is low when lanthanum oxide occurs in particles, and high when it forms a monolayer. This is similar as in the $\text{ZrO}_2/\text{SiO}_2$ example we discussed in the XPS section, but with the difference that the information now comes from the outer one or two layers only. The spectra in Fig. 10.12 indicate that La_2O_3 spreads over the support at high temperatures [28].

Two factors determine the intensity of the scattered beam: the scattering cross section for the incident ion-target atom combination and the neutralization probability of the ion in its interaction with the solid. It is the latter quantity that makes LEIS surface sensitive: 1 keV He ions have a neutralization probability of about 99% in passing through one layer of substrate atoms. Hence, the majority of ions that reach the detector must have scattered off the outermost layer. At present, there is no simple theory which describes the scattering cross section and the neutralization probability adequately. Satisfactory calibration procedures by use of reference samples exist, however.

The fact that LEIS provides quantitative information on the outer layer composition of multicomponent materials makes this technique a powerful tool for the characterization of catalysts. The somewhat limited mass resolution may, however, impede certain applications. For example, horizontal neighbours in the heavier metals range of the periodic table (e.g. Pt and Ir, Pd and Ag) are not distinguished. An interesting feature of LEIS is that atoms in the second layer can be distinguished from those in the first by a broadening of the peaks to lower energies, because an ion scattered in the second layer has a considerable chance to lose an additional amount of energy on its way back through the first layer. (Note the high step in the background on the low energy side of the Al peak of the support, in Fig. 10.12.) In addition, concentration depth profiles of the constituents can be investigated by using the sputtering action of the ion beam.

In Rutherford back scattering, RBS, one uses a primary beam of high energy H^+ or He^+ ions (1–5 MeV), which scatter from the nuclei of the atoms in the target. A fraction of the incident ions is scattered back and is subsequently analyzed for energy. As in LEIS, the energy spectrum represents a mass spectrum, but this time it is characteristic for the interior of the sample [7]. The technique has successfully been applied to determine the concentration of, for example, rhodium in model systems where the rhodium is present in sub monolayer quantities on thin, conducting oxide films [19].

10.2.5 Infrared Spectroscopy

The most common application of infrared spectroscopy in catalysis is to identify adsorbed species and to study the way in which these species are chemisorbed on the surface of the catalyst. Sometimes the infrared spectra of adsorbed probe molecules such as CO and NO give valuable information on the adsorption sites that are present on a catalyst. We will first summarize the theory behind infrared absorption [29].

Molecules possess discrete levels of rotational and vibrational energy. Transitions between vibrational levels occur by absorption of photons with frequencies ν in the infrared range (wavelength 1–1000 micrometer, wave numbers 10000–10 cm^{-1} , energy differences 1240–1.24 meV). The C–O stretch vibration, for example, is at 2143 cm^{-1} . For small deviations of the atoms in a vibrating diatomic molecule from their equilibrium positions, the potential energy $V(r)$ can be approximated by that of the harmonic oscillator:

$$V(r) = \frac{1}{2} k(r - r_{eq})^2 \quad (10.6)$$

in which k is the force constant of the vibrating bond, r the distance between the two atoms, and r_{eq} the distance at equilibrium. The corresponding vibrational energy levels are

$$E_n = \left(n + \frac{1}{2} \right) \hbar v ; \quad v = \frac{1}{2\pi} \sqrt{\frac{k}{\mu}} ; \quad \frac{1}{\mu} = \frac{1}{m_1} + \frac{1}{m_2} \quad (10.7)$$

in which $n = 0, 1, 2, \dots$, \hbar is Planck's constant, v the frequency, m_1 and m_2 are the masses of the vibrating atoms and μ is the reduced mass. Allowed transitions in the harmonic approximation are those for which the vibrational quantum number changes by one unit. A general selection rule for the absorption of a photon is that the dipole moment of the molecule must change during the vibration.

The harmonic approximation is only valid for small deviations of the atoms from their equilibrium positions. The most obvious shortcoming of the harmonic potential is that the bond between two atoms cannot break. With physically more realistic potentials, such as the Lennard-Jones or the Morse potential, the energy levels are no longer equally spaced and vibrational transitions with $\Delta n > 1$ are no longer forbidden. Such transitions are called overtones. The overtone of gaseous CO at 4260 cm^{-1} (slightly less than $2 \times 2143 = 4286 \text{ cm}^{-1}$) is an example.

The simple harmonic oscillator picture of a vibrating molecule has important implications. First, knowing the frequency, one can immediately calculate the force constant of the bond. Note from eqn. (6) that k , as coefficient of r^2 , corresponds to the curvature of the interatomic potential and not primarily to its depth, the bond energy. However, as the depth and the curvature of a potential usually change hand in hand, it is often allowed to take the infrared frequency as an indicator for the strength of the bond. Second, isotopic substitution can be useful in the assignment of frequencies to bonds in adsorbed species, because frequency shifts due to isotopic substitution (of for example D for H in adsorbed ethylene, or OD for OH in methanol) can be predicted directly.

Molecules in the gas phase have rotational freedom, and the vibrational transitions are accompanied by rotational transitions. For a rigid rotor which vibrates as a harmonic oscillator the expression for the available energy levels is:

$$E = \left(n + \frac{1}{2} \right) \hbar v + \frac{\hbar^2}{8\pi^2 I} j(j+1) \quad (10.8)$$

where j is the rotational quantum number and I the moment of inertia of the molecule. Here a third selection rule applies: $\Delta j = \pm 1$. Note that because of this third selection rule the purely vibrational transition is not observed in gas phase CO. Instead, two branches of rotational side bands appear, see Fig. 10.13 for CO.

Upon adsorption, the molecule loses its rotational freedom and now only the vibrational transition is observed, however, at a different frequency, see Fig. 10.13. In the case of CO, three factors contribute to this shift:

- mechanical coupling of the CO molecule to the heavy substrate increases the CO frequency by some 20 to 50 cm^{-1} ,

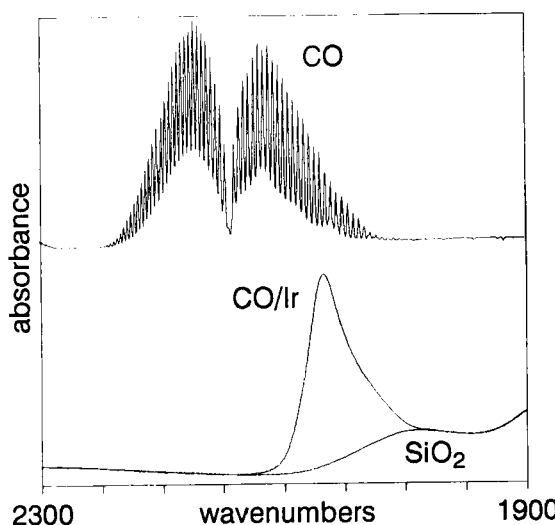


Fig. 10.13. The infrared spectrum of gas phase CO shows rotational fine structure, which is absent in the spectrum of CO adsorbed on an Ir/SiO₂ catalyst [30].

- the interaction between the C–O dipole and its image in the conducting, polarizable metal weakens the CO frequency by 25–75 cm^{−1},
- the formation of a chemisorption bond between CO and the substrate alters the distribution of electrons over the molecular orbitals and weakens the CO bond. Thus, strictly speaking, it is not correct to interpret the frequency difference between adsorbed and gas phase CO in terms of chemisorption bond strength only.

Infrared frequencies are characteristic for certain bonds in molecules and they can often be used to identify chemisorbed species on surfaces. Investigation of adsorbed species in relation to their behaviour in catalytic reactions is the main field of application for infrared spectroscopy, but falls outside the scope of this chapter. However, infrared spectra of adsorbates can sometimes also be used to recognize sites on the surface of a catalyst, as the following two examples show.

Sulphided Mo and Co–Mo catalysts, used in hydrotreating reactions, contain Mo as MoS₂. This compound has a layer structure consisting of sandwiches, each of a Mo layer between two S layers. The chemical activity of MoS₂ is associated with the edges of the sandwich where the Mo is exposed to the gas phase; the basal plane of the S^{2−} anions is largely unreactive. The infrared spectrum of NO on a sulphided Mo/Al₂O₃ catalyst (Fig. 10.14a) shows two peaks at frequencies which agree with those observed in organometallic clusters of Mo and NO groups [31]. NO on sulphided Co/Al₂O₃ also gives two infrared peaks (Fig. 10.14b), but at different frequencies as observed on MoS₂. These results suggest that NO can be used as a probe to titrate the number of Co and Mo sites in the

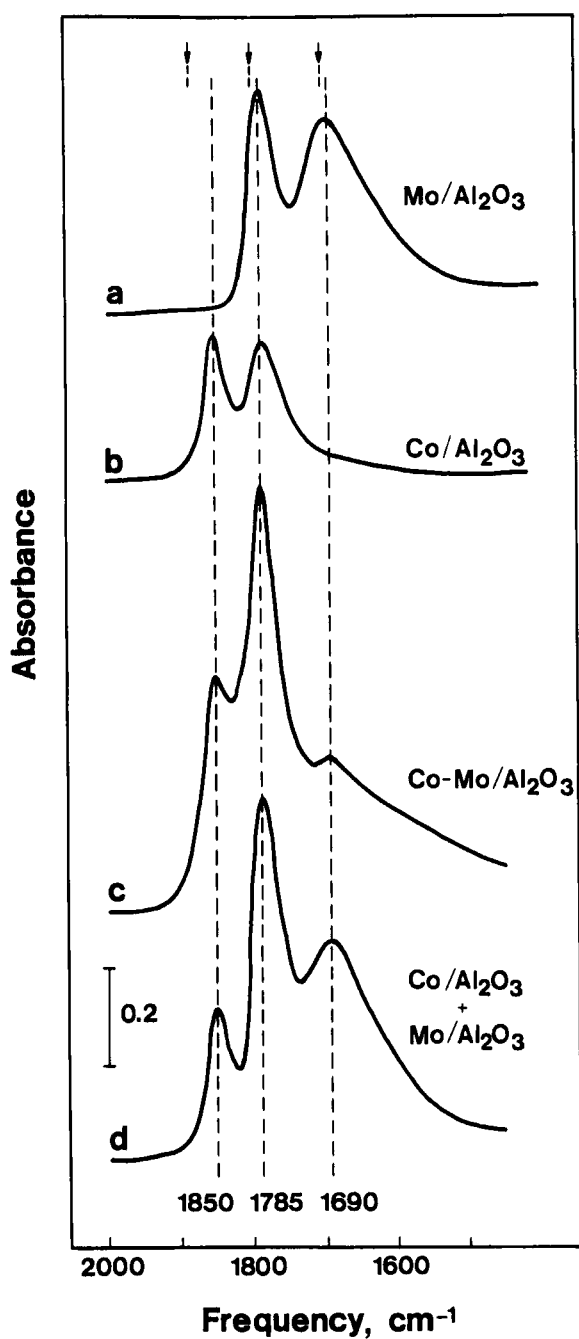


Fig. 10.14. Infrared spectra of NO probe molecules on sulphided Mo, Co, and Co-Mo hydrodesulphurization catalysts allow for titration of Co and Mo sites in the Co-Mo catalyst (from Topsøe and Topsøe [31]).

Co–Mo/Al₂O₃ catalyst. Figure 10.14c confirms that this idea works. Moreover, comparison of the intensities of the NO/Mo infrared signals on Mo/Al₂O₃ and Co–Mo/Al₂O₃ reveals that the presence of Co decreases the number of Mo atoms that are accessible to NO. This means that Co most probably decorates the edges of the MoS₂ sandwiches, because the edges constitute the adsorption sites for NO [31].

Infrared spectroscopy is also an important tool to investigate hydroxyl groups on the surfaces of oxidic catalyst supports and zeolites [32]. These OH groups may possess positive, zero or negative charge and are called acidic, neutral or basic, respectively. In solution these groups exchange with metal ion complexes (OH⁻ with a negative ion complex, H⁺ with a cation) or they provide sites where ions of opposite charge adsorb by electrostatic interaction.

As an example, let us take the (100) surface of TiO₂ in the crystallographic form of anatase. The surface is overall neutral, but possesses charged sites: in the absence of water, it contains Ti⁴⁺ cations with a net excess charge of +2/3, and two types of oxygen atoms, one with zero excess charge and the other with a net charge of -2/3 [33]. As a result, heterolytic dissociation of water occurs, in which the protons adsorb on the oxygen atoms with negative excess charge, leading to a bridging OH group of acidic character (excess charge +1/3), and the OH⁻ group attaches to the Ti ion, giving a terminal OH group of basic character (excess charge -1/3). The latter can exchange with negative ions such as {RhCl_x(OH)_y}⁻ or F⁻.

The different hydroxyl groups (see Fig. 10.15) have different vibrational properties and can be distinguished by their O–H stretch frequencies in infrared spectroscopy.

As Fig. 10.15A shows, the OH stretch region of a spectrum of TiO₂ contains at least three peaks. The one at about 3730 cm⁻¹ disappears when the surface is exchanged with F⁻ ions and corresponds to basic OH groups. The other peaks around 3670 and 3630 cm⁻¹ correspond to neutral and acidic hydroxyl groups, respectively [34]. Similar correlations exist for the O–H stretch frequencies of OH groups on alumina supports [32].

In catalyst preparation, one can determine the relative contributions of various hydroxyl groups before and after application of the active phase onto the support. In this way Sibeijn et al. [35] established that rhenium oxide attached to acidic sites of the alumina support exhibit higher activity for the metathesis of olefins than rhenium oxide on neutral or basic sites. As, however, rhenium species preferentially exchange with basic hydroxyls, one needs to go to loadings above a certain value (6 wt% for an alumina of 200 m²/gram) before the catalyst exhibits appreciable activity [35].

Another application of O–H infrared spectra is to determine to what extent the support is covered by the active phase by monitoring the total signal intensity of the hydroxyl groups as a function of catalyst loading. One should note, however,

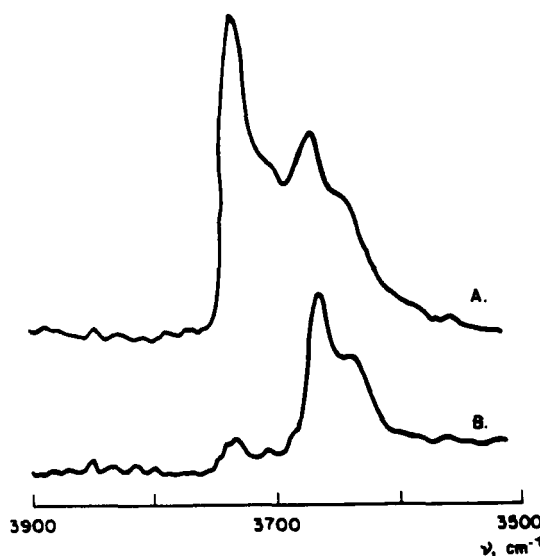


Fig. 10.15. Infrared spectra of the OH stretch region of TiO_2 , (A) before and (B) after exchange with F^- confirm that the peak around 3720 cm^{-1} is due to basic $\text{OH}^{\delta-}$ groups (from van Veen et al. [34]).

that conclusions can only be drawn on a qualitative base, because (i) the extinction coefficients of the various OH groups are unknown, (ii) the infrared signals are easily perturbed by adsorbed water, and (iii) the signal intensities can depend on temperature and concentration. For quantitative results on hydroxyl groups, infrared studies should be combined with wet chemical titrations, as described by van Veen and coworkers [34].

In summary, infrared spectroscopy is very popular for studying the adsorption of gases on supported catalysts or for studying the decomposition of infrared active catalyst precursors during catalyst preparation. Infrared spectroscopy is an *in situ* technique which is applicable in transmission or diffuse reflection mode, on real catalysts.

10.2.6 Extended X-Ray Absorption Fine Structure (EXAFS)

EXAFS is an X-ray absorption technique which gives detailed local structure information, such as the type, number and distance of neighbouring atoms [36]. As in XPS, the basic process is the photoelectric effect: a photon is absorbed by an atom or ion and an electron is emitted from an inner shell.

An EXAFS spectrum is a plot of the X-ray intensity transmitted by the sample, as a function of the energy $E = hv$ of the monochromatic X-rays. Each time E reaches the threshold for photoemission of a core electron with binding energy

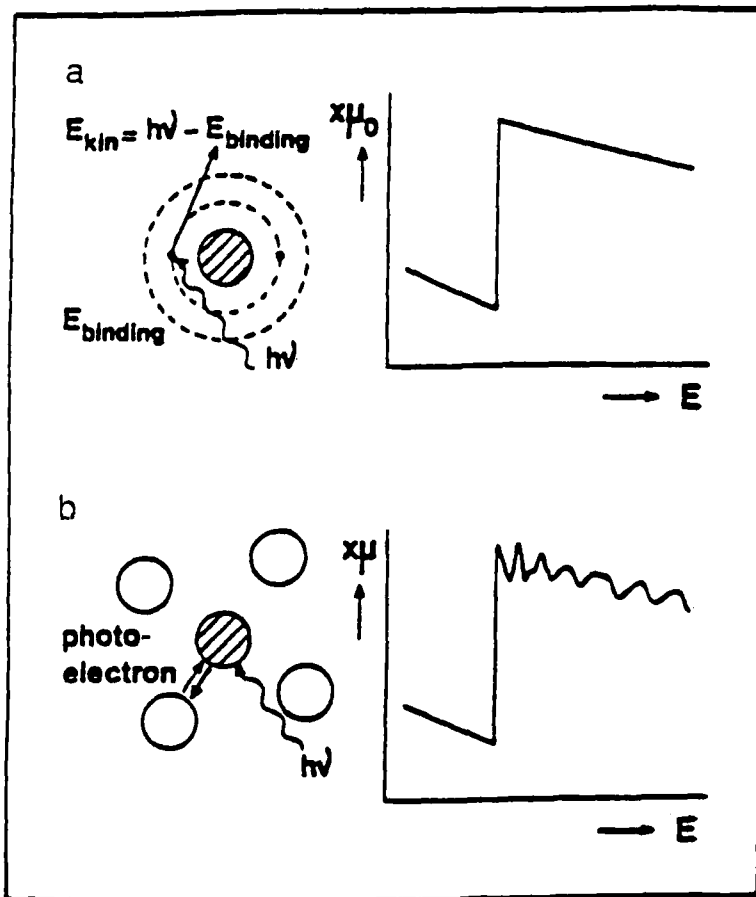


Fig. 10.16. Absorption of X-rays as a function of photon energy $h\nu$ by a free atom and by an atom in a lattice. The spherical electron wave from the central atom is scattered back by the neighbouring atoms, which leads to interference, which is constructive or destructive depending on the wavelength of the electron wave (or the kinetic energy of the electron) and the distance between the atoms. As a result, the X-ray absorption probability is modulated and the spectrum shows fine structure which represents the EXAFS spectrum [37].

E_b , the absorption cross section increases dramatically (Fig. 10.16). In a solid or a liquid, the photoelectron with kinetic energy $E_k = h\nu - E_b$ can be scattered back from neighbouring atoms to the atom where it originated. There it affects the probability that a photon can be absorbed. As electrons are waves, the back-scattered wave interferes with the original outgoing wave. Depending on the kinetic energy of the electron, which, in its turn, depends on the energy of the incoming X-rays, the interference will be constructive or destructive. The interference pattern shows up as the fine structure in the spectrum up to several hundred eV above the absorption edge.

In a monoatomic solid, each shell gives rise to a characteristic interference. This is expressed as follows in the EXAFS function $\chi(k)$:

$$\chi(k) = \sum_j A_j(k) \sin(2kr_j + \phi_j(k)) ; \quad k = \frac{2\pi}{h} \sqrt{2mE} \quad (10.9)$$

$$A_j(k) = \frac{N_j}{kr_j^2} S_0^2(k) F_j(k) e^{-2k^2\sigma_j^2} e^{-2r_j/\lambda(k)} \quad (10.10)$$

where k is the wave number, m the mass of an electron, E is kinetic energy, j labels the coordination shells around the absorbing atom, r_j is the average distance between the central atom and the atoms in the j th coordination shell and $\phi(k)$ is the phase shift. The amplitude function A contains the information on the coordination numbers N , on lattice dynamics and on structural disorder. The back-scattering amplitude F is element specific, S is a correction for relaxation processes in the absorbing atom and for multielectron excitations. These processes cause the outgoing electron to have a lower energy than $h\nu - E_b$. Exponential terms describe the effect of lattice vibrations and of structural disorder by a mean squared displacement σ^2 , as well as the attenuation of the electron wave when it travels through the solid, similarly as in XPS, UPS and AES.

The EXAFS function becomes understandable if we look at the Fourier Transform of $\chi(k)$, which resembles a radial distribution function (the probability of finding an atom at a distance r from the absorbing atom):

$$\theta_n(r) = \frac{1}{\sqrt{2\pi}} \int_{k_{\min}}^{k_{\max}} k^n \chi(k) e^{2ikr} dk \quad (10.11)$$

The function $\theta_n(r)$ represents the probability of finding an atom at a distance r . The transform is weighted with either k or k^3 , to emphasize the role of light or heavy atoms, respectively. In principle, the Fourier transform becomes more accurate when the k interval is larger, but in practice the signal to noise ratio of the spectrum sets the limit for k .

A straightforward Fourier transform of the EXAFS signal does not yield the true radial distribution function. First, the phase shift causes each coordination shell to peak at the incorrect distance. Second, due to the element specific back-scattering amplitude, the intensity may not be correct. Third, coordination numbers of distant shells will be too low mainly because of the term $1/r^2$ in the amplitude (10.10) and also because of the small inelastic mean free path of the photoelectron. The appropriate corrections can be made, however, when phase shift and amplitude functions are derived from reference samples or from theoretical calculations. Figure 10.17 illustrates the effect of phase and amplitude correction on the EXAFS of a Rh foil [38]. Note that unless the sample is that of a

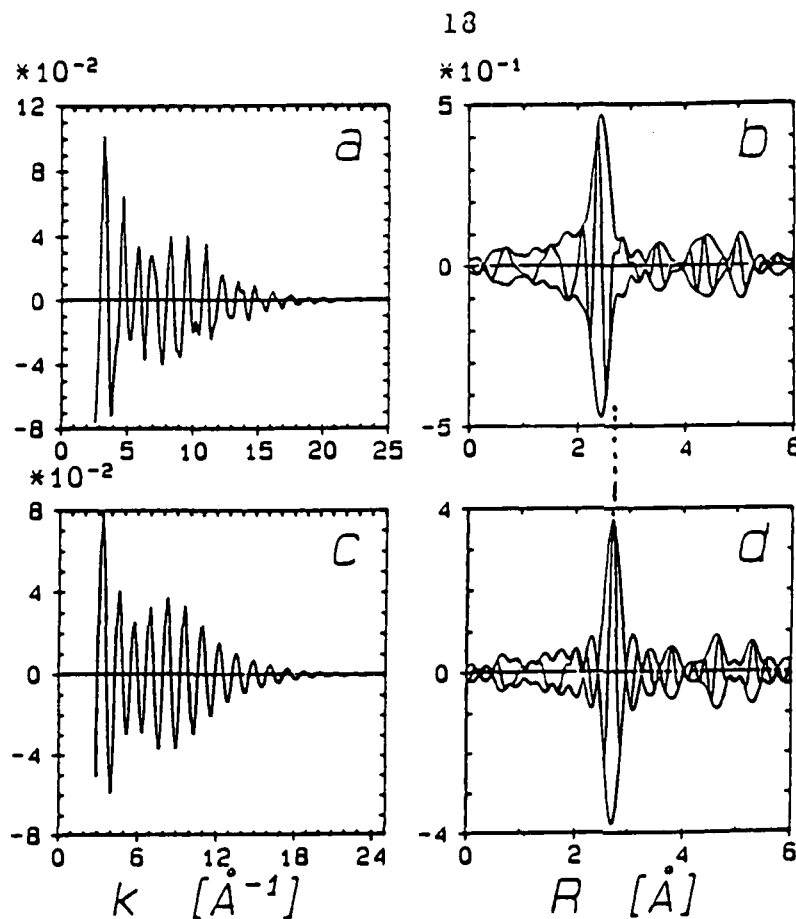
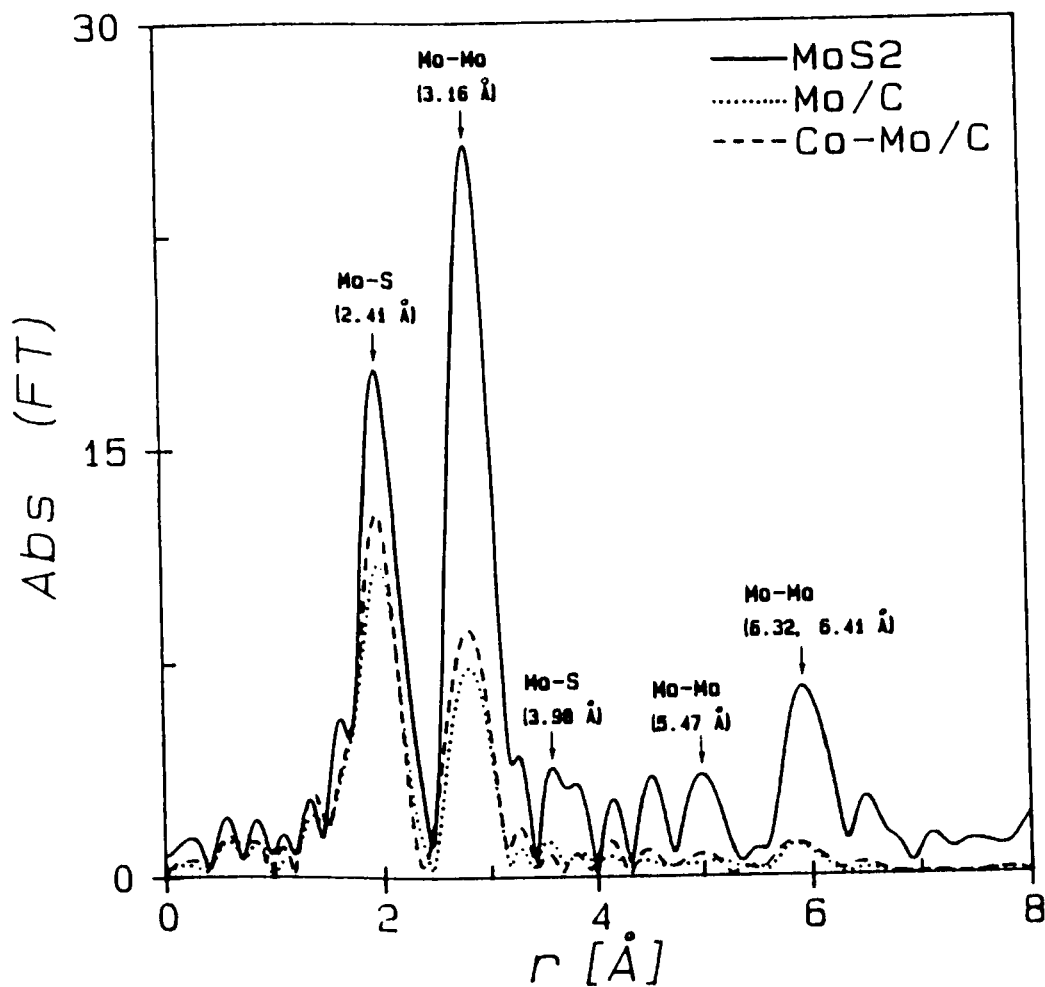


Fig. 10.17. EXAFS and Fourier transforms of rhodium metal: (a) measured EXAFS spectrum, (b) the uncorrected Fourier transform, (c) the inverse Fourier transform of the main contribution in (b), and (d) the phase and amplitude corrected Fourier transform [38].

single element, N is a fractional coordination number, i.e. the product of the real coordination number and the concentration of the element involved. Also, the EXAFS information is an average over the entire sample. As a consequence, meaningful data on supported catalysts are only obtained when the particles have a monodisperse size distribution.

Figure 10.18 shows an application of EXAFS on sulphided catalysts as used in hydrotreating processes [39]. The results in the corresponding table have been obtained by computer fitting. The great disadvantage of EXAFS is that data analysis is complicated and time consuming; considerable expertise is required to avoid ambiguities. However, if the analysis is carried out properly, one obtains structure information on the atomic scale.



	shell	N	R (Å)
MoS_2	Mo-S	6	2.41
	Mo-Mo	6	3.16
Mo/C	Mo-S	5.2 ± 0.5	2.41 ± 0.01
	Mo-Mo	2.7 ± 0.3	3.15 ± 0.01
$\text{Co}-\text{Mo}/\text{C}$	Mo-S	5.5 ± 0.5	2.40 ± 0.01
	Mo-Mo	3.2 ± 0.3	3.13 ± 0.01

Fig. 10.18. Magnitude of the Fourier Transform of the Mo K edge EXAFS spectrum of carbon-supported, sulphided Co-Mo and Mo catalysts, along with EXAFS parameters (from Bouwens et al. [39]).

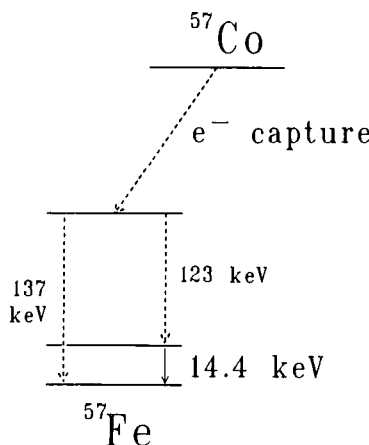


Fig. 10.19. Mössbauer spectroscopy in ^{57}Fe : the 14.4 keV source radiation is generated in a nuclear decay process starting from ^{57}Co .

10.2.7 Mössbauer Spectroscopy

Although relatively little used in catalysis, Mössbauer spectroscopy has given important information on the state of iron and cobalt in Fischer-Tropsch and hydrodesulphurization catalysts. Mössbauer spectroscopy provides the oxidation state, the magnetic field and the lattice symmetry of a number of elements such as iron, tin, iridium, and cobalt, and can be applied *in situ*. We will first describe the theory behind the Mössbauer effect and explain how a nuclear technique gives information on the state of atoms.

The Mössbauer effect (named after its discoverer, Rudolf L. Mössbauer, who demonstrated the effect in 1957) can in short be described as the recoil free emission and resonant absorption of gamma rays by nuclei [40]. The source contains nuclei in the first excited state. Figure 10.19 shows how excited iron nuclei are obtained in a nuclear decay process starting from cobalt. The 14.4 keV transition is the one that is normally used for Mössbauer spectroscopy in iron (or, more precise, in the ^{57}Fe isotope, which has a natural abundance of about 2%). The absorber contains iron with nuclei in the ground state. These nuclei could in principle absorb the radiation from the source, if their nuclear levels were separated by exactly the same energy difference as in the source. This is, in general not the case, because nuclear levels can be shifted or splitted by the so-called hyperfine interactions between the nucleus and its environment, as we will discuss in a moment. In order to cover all possible transitions between the shifted and splitted nuclear levels, one must be able to vary the energy of the source radiation. This is done by using the Doppler effect. If the source has a velocity v towards the absorber, the energy of the gamma radiation is given by

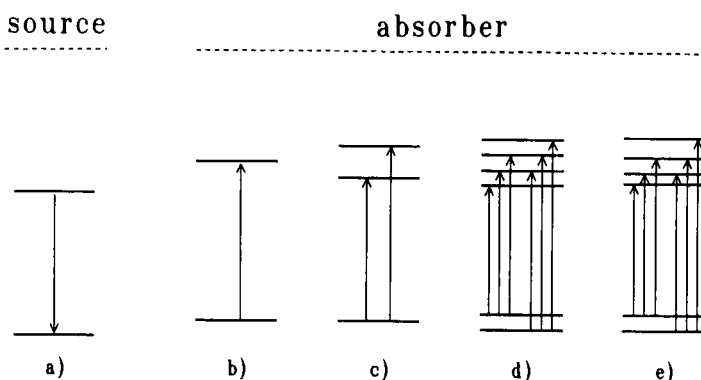


Fig. 10.20. Hyperfine interactions shift and split the nuclear levels of iron (see text) and thus make the state of the nucleus dependent on the state of the atom. Each transition corresponds to a peak in the Mössbauer spectrum, see e.g. Fig. 10.21.

$$E(v) = E_0 \left(1 + \frac{n}{c} \right) \quad (10.12)$$

in which E_0 is the energy of the stationary source and c the velocity of light. A velocity range of -10 to +10 mm/s is sufficient to cover all the shifts that can occur in iron.

Gamma rays involved in nuclear transitions are quanta of extremely narrow range in energy. It is this spectral precision that enables the detection of the so-called hyperfine interactions, the minute changes in the nuclear energy levels which result from a change in chemical state or in magnetic or electric surroundings of the atom to which the nucleus belongs.

Three hyperfine interactions play a role; they are illustrated in Fig. 10.20.

(1) The isomer shift (IS), is the consequence of the Coulomb interaction between the positively charged nucleus and the negatively charged s-electrons. The isomer shift is therefore a measure of the s-electron density at the nucleus, and yields useful information on the oxidation state of the iron in the absorber. Figure 10.20a and b show how the levels in the absorber have shifted with respect to those of the source, because the two have a different oxidation state. An example of a single line spectrum is fcc iron, as in stainless steel or in many alloys with noble metals.

(2) The electric quadrupole splitting is caused by the interaction of the electric quadrupole moment with an electric field gradient. The latter can be caused by asymmetrically distributed electrons in incompletely filled shells of the atom itself and by charges on neighbouring ions. The splitting occurs only in the excited level (Fig. 10.20c) and is proportional to the magnitude of the electric field gradient at the nucleus. The spectrum contains two peaks, the so-called quadrupole doublet. This type of spectrum is often observed with highly dispersed iron (III) oxides, see the top spectrum in Fig. 10.21.

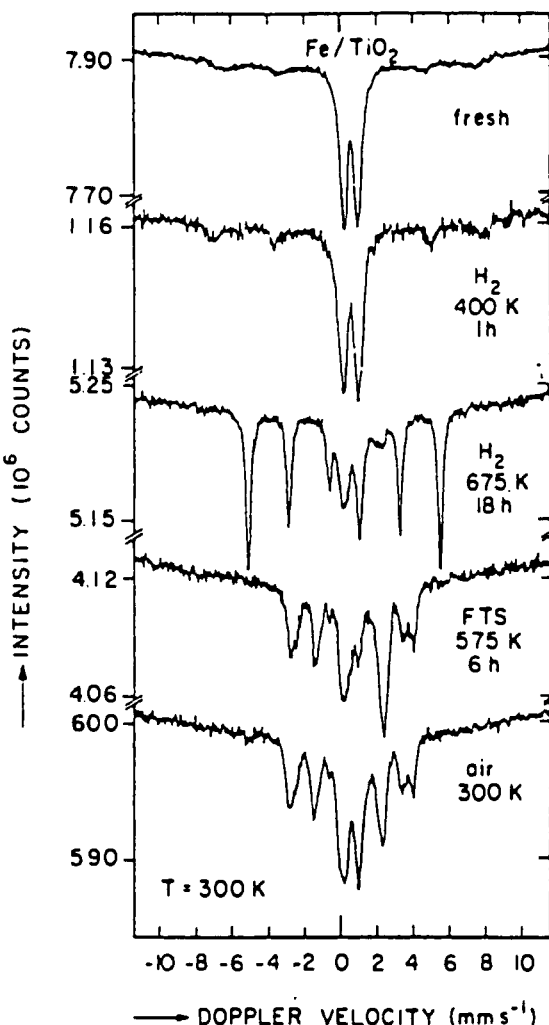


Fig. 10.21. Mössbauer spectra of an Fe/TiO_2 catalyst after different treatments (from van der Kraan et al. [44]).

(3) Magnetic hyperfine splitting or the so-called Zeeman effect arises from the interaction between the nuclear magnetic dipole moment and the magnetic field H at the nucleus. This interaction splits both nuclear levels and removes all degeneracy. From the eight possible transitions only six are allowed (Fig. 10.20d) and the spectrum contains six equidistant peaks, called sextet or sextuplet. The separation between the peaks in the spectrum is proportional to the magnetic field at the nucleus. The best known example is that of metallic or bcc iron with a magnetic hyperfine field of 33 T (330 kOe), visible in the third spectrum of Fig. 10.21 as the main contribution.

(4) If the nucleus feels both a magnetic field and an electric field gradient, and the electric quadrupole interaction is small, then the excited levels shift as indicated in Fig. 10.20e. The result is that only the inner four lines of the sextet are equidistant. This type of spectrum is measured from bulk Fe_2O_3 , with a magnetic hyperfine field of 51.5 T and a small quadrupole shift on the absorption peaks of 0.10 mm/s.

The Mössbauer effect can only be detected in the solid state. The reason is that the absorption and emission events must occur without energy losses due to recoil effects. The fraction of the absorption and emission events without exchange of recoil energy is called the recoilless fraction, f . It depends on temperature and on the energy of the lattice vibrations: f is high for a rigid lattice, but low for surface atoms [41].

A Mössbauer spectrometer consists of a radioactive ^{57}Co source on a transducer that continuously scans the desired velocity range, an absorber consisting of the catalyst and a detector to measure the intensity of the gamma radiation transmitted by the absorber as a function of the source velocity. This is the common mode of operation, called Mössbauer absorption spectroscopy, sometimes abbreviated as MAS. It is also possible to fix the ^{57}Co containing source and move a single-line ^{57}Fe absorber, in order to investigate Co-containing catalysts. This technique, called Mössbauer emission spectroscopy (MES), has successfully been applied to study Co-Mo hydrodesulphurization catalysts [42].

Mössbauer spectroscopy provides phase identification, determination of oxidation states, and incidentally structure information and particle size. A little used application is to follow in real time the kinetics of phase transitions (carburization, reduction) in catalysts by monitoring the intensities of a few selected peaks in a single velocity experiment. Examples of applications on catalysts have recently been reviewed [43].

Figure 10.21 illustrates how Mössbauer spectroscopy reveals the identity of the major iron phases in a supported iron catalyst after different treatments. The top spectrum belongs to a fresh Fe/TiO_2 catalyst, i.e. after impregnation and drying. The quadrupole doublet has an isomer shift which shows that iron is present in the ferric state, probably as small particles or a dispersed layer of an oxide or oxyhydroxide. After reduction in H_2 at 675 K the catalyst consists mainly of metallic iron, as evidenced by the sextet, along with some unreduced iron, which gives rise to two doublet contributions of Fe^{2+} and Fe^{3+} in the centre. The overall degree of iron reduction, as reflected by the relative area under the bcc-ion sextet, is high. Fischer-Tropsch synthesis at 575 K in CO and H_2 converts the metallic iron to the Hägg carbide, $\chi\text{-Fe}_5\text{C}_2$. Almost all unreduced iron is now present as Fe^{2+} . Exposure of the carburized catalyst to the air at room temperature leaves most of the carbide phase unaltered but oxidizes the ferrous to ferric iron [44].

The example is typical for many applications of Mössbauer spectroscopy in catalysis: a catalyst undergoes a certain treatment; next its Mössbauer spectrum

is measured *in situ* at room temperature. However, if the catalyst contains highly dispersed particles, the measurement of spectra at cryogenic temperatures becomes advantageous. First, because the recoil-free fraction of surface atoms increases substantially at temperatures below 300 K [41]. Second, because spectra of small particles which behave superparamagnetically at room temperature become magnetically split and therefore more informative at the temperatures of liquid nitrogen, 78 K, or liquid helium, 4.2 K [40,43,45].

10.3 CONCLUDING REMARKS

In this chapter we have limited ourselves to the most common techniques in catalyst characterization. Of course, there are many other spectroscopies which can and have been used to study catalysts, such as nuclear magnetic resonance (NMR), electron spin resonance (ESR), Raman spectroscopy, calorimetry, thermogravimetric or thermomagnetic analysis, or small-angle X-ray scattering (SAXS). Also many powerful surface science techniques, such as low energy electron diffraction (LEED), electron energy loss spectroscopy (EELS), thermal desorption spectroscopy (TDS), or scanning tunnelling microscopy (STM), have not been discussed. These methods are invaluable tools for the investigation of well defined surfaces and species adsorbed thereon, and have greatly contributed to new insights in catalysis.

10.3.1 Research Strategies

In principle, two approaches can be adopted for fundamental investigations of the relations between catalytic properties on one hand, and catalyst composition and structure on the other. The first is to model the catalytic surface, for example with that of a single crystal. By using the appropriate combination of surface spectroscopies, the desired characterization on the atomic scale is certainly possible in favourable cases. The disadvantage, however, is that although one may be able to study the catalytic properties of such samples under realistic conditions (pressures of 1 atm or higher), most of the characterization is necessarily carried out in ultra high vacuum, and not under reaction conditions.

The second approach is to study real catalysts with *in situ* techniques such as Infrared and Mössbauer spectroscopy, EXAFS and XRD, under reaction conditions, or, as is more often done, under a controlled environment after quenching of the reaction. The *in situ* techniques, however, are not sufficiently surface specific to yield the desired atom by atom characterization of the surface. At best they determine the composition of the particles. The situation is schematically represented in Fig. 10.22.

	real catalyst	single crystal
reaction conditions	XRD, TP techniques, IR, Raman spectroscopy, EXAFS, Mössbauer spectroscopy, ESR, NMR	IR, TP Techniques
vacuum	XPS, SIMS, SNMS, LEIS, RBS, TEM	all surface science techniques

Fig. 10.22. Classification of spectroscopic research in catalysis.

The dilemma is thus that investigations of real catalysts under relevant conditions by *in situ* techniques give little information on the surface of the catalyst, and that the techniques which are surface sensitive can often only be applied on model surfaces under vacuum. Bridging the gap between UHV and high pressures and between the surfaces of single crystals and of real catalysts is an important issue in catalysis.

Another point which concerns the relevance of spectroscopic research in catalysis is the following. Both catalysis and spectroscopy are disciplines which demand considerable expertise. For instance, the state of a catalyst depends often critically on the method of preparation, pretreatment or even on its environment. It is therefore essential to investigate a catalyst under carefully chosen, relevant conditions and after the proper treatment. On the other hand, no spectroscopy is really simple. The correct interpretation of spectra of catalysts requires experience based on practice and a sound theoretical background in spectroscopy, physical chemistry and solid state physics. Hence, intensive cooperation between experts in spectroscopy and experts in catalysis is probably the best way to warrant meaningful and correctly interpreted results.

Finally, it is good to realize that, although many techniques undoubtedly reveal usable information on catalysts, the information desirable from a fundamental point of view can often not be obtained. In this situation it is a good strategy to combine all techniques which tell us at least something about the catalyst. The catalysis literature contains several examples where this approach has been remarkably successful.

REFERENCES

- 1 M.J. Phillips and M. Ternan (Editors), *Proc. 9th Int. Congr. on Catalysis*, Calgary 1988, The Chemical Institute of Canada, Ottawa, 1988.
- 2 W.N. Delgass, G.L. Haller, R. Kellerman and J.H. Lunsford, *Spectroscopy in Heterogeneous Catalysis*, Academic Press, New York, 1979.
- 3 J.M. Thomas and R.M. Lambert (Editors), *Characterisation of Catalysts*, Wiley, Chichester, 1980.
- 4 J.L.G. Fierro (Editor), *Spectroscopic Characterization of Heterogeneous Catalysts*, Elsevier, Amsterdam, 1990.
- 5 R.B. Anderson and P.T. Dawson (Editors), *Experimental Methods in Catalytic Research*, Academic Press, New York, 1976.
- 6 F. Delannay (Editor), *Characterization of Heterogeneous Catalysts*, Dekker, New York, 1984.
- 7 L.C. Feldman and J.W. Mayer, *Fundamentals of Surface and Thin Film Analysis*, North Holland, Amsterdam, 1986.
- 8 G.A. Somorjai, *Chemistry in Two Dimensions: Surfaces*, Cornell University Press, Ithaca, 1981.
- 9 J.B. Cohen and L.H. Schwartz, *Diffraction from Materials*, Academic Press, New York, 1977.
- 10 H. Jung and W.J. Thomson, *J. Catal.* 128 (1991) 218.
- 11 F. Delannay, Chapter 3 in F. Delannay (Editor), *Characterization of Heterogeneous Catalysts*, Dekker, New York, 1984.
- 12 R.T.K. Baker, *Catal. Rev. - Sci. Eng.* 19 (1979) 161.
- 13 N.W. Hurst, S.J. Gentry, A. Jones and B.D. McNicol, *Catal. Rev. - Sci. Eng.* 24 (1982) 233.
- 14 H.F.J. van 't Blik and J.W. Niemantsverdriet, *Appl. Catal.* 10 (1984) 155.
- 15 J.L. Falconer and J.A. Schwarz, *Catal. Rev. - Sci. Eng.* 25 (1983) 141.
- 16 A.M. de Jong and J.W. Niemantsverdriet, *Surface Sci.* 233 (1990) 355.
- 17 G. Ertl and J. Küppers, *Low Energy Electrons and Surface Chemistry*, VCH Verlagsgesellschaft, Weinheim, 1985.
- 18 D. Briggs and M.P. Seah (Editors), *Practical Surface Analysis by Auger and X-ray Photoelectron Spectroscopy*, Wiley, New York, 1983.
- 19 H.J. Borg, L.C.A. van den Oetelaar, L.J. van IJzendoorn, and J.W. Niemantsverdriet, *J. Vac. Sci. Technol. A*, in print (July 1992).
- 20 C.D. Wagner, W.M. Riggs, L.E. Davis, J.F. Moulder, and G.E. Muilenberg, *Handbook of X-ray Photoelectron Spectroscopy*, Perkin-Elmer Corporation, Eden Prairie, 1979.
- 21 A.C.Q.M. Meijers, A.M. de Jong, L.M.P. van Gruijthuijsen and J.W. Niemantsverdriet, *Appl. Catal.* 70 (1991) 53.
- 22 H.P.C.E. Kuipers, H.C.E. van Leuven and W.M. Visser, *Surf. Interf. Anal.* 8 (1986) 235.
- 23 Spectra measured by H. Korpik and A.M. de Jong, unpublished.
- 24 J.C. Muijsers, J.W. Niemantsverdriet, I.C.M. Wehman-Ooyevaar, D.M. Grove, and G. van Koten, *Inorg. Chem.*, to be published.
- 25 L.M. Eshelman, A.M. de Jong and J.W. Niemantsverdriet, *Catal. Lett.*, 10 (1991) 201.
- 26 J.C. Vickerman, A. Brown and N.M. Reed (Editors), *Secondary Ion Mass Spectrometry*, Oxford University Press, Oxford, 1989.
- 27 A. Benninghoven, F.G. Rüdenauer and H.W. Werner, *Secondary Ion Mass spectrometry, Basic Concepts, Instrumental Aspects, Applications and Trends*, Wiley, New York, 1987.
- 28 G.C. van Leerdam, H.H. Brongersma, I.M.M. Tijburg and J.W. Geus, *Appl. Surface Sci.*, in press.
- 29 A. Fadini and F.-M. Schnepel, *Vibrational Spectroscopy*, Ellis Horwood Ltd, Chichester, 1989.

- 30 Spectra measured by L.M.P. van Gruijthuijsen and J.H.M.C. van Wolput, unpublished.
- 31 N.Y. Topsøe and H. Topsøe, *J. Catal.* 84 (1983) 386; *J. El. Spectr. Relat. Phenom.* 39 (1986) 11.
- 32 H. Knözinger and P. Ratnasamy, *Catal. Rev. - Sci. Eng.* 17 (1978) 31.
- 33 R.A. van Santen, *Theoretical Heterogeneous Catalysis*, World Scientific, 1991.
- 34 J.A.R. van Veen, F.T.G. Veltmaat and G. Jonkers, *J. Chem. Soc., Chem. Commun.* (1985) 1656.
- 35 M. Sibeijn, R. Spronk, J.A.R. van Veen and J.C. Mol, *Catal. Lett.* 8 (1991) 201.
- 36 D.C. Koningsberger and R. Prins (Editors), *X-ray Absorption*, Wiley, New York, 1987.
- 37 F.B.M. van Zon, Thesis, Eindhoven, 1988
- 38 J.H.A. Martens, Thesis, Eindhoven, 1988
- 39 S.M.A.M. Bouwens, R. Prins, V.H.J. de Beer, and D.C. Koningsberger, *J. Phys. Chem.* 94 (1990) 3711.
- 40 J.A. Dumesic and H. Topsøe, *Adv. Catal.* 26 (1976) 121.
- 41 J.W. Niemantsverdriet, A.M. van der Kraan and W.N. Delgass, *J. Catal.* 89 (1984) 138.
- 42 H. Topsøe and B.S. Clausen, *Catal. Rev. - Sci. Eng.* 26 (1984) 395.
- 43 J.W. Niemantsverdriet, *Hyperfine Interactions* 47 (1989) 219.
- 44 A.M. van der Kraan, R.C.H. Nonnekens, F. Stoop and J.W. Niemantsverdriet, *Appl. Catal.* 27 (1986) 285.
- 45 P.H. Christensen, S. Mørup and J.W. Niemantsverdriet, *J. Phys. Chem.* 89 (1985) 4898.

Chapter 11

Temperature programmed reduction and sulphiding

11.1 INTRODUCTION

Temperature programmed reduction (TPR) is a useful technique for the characterization of metal oxide catalysts. During a TPR experiment, the catalyst under investigation is placed in a fixed-bed reactor and exposed to a reducing mixture that continuously perfuses the catalyst bed, while the temperature is increased according to a linear temperature programme. The difference between the inlet and outlet concentration of the gas mixture is measured as a function of time using a thermal conductivity detector. The resulting TPR profile contains qualitative information on the oxidation state of the reducible species present and, in that sense, it is a fingerprint. The technique is intrinsically quantitative and the information obtained is of a kinetic nature and, as a consequence, directly correlated with catalytic behaviour. On the other hand, information on the structure of the species present is less straightforward than for instance that obtained by spectroscopic methods. Temperature-programmed techniques are thus complementary to spectroscopic ones and the two methods are applied in combination.

A direct application is the study and optimization of catalyst pretreatment. In industrial practice, catalysts are frequently pretreated using a temperature-programmed technique. Examples are reduction in the fat hardening catalysis and sulphiding in the hydrotreatment of oil fractions in the refinery.

Undoubtedly, more information can be extracted from a more thorough analysis of the TPR data. To stimulate this an example of a detailed modelling will be presented.

Temperature-programmed sulphiding (TPS) is another member of a family of techniques in which catalysts are characterised by subjecting them to a temperature-programme under specified conditions. The applicability of TPS is highlighted by an example in this chapter.

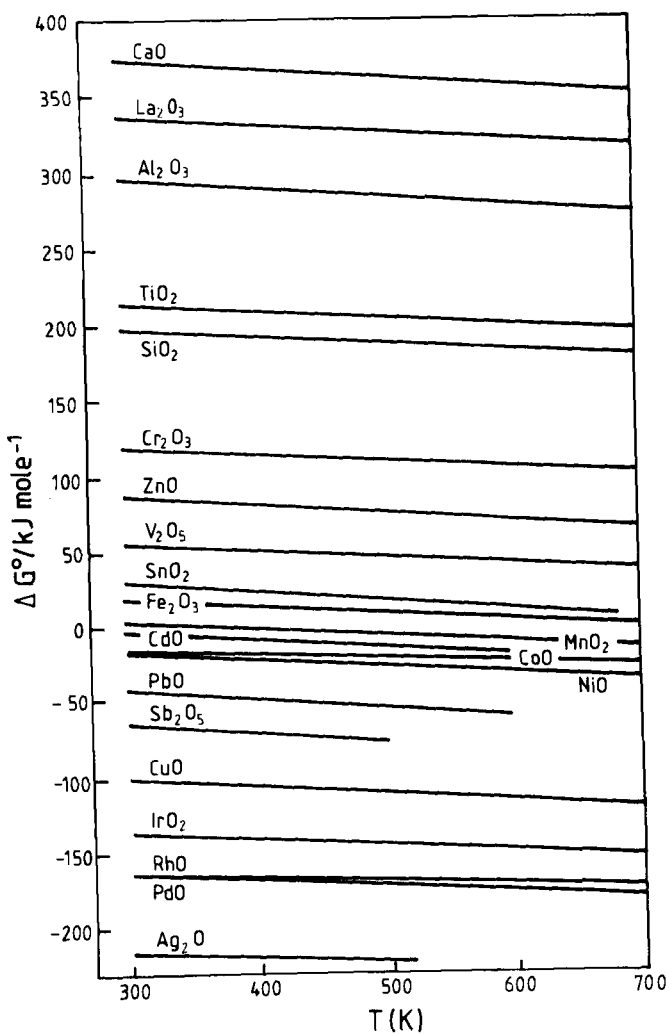


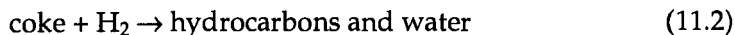
Fig. 11.1. Standard free energy, ΔG° , as a function of temperature for the process: $\text{MO} + \text{H}_2 \rightarrow \text{M} + \text{H}_2\text{O}$.

11.2 APPLICATION OF TPR

In TPR oxidic species are reduced following the general reduction path:



It should be noted that TPR is not limited to the reduction of oxides. Many species react with hydrogen and can be studied by TPR. Examples are the study of 'coke' deposits on catalysts:



and the reduction of sulphides:



The major part of this chapter is devoted to TPR of oxides but other systems are occasionally discussed.

11.3 THERMODYNAMICS

The enthalpy change, ΔG of reaction (1) is:

$$\Delta G = \Delta G^\circ + RT \ln \left(\frac{P_{\text{H}_2\text{O}}}{P_{\text{H}_2}} \right) \quad (11.4)$$

ΔG° is positive for a number of oxides [1] such as V_2O_5 , ZnO , and Fe_2O_3 (see Fig. 11.1). However, the reduction of these oxides is still thermodynamically feasible because the ratio of partial pressures in Eqn. (4) becomes sufficiently small at elevated temperature and high total flow rate the water formed is constantly swept out of the system.

11.4 APPARATUS

A flow scheme of a TPR instrument [2] is given in Fig. 11.2. The reactor containing the catalyst is situated in a furnace equipped with a temperature programmable controller. The effluent of the reactor is analyzed by one or more suitable detectors. A TCD is most commonly used for the detection of hydrogen

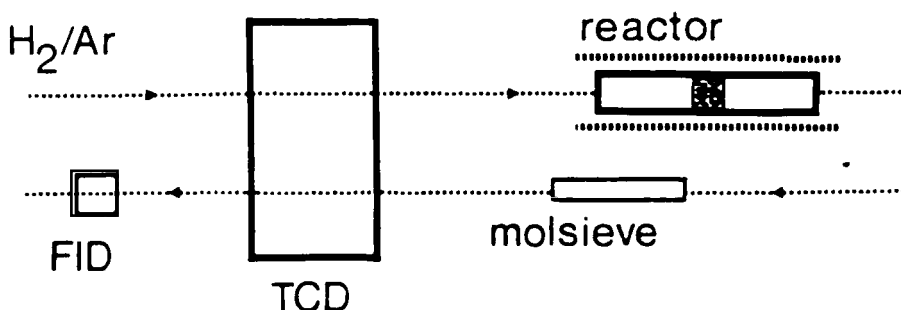


Fig. 11.2. Temperature-programmed reduction apparatus.

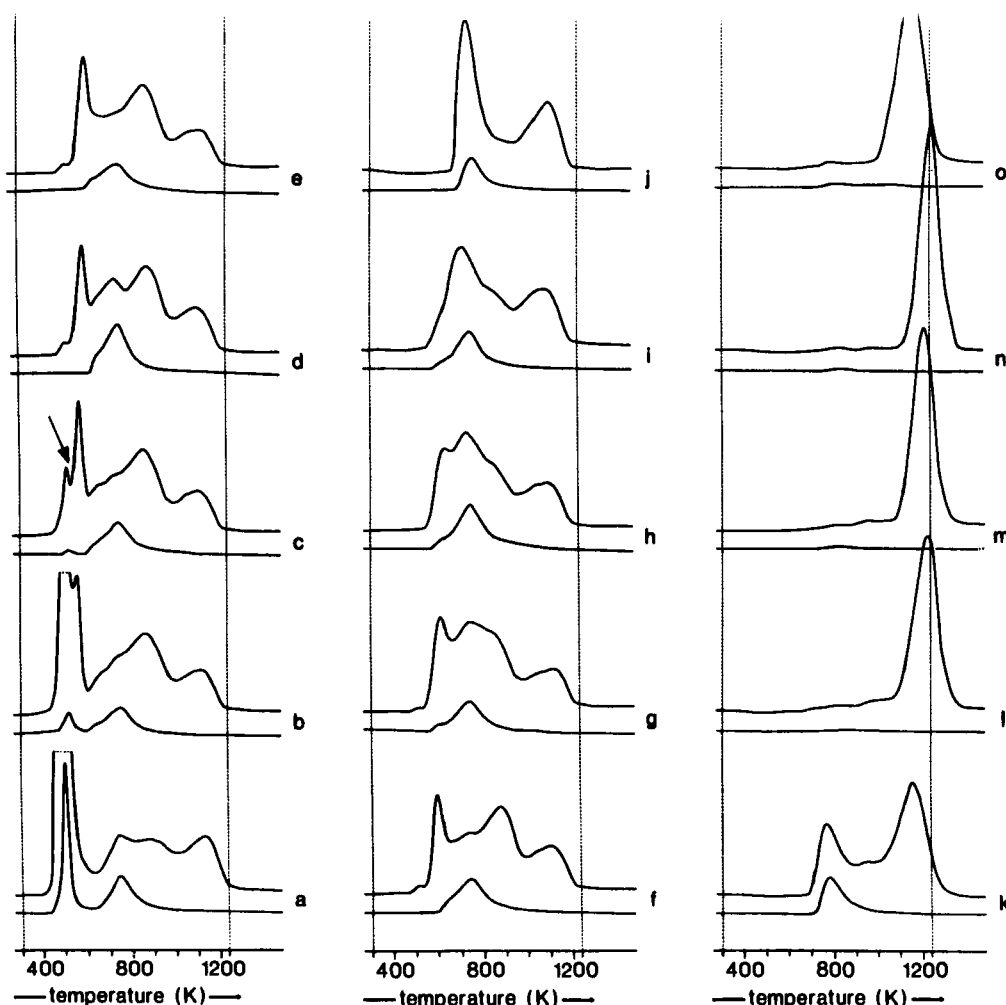


Fig. 11.3. TPR patterns of 9.1% CoO/Al₂O₃ catalysts calcined at various temperatures. Calcination temperature (K): 380 (a), 575 (b), 625 (c), 675 (d), 725 (e), 775 (f), 825 (g), 875 (h), 900 (i), 925 (j), 975 (k), 1025 (l), 1075 (m), 1175 (n), 1290 (o), the upper and lower part of each pattern represents the TCD and FID signal, respectively.

consumption. In order to obtain a quantitative signal, the H₂O produced during reduction is trapped or removed before the gas mixture reaches the TCD detector. In general, more than one detector should be used. It is convenient also to use an FID detector because porous catalysts nearly always contain adsorbed carbonaceous material, which leads to additional hydrogen consumption. The reducing mixture consists of H₂ and an inert gas. The latter should be really inert and therefore argon is well suited while N₂ is not, since it can react with hydrogen.

11.5 EXAMPLE 1: TEMPERATURE-PROGRAMMED STUDY OF CoO/Al₂O₃

The CoO/Al₂O₃ catalyst of this example [3] was prepared by pore volume impregnation of Al₂O₃ with Co(NO₃)₂ followed by drying and calcination (heating in air). It appeared that calcination conditions are critical. For instance, the colour of the sample depends strongly on the calcination temperature.

Figure 11.3 gives the TPR patterns of a series of catalysts calcined at different temperatures [3]. Clearly, they differ profoundly and reduction takes place over a wide range of temperatures. Figure 11.4 gives TPR patterns of reference compounds used for identification [3]. CoO and Co₃O₄ have relatively sharp reduction peaks at 610 and 590, respectively. Apparently, CoAl₂O₄ is very stable to reduction. The explanation is that in this spinel the CoO bonds are strongly polarized by the neighbouring Al ions. In Co₃O₄ no Al³⁺ ions are present and, as a consequence, reduction is easy. This picture is supported by the behaviour of CoMoO₄. Figure 11.5 [4] shows TPR patterns of Co₃O₄, CoAl₂O₄ and CoMoO₄. In comparison with Al ions Mo ions are soft and it may be expected that the CoO bonds are less polarized. This explains the intermediate reduction rate of CoMoO₄.

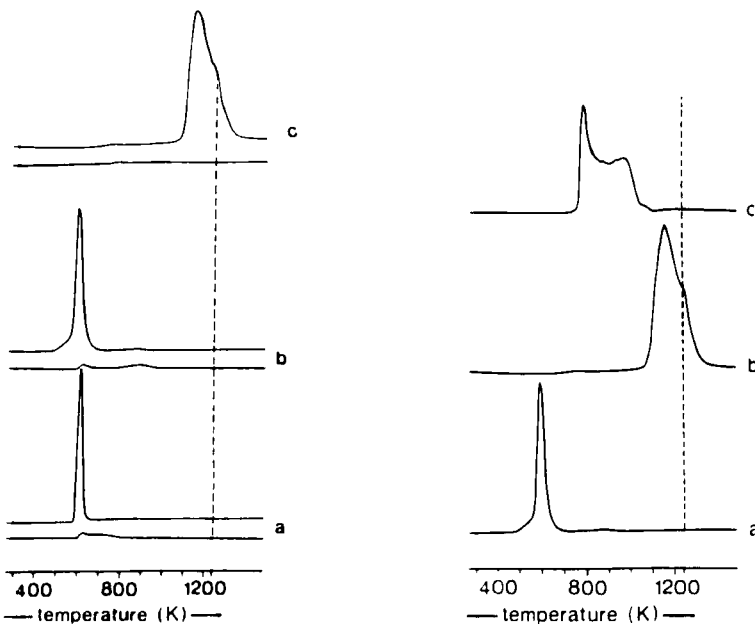


Fig. 11.4 (left). TPR patterns of reference materials. (a) CoO; (b) Co₃O₄; (c) CoAl₂O₄. The upper and lower part of each pattern represents the TCD and FID signal, respectively.

Fig. 11.5 (right). The influence of hard and soft ions on the TPR patterns (10 K/min) of Co-containing crystalline compounds. (a) Co₃O₄; (b) CoAl₂O₄; (c) CoMoO₄. Only the TCD signals are given.

When we compare these patterns with those of the series of catalysts, it is clear that CoAl_2O_4 is formed at high calcination temperature. This was confirmed by XRD. The very intense peak around 500 K of the sample calcined at the lowest temperature is due to the decomposition of nitrate groups. The patterns show that this peak only disappears when calcination is carried out above 650 K.

The sharp peak indicated in Fig. 11.3c is due to Co_3O_4 crystallites. They disappear at higher temperatures because they react with the support. Figure 11.3 also clearly shows peaks due to the hydrogenation of carbonaceous material. This is proved by the fact that they occur both in the TCD and the FID signal. The other peaks have been assigned to three other species, i.e. a Co^{3+} spinel and two surface compounds. It is clear from the peak area that Co^{3+} species must be present, besides Co^{2+} species. The structure of the compounds is not completely clear but the amounts of reducible species are known.

This example illustrates the fundamentals of TPR: quantitative operation is often possible, but additional techniques are needed for structure elucidation.

11.6 EXAMPLE 2: TEMPERATURE-PROGRAMMED SULPHIDING OF $\text{MoO}_3/\text{Al}_2\text{O}_3$

Alumina supported molybdenum oxide catalysts are extensively used in hydrotreating reactors. Under reaction conditions the oxides are not stable because they are transformed into molybdenum sulphides. In practice this step is carried out in a so-called sulphiding step. In this step the catalyst is pretreated with a mixture containing a sulphur compound. The sulphiding step was investigated by carrying out a TPS study. TPS is strictly analogous to TPR, except for the gas mixture which is here a $\text{H}_2/\text{H}_2\text{S}$ mixture.

A priori the following reactions might be expected:



The first reaction is reduction, as in TPR. Elementary sulphur is formed in the second reaction. The third reaction will be referred to as 'oxygen-sulphur exchange'. The last reaction is an oxidation.

Figure 11.6 [4] shows the TPS patterns for a series of catalysts with different loadings. The bottom curve represents the carrier. At room temperature extensive uptake of H_2S is observed. In order to measure quantitatively, an isothermal stage of ca. 1 hour is introduced at the start of the experiment.

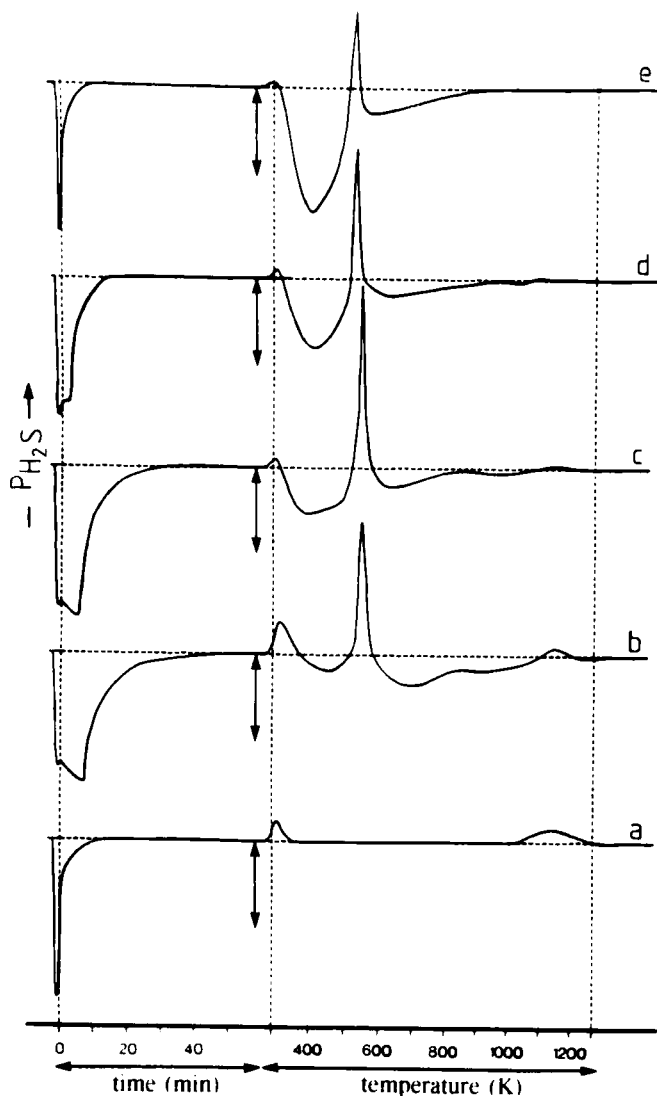


Fig. 11.6. TPS patterns (H_2S) of $\text{MoO}_3/\text{Al}_2\text{O}_3$ with varying Mo content, pretreated in Ar at room temperature. (a) 400 mg, carrier; (b) 800 mg, 0.5 atom/ nm^2 ; (c) 400 mg, 1.0 atom/ nm^2 ; (d) 200 mg, 2.2 atom/ nm^2 ; (e) 100 mg, 4.5 atom/ nm^2 . The 50% conversion level of H_2S is indicated by a double-headed arrow.

The unloaded support adsorbs some H_2S at room temperature, which is desorbed at the start of the temperature program. The small peak at the high temperature is attributed to impurities in the carrier.

All catalysts adsorb a large amount of H_2S at room temperature. From the fact that the colour of the catalyst changes during this stage we conclude that at least

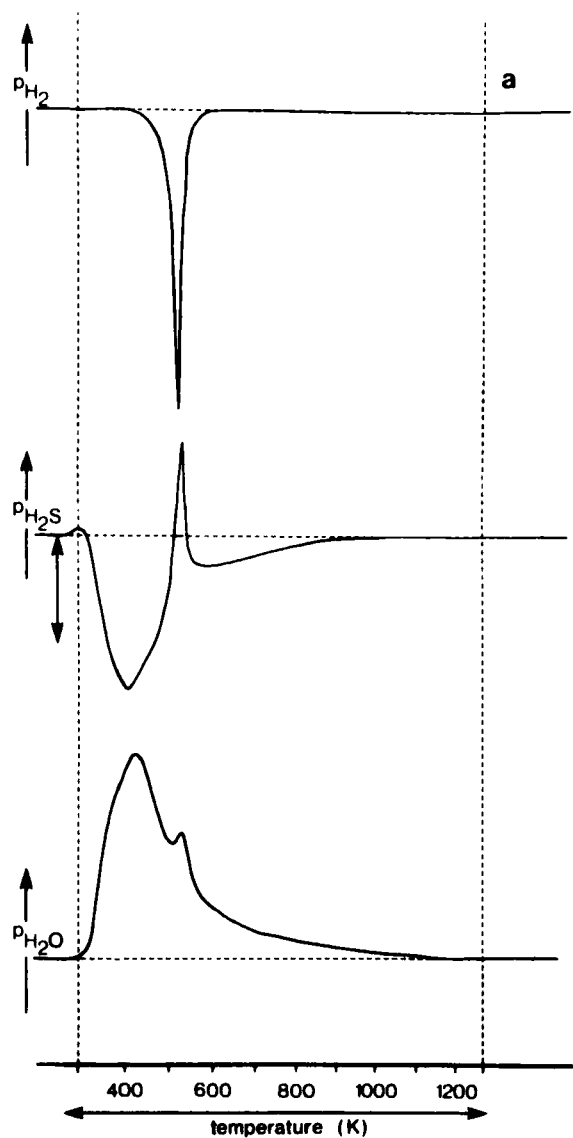


Fig. 11.7. TPS pattern (H_2S , H_2O , H_2) of $\text{MoO}_3/\text{Al}_2\text{O}_3$, 4.5 atom/nm², 100 mg, pretreated in Ar at room temperature.

partial sulphiding takes place. At the beginning of the temperature program some H_2S desorption is observed followed by continued sulphiding. It is striking that in all cases a sharp H_2S production peak exists superimposed on the sulphiding pattern.

In order to obtain information on the stoichiometry of the reaction steps, a mass spectrometer was used, besides a TCD. The results for a catalyst of inter-

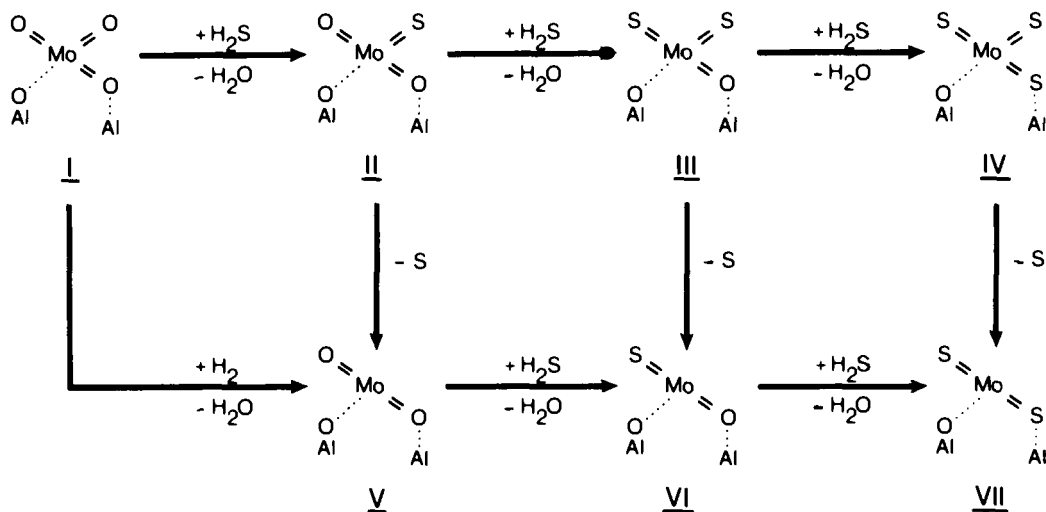


Fig. 11.8. Simplified molecular scheme of sulphiding.

mediate loading are given in Fig. 11.7. It is clear that the pattern is explained by an O-S exchange over the whole sulphiding window with hydrogenation of S superimposed on it.

On a molecular scale these results are interpreted in the scheme shown in Fig. 11.8 [4]. For simplicity the molybdenum oxide layer is represented by a tetrahedral structure. From other results and considerations of minimal steric hindrance it is concluded that the pathway via complexes III and VI is the dominant one. These patterns reveal the basic chemistry of sulphiding. They can be used for optimizing catalyst pretreatment in practical circumstances.

11.7 MODELLING

The modelling of TPR patterns has not received much attention. Nevertheless, the results depend on the experimental conditions and modelling will be necessary when the results of different authors have to be compared. Moreover, the kinetic and thermodynamic data obtained are very useful.

We present a convenient method of evaluating kinetic data from TPR patterns.

11.7.1 Theory

The reaction obeys the following stoichiometry:



Generally, it is assumed that the rate of a solid gas reaction can be represented by

the product of two factors [4], one is only dependent on the temperature and the other is only dependent on the concentrations:

$$\frac{d\alpha}{dt} = k_1 \cdot f(\alpha) \cdot f' (P_{H_2}, P_{H_2O}) \quad (11.10)$$

α is the degree of conversion of the solid reactant. Table 11.1 gives $f(\alpha)$ functions for several relevant models for reduction kinetics.

We assume differential conditions, hence the function that depends on gas-phase concentration is constant. Equation (11.10) reduces to:

$$\frac{d\alpha}{dt} = k(T) \cdot f(\alpha) \quad (11.11)$$

For a heating program with a constant heating rate β the temperature is given by:

$$T = \beta t + T_0 \quad (11.12)$$

The temperature dependence is assumed to follow the Arrhenius equation:

$$k(T) = A_0 \cdot \exp \left(\frac{-E_R}{RT} \right) \quad (11.13)$$

Combining Eqns. (11.11), (11.12), and (11.13) we obtain

$$\frac{d\alpha}{dT} = \frac{A_0}{\beta} \exp \left(\frac{-E_R}{RT} \right) \cdot f(\alpha) \quad (11.14)$$

TPR patterns (i.e. $d\alpha/dT$ versus T) can be calculated by solving the differential Eqn. (11.14), giving α explicitly as a function of T and subsequently calculating $d\alpha/dT$. The solution to the differential Eqn. (11.14) can easily be found by separation of variables and integration, which leads to:

$$g(\alpha) = \int_0^\alpha \frac{d\alpha}{f(\alpha)} = \int_{T_0}^T \frac{A_0}{\beta} \exp \left(\frac{-E_R}{RT} \right) dT \quad (11.15)$$

In Table 11.1 $f(\alpha)$ is given, besides functions $g(\alpha)$. The right-hand side can be evaluated numerically by using a 4th order rational approximation.

$$\int_{T_0}^T \exp \left(\frac{-E_R}{RT} \right) dT = \frac{E_R}{R} \frac{\exp(-x)}{x} \frac{x^3 + 18x^2 + 88x + 96}{x^4 + 20x^3 + 240x + 120} \quad (11.16)$$

This method has been found to be very accurate [5].

11.7.2 Reduction Kinetic Models

TABLE 11.1

Reduction kinetic models: ($f(\alpha)$ differential form, $g(\alpha)$ integral form Eqn. 11.15)

Model	$f(\alpha)$	$g(\alpha)$
<i>n</i> th Order	α^n	$\alpha^{n+1}/(n+1)$
Random nucleation Unimolecular decay law	$(1 - \alpha)$	$-\ln(1 - \alpha)$
Phase boundary controlled reaction (contracting area)	$(1 - \alpha)^{1/2}$	$2(1 - (1 - \alpha)^{1/2})$
Phase boundary controlled reaction (controlled volume)	$(1 - \alpha)^{2/3}$	$3(1 - (1 - \alpha)^{1/3})$
Two-dimensional growth of nuclei (Avrami-Erofeev)	$2(1 - \alpha)(-\ln(1 - \alpha))^{1/2}$	$(-\ln(1 - \alpha))^{1/2}$
Three-dimensional growth of nuclei (Avrami-Erofeev)	$3(1 - \alpha)(-\ln(1 - \alpha))^{2/3}$	$(-\ln(1 - \alpha))^{1/3}$
One-dimensional diffusion parabolic law	$1/2\alpha$	α^2
Two-dimensional diffusion	$-1/\ln(1 - \alpha)$	$(1 - \alpha)\ln(1 - \alpha) + \alpha$
Three-dimensional diffusion (Jander)	$[3(1 - \alpha)^{2/3}]/[2(1 - (1 - \alpha)^{1/3})]$	$(1 - (1 - \alpha)^{1/3})^2$
Three-dimensional diffusion (Ginstling-Brounshtein)	$3/[2((1 - \alpha)^{-1/3} - 1)]$	$1 - 2\alpha/3 - (1 - \alpha)^{2/3}$

11.7.3 Activation energy

The TPR patterns are very sensitive to the value of the activation energy which is needed for the modelling. Fortunately, this can be calculated separately from a series of experiments in which the heating rate is varied. Kissinger introduced this method in DTA measurements. It will be shown that this method can be generally used in TPR modelling. For the maximum of the TPR peak the following equations hold:

$$\left[\frac{d}{dT} \left(\frac{d\alpha}{dT} \right) \right] = 0 \quad (11.17)$$

Combination of Eqn. (11.17) with Eqn. (11.14) leads to:

$$\left[\frac{d}{dT} \left(\frac{A}{\beta} \exp \left(-\frac{E}{RT} \right) f(\alpha) \right) \right] = 0 \quad (11.18)$$

This equation reduces to:

$$\frac{d\alpha}{dT} \left[\frac{E}{RT_{\max}^2} + \left(\frac{df(\alpha)}{d\alpha} \right)_{T=T_{\max}} \left(\frac{A}{\beta} \exp \left(-\frac{E}{RT_{\max}} \right) \right) \right] = 0 \quad (11.19)$$

Assuming that $f(\alpha)$ and α are independent of the heating rate and that $d\alpha/dT$ is not equal to zero, Eqn. (11.19) can be rewritten as:

$$\ln \left(\frac{\beta}{T_{\max}^2} \right) + \ln \left(\frac{E}{RA} \right) = -\frac{E}{RT_{\max}} + \ln \left(-\frac{df(\alpha)}{d\alpha} \right)_{T=T_{\max}} \quad (11.20)$$

Consequently, plots of $\ln(\beta/T_{\max}^2)$ vs $1/T_{\max}$ are expected to give straight lines with slope $-E/R$. These plots might be called temperature-programmed 'Arrhenius plots'. This equation is used generally. We checked the validity of the assumption for the models of Table 1 and investigated the dependence of $df(\alpha)/d\alpha$ on the heating rate at the peak temperature. We found that $df(\alpha)/d\alpha$ was constant for all models. Therefore it can be concluded that the Kissinger method can usually be applied [6].

11.7.4 Recommended experimental conditions for TPR

The model Eqn. (11.14) is derived on the basis of the simplifying assumption of differential conditions which is only encountered with a low fractional conversion of hydrogen. Two other important criteria to consider are the stability and constant sensitivity of the thermal conductivity detector. The latter is the most difficult to achieve, since a thermal conductivity detectors' sensitivity depends very much on the hydrogen concentration, which changes during an experiment. This can introduce errors into the quantitative analysis if no care is taken to operate in a region where the sensitivity does not vary throughout the experiment. This can be achieved by operating at high total flow rate (50–70 Nml/min) of (60–70% H₂ in Ar) mixture. Another important factor is the temperature profile, which should be linear with time. To achieve this, a multiple-zone controlled oven is recommended. Also, a small amount of catalyst should be used to reduce the effect of the heat of reaction on the temperature profile in the reactor.

Transport effects should be avoided in qualitative analysis and kinetic studies [7]. This is accomplished by using small particles (100 µm), the ratio of reactor diameter to particle size d_t/d_p should be larger than 15, and the ratio of catalyst bed-length to the particle diameter should be larger than 20. It is also well known that the amount of sample influences the TPR profile resolution [8], i.e. multiple

reduction steps are convoluted into one peak when the amount of sample is large. We therefore recommend the use of very small amounts of sample when the objective is to distinguish between oxidic states. Finally, pretreatment of the metal oxide prior to reduction, in oxygen and argon mixture at a temperature close to the calcination temperature, leads to more reproducible TPR profiles. Reproducibility can also be achieved through cyclic temperature programmed reduction–oxidation–reduction.

11.8 EXAMPLE 3: MODELLING OF TPR OF Fe_2O_3

Figures 11.9, 11.10, and 11.11 give TPR patterns of Fe_2O_3 under various experimental conditions [9]. It is interesting to compare the three profiles a–c in Fig. 11.9. The only difference is the sample size.

The larger the sample size the higher the temperature. The explanation is that H_2O inhibits reduction. Also, a large shift is observed for large samples in Fig. 11.9, hence the assumption that the gas phase term is constant is not correct.

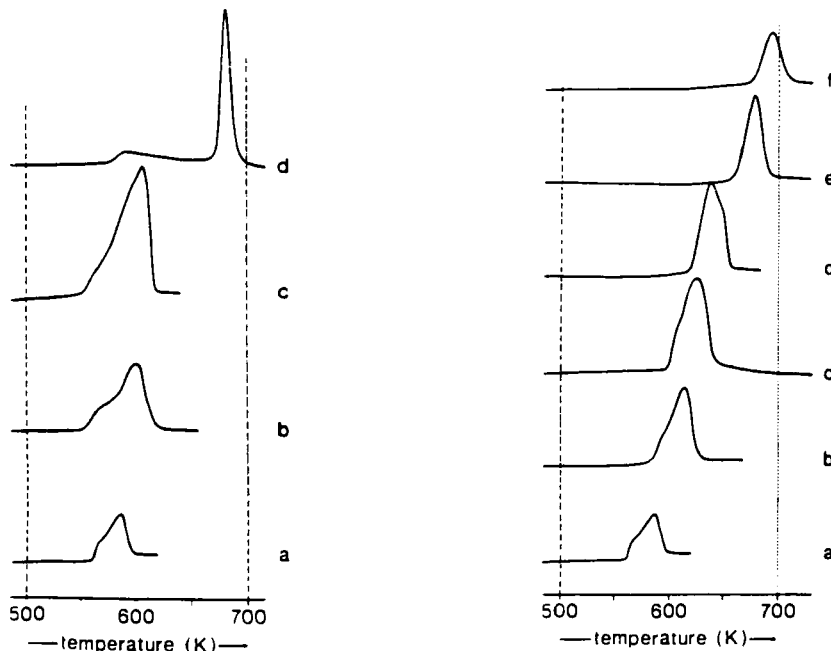


Fig. 11.9 (left). TPR patterns (0.2 K/min) of Fe_2O_3 in dry H_2/Ar (a,b,c) and in H_2/Ar saturated with 3% water(d); Fe_2O_3 sample sizes: (a) 3.6 mg; (b) 8.2 mg; (c) 15.9 mg; (d) 7.0 mg.

Fig. 11.10 (right). TPR patterns of Fe_2O_3 in dry H_2/Ar as a function of heating rate (dry series): (a) 0.2 K/min ($m = 3.6$ mg); (b) 0.5 K/min ($m = 2.8$ mg); (c) 1 K/min ($m = 1.8$ mg); (d) 2 K/min ($m = 0.91$ mg); (e) 5 K/min ($m = 0.19$ mg); (f) 10 K/min ($m = 0.08$ mg).

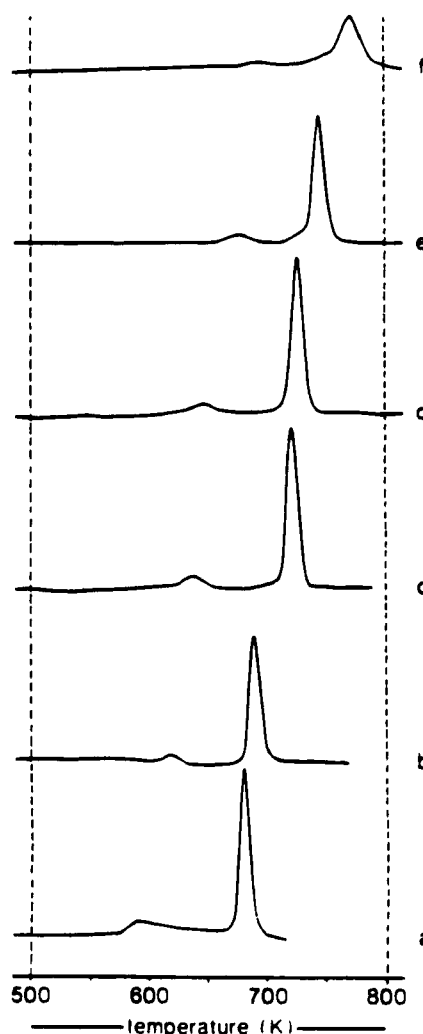
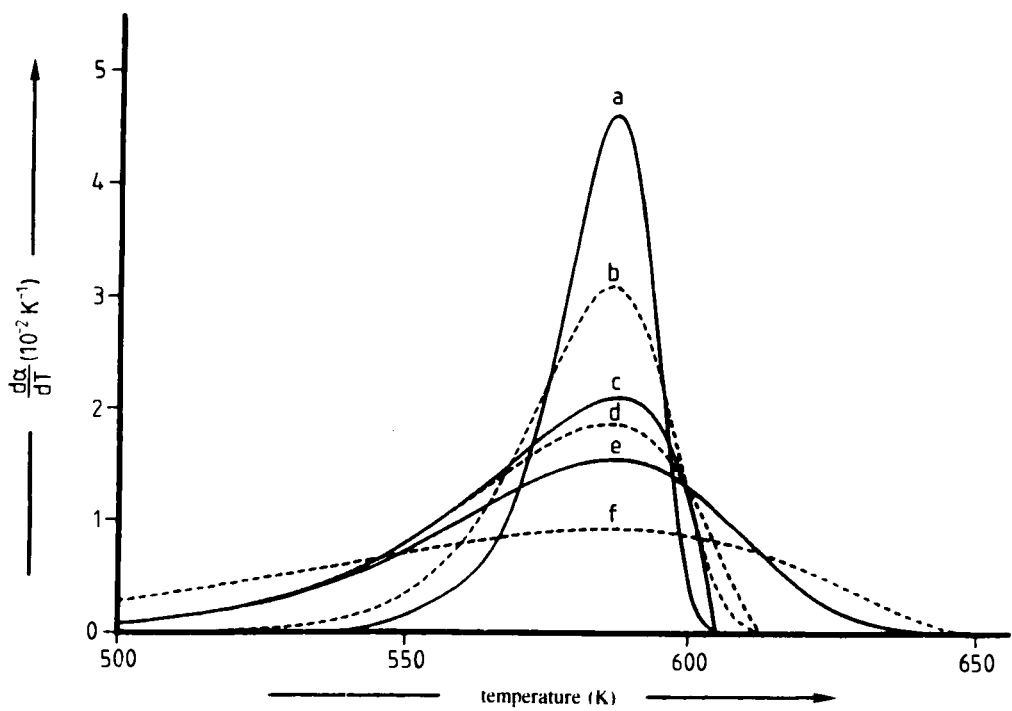
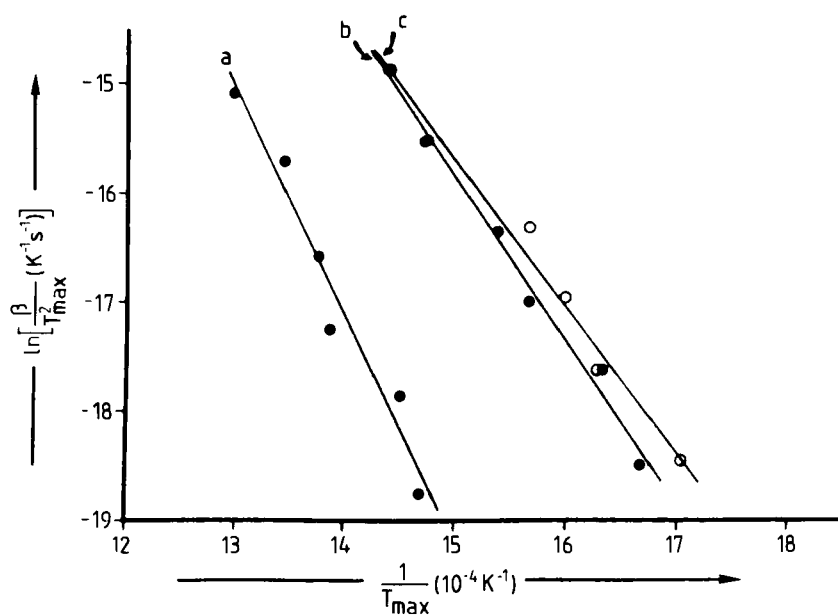


Fig. 11.11. TPR patterns of Fe_2O_3 in wet H_2/Ar (3% water) as a function of heating rate (wet series): (a) 0.2 K/min ($m = 7.0 \text{ mg}$); (b) 0.5 K/min ($m = 2.6 \text{ mg}$); (c) 1 K/min ($m = 1.5 \text{ mg}$); (d) 2 K/min ($m = 0.90 \text{ mg}$); (e) 5 K/min ($m = 0.33 \text{ mg}$); (f) 10 K/min ($m = 0.17 \text{ mg}$).

Opposite page:

Fig. 11.12. Temperature-programmed Arrhenius plots for the reduction of Fe_2O_3 . (a) main peak for wet series; (b) low temperature peak for wet series; (c) main peak for dry series ($E_a = 111 \text{ kJ/mol}$).

Fig. 11.13. Calculated $\text{Fe}_3\text{O}_4 \rightarrow \text{Fe}$ metal TPR peaks for six reduction models using $E = 111 \text{ kJ/mol}$ (TPR on dry H_2/Ar) 0.2 K/min (a) three-dimensional nucleation according to Avrami-Erofeev, (b) two-dimensional nucleation according to Avrami-Erofeev, (c) two-dimensional phase boundary, (d) three-dimensional phase boundary, (e) unimolecular decay, (f) three-dimensional diffusion according to Jander.



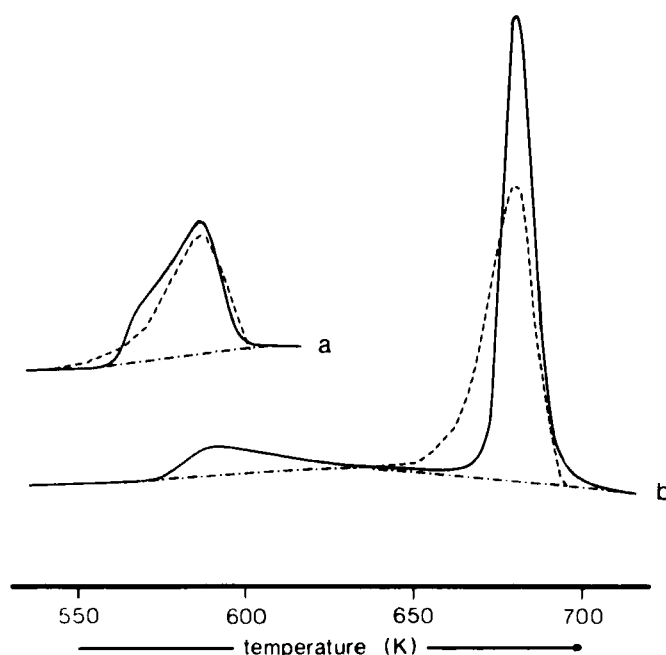


Fig. 11.14. Comparison between measured TPR patterns for Fe_2O_3 and calculated TPR peaks for $\text{Fe}_3\text{O}_4 \rightarrow \text{Fe}$ metal reduction step, using the three-dimensional nucleation model according to Avrami-Erofeev at 0.2 K/min. Calculated dotted line: (a) dry series, (b) wet series, $E = 172$ kJ/mol, $A = 3.5 \times 10^9 \text{ s}^{-1}$.

Figure 11.10 gives results of experiments where the H_2O partial pressure was kept as low as possible in order to approach differential conditions with negligible H_2O inhibition. Figure 11.11 gives results of experiments where H_2O was added on purpose. In the 'wet' series two peaks are observed, clearly due to two reduction steps, while these peaks are not resolved in the 'dry' series.

On the basis of the results given in Figs. 11.10 and 11.11, three 'Arrhenius plots' can be constructed, as given in Fig 11.12. In view of the wide range of experimental conditions it is concluded that Eqn. (11.19) is followed well, and reliable activation energies can be calculated.

These activation energies can now be used to simulate the TPR profiles. The patterns corresponding to the lowest heating rate were chosen. Figure 11.13 gives simulations for the 'dry' experiment, using the fixed value of the activation energy and T_{\max} with Eqn. (11.20) to determine A_0 for the different models given in Table 11.1. Clearly, the different models give distinctly different profiles and a model selection is possible. It appears that the sharpest curve, corresponding to Avrami-Erofeev kinetics, best describes the experimental data.

Figure 11.14a compares the model based on Avrami-Erofeev kinetics with the

experimental curve. The agreement is satisfactory in light of the fact that no adjustable parameter has been used to allow curve-fitting procedures. The difference at the leading edge is attributed to the first reduction step which is not included in the model.

For the wet series, none of the models tried is correct. We attribute this to an inhibition by water at the beginning of the peak (Fig. 11.14b) followed by a reduction process exhibiting a runaway character due to autocatalysis or thermal effect.

REFERENCES

- 1 N.W. Hurst, S.J. Gentry and A. Jones, *Catal. Rev. Sci. Eng.* 24 (2) (1982) 233.
- 2 P.J. Mangnus, Ph.D thesis, University of Amsterdam, The Netherlands, 1991.
- 3 P. Arnoldy and J. A. Moulijn, *J. Catal.* 93 (1985) 38–54.
- 4 P. Arnoldy, J.A.M. van den Heijkant, J.D. de Bok and J.A. Moulijn, *J. Catal.* 92 (1985) 25–55.
- 5 G.I. Senum and R.T. Yang, *J. Thermal Anal.* 11 (1977) 445.
- 6 A. Tarfaoui, F. Kapteijn and J.A. Moulijn, in press (1993).
- 7 J.A. Moulijn, A. Tarfaoui and F. Kapteijn, *Catal. Today*, 11 (1991) 1.
- 8 P. Malet and A. Caballero, *J. Chem. Soc., Faraday Trans.* 84 (7) (1988) 2369.
- 9 O.J. Wimmers, P. Arnoldy, and J.A. Moulijn, *J. Phys. Chem.* 90 (1986) 1331–1337.

Chapter 12

The use of adsorption methods for the assessment of the surface area and pore size distribution of heterogeneous catalysts

12.1 INTRODUCTION

It is the aim of this chapter to present a critical exposition of the use of adsorption methods for the characterization of heterogeneous catalysts. Such methods are applied to determine the *texture* of catalysts and therefore this concept has to be explained first.

By definition the texture of a solid is known if we can describe its spatial architecture in the range of dimensions between 0.3 nm (lower limit) and 1 mm (upper limit). It may also be stated that the texture of a solid body is known if we know its surface area and also the location and magnitude of all undulations in its surface. The concept of texture should be well distinguished from the concept of *structure*, which is a description of the crystallography of the material.

The chemical, physical and technical properties of catalysts and many other porous technical materials are to a very great degree determined by both their texture and their structure, but the analytical composition of the surface also plays a role. Modern surface analysis techniques, like auger electron spectroscopy (AES) and X-ray photoelectron spectroscopy (XPS) have revealed that in many cases the atomic composition of the surface of a solid material deviates strongly from the composition of the bulk material.

The study of the texture, structure and surface composition of heterogeneous catalysts plays an important role in the development of catalytic processes,

especially when sintering, poisoning and abrasion are concerned, and also in comparing batches from various manufacturers with respect to the reproducibility of new charges.

12.2 PHYSICAL ADSORPTION

In the study of the texture of catalysts use is made of the physical adsorption of gases. Physical adsorption is an increase of concentration at the gas–solid or gas–liquid interface under the influence of integrated van der Waals–London forces, also known as de Boer–Hamaker forces.

The van der Waals–London forces between molecules and atoms are well known from the term a/V^2 in the van der Waals equation:

$$(p + a/V^2)(V - b) = RT \quad (12.1)$$

where b is the volume occupied by the gas molecules and a/V^2 is a correction for the attractive forces between the gas molecules in which a is a constant, characteristic for each gas.

The total attractive interaction energy between molecules is the sum of three contributions: dipole–dipole interactions, dipole–induced dipole interactions and induced dipole–induced dipole interactions. The important feature is the dependence of all three types of interaction energy on the inverse of the *sixth* power of the separation:

$$V = -C r^{-6} \quad (12.2)$$

C being a coefficient that depends on the identity of the molecules and r being the mean distance between the molecules. V = total interaction energy.

Of course, repulsive interactions play a role as well. When molecules are squeezed together, the nuclear and electronic repulsions and the rising electronic kinetic energy begin to dominate over the attractive forces. An expression for the repulsive force between two molecules can be derived from quantum-mechanical considerations as:

$$E_{\text{rep}} = B \cdot r^{-m} \quad (12.3)$$

where B is an empirical constant and the exponent m is usually assigned the value $m = 12$.

The total potential energy between two molecules thus becomes:

$$E(r) = -C r^{-6} + B r^{-12} \quad (12.4)$$

$E(r)$ is often termed the Lennard–Jones potential.

It is important to note that the interaction energies discussed hitherto are *very weak, short-range forces*. For instance, at 25°C the average interaction energy for

pairs of molecules with a dipole moment of 1 Debye unit is about -1.4 kJ mol^{-1} when the separation is 0.3 nm. This should be compared with the average molar kinetic energy of $3/2 RT = 3.7 \text{ kJ mol}^{-1}$ at the same temperature. Due to the inverse sixth power in Eqn. 12.4 the attraction energy takes off rapidly when r is increased. This is true to a larger extent for the repulsion energy, this energy being proportional to the inverse twelfth power of the distance r .

To apply the above equations to the adsorption of a gas on a solid [1] it is necessary to consider the interaction of the surface layers of a solid composed of atoms or ions of a substance Y with isolated molecules of a gas X. The individual interactions of each atom in gas molecule X with each atom of solid Y have to be added up to obtain the potential $\phi(z)$ of a single molecule of the gas with reference to the solid:

$$\phi(z) = \sum \epsilon_{ij}(r_{ij}) \text{ or} \quad (12.5)$$

$$\phi(z) = -C_{ij} \sum_j r_{ij}^{-6} + B_{ij} \sum_j r_{ij}^{-12} \quad (12.6)$$

Here r_{ij} is the distance between the molecule i in the gas phase and the centre of atom j in the solid: ϵ_{ij} is the potential energy between i and j .

In many cases other interaction energies have still to be added to $\phi(z)$. If the solid is polar it will give rise to an electric field which will induce a dipole in the gas molecule X. The resulting interaction energy ϕ_P will be:

$$\phi_P = -\frac{1}{2} \alpha^2 F \quad (12.7)$$

where F is the field strength at the centre of the molecule and α is the polarizability of the molecule.

Further contributions to the potential energy occur when the molecule X possesses a permanent dipole and quadrupole moment.

Two important qualitative conclusions can be drawn from the above. First, the adsorbate molecules or atoms interact with a large number of adsorbent atoms or molecules and, especially at higher coverages, also with adjacent adsorbed atoms or molecules. It follows that all these interactions have to be summed. If, as a first approximation, we replace this summation with an integration in the three directions of space, the term r_{ij}^{-6} in Eqn. 12.6 reduces to r_{ij}^{-3} . It follows that physical adsorption forces are *by no means short-range forces*. Furthermore, due to integration of all interaction forces, physical adsorption forces are *relatively strong forces* as compared with the forces giving rise to the term a/V^2 in Eqn. 12.1 for the case of gases at not too high a pressure. We return to this in Section 12.7.

12.3 ADSORPTION ISOTHERMS

Adsorption isotherms are plots of the amount of gas adsorbed at equilibrium as a function of the partial pressure p/p^0 , at constant temperature. The quantity of gas adsorbed is mainly expressed as the mass of gas (usually g) or the volume of gas reduced to STP (standard temperature and pressure). The majority of isotherms which result from physical adsorption may conveniently be grouped into five classes — the five types I to V included in the classification originally proposed by Brunauer, Deming, Deming and Teller — sometimes referred to simply as the Brunauer classification [2]. The essential features of these types are indicated in Fig. 12.1.

Isotherm I is typical of adsorption in micropores, which occurs, for instance, in zeolites and in activated carbons. Isotherm II represents multilayer physisorption on a flat surface (valid for many nonporous substances). Type III and V isotherms are characteristics of weak gas-solid interactions (water adsorption on gold and bromine adsorption on silica are good examples). The type IV isotherm is frequently found in the study of heterogeneous catalysts; its shape is characteristic

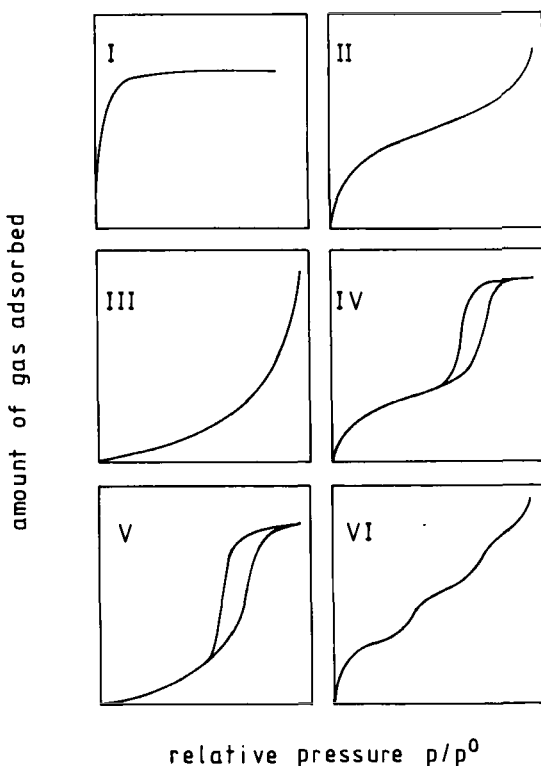


Fig. 12.1. The five types of adsorption isotherms (I to V inclusive), together with type VI, the stepped isotherm.

of multilayer adsorption accompanied by capillary condensation in mesopores.

When the surface of a nonporous adsorbent is energetically uniform the isotherm may have a step-like shape (type VI). A good example of a type VI isotherm is found in the adsorption of krypton at 90 K on carbon black, graphitized at 2700°C [3]. Type VI isotherms are of theoretical interest only.

In this review we will confine ourselves to the application of types II and IV isotherms in the determination of surface areas and pore size distributions. In practice the range of suitable adsorptives is quite narrow, by far the most commonly used one being nitrogen at its boiling point (about 77 K).

12.4 CLASSIFICATION OF PORE SIZES

The individual pores in heterogeneous catalysts and in other porous technical substances may vary greatly, both in size and in shape. An important quantity is the width of the pores, e.g. the diameter of a cylindrical pore, or the distance between the sides of a slit-shaped pore. A classification of pores according to their average width was originally proposed by Dubinin [4] and has now been officially adopted by the International Union of Pure and Applied Chemistry [5].

Widths of micropores range from 0.3 to 2 nm. Mesoporous substances have pore sizes from 2 nm up to 50 nm. Macropores run from pore widths of 50 nm up to about 10^5 nm.

Surface areas and pore size distributions of mesoporous materials are most easily studied by nitrogen adsorption and nitrogen capillary condensation. The most appropriate method for the study of macroporosity is mercury porosimetry [6,7], a technique which will not be treated here.

12.5 POROSITY OF POROUS SUBSTANCES

Relatively simple methods are available to determine the porosity of porous substances. By definition the porosity Pr is given by:

$$Pr = (V_p / V_{\text{tot}}) \times 100\% \quad (12.8)$$

where V_p is the pore volume in $\text{cm}^3 \text{ g}^{-1}$ and V_{tot} is the total volume of the porous substance, found by following the contours of the particles, in $\text{cm}^3 \text{ g}^{-1}$.

Furthermore we have:

$$V_{\text{tot}} = V_{\text{true}} + V_p \quad (12.9)$$

V_{true} , the true specific volume, may be obtained from physicochemical tables, but can also be determined pycnometrically by imbibition of the material in helium.

The total specific volume, V_{tot} , is determined pycnometrically by imbibition of the porous material in mercury at 0.1 MPa pressure. Note that most materials are not wetted by mercury. Hence, mercury will not penetrate into the pores at 0.1 MPa pressure.

As $V_{\text{true}} = V_{\text{He}}$ and $V_{\text{tot}} = V_{\text{Hg}}$, and $V_p = V_{\text{Hg}} - V_{\text{He}}$ we may write:

$$Pr = (V_{\text{Hg}} - V_{\text{He}}) / V_{\text{Hg}} \times 100\% \quad (12.10)$$

In practice the porosity varies from about 14%, as found for some zeolites, to about 70% found for highly activated carbons.

12.6 THE YARDSTICK IN THE DETERMINATION OF SURFACE AREAS

The monolayer capacity of a solid can be used to calculate its specific surface area, A , in m^2/g . The monolayer capacity is defined as the amount of adsorbate that can be accommodated in a completely filled single molecular layer, a *monolayer*, on the surface of one gram of solid. It is related to the specific surface area A by the simple equation:

$$A = n_m a_m L \quad (12.11)$$

where a_m is the average area occupied by a molecule of adsorbate in the completed monolayer and L is the Avogadro constant; n_m , the monolayer capacity, being expressed in moles of adsorbate per gram of adsorbent.

The majority of surface area determinations are carried out by making use of the area occupied by a nitrogen molecule as the yardstick, the nitrogen adsorption isotherm being measured at the boiling point of nitrogen, 77.4 K.

The value of a_m may be calculated following an early suggestion of Emmett and Brunauer [8], from the density ρ_L of liquid nitrogen at 77.4 K. In the calculation the assumption is made that the arrangement of adsorbed nitrogen molecules on a surface is just the same as it would be on a plane surface placed within the bulk liquid. This leads to the equation:

$$a_m = 1.091 (M / \rho_L L)^{2/3} \quad (12.12)$$

where $M = 28$, the molecular weight of nitrogen, and 1.091 is a packing factor for 12 nearest neighbours in the bulk liquid and six on the plane surface. The density of liquid nitrogen at 77.4 K, ρ_L , is 0.81 g cm^{-3} and L is equal to $6.022 \times 10^{23} \text{ mol}^{-1}$. Insertion of these quantities into Eqn. 12.12 gives $a_m(\text{N}_2) = 16.2 \text{ \AA}$ for the value of a_m for nitrogen at 77.4 K.

The average area occupied by other molecules can be determined by compari-

son of their monolayer capacity with that of nitrogen. The molecular area $a_m(\text{Ar})$ at 77.4 K is then found to be 13.85 Å. For krypton 20.1 Å is an appropriate value, whereas for benzene at 273 K a value 40 Å is often found in the literature.

12.7 THE LANGMUIR ADSORPTION ISOTHERM (MONOLAYER ADSORPTION) AND THE BET EQUATION (MULTILAYER ADSORPTION)

In the derivation of an isotherm describing monolayer adsorption, Langmuir [9] started from the following suppositions:

- all adsorption sites are energetically equivalent;
- the surface of the adsorbent is flat;
- there is no mutual interaction between the adsorbed molecules or atoms (no lateral interactions);
- the adsorbed molecules or atoms are localized (immobile adsorption).

As adsorption takes place on the uncovered part of the surface only, we have:

$$r_{\text{ads}} = k_a(p/p^\circ)(1 - \theta) \quad (12.13)$$

where r_{ads} is the rate of adsorption on the uncovered part of the surface, p/p° is the relative pressure and $(1 - \theta)$ is the uncovered fraction of the surface; k_a is the rate constant for adsorption.

The rate of desorption is given by:

$$r_{\text{des}} = k_d \theta \quad (12.14)$$

in which k_d is the rate constant for desorption.

At equilibrium, $r_{\text{ads}} = r_{\text{des}}$ and hence:

$$k_a(p/p^\circ)(1 - \theta) = k_d \theta \quad (12.15)$$

The adsorption equilibrium constant K is equal to k_a/k_d and hence:

$$K = \exp(-\Delta G/RT) = k_a/k_d \quad (12.16)$$

in which ΔG is the free enthalpy of adsorption.

It follows from Eqns. 12.15 and 12.16 that

$$\theta = \frac{K p/p^\circ}{1 + K p/p^\circ} \quad (12.17)$$

which is known as the Langmuir equation.

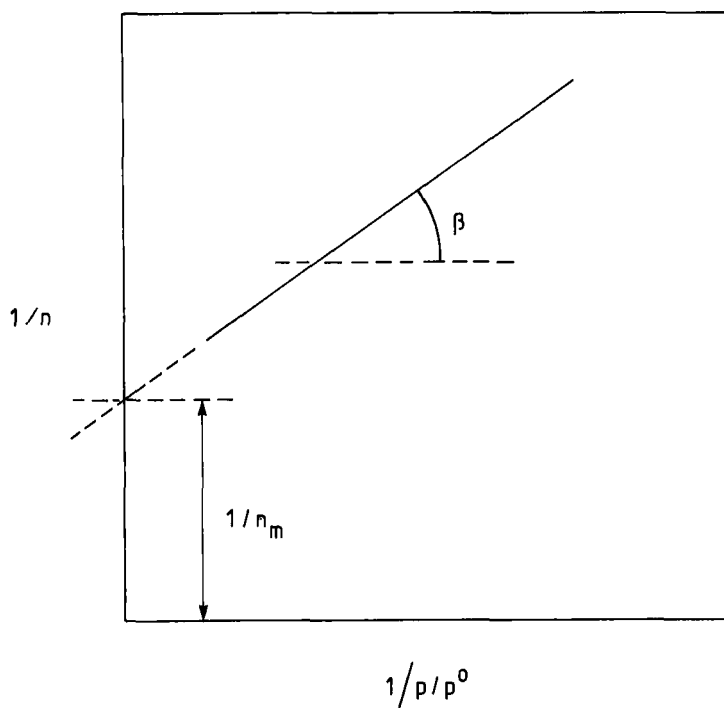


Fig. 12.2. A reciprocal plot of the Langmuir equation.

For practical purposes it is worth plotting the Langmuir equation in the so-called reciprocal form. By substitution of n/n_m for the coverage θ , in which n is the number of moles adsorbed on 1 g of adsorbent and n_m is the monolayer capacity expressed in the same units, we obtain from Eqn. 12.17:

$$1/n = 1/n_m + 1/n_m K \times 1/(p/p^0) \quad (12.18)$$

A plot of $1/n$ against $1/(p/p^0)$ should result in a straight-line relationship (see Fig. 12.2). The monolayer capacity can be calculated from the intercept $1/n_m$ and the equilibrium constant is found from tangent $\beta = 1/n_m$.

It should be emphasized that the conditions underlying the derivation of the Langmuir equation are seldom fulfilled in practice. The adsorption sites are *not* energetically equivalent, neither in a physical, nor in a chemical adsorption. In the physisorption of nitrogen on rutile, for instance, the isosteric heat of adsorption declines from 26 kJ mol^{-1} at zero coverage to only 60% of this value at full coverage [1]. Furthermore, considerable mutual interaction exists between molecules in adsorbed monolayers, especially at coverages above 0.5. Finally, physical adsorption is not localized; the physisorbed molecules have a high mobility. Nevertheless a description of adsorption equilibrium according to the Langmuir

equation is sometimes successful. The reason for this is most often that the measurements are performed under conditions at which the variation of coverage is very low.

A frequently used adsorption model that allows for adsorption in multilayers has been introduced by Brunauer, Emmett and Teller [10] and is known as the BET equation. With the exception of the assumption that the adsorption process terminates at monolayer coverage, these authors have retained all the other assumptions made in deriving the Langmuir adsorption isotherm. Hence all objections to the application of the Langmuir equation apply here, too.

A new supposition is added, viz. that the adsorption forces are short-range forces; in the first adsorbed layer the heat of adsorption is assumed to be higher than in all other adsorbed layers, where the heat of adsorption is set equal to the latent heat of condensation of the adsorbed gas. As explained in Section 12.2, this supposition is certainly incorrect.

For the derivation of the BET equation we refer to ref. 10. The equation reads:

$$\frac{p}{v(p^\circ - p)} = \frac{1}{v_m c} + \frac{c-1}{v_m c} \cdot \frac{p}{p^\circ} \quad (12.19)$$

where v is the volume of gas (STP) adsorbed and v_m is the volume of gas (STP) adsorbed in the monolayer. The quantity c is equal to $\exp(Q - L)/RT$, in which Q is the heat of adsorption in the first adsorbed layer and L is the latent heat of condensation of the gas, equal to the heat of adsorption in all following layers. The relative pressure of the gas is p/p° .

Notwithstanding its theoretical shortcomings the BET equation is the most generally used method for the determination of specific surface areas. It is applicable in cases where we are dealing with type II or type IV isotherms (see Section 12.3), but the range of partial pressures where theory and practice are in reasonable agreement is very limited (from 0.05 up to 0.3, say). This is nicely illustrated by work carried out by Harris and Sing [11], who compared experimental isotherms with the isotherm following from the BET theory (see Fig. 12.3). Figure 12.3 clearly demonstrates that the BET equation fails to reproduce the experimental data, except in the range of partial pressures from 0.05 to about 0.3, often called 'the BET region'. When applied in this restricted region, the isotherm being type II or IV, the BET method leads to a correct value of the surface area of solids within, say, 5% [1].

In zeolites, cracking catalysts and in activated carbons we deal in many cases with a combination of microporosity, mesoporosity and macroporosity. Here the isotherms are 'type I + type IV'. Strictly speaking, BET analysis is not allowed here; nevertheless it is frequently applied.

In the practical application of the BET method the volume of adsorbed gas is measured at constant temperature as a function of the partial pressure and a plot is made of $p/v(p^\circ - p)$ against p/p° (see Fig. 12.4).

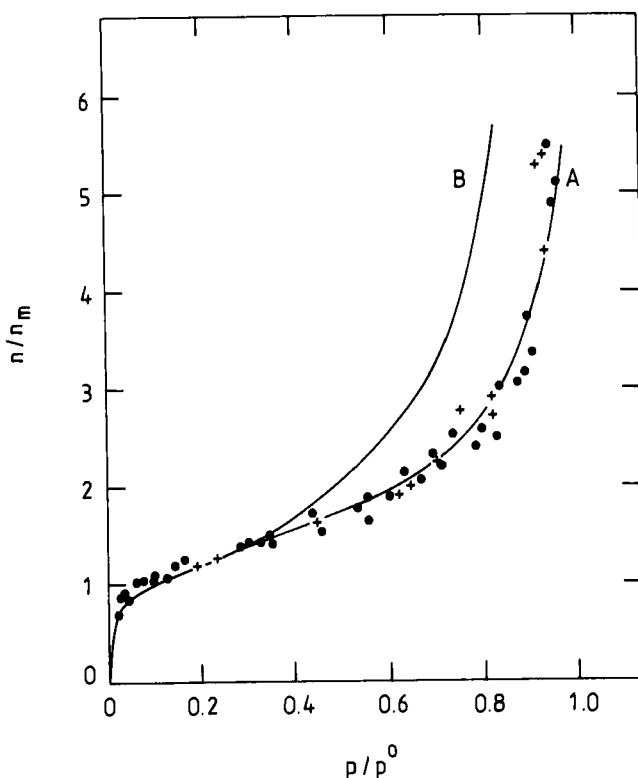


Fig. 12.3. The adsorption of nitrogen on nonporous samples of silica and alumina, the surface areas ranging from $2.6\text{--}11.5\text{ m}^2\text{ g}^{-1}$ for silica and from $58\text{--}153\text{ m}^2\text{ g}^{-1}$ for alumina. n/n_m is plotted against p/p^0 . n is the number of moles adsorbed per gram of adsorbent and n_m is the monolayer capacity, expressed in the same units. Line A: ● = silica; + = alumina. Line B: the BET isotherm (Eqn. 12.19) with c values of 100–200.

The intercept $1/v_m c$ and the tangent of α , $(c - 1)/v_m c$, readily permit the calculation of v_m and c ; n_m is found from v_m , the number of moles of adsorbate per gram of adsorbent in the monolayer. Finally, $A(\text{BET})$, the BET surface area, is calculated from Eqn. 12.11.

12.8 THE CONCEPT OF A STANDARD ISOTHERM; THE t METHOD

The t method for the determination of surface areas has been developed by de Boer and his pupils [12]. They showed that the nitrogen adsorption isotherm for a large number of nonporous solids can be represented by approximately one single curve when the ratio v_a/A is plotted as a function of the relative pressure. This so-called common t curve, a type II isotherm, is reproduced in Fig. 12.5. On the right-hand side Y axis the volume (STP) of adsorbed nitrogen per unit surface

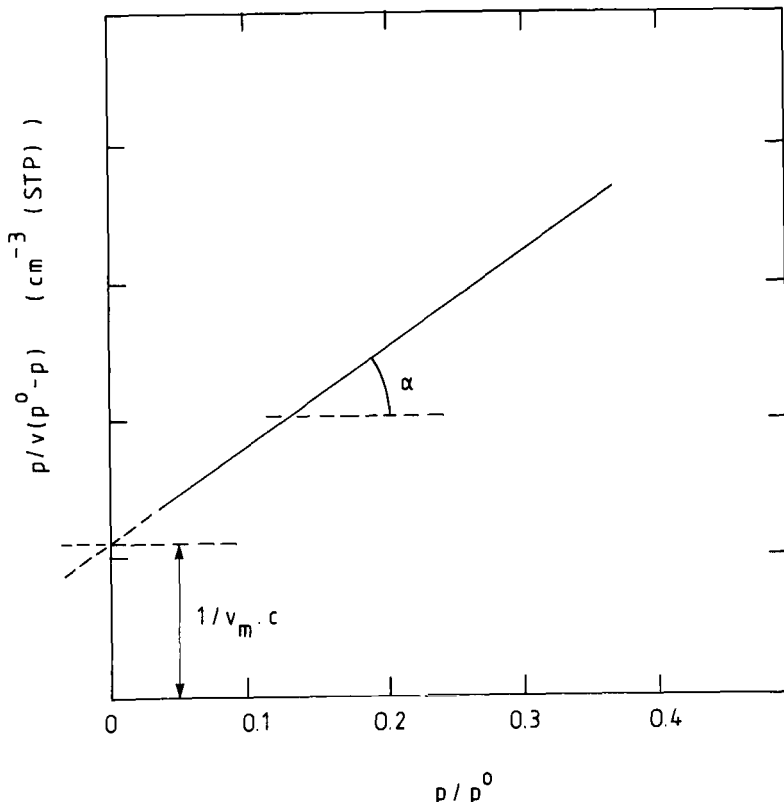


Fig. 12.4. The BET plot.

areas is indicated at 78 K. The surface areas of the nonporous solids were determined by applying the BET method. In our view it is more appropriate to make the t method independent of the BET method by calculating the surface areas of the nonporous solids from particle size distributions determined by the application of calibrated electron microscopy. Such a method is especially applicable when using smooth spherical particles of silica or titania (Aerosil-type materials).

The common t curve is valid for a relatively large number of materials. These so-called t materials are mainly oxides, like SiO_2 , Al_2O_3 , ZrO_2 , MgO and TiO_2 ; but BaSO_4 and many activated carbons also belong to this group.

For the partial pressures indicated on the ordinate we have chosen the symbol p'/p^0 in order to indicate that we are dealing here with equilibrium pressures above approximately flat surfaces. This will be seen to be important in the discussion of capillary condensation in Section 12.12.

The left-hand side abscissa gives the statistical thickness of the adsorbed multilayer, t , in nm. The t values on the abscissa are calculated as follows.

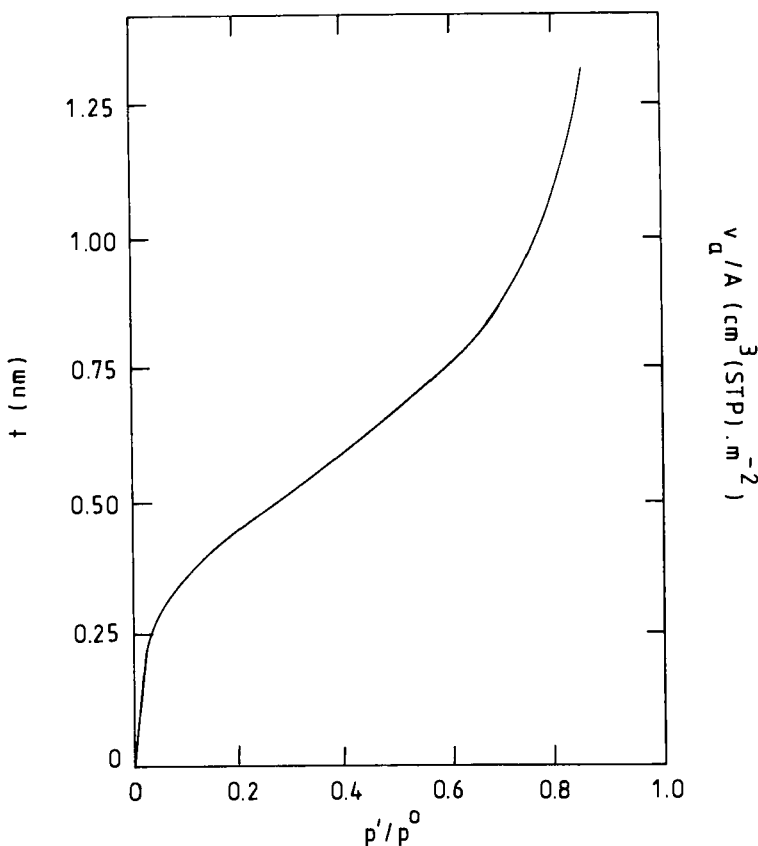


Fig. 12.5. The common t curve. Nitrogen adsorption isotherm at 78 K on nonporous solids.

The number of nitrogen molecules adsorbed in a monolayer on 1 m^2 corresponds to $0.23 \text{ cm}^3 \text{ N}_2(\text{STP})$. Hence for a t material with surface area $A(t)$ we have:

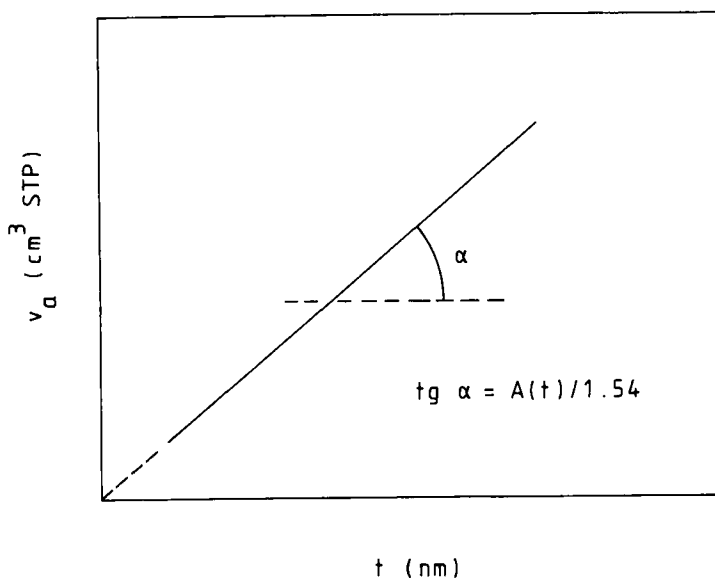
$$v_m = 0.23 \times A(t) \text{ cm}^3 \text{ N}_2(\text{STP}) \quad (12.20)$$

When $v_a \text{ cm}^3 \text{ N}_2$ is adsorbed, the statistical number of adsorbed nitrogen layers is equal to v_a/v_m . As the thickness of one layer of adsorbed nitrogen is 0.354 nm , the statistical layer thickness corresponding to v_a/v_m layers is given by:

$$t = v_a/v_m \times 0.354 \text{ nm} = \frac{v_a \times 0.345}{A(t) \times 0.23}$$

and hence:

$$A(t) = 1.54 \times v_a/t \text{ m}^2 \quad (12.21)$$

Fig. 12.6. General form of the t plot.

It follows from Eqn. 12.21 that, for every nonporous t material, a plot of v_a against t should result in a straight line running through the origin. Such a plot is called the t plot and the tangent of the straight line is a measure of $A(t)$, see Fig. 12.6.

In determining the surface area $A(t)$ of a solid, one proceeds as follows. The nitrogen adsorption isotherm at 78 K is measured. Next, this isotherm is converted into a t plot by substituting each p/p^o value for the corresponding t value. These t values are given by the common t curve. It is, however, also possible to calculate the t values from the equation:

$$t(\text{nm}) = 0.1 \left(\frac{13.99}{-\log(p/p^o) + 0.034} \right)^{1/2} \quad (12.22)$$

In the range of partial pressures from 0.1 to 0.8, Eqn. 12.22 gives a good description of the course of the common t curve.

In practice, t plots often deviate strongly from the course sketched in Fig. 12.6. However, interesting conclusions can be drawn from the derivation (see Fig. 12.7). Curve a in Fig. 12.7 is characterized by linearity and by the fact that, on extrapolation, the line runs through the origin. In this case we may conclude that we are dealing with a t material and $A(t)$ can be calculated from the tangent. For curve b in Fig. 12.7 the conclusions are the same. However, a strong upward deviation from linearity is found at a certain pressure p/p^o , corresponding to a statistical thickness t_1 ; much more nitrogen is taken up than might be expected.

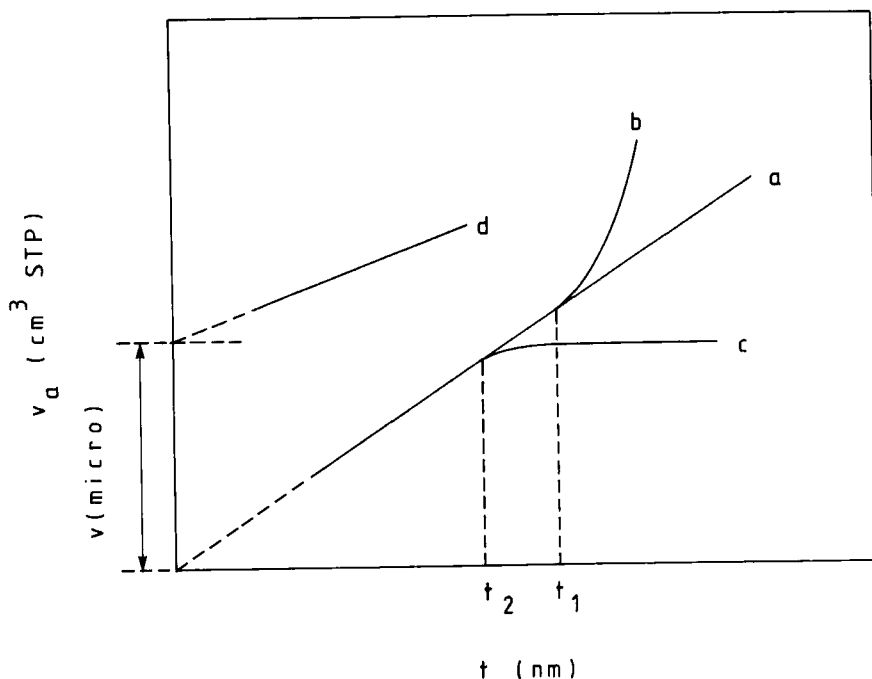


Fig. 12.7. Four different courses of the t plot.

In such a case we may conclude that, starting from t_1 , capillary condensation takes place, besides adsorption. If some narrow pores are filled up by multilayer adsorption, further adsorption does not occur on the entire surface because a part of the surface has become unavailable. The points on the t plot then begin to deviate downwards from the straight line (see point t_2 in Fig. 12.7). This situation is, for instance, encountered when slit-shaped pores are present.

The occurrence of a t plot as indicated by line d in Fig. 12.7 provides extra information. A straight line is found, and the surface area ($A(t)$) can be calculated from the tangent of the line. The positive intercept $v(\text{micro})$ is caused by a relatively large nitrogen uptake at a very low t value, which (see the common t curve, Fig. 12.6) corresponds to a very low partial nitrogen pressure. Such high nitrogen uptake at very low pressure is due to the strong adsorption of nitrogen in micropores; the micropore volume $v(\text{micro})$ can be calculated from the intercept. $A(t)$ is the total surface area minus the surface area of the micropores.

12.9 MICROPOROSITY

In microporous solids all pores, or part of them, have diameters smaller than 2 nm. Well known examples are the pores of zeolites and in activated carbons. Type I isotherms are found (see Fig. 12.1) which are characterized by a large

uptake of the adsorbate at a very low pressure, up to a p/p° value of about 0.05. A sharp knee in the isotherm is found at $p/p^\circ = 0.05\text{--}0.15$, with a horizontal plateau up to about $p/p^\circ = 0.95$. The uptake close to saturation, when converted to a liquid volume, may be taken as being actually equal to the micropore volume.

Methods for determining pore volume distributions in the micropore region have been published by Mikhail and coworkers [13], Medek [14] and by Horvath and Kawazoe [15].

Many microporous substances also contain meso and macropores. In such cases, isotherms are found which are a hybrid of isotherms type I and IV. As mentioned before (see Section 12.7), BET analysis is not allowed here.

12.10 PORE RADII AND PORE VOLUME DISTRIBUTIONS

Pore radii and pore volume distributions as a function of the pore radii may be calculated from the relative pressures at which the pores are filled or emptied. For the case of pore filling with liquid nitrogen, the relation between the pore radius, r , and the relative pressure at which filling starts, p_a/p° , is given by the Kelvin equation for pores with circular cross section:

$$p_a/p^\circ = \exp -\gamma V_L/RT(r-t) \quad (12.23)$$

With γ , the surface tension of liquid nitrogen at 77.4 K, equal to $8.72 \times 10^{-7} \text{ J cm}^{-1}$ and V_L , the molar volume of liquid nitrogen at 77.4 K, equal to $34.68 \text{ cm}^3 \text{ mol}^{-1}$, R , the gas constant equal to $8.314 \text{ kJ mol}^{-1} \text{ K}^{-1}$, and $T = 77.4 \text{ K}$ we calculate, starting from Eqn. 12.23:

$$(r-t) = 0.4078/\log(p^\circ/p_a) \quad [(r-t) \text{ in nm}] \quad (12.24)$$

At each p_a/p° value, t can be calculated from Eqn. 12.22. Hence from Eqn. 12.24 the radius of a pore can be calculated from the relative pressure p_a/p° at which capillary condensation starts.

A simple derivation of the Kelvin equation is presented by Broekhoff and van Dongen [16]. Imagine a gas B in physical adsorption equilibrium above a flat, a convex, and a concave surface, respectively (see Fig. 12.8). Considering a transfer of dN moles of vapour to the adsorbed phase at constant pressure and temperature, equilibrium requires that there will be no change in the free enthalpy of the system.

The change of the free enthalpy of the system is given by:

$$dG_{P,T} = \mu_a dN - \mu_g dN + \gamma dA \quad (12.25)$$

where μ_a is the thermodynamic potential of the adsorbed phase, μ_g the thermodynamic potential of the gas phase, γ the adsorbate/vapour surface tension and

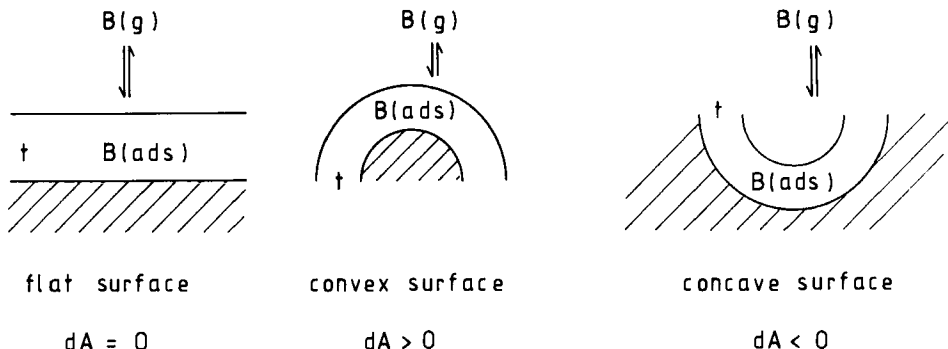


Fig. 12.8. The change of the surface A as a result of the adsorption of dN moles of gas B on a flat, a convex, and a concave surface, respectively.

dA the change in the adsorbate/vapour interface associated with the transfer of dN moles of vapour to the adsorbed phase.

At equilibrium:

$$dG_{P,T} = \mu dN - \mu_g dN + \gamma dA = 0 \quad (12.26)$$

Equation 12.26 is in fact the Kelvin equation in its primitive form. The thermodynamic potential of the gas as a function of pressure is:

$$\mu_g = \mu^{\circ}_g + RT \ln(p/p^{\circ}) \quad (12.27)$$

where μ°_g is the thermodynamic potential at standard pressure. Next, the supposition is introduced that the thermodynamic potential of the adsorbed multilayer of gas B is equal to the thermodynamic potential of the liquified gas B. At equilibrium we then have:

$$\mu_a = \mu_L = \mu^{\circ}_g \quad (12.28)$$

The ratio dA/dN is a geometric quantity, determined by the curvature of the adsorbate/vapour interface. When dealing with a concave hemispherical meniscus of the capillary condensed liquid in a cylindrical tube, it can easily be calculated that

$$dA/dN = -2 V_L/(r-t) \quad (12.29)$$

where V_L is the molar volume of the liquid.

Combining Eqns. 12.26, 12.27, 12.28 and 12.29 we obtain:

$$p/p^{\circ} = \exp -2 \gamma V_L/RT(r-t) \quad (12.30)$$

Equation 12.30 is the Kelvin equation describing capillary condensation on a concave hemispherical surface or hemispherical meniscus. Hence Eqn. 12.30

gives the relative pressure at which the emptying of a cylindrical pore with radius r , filled with capillary condensed liquid, will commence. In this case this relative pressure is indicated by p_d/p^0 :

$$p_d/p^0 = \exp (-2\gamma V_L/RT(r-t)) \quad (12.31)$$

The Kelvin expression for capillary condensation on the inner wall of a cylindrical pore is found by substitution of

$$dA/dN = -V_L/(r-t) \quad (12.32)$$

We then arrive at:

$$p_a/p^0 = \exp (-\gamma V_L/RT(r-t)) \quad (12.33)$$

which is the relative pressure at which filling of the pore commences.

Kelvin equations describing capillary evaporation from slit-shaped pores or the filling and emptying of 'ink bottle' pores can be calculated quite easily by using the appropriate expressions for dA/dN (see ref. 16).

12.11 HYSTERESIS LOOPS

Imagine a material containing cylindrical pores, all of radius r . In this idealized case the isotherm attains the following shape (Fig. 12.9). The occurrence of the hysteresis loop in Fig. 12.9 may be explained as follows. On increasing the relative pressure, capillary condensation starts from the walls of the pores in the direction

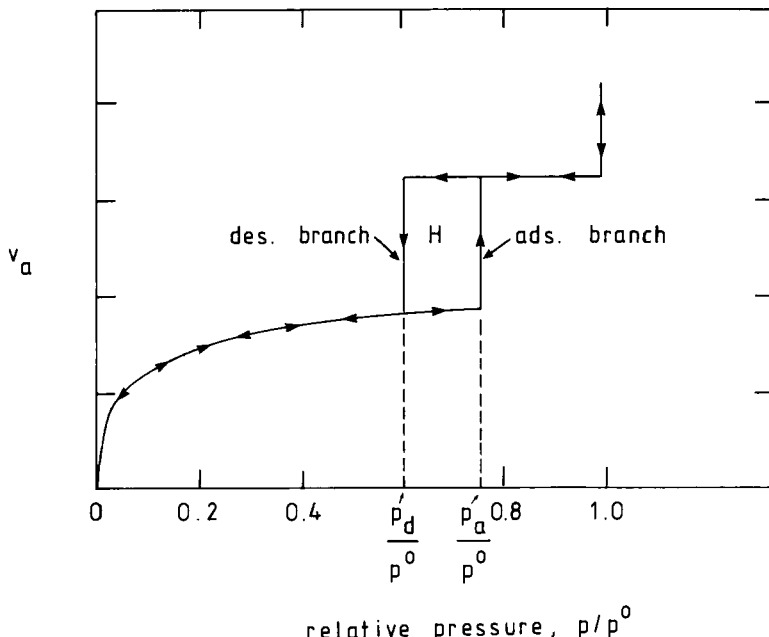


Fig. 12.9. Adsorption and desorption isotherms for a porous material, containing cylindrical pores with radius r . H is the hysteresis loop.

of the central axis of the pores. The appropriate Kelvin equation is Eqn. 12.33. Equation 12.31 is valid for emptying the pores. Combining these two equations we find:

$$(p_a/p^\circ) = p_d/p^\circ \quad (12.34)$$

Hence when capillary condensation starts, for instance, at $p_a/p^\circ = 0.8$ (the 'adsorption branch'), emptying of the pores will start at $p/p^\circ = 0.64$ (the 'desorption branch').

In practice, several types of hysteresis loops are found; their shapes are indicatives of the types of pores we are dealing with. For a full explanation we refer to refs. 1 and 16, which also describe the calculation of complete pore volume distributions.

12.12 THE CORRECTED KELVIN EQUATION

Around 1967, Broekhoff and de Boer [16], following Derjaguin [17], pointed out that the supposition introduced in the derivation of the Kelvin equation, viz. the equality of the thermodynamic potential of the adsorbed multilayer to the thermodynamic potential of the liquefied gas (see Eqn. 12.28), cannot be correct. This can be seen immediately from an inspection of the common t curve (Fig. 12.5); at each t value lower than, say, 2 nm, the relative equilibrium pressure is lower than 1, the equilibrium pressure of the liquefied gas.

The correct value of the thermodynamic potential of the adsorbed multilayer is a function if t and is given by the common t curve itself:

$$\mu_a(t) = \mu_g^\circ + RT \ln p'/p^\circ(t) = \mu_g^\circ - F(t) \quad (12.35)$$

Introduction of Eqn. 12.35 into the derivation of the Kelvin equation, along the same lines of reasoning as following in Section 12.10, gives the 'corrected Kelvin equation':

$$RT \ln(p/p^\circ) + F(t) = -\gamma V_L/(r-t) \quad (12.36)$$

This equation can be used to explain that stable adsorption on the inner wall of a capillary tube is possible up to a certain critical thickness. Capillary condensation starts from this critical thickness. The important aspect is explained further in ref. 16.

An excellent material for checking the validity of the corrected Kelvin equation is chrysotile, $Mg_3(OH)_4Si_2O_5$, which consists of hollow needles, the pore volume distribution of which can be measured both by means of calibrated electron microscopy and nitrogen capillary condensation [18]. It appears that capillary

condensation in the cylindrical pores with radii in the range 2–7 nm is quantitatively well described by the corrected Kelvin equation. If we apply the classical Kelvin equation this is not the case, and in the range of radii discussed here corrections of the order of +20% would be necessary.

12.13 CONCLUSIONS

Although the BET method for the determination of surface areas is theoretically not well founded, its application in a very restricted range of partial pressures leads to reasonably good quantitative results. This follows from the comparison of BET surface areas with surface areas following from calibrated electron microscopy (see ref. 1).

The Broekhoff-de Boer *t* method for the determination of surface areas is not based on a new theory. It is an empirical method in which the adsorption isotherm of a material of unknown surface area is compared with a standard isotherm, the 'common *t* curve', valid for '*t* materials' with a surface area of 1 m².

Pore radii and pore volume distributions can be calculated on the basis of the classical Kelvin equation which can be adapted to various pore shapes. For '*t* materials' the corrected Kelvin equation according to Broekhoff and de Boer leads to better quantitative results. The Broekhoff-de Boer theory also explains why stable adsorption on the inner walls of pores is possible up to a certain critical thickness of the adsorbed layer, without giving rise to immediate capillary condensation of the gas.

REFERENCES

- 1 S.J. Gregg and K.S.W. Sing, in *Adsorption, Surface Area and Porosity* (2nd ed.), Academic Press, London, 1982, p. 6.
- 2 S. Brunauer, L.S. Deming, W.S. Deming and E. Teller, *J. Am. Chem. Soc.*, 62 (1940) 1723.
- 3 C.A. Amberg, W.B. Spencer and R.A. Beebe, *Can. J. Chem.*, 33 (1955) 305.
- 4 M.M. Dubinin, *Zhur. Phys. Chem.*, 34 (1960) 959; *Chem Rev.*, 60 (1960) 235.
- 5 IUPAC *Manual of Symbols and Terminology*, Appendix 2, Part 1, Colloid and Surface Chemistry. *Pure Appl. Chem.*, 31 (1972) 578.
- 6 A.A. Liabastre and C.J. Orr, *Colloid Interface Sci.*, 64 (1978) 1.
- 7 A. Watson, J.O. May and B. Butterworth, *Trans. Br. Ceram. Soc.*, 46 (1957) 37.
- 8 P.H. Emmett and S. Brunauer, *J. Am. Chem. Soc.*, 59 (1937) 1553.
- 9 I. Langmuir, *J. Am. Chem. Soc.*, 38 (1916) 2221.
- 10 S. Brunauer, P.H. Emmett and E. Teller, *J. Am. Chem. Soc.*, 60 (1938) 309.
- 11 M.R. Harris and K.S.W. Sing, *Chem. Ind.*, (1959) 487.
- 12 B.C. Lippens, B.G. Linsen and J.H. de Boer, *J. Catal.*, 3 (1964) 32.
- 13 R.Sh. Mikhail, S. Brunauer and E.E. Bodor, *J. Colloid Interface Sci.*, 26 (1968) 45.
- 14 J. Medek, *Fuel*, 56 (1977) 131.

- 15 G. Horvath and K. Kawazoe, *J. Chem. Eng. Jpn.*, 6 (1983) 470.
- 16 J.C.P. Broekhoff and R.H. van Dongen, in *Physical and Chemical Aspects of Adsorbents and Catalysts*, Ch. 1, Academic Press, London, 1970, pp. 1-63.
- 17 B.V. Derjaguin, in *Proceedings of the Second International Congress on Surface Activity*, Part II, Butterworths, London, 1957, p. 154.
- 18 J.J.F. Scholten, A.M. Beers and A.M. Kiel, *J. Catal.*, 36 (1975) 23.
L.A. de Wit and J.J.F. Scholten, *J. Catal.* 36 (1975) 30.
L.A. de Wit and J.J.F. Scholten, *J. Catal.* 36 (1975) 36.

Chapter 13

Future trends

The large scale continuous processes that lie at the core of the modern chemical and petrochemical industries have their roots in scientific innovations that started nearly one hundred years ago. As Chapter 1 has described, the prime driving force for process innovation was the availability of new feedstocks and the need for new conversion processes and products. This force will remain an important one in industry. Today, for example, improved catalytic processes will be necessary to exploit natural gas resources or to produce hydrogen as an energy carrier.

While half of the large scale chemical processes currently in use are based on homogeneous catalysts, the early processes were mainly based on heterogeneous catalysts. The study of heterogeneous catalysis has led to the generation of new scientific subdisciplines, most of which are directed towards the improvement or adaptation of existing processes. This knowledge was mainly developed in industrial laboratories committed to the improvement of catalytic processes, an activity which has produced significant economic benefits. Catalysis has become established as a research discipline whose aim is an understanding of catalysis as a phenomenon.

For a long time practical catalysis remained an empirical art rather than a scientific discipline, mainly because the complexity of the catalytic systems obscured the molecular insights needed for their control in a predictive manner. The modern spectroscopic techniques available to the analytical laboratory enable detailed catalyst analysis and *in-situ* studies. Advanced inorganic and organometallic chemistry and catalyst synthesis (e.g. zeolite synthesis) are also significant. This has changed catalytic practice and has resulted in a considerable reduction of catalyst development times. Nonetheless, in catalysis, accidental discovery and high risk exploratory research are still important factors in innovation.

13.1 ENVIRONMENTAL DEMANDS

There is a long list of desirable reactions that are thermodynamically possible, but for which no direct catalytic reactions exist as yet. Examples are the direct oxidation of methane to methanol, or benzene to phenol. Environmental requirements, in particular, are giving a new direction to catalytic applications. The concentration of environmentally damaging compounds — sometimes present in minute quantities in the emission of engines, electricity plants or chemical plants — has to be further reduced. Examples are NO_x and SO_2 as well as chlorinated hydrocarbons. The removal of lead from gasoline, which was required to enable the use of automotive exhaust catalysts, led to the placing of completely new demands on refinery catalysts. There is a need for new chemicals as substitutes for such environmentally damaging products as phosgene, dimethylsulphide, hydrogen fluoride and especially compounds containing chlorine or bromine. Catalysts for the production of organic chemicals are required that replace classical organic syntheses and reduce acid consumption and the resulting salt waste products. Such processes will result in improved atom utilization.

New, preferentially stereoselective, catalytic reagents will produce enantioselectively pure products, the specific chemical activity of which reduces adverse effects when applied in agriculture or medicine. Biocatalysis will continue to play an important role here.

13.2 AUTONOMOUS DEVELOPMENTS: CHEMISTRY

At present we are beginning to understand the reaction mechanisms of many heterogeneous catalytic reactions at the molecular level. A major breakthrough came with the design of catalytic model systems, such as single crystal surfaces, enabling exhaustive structural characterization and model catalytic experiments. The surface science approach forms the basis of current developments of surface chemical reaction rate theory.

A recent trend in organometallic chemistry is the exploration of metallic clusters of increasing size, approaching the size of clusters used in heterogeneous catalysis. The two fields, with their very different historical background, have reached a stage where an appreciation of the correspondence and difference between molecular events on heterogeneous catalysts and organometallic complexes will soon become possible, leading to the exploitation of a common molecular understanding.

There is a significant difference in the ways homogeneous and heterogeneous catalysts are tuned towards higher activity or improved selectivity. The organometallic complexes used in homogeneous catalysis are optimized by choice of ligand or metal components. The main function of the ligand systems is often the

control of the geometric arrangement of the reactive complexed intermediates, thus determining the selectivity of the reaction. The predictive power of this approach is already impressive. The knowledge and means to steer the catalytic reaction will undoubtedly continue to grow.

In heterogeneous catalysis both morphology and catalyst composition can be varied. Usually small particles of a catalytically active material are dispersed on the surface of a supporting material having a high surface area. The particle size and morphology of catalyst pellets are important parameters in reactions that are diffusion limited. Zeolitic materials are unique, because they can be manufactured with micropores of molecular size, thus enabling stereoselective catalysis. Essentially, the preparation of heterogeneous catalysts is very much related to the materials science aspects of the solid–liquid interphase. Synthetic inorganic chemistry and organometallic chemistry are changing catalyst preparation by giving us the possibility to prepare active catalyst precursors under molecular control.

The continuing expansion in the possibilities afforded by computational modelling has enhanced its potential impact on catalyst improvement and design. The application of statistical mechanical techniques will enhance the predictive power of computational techniques when calculating thermodynamic or kinetic constants. An important step is the integration of molecular kinetic information with macroscopic, practical reaction conditions. The success of theoretical approaches based on transition state theories has been recently demonstrated by a prediction of the rate of the heterogeneously catalyzed ammonia synthesis reaction based on computed elementary reaction rate constants. This provides the essential bridge between molecular catalysis and process engineering.

Polymers and polymer based materials have become indispensable to our modern society. Many catalytic processes have been developed to produce the necessary intermediates. Improvements will result in significant benefits. New catalytic systems have recently been developed — initially as homogeneous catalysts but subsequently also in an immobilized form — which have led to a variety of new polymers. The choice of ligand in homogeneous catalytic systems enables high regio-, stereo- and enantiomeric control, leading to the production of new types of polymers with old monomers. Furthermore, catalysts have been found that catalyze the polymerization of otherwise unreactive monomers, such as cyclopentenes. New types of polymers with interesting properties can be produced based on ethylene and CO. The structures that can be ‘designed’ and made have increased dramatically recently, e.g. block copolymers, graft polymers, organic polymers incorporating organometallic complexes and inorganic materials, polymers with special optical properties, materials with desired molecular weight distributions, etc. With this extensive and exciting toolbox available it will be necessary to be able to predict polymer properties even more accurately because of the tremendous number of possibilities available from a catalysis point of view.

The use of antibody catalysis is attracting attention, especially because antibody catalysis is as yet the only approach available which uses an '*ab initio*' method for the development of new catalysts; for example, the antibody mimics the shape of a transition state of the substrates, thus enhancing catalytic reaction rates. Economic application may lie far in the future, however. There is no such approach available in classical metal (complex) catalysis, however, and we have to rely on the development of known catalytic reactions and the development of accidentally discovered leads.

13.3 AUTONOMOUS DEVELOPMENTS: CATALYTIC REACTION ENGINEERING

In the development of new catalytic processes it is essential to integrate catalyst preparation, catalytic testing and catalytic reactor design. Developments in catalytic reaction engineering often involve the combination of several functions in one reactor concept. Catalytically active membranes are being investigated for application at higher temperatures based on ceramic microporous materials as well as zeolites. As mentioned earlier, multifunctional catalysts, combining catalytic components of different functionality, have become very important. An example is the hydrocracking catalyst combining a hydrogenative and an acidic component. The shape and strength of catalyst particles is crucial to catalytic process applications and is an essential component of practical catalyst manufacture. In fascinating novel applications the difference between particle and reactor vanishes, e.g. in exhaust gas cleaning using monolithic converters.

In homogeneous catalysis ligand systems may define the medium for the reaction. Water-soluble ligands have been developed, but in other instances two phases have to be used. Ultrafiltration may become a useful technique for catalyst removal if one uses encapsulated homogeneous catalysts or larger oligomeric catalysts. New catalytic systems involve the use of easily functionalizable dendrimers. In all these systems a combination of catalysis and separation can be envisaged that also enhances rates and selectivity.

In the polymer field simultaneous catalytic formation and shaping of the end product or intermediate product is gaining attention, e.g. approaches have been developed which allow polymerization in extruders.

Non-stationary operations have found large scale industrial application. An important classical example is catalytic cracking, where oil is exposed with a short residence time to a rapidly deactivating zeolitic catalyst, which is regenerated in a second step by removal of deposited coke. A novel non-stationary process is selective butane oxidation over a regenerable oxidation catalyst (see Chapter 2). Undoubtedly we will see more examples of this type of process, in which the proper catalytic step and the regeneration of the catalytic sites occur in different compartments under different conditions. A nice application involves

the conversion of very inert molecules such as methane. Dissociative adsorption usually requires high temperature and pressure, but associative reactions are most selective at a lower temperature. Rapid deactivation by non-selective site reactions may also occur in catalytic systems, requiring frequent regeneration. The beauty is that catalysis and regeneration can be performed under different conditions.

The use of regenerable inorganic reagent intermediates is also very elegantly exploited in the production of organic chemicals. The generation of undesired, environmentally damaging coproducts is prevented. Alternative approaches to overcome the difficult dissociative step have also been developed. At high temperature conductive oxides can be applied as electrodes for electrocatalytic oxidation. Plasma catalytic processes have been proposed to replace high temperature thermal activation with low temperature electrical discharge activation.

Catalytic reaction engineering forms a link between chemistry and chemical engineering and is the key to catalytic process improvement and innovation. Catalysis is a branch of the chemical sciences that strongly affects frontier research in physical chemistry, organometallic chemistry and reaction engineering. The rapid development of modern chemistry and physics promises an interesting and rewarding future.

Subject Index

- π -Acceptor ligands, 204
- Acetaldehyde, 13
- Acetic acid, 15
- Acetylene, 13
 - hydrogenation of, 181
- Acrolein, 142
 - hydrogenation of, 183
- Activated clay, 11
- Activation energy, 80
- Adatoms, 91
- Adsorption (*see also* Physical adsorption), 419
 - calorimetry, 167
 - dissociation energies, 127
 - dissociative, 125
 - group, 77
 - heat of, 80, 95, 126
 - heat of dissociative adsorption, 126
 - heat of formation, 127
 - heat of oxygen adsorption, 136
 - hydrocarbons, 137
 - hysteresis loop, 435
 - molecular, 125
 - multilayer, 425
 - of carbon monoxide, 167, 173
 - of hydrogen, 176
 - oxygenases, 139
 - pore sizes, 423
 - porosity, 423
 - rate determining, 77
 - theory of dissociation, 128
- Adsorption isotherms, 73, 422, 425
 - adsorption group, 77
 - BET equation, 425, 427
 - Brunauer classification, 422
 - Brunauer, Emmett and Teller model, 427
 - isosteric heat of adsorption, 426
 - Langmuir isotherm, 74, 84, 425
 - multilayer adsorption, 423, 425
 - standard isotherm, 428
 - t method, 428
- Aerosil, 313
- AES, 378
- 'Affinity', 3
- Agostic interaction, 117
- Alkyl migration, 169
- Alkylation, 23
- Alloying, 179
- Alumina, 309
- Ammonia
 - adsorption, 144
 - synthesis, 5, 337
- Antibody catalysis, 444
- Antibonding orbital fragments, 91
- Aquagels 313
- Aromatics, 181
 - hydrogenation of, 181
- Aromatization, 26
- Association, 108, 128
- Asymmetric hydrogenation, 237
- Atropisomeric ligands, 244
- Auger electron spectroscopy (AES), 378
 - SiO_2 -supported ZrO_2 , 378
- Automotive pollution control, 16, 39
 - catalyst, 41
 - combustion, 39
 - lean burning, 40
 - three-way catalyst, 41
- Avrami-Erofeev kinetics, 416
- π -Back donation, 210
- Ballandin, 183
- Banks, 15
- BASF route, 64
- Basic sites, 143
- Batch reactors
 - multiple reactions, 253
 - selectivity, 253
 - single reaction, 252
 - yield, 253
- Bayerite, 314, 315
- Benzene, hydrogenation of, 181
- Berthelot, 9
- Berzelius, 3

- BET equation, 425, 427
- Bidentate ligands, 210
- Bifunctional catalysts, 26, 169
- Bifunctional reactions, 155, 185
- BINAP, 243, 244
- Block copolymers, 237
- Block polymers, 237
- Blyholder model, 94
- Boehmite, 314
- σ -Bond metathesis, 122
- Bonding, 89
 - adatoms, 91
 - adsorption energy, 95
 - adsorption of ammonia, 95
 - adsorption of CH_2 , 97
 - adsorption of ethylene, 95
 - adsorption of hydrogen atoms, 95
 - adsorption of methyl fragments, 95
 - antibonding orbital fragments, 91
 - Blyholder model, 94
 - bonding orbital fragments, 91
 - Chatt–Dewar–Duncanson model, 94
 - chemisorption of C atom, 91, 94
 - chemisorption of CO, 91
 - chemisorptive bond, 90
 - CO adsorption, 135
 - conservation of bond order, 99
 - d valence electron occupation, 90
 - delocalization, 90, 97
 - electron back donation, 94
 - electron donation, 94
 - elementary reaction steps on surfaces, 123
 - Fermi energy, 94
 - in organometallic coordination complexes, 99
 - island formation, 135
 - molecular adsorption, 91
 - Pauli repulsion, 92
 - surface dangling bond, 103
 - surface group orbital, 94
 - surface reactions, 135
 - valence electron distribution, 89
 - work function, 90
- Bonding mechanisms
 - α -elimination, 116
 - β -elimination, 111
 - σ -bond metathesis, 122
 - association, 108, 128, 131
 - cyclometallation, 117
 - deinsertion, 111, 112
 - desorption, 108
 - dissociation, 108, 128
 - dissociative adsorption, 125
 - Eley–Rideal mechanism, 123
 - extrusion, 112
 - heterolytic cleavage, 123
 - homolytic cleavage, 114
 - insertion, 108, 109, 134
 - ionic bond model, 143
 - Langmuir–Hinshelwood mechanism, 123, 136
 - Mars and van Krevelen mechanism, 124, 141
 - migration, 108, 109
 - nucleophilic attack, 120, 121
 - orthometallation, 115
 - oxidative addition, 108, 113
 - reductive elimination, 108, 155
 - retro-cyclometallations, 119
- Bonding orbital fragments, 91
- Bosch, 7
- Brønsted acid, hydrocarbon activation, 152
- Brønsted acidity, 145
- Brønsted basicity, 145
- Brunauer classification, 422
- Brunauer, Emmett and Teller model, 427
- Bulky phosphite ligands, 209
- Butanal, 48
- Butane, 143
- Butanol, 14
- C₂ symmetry, 231, 241
- C₅ aldehyde, 64
- Cábosil, 313
- Calcination, 405
- Caprolactam, 61
- Carbocations, 27
- Carbonylation, 15
- Carbon–carbon bond formation, 132
- Catalyst characterization, 365
 - *see also* Electron microscopy

- *see also* Extended X-ray absorption fine structure (EXAFS)
- *see also* Infrared spectroscopy
- *see also* Mössbauer spectroscopy
- *see also* Temperature programmed reactions
- *see also* X-ray diffraction (XRD)
- Catalyst shaping, 322
- Catalyst supports, *see* Support preparation
- Catalytic cracking, 26
- Catalytic cycle, 70
- 'Catalytic force', 3
- Catalytic reaction engineering, 251, 444
 - batch reactors, 252
 - multiple reactions, 253
 - selectivity, 253
 - single reaction, 252
 - yield, 253
 - continuous flow stirred tank reactors (CSTR), 257
 - maximum yield (CSTR), 260
 - experimental determination of reaction kinetics, 288
 - Biot number, 292
 - Carberry number, 294, 296
 - continuous flow stirred tank reactor, 292
 - differential method, 290
 - external transfer, 294
 - fixed bed reactors, 295
 - heat transfer, 296
 - integral method, 290
 - internal diffusion, 297
 - *j* factors, 294
 - Nusselt number, 295
 - plug flow reactor, 289
 - slurry reactors, 294
 - transport disguises, 292
 - Weisz modulus, 297
 - multicomponent diffusion, 299
 - film factor, 301
 - Stefan–Maxwell equation, 300
 - transfer coefficient, 301
 - nonisothermal reactors, 260
 - plug flow reactors, 255
 - reaction combined with transport, 262
- Carberry number, 268
- Damköhler number, 266, 273, 282
- effective diffusivity, 270
- effectiveness factor, 271, 276
- external mass transfer, 263
- external heat transfer, 268
- film theory, 280
- Hatta number, 282, 284
- heat transport, 277
- heterogeneous, 262
- homogeneous catalysis, 279
- mass transfer coefficient, 264, 281
- maximum yield, 286
- multiple reactions, 285
- Prater number, 269, 278
- Sherwood number, 283
- Thiele modulus, 271, 276
- utilization factor, 280, 284
- Catalytic reforming, 12, 23, 24
- Chain growth, 162
- Chain-end control, 226, 235
 - isotactic polymers, 229
 - syndiotactic polymers, 228
- Characterization of heterogeneous catalysts, 419
- Chatt–Dewar–Duncanson model, 94, 102
- Chemical affinity, 77
- Chemisorption
 - of C atom, 91, 94
 - of CO, 91
- Chemisorptive bond, 90
- Chiral pharmaceuticals, 237
- Cinnamic acid, 237
- Citral, 64
- Clean Air Act, 17
- Clement and Desormes, 3
- Cluster reactivity, 134
- CO adsorption, 135
- CO shift reactions, 337
- [Co(CO)₄]₂, 100
- Coal gasification, 7
- Cobalt, 49
- Coke
 - burning, 29
 - deposition, 28, 402
 - ovens, 9

- Combustion, 39
- Computational modelling, 443
- Conservation of bond order, 99
- Continuous flow stirred tank reactors (CSTR), 257
 - maximum yield, 260
- Coordination dependence of CO, 91
- Coordinative unsaturation, 110
- Cordierite, 41
- Cossee–Arlman mechanism, 38, 224
- Cracking, 9, 12, 23, 26, 29, 33, 47, 152, 154
- Crystal-face specificity, 179
- C_s symmetry, 231, 242
- Cyclic intermediates, 139
- Cyclohexane
 - dehydrogenation of, 181
- Cyclohexanone, 62
- Cyclometallation, 117
- Cylindrical internal reflectance, 220
- C–O stretching frequencies, 221

- Davy, 4
- De Boer–Hamaker forces, 420
- Deacon process, 4
- Dehydrogenation of cyclohexane, 181
- Deinsertion, 111, 112
- Delocalization, 90, 97
- Deposition–precipitation, 352
- Desorption, 83, 108
 - rate determining, 77, 83
- Deuteroformylation, 215
- Diastereotopic face discrimination, 245
- Diatomique molecules, 125
- Dienes, hydrogenation of, 181
- DIOP, 241
- DIPAMP, 241
- Disproportionation catalysts, 346
- Dissociation, 108, 128
 - energies, 127
 - of CO, 161, 163, 168
 - reactions, 76
- Dissociative adsorption of carbon monoxide, 129
- σ -Donor ligands, 204
- Double stereoselection, 235
- Driving force, 77

- Dual bed system, 17
- Dual site model, 76
- Dubinin, 423

- EDAX, 370
- EDX, 370
- Electron back donation, 94
- Electron deficiency of small metal particles, 170
- Electron donation, 94
- Electron microscopy, 368
 - electron microprobe analysis (EMA, EPMA), 370
 - energy dispersive analysis of X-rays (EDAX, EDX), 370
 - scanning electron microscopy (SEM), 369
 - scanning transmission electron microscopy (STEM), 370
 - transmission electron microscopy (TEM), 369
- Electronic effects, 207, 210
- Electronic promoters, 337
- Electrophilic attack, 192
- Electrophilic oxidation, 140
- Elementary reaction steps on surfaces, 123
- Elementary steps, 70, 71
 - in organometallic complexes, 106
- Eley–Rideal models, 76, 123
- α -Elimination, 116
- β -Elimination, 111
- EMA, 370
- Enantioface differentiation, 244
- Enantiomeric site control, 226
- Enantioselectivity, 240
- Ensemble, 161, 168, 179
 - of atoms, 134
 - size, 125
 - size effects, 179, 181
- Entrained flow reactor, 26
- Entropy of activation, 80
- Environmental aspects, 30, 32, 442
- EPMA, 370
- Epoxidation of ethene, 188
 - chlorine effect, 188
 - promotion by alkali reactions, 188

- Ethane, 143
- Ethene, oxidation of, 188
- Ethene oxide, 41, 43
- Ethylbenzene, 142
- Ethylene, 142
- Ethylene epoxide, 142, 188
- Ethylene glycol, 41
- Ethyldyne, 139
- Ewen, 230
- EXAFS, 388
- Experimental determination of reaction kinetics, 288
 - Biot number, 292
 - Carberry number, 294, 296
 - continuous flow stirred tank reactor, 292
 - differential method, 290
 - external transfer, 294
 - fixed bed reactors, 295
 - heat transfer, 296
 - integral method, 290
 - internal diffusion, 297
 - *j* factors, 294
 - Nusselt number, 295
 - slurry reactors, 294
 - transport disguises, 292
 - Weisz modulus, 297
- Extended X-ray absorption fine structure (EXAFS), 390
 - amplitude function, 390
 - back-scattering amplitude, 390
 - function $\chi(k)$, 390
 - phase shift, 390
 - radial distribution function, 390
 - sulphided Co–Mo, 392
 - sulphided Mo, 392
- Extrusion, 112, 328
- Faraday, 4
- Fermi energy, 94
- Fischer–Tropsch synthesis, 9, 160
 - carbon–carbon bond formation, 132
 - chain growth, 162
 - ensembles, 168
 - kinetics, 162
 - ligand effect, 167
- mechanism, 160
- promoters, 166, 168
- supports, 168
- using alloys, 166
- Fixed bed reactors, 31
- Fluid catalytic cracking, 12, 23, 26
- Fluidized beds, 323
- Freundlich isotherm, 75
- Friedel–Crafts acylation, 65
- Future trends, 441
 - antibody catalysis, 444
 - catalytic reaction engineering, 444
 - computational modelling, 443
 - environmental demands, 442
 - homogeneous catalysis, 444
 - non-stationary operations, 444
 - organometallic chemistry, 442
 - polymers, 443
- Gibbsite, 315
- Granulation, 324
- Haber, 5
- Haldor Topsoe process, 53
- HCo(CO)₄, 100
- Heat of adsorption, 75
- Heck and Breslow, 211
- Henry's law, 74
- Heteroatoms, hydrogenation of, 182
- Heterogeneous catalysts, characterization of, 419
- Heterolytic cleavage, 123
- High-loading supported catalysts, 337
- Higher olefins, 45
 - catalyst, 48
 - hydroformylation, 47
 - metathesis, 47
 - oligomerization, 47, 48
 - Shell process, 45
 - thermal cracking, 47
- Highest occupied molecular orbital (HOMO), 95
- History
 - acetaldehyde, 13
 - acetic acid, 15
 - acetylene chemistry, 13

- activated clay, 11
- 'affinity', 3
- ammonia synthesis, 5
- Banks, 15
- Berthelot, 9
- Berzelius, 3
- Bosch, 7
- butanol, 14
- carbonylation, 15
- 'catalytic force', 3
- catalytic reforming, 12
- Clean Air Act, 17
- Clement and Desormes, 3
- coal gasification, 7
- coke ovens, 9
- cracking, 9
- Davy, 4
- Deacon process, 4
- dual bed system, 17
- Faraday, 4
- Fischer and Tropsch, 9, 160
- fluid catalytic cracking, 12
- Haber, 5
- Hogan, 15
- Houdry, 11
- hydrogenation of coal, 9
- hydrorefining, 13
- kerosine, 11
- lead chamber process, 4
- low density polyethene, 15
- metathesis, 16
- motor vehicle emission control, 16
- Natta, 16
- Nernst, 5
- nitrogen fixation, 7
- Orlov, 160
- Ostwald, 4
- oxo process, 14
- paraffin alkylation, 12
- Phillips catalyst, 16
- polymerization, 15
- Reppe, 13, 15
- 'Rheniforming', 12
- Roelen, 14, 201
- Sabatier, 160, 176
- safety lamp, 4
- Shell higher olefin process (SHOP), 16
- Smidt, 13
- sulphuric acid, 3, 4
- Thenard, 3
- vanadium oxide, 5
- Wacker process, 14
- water-gas shift reaction, 7
- Wilkinson, 14
- Ziegler, 16
- HMn(CO)₅, 101**
- Hoffmann-La-Roche process, 65**
- Hogan, 15**
- Homogeneous catalysis, 199, 444**
- Homolytic cleavage, 114**
- Houdry, 11**
- Hydride transfer, 27**
 - reaction, 153
- Hydro-dehydrogenation, 176**
- Hydrocarbons**
 - activation, 152
 - adsorption, 137
 - isomerization, 139
 - synthesis, 171
- Hydrocracking, 33**
- Hydrodenitrogenation, 350**
- Hydrodesulphurization, 350**
- Hydroformylation, 47, 48, 65, 201**
 - π -acceptor ligands, 204
 - σ -donor ligands, 204
 - catalyst, 50
 - isomerization, 213
 - kinetic studies, 211, 215
 - ligand effects, 203, 206
 - oxo process, 48
 - phosphine ligands, 204
 - phosphites
 - electronic effects in, 207
 - steric effects in, 208
 - product linearity, 216
 - reaction, 107
 - rhodium-based, 202
 - Shell process, 202
 - Union Carbide process, 202, 216
 - with cobalt, 49
 - with rhodium, 49, 202
 - with two-phase system, 50

- Hydrogen peroxide, oxidation of, 188
 β -Hydrogen transfer, 154
Hydrogenation
 - of acetylenic compounds, 180
 - of acrolein, 183
 - of aromatics, 181
 - of benzene, 181
 - of coal, 9
 - crystal-face specificity, 179
 - of dienes, 181
 - of heteroatoms, 182
 - of olefins, 176
 - Zelinsky irreversible catalysis, 182

Hydrogenolysis, 214
 - of saturated hydrocarbons, 184

Hydroisomerization, 33
Hydronium, 151
Hydrorefining, 13
Hydrosilicate formation, 357
Hydrotreating catalysts, 348
Hydrotreatment, 23, 30, 32, 401
Hysomer process, 33
Hysteresis loops, 435

Ibuprofen, 242
ICI process, 54
Infrared spectroscopy, 383
 - CO adsorbed on Ir/SiO₂, 385
 - Co-Mo, 385
 - harmonic approximation, 384
 - hydroxyl groups, 387
 - image, 385
 - isotopic substitution, 384
 - mechanical coupling, 384
 - Mo, 385
 - MoS₂, 385
 - NO, 385
 - OH stretching, 387
 - overtones, 384
 - rhenium oxide, 387
 - rigid rotors, 384
 - rotational transitions, 384
 - sulphided Co/Al₂O₃, 385
 - sulphided Mo/Al₂O₃, 385
 - TiO₂, 387

Infrared studies, 220

Initial rate expressions, 77
Insertion, 108, 109
1,2-Insertions, 223, 229
2,1-Insertions, 223, 228
Ionic bond model, 143
Iron oxide
 - haematite, 366
 - magnetite, 366
 - reduction, 366

Island formation, 135
Isoalkane formation, 153
Isomerization, 26, 33, 153, 213
 - hydrocarbons, 139
 - hydrocracking, 33
 - hydroisomerization, 33
 - Hysomer process, 33
 - ISOSIV process, 33
 - octane number, 33
 - paraffins, 33
 - TIP process, 33

Isomorphous substitution, 146
ISOSIV process, 33
Isotactic index, 228
Isotactic polymers, 223
 - chain-end control, 229
 - site control, 231

Isotactic polypropylene, 36
Isotherms, *see* Adsorption isotherms
ISS, 381

Kaminsky, 230
Keime, 46
Kelvin equation, 433
 - corrected Kelvin equation, 436

Kerosine, 11
Kinetic factor, 77
Kinetics, 69
 - desorption rate determining, 83
 - hydroformylation, 211
 - rate determining step, 72
 - Sabatier principle, 83
 - steady state, 71, 76
 - temperature dependency, 78
 - volcano plot, 83, 136

Kissinger method, 412
Knowles, 238

- L-DOPA, 237
- Langmuir isotherm, 74, 75, 84, 425
- Langmuir–Hinshelwood models, 76, 123, 136, 137, 162
- Langmuir–Hinshelwood–Hugen–Watson models, 77, 162
- Lead chamber process, 4
- Lean burning, 40
- Lefort, 43
- LEIS, 381
- Lennard–Jones potential, 420
- Lewis acid sites, 143
- Ligand effects, 179, 203, 206
- Low density polyethene, 15
- Low energy ion scattering (LEIS), $\text{La}_2\text{O}_3/\text{Al}_2\text{O}_3$, 381, 382
- Lowest unoccupied molecular orbital (LUMO), 95
- Lurgi process, 53
- Maleic anhydride, 55
 - catalysts, 56
 - Mars–van Krevelen mechanism, 56
- Mars and van Krevelen mechanism, 56, 124, 141
- Mechanisms (*see* Bonding mechanisms)
- Menthol, 246
- Metathesis, 16, 47
 - Phillips triolefin process, 16
 - Shell higher olefin process (SHOP), 16
- Methanation, 164
- Methanol synthesis, 51, 132, 174, 337
 - catalysts, 54
 - Haldor Topsoe process, 53
 - ICI process, 54
 - Lurgi process, 53
- Methyl *t*-butyl ether, 44, 58
 - catalyst, 60
- MgO , 144, 145
- Michaelis–Menten kinetics, 77, 107
- Microporosity, 432
- Microstructure, 229
- Migration, 108, 109
- Models (*see also* Bonding mechanisms), 89
- Molecular adsorption, 91
- Molecular graphics, 242
- Molecular mechanics, 236, 242
- Molecular weight, 224
- Molybdenum sulphide, 406
- Monolith, washcoat, 41
- Monolithic honeycombs, 17
- Mordenite, 33, 36, 321
- MoS_2 , 102, 103
- Mössbauer spectroscopy, 391
 - electric quadrupole splitting, 394
 - Fe/TiO_2 , 395, 396
 - Hägg carbide, 396
 - isomer shift (IS), 394
 - magnetic hyperfine splitting, 395
 - Mössbauer absorption spectroscopy, 396
 - Mössbauer emission spectroscopy, 396
 - Zeeman effect, 395
- Motor vehicle emission control, 16, 39
- MTBE, *see* methyl *t*-butyl ether
- Multicomponent diffusion, 299
 - film factor, 301
 - transfer coefficient, 301
- Multilayer adsorption, 423
- Multiply-bound species, 138
- Naphtha, 24
- Naphtha reforming, 183
- Naproxen, 242
- Natta, 16, 226
- Nernst, 5
- $\text{Ni}(\text{PH}_3)_2$, 104
- NiO , 102
- Nitrobenzene, 142
- Nitrogen fixation, 7
- Nitrosobenzene, 142
- NMR analysis, 217, 222
 - isotactic polymers, 226
 - pentads, 226
 - triads, 226
- Non-stationary operations, 444
- Nonisothermal reactors, 260
- Noyori, 243, 244
- Nucleophilic attack, 120, 121
- Nucleophilic oxidation, 140
- Octane booster, 58

- Octane number, 24, 25, 33, 58
- Oil refinery
 - alkylation, 23
 - aromatization, 26
 - bifunctional catalyst, 26
 - catalytic cracking, 26
 - catalytic reforming, 23, 24
 - coke burning, 29
 - coke deposition, 28
 - entrained flow reactor, 26
 - environmental aspects, 30, 32
 - fluid catalytic cracking, 23, 26
 - hydrotreatment, 23, 30
 - isomerization, 26
 - octane number, 25
 - sulphur poisoning, 31
 - total isomerization process, 33
 - trickle bed reactors, 31
- Oil-drop method, 329
- Oligomerization, 46–48
- Organic peroxides, oxidation of, 188
- Organometallic coordination complexes, 99
 - Chatt–Dewar– Duncanson model, 102
 - coordination of the substrate, 108
 - $[\text{Co}(\text{CO})_4]_2$, 100
 - elementary steps, 105
 - $\text{HCo}(\text{CO})_4$, 100
 - $\text{HMn}(\text{CO})_5$, 101
 - $\text{Ni}(\text{CO})_4$, 99
 - $\text{Ni}(\text{PH}_3)_2$, 104
 - vacant site, 106
- Orlov, 160
- Ostwald, 4
- Otto engines, 40
- Oxidation, 186
 - catalysis, 187
 - of ethene, 188
 - of hydrogen peroxide, 188
 - of organic peroxides, 188
- Oxidative addition, 108, 113
- Oxo process, 14, 48, 201
- Oxygen transfer, 140
 - acroleine, 142
 - butane, 143
 - early transition metal oxides, 140
 - electrophilic oxidation, 140
 - ethane, 143
 - ethylbenzene, 142
 - ethylene, 142
 - ethylene epoxide, 142
 - late transition metals, 140
 - nitrobenzene, 142
 - nitrosobenzene, 142
 - nucleophilic oxidation, 140
 - propene, 142
 - rare earth oxides, 140
- Oxygenates, 172
- Oxygenative dehydrogenation, 176
- Paraffin alkylation, 12
- Paraffins, 33
- Particle size effects, 134
- Pauli repulsion, 92
- Pauling valency, 144
- Pelletization, 327
- Phillips catalyst, 16
- Phosphine ligands, 204
 - cone angle, 205
 - electronic parameter, 205
 - steric parameter, 205
- Phosphites
 - electronic effects in hydroformylation, 207
 - steric effects in hydroformylation, 208
- Physical adsorption, 420
 - de Boer–Hamaker forces, 420
 - Lennard–Jones potential, 420
 - van der Waals–London forces, 420
- Pichler and Schulz, 160
- Plug flow reactors, 255
- Poisoning, 176
- Polanyi relation, 129
- Polymerization, 15
 - catalyst, 38
 - chromium, 15
 - Cossee–Arlman mechanism, 38
 - Phillips catalyst, 16
 - propene, 16
 - titanium, 222
 - with titanium chloride, 37
 - Ziegler–Natta, 16, 38
 - zirconium, 222

- Polymers, 443
- Polypropylene
 - isotactic, 36
 - syndiotactic, 36
- Pore radii, 433
- Pore sizes, 419, 423
 - Dubinin classification, 423
 - macropores, 423
 - mesopores, 423
 - micropores, 423
- Pore volume distributions, 433
- Porosity, 423
- Preparation, 335
 - adsorption, 338
 - alumina-supported Pt, 343
 - ammonia synthesis, 337
 - carbon-supported Pt, 345
 - CO shift reactions, 337
 - co-impregnation, 350
 - coprecipitation, 335, 337
 - deposition–precipitation, 352
 - dry impregnation, 343
 - drying, 351
 - egg-shell distribution, 351
 - extrudates, 338, 344
 - hydrodenitrogenation, 350
 - hydrodesulphurization, 350
 - hydrosilicate formation, 357
 - hydrotreating catalysts, 348
 - impregnation, 335, 335, 338, 342
 - incipient wetness, 342
 - ion-exchange, 338
 - metathesis of olefins, 346
 - methanol synthesis, 337
 - MoO₃/Al₂O₃, 346
 - nucleation, 353
 - precipitation, 335, 335
 - precursors, 335
 - preshaped carrier bodies, 343, 359
 - Pt on silica, 343
 - Re₂O₇/Al₂O₃, 346
 - ReO₄, 348
 - selective removal, 335, 337
 - steam reforming catalysts, 337
 - supported noble-metal catalysts, 343
 - wet impregnation, 342
 - zeolites, 343
- Preshaped carrier bodies, 359
- Pressure swing adsorption, 34
- Product linearity, 216
- Promoters
 - in hydrocarbon synthesis, 171
 - selectivity, 171
- Propene, 142
- Propene epoxide, 193
- Propylene oxide, 43
- Pycnometry, 424
- Pyrogenic silica, 313
- Quasi-equilibrium, 72
- Rate expression
 - activation energy, 80
 - adsorption enthalpy, 80
 - adsorption rate determining, 77
 - catalytic cycle, 70
 - chemical affinity, 77
 - desorption rate determining, 77
 - dissociation reactions, 76
 - driving force, 77
 - dual site model, 76
 - elementary steps, 70, 71
 - Eley–Rideal models, 76
 - entropy of activation, 80
 - Freundlich isotherm, 75
 - initial rate expressions, 77
 - kinetic factor, 77
 - Langmuir isotherm, 75, 82
 - Langmuir–Hinshelwood models, 76
 - Langmuir–Hinshelwood–Huguen–Watson models, 77
 - Michaelis–Menten kinetics, 77
 - quasi-equilibrium, 72
 - rate determining step, 72
 - Sabatier principle, 83
 - single site model, 70
 - site balance, 71
 - steady-state conditions, 71
 - surface reaction rate determining, 77
 - Temkin isotherm, 75
 - transition state theory, 78
 - volcano plot, 83

- RBS, 383
- Reaction combined with transport, 262
 - Carberry number, 268
 - Damköhler number, 266, 273, 282
 - effective diffusivity, 270
 - effectiveness factor, 271, 276
 - external heat transfer, 268
 - external mass transfer, 263
 - film theory, 280
 - Hatta number, 282, 284
 - heat transport, 277
 - heterogeneous, 262
 - homogeneous catalysis, 279
 - mass transfer coefficient, 264, 281
 - maximum yield, 286
 - multiple reactions, 285
 - Prater number, 269, 278
 - Sherwood number, 283
 - Thiele modulus, 271, 276
 - utilization factor, 280, 284
- Reaction mechanisms (*see* Bonding mechanisms)
- Reactors
 - fixed bed, 31
 - riser, 29, 57
 - trickle bed, 31
 - tubular, 42, 55
- Reduction, 401
 - *see also* Temperature programmed reduction
- Reduction kinetic models, 411
- Reductive elimination, 108, 115
- Regioselectivity of polymers, 224
- Reppe, 13, 15
- Retro-cyclometallations, 119
- 'Rheniforming', 12
- RhH(PPh₃)₂(CO)₂, 219, 221
- Rhodium, 49
 - Rhodium hydroformylation, 49, 202
- Rideal mechanism, 177
- Riser reactor, 29, 57
- Roelen, 14, 201
- Rutherford back scattering (RBS), 383
- Sabatier principle, 83, 137, 160
- Safety lamp, 4
- Saturated hydrocarbon reactions, 184
- Schulz and Flory distribution, 162
- Schulz–Flory–Anderson distribution, 162
- Secondary ion mass spectrometry, 379
 - dynamic mode, 380
 - secondary ions, 380
 - silica-supported zirconium oxide, 380
- Secondary neutral mass spectrometry (SNMS), 380
- Selectivity, 171
- Self-poisoning, 161, 176
- SEM, 369
- Shell higher olefin process (SHOP), 16, 45
- Shell hydroformylation process, 202
- Shell middle distillate synthesis, 162
- ²⁹Si-NMR, 310
- Silver catalysts, 190, 192
- SIMS, 379, 380
- Single site model, 70
- Site balance, 71
- Site control, 225, 235
 - enantiomorphic, 226
 - isotactic polymers, 231
- Smidt, 13
- SMPO process, 43
- SNMS, 380
- Sol-gel method, 329
- Solid acids, 143
 - β-hydrogen transfer, 154
 - ammonia adsorption, 144
 - basic sites, 143
 - bifunctional hydroisomerization, 154
 - Brønsted acidity, 145
 - Brønsted acid–Lewis base catalysis, 151
 - Brønsted basicity, 145
 - carbonium ions, interaction with carbenium ion, 152
 - cracking, 152
 - faujasite, 147
 - formation of ethoxy species, 149
 - hydride transfer reaction, 153
 - hydrocarbon activation, 152
 - interaction with carbenium ions, 149
 - ionic bond model, 143
 - isoalkane formation, 153

- isomerization, 153
- Lewis acid sites, 143
- mechanism of protonation, 149
- MgO, 144, 145
- mordenite, 147
- Pauling valency, 144
- SiO₂, 145
- smectite clay, 146
- zeolites, 146
- Spheripol, 38
- Spinels
 - γ -Al₂O₃, 315
 - η -Al₂O₃, 315
- Spray drying, 323
- Static SIMS, 380
- Steam reforming catalysts, 337
- STEM, 370
- Stepped single crystal surface, 124
- Stereoblocks, 228, 230
- Stereocontrol, 225
- Stereogenic centres, 240
- Stereoselectivity of polymers, 224
- Steric effects, 208, 210
- Structural promoters, 337
- Styrene, 43
- Sulphides, hydrotreating, 32
- Sulphiding, 401
 - *see also* Temperature programmed sulphiding
- Sulphonated polystyrene resins, 60
- Sulphur poisoning, 31
- Sulphuric acid, 3, 4
- Support preparation, 309
 - Aerosil, 313
 - α -alumina, 309
 - γ -alumina, 304, 314
 - δ -alumina, 315
 - η -alumina, 314
 - θ -alumina, 315
 - κ -alumina, 315
 - χ -alumina, 315
 - aquagel, 313
 - bayerite, 315
 - boehmite, 314
 - Cabosil, 313
 - catalyst shaping, 322
 - extrusion, 328
 - fluidized beds, 323
 - gibbsite, 315
 - granulation, 324
 - mullite, 309
 - oil-drop method, 329
 - particle size distribution, 323
 - pelletization, 327
 - precipitated silicas, 310
 - pyrogenic silica, 313
 - silica gel, 309, 310
 - sodium silicates, 310
 - sol-gel method, 329
 - spray drying, 323
 - xerogel, 313
 - zeolites, 318
- Supported noble-metal catalysts, 343
- Supported titanium catalysts, 223
- Surface areas, 419, 424
 - monolayer capacity, 424
- Surface chemistry, 339
 - active carbon, 342
 - γ -Al₂O₃, 339
 - disproportionation catalysts, 346
 - hydroxyl groups, 340
 - oxides, 339
 - point of zero charge, 341
 - SiO₂, 339
 - surface charging model, 343
 - surface OH configurations, 340
 - TiO₂, 339, 340
- Surface dangling bond, 103
- Surface group orbital, 94
- Surface kinetics
 - Langmuir–Hinshelwood mechanism, 137
 - Polanyi relation, 129
 - reaction path, 129
 - volcano plot, 136
- Surface spectroscopy, 372
 - *see also* Auger electron spectroscopy (AES)
 - *see also* Ion scattering spectroscopy (ISS)
 - *see also* Low energy ion scattering (LEIS)

- *see also* Rutherford back scattering (RBS)
- *see also* Secondary ion mass spectrometry (SIMS)
- *see also* Ultraviolet photoelectron spectroscopy (UPS)
- *see also* X-ray photoelectron spectroscopy (XPS)
- Syndiotactic polymers
 - chain-end control, 228
- Syndiotactic polypropylene, 36
- Syndiotactic polystyrene, 222
- Synthesis gas reactions, 159
 - Fischer-Tropsch synthesis, 160
 - synthesis of higher oxygenates, 172
 - synthesis of methanol, 174
- Synthesis of higher oxygenates, 172
- Takasago process, 246
- TEM, 369
- Temkin isotherm, 75
- Temperature dependency, 78
- Temperature programmed reactions, 401
 - iron, 370
 - iron-rhodium, 370
 - rhodium, 370
 - temperature programmed desorption (TPD), 370
 - temperature programmed oxidation (TPO), 370
 - temperature programmed reaction spectroscopy (TPRS), 370
 - temperature programmed reduction (TPR), 370, 401
 - activation energy, 411
 - coke deposits, 402
 - CoO/Al₂O₃, 405
 - experimental conditions, 412
 - fat hardening, 401
 - Fe₂O₃, 413
 - Kissinger method, 412
 - modelling, 409
 - reduction kinetic models, 411
 - sulphides, 403
 - temperature programmed sulphidation (TPS), 370, 401
- hydrotreatment, 401
- MoO₃/Al₂O₃, 406
- Texture, 419
- Thenard, 3
- Thermal cracking, 47
- Through-the-metal interactions, 170
- TIP process, 33
- Titanium tetrachloride, 37
- Titanium-silicalite, 63
- Tolman parameters, 204
- Total isomerization process, 33
- TPR, 401
- TPS, 401
- Transition metal compounds
 - MoS₂, 102, 103
 - NiO, 102
 - surface dangling bond, 103
- Transition metal surfaces, 89
 - adatoms, 91
 - adsorption energy, 95
 - adsorption modes, 125, 137
 - adsorption of ammonia, 95
 - adsorption of CH₂, 97
 - adsorption of ethylene, 95
 - adsorption of hydrogen atoms, 95
 - adsorption of methyl fragments, 95
 - antibonding orbital fragments, 91
 - Blyholder model, 94
 - bonding orbital fragments, 91
 - Chatt-Dewar-Duncanson model, 94
 - chemisorption of C atom, 91, 94
 - chemisorption of CO, 91
 - chemisorptive bond, 90
 - CO adsorption, 134
 - conservation of bond order, 99
 - cyclic intermediates, 139
 - d valence electron occupation, 90
 - delocalization, 90, 97
 - diatomic molecules, 125
 - electron back donation, 94
 - electron donation, 94
 - elementary reaction steps on surfaces, 123
 - ensemble size, 125
 - ethylidyne, 139
 - Fermi energy, 94

- island formation, 135
- methoxy group, 139
- molecular adsorption, 91
- multiply-bound species, 138
- Pauli repulsion, 92
- reactivity of hydrocarbons, 137
- stepped single crystal surface, 124
- surface group orbital, 94
- surface reactions, 135
- valence electron distribution, 89
- work function, 90
- Transition state complex, 79
- Transition state theory, 78
- Trickle bed reactors, 31
- Trickle phase, 31
- Triphenyl-phosphine, 49
- Tubular reactors, 42, 55
- Two-phase system, 50
- Ultraviolet photoelectron spectroscopy, 378
- Union Carbide process, 216, 202
- α,β -Unsaturated acrolein, 183
- UPS, 378
- Valence electron distribution, 89, 90
- Van der Waals–London forces, 420
- Vanadium oxide, 5, 56
- Vanadium phosphorus oxide, 56
- Virtual pressure, 163
- Vitamin A intermediates, 63
 - BASF route, 64
 - C₅ aldehyde, 64
 - citral, 64
 - Friedel–Crafts acylation, 65
 - Hoffmann–La Roche process, 65
- Volcano plot, 83, 136
- Wacker process, 14
- Washcoat, 41
- Water–gas shift reaction, 7
- Wilke, 46
- Wilkinson, 14, 48, 202
- Wilkinson catalyst, 240
- Work function, 90
- X-ray diffraction (XRD), 365
 - Bragg relation, 366
 - Scherrer formula, 366
- X-ray line broadening, 366
- X-ray fluorescence, 365
- X-ray photoelectron spectroscopy (XPS), 372
 - binding energies, 375
 - charge potential model, 375
 - chemical shifts, 373
 - differential charging, 377
 - Kuipers' model, 377
 - monochromatic XPS, 378
 - RhCl₃, 373
 - rhodium, 373
 - ZrO₂/SiO₂, 376
- Xerogels, 313
- Zelinsky irreversible catalysis, 182
- Zeolite A, 319
- Zeolite synthesis, 318
 - crystallization, 319
 - induction period, 319
 - mordenite, 321
 - nucleation, 319
 - Zeolite A, 319
 - Zeolite Y, 320
 - ZSM-5, 322
- Zeolite Y, 320
- Zeolites (*see also* Solid acids), 89, 146, 162, 343
 - Al/Si ratio, 148
 - Brønsted acidity, 148
 - carbonium ions, interaction with carbenium ion, 152
 - cracking, 29, 152, 154
 - dimethylether from methanol, 51
 - ethylene from methanol, 51
 - formation of ethoxy species, 149
 - interaction with carbenium ions, 149
 - isomerization, 33
 - mordenite, 36
 - protonation, 149
 - of ammonia, 150
 - of ethylene, 150
 - of water, 151
 - shape-selective effect, 154
 - solution effects, 150
- Ziegler, 16
- Ziegler–Natta, 38, 222
- ZSM-5, 58, 322

STUDIES IN SURFACE SCIENCE AND CATALYSIS

Advisory Editors:

B. Delmon, Université Catholique de Louvain, Louvain-la-Neuve, Belgium
J.T. Yates, University of Pittsburgh, Pittsburgh, PA, U.S.A.

- Volume 1 **Preparation of Catalysts I.** Scientific Bases for the Preparation of Heterogeneous Catalysts. Proceedings of the First International Symposium, Brussels, October 14–17, 1975
edited by **B. Delmon, P.A. Jacobs and G. Poncelet**
- Volume 2 **The Control of the Reactivity of Solids.** A Critical Survey of the Factors that Influence the Reactivity of Solids, with Special Emphasis on the Control of the Chemical Processes in Relation to Practical Applications
by **V.V. Boldyrev, M. Bulens and B. Delmon**
- Volume 3 **Preparation of Catalysts II.** Scientific Bases for the Preparation of Heterogeneous Catalysts. Proceedings of the Second International Symposium, Louvain-la-Neuve, September 4–7, 1978
edited by **B. Delmon, P. Grange, P. Jacobs and G. Poncelet**
- Volume 4 **Growth and Properties of Metal Clusters.** Applications to Catalysis and the Photographic Process. Proceedings of the 32nd International Meeting of the Société de Chimie Physique, Villeurbanne, September 24–28, 1979
edited by **J. Bourdon**
- Volume 5 **Catalysis by Zeolites.** Proceedings of an International Symposium, Ecully (Lyon), September 9–11, 1980
edited by **B. Imelik, C. Naccache, Y. Ben Taarit, J.C. Vedrine, G. Coudurier and H. Praliaud**
- Volume 6 **Catalyst Deactivation.** Proceedings of an International Symposium, Antwerp, October 13–15, 1980
edited by **B. Delmon and G.F. Froment**
- Volume 7 **New Horizons in Catalysis.** Proceedings of the 7th International Congress on Catalysis, Tokyo, June 30–July 4, 1980. Parts A and B
edited by **T. Seiyama and K. Tanabe**
- Volume 8 **Catalysis by Supported Complexes**
by **Yu.I. Yermakov, B.N. Kuznetsov and V.A. Zakharov**
- Volume 9 **Physics of Solid Surfaces.** Proceedings of a Symposium, Bechyňe, September 29–October 3, 1980
edited by **M. Láznička**
- Volume 10 **Adsorption at the Gas–Solid and Liquid–Solid Interface.** Proceedings of an International Symposium, Aix-en-Provence, September 21–23, 1981
edited by **J. Rouquerol and K.S.W. Sing**
- Volume 11 **Metal-Support and Metal-Additive Effects in Catalysis.** Proceedings of an International Symposium, Ecully (Lyon), September 14–16, 1982
edited by **B. Imelik, C. Naccache, G. Coudurier, H. Praliaud, P. Meriaudeau, P. Gallezot, G.A. Martin and J.C. Vedrine**
- Volume 12 **Metal Microstructures in Zeolites.** Preparation - Properties – Applications. Proceedings of a Workshop, Bremen, September 22–24, 1982
edited by **P.A. Jacobs, N.I. Jaeger, P. Jirů and G. Schulz-Ekloff**
- Volume 13 **Adsorption on Metal Surfaces.** An Integrated Approach
edited by **J. Bénard**
- Volume 14 **Vibrations at Surfaces.** Proceedings of the Third International Conference, Asilomar, CA, September 1–4, 1982
edited by **C.R. Brundle and H. Morawitz**

- Volume 15 **Heterogeneous Catalytic Reactions Involving Molecular Oxygen**
by **G.I. Golodets**
- Volume 16 **Preparation of Catalysts III. Scientific Bases for the Preparation of Heterogeneous Catalysts.** Proceedings of the Third International Symposium, Louvain-la-Neuve, September 6–9, 1982
edited by **G. Poncelet, P. Grange and P.A. Jacobs**
- Volume 17 **Spillover of Adsorbed Species.** Proceedings of an International Symposium, Lyon-Villeurbanne, September 12–16, 1983
edited by **G.M. Pajonk, S.J. Teichner and J.E. Germain**
- Volume 18 **Structure and Reactivity of Modified Zeolites.** Proceedings of an International Conference, Prague, July 9–13, 1984
edited by **P.A. Jacobs, N.I. Jaeger, P. Jiří, V.B. Kazansky and G. Schulz-Ekloff**
- Volume 19 **Catalysis on the Energy Scene.** Proceedings of the 9th Canadian Symposium on Catalysis, Quebec, P.Q., September 30–October 3, 1984
edited by **S. Kaliaguine and A. Mahay**
- Volume 20 **Catalysis by Acids and Bases.** Proceedings of an International Symposium, Villeurbanne (Lyon), September 25–27, 1984
edited by **B. Imelik, C. Naccache, G. Coudurier, Y. Ben Taarit and J.C. Vedrine**
- Volume 21 **Adsorption and Catalysis on Oxide Surfaces.** Proceedings of a Symposium, Uxbridge, June 28–29, 1984
edited by **M. Che and G.C. Bond**
- Volume 22 **Unsteady Processes in Catalytic Reactors**
by **Yu.Sh. Matros**
- Volume 23 **Physics of Solid Surfaces 1984**
edited by **J. Koukal**
- Volume 24 **Zeolites: Synthesis, Structure, Technology and Application.** Proceedings of an International Symposium, Portorož-Portorose, September 3–8, 1984
edited by **B. Držaj, S. Hočvar and S. Pejovnik**
- Volume 25 **Catalytic Polymerization of Olefins.** Proceedings of the International Symposium on Future Aspects of Olefin Polymerization, Tokyo, July 4–6, 1985
edited by **T. Keii and K. Soga**
- Volume 26 **Vibrations at Surfaces 1985.** Proceedings of the Fourth International Conference, Bowness-on-Windermere, September 15–19, 1985
edited by **D.A. King, N.V. Richardson and S. Holloway**
- Volume 27 **Catalytic Hydrogenation**
edited by **L. Červený**
- Volume 28 **New Developments in Zeolite Science and Technology.** Proceedings of the 7th International Zeolite Conference, Tokyo, August 17–22, 1986
edited by **Y. Murakami, A. Iijima and J.W. Ward**
- Volume 29 **Metal Clusters in Catalysis**
edited by **B.C. Gates, L. Guczi and H. Knözinger**
- Volume 30 **Catalysis and Automotive Pollution Control.** Proceedings of the First International Symposium, Brussels, September 8–11, 1986
edited by **A. Crucq and A. Frennet**
- Volume 31 **Preparation of Catalysts IV. Scientific Bases for the Preparation of Heterogeneous Catalysts.** Proceedings of the Fourth International Symposium, Louvain-la-Neuve, September 1–4, 1986
edited by **B. Delmon, P. Grange, P.A. Jacobs and G. Poncelet**
- Volume 32 **Thin Metal Films and Gas Chemisorption**
edited by **P. Wissmann**
- Volume 33 **Synthesis of High-silica Aluminosilicate Zeolites**
edited by **P.A. Jacobs and J.A. Martens**
- Volume 34 **Catalyst Deactivation 1987.** Proceedings of the 4th International Symposium, Antwerp, September 29–October 1, 1987
edited by **B. Delmon and G.F. Froment**

- Volume 35 **Keynotes in Energy-Related Catalysis**. edited by **S. Kaliaguine**
- Volume 36 **Methane Conversion**. Proceedings of a Symposium on the Production of Fuels and Chemicals from Natural Gas, Auckland, April 27–30, 1987
edited by **D.M. Bibby, C.D. Chang, R.F. Howe and S. Yurchak**
- Volume 37 **Innovation in Zeolite Materials Science**. Proceedings of an International Symposium, Nieuwpoort, September 13–17, 1987
edited by **P.J. Grobet, W.J. Mortier, E.F. Vansant and G. Schulz-Ekloff**
- Volume 38 **Catalysis 1987**. Proceedings of the 10th North American Meeting of the Catalysis Society, San Diego, CA, May 17–22, 1987
edited by **J.W. Ward**
- Volume 39 **Characterization of Porous Solids**. Proceedings of the IUPAC Symposium (COPS I), Bad Soden a. Ts., April 26–29, 1987
edited by **K.K. Unger, J. Rouquerol, K.S.W. Sing and H. Kral**
- Volume 40 **Physics of Solid Surfaces 1987**. Proceedings of the Fourth Symposium on Surface Physics, Bechyné Castle, September 7–11, 1987
edited by **J. Koukal**
- Volume 41 **Heterogeneous Catalysis and Fine Chemicals**. Proceedings of an International Symposium, Poitiers, March 15–17, 1988
edited by **M. Guisnet, J. Barrault, C. Bouchoule, D. Duprez, C. Montassier and G. Pérat**
- Volume 42 **Laboratory Studies of Heterogeneous Catalytic Processes**
by **E.G. Christoffel**, revised and edited by **Z. Paál**
- Volume 43 **Catalytic Processes under Unsteady-State Conditions**
by **Yu. Sh. Matros**
- Volume 44 **Successful Design of Catalysts**. Future Requirements and Development. Proceedings of the Worldwide Catalysis Seminars, July, 1988, on the Occasion of the 30th Anniversary of the Catalysis Society of Japan
edited by **T. Inui**
- Volume 45 **Transition Metal Oxides**. Surface Chemistry and Catalysis
by **H.H. Kung**
- Volume 46 **Zeolites as Catalysts, Sorbents and Detergent Builders**. Applications and Innovations. Proceedings of an International Symposium, Würzburg, September 4–8, 1988
edited by **H.G. Karge and J. Weitkamp**
- Volume 47 **Photochemistry on Solid Surfaces**
edited by **M. Anpo and T. Matsuura**
- Volume 48 **Structure and Reactivity of Surfaces**. Proceedings of a European Conference, Trieste, September 13–16, 1988
edited by **C. Morterra, A. Zecchina and G. Costa**
- Volume 49 **Zeolites: Facts, Figures, Future**. Proceedings of the 8th International Zeolite Conference, Amsterdam, July 10–14, 1989. Parts A and B
edited by **P.A. Jacobs and R.A. van Santen**
- Volume 50 **Hydrotreating Catalysts**. Preparation, Characterization and Performance. Proceedings of the Annual International AIChE Meeting, Washington, DC, November 27–December 2, 1988
edited by **M.L. Occelli and R.G. Anthony**
- Volume 51 **New Solid Acids and Bases**. Their Catalytic Properties
by **K. Tanabe, M. Misano, Y. Ono and H. Hattori**
- Volume 52 **Recent Advances in Zeolite Science**. Proceedings of the 1989 Meeting of the British Zeolite Association, Cambridge, April 17–19, 1989
edited by **J. Klinowsky and P.J. Barrie**
- Volume 53 **Catalyst in Petroleum Refining 1989**. Proceedings of the First International Conference on Catalysts in Petroleum Refining, Kuwait, March 5–8, 1989
edited by **D.L. Trimm, S. Akashah, M. Absi-Halabi and A. Bishara**

- Volume 54 **Future Opportunities in Catalytic and Separation Technology**
edited by M. Misano, Y. Moro-oka and S. Kimura
- Volume 55 **New Developments in Selective Oxidation.** Proceedings of an International Symposium, Rimini, Italy, September 18–22, 1989
edited by G. Centi and F. Trifiro
- Volume 56 **Olefin Polymerization Catalysts.** Proceedings of the International Symposium on Recent Developments in Olefin Polymerization Catalysts, Tokyo, October 23–25, 1989
edited by T. Keii and K. Soga
- Volume 57A **Spectroscopic Analysis of Heterogeneous Catalysts. Part A: Methods of Surface Analysis**
edited by J.L.G. Fierro
- Volume 57B **Spectroscopic Analysis of Heterogeneous Catalysts. Part B: Chemisorption of Probe Molecules**
edited by J.L.G. Fierro
- Volume 58 **Introduction to Zeolite Science and Practice**
edited by H. van Bekkum, E.M. Flanigen and J.C. Jansen
- Volume 59 **Heterogeneous Catalysis and Fine Chemicals II.** Proceedings of the 2nd International Symposium, Poitiers, October 2–6, 1990
edited by M. Guisnet, J. Barrault, C. Bouchoule, D. Duprez, G. Pérot, R. Maurel and C. Montassier
- Volume 60 **Chemistry of Microporous Crystals.** Proceedings of the International Symposium on Chemistry of Microporous Crystals, Tokyo, June 26–29, 1990
edited by T. Inui, S. Namba and T. Tatsumi
- Volume 61 **Natural Gas Conversion.** Proceedings of the Symposium on Natural Gas Conversion, Oslo, August 12–17, 1990
edited by A. Holmen, K.-J. Jens and S. Kolboe
- Volume 62 **Characterization of Porous Solids II.** Proceedings of the IUPAC Symposium (COPS II), Alicante, May 6–9, 1990
edited by F. Rodríguez-Reinoso, J. Rouquerol, K.S.W. Sing and K.K. Unger
- Volume 63 **Preparation of Catalysts V.** Proceedings of the Fifth International Symposium on the Scientific Bases for the Preparation of Heterogeneous Catalysts, Louvain-la-Neuve, September 3–6, 1990
edited by G. Poncelet, P.A. Jacobs, P. Grange and B. Delmon
- Volume 64 **New Trends in CO Activation**
edited by L. Guczi
- Volume 65 **Catalysis and Adsorption by Zeolites.** Proceedings of ZEOCAT 90, Leipzig, August 20–23, 1990
edited by G. Öhlmann, H. Pfeifer and R. Fricke
- Volume 66 **Dioxygen Activation and Homogeneous Catalytic Oxidation.** Proceedings of the Fourth International Symposium on Dioxygen Activation and Homogeneous Catalytic Oxidation, Balatonfüred, September 10–14, 1990
edited by L.I. Simándi
- Volume 67 **Structure-Activity and Selectivity Relationships in Heterogeneous Catalysis.** Proceedings of the ACS Symposium on Structure-Activity Relationships in Heterogeneous Catalysis, Boston, MA, April 22–27, 1990
edited by R.K. Grasselli and A.W. Sleight
- Volume 68 **Catalyst Deactivation 1991.** Proceedings of the Fifth International Symposium, Evanston, IL, June 24–26, 1991
edited by C.H. Bartholomew and J.B. Butt
- Volume 69 **Zeolite Chemistry and Catalysis.** Proceedings of an International Symposium, Prague, Czechoslovakia, September 8–13, 1991
edited by P.A. Jacobs, N.I. Jaeger, L. Kubelková and B. Wichterlová

- Volume 70 **Poisoning and Promotion in Catalysis based on Surface Science Concepts and Experiments**
by M. Kiskinova
- Volume 71 **Catalysis and Automotive Pollution Control II.** Proceedings of the 2nd International Symposium (CAPoC 2), Brussels, Belgium, September 10–13, 1990
edited by A. Crucq
- Volume 72 **New Developments in Selective Oxidation by Heterogeneous Catalysis.**
Proceedings of the 3rd European Workshop Meeting on New Developments in Selective Oxidation by Heterogeneous Catalysis, Louvain-la-Neuve, Belgium, April 8–10, 1991
edited by P. Ruiz and B. Delmon
- Volume 73 **Progress in Catalysis.** Proceedings of the 12th Canadian Symposium on Catalysis, Banff, Alberta, Canada, May 25–28, 1992
edited by K.J. Smith and E.C. Sanford
- Volume 74 **Angle-Resolved Photoemission. Theory and Current Applications**
edited by S.D. Kevan
- Volume 75 **New Frontiers in Catalysis, Parts A-C.** Proceedings of the 10th International Congress on Catalysis, Budapest, Hungary, 19–24 July, 1992
edited by L. Guczi, F. Solymosi and P. Tétényi
- Volume 76 **Fluid Catalytic Cracking: Science and Technology**
edited by J.S. Magee and M.M. Mitchell, Jr.
- Volume 77 **New Aspects of Spillover Effect in Catalysis. For Development of Highly Active Catalysts.** Proceedings of the Third International Conference on Spillover, Kyoto, Japan, August 17–20, 1993
edited by T. Inui, K. Fujimoto, T. Uchijima and M. Masai
- Volume 78 **Heterogeneous Catalysis and Fine Chemicals III,**
Proceedings of the 3rd International Symposium, Poitiers, April 5 - 8, 1993
edited by M. Guisnet, J. Barbier, J. Barrault, C. Bouchoule, D. Duprez, G. Pérot and C. Montassier
- Volume 79 **Catalysis: An Integrated Approach to Homogeneous, Heterogeneous and Industrial Catalysis**
edited by J.A. Moulijn, P.W.N.M. van Leeuwen and R.A. van Santen